

**APPLICATION OF A STATE VARIABLE  
DESCRIPTION OF INELASTIC DEFORMATION  
TO GEOLOGICAL MATERIALS**

A thesis submitted for the degree  
of Doctor of Philosophy (University of London)  
and for the Diploma of University College

by

Stephen John Covey-Crump

Department of Geological Sciences,  
University College London,  
Gower Street, London, WC1E 6BT

ProQuest Number: 10630768

All rights reserved

INFORMATION TO ALL USERS

The quality of this reproduction is dependent upon the quality of the copy submitted.

In the unlikely event that the author did not send a complete manuscript and there are missing pages, these will be noted. Also, if material had to be removed, a note will indicate the deletion.



ProQuest 10630768

Published by ProQuest LLC (2017). Copyright of the Dissertation is held by the Author.

All rights reserved.

This work is protected against unauthorized copying under Title 17, United States Code  
Microform Edition © ProQuest LLC.

ProQuest LLC.  
789 East Eisenhower Parkway  
P.O. Box 1346  
Ann Arbor, MI 48106 – 1346

## ABSTRACT

The work reported in this thesis is an investigation of the potential for employing non-steady-state constitutive relations to describe the inelastic deformation properties of rock forming minerals.

Attempts to determine generally applicable constitutive equations for inelastic deformation are complicated by the severe path dependence of the deformation response and by the wide range of mechanisms by which that deformation is accomplished. In the geological literature it has been normal practice to circumvent these problems by approximating the deformation as occurring at steady-state. This presents difficulties for the description of deformation by inherently transient mechanisms, for the description of small strain deformation, and for the reliability of extrapolating laboratory mechanical properties to geological deformation conditions. In contrast, in the materials science literature several systems of inelastic constitutive equations which do not make the steady-state approximation have been proposed. One of the oldest and most widely applied of these *i.e.* that due to Hart and coworkers, was chosen for investigation here to determine its potential for geological applications.

To be successful any deformation constitutive equation must satisfy three criteria. Firstly it must provide an adequate description of the material behaviour, secondly it must be analytically / numerically integrable for deformation modelling purposes, and thirdly it must contain material parameters which can be evaluated from the results of deformation experiments. In the first half of this thesis the descriptive capacity and integrability of Hart's equations are investigated by attempting to provide a comprehensive description of inelastic deformation from the perspective offered by Hart's analysis. Hart bracketed from consideration several aspects of inelastic deformation which are of considerable geological importance *i.e.* in particular the influence of nominally deformation independent recovery processes (active at high temperatures), of solute impurities, of finely dispersed inclusions and of grain-size. Procedures for identifying the effect of these factors on the results of deformation experiments, and possible strategies for extending the analysis to accommodate them are outlined.

The second half of the thesis describes an experimental programme designed to apply Hart's description to the inelastic deformation of Carrara marble at 200 MPa confining pressure in the temperature range 120 to 700°C. The primary aim of the experimental programme was to determine whether the material parameters in Hart's description can be determined with sufficient accuracy at elevated confining pressures (given the technical limitations on the quality of the data obtained from such tests) for the approach to be of interest for the characterization of geological materials. From the results of several hundred experiments it is found that those material parameters can be evaluated sufficiently accurately. Furthermore, the proposed strategy for extending Hart's analysis to high temperatures is shown to have considerable potential. In so doing the first description of the inelastic deformation properties of calcite at temperatures below 400°C is presented, and an experimental programme is outlined which can be applied to materials of even greater geological significance.

## ACKNOWLEDGEMENTS

The work reported in this thesis and presently ongoing, has had a long gestation period. The aim has always been to work towards a description of inelastic deformation which is above all comprehensive, but yet which is also practical in the sense that the material parameters in it can be readily evaluated through experiments conducted at high confining pressures.

The fact that it has been possible to work towards such a general goal, is to a great measure due to the outstanding nature of the courses that I have been able to take in my university career. Of particular importance has been the advanced igneous / metamorphic and structural geology third year option in my undergraduate degree at Imperial College, London. It was the awesome content of this course combined with the possibility of doing varied projects all of sufficient length to allow some quality thinking time, which has proved so valuable. My thanks extend to all involved but particularly to Ernie Rutter, Kate Brodie, Paul Suddaby, Bob Thompson and Jack Nolan. A further two years at Harvard University under the auspices of Rick O'Connell, provided the mathematical literacy and a certain rigour of thinking without which much of the work presented here would never have been imagined.

The experimental work reported here has been carried out in the Rock Deformation Laboratory which was at Imperial College, London but which moved to Manchester University in July 1989. The work has involved considerable attention to experimental detail and much of this has been made possible by the lab experimental officer, Rob Holloway. It is not just his intimate knowledge of the apparatus that has been important, but also the extremely high quality of his work, for it is this more than anything which has raised the quality of the mechanical data obtained beyond even my most optimistic expectations and allowed me to draw the conclusions that I have. This combined with the fertile source of experimental and interpretative possibilities provided by Ernie Rutter has made the experimental work at times positively exciting.

Thanks are also due to my contemporary John Bloomfield. The excellence of his own experimental results on the two-phase flow problem, has been matched only by his generosity in involving me in their interpretation. The paper that we have written together has served as an inspiration for the long task of writing up the PhD.

Above all I thank my supervisors Ernie Rutter and Stan Murrell. I acknowledge with a great deal of gratitude their patience and faith in allowing me to pursue my own enquiries for what must have seemed interminable lengths of time. In particular this must have involved considerable sacrifice to Ernie as I worked on material which was only indirectly relevant to my role as his research assistant on his project on the deformation properties of ultra-fine grained materials. Without this freedom, this PhD would certainly never have been completed.

## CONTENTS

<b>Abstract</b>	<b>2</b>
<b>Acknowledgements</b>	<b>3</b>
<b>Contents</b>	<b>4</b>
<b>1. Introduction</b>	<b>11</b>
1.1 The nature of the task	11
1.1.1 Inelastic constitutive equations employed for geological materials	12
1.1.2 Inelastic constitutive equations employed in the materials' sciences	13
1.2 Scope of the present study	14
<b>PART I : THE THEORETICAL FRAMEWORK</b>	
<b>2. Theoretical framework for Hart's analysis of inelastic deformation</b>	<b>16</b>
2.1 Definitions and assumptions in the initial analysis	16
2.2 Derivation of the existence conditions : the isothermal case	17
2.3 Derivation of the existence conditions : the non-isothermal case	18
2.4 Definition of a mechanical state variable	19
2.5 Comparison of Hart's theoretical analysis with Carathéodory's treatment of the first and second laws of thermodynamics	19
<b>3. Experimental verification of the existence conditions for a state variable description of inelastic deformation</b>	<b>22</b>
3.1 Verifying that $\gamma$ and $\nu$ are unique functions of $\sigma$ and $\alpha$	22
3.1.1 Verifying that $\gamma$ is a unique function of $\sigma$ and $\alpha$	22
3.1.2 Verifying that $\nu$ is a unique function of $\sigma$ and $\alpha$	23
3.1.3 The approach of MacEwen	23
3.2 Verifying that curves of constant $\sigma^*$ are unique and form a one parameter family	24
3.2.1 The observed form of constant $\sigma^*$ curves	24
3.2.2 Verifying that constant $\sigma^*$ curves form a one parameter family	25
3.2.3 Verifying that constant $\sigma^*$ curves are unique	25
3.3 The effect of temperature	28
<b>4. Derivation of the constitutive relations</b>	<b>29</b>
4.1 Derivation of the equation of state	29
4.1.1 Constraints on the form of the plastic equation of state	29
4.1.2 Special forms adopted for the equation of state	32
4.2 Derivation of the mechanical state evolution equation	35
4.2.1 General form of the integrating factor	35
4.2.2 Special forms of the integrating factor	35
<b>5. A general model for inelastic deformation</b>	<b>40</b>
5.1 Description of the general model	40
5.1.1 General descriptions of anelastic and of plastic deformation	40
5.1.2 Presentation of the model	43
5.1.3 Deformation of the model	44
5.2 Extension of Hart's model to the deformation of anisotropic materials in the presence of multiaxial differential stresses and/or large strains	48

5.2.1 Multiaxial formulation	48
5.2.2 Finite strain formulation	49
5.2.3 Incorporation of anisotropy	51
5.3 Micromechanical interpretation of the deformation model	52
5.3.1 A qualitative outline of the micromechanical interpretation	52
5.3.2 Quantification of the micromechanical interpretation	54
<b>6. Refinements and extensions of the general model for inelastic deformation</b>	<b>59</b>
6.1 Deformation occurring near to plastic yielding	59
6.1.1 Basis for the refined inelastic deformation model	59
6.1.2 Outline of the refined Hart model	62
6.1.3 The deformation behaviour of the refined model	64
6.1.4 Further observations	72
6.2 Parameterization of $\mathcal{M}$ , $\dot{\alpha}^*$ and $M$	73
6.2.1 Parameterization of the anelastic modulus	73
6.2.2 Parameterization of $\dot{\alpha}^*$ and $M$ for $\sigma^*$ and $T$	74
6.3 The accommodation of other material characteristics / deformation variables	76
6.3.1 Solute impurities	77
6.3.2 Finely dispersed inclusions	83
6.3.3 Grain-size	87
6.3.4 'Unusual' deformation variables	89
6.4 Deformation occurring at $T > 0.45 T_m$ . (a) Recovery	90
6.4.1 Recovery processes	90
6.4.2 The effect of recovery processes on mechanical behaviour	94
6.4.3 Incorporation of recovery into Hart's analysis	95
6.5 Deformation occurring at $T > 0.45 T_m$ . (b) Grain boundary sliding	100
6.5.1 Hart's deformation model extended to include grain boundary sliding	100
6.5.2 Experimental results	102
6.5.3 A simplification of the GB - element	106
6.6 Inhomogeneous deformation	106
6.6.1 Deformation of polyphase materials	106
6.6.2 The growth of deformation instabilities	108
<b>7. Numerical modelling with the state variable analysis</b>	<b>110</b>
7.1 Simulation of deformation experiments	110
7.1.1 Formulation of the problem	110
7.1.2 Solution strategy	110
7.1.3 Results of such simulations	114
7.1.4 Multiaxial deformation experiments	114
7.2 Solution of boundary value problems	116
7.2.1 Infinitesimal strain problems	116
7.2.2 Finite strain problems	120
7.3 Limitations of the modelling scheme	126
<b>PART II : THE EXPERIMENTAL INVESTIGATION</b>	
<b>8. An outline of the experimental programme</b>	<b>129</b>
8.1 The experimental task	129
8.2 The deformation apparatus employed	131
8.2.1 Basic design	131
8.2.2 HEARD1	131
8.2.3 NIMONIC2	133
8.3 Experimental procedures	138
8.3.1 The starting material	138
8.3.2 The deformation experiments	141

8.4 Data reduction	143
8.4.1 The data reduction equations	144
8.4.2 The data reduction procedures employed	145
<b>9. An evaluation of the factors limiting data quality</b>	<b>148</b>
9.1 Calibration and data measurement errors	148
9.1.1 HEARD1	148
9.1.2 NIMONIC2	153
9.1.3 Summary of the data measurement problems	158
9.2 Problems caused by instantaneous changes in the deformation variables	159
9.2.1 The load relaxation test	159
9.2.2 The interrupted constant displacement-rate tests	161
9.3 Problems caused by the copper jacket	162
9.3.1 Formulation of the problem	162
9.3.2 Special case solutions	164
9.3.3 The errors arising from neglecting a jacket correction	164
9.4 Assumptions about material behaviour	168
9.4.1 Cataclasis	168
9.4.2 Mechanical twinning	171
9.4.3 The effect of impurities	171
9.5 Assumptions made for the convenience of data processing	172
9.5.1 Assumptions used in data reduction	172
9.5.2 Assumptions used for parameter fitting	172
9.6 Summary	174
<b>10. Equation of state I. The anelastic element</b>	<b>175</b>
10.1 Fitting the anelastic modulus	175
10.1.1 The Young's modulus of calcite	175
10.1.2 Determining the elastic and anelastic limits	176
10.2 Results	176
10.2.1 Parameter evaluation	176
10.2.2 The observed values of the anelastic modulus	177
10.2.3 Uncertainties in the values of the anelastic modulus	177
10.2.4 Final statement of the equation of state	178
10.3 Discussion	178
<b>11. Equation of state II. The friction element</b>	<b>183</b>
11.1 Fitting the parameters	183
11.1.1 Determining $M$	183
11.1.2 Determining $\dot{\alpha}^*$	183
11.2 Results	183
11.2.1 Parameter evaluation	184
11.2.2 The observed values of the material parameters	184
11.2.3 Uncertainties in the values of the material parameters	184
11.2.4 Final statement of the equation of state	185
11.3 Discussion	185
<b>12. Equation of state II. The plastic element</b>	<b>197</b>
12.1 Fitting the parameters	197
12.1.1 Determining $\lambda$	197
12.1.2 Determining $\sigma^*$ and $\dot{\epsilon}^*$	197
12.1.3 Determining $m, f_0$ and $H$	197
12.2 Results	198
12.2.1 Parameter evaluation	198

12.2.2 The observed values of the material parameters	198
12.2.3 Uncertainties in the values of the material parameters	199
12.2.4 Final statement of the equation of state	200
12.3 Discussion	200
<b>13. Evolution equation I. <math>T &lt; 0.45 T_m</math></b>	<b>216</b>
13.1 Fitting the parameters	216
13.1.1 Determining $\sigma^*$	216
13.1.2 Determining $\Lambda$	216
13.1.3 Determining $\Gamma^*$ and $\alpha^*$	217
13.1.4 Determining $\zeta$ , $\eta$ and $\sigma_0^*$	217
13.1.5 Determining $m^*$ , $f_0^*$ and $H^*$	217
13.2 Results	217
13.2.1 Parameter evaluation	217
13.2.2 The observed values of the material parameters	219
13.2.3 Uncertainties in the values of the material parameters	219
13.2.4 Final statement of the evolution equation	220
13.3 Discussion	220
<b>14. Evolution equation II. Static recovery</b>	<b>241</b>
14.1 Evaluating the recovery function	241
14.1.1 Obtaining an estimate of recovery	242
14.1.2 Correlating the recovery estimate with changes of $\sigma^*$	243
14.2 Results I. The recovery estimates	243
14.2.1 Procedures employed	244
14.2.2 The observed values of the recovery estimates	244
14.2.3 Errors in the estimates	245
14.3 Results II. Changes in mechanical state	245
14.3.1 Procedures employed	245
14.3.2 The observed changes in mechanical state	246
14.3.3 Errors in the post-annealing values of $\sigma^*$	246
14.4 Discussion	246
<b>15. Summary and comparison with steady-state flow laws</b>	<b>257</b>
15.1 Summary of the work	257
15.2 Comparison with steady-state flow laws	258
15.2.1 The steady-state approximation	258
15.2.2 Previously published flow laws for Carrara marble	262
15.3 The scope for further work	265
<b>References</b>	<b>266</b>
<b>APPENDICES</b>	
<b>A1. Derivations associated with the constitutive relations</b>	<b>275</b>
A1.1 Theory of Pfaffian forms	275
A1.1.1 Pfaffian forms in two variables	275
A1.1.2 Pfaffian forms in more than two variables	276
A1.1.3 Carathéodory's theorem	276
A1.2 Derivations of the constitutive equations	277
A1.2.1 Constraints on the constitutive relations	277
A1.2.2 The equation of state for the plastic element	278
A1.2.3 The equation of state for the friction element	279

A1.2.4 Derivation of equation 4.54	281
A1.3 Derivation of the form of anelastic load relaxation curves	281
A1.4 Derivation of the viscoplastic limit equations	282
A1.4.1 The uniaxial case	282
A1.4.2 The multiaxial case	282
A1.5 Reduction of the number of variables in Hart's equations	283
A1.5.1 Reducing the number of stress and strain-rate variables	283
A1.5.2 Reducing the number of equations	283
<b>A2. Derivations associated with the data reduction equations</b>	<b>285</b>
A2.1 Derivation of the data reduction equations	285
A2.1.1 Derivation of equations 8.5 and 8.7	285
A2.1.2 Derivation of equation 8.6	285
A2.1.3 Derivation of equation 8.20	285
A2.2 Experimental loading histories cast as stress-rates	286
A2.2.1 Constant load creep test	286
A2.2.2 Constant displacement-rate test	286
A2.2.3 Load relaxation test	287
<b>A3. Derivations associated with material parameter fitting</b>	<b>288</b>
A3.1 The fitting procedures employed in this study	288
A3.1.1 Derivation of equation 11.5	288
A3.1.2 Derivation of equation 12.3	288
A3.1.3 Determining $\sigma^*$ from the equations of state	289
A3.1.4 Derivation of equation 13.6	289
A3.1.5 Derivation of equation 13.12	290
A3.2 Alternative fitting procedures	290

## TABLES

10.1 The data used to fit the anelastic element	179
11.1 The data used to fit the friction element	187
12.1 The data used to fit the plastic element	201
13.1 The stresses supported at $\epsilon^{(t)} = 0.10$ in the constant displacement-rate experiments	222
14.1 The results of the interrupted constant displacement-rate experiments	248

## FIGURES

3.1	The deformation history independence of $\gamma$	23
3.2	The experimentally observed form of constant $\sigma^*$ curves	26
4.1	Some functions which satisfy the observed scaling property of the constant $\sigma^*$ curves	31
4.2	The $\Gamma$ function at low ( $T < 0.3 T_m$ ) homologous temperatures	36
4.3	The $\Gamma$ function at high ( $0.3 < T/T_m < 0.45$ ) homologous temperatures	37
4.4	The $\Gamma$ function at all ( $T < 0.45 T_m$ ) temperatures	38
5.1	An analogue representation of an anelastic element	41
5.2	The form of constant $\sigma^*$ curves over many orders of magnitude of strain-rate	42
5.3	An analogue representation of Hart's original deformation model	43
5.4	The response of Hart's model to the loading histories applied in deformation experiments	45
5.5	The strain-rate dependence of the elements in Hart's original model	47
5.6	The comparison of Hart's model with experimental anelastic deformation results	48
5.7	Hart's micromechanical interpretation of his deformation model	56
6.1	Comparison of real material behaviour near to the plastic yield point with that predicted by Hart's model	60
6.2	Demarcation of deformation regimes below the macroplastic limit	61
6.3	The refined Hart model for the improved description of near yield behaviour	63
6.4	The response of the refined Hart model in constant inelastic strain-rate deformation	65
6.5	The use of tension / compression loops to determine some of the parameters in the refined Hart model	67
6.6	Load relaxations conducted in the microplastic region	68
6.7	The response of the refined Hart model in stress dip experiments	70
6.8	The improved description of reload relaxation curves using the refined Hart model	72
6.9	Correlation of $\sigma^*$ with the spacing of subgrain boundaries	73
6.10	The change in scaling slope of constant $\sigma^*$ curves through three stage work hardening	75
6.11	The variation of the parameter $M$ with temperature	76
6.12	The effect of solute impurity concentration on load relaxation curves	79
6.13	The effect of solute impurity segregation during load relaxation on the results of multiple relaxation experiments conducted at low homologous temperatures	81
6.14	The effect of solute impurity segregation during load relaxation on the results of multiple relaxation experiments conducted at high homologous temperatures	84
6.15	The circumvention of finely dispersed inclusions by dislocations	85
6.16	The effect of finely dispersed inclusions on the results of multiple relaxation experiments	87
6.17	The effect of irradiation on constant $\sigma^*$ curves	91
6.18	Mechanisms of forming recrystallization nuclei	93
6.19	The mechanical consequences of recrystallization during constant strain-rate deformation	95
6.20	Fractional recovery curves generated from interrupted constant displacement-rate tests	96
6.21	Appropriate forms of the recovery function	98
6.22	Extension of Hart's original model to accommodate grain boundary sliding	101
6.23	Experimental observations of grain boundary anelasticity	103
6.24	Experimental observations of permanent grain boundary sliding	104
7.1	A summary of the inelastic equations for Hart's original model	111
7.2	The solution strategy for the simulation of uniaxial deformation experiments	112
7.3	The results of numerical simulations of uniaxial deformation experiments	115
7.4	The solution strategy for boundary value problems in infinitesimal strain	118
7.5	Numerical modelling results of boundary value problems using Hart's equations	121
7.6	The solution strategy for boundary value problems in finite strain	124
8.1	The effect of changing $\sigma^*$ and $T$ on the $\log \sigma / \log \dot{\epsilon}^{(n)}$ behaviour of Hart's original model	130
8.2	The HEARD1 deformation apparatus	132
8.3	The NIMONIC2 deformation apparatus	134
8.4	The upper closure assembly of NIMONIC2	135
8.5	The lower closure assembly of NIMONIC2	136
8.6	Comparison of the force gauge assemblies of HEARD1 and NIMONIC2	137
8.7	Photomicrographs of the Carrara marble starting material	140
8.8	An analogue model of the deformation of the apparatus axial column during a	

deformation experiment	144
8.9 Typical load / time data obtained during a load relaxation experiment	147
9.1 The effect of HEARD1 force gauge calibration errors	151
9.2 The effect of HEARD1 apparatus stiffness and displacement-rate calibration errors	153
9.3 The NIMONIC2 upper closure assembly used for the force gauge calibration	155
9.4 The effect of NIMONIC2 force gauge calibration errors	156
9.5 The effect of NIMONIC2 apparatus stiffness and displacement-rate calibration errors	157
9.6 Comparison of stress / strain curves generated on HEARD1 and NIMONIC2	158
9.7 The effect of load re-equilibration during relaxation experiments	160
9.8 A typical thermal history during an interrupted constant displacement-rate experiment	161
9.9 Correcting for the load supported by the copper jacket	163
9.10 Commercial purity copper stress / strain curves	166
9.11 The copper jacket calibration equations	167
9.12 The effect of neglecting the copper jacket calibration on the results of constant displacement-rate experiments	169
9.13 The effect of neglecting the copper jacket calibration on the results of load relaxation experiments	170
9.14 Inhomogeneities in the strain distribution through specimens deformed in compression	173
10.1 The composite stress / strain curves generated in the experiments used to determine the anelastic modulus	180
10.2 Detail of a loading curve in the anelastic experiments	181
10.3 Variation of the anelastic modulus with $\sigma^*$ and $T$	182
10.4 The sensitive of the stress / strain curve to the value of the anelastic modulus	182
11.1 Results of the multiple relaxation experiments conducted on Carrara marble at $T < 250^\circ\text{C}$	188
11.2 The master $\sigma^*$ curves from the multiple relaxation experiments conducted at $T < 250^\circ\text{C}$	192
11.3 The variation of the parameters $M$ and $\dot{\alpha}^*$ with $\sigma^*$ and $T$	193
11.4 Example plots from the relaxation data fitting exercise at $T < 250^\circ\text{C}$	194
11.5 The effect of errors in the parameter fitting exercise at $T < 250^\circ\text{C}$	195
12.1 Results of the multiple relaxation experiments conducted on Carrara marble at $T > 250^\circ\text{C}$	203
12.2 The master $\sigma^*$ curves from the multiple relaxation experiments conducted at $T > 250^\circ\text{C}$	211
12.3 The variation of the parameters $\lambda$ and $\dot{\varepsilon}^*$ with $\sigma^*$ and $T$	212
12.4 Example plots from the relaxation data fitting exercise at $T > 250^\circ\text{C}$	213
12.5 The effect of errors in the parameter fitting exercise at $T > 250^\circ\text{C}$	214
13.1 Carrara marble stress / strain curves plotted as a function of temperature at constant strain-rate	223
13.2 Carrara marble stress / strain curves plotted as a function of strain-rate at constant temperature	226
13.3 Carrara marble $\ln \sigma^* / \varepsilon^{(n)}$ curves plotted as a function of strain-rate at constant temperature	230
13.4 $\log \Gamma^* / \log \dot{\varepsilon}^{(n)}$ curves plotted as a function of $\sigma^*$ at constant temperature	234
13.5 The variation of $\Gamma^*$ with $\sigma^*$	238
13.6 The variation of $\dot{\alpha}^*$ with $\Gamma^*$ and $T$	239
13.7 Example plots from the $\sigma^*$ evolution equation fitting exercise	240
14.1 Methods of estimating recovery from the results of the interrupted constant displacement-rate experiment	242
14.2 Stress, area and strain based fractional recovery curves for Carrara marble	249
14.3 Comparisons of the stress, area and strain based recovery estimates	252
14.4 The smoothed fractional recovery curves for Carrara marble	254
14.5 $\ln \sigma^*$ / anneal duration curves for Carrara marble	255
14.6 $\sigma^* / \log$ anneal duration curves for Carrara marble	256
15.1 The question of steady-state deformation or creep-rate minima	260
15.2 Comparison of the stresses supported by Carrara marble at $\varepsilon^{(t)} = 0.10$ in experiments conducted by Rutter (1974) and in this study	264

## 1 INTRODUCTION

The characterization of the inelastic deformation properties of rock forming minerals is severely compromised by the need to determine those properties at high confining pressure in order to avoid the effects of cataclasis. The technical problems associated with deformation experiments conducted at high confining pressure constrain both the type of experiment that can be employed and the quality of the data that can be obtained, and these in turn restrict the type of description of inelastic deformation properties that can be used. Recent improvements in apparatus design and in data acquisition facilities however, offer the prospect that many of the experimental techniques employed to characterize the properties of engineering materials at room pressure, may now be viable at higher pressures. Consequently, descriptions of the inelastic deformation behaviour of geological materials which are far superior to those hitherto used may now be possible. The research reported in this thesis is an exploration of this possibility.

### 1.1 The nature of the task

To characterize the inelastic deformation properties of a material it is necessary to determine an appropriate constitutive relation. Constitutive relations are equations that describe the material response to externally applied conditions at any point within an object. Those which describe the deformation response, when combined with equilibrium and compatibility equations, allow the behaviour of a solid body to any prescribed thermal / loading history to be predicted. For the description of deformation behaviour, there are three basic categories of physical process of interest :

- (i) the stretching of interatomic bonds *i.e.* elastic deformation ;
- (ii) the switching of interatomic bonds among the various 'atoms' of the solid *i.e.* inelastic deformation, and ;
- (iii) the permanent breakage of bonds *i.e.* fracture.

The constitutive relations for elastic deformation are well understood, and are easily included in deformation models because the elastic strain experienced by a body is a good description of its elastic state. In contrast fracture is a highly complex phenomenon depending not only on the material behaviour at a point but also upon the stresses and strains across the body, and consequently few generally applicable constitutive relations to account for it have been devised (although the advances in fracture mechanics form a step in this direction). The constitutive relations for inelastic deformation form the focus of the present study.

Attempts to determine generally applicable constitutive relations for inelastic deformation are complicated by the severe path dependence of the deformation response and by the wide range of mechanisms by which that deformation is accomplished. These problems are manifest in the observation that unless the deformation path is known, the magnitude of the inelastic strain is not a reliable estimate of the mechanical state of a material *i.e.* equivalently, there exists no *mechanical* test which can determine the amount of inelastic strain a body has experienced. Consequently, any inelastic constitutive equation must incorporate not only the

external deformation state variables – temperature  $T$ , effective confining pressure  $p$ , differential stress  $\sigma$ , and inelastic strain rate  $\dot{\varepsilon}^{(n)}$  – but also some measure of the internal mechanical state  $\sigma^*$  (here defined as a variable with dimensions of stress) during deformation. This in turn requires that the constitutive relations be composed of two parts :

- (a) an equation of state :  $f(T, p, \sigma, \dot{\varepsilon}^{(n)}, \sigma^*) = 0$
- (b) a mechanical state evolution equation :  $g(T, p, \sigma, \dot{\varepsilon}^{(n)}, \sigma^*) = 0$

**1.1.1 Inelastic constitutive equations employed for geological materials.** In the geological literature it has been normal practice to circumvent the problems posed by the history dependence of inelastic deformation by approximating the deformation as occurring at steady state. The material is then viewed as deforming either at constant ‘structure’ (here used synonymously with mechanical state), or more frequently, in such a way that the structure always remains uniquely specified by the external deformation variables (*cf.* § 15.2.1). In the first case, the mechanical state of the deforming material is included within a constant material parameter, and the constitutive relation is formulated as the product of that parameter with various functions of the external deformation state variables. In the second case the mechanical state is implicitly included within some or all of the functions of the external deformation state variables. In each case the constitutive relation is an equation of state and there is no need to formulate an accompanying evolution equation.

Three equations have been widely employed to describe such steady-state inelastic deformation :

$$\dot{\varepsilon}^{(n)} = A \exp(B\sigma) \exp(-H_s/RT) \quad (1.1)$$

$$\dot{\varepsilon}^{(n)} = A \sigma^n \exp(-H_s/RT) \quad (1.2)$$

$$\dot{\varepsilon}^{(n)} = A [\sinh(B\sigma)]^n \exp(-H_s/RT) \quad (1.3)$$

where  $A$ ,  $B$ ,  $H_s$  and  $n$  are material parameters (which may have different values in the different equations) and  $R$  is the gas constant. Equation 1.1 is applied at low homologous temperatures / high strain-rates, equation 1.2 at high homologous temperatures / low strain-rates and equation 1.3 at all temperatures / strain-rates (for it reduces to the other equations under the appropriate conditions). For deformation modelling purposes, the deforming material is assumed to deform elastically at stresses below some critical yield stress and then according to equations 1.1 - 1.3 at the critical yield stress (*i.e.* it is assumed to behave as an elastic - ideally plastic body).

Several well documented problems arise from the use of equations 1.1 - 1.3 to describe the inelastic deformation of geological materials. When the equations are applied under circumstances when one deformation mechanism is controlling the bulk deformation behaviour, the functional form of the equations has some theoretical support. Consequently, the experimental strategy is to conduct deformation tests under conditions where only one mechanism is rate-controlling, and then to approximate the deformation of the material under general conditions as the sum of the constitutive relations of all the relevant mechanisms. However, this procedure ignores the ‘feedback’ relationships of the deformation mechanisms on each other. Furthermore, by requiring that the constitutive relation for each mechanism be evaluated under restricted deformation conditions, the problems that arise in the extrapolation of the constitutive relations from laboratory to natural strain-rates are exacerbated.

The steady-state approximation itself imposes significant constraints. Deformation

controlled by inherently transient mechanisms (*e.g.* deformation twinning, dislocation glide in the absence of thermally activated climb over obstacles) cannot be described satisfactorily. Indeed, both theoretical and experimental evidence suggests that steady-state deformation can never be achieved at homologous temperatures less than 0.45 (§ 15.2.1.1). Even given that steady-state *can* be achieved, equations 1.1 - 1.3 can only be applied under conditions where it actually *is* achieved, thereby posing problems for modelling relatively small strain deformations (*e.g.* such as might occur in lithospheric flexure). Peculiarly geological factors may serve to compound this effect. For example, the deformation of quartz is strongly influenced by the presence of  $H_2O$  but the diffusion of  $H_2O$  in quartz is so slow that there may be insufficient time to establish an equilibrium concentration in the lattice (and hence a steady-state deformation-rate) either prior to or within the duration of a deformation episode.

Although these problems appear to have qualitative importance, it remains unclear how significant they are for the interpretation of the results of geological deformation models. It may be that the assumptions employed in defining the modelling problem are of far greater importance than the errors introduced into the description of material behaviour by the steady-state approximation. This matter alone presents a case for evaluating alternative descriptions of the inelastic deformation properties of geological materials, for these can then be employed in the deformation models to determine their effect on the results.

**1.1.2 Inelastic constitutive relations employed in the materials' sciences.** The problem of incorporating deformation history dependence into the constitutive relations for inelastic deformation is one that has been of concern to materials' scientists, particularly with regard to engineering design problems. For such purposes, any constitutive equation must satisfy three criteria :

- (i) it must provide a sufficiently accurate description of the material behaviour ;
- (ii) it must contain material parameters that can be evaluated from the results of deformation experiments, and ;
- (iii) it must be of a form which is analytically and/or numerically integrable.

These criteria are mutually competitive. The accuracy of the description of material behaviour is improved by increasing the number of material parameters. However, the experimental task is simplified if the necessary experiments are few in number, short in duration and are technically easy to conduct, which in general requires that there be as few material parameters as possible. Integrability is generally favoured, particularly in terms of finding a numerical solution within the constraints posed by computer memory capacity, if the number of material parameters is small.

Several different systems of inelastic constitutive equations have been proposed, differing primarily in the relative emphasis they give to these three criteria (five of the most successful of these are reviewed and compared by their proponents in Miller, 1987). For the purposes of this study, that due to Hart and coworkers has been investigated. Of all the systems of equations, this has the longest pedigree, having been successfully applied to the room pressure inelastic deformation of metals, ceramics and simple ionic solids. It contains relatively few material parameters, each of which is relatively simple to evaluate experimentally, and yet extensive finite element and boundary element modelling with the equations shows that they are not only

highly competitive against the other systems of equations with respect to their computational efficiency, but that they predict deformation behaviour under highly complex thermal / loading histories remarkably accurately.

## 1.2 Scope of the present study

The work reported here is presented in two parts. In the first the descriptive capacity and integrability of Hart's equations is investigated from the perspective of potential geological applications. The former is considered by attempting to provide a comprehensive description of inelastic deformation within the context of Hart's analysis. This not only allows the system of equations proposed by Hart and coworkers to be outlined (*cf.* previous 'state of the art' reviews of Hart's analysis, describing successive developments : Hart, 1970, 1975 ; Hart *et al.*, 1975 ; Li *et al.*, 1976 ; Hart, 1976, 1978 ; Li, 1981 ; Korhonen *et al.*, 1987), but also permits an evaluation of the potential that exists for extending those equations to accommodate aspects of inelastic deformation which were bracketed from consideration by Hart but which are nevertheless of considerable geological importance. Integrability is addressed through a review of previous work on the deformation modelling capabilities of the equations.

The second part of this study is concerned with the problem of evaluating the material parameters in Hart's equations. An experimental programme designed to apply Hart's description to the inelastic deformation of Carrara marble at 200 MPa confining pressure and in the temperature range 120 to 700°C is described. The primary aim of this programme was to determine whether the material parameters in Hart's description can be determined with sufficient accuracy at elevated confining pressures, for the approach to be of interest for the characterization of the deformation properties of geological materials. A secondary aim was to determine the feasibility of some of the proposed strategies for extending the analysis to accommodate factors of geological significance not considered by Hart. The choice of Carrara marble reflects a compromise between the need to investigate a geologically significant material, and the need to consider a material which can be deformed, without cataclasis, at sufficiently low confining pressure for the technical limitations on the acquired mechanical data to be minimized. Hence, as for the choice of Hart's description from among the alternative descriptions of inelastic deformation, the choice of Carrara marble presents a best case option and provides an indication of whether or not it is worthwhile proceeding, given the presently available high pressure deformation apparatus, with the attempt to find better descriptions of inelastic properties than those presented by the steady-state approximation.

**PART I****THE THEORETICAL INVESTIGATION**

## 2 THEORETICAL FRAMEWORK FOR HART'S ANALYSIS OF INELASTIC DEFORMATION

The approach adopted by Hart in his description of inelastic deformation is methodologically similar to that used to formulate the state variable descriptions of classical thermodynamics. He begins by deriving experimentally verifiable conditions which must be satisfied if a state variable description of inelastic deformation is to exist, and then shows how, in the case where those conditions are satisfied, a variable describing the mechanical state of the deforming material can be defined. This step of the analysis is formally equivalent to Carathéodory's treatment of the first and second laws of thermodynamics, and rests like that treatment, on a purely phenomenological account of the observed material behaviour (*i.e.* no interest is taken in the mechanisms / processes by which the observed behaviour is accomplished except insofar as they affect the assumptions applied). Following verification that the state variable description existence conditions are satisfied, the functional forms of the constitutive relations are, as for their thermodynamic counterparts (*e.g.* the ideal gas law) determined empirically. Only when armed with these constitutive relations, are general models for inelastic deformation proposed and micromechanical interpretations sought to account for the results.

The first part of this account of Hart's description of inelastic deformation follows this methodological structure. The initial analysis described in § 2, the verification of the existence conditions in § 3, the determination of the constitutive relations in § 4 and the derivation of the general model of inelastic deformation in § 5. A discussion of the limitations of the description is deferred until § 6, where several developments of the inelastic deformation model aimed at accommodating these limitations are described.

### 2.1 Definitions and assumptions in the initial analysis

The derivation of the conditions which must be satisfied if a state variable description of inelastic deformation is to exist and the concomitant definition of the mechanical state variable, were first outlined by Hart (1970). He resolved the accumulated total strain  $\varepsilon^{(t)}$  at any given time in a deforming body, into three components : a time independent (excepting inertial effects) elastic strain  $\varepsilon^{(e)}$ , a time dependent recoverable (on release of the differential load) anelastic strain  $a$ , and a time dependent non-recoverable plastic strain  $\alpha$

$$\varepsilon^{(t)} = \varepsilon^{(e)} + \varepsilon^{(n)} = \varepsilon^{(e)} + a + \alpha \quad (2.1)$$

where  $\varepsilon^{(n)}$  is the time dependent part of  $\varepsilon^{(t)}$ . Noting that  $\varepsilon^{(e)}$  and  $a$  are good deformation state variables of the material, Hart restricted his initial discussion to  $\alpha$ . He further noted that in general,  $\varepsilon^{(n)}$  is composed of a grain matrix component and a grain boundary sliding component, and then restricted the analysis to conditions where the grain boundary sliding component is negligible. The analysis was also restricted to the stable, homogeneous deformation of an isotropic material under a uniaxially applied stress, in the absence of static recovery processes. These restrictions effectively limit the initial analysis to plastic deformation at homologous temperatures of less than 0.45. However, all of the restrictions have, to a greater or lesser

extent, been removed in subsequent developments (§ 5 and § 6).

## 2.2 Derivation of the existence conditions : the isothermal case

During any isothermal deformation history given the aforementioned restrictions, the variation of the applied differential stress  $\sigma$  and the material plastic strain-rate  $\dot{\alpha}$ , with the plastic strain  $\alpha$  in some increment of time, can be described by

$$d \ln \sigma = \gamma d\alpha + \nu d \ln \dot{\alpha} \quad (2.2)$$

where  $\gamma$  and  $\nu$  are measurable phenomenological parameters that are in general, dependent upon the prior deformation history, but which at any time are given by

$$\gamma = (\partial \ln \sigma / \partial \alpha)_{\dot{\alpha}} : \nu = (\partial \ln \sigma / \partial \ln \dot{\alpha})_{\alpha} \quad (2.3)$$

Equation 2.2 simply describes the smooth variation of any of the deformation variables in terms of the others. The choice of  $\ln \sigma$  and  $\ln \dot{\alpha}$  as basic variables rather than  $\sigma$  and  $\dot{\alpha}$ , is for the simplicity of the results that follow.

With a view to the desired form of the ultimate relationship required, equation 2.2 is rewritten

$$d\alpha = A d \ln \sigma + B d \ln \dot{\alpha} \quad (2.4)$$

where

$$A = 1/\gamma : B = -\nu/\gamma \quad (2.5)$$

The conditions for the existence of a state variable description of plastic deformation are then the conditions under which equation 2.4 is an exact differential *i.e.* the conditions under which the equation possesses integral solutions which are independent of the path of integration. This is the case when  $A$  and  $B$  (and hence  $\gamma$  and  $\nu$ ) are unique functions only of  $\sigma$  and  $\dot{\alpha}$  *i.e.* when

$$A = A(\sigma, \dot{\alpha}) : B = B(\sigma, \dot{\alpha})$$

or equivalently

$$\gamma = \gamma(\sigma, \dot{\alpha}) : \nu = \nu(\sigma, \dot{\alpha}) \quad (2.6)$$

and when

$$(\partial A / \partial \ln \dot{\alpha})_{\sigma} = (\partial B / \partial \ln \sigma)_{\dot{\alpha}} \quad (2.7)$$

Equation 2.4 is then directly integrable to give a state relation of the form

$$\alpha = \alpha(\sigma, \dot{\alpha}) \quad (2.8)$$

However, this implies that  $\alpha$  is a good deformation state variable which, as observed above (§ 1.1), is not generally the case. Hence, some or all of the conditions given by equations 2.6 and 2.7 must be invalid during real plastic deformation.

Despite these observations a state variable description may still exist. Provided equations 2.6 hold, then equation 2.4 is a Pfaffian form in two independent variables (§ A1.1) and it thereby follows that there always exists an integrating factor, here of the form  $\Gamma(\sigma, \dot{\alpha})$ , such that

$$\Gamma d\alpha = A \Gamma d \ln \sigma + B \Gamma d \ln \dot{\alpha} \quad (2.9)$$

is an exact differential even if equation 2.7 is not satisfied (§ A1.1.1.2). Hence the necessary and sufficient conditions for the existence of a state variable description of isothermal plastic deformation are given by equations 2.6.

### 2.3 Derivation of the existence conditions : the non-isothermal case

The influence of temperature  $T$  when static recovery processes are unimportant, may be included by the addition of an appropriate term to equation 2.2

$$d \ln \sigma = \gamma d\alpha + \nu d \ln \dot{\alpha} + H d(1/RT) \quad (2.10)$$

where

$$H \equiv [\partial \ln \sigma / \partial (1/RT)]_{\alpha, \dot{\alpha}} \quad (2.11)$$

is a third phenomenological coefficient (the apparent activation enthalpy for plastic deformation) and  $R$  is the gas constant. Rearranging equation 2.10 to the form of equation 2.4, then

$$d\alpha = A d \ln \sigma + B d \ln \dot{\alpha} + C d(1/RT) \quad (2.12)$$

where

$$C \equiv -H/\gamma \quad (2.13)$$

This is an exact differential if

$$A = A(\sigma, \dot{\alpha}, T) : B = B(\sigma, \dot{\alpha}, T) : C = C(\sigma, \dot{\alpha}, T)$$

or equivalently, if

$$\gamma = \gamma(\sigma, \dot{\alpha}, T) : \nu = \nu(\sigma, \dot{\alpha}, T) : H = H(\sigma, \dot{\alpha}, T) \quad (2.14)$$

and if

$$\begin{aligned} (\partial A / \partial \ln \dot{\alpha})_{\sigma, T} &= (\partial B / \partial \ln \sigma)_{\dot{\alpha}, T} \\ [\partial A / \partial (1/RT)]_{\sigma, \dot{\alpha}} &= (\partial C / \partial \ln \sigma)_{\dot{\alpha}, T} \\ [\partial B / \partial (1/RT)]_{\sigma, \dot{\alpha}} &= (\partial C / \partial \ln \dot{\alpha})_{\sigma, T} \end{aligned} \quad (2.15)$$

Again, the fact that  $\alpha$  is not a good deformation state variable implies that some or all of equations 2.14 and 2.15 do not hold during real plastic deformation.

Provided equations 2.14 hold, equation 2.12 is a Pfaffian form in three independent variables. However, for more than two independent variables, the theory of Pfaffian forms, although admitting the possibility, does not guarantee the existence of an integrating factor through which equation 2.12 becomes exact (§ A1.1.2) *i.e.* the satisfaction of equations 2.14 is insufficient evidence for the existence of a state variable description of non-isothermal plastic deformation. If such an integrating factor exists, and Carathéodory's theorem (§ 2.5) suggests it might, then it must be found by some new axiom of a physical character. No such axiom has been presented.

In the absence of sufficient conditions for the existence of a state variable description of non-isothermal deformation, the influence of temperature must be included by some suitable parameterization of the isothermal incremental deformation equation. For example, by normalizing  $\sigma$  with the rigidity modulus  $G$  for the material at the given temperature, and by using the temperature compensated strain-rate of Zener and Hollomon (1944), equation 2.12 becomes

$$d\alpha = A d \ln (\sigma/G) + B [d \ln \dot{\alpha} - H d(1/RT)] \quad (2.16)$$

which is a Pfaffian form in two independent variables provided  $H$  is independent of  $\sigma$  and  $\dot{\alpha}$  and  $T$  is specified. Alternatively, the material parameters may have to be specified as a function of temperature. Since the choice of an appropriate parameterization scheme is not specified by theoretical arguments, it must be governed by empirical criteria.

## 2.4 Definition of a mechanical state variable

By writing from equation 2.9

$$d \ln \sigma^* = \Gamma d\alpha = A \Gamma d \ln \sigma + B \Gamma d \ln \dot{\alpha} \quad (2.17)$$

a one parameter family of curves

$$\sigma^* = \sigma^*(\sigma, \dot{\alpha}) \quad (2.18)$$

is defined. For each fixed value of  $\sigma^*$  the corresponding curve is a solution to the Pfaffian equation

$$d \ln \sigma^* = 0$$

or equivalently (cf. equation 2.17)

$$d\alpha = 0 \quad (2.19)$$

and it further follows that this solution is unique (§ A1.1.1.1).

Equation 2.19 indicates that  $\sigma^*$  is a measure of the instantaneous mechanical 'condition' of the deforming material. Being dependent only upon the external state variables  $\sigma$  and  $\dot{\alpha}$  and, being independent of the prior deformation history, it is therefore an internal state property of the material. Hart (1970) termed  $\sigma^*$  the hardness of the material. He observed that because an infinite number of possible integrating factors exist (§ A1.1.1.2), any scheme assigning it a numerical value is arbitrary.

In principle, if equation 2.12 has an integrating factor, then for non-isothermal deformation equation 2.18 becomes

$$\sigma^* = \sigma^*(\sigma, \dot{\alpha}, T) \quad (2.20a)$$

defining a one parameter family of surfaces in  $\sigma - \dot{\alpha} - T$  space. In practice however, as discussed above (§ 2.3), it has proved necessary to parameterize equation 2.4 to include the effect of temperature (cf. equation 2.16), so that equation 2.20a becomes

$$\sigma^* = \sigma^*(\sigma, \dot{\alpha}; T) \quad (2.20b)$$

## 2.5 Comparison of Hart's theoretical analysis with Carathéodory's treatment of the first and second laws of thermodynamics

Nabarro (1989) observed that Hart's analysis, as presented above, is formally equivalent to Carathéodory's (1909) treatment of the first and second laws of thermodynamics. To demonstrate this, Carathéodory's argument as presented by Sneddon (1957, pp. 39-42) is summarized here.

It is found empirically, that in an adiabatic process the mechanical work done  $W$  is a function of the thermodynamic variables  $(y_1, \dots, y_N)$  and  $(y_1^{(0)}, \dots, y_N^{(0)})$  defining the final and initial states respectively of the system, and that it is independent of the values of those variables  $(y_1^{(i)}, \dots, y_N^{(i)})$  at some intermediate state. Thus

$$\begin{aligned} W(y_1, \dots, y_N; y_1^{(0)}, \dots, y_N^{(0)}) \\ = W(y_1, \dots, y_N; y_1^{(i)}, \dots, y_N^{(i)}) + W(y_1^{(i)}, \dots, y_N^{(i)}; y_1^{(0)}, \dots, y_N^{(0)}) \end{aligned} \quad (2.21)$$

Hence there is a function

$$U = U(y_1, \dots, y_N) \quad (2.22)$$

called the internal energy of the system such that

$$W(y_1, \dots, y_N; y_1^{(0)}, \dots, y_N^{(0)}) = U(y_1, \dots, y_N) - U(y_1^{(0)}, \dots, y_N^{(0)}) \quad (2.23)$$

However, in a non-adiabatic process the equality given by equation 2.23 does not hold. In such

instances the difference between the change in internal energy  $\Delta U$  and the work done is defined to be the *quantity of heat*  $\Delta Q$  absorbed by the system during the process *i.e.*

$$\Delta Q = \Delta U - W \quad (2.24)$$

which is the first law of thermodynamics.

Now for a gas completely specified by its pressure  $p$  and volume  $V$ , equation 2.22 becomes

$$U = U(p, V) \quad (2.25)$$

If this gas expands by an infinitesimal amount  $dV$ , the work done is  $-pdV$  and the change in internal energy is  $dU$  so that

$$\Delta Q = dU - W = A dp + B dV \quad (2.26)$$

where

$$A \equiv (\partial U / \partial p)_V : B \equiv (\partial U / \partial V)_p + p \quad (2.27)$$

Then since  $A$  and  $B$  are functions only of  $p$  and  $V$  equation 2.26 is a Pfaffian form in two independent variables. Consequently, there always exists an integrating factor  $\Upsilon(p, V)$  and an internal state variable  $S(p, V)$  such that (*cf.* equation 2.17)

$$\Upsilon \Delta Q = dS \quad (2.28)$$

*i.e.* so that equation 2.26, with each of its terms multiplied by  $\Upsilon$  is an exact differential.

If the thermodynamic system is described by  $N$  variables  $y_1, \dots, y_N$  where  $N > 2$  then equation 2.26 is replaced by a Pfaffian form of the type

$$\Delta Q = \sum_{i=1}^N Y_i dy_i \quad (2.29)$$

in which the  $Y_i$  are functions of the  $y_i$ . In this case, on the basis of the theory of Pfaffian forms alone, functions  $\Upsilon$  and  $S$  (dependent on  $N$  variables) which make equation 2.29 exact, do not necessarily exist. To establish the existence of these functions a new axiom of a physical character is required and this axiom proves to be the second law of thermodynamics.

Carathéodory was able to demonstrate that *if a Pfaffian differential form  $\Delta Y = Y_1 dy_1 + Y_2 dy_2 + \dots + Y_N dy_N$  has the property that in every arbitrarily close neighbourhood of a given point  $x_0$  there exist points  $x$  which are inaccessible from  $x_0$  along curves for which  $\Delta Y = 0$ , the corresponding Pfaffian differential equation  $\Delta Y = 0$  is integrable* (Carathéodory's theorem – see § A1.1.3 for proof). Now the second law of thermodynamics is based on the empirical observation that certain changes in state are not physically realizable (*e.g.* heat cannot flow from a cold body to a hot one without external work being done). Carathéodory therefore, uses his theorem to state the second law of thermodynamics as *arbitrarily near to any prescribed initial state there exist states which cannot be reached from the initial state as a result of adiabatic processes*. Consequently, if the first law leads to an equation of the form of equation 2.29 the second law states that arbitrarily near to the point  $(y_1^{(0)}, \dots, y_N^{(0)})$  there exist points  $(y_1, \dots, y_N)$  which are inaccessible from the initial point along paths for which  $\Delta Q = 0$ . It follows immediately from Carathéodory's theorem that there exist functions  $\Upsilon(y_1, \dots, y_N)$  and  $S(y_1, \dots, y_N)$  where

$$\Upsilon \Delta Q = dS \quad (2.30)$$

The internal state function  $S$  is the entropy of the system and it can be shown that the integrating factor  $\Upsilon$  is, apart from a multiplicative constant, a function only of the empirical temperature of the system. Defining  $\Upsilon \equiv 1/T$  where  $T$  is the thermodynamic temperature,

equation 2.30 takes the familiar form

$$\Delta Q / T = dS \quad (2.31)$$

The similarity of this analysis with the state variable formulation of Hart is apparent if it is observed that  $\Upsilon$  and  $S$  are formally equivalent to Hart's integrating factor  $\Gamma$  and his mechanical state variable  $\sigma^*$  respectively, whilst  $\Delta Q$  compares with  $d\sigma$ . The origin of the Pfaffian form in the two analyses is different, Carathéodory taking his from the first law of thermodynamics and Hart his from the incremental deformation equation. However, Carathéodory's presentation of the second law of thermodynamics would seem also to apply to Hart's analysis *i.e.* arbitrarily near to any prescribed initial state ( $\sigma, \dot{\alpha}, T$  combination) there exist other states (other  $\sigma, \dot{\alpha}, T$  combinations) that cannot be reached from the initial state without a change in strain. If true, then with Carathéodory's theorem this statement indicates that an integrating factor for the Pfaffian form for non-isothermal deformation (equation 2.12) must exist. However, without explicit knowledge of the functional forms of equations 2.14, the functional form of this integrating factor cannot be determined, thereby precluding the derivation of a relation of the kind equation 2.31.

### 3 EXPERIMENTAL VERIFICATION OF THE EXISTENCE CONDITIONS FOR A STATE VARIABLE DESCRIPTION OF INELASTIC DEFORMATION

It follows from the theoretical analysis presented above that the necessary and sufficient condition for the existence of a state variable description of inelastic deformation, provided that the deformation is isothermal, is that the incremental deformation equation (equation 2.4) is a Pfaffian form. It remains then to verify, by experiment, that this condition is satisfied during real plastic deformation.

There are two approaches to this problem. The first is to demonstrate that equations 2.6 are satisfied during real deformation, since it is these which make the incremental deformation equation a Pfaffian form. This requires showing that  $\gamma$  and  $\nu$  are unique (*i.e.* deformation history independent) functions only of  $\sigma$  and  $\dot{\alpha}$ . The second approach is to demonstrate that there exists a deformation history independent solution to the incremental deformation equation when  $d\alpha = 0$ , for then it follows (*cf.* § 2.4) that that equation must be a Pfaffian equation (and therefore by definition, a Pfaffian form when  $d\alpha \neq 0$ ). This strategy requires verifying that  $\sigma(\dot{\alpha})$  curves generated at constant mechanical state are unique (*i.e.* again, that they are deformation history independent) and form a one parameter ( $\sigma^*$ ) family.

Both strategies have been utilized although it has been the second approach that has received the widest application, primarily because it also provides information for the derivation of the constitutive relations between the deformation state variables.

#### 3.1 Verifying that $\gamma$ and $\nu$ are unique functions of $\sigma$ and $\dot{\alpha}$

The unique dependence of  $\gamma$  and  $\nu$  on  $\sigma$  and  $\dot{\alpha}$  has been demonstrated for each parameter individually, and by showing that a composite function of  $\gamma$  and  $\nu$  is uniquely dependent on  $\sigma$  and  $\dot{\alpha}$ .

**3.1.1 Verifying that  $\gamma$  is a unique function of  $\sigma$  and  $\dot{\alpha}$ .** To demonstrate that  $\gamma$  is a unique function only of  $\sigma$  and  $\dot{\alpha}$  it is necessary to show that the slope of the  $\ln \sigma$  versus  $\alpha$  curve during constant  $\dot{\alpha}$ , isothermal deformation (*i.e.*  $\gamma$ , equation 2.3) is at any instant specified by the  $\sigma$  and  $\dot{\alpha}$  at that time irrespective of the value of  $\alpha$ . This has been demonstrated for Type 316 stainless steel, high purity niobium (both at 22°C) and 1100 aluminium alloy (22 and 200°C) by Wire *et al.* (1976), and for OFHC copper (22°C) by Korhonen *et al.* (1985b). In each case, the shape of the  $\ln \sigma / \epsilon^{(n)}$  curve obtained in constant displacement-rate experiments was compared with that obtained in tests where the displacement-rate was suddenly changed several times during the experiment. In making the comparison it was assumed that for  $\epsilon^{(n)} > 0.005$ ,  $\dot{\alpha} = \epsilon^{(n)}$  so that the anelastic contribution to the inelastic deformation could be neglected (see § 5.1.3 for a justification of this approximation). It was observed that the curves produced in the displacement-rate change experiments could be translated parallel to the  $\epsilon^{(n)}$  axis so that they superposed onto the curves produced at the corresponding displacement-rate in the uninterrupted tests (figure 3.1). Hence the slope of the curves was specified by the stress alone at given strain-rate, and not by the magnitude of the inelastic strain (which was different in the various experiments). Comparison of the results obtained at different displacement-rates

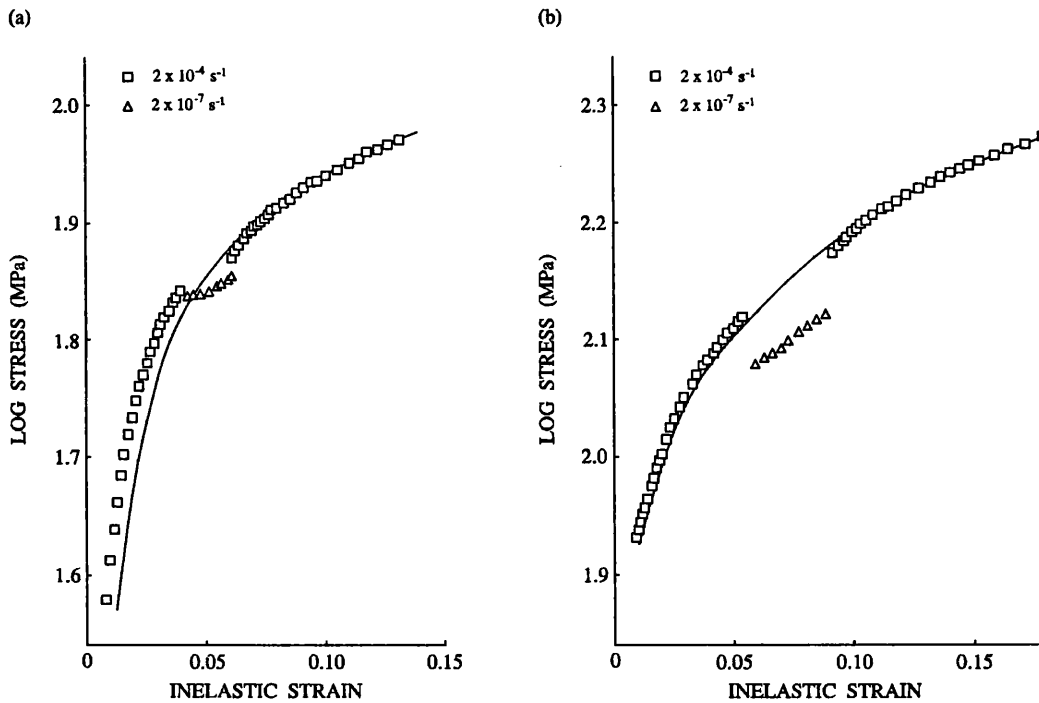


FIG. 3.1. Room temperature, displacement-rate change experiments showing the deformation history independence of  $\gamma = (\partial \ln \sigma / \partial \alpha)_\alpha$  in (a) 1100 aluminium alloy and (b) high purity niobium. In each case the points are for a specimen deformed at the indicated inelastic strain-rate, while the solid line is for a specimen deformed at a strain-rate of  $2 \times 10^{-4} \text{ s}^{-1}$ . The solid line has been translated parallel to the strain axis to show the strain-rate independence of  $\gamma$  (redrawn after Wire *et al.*, 1976).

confirmed the strain-rate dependence of  $\gamma$ .

**3.1.2 Verifying that  $\nu$  is a unique function of  $\sigma$  and  $\dot{\alpha}$ .** To demonstrate that  $\nu$  is a unique function only of  $\sigma$  and  $\dot{\alpha}$  it is necessary to show that the slope of the  $\ln \sigma$  versus  $\ln \dot{\alpha}$  curve obtained at given value of  $\alpha$  under isothermal conditions (*i.e.*  $\nu$ , equation 2.3) is specified only by  $\sigma$  and  $\dot{\alpha}$  irrespective of the magnitude of  $\alpha$ . Since such a curve is a curve at constant  $\sigma^*$  this exercise is equivalent to verifying that curves of constant  $\sigma^*$  are unique and form a one parameter family. As discussed below (§ 3.2), this has been confirmed for a wide variety of materials.

**3.1.3 The approach of MacEwen.** MacEwen (1982) began with an alternative formulation of the isothermal incremental deformation equation (equation 2.2)

$$d\alpha = (d\sigma/A) - (d\ln\dot{\alpha}/B) \quad (3.1)$$

where

$$A \equiv (\partial\sigma/\partial\alpha)_\sigma \quad ; \quad B \equiv -(\partial\ln\dot{\alpha}/\partial\alpha)_\sigma \quad (3.2)$$

The existence of a state variable description of plastic deformation is demonstrated if it is shown that  $A$  and  $B$  are unique functions of  $\sigma$  and  $\dot{\alpha}$ . Alternatively, it follows from equation 3.1 that

$$C \equiv (\partial\sigma/\partial\ln\dot{\alpha})_{\text{state}} = A/B \quad (3.3)$$

Hence the existence of the state variable description is demonstrated by showing that  $C$  is a unique function of  $\sigma$  and  $\dot{\alpha}$ . Since this requires the ambiguous procedure of defining a

mechanical state variable, both the equalities given in equation 3.3 must be demonstrated and not just the unique dependence of  $(\partial\sigma / \partial \ln \dot{\alpha})_{state}$  on  $\sigma$  and  $\dot{\alpha}$  for the chosen state variable. It then follows that if the equality holds, the mechanical state is adequately described by the chosen variable and a state variable description of the deformation exists, but that if it does not, either the chosen variable does not fully characterize the mechanical state or a state variable description does not exist (*i.e.* the existence of a state variable description is not disproved).

MacEwen conducted room temperature experiments on polycrystalline zirconium. He treated the mechanical state as being uniquely specified by the flow stress. Two deformation paths were investigated : (1) a sequence of constant true strain-rate, load relaxation, constant true strain-rate, constant true stress creep repeated until a total strain of about 0.1 had been attained and, (2) a sequence of constant true strain-rate, sudden increase in strain-rate, sudden decrease to re-establish the base strain-rate, constant true stress, again repeated until a total strain of about 0.1.  $C = (\partial\sigma / \partial \ln \dot{\alpha})_{flow\ stress}$  was determined from the load relaxation tests on path (1) and the strain-rate change tests on path (2), and shown to be a unique function of the flow stress.  $A$  was determined from the constant strain-rate stress / strain curve immediately before the onset of a creep test, and  $B$  from the creep curve immediately after (allowing for anelastic effects) the onset of that test. The comparison of  $A / B$  with the value of  $C$  calculated from the determined  $C$  / flow stress function showed that the equality given by equation 3.3 was satisfied for all sixteen creep tests conducted, irrespective of the deformation history.

Although MacEwen found that the mechanical state of zirconium is strain-rate independent at room temperature, experiments on other materials show that at  $T > 0.3 T_m$  (where  $T_m$  is the material's absolute melting temperature) this is not generally the case (§ 4.2.2). This emphasizes the fact that these verifications of the state variable description existence conditions are applicable only for the deformation conditions under which they were established.

### 3.2 Verifying that curves of constant $\sigma^*$ are unique and form a one parameter family

To demonstrate that curves of constant  $\sigma^*$  form a one parameter family it is necessary to show that at given temperature, the set of  $\sigma(\dot{\alpha})$  curves, where each curve is obtained at given value of  $\dot{\alpha}$  (*i.e.* at given mechanical state), are a set of  $\sigma^*$  contours (level curves) of the surface

$$f(\sigma, \dot{\alpha}, \sigma^*) = 0 \quad (3.4)$$

Uniqueness may then be verified by demonstrating that the  $\sigma(\dot{\alpha})$  curve at given  $\sigma^*$  is the same irrespective of the deformation history required to obtain that value of  $\sigma^*$ .

**3.2.1 The observed form of constant  $\sigma^*$  curves.** In numerous investigations, the experimental problem of determining the relationship between  $\sigma$  and  $\dot{\alpha}$  for a specimen whilst  $d\alpha = 0$  has been solved by using the load relaxation test, which can generate within strains of a fraction of one percent, stress and strain-rate data over several orders of magnitude of these variables. The usual experimental procedure is to deform the specimen to a given flow stress (and hence given  $\sigma^*$ ) and then to conduct a load relaxation to determine the  $\sigma(\dot{\varepsilon}^{(n)})$  curve. Subsequently the specimen is reloaded to a higher flow stress and another relaxation carried out. This process is repeated until a requisite number of curves, each of different  $\sigma^*$ , have been obtained. Providing the loading phase prior to each relaxation is taken beyond the yield stress  $\dot{\alpha} \approx \dot{\varepsilon}^{(n)}$  and anelastic effects are negligible (§ 5.1.3). Although the load relaxation test is the most time efficient

method of obtaining  $\sigma^*$  curves, the same information can be gathered from the stress dip test (Birocheau and Oytana, 1983 ; Korhonen *et al.*, 1985a).

A wide variety of materials have been investigated including metals, metallic alloys, a metallic glass and several simple ionic solids. Homologous temperatures (*i.e.*  $T/T_m$ ) of less than 0.45 and strain-rates of between  $10^{-3}$  and  $10^{-10}$  s $^{-1}$  have been explored. Importantly, the results show that the general form of the constant  $\sigma^*$  curves is essentially material independent. For all the materials studied, the curves in  $\log \sigma - \log \dot{\alpha}$  space are concave upward at low homologous temperatures ( $T < 0.25 T_m$ ), concave downward at high homologous temperatures ( $T > 0.3 T_m$ ), and at intermediate temperatures are linear or, if extended over a sufficient strain-rate range, may contain an inflection point, being concave downward at low strain-rates and concave upward at high strain-rates (figure 3.2).

**3.2.2 Verifying that constant  $\sigma^*$  curves form a one parameter family.** The verification that constant  $\sigma^*$  curves form a one parameter family has been greatly facilitated by the observation that for almost all materials investigated, a scaling relation exists whereby all of the  $\sigma(\dot{\varepsilon}^{(n)})$  curves generated at given temperature may be superposed by a translation, without rotation, along a constant direction of slope

$$\mu = (\partial \log \sigma / \partial \log \dot{\alpha})_{\nu, T} \quad (3.5)$$

Stated more precisely using the change of variables  $x = \log \dot{\varepsilon}^{(n)}$ ,  $y = \log \sigma$  and  $z = \log \sigma^*$ , then

$$\left( \frac{\partial y}{\partial x} \right)_{x, z_1} = \left( \frac{\partial y}{\partial x} \right)_{x + \Delta x, z_2} \quad (3.6)$$

*i.e.* points of equal derivatives on two curves parameterized in  $z$  in the  $x, y$  plane superpose, and, the scaling direction

$$\mu = \Delta y / \Delta x = \text{constant} \quad (3.7)$$

is independent of the variables (figure 3.2b,d). This scaling property confirms that the curves do indeed belong to a one parameter family and that that parameter is  $\sigma^*$ .

In all investigations of the form of the constant  $\sigma^*$  curves, the existence of the scaling property has been tested only by visual inspection of the quality of the superposition of the curves onto a common master. This fails to distinguish between apparent and real scaling, and also requires that the curves have sufficient curvature to define a unique scaling direction. In practice these problems are significant only when the data is collected over a small strain-rate range or at temperatures of about  $0.3 T_m$ . More rigorous tests based on the form of the general function that gives rise to equations 3.6 and 3.7, can be employed once constitutive relations have been fitted to the data (§ 4.1.1.1).

**3.2.3 Verifying that the constant  $\sigma^*$  curves are unique.** Hart (1970) suggested that if  $\sigma^*$  is a unique function of  $\sigma$  and  $\dot{\alpha}$  then no two constant  $\sigma^*$  curves obtained from the same material should intersect. However, this is not in general correct. In a constant stress creep test where the deforming phase passes through a creep-rate minimum, there exist two states of the material which creep at the same  $\dot{\alpha}$  under the same  $\sigma$  but which are clearly different because in one case the creep-rate decelerates while in the other it accelerates. The intersection of the constant  $\sigma^*$  curves in this case reflects the fact that the curves are contours in the  $\sigma - \dot{\alpha}$  plane, to a surface (equation 3.4) which 'doubles back on itself' in the third ( $\sigma^*$ ) dimension. Nabarro (1989) observed that this situation is analogous to the surface  $T(p, V)$  representing the equation of

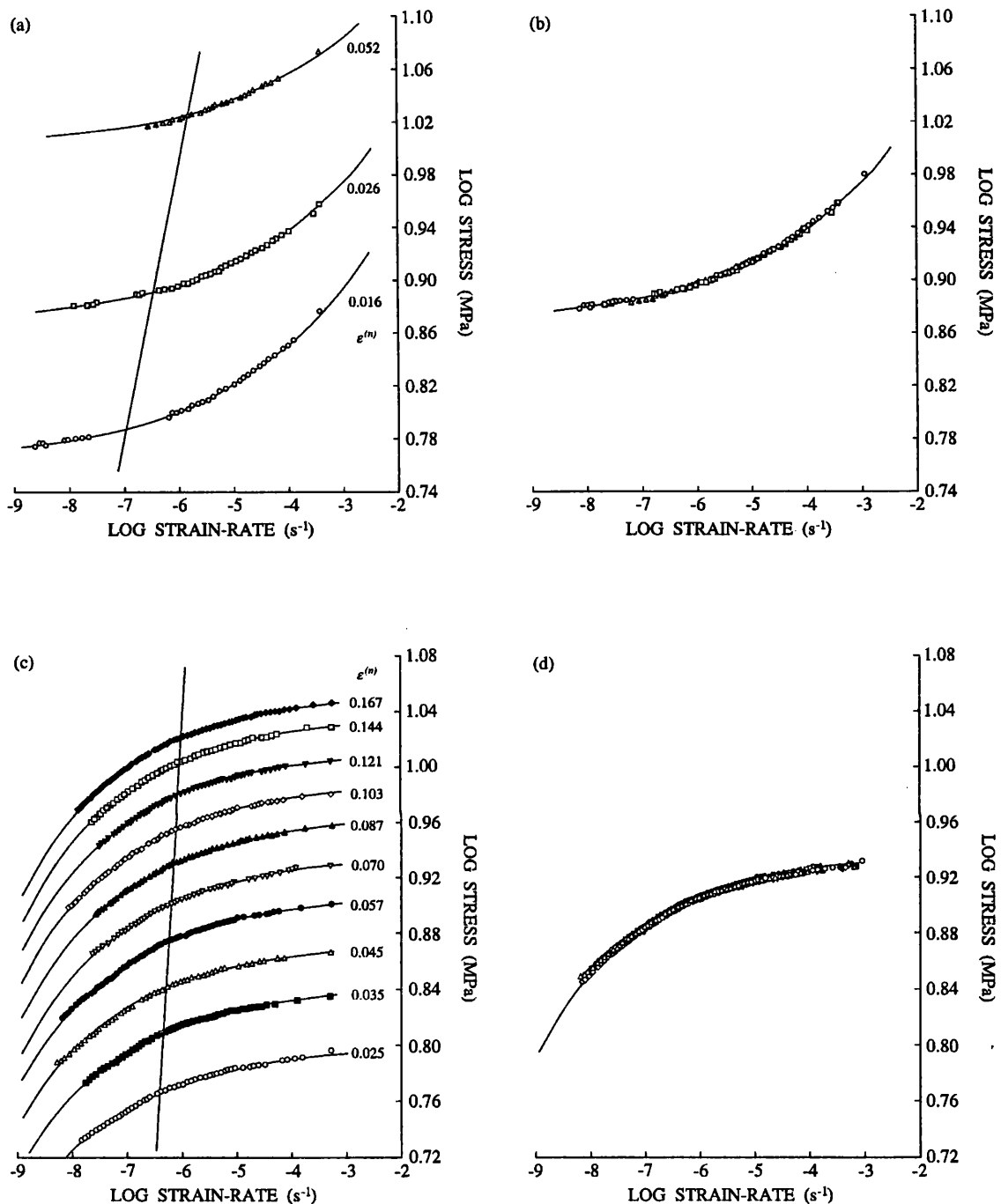


FIG. 3.2. Constant  $\sigma^*$  curves generated by load relaxation experiments conducted after constant displacement-rate loading to the indicated inelastic strains. (a) Low homologous temperature behaviour demonstrated at room temperature by single crystals of LiF. Translation of the curves along the indicated line yields the master curve shown in (b) (redrawn after Lerner *et al.*, 1979). (c) High homologous temperature behaviour demonstrated at room temperature by single crystals of AgCl loaded in the [100] direction. Translation of the curves along the indicated line yields the master curve shown in (d) (redrawn after Lerner and Kohlstedt, 1982).

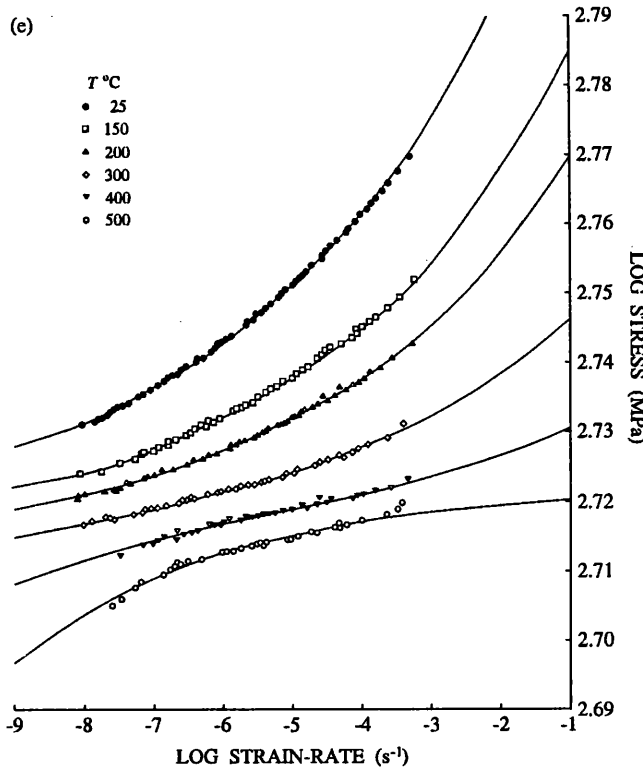


FIG. 3.2 contd. Load relaxation data obtained at different temperatures but at approximately the same  $\sigma^*$  in Type 316 stainless steel, showing the effect of temperature on the concavity of  $\sigma^*$  curves. The stress values are rigidity modulus corrected for temperature to room  $T$  (redrawn after Huang *et al.*, 1977).

state for  $\text{H}_2\text{O}$  in the range  $0 - 10^\circ\text{C}$ . This surface is approximately a portion of a circular cylinder with its axis pointing in the direction (-2026 MPa, 1 unit strain,  $2000^\circ\text{C}$ ). Hence at atmospheric pressure, a given volume may correspond to  $T \approx 2^\circ\text{C}$  or to  $T \approx 6^\circ\text{C}$ .

The only way to verify uniqueness is to compare constant  $\sigma^*$  curves generated at the same  $\sigma^*$  but after different deformation histories. In almost all experimental studies the pre-straining prior to the determination of constant  $\sigma^*$  curves has been by monotonic, constant displacement-rate deformation, without investigation of the effect of different deformation histories. However, Tanoue and Matsuda (1982, 1984) and Tanoue *et al.* (1983) found that in polycrystalline molybdenum, neither the displacement-rate used nor complex pre-strain histories involving loading or strain-rate cycling had any effect on the shape of the curves. In contrast, Szwarcengen *et al.* (1976) found that whilst both monotonic and cyclic loading histories produced one parameter families of curves in high purity (99.97%) polycrystalline iron, the scaling slope  $\mu$  was different in each case. This implies that the shape of the master  $\sigma^*$  curve for this material is a function of deformation history and hence that the  $\sigma^*$  curves are not unique. Differences in starting material pre-treatments, particularly in the annealing treatment given to heavily cold-worked materials, have also been observed to produce different sets of one parameter  $\sigma^*$  curves in a number of materials (in various stainless steels, Povolo and Tinivella, 1984a,b, Thomas and Yagge, 1975, Yamada and Li, 1973; in zircaloy-4, Povolo and Capitani, 1984, Povolo and Higa, 1980, Povolo and Peszkin, 1983; in molybdenum, Tanoue and

Matsuda, 1982 ; in Inconel, Povolo and Reggardo, 1988 ; in LiF, Lerner *et al.*, 1979).

The fact that under given pre-treatment one parameter families of curves are still observed in these materials, suggests that the apparent failure of uniqueness may be due to substantial microstructural changes induced by the pre-treatment (or, in the case of Swearengen *et al.*, by the deformation) which, from the perspective of Hart's analysis, effectively render the starting material as a new substance. Microstructural changes which could produce this effect include the precipitation or rearrangement of second phase particles or the loss of the homogeneity or isotropy (though the development of a fabric) of the deformation. Such effects, while not accommodated in the theoretical framework of the state variable analysis, may however, be included by a suitable parameterization of the material parameters in the final constitutive relations (§ 6.3).

### 3.3 The effect of temperature

The effect of temperature on the concave upward  $\sigma^*$  curves generated at  $T < 0.25 T_m$  has been fully investigated only for molybdenum (Tanoue and Matsuda, 1982, 1984 ; Tanoue *et al.*, 1983), although some experimental results have been reported for Type 316 stainless steel (Huang *et al.*, 1977) and zircaloy-4 (Huang *et al.*, 1979). It is found to affect both the position in  $\sigma$  -  $\dot{\alpha}$  space and the shape of the curves, the latter being reflected in an increase of scaling slope  $\mu$  with temperature. The positional effect can be accommodated with a Zener-Hollomon type temperature parameterization (equation 2.16) but only with an apparent activation enthalpy which varies with temperature (Huang *et al.*, 1977). To describe the shape change the temperature parameterization scheme employed must involve specifying the material parameters in the final constitutive relations as a function of temperature.

The effect of temperature on the concave downward  $\sigma^*$  curves generated at  $T > 0.3 T_m$  has been investigated for  $\text{UO}_2$  (Roberts, 1974) and for Cr-Mo-V steel (Woodford, 1975), and been shown to affect only the position of the curves in  $\sigma$  -  $\dot{\alpha}$  space and not their shape (*i.e.* the scaling slope is independent of temperature). In this case the Zener-Hollomon parameterization with a temperature independent apparent activation enthalpy can fully account for temperature.

## 4 DERIVATION OF THE CONSTITUTIVE RELATIONS

Having verified by experiment that a state variable description of plastic deformation exists for real materials, it is necessary to derive the constitutive relations which comprise that description. This involves the twin tasks of (a) determining the equation of state that interrelates the internal and external state variables of the deformation system at any given time, and of (b) determining the internal state variable evolution equation which allows the integration of the incremental deformation equation along any deformation path of interest. Since the theoretical analysis (§ 2) does not address the functional form of these constitutive relations, this exercise is necessarily (at least in principle) empirical.

### 4.1 Derivation of the equation of state

The preceding discussion has shown that the isothermal, plastic deformation system is characterized by the two external state variables  $\sigma$  and  $\alpha$  together with the internal state variable  $\sigma^*$ . The equation of state for this system is therefore a relationship between only these three variables.

**4.1.1 Constraints on the form of the plastic equation of state.** The required relationship between the deformation variables is some function that describes the surface denoted by equation 3.4. The general form of this function is constrained to be one that produces the observed scaling behaviour of the  $\sigma^*$  level curves to this surface (§ 3.2.2), while the particular equation chosen to represent that general form must satisfy the criteria which actually make it an equation of state. In addition, the scaling property also constrains the functional interrelationships of the material parameters in the special form.

**4.1.1.1 The general function which produces the observed scaling behaviour :** The general form of a one parameter  $z$  family of  $y(x; z)$  curves with a scaling relation  $M_R = \Delta x / \Delta y = 0$  (that is curves which can be made to superpose by a translation parallel to the  $y$  axis) is

$$y(x; z) = z + f(x) \quad (4.1)$$

where  $f$  is an arbitrary function (Fortes and Emilia Rosa, 1984). For scaling along a linear translation path in any direction, equation 4.1 becomes (Povolo, 1985)

$$g(A_i x_i) = B_i x_i + B_4 \quad i = 1, 2, 3 \quad (4.2)$$

where the variables  $x_1, x_2$  and  $x_3$  have been used in place of the  $x, y, z$  nomenclature, where  $g$  is a real function which is continuous, single-valued and differentiable and  $A_i, B_i, B_4$  are real constants, and where the Einstein suffix convention of summation over repeated indices within a given term is implied.

Povolo (1985) verified that equation 4.2 produces a scaling slope which is independent of the variables (*i.e.* the scaling property formulated as equation 3.7) by rewriting it as

$$F = g(A_i x_i) - B_i x_i - B_4 = 0 \quad (4.3)$$

Taking increments of equation 4.3

$$F_i \Delta x_i = g'(u) (A_i \Delta x_i) - (B_i \Delta x_i) = 0 \quad (4.4)$$

where  $u = A_i x_i$ ,  $g'(u) = dg/du$  and  $F_i = \partial F / \partial x_i$  (§A1.2.1.1). For fixed increments  $\Delta x_i$ , equation 4.4 can be satisfied only if

$$A_i \Delta x_i = 0 \quad (4.5)$$

$$B_i \Delta x_i = 0 \quad (4.6)$$

Combining equations 4.5 and 4.6 then

$$\Delta x_k / \Delta x_i = (A_i B_j - B_i A_j) / (A_j B_k - B_j A_k) \quad i \neq j \neq k \quad (4.7)$$

(§A1.2.1.2) which defines three scaling relationships which are all independent of the variables. The fact that scaling behaviour in one plane leads to scaling in the other two may be used as a test of whether or not the observed scaling in one plane is real or apparent, for not only must scaling be observed in the other two planes but the scaling slopes in all three planes must be related according to equation 4.7 (Povolo and Fontelos, 1987a).

The scaling property formulated as equation 3.6 *i.e.* that points of equal derivatives should be superposed, was shown by Povolo and Fontelos (1987b) to be satisfied by equation 4.2 in the case that equation 4.3 can be used to define a function  $x_j = \psi(x_i, x_k)$  where  $i \neq j \neq k$ . In such circumstances (which must apply if equation 4.2 is to define an equation of state, § 4.1.1.2), the theorems for the derivatives of implicit functions (*cf.* equations 4.15) can be used to show that

$$(\partial x_j / \partial x_i)_k = - [g'(u) A_i - B_i] / [g'(u) A_j - B_j] \quad (4.8)$$

From equation 4.5

$$u = A_i x_i = A_i (x_i + \Delta x_i) \quad (4.9)$$

and therefore using equation 4.9 in 4.8, then  $(\partial x_j / \partial x_i)_k$  as defined at point  $(x_1, x_2, x_3)$ , equals that defined at every other point  $(x_1 + \Delta x_1, x_2 + \Delta x_2, x_3 + \Delta x_3)$  on the scaling path.

Since equation 4.2 satisfies the observed scaling properties (equations 3.6 and 3.7) of the constant  $\sigma^*$ ,  $\sigma(\alpha)$  curves, it is, with the appropriate change of variables, the general form for the plastic equation of state. Restating equation 4.2 in  $x, y, z$  nomenclature, then

$$g(A_1 x + A_2 y + A_3 z) = B_1 x + B_2 y + B_3 z + B_4 \quad (4.10)$$

where, since the scaling is observed in logarithmic space,  $x = \log \alpha$ ,  $y = \log \sigma$ ,  $z = \log \sigma^*$  and  $B_4 = \log C$  (where  $C$  is a real constant). To satisfy the variable independent scaling property, the  $A_i$  and  $B_i$  in equation 4.10 must satisfy equation 4.7, *i.e.*

$$\Delta y / \Delta x = (A_1 B_3 - B_1 A_3) / (A_3 B_2 - B_3 A_2) = 1 / M_R \quad (4.11)$$

where  $M_R$  is the reciprocal of the scaling slope (equation 3.5). Several functions of the form of equation 4.10 which satisfy equation 4.11 were listed by Povolo (1985) and these are shown in figure 4.1 together with their equivalents on the change of variables.

**4.1.1.2 The conditions to be satisfied for the special form to be an equation of state :** For equation 4.10 to be an equation of state it is necessary that any one of the variables be a unique function of the others or, equivalently, that the differential of each variable be a perfect differential. Hence writing equation 4.10 (*cf.* equation 4.3) as

$$F(x, y, z) = g(A_1 x + A_2 y + A_3 z) - B_1 x - B_2 y - B_3 z - B_4 = 0 \quad (4.12)$$

then a function  $z = \psi(x, y)$  must exist and the differential

$$dz = (\partial \psi / \partial x)_y dx + (\partial \psi / \partial y)_x dy \quad (4.13)$$

must be exact. The necessary and sufficient condition for equation 4.13 to be exact is that

$$\frac{\partial}{\partial y} (\partial \psi / \partial x)_y = \frac{\partial}{\partial x} (\partial \psi / \partial y)_x \quad (4.14)$$

where the derivatives of the functions  $(\partial \psi / \partial x)_y$  and  $(\partial \psi / \partial y)_x$  are both continuous. Using the

$$\begin{aligned}
g(x - M_R y) &= B_1 x + B_3 z + B_4 & \Rightarrow f(\dot{\alpha} / \sigma^{M_R}) &= C \dot{\alpha}^{B_1} \sigma^{* B_2} \\
g(x - M_R y) &= B_2 y + B_3 z + B_4 & \Rightarrow f(\dot{\alpha} / \sigma^{M_R}) &= C \dot{\alpha}^{B_2} \sigma^{* B_3} \\
g(M_R y + z) &= B_1(x + z) + B_4 & \Rightarrow f(\sigma^{M_R} \sigma^*) &= C(\dot{\alpha} \sigma^*)^{B_1} \\
g(x + M_R z) &= B_2(y + z) + B_4 & \Rightarrow f(\dot{\alpha} \sigma^{* M_R}) &= C(\sigma \sigma^*)^{B_2} \\
g(x + z) &= M_R y + z + B_4 & \Rightarrow f(\dot{\alpha} \sigma^*) &= C \sigma^* \sigma^{M_R} \\
g(y + z) &= x + M_R z + B_4 & \Rightarrow f(\sigma \sigma^*) &= C \dot{\alpha} \sigma^{* M_R} \\
g(y - z) &= x - M_R z + B_4 & \Rightarrow f(\sigma / \sigma^*) &= C \dot{\alpha} \sigma^{*-M_R}
\end{aligned}$$

FIG. 4.1. Some functions which satisfy the observed scaling behaviour of constant  $\sigma^*$  curves in  $\log \sigma$  -  $\log \dot{\alpha}$  space i.e. which are special forms of equation 4.10 that also satisfy equation 4.11 (after Povolo, 1985).

change of variables,  $u = A_1 x + A_2 y + A_3 z$  (as previously, § 4.1.1.1) and the theorems for the derivatives of implicit functions (e.g. Hildebrand, 1976, pp. 342-346) then

$$\left( \frac{\partial \psi}{\partial x} \right)_y = - \frac{(\partial F / \partial x)_{y,z}}{(\partial F / \partial z)_{x,y}} = - \frac{[g'(u) A_1 - B_1]}{[g'(u) A_3 - B_3]} \quad (4.15a)$$

$$\left( \frac{\partial \psi}{\partial y} \right)_x = - \frac{(\partial F / \partial y)_{x,z}}{(\partial F / \partial z)_{x,y}} = - \frac{[g'(u) A_2 - B_2]}{[g'(u) A_3 - B_3]} \quad (4.15b)$$

so that equation 4.14 yields

$$\psi_{xy} = \psi_{yx} = - g''(u) \left\{ \frac{(A_1 A_2 + A_2 A_3 \psi_x + A_1 A_3 \psi_y + A_3^2 \psi_x \psi_y)}{[g'(u) A_3 - B_3]} \right\} \quad (4.16)$$

where  $\psi_x = (\partial \psi / \partial x)_y$ ,  $\psi_y = (\partial \psi / \partial y)_x$ ,  $\psi_{yx} = (\partial / \partial x)(\partial \psi / \partial y)_x$  and  $\psi_{xy} = (\partial / \partial y)(\partial \psi / \partial x)_y$  (§ A1.2.1.3). Hence from equation 4.16, equation 4.13 is exact if  $g'(u) A_3 - B_3 \neq 0$  or

$$g'(u) \neq B_3 / A_3 \quad (4.17)$$

Therefore, while the general form of the plastic constitutive relation is given by equation 4.10, the special form chosen must also satisfy equation 4.11 if it is to give rise to variable independent scaling, and equation 4.17 if it is to be an equation of state. These constraints, presented here according to the analysis of Povolo (1985), are sufficiently general to allow them to be applied to a wide variety of plastic constitutive relations in addition to those arising from Hart's analysis (Povolo and Marzocca, 1983b ; Povolo and Rubiolo, 1983a,b ; Povolo *et al.*, 1984).

**4.1.1.3 Constraints on the functional interrelationships of the material parameters in the special form** : Povolo and Marzocca (1983a) outlined the constraints the scaling property imposes on the functional interrelationships between the material parameters in any special form of equation 4.10.

Theoretical expressions used to describe load relaxation data can be represented as

$$f(\sigma / \sigma_0, \dot{\alpha} / \dot{\varepsilon}^*, \beta) = 0 \quad (4.18)$$

where  $\sigma_0$ ,  $\dot{\varepsilon}^*$  and  $\beta$  are parameters which depend upon the particular theoretical model considered (with  $\beta$  being an implicit function of  $\sigma / \sigma_0$  and  $\dot{\alpha} / \dot{\varepsilon}^*$ ), and  $f$  is a general function

(Povolo, 1981). The substitution  $\dot{\alpha} = \dot{\varepsilon}^{(n)}$  is used in equation 4.18 with the caveat that prior to the relaxation the specimen is loaded beyond the yield point so that anelastic effects are negligible (§ 5.1.3). Taking increments of equation 4.18

$$\frac{\partial f}{\partial \log(\sigma/\sigma_0)} \Delta \log(\sigma/\sigma_0) + \frac{\partial f}{\partial \log(\dot{\alpha}/\dot{\varepsilon}^*)} \Delta \log(\dot{\alpha}/\dot{\varepsilon}^*) + \frac{\partial f}{\partial \log \beta} \Delta \log \beta = 0 \quad (4.19)$$

with the additional constraints along the scaling path that

$$\left[ \frac{\partial f}{\partial \log(\sigma/\sigma_0)} \right]_{(\dot{\alpha}/\dot{\varepsilon}^*)} = \frac{\partial f}{\partial \log(\sigma/\sigma_0)} + \frac{\partial f}{\partial \log \beta} \frac{\partial \log \beta}{\partial \log(\sigma/\sigma_0)} = 0 \quad (4.20a)$$

$$\left[ \frac{\partial f}{\partial \log(\dot{\alpha}/\dot{\varepsilon}^*)} \right]_{(\sigma/\sigma_0)} = \frac{\partial f}{\partial \log(\dot{\alpha}/\dot{\varepsilon}^*)} + \frac{\partial f}{\partial \log \beta} \frac{\partial \log \beta}{\partial \log(\dot{\alpha}/\dot{\varepsilon}^*)} = 0 \quad (4.20b)$$

On substituting equations 4.20 into equation 4.19 then

$$\frac{\partial \log \beta}{\partial \log(\sigma/\sigma_0)} \Delta \log(\sigma/\sigma_0) + \frac{\partial \log \beta}{\partial \log(\dot{\alpha}/\dot{\varepsilon}^*)} \Delta \log(\dot{\alpha}/\dot{\varepsilon}^*) = \Delta \log \beta \quad (4.21)$$

Introducing

$$h = h(\sigma/\sigma_0, \dot{\alpha}/\dot{\varepsilon}^*, \beta) = \partial \log \beta / \partial \log(\sigma/\sigma_0) \quad (4.22a)$$

$$g = g(\sigma/\sigma_0, \dot{\alpha}/\dot{\varepsilon}^*, \beta) = \partial \log \beta / \partial \log(\dot{\alpha}/\dot{\varepsilon}^*) \quad (4.22b)$$

equation 4.21 in turn becomes

$$h \Delta \log(\sigma/\sigma_0) + g \Delta \log(\dot{\alpha}/\dot{\varepsilon}^*) = \Delta \log \beta \quad (4.23)$$

This expression then relates the increments on the variables  $\sigma$  and  $\dot{\alpha}$  that are compatible with the increments on the parameters  $\sigma_0$ ,  $\dot{\varepsilon}^*$  and  $\beta$  in any special form of equation 4.10 given the fact of the scaling relation. To be consistent with the observation that the scaling direction is independent of the state variables, solutions to equation 4.23 which are independent of  $\sigma/\sigma_0$ ,  $\dot{\alpha}/\dot{\varepsilon}^*$  and  $\beta$  are required.

**4.1.2 Special forms adopted for the equation of state.** Two different special forms of equation 4.10 have been widely used for the isothermal plastic equation of state ; one applicable at low homologous temperatures producing concave upward  $\sigma^*$  curves in  $\log \sigma - \log \dot{\alpha}$  space, and the other applicable at high homologous temperatures producing the concave downward curves.

**4.1.2.1 High homologous temperatures :** The special form used at high homologous temperatures was introduced by Hart *et al.* (1975) as

$$\ln(\sigma^*/\sigma) = (\dot{\varepsilon}^*/\dot{\alpha})^\lambda \quad (4.24)$$

where  $\lambda$  is a constant and  $\sigma^*$  and  $\dot{\varepsilon}^*$  appear as normalization factors.

To find the interrelationships between  $\lambda$ ,  $\sigma^*$  and  $\dot{\varepsilon}^*$  consistent with scaling behaviour, equation 4.24 is written as

$$\sigma/\sigma^* = \exp[-(\dot{\alpha}/\dot{\varepsilon}^*)^\lambda] \quad (4.25)$$

Making the change of variables  $\sigma_0 = \sigma^*$  and  $\beta = \lambda$  then from equations 4.22 (§ A1.2.2.1)

$$h = \partial \log \beta / \partial \log(\sigma/\sigma_0) = 1 / [\beta (\dot{\alpha}/\dot{\varepsilon}^*)^\beta \ln(\dot{\alpha}/\dot{\varepsilon}^*)] \quad (4.26a)$$

$$g = \partial \log \beta / \partial \log(\dot{\alpha}/\dot{\varepsilon}^*) = -1 / \ln(\dot{\alpha}/\dot{\varepsilon}^*) \quad (4.26b)$$

With equations 4.26, equation 4.23 has solutions which are independent of  $\sigma/\sigma_0$ ,  $\dot{\alpha}/\dot{\varepsilon}^*$  and  $\beta$  only if

$$\Delta \log \beta = \Delta \log(\sigma/\sigma_0) = \Delta \log(\dot{\alpha}/\dot{\varepsilon}^*) = 0 \quad (4.27)$$

that is if

$$\Delta \log \lambda = 0 \quad ; \quad \Delta \log \sigma = \Delta \log \sigma^* \quad ; \quad \Delta \log \dot{\alpha} = \Delta \log \dot{\varepsilon}^* \quad (4.28)$$

Hence to be consistent with the variable independent scaling property (equation 3.7),  $\lambda$  must be the same value for all the constant  $\sigma^*$  curves (*i.e.* it must not change along the scaling path) and  $\sigma^*$  and  $\dot{\varepsilon}^*$  must be related as (equation 3.5)

$$\mu = \Delta \log \sigma / \Delta \log \dot{\alpha} = \Delta \log \sigma^* / \Delta \log \dot{\varepsilon}^* \quad (4.29)$$

that is as

$$\dot{\varepsilon}^* = C (\sigma^*)^{1/\mu} \quad (4.30)$$

where  $C$  is a constant.

Making the change of variables  $x = \log \dot{\alpha}$ ,  $y = \log \sigma$ ,  $z = \log \sigma^*$ , and substituting equation 4.30, equation 4.24 can be rearranged ( $\S$  A1.2.2.2) to give

$$z - y - (1/\ln 10) \{ \exp [\lambda \ln 10 (\log C + mz - x)] \} = 0 \quad (4.31)$$

where  $m = (1/\mu)$ . It is then readily seen that equation 4.24 is a special form of equation 4.10 with

$$\begin{aligned} A_1 &= -1 \quad ; \quad A_2 = 0 \quad ; \quad A_3 = m \\ B_1 &= 0 \quad ; \quad B_2 = 1 \quad ; \quad B_3 = -1 \quad ; \quad B_4 = 0 \end{aligned} \quad (4.32)$$

From equation 4.11, the scaling slope is given by  $\mu = (1/m)$  in accordance with the way  $m$  was defined in equation 4.31. The condition for equation 4.24 to be an equation of state is, from equations 4.17 and 4.32 ( $\S$  A1.2.2.3)

$$\ln (\sigma^* / \sigma) \neq 1/\lambda m \quad (4.33)$$

This inequality does not necessarily always hold. Since the condition of continuity requires the inequality to hold throughout the domain in which the equation of state is applicable, then it follows that for equation 4.24 to be an equation of state either

$$(\sigma^* / \sigma) > \exp (1/\lambda m) \quad (4.34a)$$

or

$$(\sigma^* / \sigma) < \exp (1/\lambda m) \quad (4.34b)$$

must be true for all  $\dot{\alpha}$ . The experiments conducted to investigate the high homologous temperature equation of state have all been in the domain given by equation 4.34b.

**4.1.2.2 Low homologous temperatures :** Since the low homologous temperature  $\log \sigma - \log \dot{\alpha}$  constant  $\sigma^*$  curves have the same scaling relationship as those at high homologous temperatures, and differ from them only in being concave upward rather than concave down, the plastic equation of state at such temperatures can be expected to be described by an inverted form of equation 4.24, *i.e.* by

$$\ln (\sigma / \sigma^*) = (\dot{\alpha} / \dot{\varepsilon}^*)^\lambda \quad (4.35)$$

However, although equation 4.35 can describe the  $\sigma^*$  curves, the recognition that at these temperatures dislocation glide kinetics control the rate of plastic deformation, has led to a form with greater micromechanical significance being chosen. Splitting the flow stress  $\sigma$  into internal stress  $\sigma_a$  and effective stress  $\sigma_f$  components such that

$$\sigma = \sigma_a + \sigma_f \quad (4.36)$$

Hart (1976) proposed that the special form for the low homologous temperature equation of state be

$$\dot{\alpha} = \dot{\alpha}^* (|\sigma_f| / G)^M \operatorname{sgn}(\sigma_f) \quad (4.37)$$

where  $\dot{\alpha}^*$  is a rate parameter (which is constant at given mechanical state and at given temperature),  $M$  is a constant,  $G$  is the rigidity modulus and  $\text{sgn}(\sigma_f)$  is the signum function whose value is simply the sign of its argument (the signum is omitted in all the equations below where both  $\dot{\alpha}$  and  $\sigma_f$  are positive). Equation 4.37 has the same functional form as the Johnston-Gilman equation which combines the empirically observed relationships between dislocation glide velocity, plastic strain-rate and effective stress (as defined in equation 4.36) – § 6.2.2.1. It may also be shown (§ A1.2.3.1) that on making the approximation

$$\sigma^* = \sigma_a \quad (4.38)$$

(permissible at present because  $\sigma^*$  is arbitrarily defined, § 2.4) and using equation 4.36, equation 4.37 is equivalent to equation 4.35 with

$$\lambda = 1/M ; \quad \dot{\varepsilon}^* = \dot{\alpha}^* (\sigma^* / G)^M \quad (4.39)$$

To find the interrelationships between  $\dot{\alpha}^*$ ,  $\sigma^*$ ,  $G$  and  $M$  that are consistent with scaling behaviour, equations 4.36 and 4.38 are used to rewrite equation 4.37 as

$$\dot{\alpha} = \dot{\alpha}^* [(\sigma - \sigma^*) / G]^M \quad (4.40)$$

On rearranging and making the change of variables

$$\sigma_0 = \sigma^* ; \quad \beta = 1/M ; \quad \dot{\varepsilon}^* = \dot{\alpha}^* (\sigma^* / G)^M \quad (4.41)$$

equation 4.40 becomes

$$(\sigma / \sigma_0) = (\dot{\alpha} / \dot{\varepsilon}^*)^\beta + 1 \quad (4.42)$$

so that from equations 4.22

$$h = \partial \log \beta / \partial \log (\sigma / \sigma_0) = (\sigma / \sigma_0) / [\beta (\dot{\alpha} / \dot{\varepsilon}^*)^\beta \ln (\dot{\alpha} / \dot{\varepsilon}^*)] \quad (4.43a)$$

$$g = \partial \log \beta / \partial \log (\dot{\alpha} / \dot{\varepsilon}^*) = -1 / \ln (\dot{\alpha} / \dot{\varepsilon}^*) \quad (4.43b)$$

(§ A1.2.3.2). Again, as for the high homologous temperature case, the need for solutions to equation 4.23 that are independent of  $\sigma / \sigma_0$ ,  $\dot{\alpha} / \dot{\varepsilon}^*$  and  $\beta$  requires

$$\Delta \log \beta = \Delta \log (\sigma / \sigma_0) = \Delta \log (\dot{\alpha} / \dot{\varepsilon}^*) = 0 \quad (4.44)$$

and so from equation 4.41

$$-\Delta \log M = 0 ; \quad \Delta \log \sigma = \Delta \log \sigma^* ; \quad \Delta \log \dot{\alpha} = \Delta \log \dot{\varepsilon}^* \quad (4.45)$$

Hence to be consistent with the variable independent scaling property (equation 3.7),  $M$  must be the same value for all the constant  $\sigma^*$  curves (*i.e.* it must not change along the scaling path), and  $\dot{\varepsilon}^*$  and  $\sigma^*$  must be related as (equation 3.5)

$$\mu = \Delta \log \sigma / \Delta \log \dot{\alpha} = \Delta \log \sigma^* / \Delta \log \dot{\varepsilon}^* = (M + \partial \log \dot{\alpha}^* / \partial \log \sigma^*)^{-1} \quad (4.46)$$

where the last equality in equation 4.46 follows from equation 4.41.

Making the change of variables  $x = \log \dot{\alpha}$ ,  $y = \log \sigma$ ,  $z = \log \sigma^*$ , equation 4.40 can be rearranged (§ A1.2.3.3) to give

$$(\log \dot{\alpha}^* - M \log G) + Mz - x + M \log \{\exp [\ln 10 (y - z)] - 1\} = 0 \quad (4.47)$$

Provided that the dependence of  $\dot{\alpha}^*$  on  $\sigma^*$  is given by

$$\log \dot{\alpha}^* = A + B \log \sigma^* \quad (4.48)$$

where  $A$  and  $B$  are constants, it is then readily seen that equation 4.40 is a special form of equation 4.10 with

$$A_1 = 0 ; \quad A_2 = 1 ; \quad A_3 = -1$$

$$B_1 = 1 ; \quad B_2 = 0 ; \quad B_3 = -(B + M) ; \quad B_4 = -(A - M \log G) \quad (4.49)$$

From equation 4.11 the scaling slope is given by  $\mu = (B + M)^{-1}$  in accordance with equation 4.46. The condition for equation 4.40 to be an equation of state is, from equations 4.17 and 4.49

$$(\sigma^* / \sigma) \neq B / (B + M) \quad (4.50)$$

(§ A1.2.3.4) which in the case that  $\dot{\alpha}^*$  is independent of  $\sigma^*$ , is always satisfied.

**4.1.2.3 Temperature parameterization :** The parameterization of equations 4.24 and 4.37 for temperature follows from the observed effect of temperature on the constant  $\sigma^*$  curves (§ 3.3).

At high homologous temperatures, temperature affects only the position of the  $\sigma^*$  curves and has no effect on their shape. Since this means that the scaling slope is independent of temperature, it follows from the analysis presented in equations 4.26 - 4.30, that  $\lambda$  is temperature independent, and that position effect of temperature is accommodated wholly within the constant  $C$  in equation 4.30. Hart *et al.* (1975) proposed that equation 4.30 be

$$\dot{\varepsilon}^* = (\sigma^* / G)^m f_0 \exp(-H/RT) \quad (4.51)$$

where  $\sigma^*$  is scaled by the rigidity modulus  $G$  (which is implicitly temperature dependent),  $m$  is the reciprocal of the scaling slope,  $f_0$  is a frequency factor,  $H$  is an activation enthalpy and  $R$  is the gas constant.

At low homologous temperatures, temperature affects both the position and the shape of the  $\sigma^*$  curves. Since the effect on shape implies that the scaling slope is dependent on temperature, it follows from equation 4.46 that  $M$  and/or  $\partial \log \dot{\alpha}^* / \partial \log \sigma^*$  depend on temperature. The position effect indicates that  $\dot{\alpha}^*$  is temperature dependent. No explicit forms for these temperature dependencies have been proposed, although theoretical considerations offer some constraints (§ 6.2.2.2).

## 4.2 Derivation of the mechanical state evolution equation

The plastic equations of state outlined above completely specify the plastic state of a deforming material at any instant. However, they do not indicate how that state changes as deformation proceeds. To determine this it is necessary to find some function of the state variables which describes how the internal state variable  $\sigma^*$  changes with plastic strain. From equation 2.17, noting the definitions used in equation 2.5

$$d \ln \sigma^* = \Gamma d\alpha = (\Gamma / \gamma) (d \ln \sigma - \nu d \ln \dot{\alpha}) \quad (4.52)$$

so that this task is formally equivalent to finding the functional form of the integrating factor  $\Gamma$ .

**4.2.1 General form of the integrating factor.** For the adopted equations of state at both low and high homologous temperatures (*i.e.* equations 4.24 and 4.37), along the scaling path

$$\mu = d \ln \sigma / d \ln \dot{\alpha} ; \quad d \ln \sigma = d \ln \sigma^* \quad (4.53)$$

(equations 4.28, 4.29 and 4.45, 4.46). Substituting these identities into equation 4.52 and solving for  $\Gamma$  then

$$\Gamma = \gamma \mu / (\mu - \nu) \quad (4.54)$$

(§ A1.2.4, Wire *et al.*, 1976). Equation 4.54 represents the general form of the integrating factor in terms of  $\gamma$  and  $\nu$  (which are unspecified functions of  $\sigma$  and  $\dot{\alpha}$ ) given that the special form chosen for the equation of state leads to the identities expressed in equation 4.53.

**4.2.2 Special forms for the integrating factor.** The general form of the integrating factor, equation 4.54, is expressed as a function of  $\sigma$  and  $\dot{\alpha}$  through the dependence of  $\gamma$  and  $\nu$  on those variables. However, since this integrating factor is the function that describes the evolution of the mechanical state  $\sigma^*$  with deformation, it is more convenient to express it as a function of  $\sigma$  and  $\sigma^*$ . This presents no difficulty because the equations of state allow the third state variable

to be determined from the other two.

**4.2.2.1 Low homologous temperatures :** In all the experiments that have been conducted,  $\Gamma$  is strain-rate independent at low homologous temperatures. Suzuki *et al.* (1982) demonstrated this in a series of constant displacement-rate tests on zircaloy-2. Calculating  $\sigma_f$  in the low homologous temperature equation of state (equation 4.37) by employing previously determined values of the parameters in that equation and the imposed strain-rate of the test, they used equation 4.36 to plot their stress / strain curves as curves of  $\sigma_a$  versus  $\alpha$ . The  $\sigma_a / \alpha$  curves generated at different strain-rates are coincident (figure 4.2a) thereby establishing that  $d\sigma_a / d\alpha$  is independent of  $\dot{\alpha}$ . The strain-rate independence of  $\Gamma = d \ln \sigma^* / d\alpha$  then follows by verifying that  $\sigma^* \approx \sigma_a$  (equation 4.38) which was shown by determining  $\sigma^*$  from load relaxations conducted at several points along the  $\sigma_a / \alpha$  curve.

The strain-rate independence of  $\Gamma$  at low homologous temperatures has also been demonstrated in high purity niobium and Type 316 stainless steel (Wire *et al.*, 1976 ; Korhonen *et al.*, 1985b). Korhonen *et al.* (1985b) plotted  $\Gamma$  as a function of  $\sigma^*$  and found that irrespective of  $\dot{\alpha}$

$$\Gamma = [\zeta / (\sigma^* - \sigma_0^*)]^\eta \quad (4.55)$$

where  $\zeta$ ,  $\eta$  and  $\sigma_0^*$  are constants (figure 4.2b). They observed that the  $\dot{\alpha}$  independence of  $\Gamma$  suggests that  $\zeta$ ,  $\eta$  and  $\sigma_0^*$  are all temperature independent.

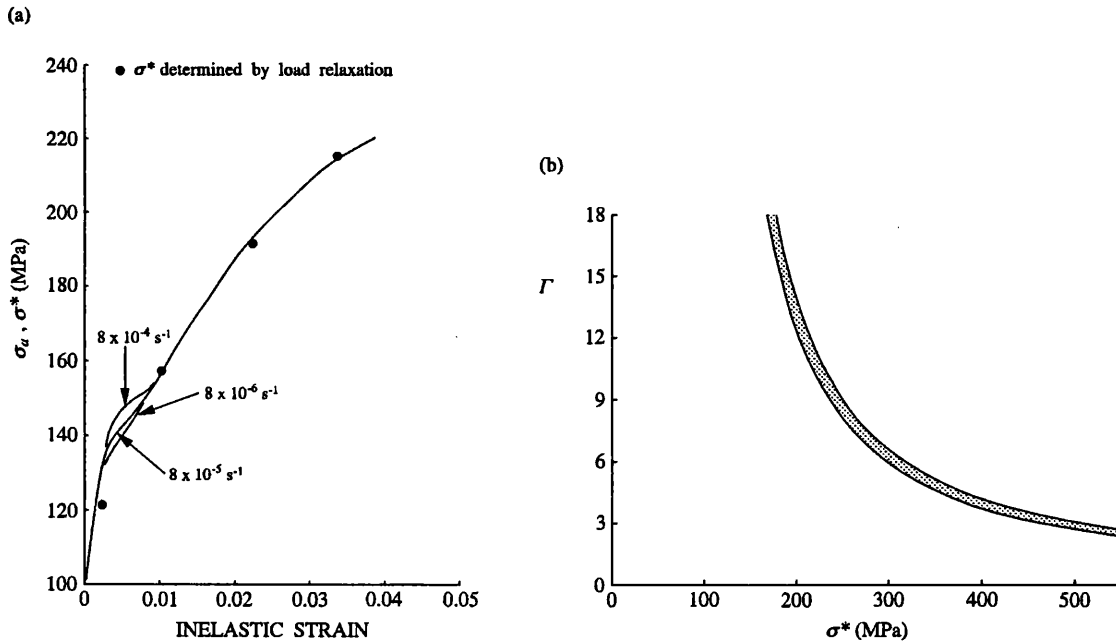


FIG. 4.2. The  $\Gamma$  function at low homologous temperatures. (a)  $\sigma_a / \varepsilon^{(n)}$  curves in zircaloy-2 at 200°C as determined from constant displacement-rate  $\sigma / \varepsilon^{(t)}$  curves using calculated values of  $\sigma_f$ . At  $\varepsilon^{(n)} > 0.01$  the curves are strain-rate independent and  $\sigma^* \approx \sigma_a$ . Hence it follows that  $\Gamma$  is strain-rate independent (redrawn after Suzuki *et al.*, 1982). (b) The dependence of  $\Gamma$  on  $\sigma^*$  in Type 316 stainless steel at room temperature as determined from constant displacement-rate tests at several strain-rates in the range  $3 \times 10^{-3}$  to  $3 \times 10^{-5} \text{ s}^{-1}$ . No strain-rate dependence can be seen (redrawn after Korhonen *et al.*, 1985b).

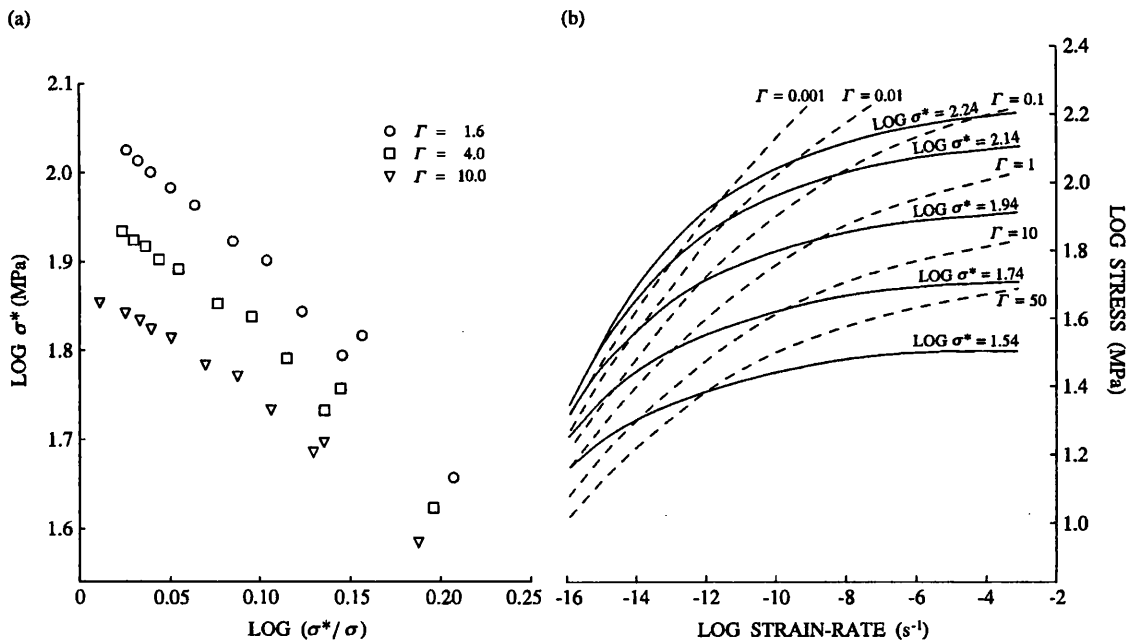


FIG. 4.3. The  $\Gamma$  function at high homologous temperatures. (a) Constant  $\Gamma$  data obtained from 1100 aluminium alloy at temperatures of between room and 250°C and after loading at several different strain-rates in the range  $2.5 \times 10^{-3}$  to  $6.3 \times 10^{-6} \text{ s}^{-1}$ . The stress values are rigidity modulus corrected for temperature to their values at room  $T$  (redrawn after Hart *et al.*, 1975). (b) Curves of constant  $\Gamma$  and constant  $\sigma^*$  in  $\log \sigma / \log \dot{\varepsilon}^{(n)}$  space, where the  $\Gamma$  curves are calculated from equation 4.56 and the  $\sigma^*$  curves from equation 4.24, both using room temperature material parameters for 1100 aluminium alloy (redrawn after Ellis *et al.*, 1975).

**4.2.2.2 High homologous temperatures :** Experiments on 1100 aluminium alloy (Wire *et al.*, 1976), high purity aluminium and OFHC copper (Korhonen *et al.*, 1985b) have all shown  $\Gamma$  to be  $\dot{\varepsilon}$  dependent at high homologous temperatures. Curves of constant  $\Gamma$  in  $\log \sigma^* - \log (\sigma^* / \sigma)$  space are linear (figure 4.3a) which prompted Hart *et al.* (1975) to suggest that

$$\Gamma = C(\sigma^A / \sigma^{*B}) \quad (4.56)$$

where  $A$ ,  $B$  and  $C$  are constants. They also found that equation 4.56 could be parameterized for temperature by normalizing both  $\sigma$  and  $\sigma^*$  by the rigidity modulus at the specified temperature. Ellis *et al.* (1975) showed that on a  $\log \sigma - \log \dot{\varepsilon}$  plot curves of constant  $\Gamma$  given by equation 4.56 are concave downward (figure 4.3b).

**4.2.2.3 A special form applicable for all temperatures :** The experimental results for  $\Gamma$  may be represented for all temperatures as the product of an athermal strain-rate independent term  $\Gamma^*$  and a thermal strain-rate dependent term :

$$\Gamma = \Gamma^* (\sigma_a / \sigma^*)^{\zeta / \sigma^*} = (\zeta / \sigma^*)^{\eta} (\sigma_a / \sigma^*)^{\zeta / \sigma^*} \quad (4.57)$$

where  $\zeta$  and  $\eta$  are constants (Li, 1981). At low homologous temperatures where  $\sigma_a \approx \sigma^*$ , equation 4.57 reduces to equation 4.55 with  $\sigma_0^* = 0$ .

Korhonen *et al.* (1985b) investigated equation 4.57 in detail and reformulated it in terms of  $\dot{\varepsilon}$ . Plotting curves of constant  $\sigma^*$  in  $\log \Gamma - \log \dot{\varepsilon}$  space they found a scaling behaviour similar to that observed for constant  $\sigma^*$  curves in  $\log \sigma - \log \dot{\varepsilon}$  space (figure 4.4a). This suggested that

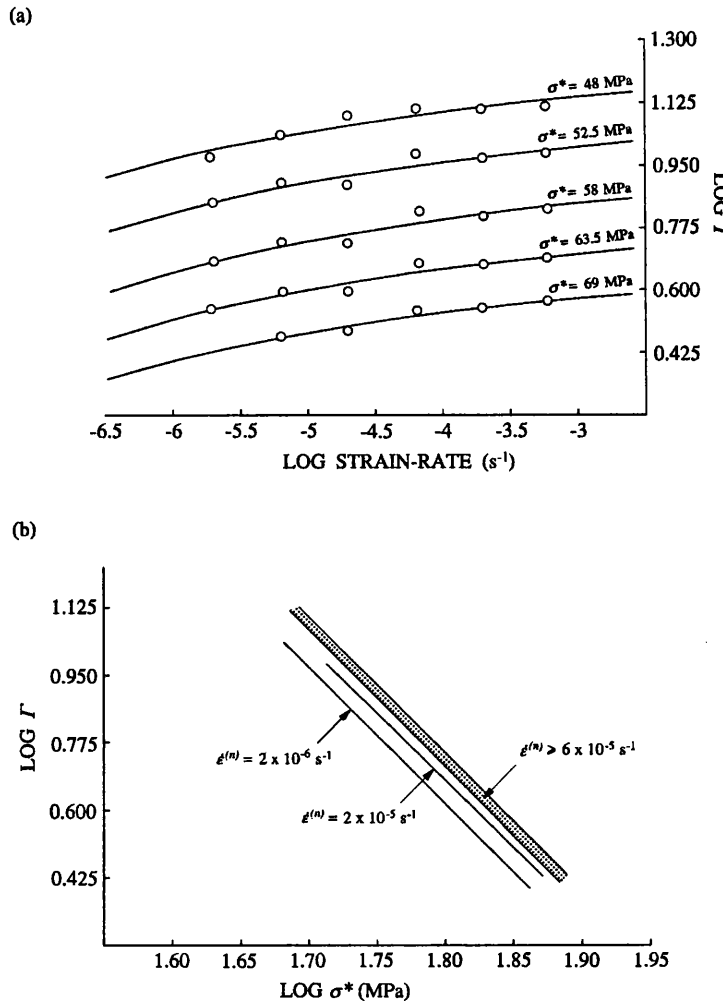


FIG. 4.4. The  $\Gamma$  function at all temperatures. (a) Curves of constant  $\sigma^*$  in  $\log \Gamma / \log \dot{\epsilon}^{(n)}$  space for the room temperature (high homologous temperature) deformation of commercial purity aluminium. A master curve may be constructed by rigid body translation (redrawn after Korhonen *et al.*, 1985b). (b) The dependence of  $\Gamma$  on  $\sigma^*$  in commercial purity aluminium at room temperature and several different strain-rates. The data indicates a power law relationship between the two variables at given strain-rate and thereby confirms the functional form of equation 4.55 (with  $\sigma_0^* = 0$ ) at high strain-rates where  $\Gamma$  is approximately strain-rate independent (redrawn after Korhonen *et al.*, 1985b).

(*cf.* equation 4.24)

$$\Gamma = \Gamma^* \exp [ -(\dot{\alpha}^* / \dot{\alpha})^\Lambda ] \quad (4.58)$$

where (*cf.* equation 4.30)

$$\dot{\alpha}^* = C (\Gamma^*)^{1/\mu^*} \quad (4.59)$$

$\Lambda$  and  $C$  are constants, and  $\mu^*$  is the scaling slope. The parameter  $\dot{\alpha}^*$  provides a measure of the strain-rate sensitivity of work hardening such that if  $\dot{\alpha} \gg \dot{\alpha}^*$  no strain-rate dependence is observed. Hence at high strain-rates even at relatively high temperatures, no strain-rate dependence is expected, and  $\Gamma = \Gamma^*$  should be given by equation 4.55. They confirmed this in high purity aluminium (figure 4.4b) and OFHC copper, finding in common with equation 4.57, that  $\sigma_0^* = 0$ . They suggested that the need to have the  $\sigma_0^*$  parameter implies that the flow stress

in some materials contains an additional component besides that of dislocation interactions. Such interactions may arise for example, between dislocations and grain boundaries (§ 6.3.3), and hence  $\sigma_0^* \neq 0$  may be expected in materials of fine grain-size. The temperature dependence of equation 4.58 has not been investigated but given that an Arrhenius dependence of the rate parameter  $\dot{\alpha}^*$  is probable, Korhonen *et al.* (1985b) suggested (*cf.* equation 4.51)

$$\dot{\alpha}^* = (\Gamma^*)^{m^*} f_0^* \exp(-H^*/RT) \quad (4.60)$$

where  $m^* = 1/\mu^*$ ,  $f_0^*$  is a frequency factor and  $H^*$  is an apparent activation enthalpy.

Equations 4.55, 4.58 and 4.60, which represent Korhonen *et al.*'s special form for  $\Gamma$ , and the alternative expression equation 4.57, are equivalent. Writing equation 4.57 as

$$\Gamma = \Gamma^* (\sigma_a / \sigma^*)^{f(\sigma^*)} \quad (4.61a)$$

or equivalently as

$$\ln(\Gamma^* / \Gamma) = f(\sigma^*) \ln(\sigma_a / \sigma^*) \quad (4.61b)$$

then on substituting the high temperature equation of state (equation 4.24)

$$\ln(\Gamma^* / \Gamma) = f(\sigma^*) [(\dot{\epsilon}^* / \dot{\alpha})^\lambda] \quad (4.62)$$

For a given  $\Gamma^*$  (or  $\sigma^*$ ), and with the definition

$$\dot{\alpha}^* \equiv [f(\sigma^*)]^{1/\lambda} \dot{\epsilon}^* \quad (4.63)$$

equation 4.62 becomes

$$\ln(\Gamma^* / \Gamma) = (\dot{\alpha}^* / \dot{\alpha})^\lambda \quad (4.64)$$

which is the same as equation 4.58 with  $\lambda = \Lambda$ . This latter equality seems to be confirmed by existing experimental results.

## 5 A GENERAL MODEL FOR INELASTIC DEFORMATION

The preceding discussion has been restricted to the case of the stable, homogeneous, grain matrix plastic deformation of an isotropic material under a uniaxially applied differential stress. Any contribution to the deformation from elastic, anelastic or grain boundary sliding processes has been neglected and it has been assumed that time dependent microstructural changes do not exert any influence. All the experiments described above have been conducted and interpreted within the confines of these conditions.

The results are now combined with a simple state variable description of anelastic deformation to delimit a general phenomenological model of inelastic deformation in the absence of grain boundary sliding and time dependent microstructural changes. This model is then extended to the general case of the deformation of an anisotropic material under triaxially applied differential stresses. Finally a micromechanical interpretation of the model is offered.

### 5.1 Description of the general model

The task of devising a general model for inelastic deformation which incorporates the results discussed above, is one of finding a description that will reduce to some anelastic equation of state when anelastic processes dominate the deformation, and to some general plastic equation of state (which under the appropriate conditions must itself reduce to the low and high homologous temperature equations of state, equations 4.37 and 4.24 respectively) when plastic processes dominate it.

**5.1.1 General descriptions of anelastic and of plastic deformation.** The first task is to determine general descriptions of both anelastic and plastic deformation.

*5.1.1.1 Anelastic deformation* : Within the context of the present analysis, anelastic deformation has been phenomenologically defined as that part of the total strain which is both time-dependent and recoverable (§ 2.1). It may therefore be represented by a two branch analogue model (figure 5.1 ; Hart, 1979) containing a viscous element (shown as a dashpot in figure 5.1) and a strain storage element (the spring). The constraint conditions for the deformation of such a model are

$$\sigma = \sigma_1 + \sigma_2 \quad (5.1)$$

$$\dot{\alpha} = \dot{\varepsilon}_1 = \dot{\varepsilon}_2 \quad (5.2)$$

where  $\sigma_1, \sigma_2$  are the differential stresses and  $\dot{\varepsilon}_1, \dot{\varepsilon}_2$  are the strain-rates acting in the respective branches 1 and 2, and  $\sigma$  and  $\dot{\alpha}$  are the total differential stress and total strain-rate respectively. Assuming that the strain storage element is linear and that the viscous element is governed by a power law, then the constitutive relations for the two elements may be written

$$\sigma_1 = \mathcal{M} \varepsilon_1 \quad (5.3)$$

$$\dot{\varepsilon}_2 = A (\sigma_2 / G)^B \quad (5.4)$$

where  $\mathcal{M}, A, B$  and  $G$  (the rigidity modulus) are constants at given mechanical state and temperature. Combining equations 5.1 to 5.4 yields

$$\dot{\alpha} = A [(\sigma - \sigma_1) / G]^B = A [(\sigma - \mathcal{M} \alpha) / G]^B \quad (5.5)$$

where the identity  $\alpha = \varepsilon_1 = \varepsilon_2$  (i.e. the strains in the two branches are equal as follows from

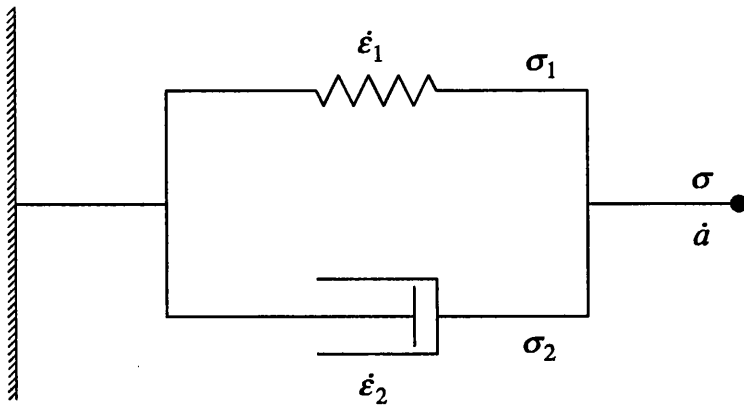


FIG. 5.1. An analogue representation of an anelastic element.

equation 5.2) has been used.

Since the anelastic strain  $a$  is a good state variable then, provided the functional forms of equations 5.3 and 5.4 are valid and the magnitudes of  $\mathcal{M}$ ,  $A$  and  $B$  at given  $\sigma^*$  and  $T$  are independent of the deformation history, equation 5.5 is an equation of state for anelastic deformation. Existing experimental data indicates that these conditions are satisfied (§ 5.1.3.3).

**5.1.1.2 Plastic deformation :** In the previous discussion it has been observed that at  $T < 0.3 T_m$  plastic deformation is characterized by upwardly concave constant  $\sigma^*$  curves in  $\log \sigma - \log \dot{\alpha}$  space, while at  $0.3 < T / T_m < 0.45$  those constant  $\sigma^*$  curves are downwardly concave. The former curves may be described by equation 4.37 and the latter by equation 4.24. It has also been observed that within each temperature regime a Zener-Hollomon type temperature compensated strain-rate can be employed to superpose at least the strain-rate location of curves of a given  $\sigma^*$  (§ 3.3). The implication is therefore, that if a curve of given  $\sigma^*$  is extended over a sufficiently large range of strain-rates, it will change from being concave upward to being concave downward as strain-rate decreases (figure 5.2a). This conclusion is supported by the observed mixed concavity of the  $\sigma^*$  curves generated at  $T \approx 0.3 T_m$  (figure 3.2e), and by the results of Henderson *et al.* (1984) who extended a room temperature constant  $\sigma^*$  curve for commercial purity aluminium to strain-rates of  $10^2 \text{ s}^{-1}$  and found that the concave downward curve obtained under normal laboratory strain-rates became concave upward at higher strain-rates (figure 5.2b).

Inspection of equation 4.37 (in the form of equation 4.40) shows that it can only describe concave upward curves, and that these curves approach  $\sigma^*$  asymptotically as  $\log \dot{\alpha}$  tends to minus infinity. Similarly equation 4.24 can only describe concave downward curves which approach  $\sigma^*$  asymptotically as  $\log \dot{\alpha}$  tends to infinity. This behaviour suggests that provided the same scheme for assigning a value to  $\sigma^*$  is adopted for both equations, it should be possible to combine them into one equation which has the desired mixed concavity. In selecting a form which had micromechanical significance for the equation of state at low homologous temperatures (§ 4.1.2.2), it was convenient to identify  $\sigma^*$  with the internal stress  $\sigma_a$  (equation 4.38), which at these temperatures is approximately equal to the mechanical threshold stress (*i.e.* the stress at which most of the gliding dislocations in the deforming material can

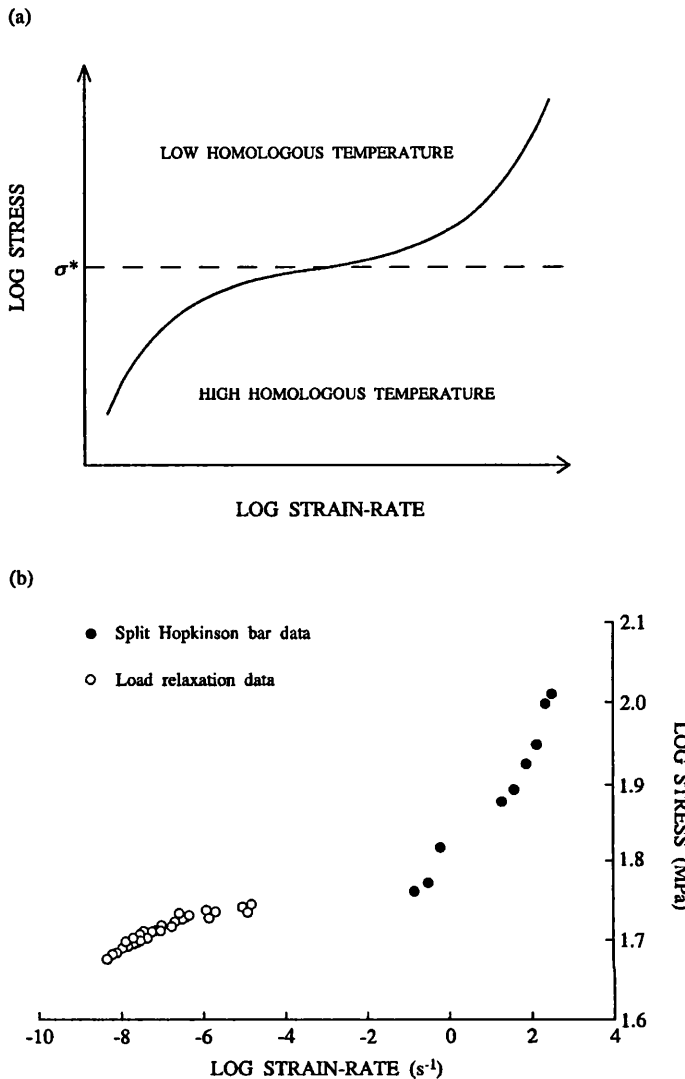


FIG. 5.2. Constant  $\sigma^*$  curves extended over many orders of magnitude of strain-rate. (a) A schematic  $\sigma^*$  curve extended over a sufficiently wide range of strain-rates to show the change in concavity which has previously here been associated with different temperature regimes. To identify  $\sigma^*$  with the mechanical threshold stress is to define  $\sigma^*$  as the stress at the inflection point of the curve. (b) An approximately constant  $\sigma^*$  curve for the room temperature deformation of commercial purity aluminium, showing the mixed concavity suggested by (a). The load relaxation data was obtained by Henderson *et al.* (1984) after constant displacement-rate loading to  $\varepsilon^{(n)} = 0.09$ . The high strain-rate data was obtained using the split Hopkinson bar technique by Hauser (1966) and corresponds to  $\varepsilon^{(n)} = 0.08$  (redrawn after Henderson *et al.*, 1984).

mechanically overcome the obstacles to their motion). Retaining this identification and observing that at stresses below the threshold stress  $\sigma \approx \sigma_a$ , then substituting equations 4.24 and 4.37 into equation 4.38 yields

$$\sigma = G(\dot{\alpha}/\dot{\alpha}^*)^{1/M} + \sigma^* \exp [ -(\dot{\varepsilon}^* / \dot{\alpha})^\lambda ] \quad (5.6)$$

Equation 5.6 then describes plastic deformation at all  $T < 0.45 T_m$ , as has been confirmed by Huang *et al.* (1977 ; 1979) who successfully used it to describe constant  $\sigma^*$  curves generated from Type 316 stainless steel and zircaloy-4 over a wide range of temperatures.

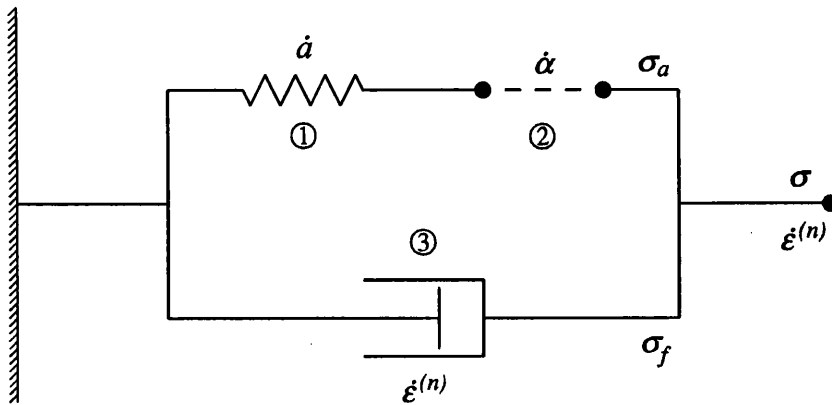


FIG. 5.3. An analogue representation of Hart's (1976) model for grain matrix inelastic deformation.

**5.1.2 Presentation of the model.** The functional similarity of equation 4.40 (the low homologous temperature equation of state) and the first identity of equation 5.5 (the constitutive relation for the viscous element of the anelastic model subject to the stress constraint condition, equation 5.1), allowed Hart (1976) to propose the model illustrated in figure 5.3 as an analogue for a general inelastic deformation. This model consists of three elements labelled 1, 2 and 3, which are conveniently referred to by the names  $a$  - element (or anelastic element),  $\dot{\alpha}$  - element (or plastic element) and  $\dot{\varepsilon}^{(n)}$  - element (or friction element) respectively.

The constraint conditions for the deformation of the model are

$$\sigma = \sigma_a + \sigma_f \quad (5.7)$$

$$\dot{\varepsilon}^{(n)} = \dot{\alpha} + da/dt \quad (5.8)$$

where  $\sigma$  is the applied differential stress (of uniaxial symmetry),  $\sigma_a$  and  $\sigma_f$  are the differential stresses operative in each branch of the model,  $\dot{\varepsilon}^{(n)}$  is the total inelastic strain-rate,  $\dot{\alpha}$  is the strain-rate of the  $\dot{\alpha}$  - element, and  $a$  is the stored but recoverable anelastic strain. It is emphasized that  $\dot{\varepsilon}^{(n)}$  and  $\dot{\alpha}$  are not time derivatives of state quantities but are simply rates. This distinction is made to ensure that the evolution laws for  $a$  and  $\sigma^*$  in the model are independent of the rigid motions of the material, though in the following the dot notation for the time derivative of  $a$  is used for simplicity.

The constitutive relations for the component elements are as follows (with the definition of parameters restated for clarity) :

– the anelastic element is described by equation 5.3

$$\sigma_a = \mathcal{M}a \quad (5.9)$$

where  $\mathcal{M}$  is the anelastic modulus which is in general a function of  $\sigma^*$  and  $T$ .

– the plastic element is described by the high homologous temperature equation of state (equation 4.24) as parameterized for temperature (equation 4.51)

$$\ln(\sigma^*/\sigma_a) = (\dot{\varepsilon}^*/\dot{\alpha})^\lambda \quad (5.10)$$

$$\dot{\varepsilon}^* = (\sigma^*/G)^m f_0 \exp(-H/RT) \quad (5.11)$$

where  $\lambda$ ,  $m$  (the reciprocal of the scaling slope for high temperature constant  $\sigma^*$  curves),  $f_0$  and

$H$  (an activation enthalpy) are material constants,  $G$  is the rigidity modulus (which is temperature dependent) and  $R$  is the gas constant.

– the friction element is described by the low homologous temperature equation of state (equation 4.37)

$$\dot{\varepsilon}^{(n)} = \dot{a}^* (\sigma_f / G)^M \quad (5.12)$$

where  $\dot{a}^*$  is a temperature and mechanical state dependent rate parameter and  $M$  is a material constant.

The  $\sigma^*$  evolution equation for the model is written as

$$d(\ln \sigma^*) / dt = \dot{\alpha} \Gamma(\sigma^*, \sigma_a) - \mathcal{R}(\sigma^*, T) \quad (5.13)$$

where  $\mathcal{R}(\sigma^*, T)$  is an unspecified recovery function (treated as zero throughout the preceding discussion) which incorporates all time dependent microstructural changes that influence the magnitude of  $\sigma^*$ , and  $\Gamma$  is given by equations 4.55, 4.58 and 4.60 which become in the model

$$\Gamma = \Gamma^* \exp [ -(\dot{\alpha}^* / \dot{\alpha})^\Lambda ] \quad (5.14)$$

$$\Gamma^* = [\zeta / (\sigma^* - \sigma_0^*)]^\eta \quad (5.15)$$

$$\dot{\alpha}^* = (\Gamma^*)^{m^*} f_0^* \exp (-H^* / RT) \quad (5.16)$$

where  $\Lambda$ ,  $\zeta$ ,  $\eta$ ,  $\sigma_0^*$ ,  $m^*$  (the reciprocal of the scaling slope for constant  $\sigma^*$  curves in  $\log \Gamma$ - $\log \dot{\alpha}$  space),  $f_0^*$  and  $H^*$  (an activation enthalpy) are material constants.

**5.1.3 Deformation of the model.** Before demonstrating that the model does reduce to the anelastic and plastic equations of state (equations 5.5, 4.37 and 4.24) under the appropriate conditions, it is convenient to consider its response to the conditions imposed in constant stress creep, constant inelastic strain-rate and load relaxation experiments. To simplify the discussion of the first two of these tests, any variation of  $\mathcal{M}$  or  $\dot{a}^*$  during deformation (i.e. with  $\sigma^*$ ) is assumed to be negligible.

**5.1.3.1 Behaviour under the conditions that pertain in deformation experiments :** The response of the model in a constant stress creep test (where  $\sigma$  is greater than the elastic limit and initially  $\sigma_a < \sigma^*$ ) is shown in figure 5.4a-c. In the early stages of the test  $\sigma^* / \sigma_a$  is large so that  $\dot{\alpha} \approx 0$  (equation 5.10). Consequently,  $\dot{\varepsilon}^{(n)} = \dot{a} = \dot{\sigma}_a / \mathcal{M}$  (equations 5.8 and 5.9). While  $\dot{\alpha} \approx 0$ ,  $d\dot{\varepsilon}^{(n)} = da$  and  $\sigma_a$  increases (equation 5.9) so that  $\sigma_f$  decreases (equation 5.7) and with it  $\dot{\varepsilon}^{(n)}$  (equation 5.12). With the increase of  $\sigma_a$ ,  $\sigma^* / \sigma_a$  decreases, eventually becoming small enough for  $\dot{\alpha}$  to be non-negligible. Further increases in  $\sigma_a$  lead to a rapid rise of  $\dot{\alpha}$  (equation 5.10) so that since it must still be that  $\dot{a} = \dot{\sigma}_a / \mathcal{M}$ , as  $\dot{\alpha}$  comes to dominate the left hand side of equation 5.8,  $\dot{\sigma}_a$  must decrease. If steady state creep is attained  $\dot{\sigma}_f = 0$  (equation 5.12) and hence  $\dot{\sigma}_a = 0$  (equation 5.7) and therefore  $\dot{a} = 0$  and  $\dot{\varepsilon}^{(n)} = \dot{\alpha}$ .

The response of the model in a constant inelastic strain-rate test (where initially  $\sigma_a < \sigma^*$ ) is shown in figure 5.4d-e. Throughout the test  $\dot{\varepsilon}^{(n)}$  is constant and so  $\sigma_f$  is constant (equation 5.12). Again initially  $\sigma^* / \sigma_a$  is large so that  $\dot{\alpha} \approx 0$ ,  $d\dot{\varepsilon}^{(n)} = da$  and  $\sigma_a$  increases. The stress / inelastic strain curve is linear and of slope  $\mathcal{M}$  (equation 5.9). Once  $\sigma_a$  has increased sufficiently for  $\dot{\alpha}$  to be non-negligible,  $\dot{\sigma}_a$  again diminishes so that  $\dot{\alpha}$  decreases (equation 5.7), and since the inelastic strain-rate is constant the slope of the stress / inelastic strain curve decreases. In the limit  $\dot{\sigma} = 0$ , then  $\dot{\sigma}_a = 0$  and  $\dot{\varepsilon}^{(n)} = \dot{\alpha}$ .

The response of the model during a load relaxation is given for the case in which the relaxation is conducted after pre-straining to beyond the yield stress. In such circumstances  $\sigma_a$

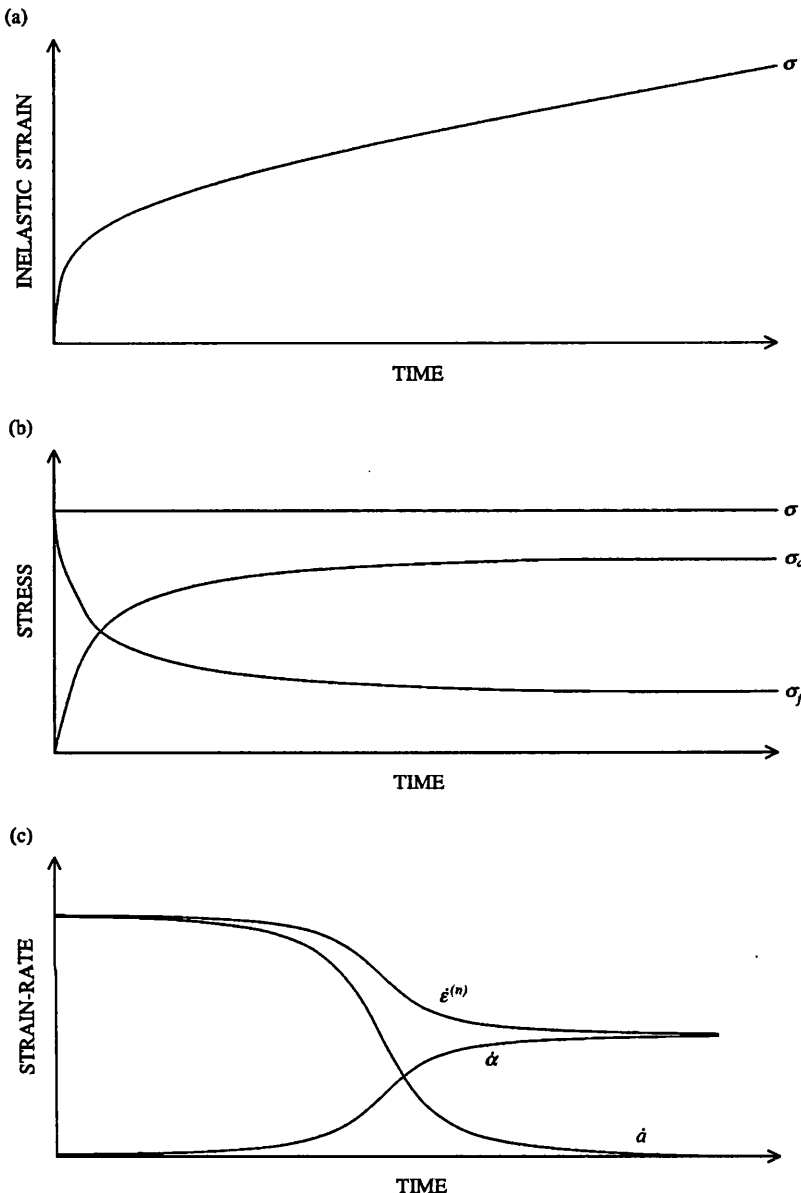


FIG. 5.4. The response of Hart's model in deformation experiments. (a) - (c) Response in a constant stress creep test.

is of sufficient magnitude for  $\dot{\alpha}$  to be non-negligible. For all materials of interest, at these conditions  $\sigma_f \ll \sigma_a$  so that  $\dot{\sigma} \approx \dot{\sigma}_a = \mathcal{M} \dot{\alpha}$  (equations 5.7 and 5.9). During the relaxation

$$\dot{\sigma} = \kappa \dot{\epsilon}^{(n)} \quad (5.17)$$

where  $\kappa$  is an effective modulus for the specimen and load train (§ A2.2.3). Hence substituting for  $\dot{\sigma}$

$$\dot{\alpha} = \kappa \dot{\epsilon}^{(n)} / \mathcal{M} \quad (5.18)$$

which combining with equation 5.8 and rearranging gives

$$\dot{\alpha} = [1 - (\kappa / \mathcal{M})] \dot{\epsilon}^{(n)} \quad (5.19)$$

For most deformation apparatus  $\kappa \ll \mathcal{M}$  so that  $\dot{\alpha} \approx \dot{\epsilon}^{(n)}$ . Even when this is not the case equation 5.19 indicates that on a  $\log \sigma - \log \dot{\epsilon}^{(n)}$  plot,  $\log \dot{\alpha}$  differs from  $\log \dot{\epsilon}^{(n)}$  only by a constant (i.e.  $\log [1 - (\kappa / \mathcal{M})]$ ) and hence the shape of the relaxation curves is unaffected. It

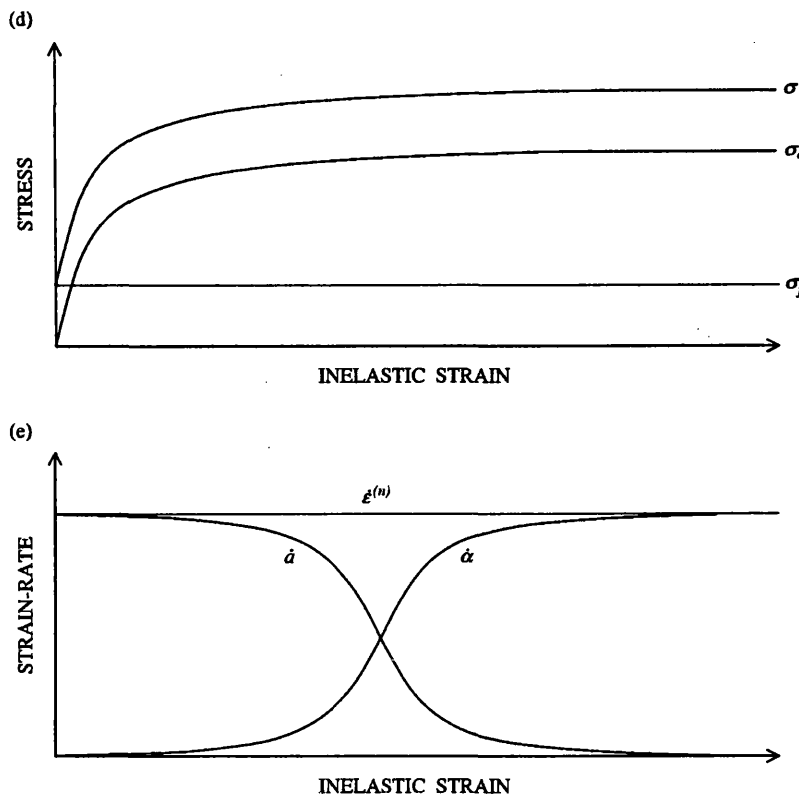


FIG. 5.4 contd. (d) - (e) Response of Hart's deformation model in a constant inelastic strain-rate experiment.

is this observation which allowed the effect of anelasticity to be ignored in the experiments described above (§ 3 and § 4).

The response of the model during a load relaxation conducted when  $\sigma_a$  is not much greater than  $\sigma_f$  (i.e. when  $\dot{\alpha} \approx 0$  throughout pre-straining) is considered below (§ 6.1.3.5).

**5.1.3.2 Anelastic and plastic behaviour :** The general deformation response of the model is illustrated by its behaviour in the differential stress regimes  $\sigma_a \ll \sigma^*$ ,  $\sigma < \sigma^*$  and  $\sigma > \sigma^*$ .

For  $\sigma_a \ll \sigma^*$  then  $\dot{\alpha}$  is negligibly small (equation 5.10). Under these conditions the plastic element is effectively frozen and the model reduces to the anelastic analogue model shown in figure 5.1. The constitutive behaviour is, with  $\dot{\alpha} = 0$  and equations 5.7, 5.8 and 5.12

$$\dot{\alpha} = \dot{\alpha}^* [(\sigma - \sigma_a) / G]^M = \dot{\alpha}^* [(\sigma - \mathcal{M}a) / G]^M \quad (5.20)$$

which is the same as the anelastic equation of state (equation 5.5, with  $\dot{\alpha}^* = A$  and  $M = B$ ).

At larger stresses (i.e. at stresses large enough for  $\dot{\alpha}$  to be non-negligible) for all materials of interest,  $\sigma_f \ll \sigma_a$  and within an inelastic strain of 0.01,  $\dot{\alpha} \ll \dot{\alpha}^*$  (cf. figures 5.4c,e). Under such circumstances  $\dot{\alpha} \approx \dot{\varepsilon}^{(n)}$ , so that on rearranging equations 5.10 and 5.12 for  $\sigma_a$  and  $\sigma_f$  respectively, and substituting equation 5.7, then

$$\sigma = G(\dot{\alpha} / \dot{\alpha}^*)^{1/M} + \sigma^* \exp [ -(\dot{\varepsilon}^* / \dot{\alpha})^\lambda ] \quad (5.21)$$

which is the equation for a general plastic deformation (equation 5.6). The behaviour of equation 5.21 is shown graphically in figure 5.5. For  $\sigma < \sigma^*$  then with  $\sigma_f \ll \sigma_a$  (or alternatively with the observation that this stress state pertains when  $\dot{\alpha}$  is relatively small) equation 5.21 becomes

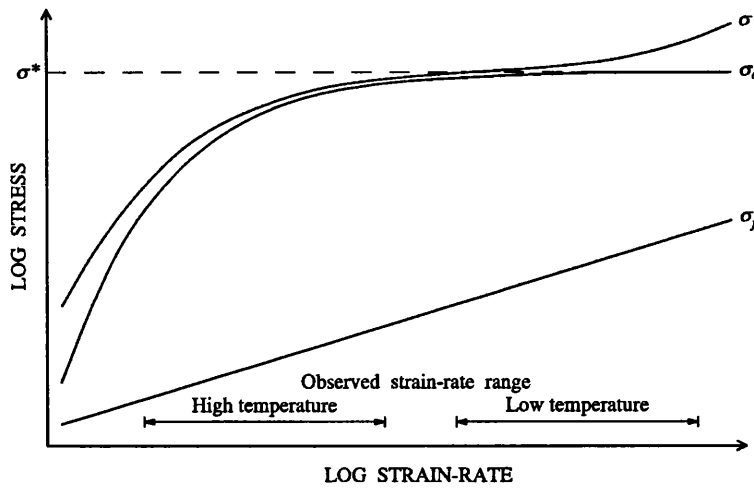


FIG. 5.5. A schematic representation of the strain-rate dependence of the flow stress at given  $\sigma^*$  as implied by equation 5.21 representing general plastic deformation (redrawn after Hart, 1976).

$$\sigma \approx \sigma^* \exp [ -(\dot{\varepsilon}^* / \dot{\alpha})^\lambda ] \quad (5.22)$$

which is the high homologous temperature plastic equation of state (equation 4.24). Hence under these conditions the plastic element controls the rate of deformation. For  $\sigma > \sigma^*$  then with  $\sigma_a = \sigma^*$  (equation 4.38, or alternatively with the observation that this stress state pertains when  $\dot{\alpha}$  is relatively large) equation 5.21 becomes

$$\sigma = G(\dot{\alpha} / \dot{\alpha}^*)^{1/M} + \sigma^* \quad (5.23)$$

which is the low homologous temperature plastic equation of state (equation 4.37 in the form of equation 4.40). Under these conditions it is the friction element that controls the rate of deformation.

*5.1.3.3 Experimental testing of the model* : Equations 5.20 - 5.23 show that Hart's model does reduce to the expressions proposed for completely anelastic and completely plastic deformation. However, if the model is to provide a satisfactory description of inelastic deformation, it must also be shown that the values of  $\dot{\alpha}^*$  and  $M$  in equation 5.20 are the same (at the appropriate  $\sigma^*$  and  $T$ ) as their values in equation 5.23. Moreover it remains to be shown that the value of  $\mathcal{M}$  at given  $\sigma^*$  and  $T$  is independent of the deformation history *i.e.* that equation 5.20 is an equation of state for anelasticity.

The first of these requirements has been examined using the stress dip test as conducted at  $\sigma \ll \sigma^*$  (Nir *et al.*, 1976). Rewriting equation 5.20 as

$$\dot{\alpha} = \dot{\alpha}^* (\mathcal{M} / G)^M [a_s - a]^M \quad (5.24)$$

where  $a_s = (\sigma / \mathcal{M})$  is a saturation anelastic strain for given stress, then on integrating with respect to time

$$(a_s - a_0)^{1-M} - (a_s - a)^{1-M} = (1 - M) \dot{\alpha}^* (\mathcal{M} / G)^M (t - t_0) \quad (5.25)$$

where  $a_0$  is the anelastic strain at  $t_0$ . Non-linear least squares fitting procedures can then be applied to the recovered strain / time data to determine the values of  $\dot{\alpha}^*$  and  $M$ . Equation 5.25 provides an excellent description of the stress change data obtained from a number of materials (figure 5.6), and the values of  $\dot{\alpha}^*$  and  $M$  determined in this way have been shown to agree

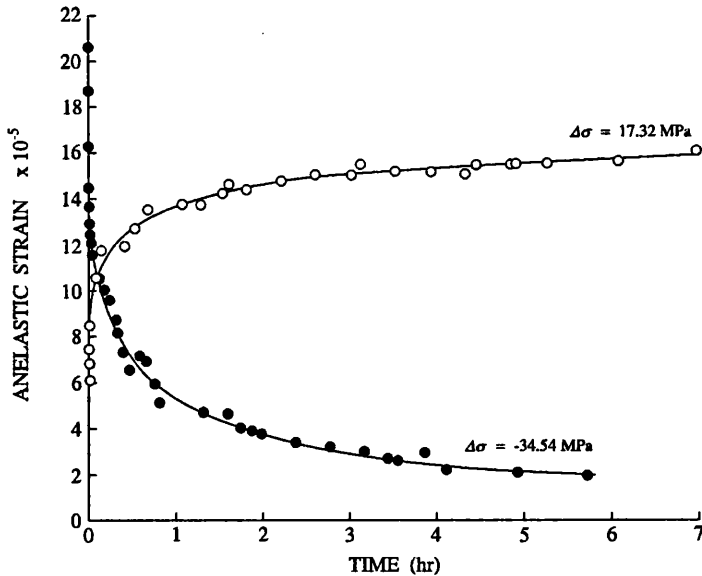


FIG. 5.6. Loading and unloading data for the grain matrix anelastic deformation of Type 316 stainless steel at room temperature after stress changes in a constant stress creep test where  $\sigma < \sigma^*$ . The curves are best fits of equation 5.25 to the data and yield the same values of  $\dot{\alpha}^*$  and  $M$  as determined from load relaxation experiments (redrawn after Nir *et al.*, 1977).

within experimental error, with those obtained from load relaxation tests conducted at similar  $\sigma^*$  (Nir *et al.*, 1977; Suzuki *et al.*, 1982; Suzuki and Okubo, 1984).

Alexopoulos *et al.* (1981) verified (for commercial purity aluminium and Type 304 stainless steel, both at room temperature) the deformation history independence of the magnitude of  $\mathcal{M}$  at given  $\sigma^*$  and  $T$ . They determined  $\mathcal{M}$  from the slope of the stress / inelastic strain curve prior to plastic yielding in constant displacement-rate experiments, and found that repeated loading and unloading where the maximum stress was always less than the plastic yield stress (so that  $\sigma^*$  remained constant) had no effect on  $\mathcal{M}$ . They also verified that  $\mathcal{M}$  was strain-rate independent.

## 5.2 Extension of Hart's model to the deformation of anisotropic materials in the presence of multiaxial differential stresses and/or large strains

The introduction of a tensorial notation into equations 5.7 - 5.16 makes it possible to consider the potential for extending Hart's uniaxial deformation model to the case of deformation under multiaxially applied differential stresses, and to circumstances where the rigid body motions of the deforming material are non-negligible. By defining a suitable anisotropy tensor, the potential for incorporating material anisotropy into the model may also be investigated.

**5.2.1 Multiaxial formulation.** In the small strain, multiaxial extension of Hart's deformation model (e.g. Korhonen *et al.*, 1987), the tensorial inelastic strain-rate is considered to be composed of anelastic and plastic components such that (*cf.* equation 5.8)

$$\dot{\varepsilon}_{ij}^{(n)} = \dot{\alpha}_{ij} + \dot{d}_{ij} \quad (5.26)$$

Deformation is assumed to be incompressible (i.e.  $\dot{\varepsilon}_{kk}^{(n)} = 0$ ) allowing the use of the stress deviator  $s_{ij} = \sigma_{ij} - (1/3) \sigma_{kk} \delta_{ij}$  (where  $\delta_{ij}$  is the Kronecker delta) which, corresponding to equation 5.7, is divided into two components

$$s_{ij} = s_{ij}^{(a)} + s_{ij}^{(f)} \quad (5.27)$$

Given that the deforming material is isotropic, Levy-Mises type flow relations (i.e.  $\dot{\varepsilon}_{ij}^{(n)} = A \sigma_{ij}$ , where  $A$  is some scalar) can be used to describe the interrelationship of corresponding stress and strain-rate components. The flow relations that have been proposed are

$$\begin{aligned} \dot{\varepsilon}_{ij}^{(n)} &= (3/2) (\dot{\varepsilon}^{(n)} / \sigma_f) s_{ij}^{(f)} \\ \dot{\alpha}_{ij} &= (3/2) (\dot{\alpha} / \sigma_a) s_{ij}^{(a)} \\ a_{ij} &= (3/2) (a / \sigma_a) s_{ij}^{(a)} \end{aligned} \quad (5.28)$$

in which the six scalar invariants are defined as

$$\begin{aligned} \sigma &= [(3/2) s_{ij} s_{ij}]^{1/2} ; \quad \dot{\varepsilon}^{(n)} = [(2/3) \dot{\varepsilon}_{ij}^{(n)} \dot{\varepsilon}_{ij}^{(n)}]^{1/2} \\ \sigma_a &= [(3/2) s_{ij}^{(a)} s_{ij}^{(a)}]^{1/2} ; \quad \dot{\alpha} = [(2/3) \dot{\alpha}_{ij} \dot{\alpha}_{ij}]^{1/2} \\ \sigma_f &= [(3/2) s_{ij}^{(f)} s_{ij}^{(f)}]^{1/2} ; \quad a = [(2/3) a_{ij} a_{ij}]^{1/2} \end{aligned} \quad (5.29)$$

These scalar invariants can then be considered as effective stresses and strain-rates which are related to the uniaxial equations 5.9 - 5.16. Equations 5.28, which are of the type employed in the Prandtl-Reuss prescription for plasticity, require experimental verification.

Bammann and Krieg (1987) observed that the multiaxial generalization described above contains some 'quirks' that are not present in the uniaxial model. For example, from the definitions given in equation 5.29 all six scalar invariants must always be positive no matter in which direction  $\dot{\varepsilon}_{ij}^{(n)}$  (or  $s_{ij}$ ) is operating. Another problem arises from the fact that in the multiaxial model, like the uniaxial one, the inelastic strain-rate coincides with the direction of the deviatoric external stress. Bammann and Krieg (1987) present an example to illustrate the absurdities this can lead to. If the stress state given by  $s_{11} = 100$  MPa with all other  $s_{ij}$  equal to zero is applied for a time sufficient for  $\sigma_a$  to rise to 100 MPa, then from equations 5.29,  $\sigma = 122$  MPa and from equations 5.7, 5.12 and 5.28,  $\dot{\varepsilon}_{11}^{(n)} = C (22)^M$  (where  $C$  is a combination of material constants) with all other  $\dot{\varepsilon}_{ij}^{(n)}$  zero. If the stress state is then suddenly changed to  $s_{22} = 0.1$  MPa with all other  $s_{ij}$  zero,  $\sigma = 0.12$  MPa but  $\sigma_a$ , which being an internal stress cannot change instantly, remains 100 MPa. Again from equations 5.7, 5.12 and 5.28,  $\dot{\varepsilon}_{22}^{(n)} = C (100)^M$  with all other  $\dot{\varepsilon}_{ij}^{(n)}$  being zero. For real materials  $M \approx 5$  so that the strain-rate in the 22 - direction is extremely large for a near zero  $s_{22}$  stress.

These problems are peculiar to the multiaxial generalization and can possibly be eliminated by making small changes in the mathematical formulation described above. Their significance remains uncertain given that the multiaxial equations in the form presented here have been successfully applied in a wide range of deformation modelling problems (§ 7.2.1).

**5.2.2 Finite strain formulation.** In accordance with the requirements of any constitutive equation of state, Hart defined his equations to be independent of any rigid body motions of the deforming material. Throughout the preceding discussion such motions have been ignored by making the implicit assumption that they are negligible. However, the analysis is easily extended to accommodate them (Van Arsdale *et al.*, 1980 ; Mukherjee and Chandra, 1984).

**5.2.2.1 Basic definitions :** Referring to the same set of spatially fixed orthogonal cartesian coordinates, the position of a material particle in a reference configuration of a three

dimensional body is specified by coordinates  $X_i$ , and in the current ('deformed') configuration by coordinates  $x_i$ . The displacement vector  $u_i$  is defined as

$$x_i = X_i + u_i \quad (5.30)$$

The velocity of this material point during deformation is denoted by  $v_i$ . The velocity gradient tensor  $L_{ij}$  is split into symmetric and anti-symmetric parts

$$L_{ij} = d_{ij} + \Omega_{ij} \quad (5.31)$$

where the deformation-rate  $d_{ij}$  is the symmetric part

$$d_{ij} = \frac{1}{2} \left( \frac{\partial v_i}{\partial x_j} + \frac{\partial v_j}{\partial x_i} \right) = d_{ji} \quad (5.32)$$

and the spin-rate  $\Omega_{ij}$  is the anti-symmetric part

$$\Omega_{ij} = \frac{1}{2} \left( \frac{\partial v_i}{\partial x_j} - \frac{\partial v_j}{\partial x_i} \right) = -\Omega_{ji} \quad (5.33)$$

To be independent of the rigid motions of the deforming body (*i.e.* to be coordinate frame independent), the constitutive relations must be formulated in terms of  $d_{ij}$ , that is the rate variables which are not time derivatives of anything (the inelastic and plastic strain-rates) must be recast as deformation-rate variables. In addition, time differentiation (of  $\sigma^*$  and  $a_{ij}$ ) must be conducted in a coordinate frame which undergoes the same rigid motions as the body. Following Oldroyd (1950, 1958 ; or see Harris, 1977, pp. 85f) it may easily be shown from the definition of a covariant second rank tensor  $A_{ij}$  (assuming that the tensor has zero weight) that

$$\frac{\delta A_{ij}}{\delta t} = \frac{\partial A_{ij}}{\partial t} + v_k \frac{\partial A_{ij}}{\partial x_k} + \Omega_{jl} A_{il} + \Omega_{ik} A_{kj} + d_{lj} A_{il} + d_{ki} A_{kj} \quad (5.34a)$$

while similarly from the definition of a contravariant second rank tensor, that

$$\frac{\delta A_{ij}}{\delta t} = \frac{\partial A_{ij}}{\partial t} + v_k \frac{\partial A_{ij}}{\partial x_k} + \Omega_{jl} A_{il} + \Omega_{ik} A_{kj} - d_{lj} A_{il} - d_{ki} A_{kj} \quad (5.34b)$$

where  $\delta/\delta t$  is the time derivative (henceforth referred to as the convective derivative) in a coordinate frame which translates, rotates and deforms with the material body. Although, as observed by Oldroyd (1958), the convected derivative is the time derivative which arises most naturally in the development of general frame invariant constitutive relations, the need to distinguish associated covariant and contravariant tensors makes it inconvenient to use in practice. Instead it is more usual to consider a coordinate frame which translates and rotates with the material body but which remains rigid (*i.e.* remains an orthogonal cartesian frame thereby removing the distinction between covariance and contravariance). For such a frame  $d_{ij} = 0$  so that equations 5.34 reduce to

$$\frac{\delta A_{ij}}{\delta t} = \frac{\partial A_{ij}}{\partial t} + v_k \frac{\partial A_{ij}}{\partial x_k} + \Omega_{jl} A_{il} + \Omega_{ik} A_{kj} = -\frac{\mathcal{D}A_{ij}}{\mathcal{D}t} \quad (5.35)$$

where  $\mathcal{D}/\mathcal{D}t$  is the so-called Jaumann (or corotational) derivative. The Jaumann derivative is frame invariant as may be seen by substituting equation 5.35 into either of equations 5.34 (here equation 5.34a)

$$\frac{\delta A_{ij}}{\delta t} = -\frac{\mathcal{D}A_{ij}}{\mathcal{D}t} + d_{lj} A_{il} + d_{ki} A_{kj} \quad (5.36)$$

Hence, provided  $A_{ij}$  (and therefore its convective derivative) is a suitable variable in frame

invariant constitutive relations, and since  $d_{ij}$  is also such a variable, then so must be the Jaumann derivative. This frame invariance means that either the convective or the Jaumann derivative may be used in the constitutive equations, as convenient.

Finally, it is observed that for a scalar variable the Jaumann derivative reduces to the familiar material derivative  $D/Dt$

$$\frac{\mathcal{D}A}{Dt} = \frac{\partial A}{\partial t} + v_k \frac{\partial A}{\partial x_k} = \frac{DA}{Dt} \quad (5.37)$$

(i.e. effectively it reduces to a derivative in a rigid coordinate frame which translates with the material point but does not rotate with it, that is  $\Omega_{ij} = 0$ ).

**5.2.2.2 Formulation of the equations :** From the preceding definitions, the multiaxial equations 5.26 - 5.29 become (again assuming the inelastic deformation is incompressible)

$$d_{ij}^{(n)} = d_{ij}^{(p)} + \dot{a}_{ij} \quad (5.38)$$

$$s_{ij} = s_{ij}^{(a)} + s_{ij}^{(f)} \quad (5.39)$$

$$d_{ij}^{(n)} = (3/2) (d^{(n)} / \sigma_f) s_{ij}^{(f)} \quad (5.40)$$

$$d_{ij}^{(p)} = (3/2) (d^{(p)} / \sigma_a) s_{ij}^{(a)} \quad (5.40)$$

$$a_{ij} = (3/2) (a / \sigma_a) s_{ij}^{(a)}$$

in which the six scalar invariants are defined as

$$\begin{aligned} \sigma &= [(3/2) s_{ij} s_{ij}]^{1/2} & d^{(n)} &= [(2/3) d_{ij}^{(n)} d_{ij}^{(n)}]^{1/2} \\ \sigma_a &= [(3/2) s_{ij}^{(a)} s_{ij}^{(a)}]^{1/2} & d^{(p)} &= [(2/3) d_{ij}^{(p)} d_{ij}^{(p)}]^{1/2} \\ \sigma_f &= [(3/2) s_{ij}^{(f)} s_{ij}^{(f)}]^{1/2} & a &= [(2/3) a_{ij} a_{ij}]^{1/2} \end{aligned} \quad (5.41)$$

with the following modifications to equations 5.9 - 5.16

$$\sigma_a = \mathcal{M}a \quad (5.42)$$

$$\ln(\sigma^* / \sigma_a) = (\dot{\varepsilon}^* / d^{(p)}) \lambda \quad (5.43)$$

$$d^{(n)} = \dot{a}^* (\sigma_f / G)^M \quad (5.44)$$

$$d\sigma^*/dt = \dot{\sigma}^* = d^{(p)} \sigma^* \Gamma(\sigma^*, \sigma_a) - \sigma^* \mathcal{R}(\sigma^*, T) \quad (5.45)$$

where  $\dot{a}_{ij}$  is the Jaumann derivative given by substituting  $a_{ij}$  for  $A_{ij}$  in equation 5.35 and  $\dot{\sigma}^*$  is the material derivative given by substituting  $\sigma^*$  for  $A$  in equation 5.37 (recognizing that in Hart's model  $\sigma^*$  is a scalar). Since the multiaxial formulation used in this case (equations 5.38 - 5.41) is the same as that employed at small strains (equations 5.26 - 5.29), the same problems arise (§ 5.2.1).

**5.2.3 Incorporation of anisotropy.** Hart (1976) provided for the incorporation of anisotropy in his original presentation of the inelastic deformation model. He distinguished two types of anisotropy, the first arising from the anisotropy of the crystal structure and the second from the deformation history. Of these the flow anisotropy that results from the deformation history is explicitly contained within the constitutive equations of the model, and consequently requires no further attention.

To incorporate crystalline anisotropy it is assumed that the components  $a_{ij}$ ,  $\dot{a}_{ij}$  and  $\dot{\varepsilon}_{ij}^{(n)}$  (or  $a_{ij}$ ,  $d_{ij}^{(p)}$  and  $d_{ij}^{(n)}$ ) share the same anisotropy. Then each of the flow equations 5.28 (or 5.40) can be rewritten as anisotropic tensor relations involving the same anisotropy tensor  $K_{ij;kl}$ . This anisotropy tensor is prescribed to have the same properties as those of an anisotropic elastic coefficient tensor for an elastically incompressible material, i.e.

$$K_{ij;kl} = K_{ji;kl} = K_{ij;lk} \quad (5.46a)$$

$$K_{ij;kl} = K_{kl;ij} \quad (5.46b)$$

$$K_{ii;kl} = K_{ij;kk} = 0 \quad (5.46c)$$

Equation 5.46c indicates that in general  $K_{ij;kl}$  does not possess an inverse. However, Hart (1976) defined a semi-inverse  $K_{ij;kl}^*$  which satisfies the relationship

$$K_{ij;kl}^* K_{kl;mn} = (1/2)(\delta_{im}\delta_{jn} + \delta_{in}\delta_{jm}) - (1/3)(\delta_{ij}\delta_{mn}) \quad (5.47)$$

(where  $\delta_{ij}$  is the Kronecker delta) and which acts as an inverse only when the invariant operands are employed. Now the flow equations 5.28 (or 5.40) are of the form

$$x_{ij} = (3/2)(x/X) K_{ij;kl} X_{kl} \quad (5.48a)$$

$$X_{ij} = (2/3)(X/x) K_{ij;kl}^* x_{kl} \quad (5.48b)$$

where the dummy variables  $x_{ij}$  and  $X_{ij}$  represent the appropriate strain or strain-rate variable and the appropriate stress variable respectively. To fix the form of the invariants  $x$  and  $X$  it is necessary that they satisfy the relationship

$$X_{ij} x_{ij} = X x \quad (5.49)$$

Then from equation 5.48a

$$X_{ij} x_{ij} = (x/X)(3/2)(X_{ij} K_{ij;kl} X_{kl}) \quad (5.50)$$

which on comparison with equation 5.49 yields

$$X = [(3/2)(X_{ij} K_{ij;kl} X_{kl})]^{1/2} \quad (5.51a)$$

Similarly

$$x = [(2/3)(x_{ij} K_{ij;kl}^* x_{kl})]^{1/2} \quad (5.51b)$$

Equations 5.51 replace equations 5.29 (or 5.41) and anisotropy is incorporated, excepting the problems raised by Bamann and Krieg (1987) with the multiaxial formulation (§ 5.2.1).

### 5.3 Micromechanical interpretation of the deformation model

The state variable description outlined in the preceding discussion has been developed without recourse to any micromechanical arguments. However, it is possible to establish a connection between the features of the analogue model developed from the analysis (figure 5.3), and the processes occurring during inelastic deformation.

**5.3.1 A qualitative outline of the micromechanical interpretation.** The attempt to find a state variable description of inelastic grain matrix deformation is effectively an attempt to find some description of the collective dislocation flux in a deforming material, and its dependence on the external deformation variables.

**5.3.1.1 General factors influencing the dislocation flux :** The motion of a dislocation within a deforming crystal is limited on the atomic scale by the Peierls-Nabarro hills and on a larger scale by the interaction of the dislocation both with other dislocations (e.g. those moving on other slip systems, caught in dislocation tangles or arranged in subgrain walls) and with second phase particles. In general, the release of dislocations from these obstacles requires some thermally activated process which is to some degree stress assisted. Hence it proves convenient to distinguish

(a) a situation where the applied stress is greater than some critical (threshold) value for stress controlled barrier circumvention so that the barriers present merely a 'friction-type' obstacle, i.e. once the critical stress is attained the dislocation can move and continue to do so at that stress (subject to spatial variations in obstacle size) without thermal assistance and without any

wait-time at the obstacles, and

(b) a situation where the applied stress is less than this critical value and the dislocation must wait for thermal assistance to overcome the obstacle.

In general, the critical stress  $\sigma_L$  required to overcome the Peierls-Nabarro hills is much smaller than the critical stress  $\sigma_B$  required to overcome the long range obstacles. Hence when  $\sigma_L < \sigma < \sigma_B$  the dislocation flux in long range obstacle free regions of crystal exceeds the rate of passage through those barriers. Consequently, the mobile dislocations are forced to pile up behind the barriers, thereby raising the driving force for barrier penetration and generating back stresses (internal stresses) that slow the dislocation flux through the obstacle free regions.

Strong barrier passage at  $T < 0.5 T_m$  is accomplished by (Nabarro, 1989) :

- (a) cutting of repulsive forest dislocations [obstacle controlled dislocation glide],
- (b) cross-slip at some pre-existing constriction such as a unit jog or the node of an attractive junction *i.e.* cross-slip rate controlled by the reassociation of dissociated dislocations prior to the cross-slip step [constriction controlled cross-slip],
- (c) cross-slip at some general point *i.e.* cross-slip rate controlled by the re-dissociation of the dislocation on the new glide plane after the cross-slip step [dissociation controlled cross-slip], and
- (d) climb of dislocations accommodated by the diffusion of vacancies generated during the deformation.

Of these processes (a) and (b) are thermally assisted but stress controlled, depending primarily on the stacking fault energy but being independent of the mobility of lattice vacancy point defects. Process (c) is more strongly thermally assisted but can occur at low temperatures if the stress is sufficiently high. It too is a function of stacking fault energy. Process (d) is stress assisted but thermally controlled, being strongly dependent on the concentration and mobility of lattice vacancies. Reflecting these controls, processes (a) and (b) are more significant at high stresses / low temperatures and require no wait-time at the barrier. At lower stresses, particularly with increasing temperature, process (c) dominates but requires some wait-time. Process (d) becomes rate competitive only at low stresses and high temperatures ( $T > 0.3 T_m$  are required before vacancy mobility is sufficient). It becomes more significant as the vacancies generated by the deformation increase (the thermal equilibrium concentration of vacancies remains too small for it at all  $T < 0.5 T_m$ ) and the barrier wait-time correspondingly decreases.

**5.3.1.2 Comparison with Hart's deformation model :** The three elements of Hart's deformation model may be identified with these influences on the dislocation flux. The friction element represents dislocation motion as restricted by the Peierls-Nabarro hills, the plastic element represents dislocation motion as restricted by the rate of long range barrier circumvention, and the anelastic element represents the dislocation pile-ups behind the long range barriers.

Three stress regimes are of interest (*cf.* § 5.1.3.2). When  $\sigma_L < \sigma \ll \sigma_B$  the dislocations pile up behind the long range barriers but cannot overcome them *i.e.* the plastic element is inactive. A stored strain is produced which is recovered on release of the applied stress and the deformation is completely anelastic. When  $\sigma_B < \sigma$  the strong barriers may be overcome by stress controlled mechanisms (processes a and b) with no wait-time. The friction element is rate-controlling because the plastic element opens as fast as is required, and the deformation is

of low homologous temperature plastic type. The fact that the corresponding material parameters in the anelastic deformation equation (equation 5.20) and the low homologous temperature plastic deformation equation (equation 5.23) have the same value (§ 5.1.3.3), suggests that at these high stresses processes (a) and (b) have no kinetic significance (*i.e.* the rate of deformation is controlled by the resistance posed by the Peierls-Nabarro hills, as at lower stresses). When  $\sigma_L < \sigma < \sigma_B$  the strong barriers can only be overcome by strongly thermally assisted mechanisms (processes c and d). Because these require a wait-time, the plastic element is rate controlling and the deformation is of high homologous temperature plastic type. Process (c) will generally be the most significant control of the kinetics of deformation under these conditions, particularly at the lower temperatures.

The total applied differential stress follows as the sum of the friction stress  $\sigma_f$  and the internal stress of the pile-up  $\sigma_a$ .

**5.3.1.3 Identity of the mechanical state variable :** Given this micromechanical interpretation of Hart's deformation model,  $\sigma^*$  which is associated specifically with the plastic element, must be some significant moment of the spatial distribution of the long range barriers. The identification of  $\sigma^*$  with the threshold stress made previously (§ 5.1.1.2) is entirely consistent with this, given that the threshold stress is taken as the macroscopic stress ( $\sigma_B$ ) required for the stress controlled, strong barrier circumvention processes to be widely viable throughout the deforming material.

In terms of some microstructurally observable feature, at low homologous temperatures the fact that the internal stress  $\sigma_a$  equals the threshold stress allows the use of the familiar expressions (*e.g.* Kocks *et al.*, 1975, pp. 39-40)

$$\sigma^* = \sigma_a = \Phi_1 G b / l = \Phi_2 G b \rho^{1/2} \quad (5.52)$$

where  $\Phi_1$  and  $\Phi_2$  are constants,  $G$  is the rigidity modulus,  $b$  is the Burgers vector,  $l$  is half the average spacing of the obstacles and  $\rho$  is the total (sessile and mobile) dislocation density. Hence in principle,  $\sigma^*$  may be quantified from the dislocation density. At high homologous temperatures where the threshold stress does not equal the internal stress (*i.e.*  $\sigma^* = \sigma_a$  is not true), some inverse correlation between  $\sigma^*$  and 'subgrain' size may be more appropriate, but as yet this has received little attention (although see § 6.1.4 ; Stone, 1991).

**5.3.1.4 Strain hardening behaviour :** The athermal component of the hardening behaviour represents the increasing strength / density of the long range barrier network as the dislocation density increases during deformation. The strain-rate dependent part of the hardening behaviour reflects the mediation of this increased dislocation density by the loss of dislocations during the thermally activated barrier circumventing processes (through for example, the annihilation of opposite dislocations by diffusion aided but deformation driven dislocation climb).

**5.3.2 Quantification of the micromechanical interpretation.** Hart (1984), developing some earlier work (Hart and Solomon, 1973 ; Hart *et al.*, 1975), showed that the micromechanical interpretation of his deformation model can be given a more rigorous basis than that discussed above. To accomplish this he represented the deforming material as a collection of 'slip-zones', defining each slip-zone as a clear region of glide plane bounded at each end by a barrier to dislocation motion. He then considered the dislocation pile-ups behind the barriers using continuum dislocation theory (*e.g.* Hirth and Lothe, 1982, pp. 764f).

**5.3.2.1 Formulation of the problem :** Hart considered the simple case in which the slip-zones belong to a planar array in a single slip system. He took the planar projection through the system which contains the slip direction, and thereby reduced the problem to one of the glide and storage of screw dislocations along one dimensional idealizations of the slip-zones (figure 5.7a). To complete the initial formulation of the problem, he considered the average slip-zone, defined it to be of length  $2l$  with barriers located at  $\pm l$ , and defined  $\mathcal{N}^0$  as the number of slip-zones per unit area of the projection plane,  $G$  as the rigidity modulus and  $b$  as the Burgers vector of the slip system (figure 5.7b).

**5.3.2.2 The static case :** When the dislocations cannot penetrate the barriers at the end of the slip-zone and they have been generated from a source within the zone in pairs of equal and opposite Burgers vector under the action of an applied stress  $\sigma$ , then the pile-up configuration is one of static equilibrium. The equilibrium condition then gives

$$\sigma + \frac{Gb}{2\pi} \int_{-l}^{+l} dx' \frac{\rho(x')}{(x - x')} = 0 \quad (5.53)$$

where  $-l < x < +l$ ,  $\rho(x)$  is the net dislocation density across the slip-zone and the integral is defined in terms of its Cauchy principal value. Solving for  $\rho(x)$

$$\rho(x) = (2\sigma/Gb) \frac{x/l}{[1 - (x/l)^2]} \quad (5.54)$$

(figure 5.7c). The total shear in the zone generated by a dislocation source at the origin is

$$\mathcal{T} = b \int_{-l}^{+l} dx [x \rho(x)] \quad (5.55)$$

which on substituting  $\rho(x)$  from equation 5.54 becomes

$$\mathcal{T} = \pi l^2 \sigma / G \quad (5.56)$$

The total stored strain  $a$  from the pile-up is

$$a = \mathcal{N}^0 \mathcal{T} = \pi l^2 \mathcal{N}^0 (\sigma / G) = \sigma / \mathcal{M} \quad (5.57)$$

where  $\mathcal{M}$  is the anelastic modulus, which is seen to be given by

$$\mathcal{M} = G / (\pi l^2 \mathcal{N}^0) \quad (5.58)$$

**5.3.2.3 The non-zero dislocation flux case :** When the dislocations can penetrate the barriers the pile-up is not static. If  $v(x)$  is the dislocation velocity for positive dislocations at each point of the slip-zone then the positive dislocation flux  $\phi(x)$  past each point is given by

$$\phi(x) = |\rho(x)| v(x) \quad (5.59)$$

Experimental results (Gupta and Li, 1970) show that  $v(x)$  depends upon the local effective friction stress  $\sigma_f$  so that equation 5.59 may be written

$$\phi(x) = |\rho(x)| v[\sigma_f(x)] \quad (5.60)$$

where (cf. § 6.2.2.1)

$$v[\sigma_f(x)] = v_0 (\sigma_f / G)^{M^*} \quad (5.61)$$

in which  $v_0$  and  $M^*$  are material constants. Since for real materials  $M^* > 5$ , then effectively  $v = 0$  for  $\sigma_f < \sigma_c$  where  $\sigma_c$  is a critical value of stress, and  $v$  can take any required value for  $\sigma_f = \sigma_c$  (Coulomb friction). This implies that during flow  $\sigma_f$  is constant over the interval  $-l$  to  $+l$ , which is significant because by writing

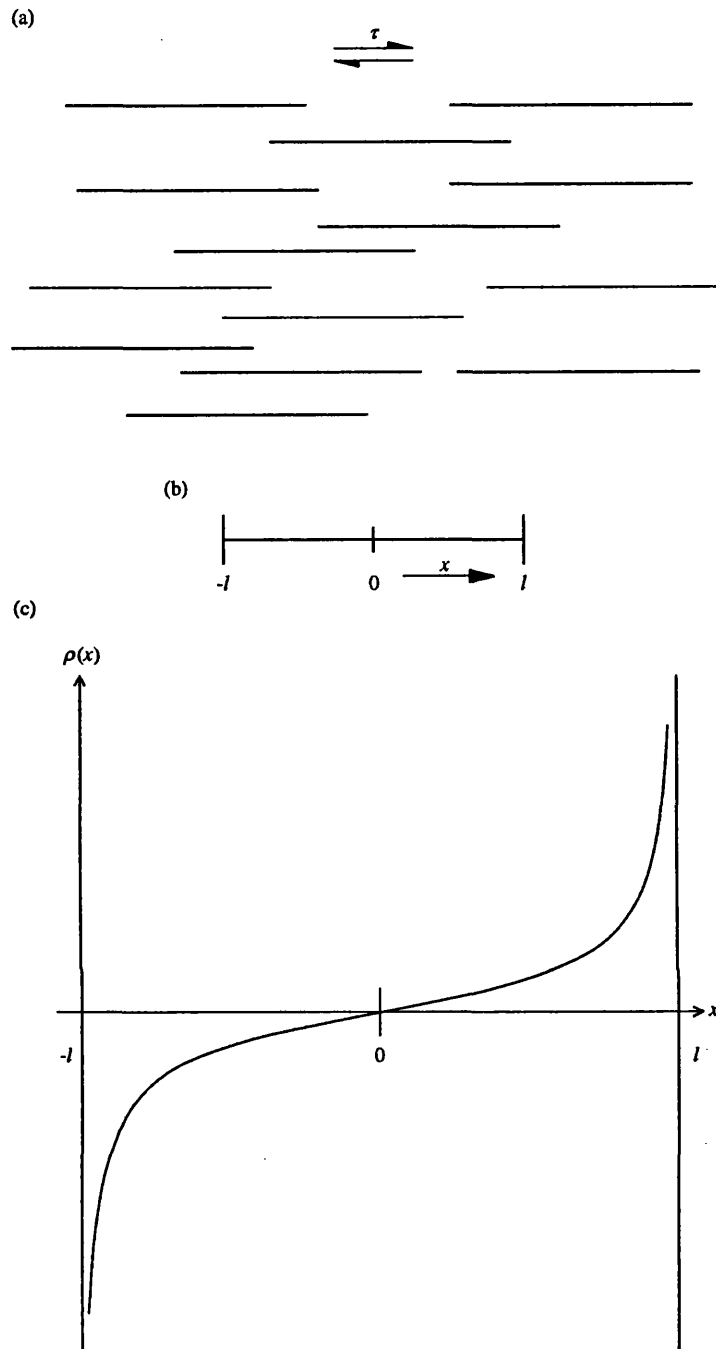


FIG. 5.7. Hart's micromechanical interpretation of his model. (a) A schematic distribution of slip-zones intersecting a plane of projection. The slip-zones are under a planar shear stress  $\tau$  with Burgers vector  $b$  in the plane. (b) The geometry of an average slip-zone as used for the model computations. (c) The net dislocation density  $\rho(x)$  across a slip-zone which is under an applied stress (all figures redrawn after Hart, 1984 and Jackson *et al.*, 1981).

$$\sigma = \sigma_a + \sigma_f \quad (5.62)$$

then if  $\sigma_f$  is independent of  $x$ , it follows that  $\sigma_a$  is independent of  $x$  (for  $\sigma$  is constant in this analysis). This in turn means that the dislocation distribution  $\rho(x)$  is a static equilibrium distribution *i.e.* it is independent of the dislocation flux and a function only of  $\sigma$  or if preferred  $\sigma_a$ .

The Coulomb friction nature of equation 5.61 may easily be demonstrated for the special case of a stationary dislocation flux (*i.e.*  $\phi(x)$  has a constant value  $\phi$  for all  $x$ ) by rearranging it and substituting equation 5.60

$$(\sigma_f/G) = [\phi / (v_0 |\rho(x)|)]^{1/M^*} \quad (5.63)$$

Using values of  $M^* = 7$  and the static equilibrium values of  $\rho(x)$  given by equation 5.54, then equation 5.63 shows  $\sigma_f$  to be independent of  $x$  (except near the barriers where the slip-zone model is too simple to describe accurately the behaviour).

**5.3.2.4 The static case revisited :** The observation that the distribution of dislocations is a static equilibrium one for at least the case of a stationary state of dislocation flux, suggests that the static equations 5.53 - 5.58 may be recast in terms of  $\sigma_a$  rather than  $\sigma$ . In this way equation 5.57 becomes

$$\sigma_a = \mathcal{M}a \quad (5.64)$$

which is the constitutive relation for the anelastic element of Hart's deformation model (equation 5.9).

Constraints on the form of the constitutive relation for the plastic element may also be attained by a consideration of the force  $\mathcal{F}$  acting on the blocked dislocation at either end of the pile-up. This is given by the work per unit edge length required to extend the length of the slip-zone per unit amount

$$\mathcal{F} = (\pi/2)(l/G)\sigma_a^2 \quad (5.65)$$

Introducing the parameter  $\mathcal{F}^*$  to characterize the critical strength of the barrier then the critical value  $\sigma^*$  of  $\sigma_a$  is

$$\mathcal{F}^* = (\pi/2)(l/G)\sigma^{*2} \quad (5.66)$$

If as seems reasonable, the rate of barrier penetration depends upon the ratio  $\mathcal{F}/\mathcal{F}^*$ , then

$$(\mathcal{F}/\mathcal{F}^*) = (\sigma_a/\sigma^*)^2 \quad (5.67)$$

so that the strain-rate for the plastic element should be a function of  $(\sigma_a/\sigma^*)$  as indicated by equation 5.10.

**5.3.2.5 The constraint equations :** The strain-rate constraint equation for Hart's deformation model (equation 5.8) can be derived from this slip-zone model. To do this Hart (1984) considered the general case of non-stationary dislocation flux.

The local dislocation flux is defined in equation 5.59. The value of  $\phi$  at the barriers represents the time rate of dislocation passage through the barriers. This can be expressed as an effective plastic strain-rate  $\dot{\alpha}$  given by

$$\dot{\alpha} = 2\mathcal{N}^0 b l \phi \quad (5.68)$$

The observable macroscopic strain-rate  $\dot{\varepsilon}^{(n)}$  is given by

$$\dot{\varepsilon}^{(n)} = \mathcal{N}^0 b \int_{-l}^{+l} dx |\rho(x)| v(x) \quad (5.69)$$

whilst the stored anelastic strain  $a$  has already been determined as (equation 5.57)

$$a = \mathcal{N}^0 \mathcal{T} = \mathcal{N}^0 b \int_{-l}^{+l} dx [x \rho(x)] \quad (5.70)$$

The equation for the conservation of dislocations is

$$\frac{d\phi(x)}{dx} + \frac{d\rho(x)}{dt} = 0 \quad (5.71)$$

Multiplying equation 5.71 by  $x$  and integrating from  $-l$  to  $+l$  then

$$\int_{-l}^{+l} dx \phi(x) = \int_{-l}^{+l} dx x \frac{d\rho(x)}{dt} + \int_{-l}^{+l} dx \frac{d}{dx} [x\phi(x)] + \int_{-l}^{+l} dx x\rho(x) + 2l\phi \quad (5.72)$$

where  $\phi$  is the value of  $\phi(x)$  at the barrier, and where use has been made of the identity

$$\frac{d}{dt} [x\phi(x)] = \phi(x) + x \frac{d\phi(x)}{dx} \quad (5.73)$$

When equation 5.72 is multiplied by  $\mathcal{N}^0 b$ , and equations 5.68 - 5.70 are used then

$$\dot{\varepsilon}^{(n)} = \dot{\alpha} + da/dt \quad (5.74)$$

which is equation 5.8.

The stress constraint equation in Hart's deformation model (equation 5.5) has already been demonstrated for the slip-zone model by showing that the dislocation velocity function (equation 5.61) is approximately a Coulomb friction law (*cf.* equation 5.63).

## 6 REFINEMENTS AND EXTENSIONS OF THE GENERAL MODEL FOR INELASTIC DEFORMATION

The general model for inelastic deformation introduced by Hart (1976) and described above (§ 5), successfully accounts for the principal features of anelastic and plastic deformation at temperatures of less than  $0.45 T_m$ . However, there remain a number of problems which must be addressed before the model can be said to provide a complete description of inelastic deformation :

- (a) the description of deformation occurring near to the plastic yield point,
- (b) the temperature and mechanical state dependencies of the anelastic modulus  $\mathcal{M}$  (equation 5.9), and of  $\dot{\alpha}^*$  and  $M$  in the constitutive relation for the friction element (equation 5.12),
- (c) the effects of as yet unconsidered aspects of both the deforming material (*e.g.* the influence of solute impurities, finely dispersed particles, grain-size) and the deformation environment (*e.g.* pressure, the presence of fluids),
- (d) the description of deformation at temperatures greater than  $0.45 T_m$ , and
- (e) the description of polyphase deformation and of inelastic deformation which is in other ways inhomogeneous.

In the following discussion each of these issues is considered in turn. The refinements and extensions which have been applied to the model since its formulation are described, and the potential for accommodating the remaining problems is evaluated.

### 6.1 Deformation occurring near to plastic yielding

Although Hart's deformation model accounts for purely anelastic and purely plastic deformation (§ 5.1.3.2), it is found to be less accurate in its description of deformation occurring near to the plastic yield point. In real materials plastic yielding is much less rapid than predicted by the model (figure 6.1), real materials may accumulate some irrecoverable strain before they plastically yield and, the Bauschinger effect (where a previously deformed specimen is stronger when reloaded in the forward direction than when reloaded in the reverse direction) is much larger in real materials than predicted by the model (the model predicts some Bauschinger effect via the weak dependence of the friction stress  $\sigma_f$  on the strain-rate, which may cause some of the 'anelastic' strain to be trapped during complete unloading and then released as the loading is reversed).

To accommodate these problems a 'refined Hart model' has been proposed in which the anelastic element in the original model is replaced by a compound element. The basis for the modification is a more precise phenomenological description of the deformation occurring prior to plastic yielding.

**6.1.1 Basis for the refined inelastic deformation model.** Phenomenologically, the near yield point behaviour of real materials is conveniently described with reference to the stress / strain loops produced by loading and unloading in a constant displacement-rate test. Several such loops are shown schematically in figure 6.2a. At stresses below the elastic limit  $\sigma_E$ , the material deforms in a fully time independent elastic manner, while at higher stresses the presence of a

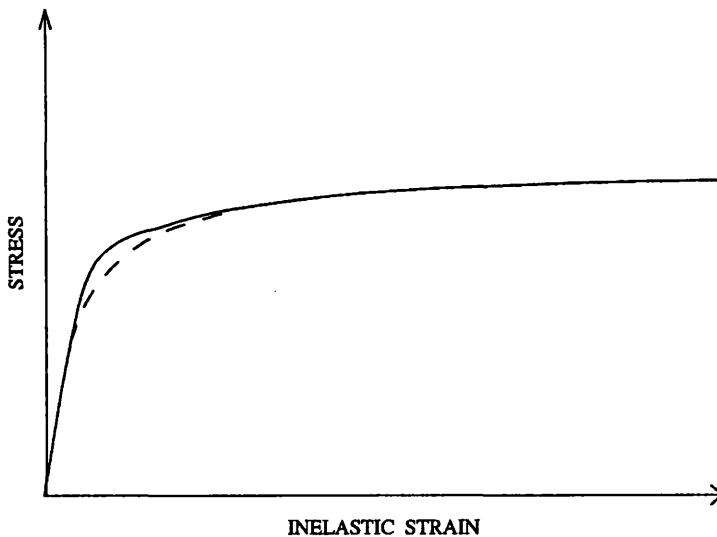


FIG. 6.1. Schematic comparison of real material behaviour (dashed curve) with that predicted by Hart's inelastic deformation model (solid curve) in a constant displacement-rate test.

time dependent inelastic strain results in the formation of a hysteresis loop. For stresses below the so-called anelastic limit  $\sigma_A$ , the hysteresis loops are closed reflecting the fact that the inelastic deformation is a completely recoverable anelastic strain, while at stresses greater than  $\sigma_A$  the hysteresis loops cease to be closed indicating the existence of an irrecoverable plastic strain. This plastic strain is conveniently described as microplastic when it is produced at stresses less than the yield stress  $\sigma_Y$ , and as macroplastic at greater stresses. Thus the stress / strain curve produced in a constant displacement-rate test exhibits four regions demarcated by  $\sigma_E$ ,  $\sigma_A$  and  $\sigma_Y$  (figure 6.2b). They are region I – elastic ; region II – anelastic ; region III – microplastic and ; region IV – macroplastic. Comparison with figure 6.1 shows that the only difference between the behaviour of real materials and Hart's model is in the microplastic region which does not exist in the model.

From a micromechanical perspective, the fact that the problems with Hart's model seem to originate at pre-yield strains, suggests that Hart's (1984) dislocation pile-up interpretation of inelastic deformation under those conditions (§ 5.3) is oversimplified. In that interpretation, the existence of *well defined* pile-ups on single slip planes was assumed. Although such structures are observed in many materials, in many others where easy cross-slip can occur, they are not. However, as observed by Jackson *et al.* (1981) some sort of dislocation pile-up is a prerequisite for plastic yielding behaviour, and so the essential features of a stress concentration leading to barrier penetration will remain whether or not that pile-up is a simple two-dimensional structure or an extended dislocation cloud. A second approximation of Hart's interpretation is that the inelastic behaviour can be explained with an array of equal strength ( $\sigma^*$ ) barriers to dislocation motion. The fact that the barrier structure results from prior macroplastic flow and that the self-correcting nature of such flow tends to limit structural inhomogeneity, suggests that this is a reasonable approximation at large (greater than 0.01) strains. However, there remains the possibility that weak barriers to dislocation motion within

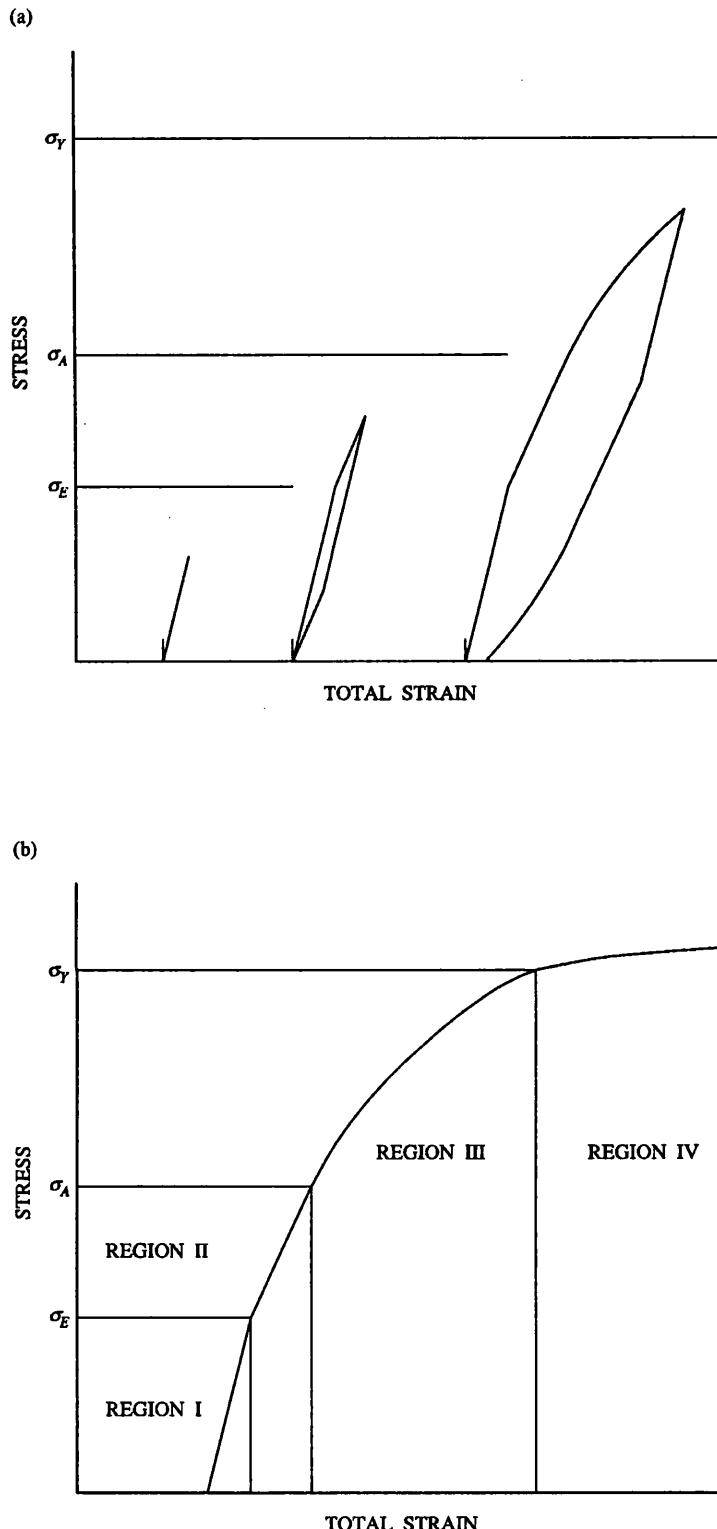


FIG. 6.2. Real material behaviour at stresses near the macroplastic yield point. (a) A schematic representation of three constant displacement-rate stress / strain curves with the peak stress below the elastic limit, the anelastic limit and the macroplastic yield stress respectively. (b) Demarcation of a constant displacement-rate stress / strain curve into elastic (I), anelastic (II), microplastic (III) and macroplastic (IV) regions on the basis of the behaviour illustrated in (a).

Hart's idealized slip-zones influence the deformation under conditions where macroplastic flow cannot take place.

The effect of introducing weak barriers into Hart's slip-zones may be qualitatively assessed. Under the action of an applied differential stress the static equilibrium dislocation density across a slip-zone is shown in figure 6.3a (cf. figure 5.7c). This shows the piling up of dislocations at low stresses ( $\sigma < \sigma_A$ ) behind the weak barriers, a phase of deformation which has the same linear anelastic characteristics as observed in the original Hart model. At sufficiently high stress (*i.e.*  $\sigma > \sigma_A$ ) the dislocations are able to surmount the weak barriers while being unable (if  $\sigma < \sigma_Y$ ) to penetrate the strong ones at either end of the slip-zone. In this way microplastic deformation is produced. At still higher stresses (*i.e.*  $\sigma > \sigma_Y$ ) the strong barriers can be overcome and macroplastic deformation occurs as described previously.

**6.1.2 Outline of the refined Hart model.** The weak barrier model has the important characteristic of leaving untouched those parts of the deformation that Hart's model describes well *i.e.* the anelastic and macroplastic regions of figure 6.2b.

In Hart's original model there was only one type of dislocation pile-up, and hence only one pile-up element with one anelastic state variable to characterize it, was required. In the weak barrier model there are two types of pile-up and consequently two pile-up elements with two anelastic state variables are required. In addition an element for weak barrier passage, with associated internal state variable, is needed.

A suitable modification of Hart's model has been proposed by Jackson *et al.* (1981). They replaced the anelastic element of Hart with three new elements, leaving Hart's other two elements unmodified (figure 6.3b). The long range dislocation pile-up distribution is represented by the  $a_1$  - element, the short range pile-ups are represented by the  $a_1$  - and  $a_2$  - elements acting together, and the passage through the weak barriers is represented by the  $\alpha_2$  - element. The constraint equations for the deformation of the model (replacing equations 5.7 and 5.8) are

$$\sigma = \sigma_f + \sigma_a = \sigma_f + \sigma_{a1} + \sigma_{a2} \quad (6.1)$$

$$\dot{\varepsilon}^{(n)} = \dot{\alpha}_1 + \dot{a}_1 = \dot{\alpha}_1 + \dot{a}_2 + \dot{a}_2 \quad (6.2)$$

The constitutive relations for the anelastic elements are

$$\sigma_{a1} = \mathcal{M}_1 a_1 \quad (6.3)$$

$$\sigma_{a2} = \mathcal{M}_2 a_2 \quad (6.4)$$

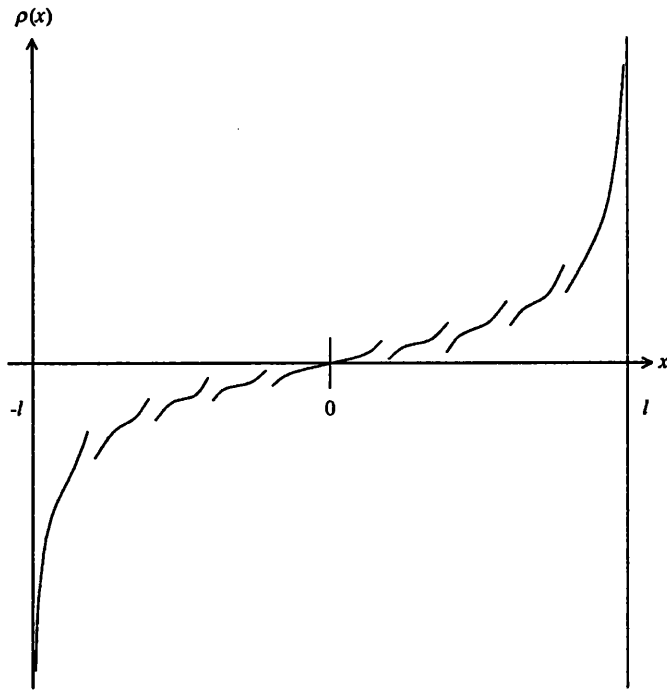
where  $\mathcal{M}_1$  and  $\mathcal{M}_2$  are two new anelastic moduli which are in general dependent upon  $\sigma^*$  and  $T$ . The constitutive relation for the microplastic element is assumed to be of the same form as that of Hart's plastic element (equations 5.10 and 5.11) since both involve leakage through barriers *i.e.*

$$\ln(\sigma_2^* / \sigma_{a2}) = (\dot{\varepsilon}_2^* / \dot{\alpha}_2)^{\lambda_2} \quad (6.5)$$

$$\dot{\varepsilon}_2^* = (\sigma_2^* / G)^{m_2} f_2 \exp(-H/RT) \quad (6.6)$$

In this way the state variable  $\sigma_2^*$  characterizes the weak barriers. The remaining two elements have the same constitutive relations as in Hart's original model (*i.e.* equations 5.10 - 5.16). All that remains to be defined is the  $\sigma_2^*$  evolution equation. Given that the weak barriers have a distribution of strengths, the evolution of  $\sigma_2^*$  must reflect the sampling of progressively stronger

(a)



(b)

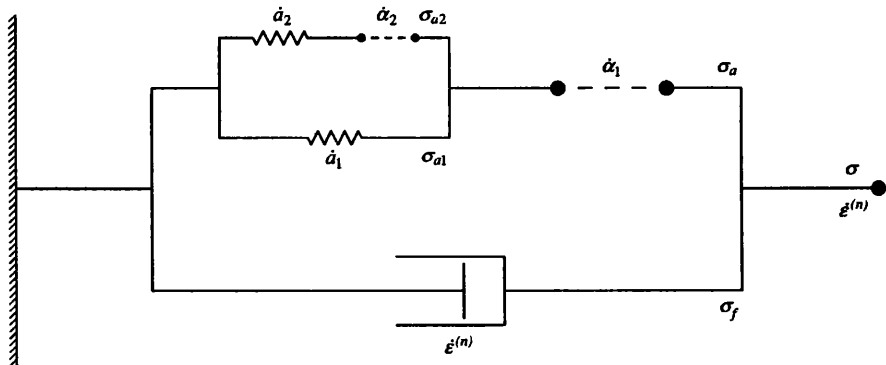


FIG. 6.3. Modifications of Hart's inelastic deformation model which improve the description of near yield behaviour. (a) The effect of introducing weak barriers to dislocation motion on the dislocation density across one of Hart's slip-zones (cf. figure 5.7c ; redrawn after Jackson *et al.*, 1981). (b) An analogue representation of the refined Hart model.

barriers as deformation proceeds.  $\sigma_2^*$  is therefore a function of stress. Jackson *et al.* (1981) found that for high purity aluminium at 25°C

$$\sigma_2^* = \sigma_{a2} \exp(c_2 \sigma_{a2}) \quad (6.7)$$

where  $c_2$  is a material constant. Equation 6.7 implies that the weakest barriers to dislocation are very weak ( $\sigma_2^*$  is very small as  $\sigma_{a2} \rightarrow 0$ ). Its difference from the  $\sigma^*$  evolution equations 5.14 - 5.16 reflects the fact that the latter represent real microstructural change during deformation and not merely sampling effects.

Equations 6.1 - 6.7 are presented in uniaxial form, but they may be generalized into a multiaxial formulation which also includes anisotropy by following the same procedures as outlined in § 5.2.

**6.1.3 The deformation behaviour of the refined model.** The refinements to Hart's model have been introduced from a qualitative consideration of the deformation processes occurring near to the plastic yield point. It is therefore necessary to verify that the constitutive relations can quantitatively describe real deformation under conditions where the new elements contribute significantly to the material behaviour, and that those relations are equations of state. To this end the response of the refined model under various loading conditions is considered and compared with experimental results.

**6.1.3.1 Expressions for  $\sigma_{a2}$  and  $\dot{\alpha}_2$ :** The additional branch in the refined model complicates the prediction of its deformation response. Hence in order to simplify the following discussion expressions for  $\sigma_{a2}$  and  $\dot{\alpha}_2$  are derived.

From equations 6.1 and 6.3

$$\sigma_{a2} = \sigma - \sigma_f - \mathcal{M}_1 a_1 \quad (6.8)$$

Rearranging equation 6.2 for  $a_1$ , integrating and substituting the result into equation 6.8

$$\sigma_{a2} = \sigma - \sigma_f - \mathcal{M}_1 \left( \dot{\varepsilon}^{(n)} - \alpha_0 - \int_0^t \dot{\alpha}_1 dt \right) \quad (6.9)$$

where  $\alpha_1$  is the sum of the macroplastic strain accumulated prior to ( $\alpha_0$ ) and during the deformation.

From equations 6.2 and 6.4

$$\dot{\alpha}_2 = \dot{\varepsilon}^{(n)} - \dot{\alpha}_1 - (\dot{\sigma}_{a2} / \mathcal{M}_2) \quad (6.10)$$

Differentiating equation 6.9 to find  $\dot{\sigma}_{a2}$  and substituting the result into equation 6.10, then after rearranging

$$\dot{\alpha}_2 = \{(\dot{\varepsilon}^{(n)} - \dot{\alpha}_1)[1 + (\mathcal{M}_1 / \mathcal{M}_2)]\} - [(\dot{\sigma} - \dot{\sigma}_f) / \mathcal{M}_2] \quad (6.11)$$

**6.1.3.2 Constant inelastic strain-rate test:** Figure 6.4a,b shows the response of the refined model in a constant inelastic strain-rate test. These figures have been deduced in the same manner as used to determine the response of the original model under the same loading conditions (§ 5.1.3.1).

At the point of inelastic yielding ( $\sigma = \sigma_E$ ) all the strain-rates are zero. After yielding  $\dot{\varepsilon}^{(n)}$  is constant and so from equation 5.12,  $\sigma_f$  is constant. Hence as  $\sigma$  increases  $\sigma_a = \sigma_{a1} + \sigma_{a2}$  increases (equation 6.1). While  $(\sigma^* / \sigma_a)$  and  $(\sigma_2^* / \sigma_{a2})$  remain large, equations 5.10 and 6.5 ensure that  $\dot{\alpha}_1 \approx \dot{\alpha}_2 \approx 0$ . Therefore from equation 6.2

$$\dot{\varepsilon}^{(n)} = \dot{\alpha}_1 = \dot{\alpha}_2 = \text{constant} \quad (6.12)$$

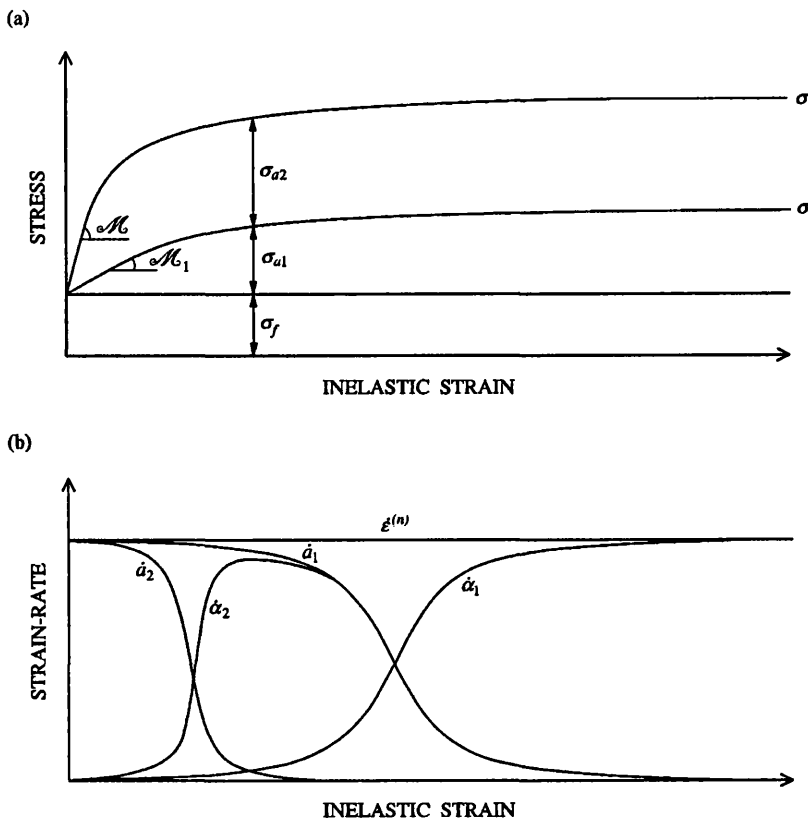


FIG. 6.4. The response of the refined Hart model in a constant inelastic strain-rate test.

and the deformation is purely anelastic. From equations 5.12, 6.1 and 6.12, the purely anelastic response of the refined model is

$$\dot{a}_1 = \dot{a}_2 = \dot{a}^* [(\sigma - \sigma_{a1} - \sigma_{a2}) / G]^M \quad (6.13)$$

which is the same as equation 5.20.

During the anelastic deformation phase, from equations 6.1, 6.3 and 6.4

$$\sigma = \mathcal{M}_1 a_1 + \mathcal{M}_2 a_2 + \sigma_f \quad (6.14)$$

Differentiating

$$\frac{d\sigma}{d\epsilon^{(n)}} = \mathcal{M}_1 \frac{da_1}{d\epsilon^{(n)}} + \mathcal{M}_2 \frac{da_2}{d\epsilon^{(n)}} + \frac{d\sigma_f}{d\epsilon^{(n)}} \quad (6.15)$$

which becomes, from equation 6.12 (i.e.  $d\epsilon^{(n)} = da_1 = da_2$ ) and the observation that  $\sigma_f$  is constant

$$d\sigma / d\epsilon^{(n)} = \mathcal{M}_1 + \mathcal{M}_2 \quad (6.16)$$

Thus the slope of the stress / strain curve in the anelastic region is  $(\mathcal{M}_1 + \mathcal{M}_2)$  which on comparison with the same in the Hart's original model yields

$$\mathcal{M} = \mathcal{M}_1 + \mathcal{M}_2 \quad (6.17)$$

Since the magnitude of  $\mathcal{M}$  at given  $\sigma^*$  and  $T$  is independent of the deformation history (§ 5.1.3.3), then equation 6.17 indicates that it is sufficient to show that either  $\mathcal{M}_1$  or  $\mathcal{M}_2$  are similarly independent of deformation history for it to be verified that both equations 6.3 and 6.4 are good state relations. Furthermore it follows that if under isothermal conditions  $\mathcal{M}_1$  is dependent only on  $\sigma^*$  then  $\mathcal{M}_2$  must be independent of  $\sigma^*$ , thereby confirming the supposition

that changes in  $\sigma_2^*$  do not reflect changes in the obstacle structure but rather a weak barrier sampling effect for a given structure.

When during loading  $\sigma = \sigma_A$ , then  $(\sigma_2^* / \sigma_{a2})$  attains a value sufficient for yielding of the  $\alpha_2$  - element. At the beginning of the test  $\sigma_2^*$  is the strength of the weakest barrier, and so this occurs when  $\sigma_{a2}$  is approximately equal to that strength. As  $\sigma_{a2}$  continues to increase, initially a large number of barriers can be overcome (equation 6.7) so that  $\dot{\alpha}_2$  rises rapidly. Hence since (equation 6.2)

$$\dot{\varepsilon}^{(n)} = \dot{\alpha}_1 = \dot{\alpha}_2 + \dot{\alpha}_2 = \text{constant} \quad (6.18)$$

then  $\dot{\alpha}_2$  diminishes. This in turn requires (equation 6.4) that  $\dot{\sigma}_{a2}$  decreases, and since  $\dot{\sigma}_f$  is zero and from equations 6.3 and 6.18  $\dot{\sigma}_{a1}$  is constant, then from equation 6.1  $\dot{\sigma}$  must diminish. Thus the slope of the stress / strain curve decreases.

As the remaining weak barriers become fewer in number and stronger,  $\sigma_2^*$  starts to increase more rapidly so that the rate of increase of  $\dot{\alpha}_2$  decreases. In the final stages of microplastic flow as  $\sigma \rightarrow \sigma_Y$ , all the weak barriers can be overcome and the model becomes like the original weak barrier free one, with

$$\dot{\varepsilon}^{(n)} = \dot{\alpha}_1 = \dot{\alpha}_2 \quad (6.19)$$

i.e.  $\dot{\alpha}_2 = 0$ . The slope of the stress / strain curve is then given by  $\mathcal{M}_1$ , which for real materials is less than  $0.5 \mathcal{M}$  implying that  $\mathcal{M}_1 < \mathcal{M}_2$ .

At  $\sigma = \sigma_Y$ ,  $(\sigma^* / \sigma_a)$  attains a value where the  $\alpha_1$  - element becomes active, and thereafter macroplastic deformation continues as described for the original model.

**6.1.3.3 Constant inelastic strain-rate cyclic tests :** The response of the refined model to loading / unloading or tension / compression cyclic deformation under constant inelastic strain-rate conditions, may be readily deduced from micromechanical arguments.

In the early stages of unloading after deformation into the macroplastic region, leakage of dislocations through the strong barriers continues until the back stress in the dislocation pile-up exceeds the applied stress driving the leakage. When this occurs dislocations begin to move backwards and start to pile up against the weak barriers in the opposite direction. Eventually the difference between the applied stress and the back stress becomes sufficient for reverse leakage over these weak barriers. Upon load reversal the applied stress adds to the back stress, enhancing the reverse microplasticity, and leading eventually to the premature macroplastic yielding which constitutes the Bauschinger effect. Thus the Bauschinger effect is seen to be due to the trapping of 'anelastic' strain upon unloading, behind the weak barriers.

Examination of cyclic constant inelastic strain-rate stress / strain curves, where the cycle is symmetric (i.e. where there is no Bauschinger effect) and the maximum stress is less than  $\sigma_Y$  (so that during the deformation  $d\alpha_1 = 0$  and hence also  $\sigma^*$  is constant), provides further insight into the anelastic properties of the refined model. Symmetry of the cycle may be obtained by repeating the cycle several times so as to saturate the pile-ups in each direction. Once saturation behaviour is attained the strength of the weakest barrier is very small, so that at  $\sigma_A$ ,  $\sigma_{a2} \approx 0$ . Hence, provided  $\sigma_{a1} \gg \sigma_f$  then from equation 6.1,  $\sigma_{a1} \approx \sigma_A$ . Using these results equation 6.9 becomes at  $\sigma_A$

$$\sigma_{a1} = \sigma_A = \mathcal{M}_1 (\dot{\varepsilon}^{(n)} - \alpha_0) \quad (6.20)$$

The symmetry of the cycle indicates that at the centre of the loop the specimen contains neither

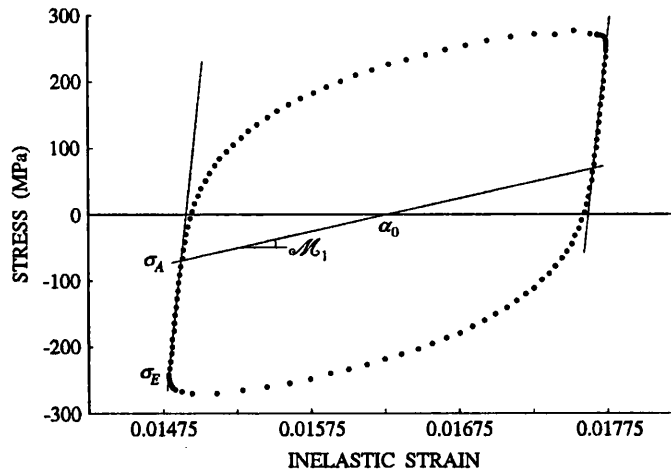


FIG. 6.5. Stress / inelastic strain data obtained for Type 316 stainless steel in room temperature, constant displacement-rate, tension / compression cycles where the maximum stress was less than the macroplastic yield stress. The slope of the line through  $\sigma_A$  and  $\alpha_0$  (the centre of the loop) yields  $\mathcal{M}_1$  (redrawn after Alexopoulos *et al.*, 1982).

anelastic nor microplastic strain. Consequently that centre gives the value of  $\alpha_0$  and equation 6.20 yields the value of  $\mathcal{M}_1$  (figure 6.5). This method of determining  $\mathcal{M}_1$  is in practice, more reliable than that of using the slope of the stress / inelastic strain curve as  $\sigma \rightarrow \sigma_Y$  in a constant inelastic strain-rate test. By running cycles of different amplitude while always maintaining  $\sigma < \sigma_Y$ , then the deformation history independence of  $\mathcal{M}_1$  (and hence  $\mathcal{M}_2$  – equation 6.17) at given  $\sigma^*$  can be verified. There have been no published results attempting to show this.

The behaviour of the  $\alpha_2$  – element is conveniently investigated by interrupting the cyclic constant inelastic strain-rate test at various stress levels, in order to conduct load relaxations. These relaxations are at constant  $\sigma_2^*$  because since  $\sigma$  decreases during the relaxation, the deformation that occurs in it is controlled by the strongest barriers sampled at its beginning. The cyclic test is a good method of pre-straining because it provides a complex deformation path by which to investigate the deformation history independence of the constant  $\sigma_2^*$  curves. Moreover it provides the value of  $\alpha_0$  necessary to evaluate  $\sigma_{a2}$  (equation 6.21) and the value of  $\mathcal{M}_2$  (through  $\mathcal{M}_1$  and equation 6.17) necessary to evaluate  $\alpha_2$  (equation 6.22). Alexopoulos *et al.* (1982) published suites of  $\sigma_2^*$  curves obtained in this way (figure 6.6a,b). These curves share the same properties as the macroplastic  $\sigma^*$  curves, being concave downward in  $\log \sigma / \log \dot{\varepsilon}^{(n)}$  space at high homologous temperatures and concave upward at low homologous temperatures, while also having the scaling property. This supports the proposed form for the constitutive relations of the  $\alpha_2$  – element and suggests that as for macroplastic deformation, at low  $T_m$  the weak barrier circumventing processes are mechanically activated so that glide friction is microplastic strain-rate controlling, whilst at high  $T_m$  the barrier circumventing processes are thermally activated and they are rate controlling. Given that at high homologous temperatures  $\sigma_{a2} \gg \sigma_f$  then the curves of figure 6.6a may be transformed into  $\log \sigma_{a2} / \log \alpha_2$  space using equations 6.9 and 6.11 (remembering that as long as the maximum stress on the cycles is less than  $\sigma_Y$ ,  $d\alpha_1 = 0$ )

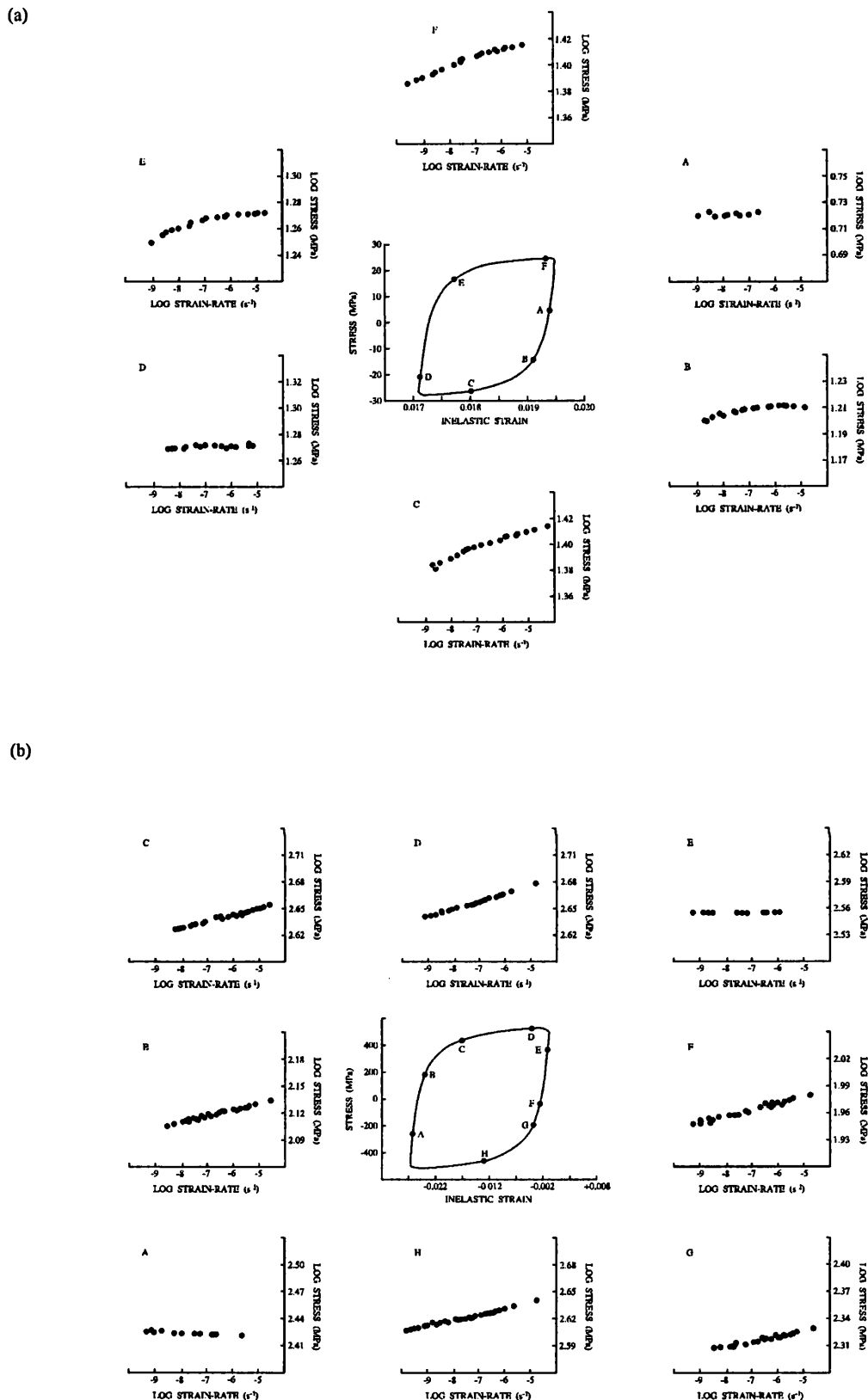


FIG. 6.6. Stress / inelastic strain-rate data obtained for (a) aluminium and (b) Type 316 stainless steel from load relaxations conducted at the indicated points in room temperature, constant displacement-rate tension / compression cycles. The stresses all lie in the microplastic region. The aluminium displays high homologous temperature behaviour and the stainless steel low homologous temperature behaviour (redrawn after Alexopoulos *et al.*, 1982).

$$\sigma_{a2} = \sigma - \mathcal{M}_1 (\varepsilon^{(n)} - \alpha_0) \quad (6.21)$$

$$\dot{\alpha}_2 = [1 + (\mathcal{M}_1 / \mathcal{M}_2)] \varepsilon^{(n)} - [\dot{\sigma} / \mathcal{M}_2] \quad (6.22)$$

and the parameters in the constitutive equations 6.5 and 6.6 determined from them. With the observation that at low homologous temperatures  $\sigma_{a2} \approx \sigma_2^*$  the parameters in the friction element can be determined directly from the  $\log \sigma / \log \varepsilon^{(n)}$  curves, and these should agree with those parameters as determined under glide friction controlled macroplastic deformation. This has yet to be systematically verified.

**6.1.3.4 Stress dip tests :** The typical response to a stress reduction during a constant stress creep test is shown schematically in figure 6.7a. Prior to the reduction the specimen undergoes steady creep under an applied stress  $\sigma_I$  and at strain-rate  $\dot{\varepsilon}_I$ . After the reduction to  $\sigma_{II}$  there is a transient region during which there is a rearrangement of the mobile dislocation structure, before a new creep rate  $\dot{\varepsilon}_{II}$  is established. The immediately post-transient behaviour is described as isostructural because since the strains encompassed by the transient region are small, the mechanical state of the specimen as given by the immobile dislocation structure, is effectively unchanged. As creep continues however, the state does change and a new steady strain-rate  $\dot{\varepsilon}_{III}$  is developed.

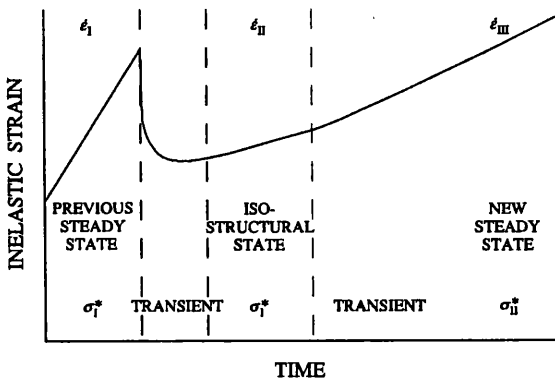
In terms of the refined model, the transient region can be considered as a continued forward flow through the strong barriers at a reduced stress with concurrent anelastic and microplastic back flow. Korhonen *et al.* (1985a) observed that the nature of the back flow is most easily considered when the forward flow decays rapidly, which is the case when  $\sigma_I \gg \sigma_{II}$  or  $\sigma_{II} \approx 0$ . In this situation the stress dip test is effectively a creep recovery test in which strain versus time data are recorded after a stress drop. The results of such tests are conveniently plotted as remaining recoverable strain  $\varepsilon_R$  versus strain-rate, because  $\varepsilon_R = a_1$  is proportional to the stored internal stress  $\sigma_{a1}$ . Generally these plots display two regions of different back flow kinetics, a high strain-rate anelastic region and a low strain-rate microplastic region (figure 6.7b). For the case where  $\sigma_{II} \approx 0$  and where there is no microplastic flow, then the anelastic back flow is given by equation 6.13

$$\begin{aligned} \dot{\varepsilon}^{(n)} &= \dot{a}^* (|\sigma_a| / G)^M = \dot{a}^* (\mathcal{M} / G)^M |a|^M \\ &= \dot{a}^* (\mathcal{M} / G)^M |a_1 - a_{1F}|^M \end{aligned} \quad (6.23)$$

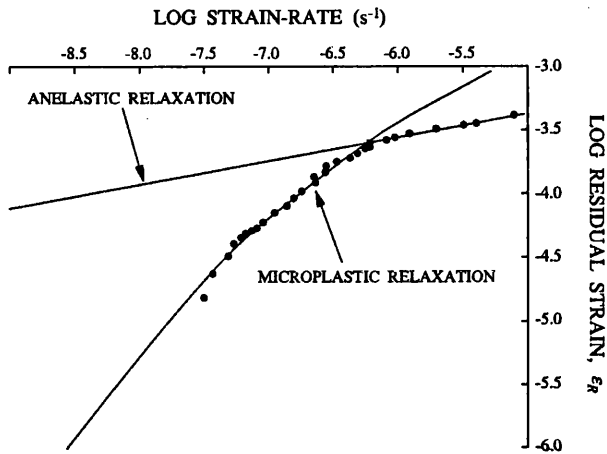
where  $a_{1F}$  is the value of  $a_1$  at the end of anelastic relaxation when  $\sigma_a \approx 0$ . Hence on a  $\log \varepsilon_R$  versus  $\log \dot{\varepsilon}^{(n)}$  plot the anelastic region is concave upward (figure 6.7b,c). If the temperature is sufficient, when the driving force for friction controlled flow is small, thermally activated barrier circumventing processes become rate competitive. This is the case when  $\sigma_a \approx 0$  at which point  $\sigma_{a1} \approx -\sigma_{a2}$  and  $\dot{\sigma}_{a1} \approx -\dot{\sigma}_{a2}$ . Consequently, from equation 6.2, 6.3, 6.4 and 6.17  $\dot{\alpha}_2 = \dot{a}_1 - \dot{a}_2 \approx -\dot{\sigma}_{a2} / \mathcal{M}$  and so  $\dot{\varepsilon}^{(n)} = \mathcal{M} \dot{\alpha}_2 / \mathcal{M}_1$ . Also  $\varepsilon_R = a_1 = \sigma_{a2} / \mathcal{M}_1$ . Hence a plot of  $\log \varepsilon_R$  versus  $\log \dot{\varepsilon}^{(n)}$  should describe the  $\dot{\alpha}_2$  - element constitutive relation (equation 6.5), provided  $\sigma_2^*$  remains constant during the test (which is reasonable given that the stress is decreasing). Such plots will then display a change in concavity as the deformation changes from anelastic to microplastic (figure 6.7b,c).

**6.1.3.5 Stress relaxation test :** A final deformation response of the refined model that is of particular interest is that occurring in a stress relaxation conducted after reloading to just below the initial stress of a prior relaxation run. Several such experiments have been reported (e.g.

(a)



(b)



(c)

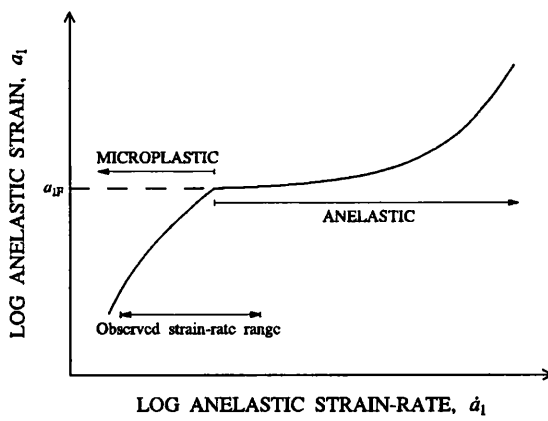


FIG. 6.7. The response of the refined Hart model in stress dip tests. (a) A schematic strain / time curve showing a stable creep region followed by several stages of deformation behaviour after a stress reduction. (b) Residual (remaining recoverable) strain / creep recovery-rate data for aluminium at 400°C obtained in a creep recovery test (i.e. a stress dip test in which the load is completely removed). (c) Schematic representation of the creep recovery characteristics shown in (b) but extended over a much wider strain-rate range (all figures redrawn after Korhonen *et al.*, 1985a).

Hart and Solomon, 1973 ; Korhonen and Li, 1982). Typically the high strain-rate part of the  $\log \sigma$  versus  $\log \dot{\varepsilon}^{(n)}$  curve produced in the second relaxation has a much greater stress sensitivity than the corresponding part of the initial curve, but at low strain-rates the two curves merge and are thereafter coincident (figure 6.8a).

Both the original and the refined model can account for this behaviour. Upon reloading after a stress relaxation, the mobile dislocations pile up behind the barriers to their motion. Strong barrier passage does not become significant until the flow stress is attained. Consequently, if reloading is stopped before the flow stress is reached, the initial part of the relaxation is dominated by anelastic and (in the refined model given that the reloading stress is sufficient for weak barrier passage) microplastic deformation. This remains the case until the strain-rate has decreased sufficiently for the strong barrier circumventing processes to become rate competitive, at which point the relaxation curve follows that predicted by the constitutive relation for the macroplastic element. Since during reloading the strong barrier structure remains unaltered, the mechanical state of the material is the same for the two relaxations, and so the low strain-rate portions of the two relaxation curves should be the same.

The original Hart model predicts that the reloading transient defines a broad upwardly concave curve in  $\log \sigma / \log \dot{\varepsilon}^{(n)}$  space. This may be seen by rearranging equation 5.12 for  $\sigma_f$  and substituting it and equation 5.9 into equation 5.7. Then on rearranging

$$(\sigma - \mathcal{M}a) / G = (\dot{\varepsilon}^{(n)} / \dot{a}^*)^{1/M} \quad (6.24)$$

Now the integrated form of the stress relaxation equation (equation 5.17) when the deformation is entirely anelastic is

$$(\sigma - \sigma_0) = \kappa(a - a_0) \quad (6.25)$$

where the subscript 0 refers to the start of the relaxation. This may be rewritten (entirely by algebraic manipulation, § A1.3) as

$$\frac{(\sigma - \mathcal{M}a)}{G} = \left( \frac{1}{G} - \frac{\mathcal{M}}{G\kappa} \right) \left( \sigma + \frac{(\sigma_0 - \kappa a_0)}{[(\kappa/\mathcal{M}) - 1]} \right) \quad (6.26)$$

Then defining

$$\frac{1}{\mathcal{M}^{(a)}} = \left( \frac{1}{G} - \frac{\mathcal{M}}{G\kappa} \right) \quad ; \quad \sigma_a^{(a)} = \frac{-(\sigma_0 - \kappa a_0)}{[(\kappa/\mathcal{M}) - 1]} \quad (6.27)$$

and equating equations 6.24 and 6.26

$$[\sigma - \sigma_a^{(a)}] / \mathcal{M}^{(a)} = (\dot{\varepsilon}^{(n)} / \dot{a}^*)^{1/M} \quad (6.28)$$

which, since  $\sigma_a^{(a)}$  and  $\mathcal{M}^{(a)}$  are constants, is the same form as the equation for the low homologous temperature constant  $\sigma^*$  curves (equation 6.24 with  $\sigma_a = \mathcal{M}a \approx \sigma^*$ ).

For real materials equation 6.28 yields very flat anelastic relaxation curves over the strain-rates of interest and cannot properly describe the results shown in figure 6.8a. In the refined model the anelastic initial portion of the curves is also described by equation 6.28, since equations 5.12, 6.1, 6.2, 6.3 and 6.17 together yield the same equation 6.24, given  $a = a_1 = a_2$  which is satisfied through the definition of  $a_0$  in equation 6.25. However, in the refined model, before the second relaxation curve merges with the initial one it passes through an  $\dot{\alpha}_2$  - element controlled region where the shape of the curve is given by equation 6.5. Jackson *et al.* (1981) determined the material parameters in the constitutive relations of the refined model for high purity aluminium and then carried out a numerical simulation of the experiments shown in

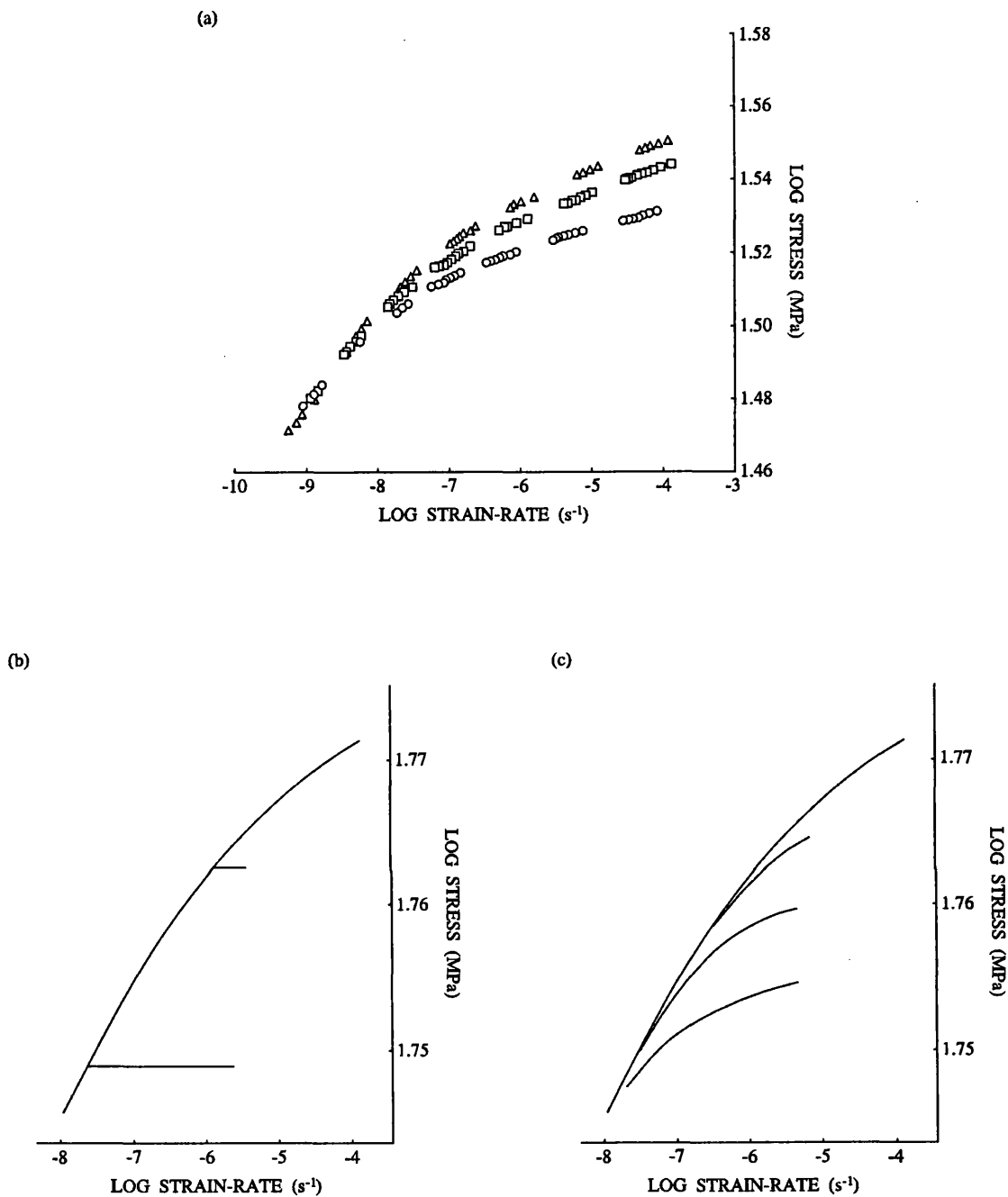


FIG. 6.8. The room temperature load relaxation behaviour of aluminium after reloading (lower curves) to a stress below that at the start of an initial relaxation (upper curve in each figure). (a) Observed behaviour (redrawn after Hart and Solomon, 1973). (b) and (c) Numerical simulations using the material parameters for aluminium ; (b) in Hart's original model and (c) in the refined model (redrawn after Jackson *et al.*, 1981).

figure 6.8a. The results are shown in figure 6.8c and compared with a simulation for the original model (figure 6.8b). The refined model is seen to be an excellent description.

**6.1.4 Further observations.** The refined model described above envisages, during microplastic deformation, that mobile dislocations move among barriers whose strength and distribution remain fixed as deformation proceeds. This is presumably an oversimplification but

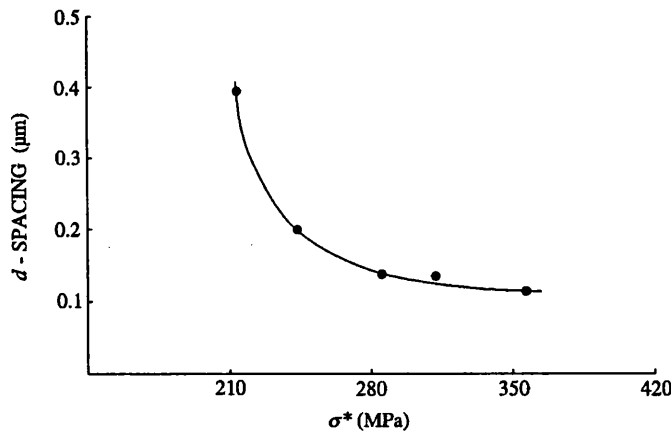


FIG. 6.9. The correlation between  $\sigma^*$  and the spacing of well defined subgrain boundaries on the activated slip planes in Type 316 stainless steel deformed at room temperature (redrawn after Alexopoulos *et al.*, 1982).

the success of the model suggests that it is a good approximation. At the temperatures at which the refined model has been tested the weak barrier structure remains stable against thermal recovery. However, it may be expected that the influence of such recovery will commence at lower temperatures than the 0.45  $T_m$  found for macroplastic flow.

Alexopoulos *et al.* (1982) attempted to correlate the structural parameters  $\sigma^*$ ,  $\sigma_2^*$ ,  $\mathcal{M}_1$  and  $\mathcal{M}_2$  with features in the deformation microstructure of Type 316 stainless steel. They found that  $\sigma^*$  correlated with the spacing of well defined subgrain boundaries on the activated slip planes (figure 6.9), and  $\sigma_2^*$  with the spacing of partially developed subgrain boundaries between the activated slip planes. The ratio of the square of the spacing between the well defined and the partially developed subgrain boundaries was found to be inversely proportional to the ratio of  $\mathcal{M}_1$  and  $\mathcal{M}_2$  (*cf.* equation 5.58).

## 6.2 Parameterization of $\mathcal{M}$ , $\dot{\alpha}^*$ and $M$

Hart (1976) introduced the parameters  $\mathcal{M}$  (equation 5.9) and  $\dot{\alpha}^*$  and  $M$  (equation 5.12) as material constants and in a number of experimental studies they have been treated as such. However, comparison of equations 5.9 and 5.12 with theoretically derived expressions provides a physical interpretation of these parameters which indicates that  $\mathcal{M}$  and  $\dot{\alpha}^*$  are a function of  $\sigma^*$  and that all three parameters are a function of  $T$ .

**6.2.1 Parameterization of the anelastic modulus.** In presenting the continuum dislocation theory analysis of Hart's model (§ 5.3.2), it was found that the anelastic modulus  $\mathcal{M}$  was given by (equation 5.58)

$$\mathcal{M} = G / (\pi l^2 \mathcal{N}^0) \quad (6.29)$$

where  $G$  is the rigidity modulus,  $l$  is the half distance between the long range barriers to dislocation motion and  $\mathcal{N}^0$  is a slip-zone density. With increasing  $\sigma^*$ ,  $l$  may be expected to decrease and  $\mathcal{N}^0$  to increase. Hence  $\mathcal{M}$  will be some function of  $\sigma^*$ . With increasing  $T$  at given  $\sigma^*$ ,  $l$  remains constant,  $\mathcal{N}^0$  increases (as more slip-zones are activated) and  $G$  decreases. Hence  $\mathcal{M}$  should decrease with increasing  $T$ .

There have been no systematic studies of the mechanical state and temperature dependencies of the anelastic modulus. However, Alexopoulos *et al.* (1981) determined  $\mathcal{M}$  at different  $\sigma^*$  in high purity aluminium and although they did not state it, it is apparent from their figure of the results that  $\mathcal{M}$  increased with  $\sigma^*$ . A decrease in  $\mathcal{M}$  with increasing  $T$  has been observed by Wire *et al.* (1981) in their analysis of the results of pressurization tests on Type 316 stainless steel tubes.

**6.2.2 Parameterization of  $\dot{\alpha}^*$  and  $M$  for  $\sigma^*$  and  $T$ .** The mechanical state and temperature dependencies of  $\dot{\alpha}^*$  and  $M$  can be ascertained by comparing equation 5.12 with two other commonly employed descriptions of the kinetics of dislocation glide ; the Johnston-Gilman equation and the absolute reaction rate equation for thermally activated glide.

**6.2.2.1 Mechanical state dependence :** Orowan (1940) showed that when isothermal plastic deformation is rate controlled by the kinetics of dislocation glide

$$\dot{\alpha} = \Phi b \rho_m \bar{v} \quad (6.30)$$

where  $\Phi$  is a geometric factor,  $b$  is the magnitude of the Burgers vector,  $\rho_m$  is the mobile dislocation density and  $\bar{v}$  is the mean dislocation velocity. Johnston and Gilman (1959) suggested, and Gupta and Li (1970) confirmed, that

$$\bar{v} = v_0 (\sigma_f / G)^{M^*} \quad (6.31)$$

where  $v_0$  and  $M^*$  are material constants. Combining equations 6.30 and 6.31 yields the Johnston-Gilman equation

$$\dot{\alpha} = \Phi b \rho_m v_0 (\sigma_f / G)^{M^*} \quad (6.32)$$

Equating equation 5.12 and 6.32 using  $\dot{\epsilon}^{(n)} \approx \dot{\alpha}$  gives

$$\dot{\alpha}^* = \Phi b \rho_m v_0 \quad (6.33)$$

$$M = M^* \quad (6.34)$$

Beyond plastic yielding during the isothermal loading of a polycrystal, it can be reasonably expected that  $(\Phi b)$ ,  $v_0$  and  $M^*$  are constant. It therefore follows from equations 6.33 and 6.34, that  $M$  is independent of  $\sigma^*$  and that  $\dot{\alpha}^*$  varies with  $\sigma^*$  according to the dependence of  $\rho_m$  on  $\sigma^*$ . Furthermore, given these conditions  $\rho_m$  must be uniquely specified by  $\sigma^*$  (and does not change for example, during a load relaxation conducted at constant  $\sigma^*$ ), and the scaling slope  $\mu$  for constant  $\sigma^*$  curves in  $\log \sigma - \log \dot{\alpha}$  space must be given by (equation 4.46)

$$\mu = (M + \partial \log \dot{\alpha}^* / \partial \log \sigma^*)^{-1} = (M^* + \partial \log \rho_m / \partial \log \sigma^*)^{-1} \quad (6.35)$$

a result which has been obtained elsewhere (Tanoue and Matsuda, 1982 ; Povolo and Marzocca, 1983c). Equation 6.35 indicates that if there is a linear scaling slope then there must be (at least empirically) a power law relationship between  $\rho_m$  and  $\sigma^*$  (*cf.* equation 4.48).

The  $\sigma^*$  independence of  $M$  is a prerequisite for the scaling behaviour of constant  $\sigma^*$  curves in  $\log \sigma / \log \dot{\alpha}$  space (§ 4.1.2.2). The variation of  $\dot{\alpha}^*$  with  $\sigma^*$  has not been studied systematically although Korhonen *et al.* (1985b) observed a linear relation between  $\dot{\alpha}^{*-1/M}$  and  $\sigma^*$  in Type 316 stainless steel at room temperature. No use has yet been made of equation 6.35 because of the notoriously difficult problem of distinguishing mobile from immobile dislocations in micrographs of deformation textures (*e.g.* Kocks *et al.*, 1975, pp. 89-93).

Although the assumption that  $(\Phi b)$ ,  $v_0$  and  $M^*$  are constant beyond plastic yielding is reasonable in polycrystals, in single crystals all three terms can be expected to change as new slip systems become active. The implication from equations 6.33 and 6.34 is that  $\dot{\alpha}^*$  and  $M$  will

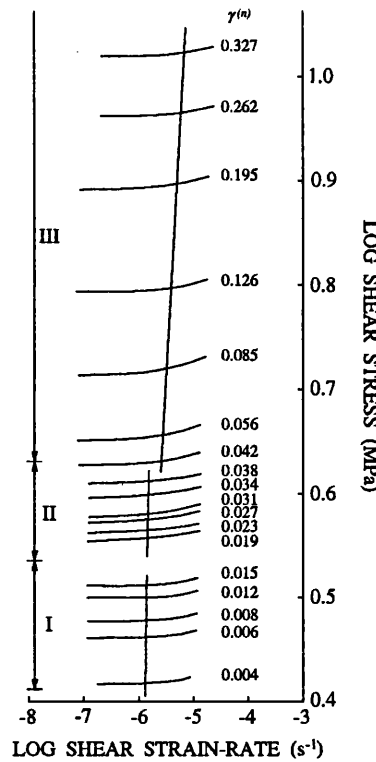


FIG. 6.10. The change in scaling slope of constant  $\sigma^*$  curves during three stage work hardening in aluminium single crystals deformed at  $-86^\circ\text{C}$  (redrawn after Tanoue *et al.*, 1988).

show corresponding variations but that between activation of new slip systems they will demonstrate the same relationship with  $\sigma^*$  as observed in polycrystals. This has been confirmed by Tanoue *et al.* (1988) and Tanoue (1991) who found that although the scaling slope  $\mu$  for constant  $\sigma^*$  curves in  $\log \sigma / \log \dot{\alpha}$  space changed as single crystals of aluminium, zinc and copper passed through three stage work hardening, within each stage  $\mu$  was constant (figure 6.10).

**6.2.2.2 Temperature dependence :** Absolute reaction rate theory indicates that the temperature dependence of dislocation glide can be described by an Arrhenius equation of the form

$$\dot{\varepsilon}^{(n)} = \dot{\varepsilon}_0^{(n)} \exp [-G_f(\sigma_f) / kT] \quad (6.36)$$

in which  $\dot{\varepsilon}_0^{(n)}$  is a constant,  $G_f(\sigma_f)$  is the Gibbs free energy of activation for the glide process and  $k$  is the Boltzmann constant (*e.g.* Kocks *et al.*, 1975). By equating equations 5.12 and 6.36 then it follows that  $G_f(\sigma_f)$  must be (at least empirically) of the form

$$G_f = A - B \ln (\sigma_f / G) \quad (6.37)$$

where  $A$  and  $B$  are constants. Then

$$\dot{\varepsilon}^{(n)} = \dot{\alpha}^* (\sigma_f / G)^M = [\dot{\varepsilon}_0^{(n)} \exp (-A / kT)] (\sigma_f / G)^{B/kT} \quad (6.38)$$

so that

$$\dot{\alpha}^* = \dot{\varepsilon}_0^{(n)} \exp (-A / kT) \quad (6.39)$$

$$M = B / kT \quad (6.40)$$

The temperature dependence of  $M$  has been investigated in polycrystalline molybdenum by

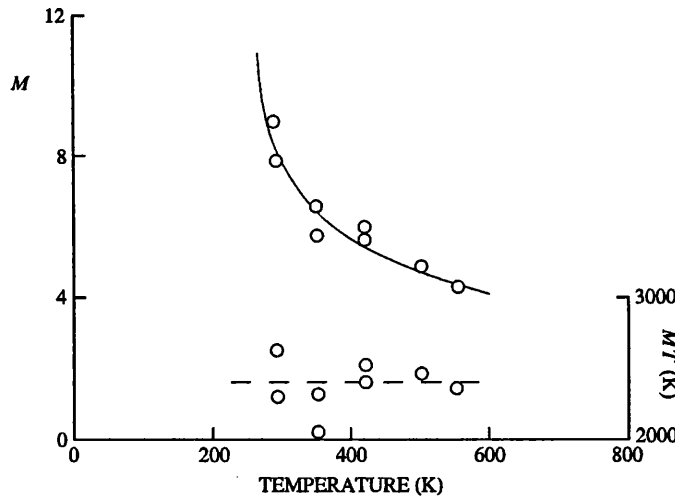


FIG. 6.11. The change in  $M$  with temperature in molybdenum. The constancy of  $MT$  validates equation 6.40 (redrawn after Tanoue and Matsuda, 1984).

Tanoue and Matsuda (1982 ; 1984) and Tanoue *et al.* (1983). They observed that  $MT$  was constant (figure 6.11) as predicted by equation 6.40. Huang *et al.* (1977 ; 1979) reported  $M$  to be temperature independent in Type 316 stainless steel and zircaloy-4, but this may be due to the method they used to determine it from their load relaxation curves (§ 11.2.3).

The temperature dependence of  $\dot{\alpha}^*$  has not been studied systematically. Huang *et al.* (1977) observed that  $G / \dot{\alpha}^{*1/M}$  decreased with increasing temperature in Type 316 stainless steel, but not exponentially. However, again this conclusion is severely compromised by their method of determining  $M$  (§ 11.2.3).

### 6.3 The accommodation of other material characteristics / deformation variables

Hart's inelastic deformation model has been presented for a material which is nominally pure (*i.e.* one in which any impurities are of no consequence for the material behaviour) and which has grain-size independent mechanical properties. It has also been assumed that the only extrinsic variables of interest for characterizing the deformation at given  $T$ , are  $\sigma$  and  $\dot{\varepsilon}^{(n)}$ . The mechanical state  $\sigma^*$  of the deforming material is then controlled by the strong barrier network (effectively the evolving deformation microstructure) which is uniquely specified by  $\sigma$  and  $\dot{\varepsilon}^{(n)}$ , while the material parameters are controlled by dislocation-defect interactions and are material constants or are uniquely specified by  $\sigma^*$  and/or  $T$ .

In real deforming materials both grain-size and impurities (*i.e.* impurity solutes or finely dispersed inclusions) exert an influence on the deformation behaviour. In addition other features of the deformation environment such as the isostatic pressure or the presence of fluids may be significant. If Hart's deformation model is to have general application therefore, then it must be able to accommodate the effects produced by these factors.

The potential for incorporating the aforementioned factors into Hart's model is considered below. Although the influence of each on inelastic deformation properties has received extensive theoretical and experimental attention, there have been few attempts to treat them

within the context of Hart's analysis. Consequently, the discussion of each factor begins with a qualitative deduction of its effects on the results of load relaxation tests conducted after constant displacement-rate loading (here referred to as multiple relaxation experiments). This not only provides a basis for considering the potential for extending Hart's model to include such effects, but also allows those experiments influenced by them to be identified so that (in lieu of such extensions) they are not used in fitting the equations of state.

**6.3.1 Solute impurities.** Solute impurities influence inelastic deformation behaviour through their elastic, electrostatic and/or chemical interactions with the dislocations in the solvent phase. Elastic interactions arise when the solute atoms differ in size and in elastic properties from the solvent atoms. The size effect reflects the interaction of the elastic strain fields associated with both solute and dislocation, while the effect of the difference in elastic properties arises from the fact that a dislocation has to do less work when moving through an area of lattice containing elastically softer solutes (and conversely more when moving through an area with elastically harder solutes) than when moving through the pure lattice. Electrostatic interactions occur between electrostatically charged impurities and dislocations in ionic materials which carry a local excess of charge (or in metals where the dislocation has an asymmetric distribution of the conduction electrons). Chemical interactions may arise when the structural changes associated with stacking faults lead to variations in cohesive energy between the atoms, and hence variations in the local equilibrium concentration of solute impurities.

These interactions present a driving force for the segregation of solute atoms towards or away from dislocations, and thereby effectively attempt to limit dislocation mobility to that of the impurities. In order to move, a dislocation must either to overcome these interactions or to drag an accumulating solute atmosphere with it. If unable to do either it is rendered immobile.

**6.3.1.1 Factors influencing the magnitude of the solute effect :** The significance of solute impurities for dislocation motion depends upon their composition, concentration, distribution and mobility.

Solute composition exerts its influence through the effect that the size, elastic properties, valence and electronic structure of the solute atoms have on the solute-dislocation interactions. This effect varies with temperature. Thus for example, the significance of the dimensional mismatch between the solute and solvent atoms (*i.e.* of the elastic interaction) decreases with increasing temperature as the solvent lattice is able to tolerate larger distortions.

The solute distribution influences the mechanism by which dislocations must overcome the impurities. In materials in which the solute is ordered into a superlattice it is energetically favourable for dislocations to move in pairs or groups such that the total Burgers vector of the group is equivalent to the identity distance of the superlattice in the slip direction. If the solute atoms are clustered, then each cluster may act like a crystallographically incoherent inclusion and require the dislocations to undergo large changes in curvature in overcoming them (*cf.* § 6.3.2). Solutes interacting with the mobile dislocations (*i.e.* located near them) are more significant than those located in the immobile dislocation network.

Solute mobility determines whether the solute can redistribute itself in the solvent lattice in response to the solute-dislocation interactions. The consequences for dislocation motion are complex, because although high mobilities increase the concentration of impurities in the

neighbourhood of (*i.e.* interacting with) a dislocation, they also increase the ability of the solute to move with it. The significance of solute mobility and the factors (most notably temperature) which affect it, is therefore strongly dependent on the magnitude of the solute-dislocation interactions and the factors which affect them.

**6.3.1.2 The effect of solute impurities on multiple relaxation experiments :** The effect of solute impurities on multiple relaxation experiments is described for a solute of given composition which is initially uniformly and randomly distributed through the solvent.

At low temperatures the solutes are approximately immobile and so dislocations must be able to break-free of their interactions with them before they can move. In such circumstances there is no change in solute concentration in the neighbourhood of the dislocations, either during or between relaxations *i.e.* the solute impurity effect remains constant throughout the experiment. Hence the suite of relaxation curves generated differ only from that for the pure material through the values of the material parameters in the appropriate equation of state. Such behaviour has been observed by Tanoue and coworkers (Tanoue *et al.*, 1983 ; Tanoue and Matsuda, 1984) in some experiments on polycrystalline molybdenum specimens of varying purity, *i.e.* they observed that at given temperature and specimen purity the relaxation curves demonstrated good scaling behaviour, but that both the scaling slope and its dependence on temperature were a function of impurity content (figure 6.12a,b).

At slightly higher temperatures the solute mobility is insufficient to allow diffusive solute segregation during the load relaxations, but may be sufficient to allow those solutes encountered by the mobile dislocations during the loading phase to be dragged with them. Because the solute mobility is low, only a small increase in concentration near the dislocation is required to render it immobile. This serves to concentrate the solutes in the immobile dislocation network, leaving the rest of the lattice relatively 'clean' for the later dislocations. In such cases the relaxation curves do not form a one parameter family because the effective solute concentration is changing between (though not during) relaxations. No experiments conducted within the context of Hart's analysis have shown this type of behaviour. However, Gupta and Li (1970) observed that in impure niobium and tantalum  $M^*$  ( $= M$ , equation 6.34) decreased rapidly during the first few percent strain, asymptoting to the value for the pure material.

At higher temperatures diffusive solute segregation leads to a significant redistribution of the impurities during load relaxation. As the relaxation progresses and the drag exerted by the impurity atmosphere increases, the slope of the relaxation curve becomes progressively smaller than observed in the absence of segregation. With increasing pre-strain this effect decreases because the affected dislocations become part of the immobile network, and consequently the relaxation curves do not form a one parameter family. When relaxation is affected by ongoing solute segregation, the subsequent reloading stress / strain curves show reloading peaks. These peaks reflect the fact that because of the solute segregation there are relatively few dislocations which can move at the velocity required by the imposed reloading strain-rate. To accomplish the deformation the velocity of those few dislocations, and therefore the stress, must be high (*cf.* equations 6.30 and 6.31). At some critical stress (the yield peak) the dislocations are able to break-free of their solute atmospheres (or dislocation sources become active) so that the

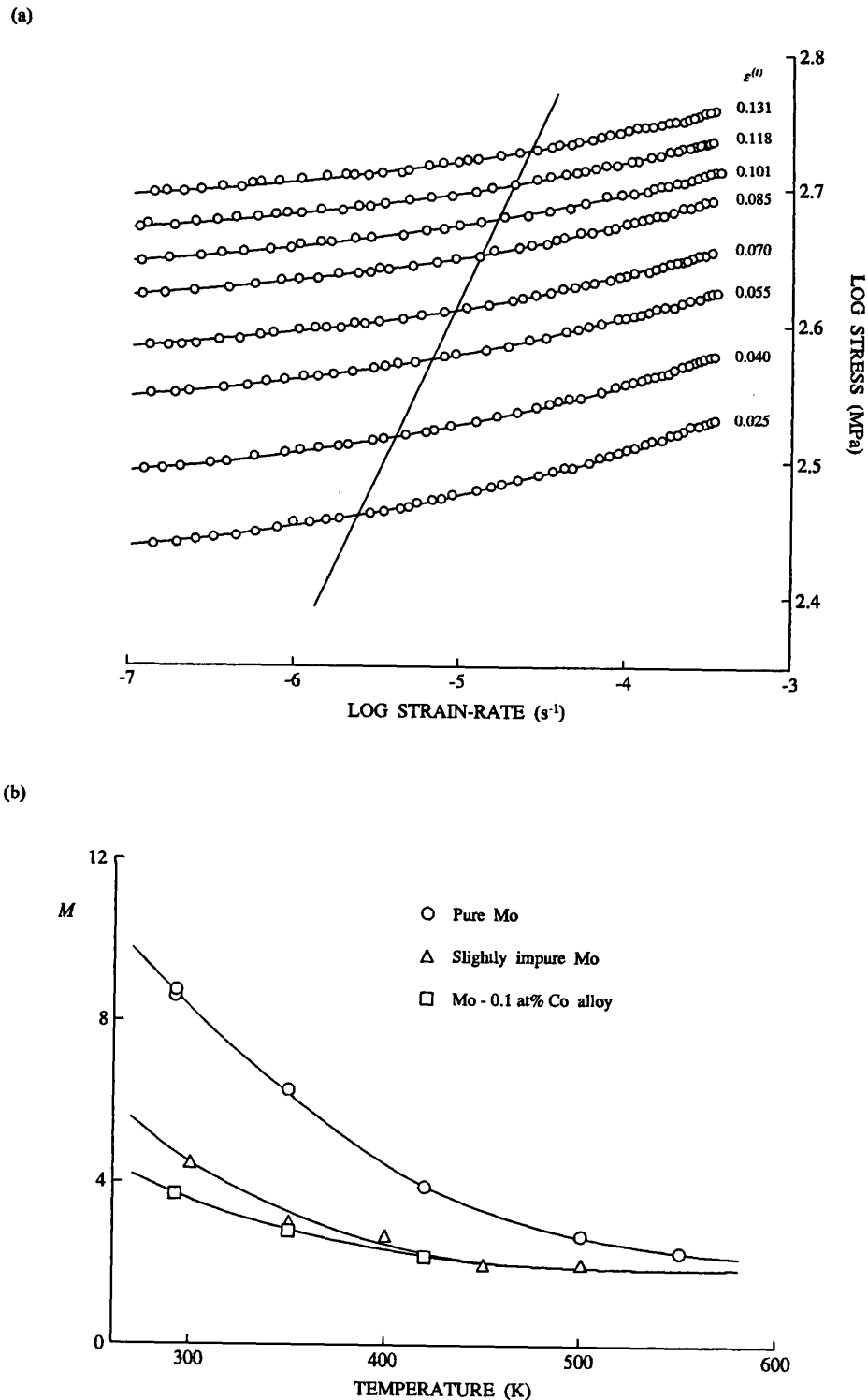


FIG. 6.12. The effect of solute impurities on the relaxation curves of molybdenum. (a) Curves generated from Mo-0.1 at% Co alloy at room temperature showing the usual scaling behaviour, although (b)  $M$  and its temperature dependence varies with purity (redrawn after Tanoue *et al.*, 1983).

average dislocation velocity, and with it the stress, decreases. The deviation of the relaxation curve from that generated in the absence of segregation, and the size of the subsequent yield drop on reloading, vary with temperature in correspondence with the magnitude of solute-dislocation interactions and solute mobility. In general, with increasing temperature they rise to a maximum beyond which they decrease as the driving force for segregation diminishes and the solute mobility becomes too great to hinder dislocation motion. All these features have been observed by Huang *et al.* (1979) in zircaloy-4 (figure 6.13a-c). The reload stress / strain curves show yield drops which decrease in size with increasing strain and which increase to a maximum size at about 300°C (figure 6.13a), while the low strain-rate portions of the relaxation curves deviate from the curves predicted in the absence of solute segregation in a manner which decreases with increasing strain (figure 6.13b). From the results shown in figure 6.13c, it is apparent that the changing significance of solute segregation with strain means that the observed relaxation curves do not belong to a one-parameter family.

As temperature is further increased, the solute mobility becomes too great to hinder the mobile dislocations and the yield peaks disappear. However, near the end of a relaxation when the driving force for further deformation is low, the segregated solute concentration may still be sufficient to reduce the rate of relaxation. This may then lead to a sigmoidal relaxation curve (*cf.* figure 6.14a).

**6.3.1.3 Towards a solute parameterization. (a) General remarks :** Solute impurities affect the rate of dislocation motion rather than the scale of the strong barrier network, and hence are appropriately included in Hart's model by a parameterization of  $\dot{\alpha}^*$  and/or  $M$  (friction element), and  $\varepsilon^*$  and/or  $\lambda$  (plastic element). Such a parameterization must describe the change in magnitude of the material parameters as a function of the solute-dislocation interaction, and accordingly must include some specification of the solute-dislocation interaction as a function of solute composition, concentration, distribution and mobility. The large number of factors influencing the form of these functions makes this a formidable task. The best prospect of a solution lies in combining empirical observations of the solute effect on the parameters with theoretical models of solute impeded dislocation motion. This in turn requires a detailed physical interpretation of those material parameters.

**6.3.1.4 Towards a solute parameterization. (b) The friction element :** The task of determining the effect of solute impurities on the material parameters of the friction element is simplified by the possibility of conducting experiments under conditions in which the solutes are immobile. Hence the influence of solute composition, concentration and distribution on  $\dot{\alpha}^*$  and  $M$  may be directly determined by conducting suites of relaxations on specimens where these variables are controlled. The experiments of Tanoue and coworkers cited above (§ 6.3.1.2) may be used in this way. Their observation that the scaling slope of the relaxation curves generated from specimens of different purity was a function of purity, means that  $M$  and/or the power law exponent in the relationship between  $\dot{\alpha}^*$  and  $\sigma^*$  is a function of solute concentration (equation 6.35). By using the Gupta-Li method to determine  $M^*$  ( $= M$ , equation 6.34), Tanoue and Matsuda (1984) showed that in their experiments the value of  $M^*$  equals the reciprocal of the scaling slope (*i.e.*  $\partial \log \dot{\alpha}^* / \partial \log \sigma^* = 0$ ), and hence it follows that the power law exponent in the relationship between  $\dot{\alpha}^*$  and  $\sigma^*$  is independent of purity but that  $M$  is not. Tanoue and

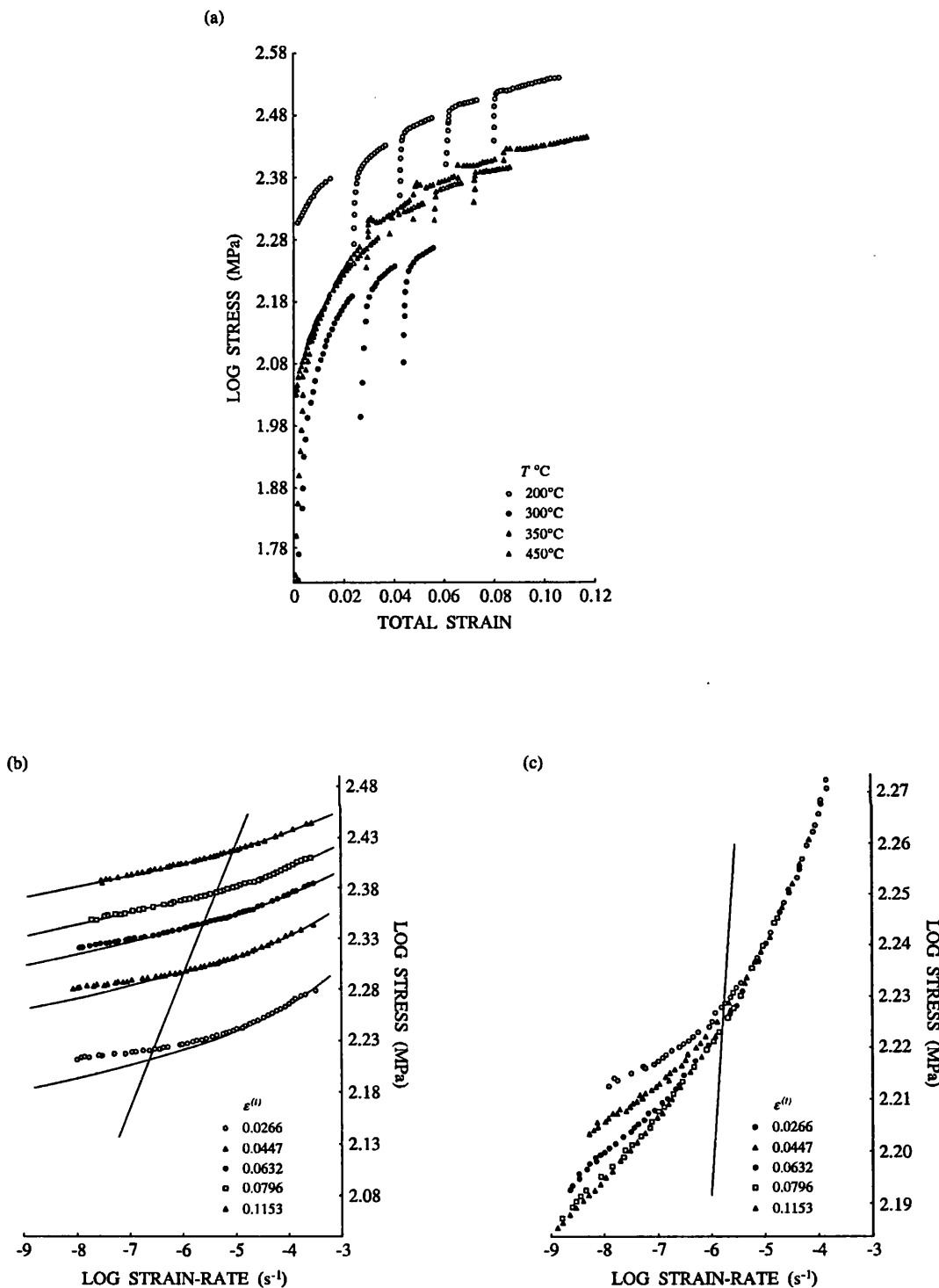


FIG. 6.13. The effect of ongoing solute segregation to the mobile dislocations during load relaxation of zircaloy-4. (a) Reloading peaks in the stress / strain curves and their variation with strain and temperature. (b) Actual relaxation curves generated at 300°C compared with the predicted behaviour in the absence of segregation (solid curves). (c) Translation of the curves in (b) along the indicated 'segregation-free' scaling direction, demonstrating the systematic failure of the scaling property (all figures redrawn after Huang *et al.*, 1979).

coworkers did not consider the effect of impurity concentration on the magnitude of  $\dot{\alpha}^*$ . However, Gypen and Deruyttere (1982) applied the absolute reaction rate equation for dislocation glide (equation 6.36) to the deformation of various tantalum based alloys and found that  $\dot{\epsilon}_0^{(n)}$  was independent of solute content. The implication is that solute concentration does not affect  $\dot{\alpha}^*$  at given temperature (equation 6.39).

The observation that  $\dot{\alpha}^*$  is independent of solute concentration implies that solutes do not affect  $v_0$  or the  $\rho_m(\sigma^*)$  function (equation 6.33). If this is true in general, then the retarding effect of solutes on relaxation-rates in tests where ongoing segregation is significant, does not result from a reduction in the mobile dislocation density (the relaxation is at constant  $\sigma^*$ ) *i.e.* the solutes do not completely pin the dislocations, or if they do then new dislocations are generated to take their place. The dependence of  $M$  on solute concentration is difficult to interpret. For almost all theoretical dislocation glide models where glide is rate-controlled by the lattice resistance, the activation energy can be expressed as

$$G_f(\sigma_f) = G_{f0} \left[ 1 - (\sigma_f / \sigma_p)^{q_1} \right]^{q_2} \quad (6.41)$$

in which  $G_{f0}$  is the value of  $G_f$  when  $\sigma_f = 0$ ,  $\sigma_p$  is the Peierls stress and  $q_1$  and  $q_2$  are constants which depend on the model or more specifically, on the profile of the Peierls-Nabarro hills (Kocks *et al.*, 1975). This functional form for  $G_f(\sigma_f)$  differs from that prescribed by equation 6.37 but since the latter arises from a purely empirical relation (*i.e.* the constitutive relation for the friction element, equation 5.12), all that is required is that  $G_f$  be given by a function that can be approximated by equation 6.37. Calculating  $G_f(\sigma_f)$  from a fit of equation 6.37 to their data, and assuming that  $G_{f0}$  and  $\sigma_p$  are constant, Tanoue and Matsuda (1984) showed that their changes in  $M$  with composition correlated with changes in  $q_1$  and  $q_2$  *i.e.* with the profile of the Peierls-Nabarro hills.

**6.3.1.5 Towards a solute parameterization. (c) The plastic element :** The task of determining the effect of solute impurities on the material parameters in the plastic element is complicated by the fact that at the temperatures where the plastic element controls the deformation behaviour diffusive solute segregation is important. Hence during a relaxation the solute effect changes. Even a qualitative consideration is rendered difficult because the constitutive relation for the plastic element (equation 5.10) does not correspond to the form of any of the theoretically derived dislocation creep equations.

The effect of solute impurities on the plastic element reflects their influence on long range barrier circumvention. Such an influence arises for example, from the effect of solute impurities on stacking fault energy (and hence on rates of cross-slip), or from impurities filling the vacant lattice sites (*i.e.* the jogs) along a dislocation during its 'wait-time' at the barrier. In the absence of a theoretical interpretation of  $\lambda$  and  $\dot{\epsilon}^*$ , then to gain some understanding of their physical meaning which can serve as a basis for considering the solute effect, it is necessary to fit both equation 5.10 and the theoretical creep equations to the same data in the same variable space. The only published attempt to do this is by Povolo and Marzocca (1981). Comparing equation 5.10 with a creep equation based on the thermally assisted motion of jogged screw dislocations (that of Barrett and Nix, 1965), they found that  $\lambda$  was a function of the stress exponent of the stress dependence of the mobile dislocation density (assuming a power law dependence of  $\rho_m$

on the flow stress), and that  $\dot{\varepsilon}^*$  was a function of the self-diffusion coefficient, temperature and the average spacing between jogs. If it is then assumed that the stress exponent of the stress dependence of the mobile dislocation density is unaffected by the presence of solute impurities, it follows that the solute effect is contained wholly within  $\dot{\varepsilon}^*$ . In the case that solute impurities exert their influence solely through their effect on vacancy concentration and mobility, the solute effect is like that of temperature and reduces an effect on the jump frequency parameter  $f_0$  (equation 5.11).

There is some experimental support for these predictions. Lerner and Kohlstedt (1982) found that the high strain-rate portion of the sigmoidal relaxation curves generated in Cd<sup>2+</sup> doped AgCl single crystals (figure 6.14a) superpose onto the relaxation curves generated from the pure material. This implies that the solutes do not influence  $\lambda$ . Korhonen and Li (1982) reported a time dependent variation of  $\dot{\varepsilon}^*$  in some room temperature load relaxations conducted on commercial purity aluminium. They conducted a number of relaxations after reloading to a stress just below the initial stress of a prior relaxation run, and found that instead of merging with the initial curve (§ 6.1.4.5, figure 6.8a), the later relaxations crossed over the earlier ones (cf. figure 6.14b). By fitting the equation of state to the curves they found that  $\lambda$  and  $\sigma^*$  were constant for each relaxation but that  $\dot{\varepsilon}^*$  decreased with each successive run. Although the variation of  $\dot{\varepsilon}^*$  was not explained it is compatible with the expected influence of an increasing segregation of solute impurities, the importance of which is emphasized by the reported observation of a yield drop during reloading after the last relaxation. Wire *et al.* (1981) also reported a time dependent  $\dot{\varepsilon}^*$  (but constant  $\lambda$ ) in Type 316 stainless steel, and were able to accommodate all the variation within  $f_0$ .

**6.3.1.6 Towards a solute parameterization. (d) Summary :** Before a full parameterization of Hart's model for the effect of solute impurities is attempted, a much closer comparison of his equations with theoretical solute impeded dislocation glide / creep models is required. The limited experimental evidence described above suggests that solute impurities change the magnitude of  $M$  but not  $\dot{\alpha}^*$  (friction element) and  $\dot{\varepsilon}^*$  but not  $\lambda$  (plastic element), and that such effects are a function of temperature. Until a solute parameterization is obtained, it is therefore important to recognize the potential for interpretative difficulties when applying Hart's analysis to impure materials.

**6.3.2 Finely dispersed inclusions.** Finely dispersed inclusions / second phase particles influence inelastic deformation behaviour by presenting barriers to dislocation motion which the dislocations must either cut through or go around. In considering this effect, of interest are only those particles which are similar in size to the strain field of a single dislocation. The influence of larger particles is considered elsewhere (§ 6.6.1).

**6.3.2.1 Factors influencing the magnitude of the effect due to inclusions :** The significance of the effect due to inclusions depends upon the work required for the dislocations to overcome them.

To cut through an inclusion (figure 6.15a) work must be done (a) to overcome the elastic interactions between dislocation and inclusion, (b) to force the dislocation through the inclusion lattice, and (c) to create new matrix-inclusion boundaries (*i.e.* a step on either side of the inclusion). The magnitude of the elastic dislocation-inclusion interactions depends upon the

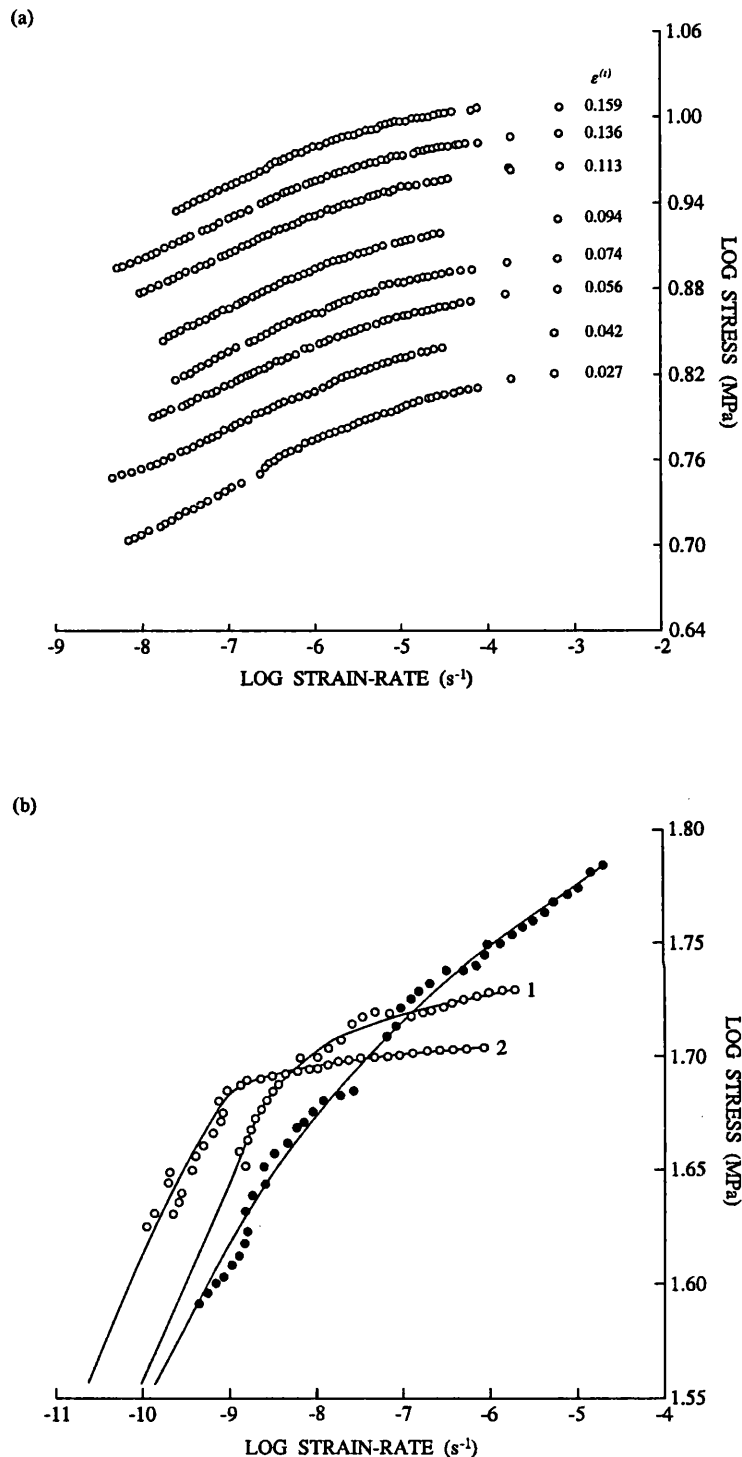
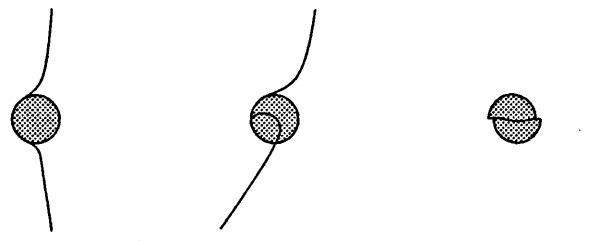


FIG. 6.14. Effect of solute impurities on the plastic element. (a) Slightly sigmoidal load relaxation curves generated from Cd<sup>2+</sup> doped AgCl single crystals at room temperature. The sigmoidal form is attributed to the progressively increasing influence of solute segregation as the driving force for relaxation diminishes (redrawn after Lerner and Kohlstedt, 1982). (b) Crossing load relaxation curves generated from commercial purity aluminium at room temperature after reloading to stresses below the initial stress of the first relaxations. The crossing behaviour results from changes in  $\dot{\epsilon}^*$  induced by solute segregation during the relaxations (redrawn after Rohde *et al.*, 1981).

(a)



(b)

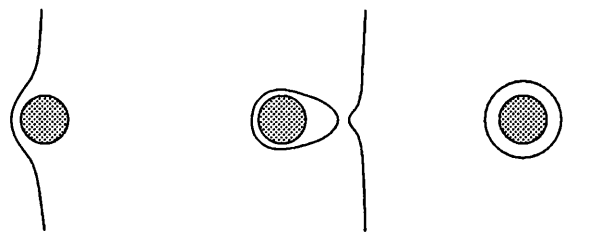


FIG. 6.15. The circumvention of finely dispersed inclusions by dislocations. (a) The dislocation cuts through the inclusion or (b) it bows around it.

difference in atomic volume between matrix and particle. The work required to force a dislocation through the inclusion enters the problem because if the mechanical properties of matrix and inclusion differ, then there is a corresponding difference in the stress needed to move the dislocation through the inclusion rather than the matrix. The work required to create new matrix-inclusion boundaries depends upon their interfacial energy. If the inclusion has an ordered lattice, work must also be done to create a disordered interface across the slip plane. Furthermore, if the lattice parameters of matrix and inclusion differ, misfit dislocations must be created at the matrix-inclusion interface.

To go around an inclusion (figure 6.15b) work must be done to force the dislocation to undergo large changes in curvature. The necessary changes in curvature depend upon inclusion size, shape and spacing, and upon the magnitude of the elastic dislocation-inclusion interactions. Since the radius of curvature of a dislocation is inversely proportional to the applied stress, the work required is also a function of those variables. However, usually when the inclusions are mechanically strong, incoherent and widely spaced, it requires less work to go around an inclusion than to cut through it.

In summary, the significance of the inclusion effect depends on microstructural (particle size, shape, number and distribution), crystallographic (the difference between the inclusion and matrix lattices) and mechanical (the difference in mechanical properties between inclusion and matrix) factors. All of these may vary with temperature. Variations in microstructure induced by temperature changes (*e.g.* the precipitation, growth or redistribution of the inclusions) are particularly significant because they may lead to a change in the way the

dislocations overcome the inclusions. However, the variation of the other factors may also be important. Thus for example, the elastic dislocation-inclusion interactions may vary considerably with temperature if the thermal expansion coefficients of matrix and inclusion are significantly different.

*6.3.2.2 The effect of inclusions on multiple relaxation experiments* : The effect of a random dispersion of inclusions on a load relaxation at given  $\sigma^*$  and  $T$  is a function of stress. At high stresses, the dislocations can readily overcome the inclusions and the relaxation proceeds as for the pure material. However, as the stress decreases the inclusions become more significant and the rate of relaxation diminishes faster than observed in the inclusion-free material. Finally at low stresses the rate of relaxation is controlled by the rate at which the inclusions can be overcome, and the relaxation then proceeds as for the pure material but displaced to a higher  $\sigma^*$  curve than the one on which it began. The influence of inclusions on the shape of the relaxation curve decreases with increasing  $\sigma^*$  as the barriers posed by the immobile dislocation network become more significant relative to those presented by the inclusions. Those relaxations most heavily influenced show yielding peaks on the reloading stress / strain curves as the mobile dislocations are forced to break-free of the inclusions before they can move. The effect of inclusions on multiple relaxation experiments is therefore qualitatively similar to that produced by diffusive solute segregation (§ 6.3.1.2). However, there is a less systematic temperature dependence in inclusion influenced experiments, reflecting the complex effect temperature has on determining the inclusion circumvention mechanism and its potential for permitting microstructural evolution.

The effect of inclusions on multiple relaxation experiments has been observed by Lerner and Kohlstedt (1982). They compared the room temperature deformation of pure AgCl single crystals with that of AgCl single crystals containing ultravioletly induced (prior to the deformation)  $\text{Ag}^0$  particles. The resulting relaxation and reloading stress / strain curves (figure 6.16a-c) show all the features described above. The effect of an evolution in the inclusion microstructure during relaxation has been invoked by Povolo and coworkers (Povolo and Tinivella, 1984a,b ; Povolo and Reggiardo, 1988) to explain the failure of various stainless steels (at 300 and 500°C) and Inconel (at 500°C) to form a one-parameter family of relaxation curves.

*6.3.2.3 Towards a parameterization for the inclusion effect* : Finely dispersed inclusions affect the scale of the strong barrier network rather than the rate of dislocation motion, and hence are most appropriately included in Hart's model by a parameterization of the  $\sigma^*$  evolution equation. This parameterization must express the changing role of the inclusion as a barrier to dislocation motion, as a function of both  $\sigma$  and  $\sigma^*$ . It must also be specified as a function of the inclusion circumvention mechanism. This follows from for example, the observation that when a dislocation goes around an inclusion by the mechanism shown in figure 6.15b, a dislocation is left ringing the inclusion, thereby opposing further slip on the slip plane and forcing the material to work harden (*i.e.* increase in  $\sigma^*$ ) more rapidly than if the inclusion had been cut through.

The dependence on the inclusion circumvention mechanism complicates the parameterization task because of the large number of factors influencing that mechanism. This

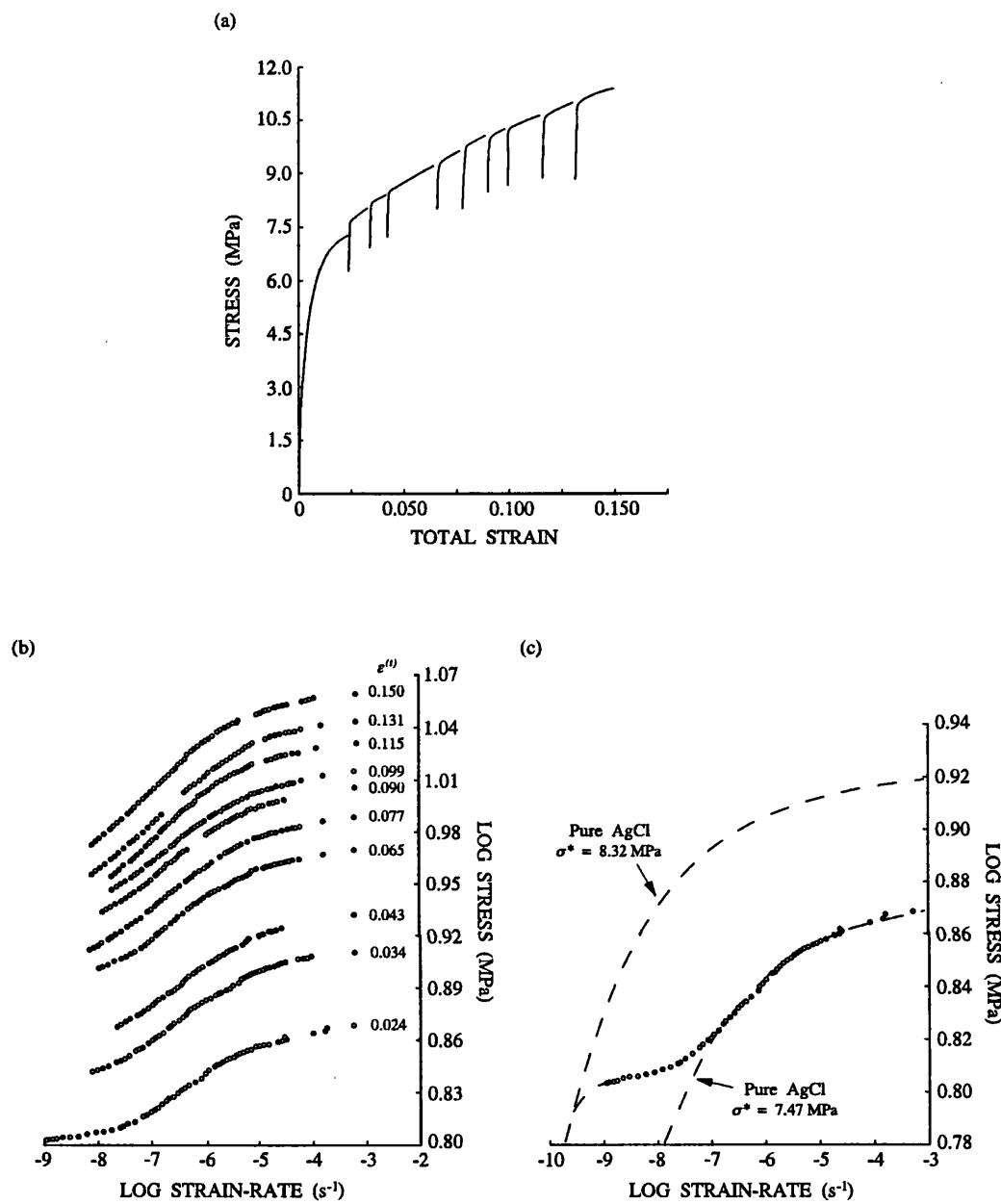


FIG. 6.16. The effect of finely dispersed  $\text{Ag}^0$  particles on the load relaxation behaviour of  $\text{AgCl}$  single crystals at room temperature. (a) The stress / strain curves and (b) the corresponding load relaxations. The sigmoidal form of the relaxation curves is attributed (c) to the increasing significance of the  $\text{Ag}^0$  particles as strong barriers to dislocation motion as the driving force for relaxation diminishes (redrawn after Lerner and Kohlstedt, 1982).

is emphasized by the difficulty of predicting the temperature dependence of the inclusion effect, and is particularly problematic when the inclusion microstructure evolves during deformation. It seems probable that before any parameterization can be attempted, a much closer comparison of Hart's equations with theoretical creep and work hardening models will be required.

**6.3.3 Grain-size.** Grain-size affects the inelastic deformation behaviour of polycrystalline materials through the role grain boundaries play in the deformation. Grain boundaries demarcate regions of polycrystal which are of different crystallographic orientation and which

consequently respond differently to a given stress field. They therefore present both obstacles to dislocation motion and sites where large strain gradients must be accommodated if strain compatibility between neighbouring grains is to be maintained.

As obstacles to dislocation motion, grain boundaries force dislocations to pile up behind them. When the resulting stress concentration becomes sufficient to activate dislocation sources in the neighbouring grain (or grain boundary), the deformation is able to propagate across the boundary. This stress concentration increases with the number of contributing dislocations, which in turn increases with the distance between dislocation source and barrier. Given that the maximum distance available between source and barrier decreases with grain-size, decreasing grain-size decreases the stress concentration and therefore makes the propagation of the deformation more difficult (*i.e.* strengthens the material).

The large strain gradients in the grain boundary are mechanically significant because they require a proportionately large number of dislocations to accommodate them. While these dislocations do not achieve the general strain (*i.e.* they are only geometrically necessary), they do increase the local dislocation density and hence increase the strength of the grain boundary as an obstacle to dislocation motion. This effect increases with the volume fraction of grain boundaries and hence contributes to the strengthening of materials as grain-size decreases.

Empirically it is found that the dependence of the flow stress on grain-size is given by the Hall-Petch equation

$$\sigma = \sigma_{hp} + k_{hp} d^{-1/2} \quad (6.42)$$

where  $\sigma_{hp}$  and  $k_{hp}$  are material parameters and  $d$  is the grain-size. In the case that the grain-size sensitivity is independent of strain (*i.e.* the magnitudes of  $\sigma_{hp}$  and  $k_{hp}$  are deformation independent), equation 6.42 predicts that the stress / strain curves generated in isothermal constant strain-rate tests on specimens of different grain-size, differ only by a translation parallel to the stress axis. However, if the grain-size sensitivity is strain dependent, such stress / strain curves crosscut.

**6.3.3.1 Factors influencing grain-size sensitivity :** The extent to which the inelastic deformation properties of a material are grain-size sensitive depends upon the importance of the grain boundary as a barrier to dislocation motion relative to those factors limiting dislocation motion within the grain. This is expressed in equation 6.42 by the relative magnitudes of  $\sigma_{hp}$  (which reflects the within grain factors) and  $k_{hp} d^{-1/2}$  (reflecting the significance of the grain boundaries). Anything increasing  $\sigma_{hp}$  relative to  $k_{hp} d^{-1/2}$  therefore decreases the grain-size effect.

The rate of dislocation motion in the grain interiors is affected, as discussed previously, by temperature, solute impurities and finely dispersed inclusions. The importance of the grain boundaries as obstacles to dislocation motion is determined primarily by the number of slip systems available and by the structure of the grain boundary. A large number of slip systems enables deformation to propagate across the grain boundary more easily while also making it easier to accommodate the large strain gradients near the boundary. The structure of the grain boundary, which may be affected by temperature, solute impurities and finely dispersed inclusions, determines the ease with which it can act as a dislocation source and hence assist in propagating the deformation. In general therefore, grain-size sensitivity (*i.e.* the magnitudes of

$\sigma_{hp}$  and  $k_{hp}$ ) is a function of impurity content and temperature.

The grain-size sensitivity may also be strain dependent if the role of solute impurities and finely dispersed inclusions, both on within grain dislocation motion and on grain boundary structure, varies during the deformation. Similarly the development of a crystallographic preferred orientation may change the role played by the number of available slip systems, by altering the ease with which deformation may be propagated between grains, and by affecting the number of geometrically necessary dislocations required.

**6.3.3.2 The effect of grain-size on multiple relaxation experiments :** Except for ultrafine grained materials where the obstacle posed by the grain boundary dominates the strong barrier network, grain-size does not influence within grain dislocation motion and hence should not affect load relaxation behaviour. This has been confirmed by Tanoue and coworkers (Tanoue *et al.*, 1983 ; Tanoue and Matsuda, 1984) who deformed pure molybdenum specimens of various grain-sizes (17 – 1500  $\mu\text{m}$ ) at several different temperatures in the low homologous temperature regime. Good scaling behaviour was observed in each suite of relaxations with the scaling slope being grain-size independent.

**6.3.3.3 Towards a grain-size parameterization :** By being obstacles to dislocation motion and sites of high dislocation density, grain boundaries can be expected to influence the development of the strong barrier network during deformation but not the barrier circumvention or dislocation glide processes themselves. Hence the equations of state in Hart's model should be grain-size independent (as indicated by the results of Tanoue and coworkers, § 6.3.3.2) but the  $\sigma^*$  evolution equation (equations 5.14 – 5.16) should not be.

Where the grain-size sensitivity is independent of strain, it may be fully incorporated by parameterizing the term  $\sigma_0^*$  for grain-size (*cf.* § 4.2.2.3). Where there is a strain dependence, other parameters in equations 5.14 – 5.16 will be affected. A closer comparison of Hart's equations with theoretical work hardening models is required before further conclusions can be drawn.

**6.3.4 'Unusual' deformation variables.** Inelastic deformation is affected by several features of the deformation environment besides  $\sigma$ ,  $\dot{\varepsilon}^{(n)}$  and  $T$ . Among the most significant of these are the isostatic pressure, the composition and pressure of any fluids (liquid or gaseous) present, and the presence of a source of irradiation. The incorporation of the effects of these extra deformation variables into Hart's analysis must be done on a case by case basis and be founded upon an account of the way in which variable of interest exerts its influence on the deformation. To illustrate this procedure, an attempt to incorporate the effects of a source of irradiation (which is the only one of these variables to have received attention within the context of Hart's analysis) is described.

On entering a crystalline solid, fast moving atomic particles emitted from a radiation source generate vacancy and interstitial point defects which may develop, either *in situ* or by diffusion, into vacancy or interstitial dislocation loops. If the particle is of sufficient energy, the knock-on effects after a collision may involve many hundreds of atoms and lead to locally depleted zones of lattice. Both the vacancy / interstitial loops and the depleted zones can form strong obstacles to dislocation motion and thereby strengthen the irradiated material. However, isolated excess vacancies may enhance diffusive accommodated barrier circumvention

processes and lead to a weakening effect. The incorporation of irradiation into Hart's analysis therefore requires both a description of the effect of the accumulated microstructural damage due to the radiation *fluence*, and a description of the effect of the supersaturation of point defects due to the current radiation *flux*.

Hart and Li (1977) proposed that the fluence effect could be accommodated into the equation of state for the plastic element (equation 5.10) by changes in  $\sigma^*$  and  $\varepsilon^*$  (*i.e.*  $\lambda$  is unaffected), while the flux effect could be accommodated wholly by changes in  $\varepsilon^*$  (since it acts like temperature). If correct then irradiation should result in a rigid body translation of the constant  $\sigma^*$  curves in  $\log \sigma - \log \dot{\varepsilon}$  space (figure 6.17a). There is some experimental support for this. Lerner and Kohlstedt (1982) found that  $\gamma$ -irradiated single crystals of AgCl produced a family of  $\sigma^*$  curves which had a different scaling slope to that of the unirradiated crystals (implying a change in  $\varepsilon^*$  through  $m$ , equation 5.11 and § 4.1.2.1), but that the two families superposed after a rigid translation (figure 6.17b). Similar results were obtained for  $\gamma$ -irradiated single crystals of NaCl (Lerner and Kohlstedt, 1981). There has been no attempt to quantify the fluence or flux effects, nor to determine their effect on either the equation of state for the friction element or the  $\sigma^*$  evolution equation.

Although the experimental data is limited, there seems little reason to doubt that Hart's analysis can accommodate the effects of irradiation. The ability of the analysis to incorporate other environmental variables remains to be determined.

#### 6.4 Deformation occurring at $T > 0.45 T_m$ . (a) Recovery

In the preceding discussion (prior to § 6.3) it has been assumed that inelastic deformation is fully accommodated by the grain matrix, and that the plastic mechanical state can be changed only by such deformation under the action of an applied differential stress (*cf.* § 2.1). However, at temperatures above  $0.45 T_m$  diffusive processes become sufficiently active to allow the operation of grain boundary sliding processes, and to cause thermally induced, nominally deformation independent changes in mechanical state (*i.e.* recovery). Before Hart's analysis can be extended to higher temperatures it is therefore necessary that some description be found for both these aspects of high temperature deformation.

The incorporation of high temperature recovery into Hart's analysis has received little attention and consequently the following discussion is concerned primarily with outlining a possible approach to this problem. The accommodation of grain boundary sliding has been given much greater consideration and is described in § 6.5.

**6.4.1 Recovery processes.** By definition, a recovery process is one that provides a negative contribution to the athermal work hardening-rate. The athermal work hardening-rate is a measure of the rate of increase of elastic strain energy accompanying the accumulation of dislocations. Hence any process which either removes dislocations or rearranges them into a lower energy configuration is a recovery process.

It has been conventional to refer to recovery occurring during deformation as *dynamic*, and that occurring after deformation as *static*. However, in the following discussion a recovery process will be considered dynamic only if it requires a differential stress to be active. By default all other recovery processes will be regarded as static, even when they operate during

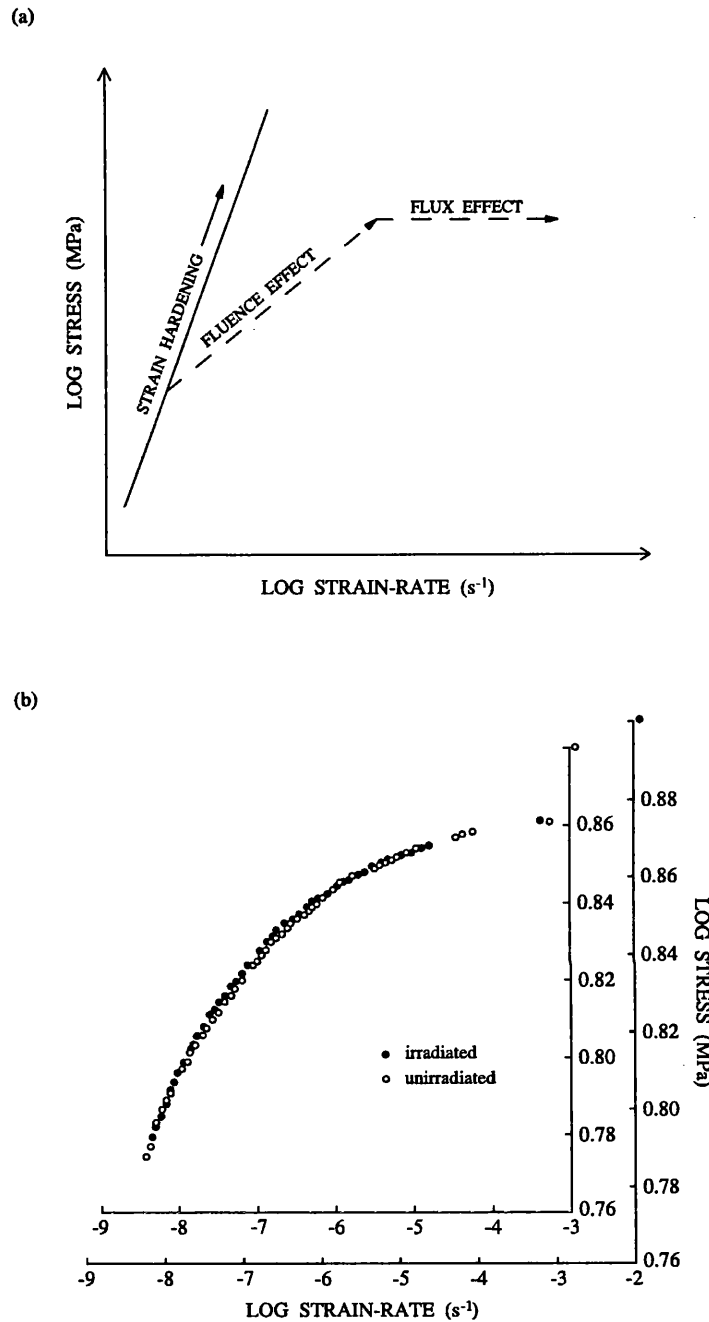


FIG. 6.17. The effect of irradiation on constant  $\sigma^*$  curves. (a) The predicted effect on a given point of a  $\sigma^*$  curve (redrawn after Hart and Li, 1977). (b) The effect of  $\gamma$ -irradiation on the relaxation curves of AgCl single crystals at room temperature. The irradiated and unirradiated curves superpose but the scaling direction is influenced by the irradiation (redrawn after Lerner and Kohlstedt, 1982).

deformation. This stronger definition is more suited to Hart's analysis and is apposite on mechanistic grounds.

**6.4.1.1 Dynamic recovery processes (*sensu stricto*)** : Dynamic recovery is driven by an externally applied differential stress and, as defined here, results only from the annihilation of dislocations during strong barrier circumvention (*cf.* § 5.3.1.4). In anisotropic materials it may in principle, also result from the elimination of dislocations during stress induced boundary

migration. However, the driving force for this boundary migration – the difference in elastic strain energy (reflecting the anisotropy of the elastic constants) between two subgrains / grains differently oriented with respect to the applied differential stress – is in general, insufficient to make the process important (Paterson, 1973). The rate of dynamic recovery is therefore a function of those factors influencing the rate of strong barrier circumvention *i.e.*  $\sigma$  and  $\alpha$  (and hence  $\sigma^*$ ),  $T$  (the strong barrier circumventing processes are thermally activated, § 5.3.1.1), and material characteristics such as purity and grain-size (§ 6.3).

In restricting dynamic recovery to these processes, the assumption is made that apparently dynamic recovery processes (*e.g.* subgrain formation) are actually static processes which occur at enhanced rates under applied differential stress because of the maintenance of high levels of  $\sigma^*$  (through the continuous generation of new dislocations).

**6.4.1.2 Static recovery processes (*sensu lato*)** : Static recovery processes are driven by the local elastic stresses arising from the presence of lattice defects. These stresses may cause (a) dislocation motion, leading to the annihilation of the dislocations of opposite sign which meet each other and to the rearrangement of dislocations into low energy configurations (*i.e.* into a subgrain network), and (b) strain induced boundary migration leading to the elimination of dislocations in the migrating grain boundary.

In a material of given purity and grain-size, the rate of static recovery is, by definition, a function only of  $\sigma^*$  and  $T$ . Since the driving force for such recovery is relatively small, a high concentration and mobility of vacancy point defects is required. Static recovery by dislocation motion becomes rate significant at  $T > 0.45 T_m$ , although it may be important at slightly lower temperatures if the vacancies generated by deformation are of sufficient concentration. It is influenced by solute impurities, finely dispersed inclusions and grain-size through the way that these affect dislocation mobility (§ 6.3). Static recovery by boundary migration becomes rate significant at  $T > 0.5 T_m$  if the driving force is sufficient. It is strongly dependent on the vacancy concentration at the boundary for this determines the number of sites on either side of the boundary that atoms can jump to or from. Hence boundary mobility increases with increasing  $\sigma^*$ , with increasing misorientation of the lattices across the boundary, and with decreasing grain-size. It is also strongly influenced by impurity solutes and finely dispersed inclusions for these interact with the boundaries in the same way that they interact with dislocations (§ 6.3.1.1 and 6.3.2.1).

The relative importance of dislocation motion and boundary migration as agents of static recovery reflects the influence of the factors described above on the relative mobility of dislocation and boundary. At comparatively low temperatures and mechanical states, the grain boundaries are immobile and recovery occurs entirely through dislocation annihilation and subgrain formation. In the presence of an externally applied differential stress, the continual generation of new dislocations and their accommodation into the subgrain walls may reduce the dislocation spacing in those walls and thereby lead to a progressive increase in the misorientation of the lattices across the subgrain boundary. Eventually the misorientation may be such that the subgrain becomes a new grain (rotation recrystallization). At higher temperatures and mechanical states, the subgrain / grain boundaries become mobile. This allows recovery to proceed by the formation of relatively strain-free nuclei which then grow rapidly to

replace the deformed aggregate (migration recrystallization). The recrystallization nuclei may be formed by the grain boundary bulging mechanism or by the progressive misorientation of subgrains with respect to their neighbours (by incorporation of increasing numbers of dislocations in the subgrain walls, by subgrain impingement and/or by grain coalescence, figure 6.18). Growth occurs at some critical lattice misorientation across the boundary which is a function of the boundary structure and the difference in strain energy across it. In general, at given temperature increasing the concentration of solute impurities and of finely dispersed inclusions increases the mechanical state required for the onset of boundary migration. However, the precise effect depends on the magnitude of the solute / inclusion interactions with the dislocations / boundaries, for this determines whether the dislocations / boundaries break-free of the solutes / inclusions, whether they drag them with them, or whether they are pinned by them. Solute impurities may even enhance boundary migration if differences in impurity concentration across the boundary lead to significant differences in chemical potential (and hence to chemically induced boundary migration). Decreasing grain-size at given temperature lowers the mechanical state required for boundary migration.

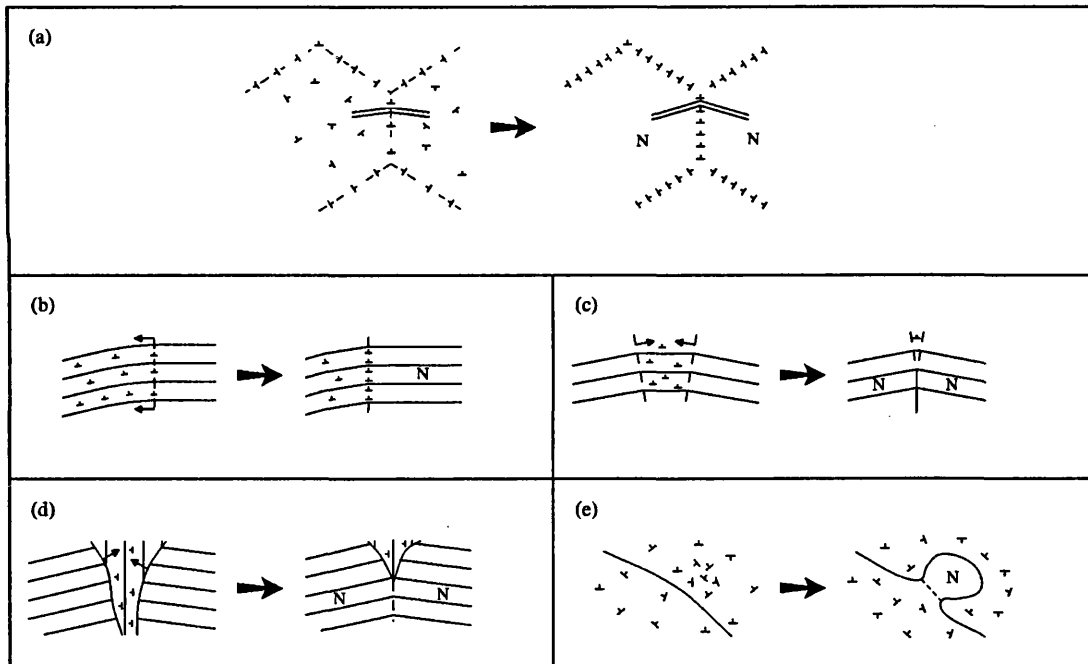


FIG. 6.18. Mechanisms of forming recrystallization nuclei.

(a) Rotation recrystallization – the progressive misorientation of neighbouring subgrains through the removal of dislocations from the subgrain interiors to the subgrain walls.

(b), (c) Subgrain boundary migration – (b) the progressive misorientation of neighbouring subgrains through the incorporation of those dislocations encountered by the migrating boundaries into the subgrain walls ; (c) the formation of a relatively mobile subgrain wall through the consumption of a relatively highly strained intervening subgrain (subgrain impingement).

(d), (e) Grain boundary migration – (d) the formation of a subgrain wall by the coalescence of two grains of similar orientation through consumption of the intervening grains (grain coalescence) ; (e) the grain boundary bulging mechanism which must be assisted by one or more of (a) to (d) to close the bulge.

In the figures the heavy solid lines are grain boundaries, the dashed lines are subgrain boundaries, the light lines indicate the lattice orientation and N the recrystallization nuclei.

**6.4.2 The effect of recovery processes on mechanical behaviour.** The effect of recovery processes on the mechanical properties of an isotropic, pure material of given grain-size is described for recovery occurring before and after constant displacement-rate deformation. It is assumed that any changes in grain-size are insufficient to make grain boundary sliding rate-significant.

**6.4.2.1 Recovery during deformation :** The operation of recovery processes during deformation characteristically leads to three types of constant displacement-rate stress / strain curves.

Under conditions where the grain boundaries are immobile the stress / strain curves show a progressively decreasing rate of work hardening as the deformation proceeds (curve 1, figure 6.19a). Rotation recrystallization has no important effect on the curves except for the strengthening that results from the decrease in the grain-size (§ 6.3.3).

Under conditions where the boundaries are mobile and where  $\sigma^*$  is large (when grain boundary migration begins at large stresses or in materials of large grain-size), the stress / strain curves show a single peak stress followed by strain softening (curve 2, figure 6.19a). This behaviour results from successive cycles of recrystallization which are out of phase (figure 6.19b) because there are large strain (*i.e.*  $\sigma^*$ ) gradients across individual grains. Such recrystallization leads to 'necklace' type textures and can be described as growth controlled because the growth of the new grains ceases when the driving force for it is destroyed by the concurrent deformation.

Under conditions where the boundaries are mobile and where  $\sigma^*$  is small (when grain boundary migration begins at small stresses or in materials of small grain-size), the stress / strain curves display periodic oscillations in stress (curve 3, figure 6.19a). This behaviour also results from successive cycles of recrystallization, but in this instance the magnitude of the strain gradients across individual grains is smaller and the cycles are more in phase (figure 6.19c). The growth of new grains is terminated by boundary impingement and so the recrystallization can be described as nucleation controlled.

**6.4.2.2 Recovery after deformation :** The effect of recovery processes operating after deformation can be investigated by loading a specimen to a given strain and by then offloading and annealing it for a given period. The specimen may then be removed for analysis of the recovered microstructure or it may be reloaded under the original deformation conditions to determine the amount of recovery. In such interrupted constant displacement-rate tests, the amount of recovery is estimated from a comparison of the deformation behaviour before and after the anneal (most commonly from a comparison of the reloading yield stress with the flow stress at the end of the initial loading, but see § 14.1.1 for an extended discussion), and is presented as curves of *fractional recovery* versus log anneal time for given pre-strain and anneal temperature (figure 6.20a,b). Under conditions where the boundaries are mobile such curves are typically sigmoidal with slopes that vary from shallow to steep to shallow as time increases. Microstructural observations show that the initial shallow portion of the curve corresponds to recovery by dislocation annihilation and subgrain formation, while the steep portion marks the onset and progression of migration recrystallization (*cf.* the indicated percentage recrystallization figures on the curves shown in figure 6.20a). The final shallow portion of the curves corresponds to the further reorganization of those dislocations remaining

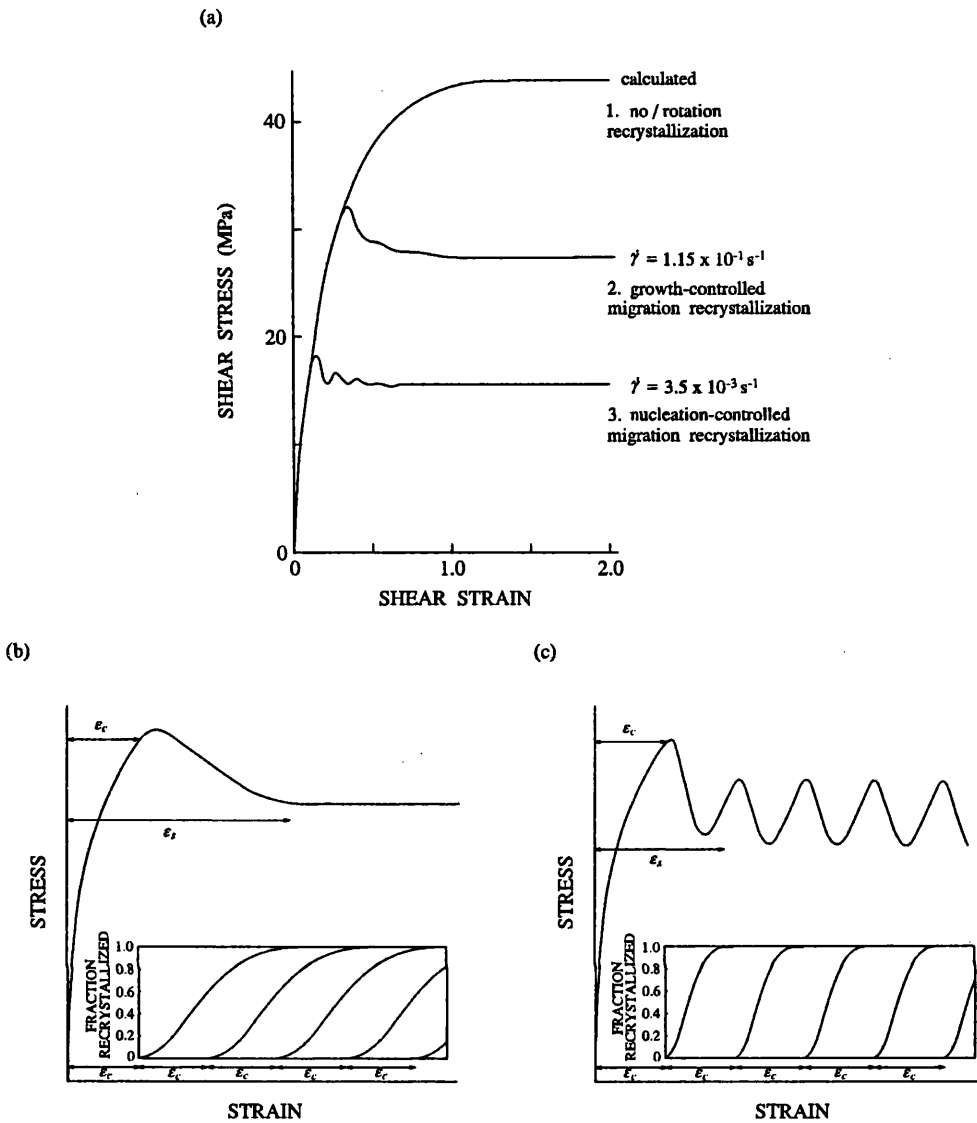


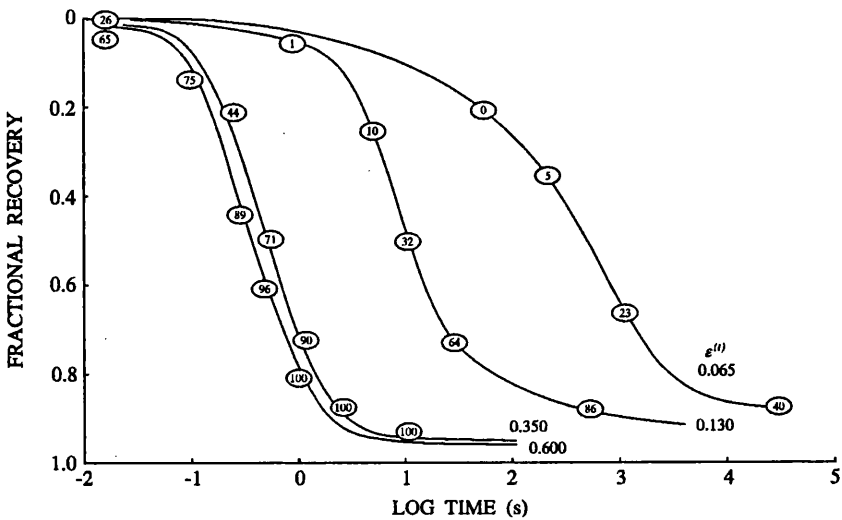
FIG. 6.19. The mechanical consequences of recrystallization during constant strain-rate tests. (a) The behaviour of 99.9% nickel deformed in torsion at 934°C and the indicated strain-rates. The strain-rate is used to control the stress at which recrystallization begins (redrawn after Sellars, 1978). The form of the stress / strain curves for (b) growth-controlled and (c) nucleation-controlled migration recrystallization may be interpreted in terms of the length  $\varepsilon_s$  of each recrystallization cycle relative to the critical strain  $\varepsilon_c$  required to initiate the cycle (redrawn after Luton and Sellars, 1969).

after complete recrystallization. Increasing the mechanical state and/or the temperature steepens the initial shallow portion of the recovery curve by enhancing the efficiency of the dislocation annihilation and reorganization processes, while it also translates the steep portion of the curve towards short times by decreasing the incubation time required for recrystallization.

**6.4.3 Incorporation of recovery into Hart's analysis.** Within the context of Hart's analysis, recovery processes are those processes which diminish the rate of increase of  $\sigma^*$  given by the athermal ( $\Gamma^*$ ) term in the  $\sigma^*$  evolution equation (equation 5.13). Rewriting equation 5.13 to make the recovery terms explicit yields

$$d(\ln \sigma^*)/dt = \alpha [\Gamma^*(\sigma^*) - R^*(\sigma^*, \sigma_a)] - \mathfrak{R}(\sigma^*, T) \quad (6.43)$$

(a)



(b)

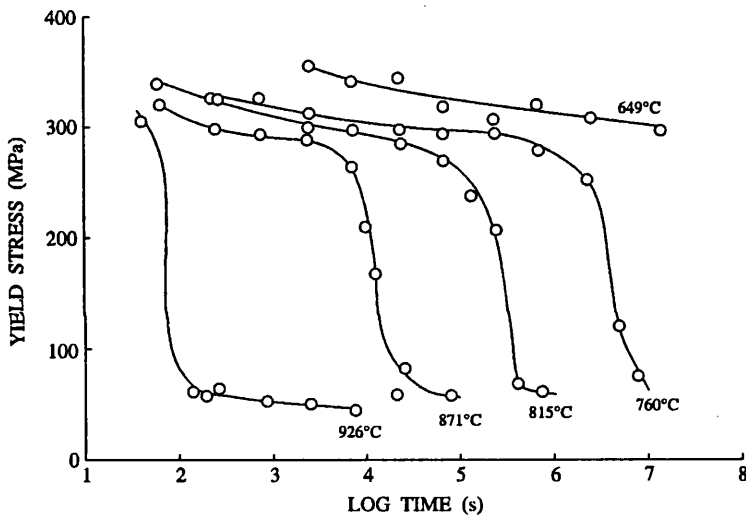


FIG. 6.20. Fractional recovery curves produced from interrupted constant displacement-rate tests. (a) Recovery of OFHC copper at 550°C after deformation to four different pre-strains. Recovery was estimated using equation 14.4 and the numbers on the curves indicate the volume fraction recrystallization (redrawn after Kwon and DeArdo, 1990). (b) Recovery of 20% cold-worked Type 316 stainless steel at five different anneal temperatures. Recovery was estimated by the 0.2% yield stress at 538°C which is approximately equal to  $\sigma^*$  (redrawn after Alexopoulos *et al.*, 1982; data is that of Paxton, 1974).

where the athermal term  $\Gamma^*(\sigma^*)$  is given by equation 5.15, and  $R^*(\sigma^*, \sigma_a)$  and  $\mathfrak{R}(\sigma^*, T)$  describe dynamic recovery (*sensu stricto*) and static recovery (*sensu lato*) respectively. Dynamic recovery is fully accommodated within the  $\Gamma(\sigma^*, \sigma_a)$  function in equation 5.13, and so  $R^*(\sigma^*, \sigma_a)$  may be determined from equations 5.14 - 5.16. Since this is unnecessary, the following discussion is restricted to the  $\mathfrak{R}(\sigma^*, T)$  function. It is assumed that the  $\mathfrak{R}(\sigma^*, T)$  function can be expressed as the sum of a component due to dislocation motion and a component due to boundary migration.

**6.4.3.1 Static recovery by dislocation motion :** To determine the component of  $\mathfrak{R}(\sigma^*, T)$  due to

dislocation motion, it is necessary to find some function which describes the time rate of change of mechanical state produced by dislocation annihilation and subgrain formation in terms of the current value of  $\sigma^*$  and the temperature. This may be done using interrupted constant displacement-rate tests to construct curves of  $d\sigma^*$  versus anneal time for various annealing temperatures and after different pre-strains. The deformation must be conducted under conditions where  $\sigma^*$  is determinable as a function of loading strain (*i.e.* at  $T < 0.45 T_m$ ), and if recovery by a boundary migration mechanism occurs during the anneal, only data from the shallow sloping portions of the fractional recovery curves should be used.

The only attempt to determine such a recovery function is that of Yamada (1977). He annealed 20% cold worked Type 316 stainless steel for various durations at temperatures of 600 to 700°C, and determined  $\sigma^*$  after each anneal from room temperature load relaxations conducted just beyond the plastic yield point. He observed that  $\sigma^*$  decreased monotonically to a temperature dependent limiting value  $\sigma_\infty^*$  (figure 6.21a), and so assumed that  $d\sigma^*/dt$  was proportional to the difference between the current and asymptotic value of  $\sigma^*$

$$\mathfrak{R}(\sigma^*, T) = -d(\ln \sigma^*)/dt = -(\sigma^* - \sigma_\infty^*)/(\sigma^* t_1) \quad (6.44)$$

where  $t_1$  is a temperature dependent time constant.

Yamada's results were complicated by the formation of precipitates during annealing, thereby raising questions concerning the general applicability of equation 6.44 and the existence of  $\sigma_\infty^*$  at long (*e.g.* geological) times. Static recovery by dislocation processes is more commonly represented as (*e.g.* Honeycombe, 1968)

$$x = A - B(\ln t - H_f/RT) \quad (6.45)$$

where  $x$  is some increment of a physical or mechanical property above that of the undeformed material,  $A$  and  $B$  are constants, and an Arrhenius temperature compensated time has been employed. Using  $x = \sigma^*$ , Yamada's results are equally well described by equation 6.45 (figure 6.21b). Equation 6.45 implies that  $d\sigma^*/dt$  is independent of  $\sigma^*$ , suggesting that  $\sigma^*$  affects merely the scale of the dislocation recovery processes (*e.g.* subgrain-size) and not their kinetics. However, as presented here it yields a function for  $\mathfrak{R}$  which contains time as a variable.

Further theoretical and experimental work is required before a general  $\mathfrak{R}$  function for dislocation processes can be determined. In addition some function describing the progression of rotation recrystallization and the resulting grain-size is required for use in the grain-size parameterized  $\Gamma(\sigma^*, \sigma_a)$  function (§ 6.3.3).

**6.4.3.2 Static recovery by boundary migration :** To determine the component of  $\mathfrak{R}(\sigma^*, T)$  due to boundary migration, it is necessary to find some function which describes the time rate of change of mechanical state during a recrystallization cycle (*i.e.* as the volume fraction of recrystallized grains increases), while expressing the rate of recrystallization as a function of  $\sigma^*$  and  $T$ .

Within the context of Hart's analysis the only attempts to describe recovery by boundary migration have been to employ empirical fits to the steeply sloping portions of the recovery curves shown in figure 6.20b (Wire *et al.*, 1979 ; 1981). However, deformation induced recrystallization like other phase transformations, may be treated formally as a nucleation and growth process in which the important parameters are the nucleation and growth rates of the recrystallizing grains. The volume fraction  $X_{rx}$  of the recrystallized material is then described

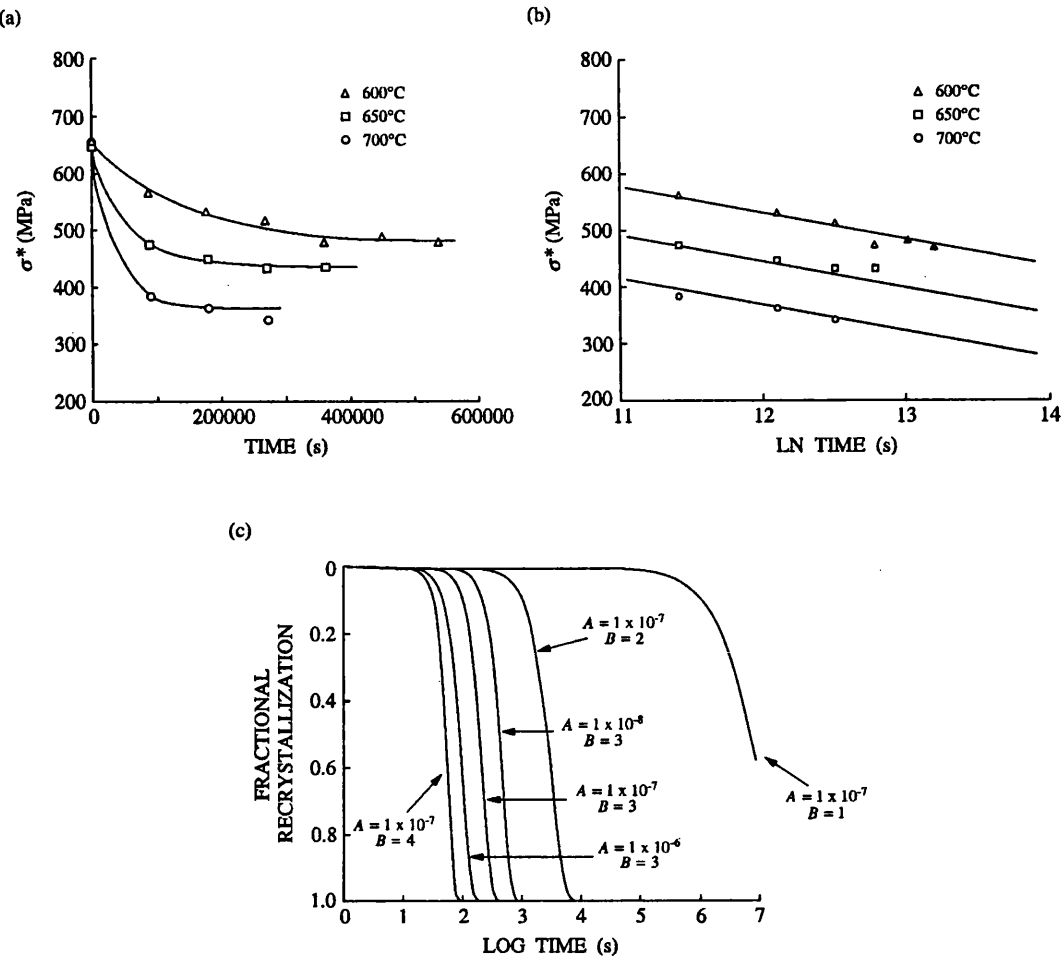


FIG. 6.21. Towards a recovery function. (a) The change in  $\sigma^*$  during static annealing of 20% cold-worked Type 316 stainless steel. The value of  $\sigma^*$  after annealing was determined from room temperature load relaxations conducted at just beyond the plastic yield point. The curves are the fits of the data to equation 6.44 (redrawn after Yamada, 1977). (b) The data of (a) replotted according to equation 6.45. (c) The effect of the parameters  $A$  and  $B$  in the Avrami equation (equation 6.46) on the fractional recrystallization curves predicted by that equation.

by the Avrami equation (e.g. Tiller, 1991)

$$X_{rx} = 1 - \exp(-At^B) \quad (6.46)$$

(cf. figure 6.21c) where  $A$  is a constant which depends on the nucleation and growth rates, and  $B$  is constant which reflects the geometry of the nucleation / growth situation. It follows that the  $\mathcal{R}(\sigma^*, T)$  function can be found by fitting equation 6.46 to data supplied from the microstructural analysis of interrupted constant displacement-rate tests, while using the mechanical data from those tests (after subtracting the component of recovery due to dislocation motion) to determine  $d\sigma^*$  as a function of  $X_{rx}$ . The  $\sigma^*$  and  $T$  dependence of the recovery function then resides in  $A$  and reflects the dependence of the nucleation and growth rates on those variables. Since the nucleation and growth rate dependence of  $A$  is specified in various theoretical models, this approach has the benefit of allowing experimentally determined values of  $A$  to be given a physically meaningful interpretation (thereby easing the consideration

of, for example, solute impeded boundary migration).

The Avrami equation has been applied successfully to the results of interrupted constant displacement-rate tests in several studies (e.g. Laasraoui and Jonas, 1991), and  $A$  has been found to be a well behaved function of pre-strain, loading strain-rate and temperature. This suggests that equation 6.46 can be used to describe the boundary migration component of  $\mathfrak{R}(\sigma^*, T)$ . However, further work is necessary, particularly with respect to the complications that might arise from the simultaneous operation of several different nucleation mechanisms, before this possibility can be fully evaluated. Some function describing the recrystallized grain-size is also required, both for use in the grain-size parameterized  $\Gamma(\sigma^*, \sigma_a)$  function and to allow for the effects of that grain-size on any subsequent cycles of recrystallization.

**6.4.3.3 Employing the recovery function during deformation :** The approach to characterizing recovery outlined here relies on the interrupted constant displacement-rate test for parameter evaluation and is therefore most suited to describing changes of  $\sigma^*$  after deformation. Two practical limitations may arise in using it to describe recovery during deformation. Firstly, since static recovery processes are operative at all  $T > 0.45 T_m$ , the  $\Gamma(\sigma^*, \sigma_a)$  function (incorporating dynamic recovery) at these temperatures must either be determined from constant displacement-rate tests using a previously determined  $\mathfrak{R}(\sigma^*, T)$  function, or by extrapolating  $\Gamma$  from its observed temperature dependence at  $T < 0.45 T_m$  (equations 5.14 and 5.16). Both alternatives carry potentially large errors, the former reflecting the errors in determining  $\mathfrak{R}$ , and the latter the errors in determining the temperature dependence of  $\Gamma$  under conditions in which that dependence is relatively small. Secondly, the use of the interrupted constant displacement-rate test to determine the parameters in  $\mathfrak{R}(\sigma^*, T)$  underestimates the contribution of recovery mechanisms which rely on  $\sigma^*$  being dynamically maintained. This problem is particularly pertinent under circumstances where the formation of recrystallization nuclei by the subgrain misorientation is important. The significance of these problems is difficult to evaluate in the absence of experimental data. However, once an  $\mathfrak{R}(\sigma^*, T)$  function has been determined, they can be investigated by using it to simulate appropriate deformation experiments and then by comparing the simulations with actual experimental results (cf. § 7.2).

The method of applying the recovery functions described here when modelling deformation at  $T > 0.45 T_m$  would be similar to that used by Luton and Sellars (1969) to model constant strain-rate stress / strain curves during cyclic recrystallization. They used the Avrami equation to determine the (volume fraction) increment of recrystallization  $X_{rx}^{(i)}$  occurring in uniform increments of time (strain) once a critical strain  $\varepsilon_c$  for initiating recrystallization had been attained. As each increment recrystallized it was assumed that its flow stress fell instantaneously to zero and then followed the initial ( $\varepsilon < \varepsilon_c$ ) stress / strain curve. Hence the flow stress  $\sigma_{rx}^{(i)}$  of each increment was obtained after each increment of time. The flow stress  $\sigma_{unrx}$  of the unrecrystallized material was assumed to follow the extrapolation of the unrecrystallized material, so that the bulk stress was given by

$$\sigma = \sum_0^i X_{rx}^{(i)} \sigma_{rx}^{(i)} + \left(1 - \sum_0^i X_{rx}^{(i)}\right) \sigma_{unrx} \quad (6.47)$$

A new recrystallization cycle was assumed to begin again in each volume increment when the

critical strain was attained (cf. figure 6.19b,c). In the present analysis the application of the Avrami equation would be governed by some critical value of  $\sigma^*$  (not  $\varepsilon_c$ ) and the stresses  $\sigma_{rx}^{(i)}$  and  $\sigma_{unrx}$  by Hart's equations (incorporating the recovery function for recovery by dislocation motion).

## 6.5 Deformation occurring at $T > 0.45 T_m$ . (a) Grain boundary sliding

Grain boundaries are approximately planar regions with a thickness of atomic dimensions within a polycrystal. Being regions of a relatively high degree of atomic disorder, their mechanical properties differ from the grain matrix and hence a resolved shear stress acts along them during deformation. This stress induces a boundary parallel shear which is termed grain boundary sliding. At  $T < 0.45 T_m$  the shear is accommodated by recoverable elastic and anelastic deformation, but at higher temperatures the enhanced activity of diffusive processes allows it to produce a permanent plastic strain.

An extension of Hart's analysis to incorporate grain boundary sliding has been developed by Li and coworkers (Li, 1981 ; Alexopoulos *et al.*, 1982). In the following discussion this extended model is described.

**6.5.1 Hart's deformation model extended to include grain boundary sliding.** The extension of Hart's model proposed by Li and coworkers is shown in analogue form in figure 6.22a. It comprises a grain matrix branch (labelled 1) connected in parallel with a grain boundary sliding branch (labelled 2). Each branch contains an elastic (E) and a grain matrix (M) element connected in series, while branch 2 has an additional grain boundary (GB) element. The elastic elements account for the elastic deformation (matrix and boundary) of the aggregate and to simplify the present discussion are assumed to be linear with a common Young's modulus  $E$ . The grain matrix elements account for the grain matrix inelastic deformation and each have the same structure as Hart's original model (figure 5.3, or its refinement, figure 6.3b). The grain boundary element accounts for inelastic grain boundary sliding. The constraint equations for the model are

$$\sigma = P\sigma_1 + (1 - P)\sigma_2 \quad (6.48)$$

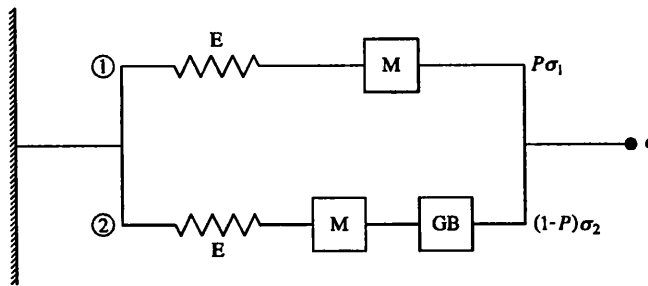
$$\dot{\varepsilon}^{(t)} = \dot{\varepsilon}_1^{(e)} + \dot{\varepsilon}_1^{(n)} = \dot{\varepsilon}_2^{(e)} + \dot{\varepsilon}_2^{(n)} + \dot{\varepsilon}_g^{(n)} \quad (6.49)$$

where the numerical subscripts refer to the branch labels,  $\dot{\varepsilon}_g^{(n)}$  is the grain boundary shear-rate and  $P$  is a stress partitioning factor which effectively indicates the stress concentration in the grain boundary 'phase'. The model reduces to Hart's original model if there is no grain boundary sliding because at the elastic limit (and consequently for all greater strains where  $\dot{\varepsilon}_g^{(n)} = 0$ ),  $\sigma = \sigma_1 = \sigma_2$  since  $\dot{\varepsilon}^{(t)} = \dot{\varepsilon}_1^{(e)} = \dot{\varepsilon}_2^{(e)}$ .

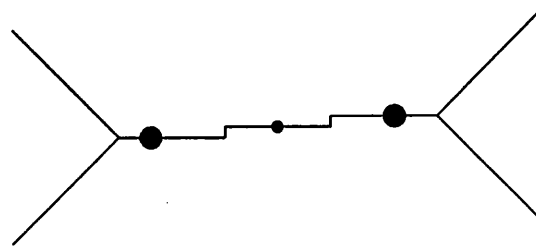
Given this extended model, the problem of incorporating grain boundary sliding reduces to one of prescribing a suitable constitutive relation for the GB - element. Figure 6.22b shows schematically a segment of grain boundary containing grain vertices, steps and second phase particles. In principle, if this representation contains all the features that are significant in controlling the rate of grain boundary deformation, then the GB - element can be depicted by the same analogue model as chosen to represent grain matrix deformation (figure 6.22c). The constraint equations and constitutive relations are once more

$$\sigma_2 = \sigma_{ag} + \sigma_{fg} \quad (6.50)$$

(a)



(b)



(c)

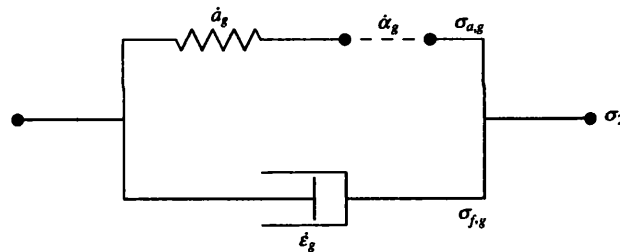


FIG. 6.22. Extension of Hart's deformation model to include grain boundary sliding. (a) An analogue representation of the extended model. (b) A schematic representation of a segment of grain boundary showing grain vertices, steps and second phase particles. (c) An analogue representation of the grain boundary (GB) element (figures modified after Li, 1981).

$$\dot{\varepsilon}_g = \dot{\alpha}_g + da_g/dt \quad (6.51)$$

$$\sigma_{a,g} = \mathcal{M}_g a_g \quad (6.52)$$

$$\ln (\sigma_g^* / \sigma_{a,g}) = (\dot{\varepsilon}_g^* / \dot{\alpha}_g)^{\lambda_g} \quad (6.53)$$

$$\dot{\varepsilon}_g^{(n)} = \dot{a}_g^* (\sigma_{f,g} / G)^{M_g} \quad (6.54)$$

In this instance the  $a_g$ - and  $\dot{\varepsilon}_g$ -elements acting together constitute grain boundary anelasticity. The constitutive relation of the  $\dot{\varepsilon}_g$ -element, which represents the frictional resistance to grain boundary shear, reflects grain boundary sliding rates controlled by grain boundary diffusive mass transfer processes. The constitutive relation for the  $\dot{\alpha}_g$ -element, which represents the resistance to boundary shear posed by the steps and other inhomogeneities

in the boundary, reflects boundary sliding rates controlled by grain matrix deformation at the sites of these obstacles.

**6.5.2 Experimental results.** Discussion of the experiments investigating grain boundary deformation processes is here restricted to those conducted from the perspective of the state variable analysis.

**6.5.2.1 Grain boundary anelasticity :** Nir *et al.* (1976) investigated the room temperature anelastic deformation of high purity aluminium, both in single crystals and in polycrystals. Using stress dip tests they identified the grain boundary anelastic component as that part of the deformation absent in the single crystals. They observed that it was very small in comparison with the grain matrix anelasticity, that equation 6.54 recast in its anelastic form (*cf.* equation 5.20)

$$\dot{a}_g = \dot{a}_g^* [(\sigma_2 - \mathcal{M}_g a_g)/G]^{M_g} \quad (6.55)$$

was obeyed with  $M_g = 1$ , and that  $\dot{a}_g^*$  was such that the grain boundary anelastic deformation was completely recovered within one second of the stress dip (figure 6.23a). Similar results have been reported for Type 316 stainless steel (Nir *et al.*, 1977) suggesting that grain boundary anelasticity can in general be neglected at low temperatures (as it has been throughout the preceding discussion).

Grain boundary anelasticity has an important influence on the shape of the stress / strain curves generated in constant displacement-rate tests. Between the elastic and anelastic limits

$$\varepsilon^{(t)} = \varepsilon_1^{(e)} + a_{M1} \quad (6.56)$$

where  $a_{M1}$  is the strain of the anelastic element in the matrix element of branch 1 (equation 6.49). For a constant displacement-rate test it then follows that

$$d\sigma_1/d\varepsilon^{(t)} = [(1/E) + (1/\mathcal{M})]^{-1} \quad (6.57)$$

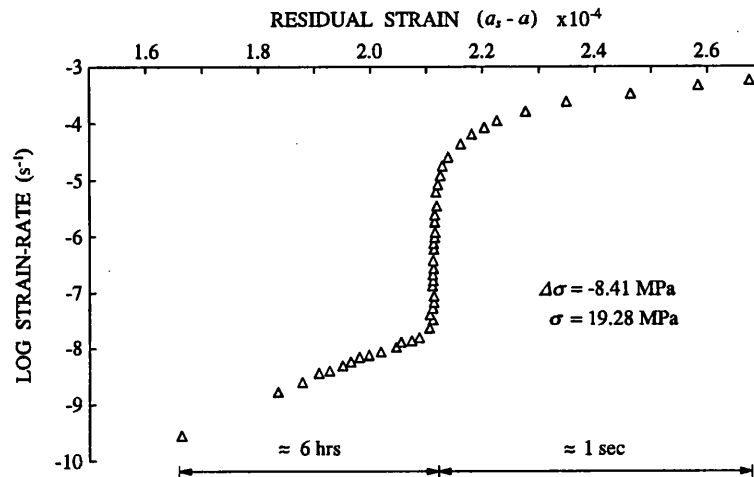
(§ 10.1). At low temperatures (*i.e.*  $T < 0.45 T_m$ ) grain boundary sliding is negligible, and so  $d\sigma \approx d\sigma_1 \approx d\sigma_2$  (§ 6.5.1) and equation 6.57 describes the slope of the stress / total strain curve. At intermediate temperatures this is not the case because  $d\sigma_1 \neq d\sigma_2$ . However, at very high temperatures, the grain boundary element becomes sufficiently weak to accommodate all the deformation required of branch 2. Above the elastic limit then  $d\sigma_2 \approx 0$  and hence from equation 6.48  $d\sigma \approx P d\sigma_1$ . Substituting this result into equation 6.57 yields

$$d\sigma/d\varepsilon^{(t)} = P/[(1/E) + (1/\mathcal{M})] \quad (6.58)$$

which is significant because it allows  $P$  to be determined. This method of evaluating  $P$  has been successfully employed in characterizing the grain boundary sliding behaviour of pure nickel (Li, 1981 ; Alexopoulos *et al.*, 1982). It was found essential to take a series of measurements at several temperatures so that the influence of boundary sliding could be unambiguously demonstrated, and it was also observed that the condition  $d\sigma_2 \approx 0$  held only at stresses considerably above the elastic limit (figure 6.23b).

**6.5.2.2 Permanent grain boundary sliding :** The influence of permanent grain boundary sliding on load relaxation curves has been reported in several experiments (Wire *et al.*, 1974 ; Roberts, 1974 ; Woodford, 1976 ; Huang *et al.*, 1979 ; Keusseyan *et al.*, 1981 ; and others reported in Ellis *et al.*, 1975 ; Li *et al.*, 1976 ; Li, 1981 ; Korhonen *et al.*, 1987). In these studies the grain boundary sliding component was identified by comparison with sliding-free curves either

(a)



(b)

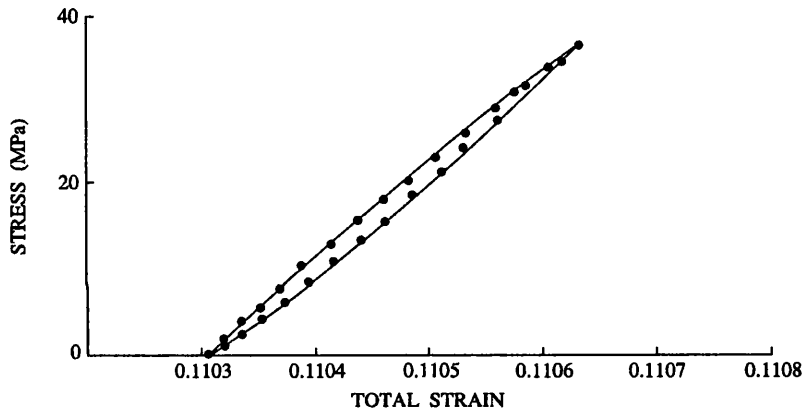


FIG. 6.23. Grain boundary anelasticity. (a) The remaining recoverable strain in a stress dip test conducted on high purity polycrystalline aluminium at room temperature. Comparison with the results from single crystals shows that the grain boundary anelasticity is responsible for the strain recovered in the first second of the test (redrawn after Nir *et al.*, 1976). (b) Stress / strain data for pure nickel at 600°C in a constant displacement-rate loading / unloading cycle where the peak stress is less than the anelastic limit. The solid line is a simulation using the full grain boundary sliding model shown in figure 6.22a (redrawn after Alexopoulos *et al.*, 1982).

generated from single crystals or calculated using the equation of state as determined at  $T < 0.45 T_m$  and extrapolated to the experimental conditions.

The results show that relaxation curves at given  $\sigma^*$  but different  $T$  may be superposed by a translation parallel to the  $\log \dot{\varepsilon}^{(n)}$  axis in  $\log \sigma / \log \dot{\varepsilon}^{(n)}$  space (figure 6.24a,b). At large  $\dot{\varepsilon}^{(n)}$  the material follows a grain matrix (sliding absent)  $\sigma^*$  curve, but as  $\dot{\varepsilon}^{(n)}$  decreases there is a progressive deviation from this curve until the material merges with another matrix curve of lower  $\sigma^*$ . In some materials the slope of the relaxation curve between the two matrix curves is steep enough for it to take a sigmoidal form (figure 6.24c). For relaxation curves generated at

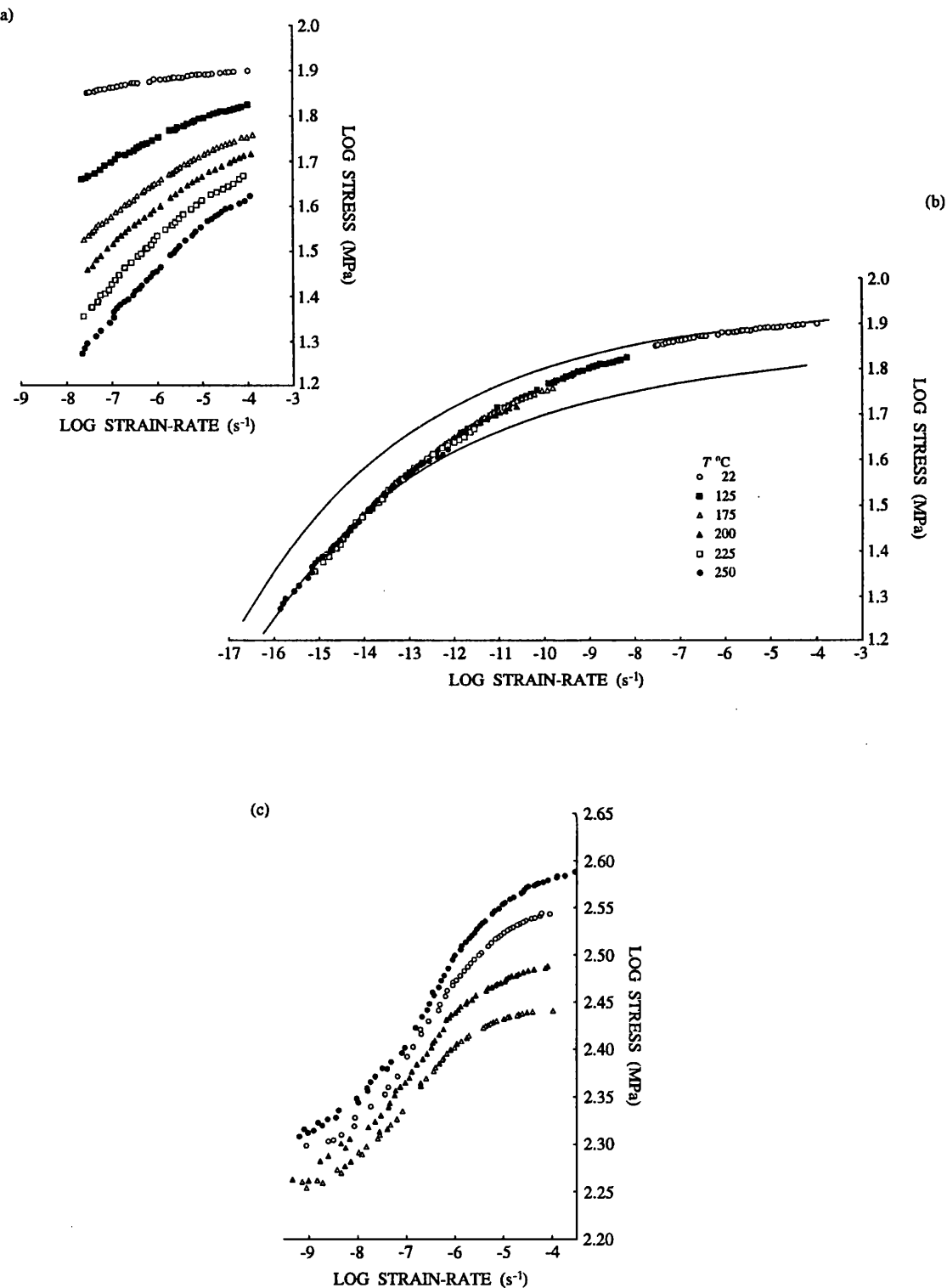


FIG. 6.24. Permanent grain boundary sliding. (a), (b) Relaxation curves generated in 1100 aluminium alloy at several temperatures but at approximately constant initial  $\sigma^*$ . The curves may be superposed by a translation parallel to the strain-rate axis but the resulting master curve deviates from constant  $\sigma^*$  curves (the solid lines). The stress values are rigidity modulus corrected for temperature to their values at room  $T$  (redrawn after Li *et al.*, 1976). (c) Relaxation curves generated in Type 316 stainless steel at 650°C but at different initial  $\sigma^*$ . The grain boundary sliding rate is sufficiently fast for the curves to be sigmoidal (redrawn after Li *et al.*, 1976).

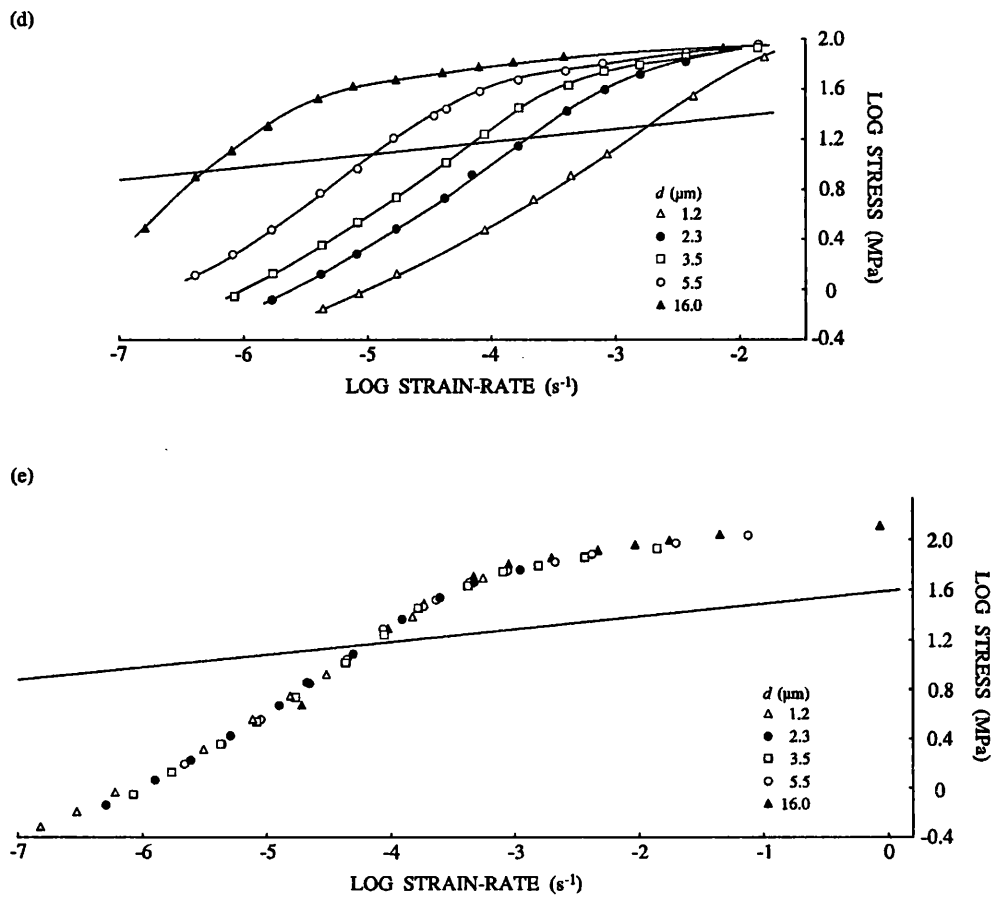


Fig. 6.24 contd. (d), (e) Curves of approximately constant initial  $\sigma^*$  generated at room temperature in Sn-5% Bi alloy polycrystals of various mean grain-size. The curves of different grain-size may be superposed along the indicated scaling direction (redrawn after Tonejc and Poirier, 1975 ; original data of Alden, 1967).

given  $T$  but different  $\sigma^*$ , increasing  $\sigma^*$  increases the strain-rate at which the deviation from the upper curve begins *i.e.* increasing  $\sigma^*$  acts like increasing  $T$  (figure 6.24a,c).

Results from commercial purity lead (Wire *et al.*, 1974) and Sn - 5% Bi alloy (Tonejc and Poirier, 1975) indicate that decreasing grain-size (which increases the viability of grain boundary sliding processes) increases the slope of the relaxation curve between the two matrix curves and/or increases the strain-rate at which deviation from the upper matrix curve begins (figure 6.24d). In the Sn - 5% Bi alloy, curves generated at given  $\sigma^*$  but different grain-size could be superposed along a linear translation path (figure 6.24d,e).

The form of the relaxation curves indicates that grain boundary sliding processes are a significant influence on the rates of deformation only at intermediate strain-rates. Within the context of the grain boundary sliding model (figure 6.22a) this may be rationalized in the following way. At high strain-rates the grain boundaries are essentially rigid in comparison to the grain matrix (*i.e.*  $\dot{\varepsilon}_g^{(n)} \approx 0$ ), and so they remain unrelaxed and the deformation proceeds as in Hart's original model. At intermediate strain-rates both boundary sliding rates and matrix deformation are important. However, at low strain-rates the grain boundaries are able to slide very easily. The GB - element accommodates all the deformation in branch 2 and the matrix

element on branch 1 controls the relaxation-rate. It then follows that the logarithmic stress difference between the two matrix curves is the stress factor  $P$ . The magnitude of  $P$  determined in this way matches that determined from the constant displacement-rate tests (Li, 1981 ; Alexopoulos *et al.*, 1982) and thereby supports the validity of the grain boundary sliding model.

**6.5.3 A simplification of the GB – element.** Since grain boundary anelasticity is small, the GB – element can be approximated as a one component element. Two possibilities arise for the constitutive relation

$$\ln (\sigma_g^* / \sigma_2) = (\dot{\varepsilon}_g^* / \dot{\varepsilon}_g^{(n)})^{\lambda_g} \quad (6.59)$$

$$\dot{\varepsilon}_g^{(n)} = \dot{a}_g^* (\sigma_2 / G)^M \quad (6.60)$$

The former represents grain boundary sliding accommodated wholly by grain matrix deformation at the sites of the boundary inhomogeneities ; the latter grain boundary sliding accommodated wholly by grain boundary diffusion. The portion of the relaxation curves influenced by the GB – element can be modelled by either equation, and so to distinguish between the two alternatives it is necessary to determine more precisely the component of the deformation which is due purely to boundary sliding. In principle this may be done by calculating and subtracting the grain matrix deformation from relaxation curves. However, this in turn requires a precise knowledge of the static recovery function which, as discussed above (§ 6.4), is lacking. In advance of a rigorous characterization of static recovery, it may be that some constraints can be provided from experiments conducted under superplastic conditions where grain boundary sliding dominates the matrix deformation.

## 6.6 Inhomogeneous deformation

The incremental deformation equation on which the state variable analysis is based (equation 2.2), is applicable only within regions of homogeneous deformation. However, Hart's analysis may be applied to inhomogeneously deforming materials if it is possible to delimit subareas which deform homogeneously.

**6.6.1 Deformation of polyphase materials.** The deformation of polyphase materials is inherently heterogeneous because of the different mechanical properties of the constituent phases. If the heterogeneous nature of the polyphase flow is on a large scale in comparison with the scale of the inherently non-uniform deformation of crystal plasticity involving dislocations (*i.e.* if strong interactions between the phases at the dislocation scale are negligibly small), then the mechanical behaviour of the component phases is the same whether or not they are in a single-phase or a polyphase aggregate, and the polyphase deformation problem becomes one of determining how the aggregate mechanical properties depend upon those of its constituents.

Strong interactions between the phases arise when the grain-size of one of the phases is sufficiently small for that phase to influence directly the motion of individual dislocations in the others, or when the grain-size of one or more of the phases is sufficiently small for its work hardening behaviour to be influenced by the interactions between its statistically necessary and geometrically necessary dislocations (respectively, dislocations which produce the deformation, and dislocations which merely solve strain incompatibility problems at the grain boundaries without contributing to the deformation, *cf.* § 6.3.3 ; Ashby, 1971). It therefore follows that the

single-phase mechanical properties of a material may be used in polyphase aggregates when the grain-size of all the phases is large (the coarse microstructure approximation). Apart from this intuitive argument, there is no theoretical justification for the coarse microstructure approximation. However, it is widely employed in continuum models of polyphase deformation (e.g. Chen and Argon, 1979), and experimental results from various metal alloys suggest that it is valid wherever the grain-sizes of all the phases exceeds a few microns (Fischmeister and Karlsson, 1977). Deformation under circumstances where there are strong interactions between the phases has been discussed previously (§ 6.3.2).

**6.6.1.1 Geometric constraints on polyphase deformation :** The relationship between the stresses and strains experienced by the phases in a polyphase aggregate may be derived from the fundamental stereological relationship

$$(L_i / L_t) = (A_i / A_t) = (V_i / V_t) \quad (6.61)$$

where  $(L_i / L_t)$  is the mean length fraction of the  $i$ th phase on test lines through the aggregate,  $(A_i / A_t)$  is the mean areal fraction of the  $i$ th phase on a section through the aggregate, and  $(V_i / V_t)$  is the volume fraction of the  $i$ th phase in the aggregate (Underwood 1970). This relation holds independently of the orientation of the test lines / surfaces and also of the size, shape, orientation and distribution of the  $i$ th phase, provided the measurements are obtained from statistically representative lines / sections / volumes. By resolving the total force  $\mathcal{F}_t$  acting on the aggregate into partial forces  $\mathcal{F}_i$  acting on each phase

$$\mathcal{F}_t = \sum_i \mathcal{F}_i = \sum_i \mathcal{F}_i (A_i / A_t) \quad (6.62)$$

where  $A_i$  are the respective phase areas. Dividing by the total area  $A_t$  and using equation 6.61, then

$$\sigma_t = \sum_i (V_i / V_t) \sigma_i \quad (6.63)$$

in which  $\sigma_t$  is the stress acting on the aggregate and  $\sigma_i$  is the total stress acting on the  $i$ th phase. Similarly, resolving the total shortening  $\Delta L_t$  of the aggregate in terms of its components in the two phases

$$\Delta L_t = \sum_i \Delta L_i = \sum_i \Delta L_i (L_i^{(0)} / L_t^{(0)}) \quad (6.64)$$

where the superscript 0 refers to the initial length. Dividing by  $L_t^{(0)}$  and using equation 6.61

$$\varepsilon_t = \sum_i (V_i / V_t) \varepsilon_i \quad (6.65)$$

in which  $\varepsilon_t$  is the engineering strain acting on the aggregate and  $\varepsilon_i$  is the total engineering strain acting on the  $i$ th phase.

Equations 6.63 and 6.65 provide geometric constraints on the deformation of polyphase aggregates. In two-phase aggregates they become (using strain-rates for the strain terms in equation 6.65)

$$\sigma_t = (1 - X_\beta) \sigma_\alpha + X_\beta \sigma_\beta \quad (6.66)$$

$$\varepsilon_t = (1 - X_\beta) \dot{\varepsilon}_\alpha^{(t)} + X_\beta \dot{\varepsilon}_\beta^{(t)} \quad (6.67)$$

where  $\sigma_\alpha$ ,  $\sigma_\beta$  and  $\dot{\varepsilon}_\alpha^{(t)}$ ,  $\dot{\varepsilon}_\beta^{(t)}$  are the stresses and strain-rates in the  $\alpha$  and  $\beta$  phases,  $X_\beta$  is the  $\beta$  phase volume fraction, and by convention  $\beta$  is the strong phase. Equations 6.66 and 6.67 take no

account of the distribution of the two phases through the aggregate. Hence the component stresses and strains are defined as if all the grains of given phase are arranged in an end-loaded, single-phase polycrystal. In real microstructures however, the phases are, in general, discontinuously distributed. The stresses in the strong phase therefore reflect not pure end-loading, but rather an end-load component (equalling the stress in the weak phase), plus a component which is due to the transfer of load from the weak to strong phase through the shear stresses generated by the difference in deformation-rates across their shared boundaries. The potential extent of this load transfer depends upon the strong phase / strong phase boundary area (*i.e.* it increases as that boundary area decreases). Hence it is to be expected that equations 6.66 and 6.67 will be modified by some microstructural variable which accounts for this area. Strong phase contiguity is precisely such a variable.

Contiguity is defined for a phase as the fraction of the total surface area of that phase which it shares with itself. Accordingly, the strong phase contiguity  $C_\beta$  is defined as

$$C_\beta = 2S_{\beta\beta} / (2S_{\beta\beta} + S_{\alpha\beta}) \quad (6.68)$$

where  $S_{\beta\beta}$  is the shared boundary area between  $\beta$ -grains and  $S_{\alpha\beta}$  is the area of interphase boundary, both per unit volume. Existing experimental results on synthetic two-phase aggregates can be described by

$$\sigma_t = (1 - C_\beta X_\beta) \sigma_\alpha + C_\beta X_\beta \sigma_\beta \quad (6.69)$$

$$\dot{\epsilon}_t = (1 - C_\beta X_\beta) \dot{\epsilon}_\alpha^{(t)} + C_\beta X_\beta \dot{\epsilon}_\beta^{(t)} \quad (6.70)$$

(Gurland, 1979 ; Bloomfield and Covey-Crump, 1992). In the case that all the grains of the strong phase are arranged in a continuous framework in the loading direction,  $C_\beta = 1$  and equations 6.69 and 6.70 reduce to equations 6.66 and 6.67. However, for  $C_\beta \neq 1$  there is as yet no theoretical justification for equations 6.69 and 6.70.

**6.6.1.2 Towards a state variable model for two-phase deformation :** Equations 6.69 and 6.70, together with the constitutive relations interrelating the stress and strain-rates of the constituent phases, are four sets of equations in the variables  $\sigma$ ,  $\dot{\epsilon}^{(t)}$ ,  $\sigma_\alpha$ ,  $\dot{\epsilon}_\alpha^{(t)}$ ,  $\sigma_\beta$ ,  $\dot{\epsilon}_\beta^{(t)}$ ,  $C_\beta$  and  $X_\beta$ . These are bulk properties which must each be defined over the whole of some statistically homogeneous domain of the aggregate. In any conceivable two-phase deformation problem, two of these variables (typically  $\dot{\epsilon}^{(t)}$  and  $X_\beta$ ) are prescribed, and so two more equations are required to complete the deformation model. These must be relationships describing the evolution of strong phase contiguity and the stress or strain-rate partitioning with deformation. No attempt to posit such relationships has yet been made.

**6.6.2 The growth of deformation instabilities.** There have been several attempts to use the incremental deformation equation (equation 2.2) to determine the growth-rate of instabilities following creep-rate minima (see Lin *et al.*, 1981). In these studies, the incremental equation is applied separately to stable and unstable areas of the deforming material, and the development of spatial differences in load bearing capacity across the sample is calculated. Typically the two types of area are assumed to have the same mechanical properties throughout the growth of the instability despite their grossly different deformation histories, and consequently there can be a large overestimate of the instability growth-rate (Ferron and Mhila-Touati, 1982). Hart's analysis provides a means of overcoming this problem.

There have been no studies of this type. However, the analyses of deformation instability

growth-rates generally lead to predictions of the creep-rupture strains. In circumstances where the creep-rupture strain is constant, the state variable analysis may be used to predict creep-rupture times. This time  $t_{rup}$  is given by

$$t_{rup} = \alpha_{rup} / \dot{\alpha} \quad (6.71)$$

where  $\alpha_{rup}$  is the failure strain. Substituting the equation of state for the plastic element (equations 5.10 and 5.11) for  $\dot{\alpha}$  and rearranging

$$\ln t_{rup} = A + (1/\lambda) \ln [\ln (\sigma_{rup}^* / \sigma_a)] + H/RT \quad (6.72)$$

where  $\sigma_{rup}^*$  is the magnitude of  $\sigma^*$  at the rupture strain and  $A$  is a constant. Johnson *et al.* (1977) found that equation 6.72 provided an excellent description of creep-rupture times in Type 316 stainless steel and two other commercial alloys.

## 7 NUMERICAL MODELLING WITH THE STATE VARIABLE ANALYSIS

The constitutive equations which comprise Hart's analysis can be integrated with time to determine the mechanical response of a given material along any specified thermomechanical path. There have been numerous attempts to carry out such integrations, both to simulate deformation experiments to test the descriptive capability of the equations, and to solve boundary value problems to evaluate the potential of the equations for engineering applications. In the following discussion the procedure that has been employed in this deformation modelling is outlined and the results described.

### 7.1 Simulation of deformation experiments

The integration of Hart's model to simulate isothermal uniaxial deformation experiments is particularly simple.

**7.1.1 Formulation of the problem.** The governing equations for the problem are

(a) kinematic

$$\dot{\varepsilon}^{(t)} = \dot{\varepsilon}^{(e)} + \dot{\varepsilon}^{(n)} \quad (7.1)$$

(b) constitutive

$$\dot{\varepsilon}^{(e)} = \dot{\sigma} / E \quad (7.2)$$

$$\dot{\varepsilon}^{(n)} = f(\sigma, q_k, T) \quad (7.3)$$

$$\dot{q}_k = g(\sigma, q_k, T) \quad (7.4)$$

where  $q_k$  are the internal state variables and all other variables are as defined previously. The constitutive equations 7.3 - 7.4 depend on the particular version of Hart's model that is employed. The equations for the original model (figure 5.3) where  $q_k = \sigma^*$ , are restated in figure 7.1a for ease of reference.

Equations 7.1 - 7.4 are subject to the loading history prescribed by the type of deformation test. This loading history should be cast in terms of  $\dot{\sigma}$ . For example it is easy to show that creep under constant load yields (§ A2.2.1)

$$\dot{\sigma} = \sigma \dot{\varepsilon}^{(n)} \quad (7.5)$$

(or for constant stress creep,  $\dot{\sigma} = 0$ ), while deformation at constant displacement-rate yields (§ A2.2.2)

$$\dot{\sigma} = \kappa [(\dot{\mathcal{X}}^0 / L) + \dot{\varepsilon}^{(n)}] \quad (7.6)$$

(or for constant inelastic strain-rate,  $\dot{\sigma} = \dot{\sigma}_a$ ) where  $\kappa$  is an effective modulus for the specimen and load train,  $\dot{\mathcal{X}}^0$  is the apparatus crosshead displacement-rate and  $L$  is the elastic length of the specimen (§ 8.4).

**7.1.2 Solution strategy.** The following solution strategy (figure 7.2) was specified by Korhonen *et al.* (1987).

**7.1.2.1 Initial conditions :** The initial values of  $\sigma^*$ ,  $\sigma_a$  and  $\dot{\varepsilon}^{(n)}$  are prescribed, together with the initial applied stress  $\sigma$ . The value of  $\sigma_a$  may be prescribed by that of  $\dot{\varepsilon}^{(n)}$ . For example, if at the start time  $\dot{\varepsilon}^{(n)} = 0$ , then  $a = 0$  and hence from equation F3,  $\sigma_a = 0$ .

**7.1.2.2 Calculation of the rates :** Using equations F1, F2, F4 and F5 (where the F refers to the equation numbering in figure 7.1) the strain-rates  $\dot{\varepsilon}^{(n)}$ ,  $\dot{a}$  and  $\dot{\sigma}$  are calculated. The stress-rates

FIG. 7.1 A summary of the inelastic equations for Hart's original model.

## (a) Uniaxial equations

$$\dot{\varepsilon}^{(n)} = \dot{a} + \dot{\alpha} \quad (F1)$$

$$\sigma = \sigma_a + \sigma_f \quad (F2)$$

$$\sigma_a = \mathcal{M}a \quad (F3)$$

$$\dot{\varepsilon}^{(n)} = \dot{a}^* (\sigma_f / G)^M \quad (F4)$$

$$\dot{\alpha} = \left[ \ln \left( \frac{\sigma^*}{\sigma_a} \right) \right]^{-1/\lambda} \left( \frac{\sigma^*}{G} \right)^m f_0 \exp \left( \frac{-H}{RT} \right) \quad (F5)$$

$$\dot{\alpha}^* = \dot{\alpha} \sigma^* \Gamma(\sigma^*, \sigma_a) - \sigma^* \mathcal{R}(\sigma^*, T) \quad (F6)$$

(b) Multiaxial equations for infinitesimal strains given that  $\dot{\varepsilon}_{kk}^{(n)} = 0$  (i.e. the inelastic deformation is incompressible).

$$\dot{\varepsilon}_{ij}^{(n)} = \dot{a}_{ij} + \dot{\alpha}_{ij} \quad (F7)$$

$$s_{ij} = s_{ij}^{(a)} + s_{ij}^{(f)} \quad (F8)$$

$$\dot{\varepsilon}_{ij}^{(n)} = (3/2) (\dot{\varepsilon}^{(n)} / \sigma_f) s_{ij}^{(f)} \quad (F9)$$

$$\dot{\alpha}_{ij} = (3/2) (\dot{\alpha} / \sigma_a) s_{ij}^{(a)} \quad (F10)$$

$$a_{ij} = (3/2) (a / \sigma_a) s_{ij}^{(a)}$$

$$\sigma = [(3/2) s_{ij} s_{ij}]^{1/2} ; \quad \dot{\varepsilon}^{(n)} = [(2/3) \dot{\varepsilon}_{ij}^{(n)} \dot{\varepsilon}_{ij}^{(n)}]^{1/2}$$

$$\sigma_a = [(3/2) s_{ij}^{(a)} s_{ij}^{(a)}]^{1/2} ; \quad \dot{\alpha} = [(2/3) \dot{\alpha}_{ij} \dot{\alpha}_{ij}]^{1/2}$$

$$\sigma_f = [(3/2) s_{ij}^{(f)} s_{ij}^{(f)}]^{1/2} ; \quad a = [(2/3) a_{ij} a_{ij}]^{1/2}$$

and where equations F3 - F6 apply.

(c) Multiaxial equations for finite strains given that  $d_{kk}^{(n)} = 0$  (i.e. the inelastic deformation is incompressible).

$$d_{ij}^{(n)} = d_{ij}^{(p)} + \dot{a}_{ij} \quad (F11)$$

$$s_{ij} = s_{ij}^{(a)} + s_{ij}^{(f)} \quad (F12)$$

$$d_{ij}^{(n)} = (3/2) (d^{(n)} / \sigma_f) s_{ij}^{(f)} \quad (F13)$$

$$d_{ij}^{(p)} = (3/2) (d^{(p)} / \sigma_a) s_{ij}^{(a)} \quad (F14)$$

$$a_{ij} = (3/2) (a / \sigma_a) s_{ij}^{(a)}$$

$$\sigma = [(3/2) s_{ij} s_{ij}]^{1/2} ; \quad d^{(n)} = [(2/3) d_{ij}^{(n)} d_{ij}^{(n)}]^{1/2}$$

$$\sigma_a = [(3/2) s_{ij}^{(a)} s_{ij}^{(a)}]^{1/2} ; \quad d^{(p)} = [(2/3) d_{ij}^{(p)} d_{ij}^{(p)}]^{1/2}$$

$$\sigma_f = [(3/2) s_{ij}^{(f)} s_{ij}^{(f)}]^{1/2} ; \quad a = [(2/3) a_{ij} a_{ij}]^{1/2}$$

$$\sigma_a = \mathcal{M}a \quad (F15)$$

$$d^{(n)} = \dot{a}^* (\sigma_f / G)^M \quad (F16)$$

$$d^{(p)} = \left[ \ln \left( \frac{\sigma^*}{\sigma_a} \right) \right]^{-1/\lambda} \left( \frac{\sigma^*}{G} \right)^m f_0 \exp \left( \frac{-H}{RT} \right) \quad (F17)$$

$$\dot{\alpha}^* = d^{(p)} \sigma^* \Gamma(\sigma^*, \sigma_a) - \sigma^* \mathcal{R}(\sigma^*, T) \quad (F18)$$

$\dot{\alpha}^*$ ,  $\dot{\sigma}_a$  and  $\dot{\sigma}$  then follow from equations F3 and F6 and the appropriate loading condition (e.g. equation 7.5 or 7.6), while  $\dot{\varepsilon}^{(e)}$  and  $\dot{\varepsilon}^{(f)}$  are given by equations 7.1 and 7.2. In the instance that  $\dot{\varepsilon}^{(n)} = 0$ ,  $\sigma_a = 0$  and hence  $\dot{\alpha} = 0$  (equation F5) and  $\sigma_f = \sigma$  (equation F2).  $\dot{\varepsilon}^{(n)}$  is then given by equation F4 and  $\dot{a} = \dot{\varepsilon}^{(n)}$  (equation F1). Finally  $\dot{\sigma}_a$  follows from equation F3 and, in the absence of static recovery,  $\dot{\sigma}^* = 0$  (equation F6).

**7.1.2.3 Time integration :** The values of  $\sigma^*$ ,  $\sigma_a$  and  $\dot{\varepsilon}^{(n)}$  are determined at a new time  $t + \Delta t$  by using their values and time-rates of change at  $t$  and a suitable numerical integration scheme (i.e. new value = old value + rate  $\times$  time increment).

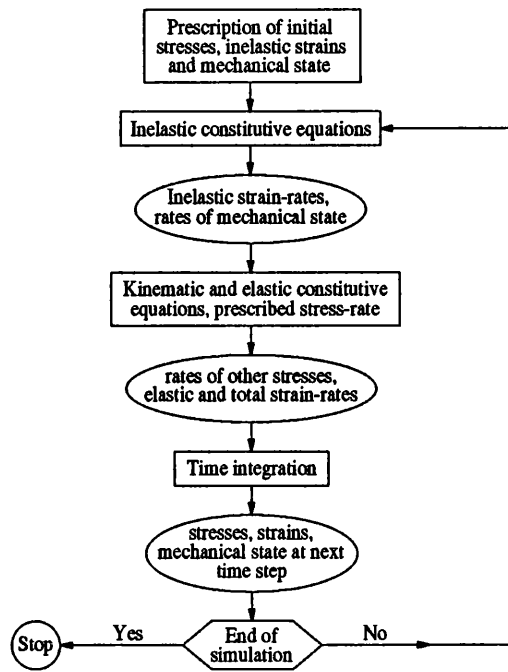


FIG. 7.2. Flow diagram illustrating the solution strategy for the simulation of isothermal uniaxial deformation experiments.

The time integration of Hart's equations is complicated by the fact that they are not only highly non-linear, but that they are also, in some regimes, mathematically stiff (*i.e.* they cannot be integrated with an explicit integration algorithm without there being a loss of stability). Mathematical stiffness is a problem inherent in all systems of constitutive equations for time-dependent plasticity because an elastic regime is not assumed and so the flow laws must be capable of approximating such a regime whilst also showing yielding behaviour, *i.e.* the plastic strain-rate must inevitably be a strongly increasing function of the applied stress (Bammann and Krieg, 1987). In Hart's equations the stiffness arises when  $\sigma_a \approx \sigma^*$  (*i.e.* at high strain-rates / low homologous temperatures, figure 5.5), for then the equation for the plastic element (equation F5) becomes almost singular. Two strategies have been employed to overcome this. One is to retain Hart's equations as they are and to employ an implicit time integration scheme which is unconditionally stable (Cordts and Kollmann, 1986). The other is to employ an amended form of equation F5 when  $\sigma_a$  exceeds a critical fraction of  $\sigma^*$ , and then to use an explicit integration scheme with tight, automatic time-step size control. The advantage of using an explicit scheme lies in its simplicity and hence the ease with which it may be implemented. For this reason this is the strategy which has been preferred.

The amended form of equation F5 which has been employed is

$$\dot{\sigma} = \dot{\varepsilon}^{(n)} / [1 + (\sigma^* \Gamma / \mathcal{M})] \quad (7.7)$$

which may be easily derived by algebraic manipulation of equations F1, F3 and F6 on the assumption that when  $\sigma_a \approx \sigma^*$  then  $\dot{\sigma}_a \approx \dot{\sigma}^*$  (§ A1.4.1). This so-called 'viscoplastic limit' approximation is typically applied if  $\sigma_a > 0.99 \sigma^*$ . Its effect on the deformation modelling

results has been investigated both theoretically and numerically and been shown to be negligible (Hui, 1985).

The choice of integration scheme has been investigated by Kumar *et al.* (1980) who, after comparing several different schemes, found that for the specific task of integrating Hart's equations a simple Euler strategy yielded results of practically the same accuracy as more elaborate methods. The Euler scheme is easily illustrated with the example of a single differential equation

$$\frac{dy}{dt} = f(y, t) \quad (7.8)$$

Expanding  $y_{k+1}$  in terms of  $y_k$  (Hildebrand, 1968, pp. 93f)

$$y_{k+1} = y_k + \Delta t_k (f_k + \frac{1}{2} \Delta f_k + \frac{5}{12} \Delta^2 f_k + \dots) \quad (7.9)$$

where  $\Delta f_k = f_k - f_{k-1}$  is the first backword difference of  $f_k$ . Assuming that the rates of the quantities being integrated remain constant over a small time-step  $\Delta t_k$  then

$$y_{k+1} = y_k + \Delta t_k f_k \quad (7.10)$$

The success of the scheme is highly dependent on the selection of the size of the time-step  $\Delta t_k$ . If the step at any time is too large then the assumption of constant rate over the step is violated, while if it is too small excess computational effort is required. Some automatic time-step size control is therefore necessary. This may be done by monitoring the rates during the simulation and varying  $\Delta t_k$  such that it always falls between prescribed limits of some suitably defined 'error'. Kumar *et al.* (1980) defined their error estimate  $e$  as

$$e = |\Delta t_k \Delta f_k| / |y_k| \quad (7.11)$$

and found the optimum error bounds to be

$$e_{max} = 10^{-3} ; e_{min} = 10^{-4} \quad (7.12)$$

The time-step size control algorithm then proceeds as follows

$e_{max} < e$  : replace  $\Delta t_k$  by  $\Delta t_k/2$ ; recompute  $e$

$e < e_{max}$  : accept  $\Delta t_k$ ; calculate  $y_{k+1}$

with the time-step for the next step  $\Delta t_{k+1}$  being decided according to

$$e_{min} < e < e_{max} : \Delta t_{k+1} = \Delta t_k$$

$$e < e_{max} : \Delta t_{k+1} = 2 \Delta t_k$$

Banthia and Mukherjee (1985) observed that since the variable  $y_k$  reflects the entire prior deformation history, the use of equation 7.11 means that the choice of time-step is influenced by that history. They achieved a considerable improvement in the efficiency of the integration scheme by defining

$$e = \frac{\Delta t_k |\Delta f_k|}{\text{MAX}[|f_k|, |f_{k-1}|]} \quad (7.13)$$

and using only an upper error bound, optimally defined by

$$e_{max} = 2 \times 10^{-6} / \dot{\epsilon}^{(n)} \quad (7.14)$$

By choosing an error bound which is inversely proportional to the inelastic strain-rate, Banthia and Mukherjee exploit the fact that the equations become stiffer as the inelastic strain-rate increases.

In the numerical integration of Hart's equations the stress, internal state and strain variables are integrated. Hence the time-step chosen must be the optimum one for all these

variables. In this case equation 7.8 is generalized for a system of equations

$$dy^{(i)}/dt = f^{(i)}(y^{(i)}, t) \quad (7.15)$$

and an error vector  $e^{(i)}$  obtained. Adjustments to  $\Delta t_k$  can then be made by using a suitable vector norm  $L^{(k)}$

$$e = L^{(k)}(e^{(i)}) \quad (7.16)$$

Three commonly utilized norms are

$$L^{(1)} = \sum_i |e^{(i)}| \quad ; \quad L^{(2)} = \left[ \sum_i (e^{(i)})^2 \right]^{1/2}$$

$$L^{(\infty)} = \text{MAX} |e^{(i)}| \quad (7.17)$$

**7.1.2.4 Calculation of new rates :** Once the new values of the primary stress variables and inelastic strain have been determined, the new strain-rates may be calculated in the manner described in § 7.1.2.2. A further time integration can then be conducted, and so on until the final desired time.

**7.1.3 Results of such simulations.** Constant stress creep, constant strain-rate, stress and strain-rate dip and load relaxation tests have all been simulated using the constitutive equations of Hart's original model (Li *et al.*, 1976 ; Kumar *et al.*, 1980 ; Li, 1981 ; Suzuki *et al.*, 1982 ; Suzuki and Okubo, 1984). In figure 7.3a a measured constant stress creep curve for nickel at 424°C is compared with that simulated using parameters determined from constant displacement-rate and load relaxation experiments (Li, 1981). The excellent agreement between the two emphasizes the descriptive power of Hart's model.

Simulations with the refined Hart model (figure 6.3b) have also been conducted. Figure 7.3b compares experimental and simulated stress / inelastic strain data for a constant displacement-rate tension / compression cycle where the maximum stress is in the microplastic region. Simulations of a variety of other loading histories using the refined model are described in Jackson *et al.* (1981) and Korhonen *et al.* (1985a).

**7.1.4 Multiaxial deformation experiments.** In the preceding discussion it has been assumed that the effects of material rotations in the specimen during deformation are negligible. However, in some loading configurations, most notably in combined tension -torsion tests, such material rotations form an integral part of the test because they permit testing of material properties under a much broader range of loading stresses than in the uniaxial configuration.

The extension of the foregoing analysis to incorporate genuinely multiaxial loading has been described by Van Arsdale *et al.* (1980). They replaced equations 7.1 - 7.4 with the following tensor relations

$$d^{(t)} = d^{(n)} - (\varepsilon^{(e)} \cdot d^{(n)} + d^{(n)} \cdot \varepsilon^{(e)}) + \dot{\varepsilon}^{(e)} \quad (7.18)$$

$$\varepsilon^{(e)} = \frac{1}{2G} \left( \sigma - \frac{\nu_p}{1+\nu_p} \sigma \cdot I \right) \quad (7.19)$$

$$d^{(n)} = f(\sigma, q_k, T) \quad (7.20)$$

$$\dot{q}_k = g(\sigma, q_k, T) \quad (7.21)$$

where the deformation-rate tensors are used in place of the strain-rates (§ 5.2.2.2),  $I$  is the identity tensor and  $\nu_p$  is Poisson's ratio. The elastic strain is measured with respect to the current configuration of the body (hence the form of equation 7.18), and hence the elastic

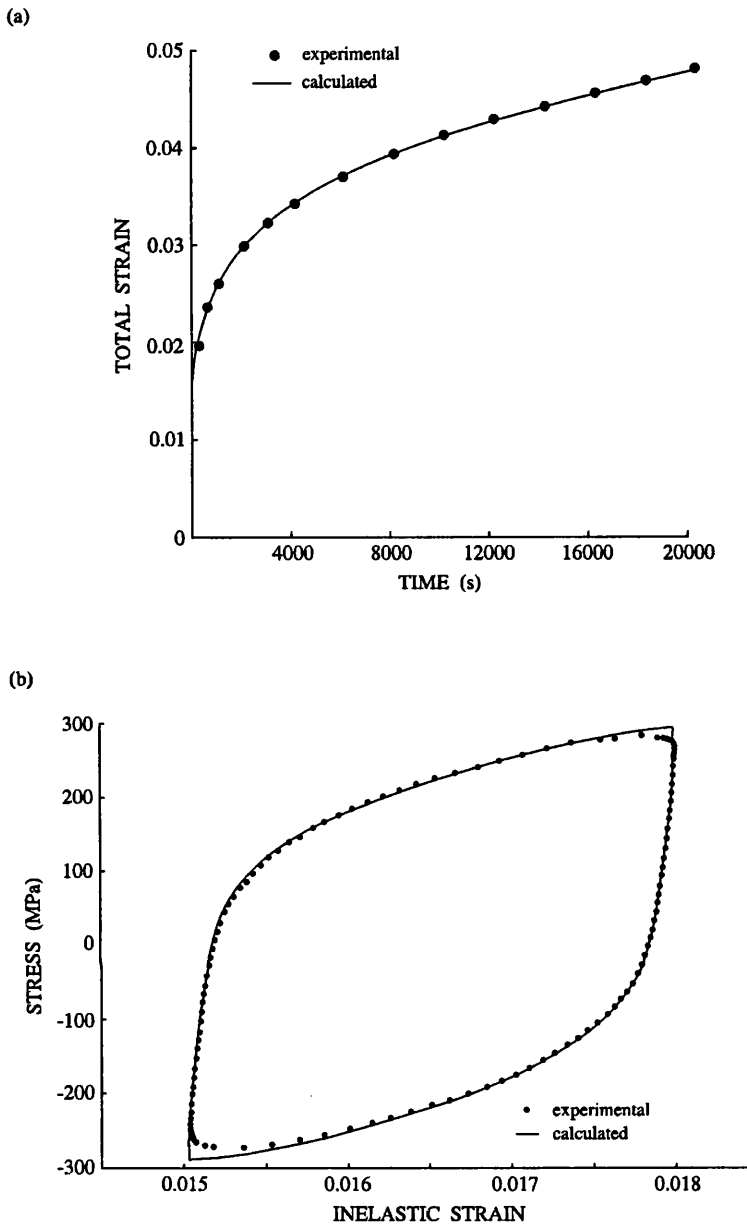


FIG. 7.3. Numerical simulations of uniaxial deformation experiments. (a) Simulated and experimental constant load creep curves for 3% cold-worked nickel at 424°C using Hart's original model (redrawn after Li, 1981). (b) Simulated and experimental constant displacement-rate tension/compression loops in Type 316 stainless steel at room temperature using the refined Hart model. The maximum stress is less than the macroplastic yield stress (redrawn after Alexopoulos *et al.*, 1982).

strain-rate  $\hat{\varepsilon}^{(e)}$  is the convective derivative. The other time derivatives are specified as Jaumann derivatives which become for the internal state variables (since they are scalars in Hart's equations) the material derivative  $\hat{q}_k$  (§ 5.2.2.1). As before the constitutive equations 7.20 - 7.21 depend on the particular version of Hart's model that is employed. The equations for the original model are restated in figure 7.1c. Also as before, it is assumed that the stress-rate is prescribed as a function of time by the loading configuration.

The solution strategy proceeds as described in § 7.1.2 except that in the multiaxial

formulation the viscoplastic limit equation (equation 7.7) becomes (§ A1.4.2)

$$d^{(p)} = \frac{s_{ij}^{(a)} d_{ij}^{(n)} / \sigma_a}{1 + (\sigma^* \Gamma / \mathcal{M})} \quad (7.22)$$

Van Arsdale *et al.* (1980) expanded the full tensor relations 7.18 - 7.21 to solve the problem of the isothermal torsion of a thin-walled cylinder at low homologous temperatures. By introducing a novel vector representation of the deformation variables, Hart (1982) simplified the solution to this problem and extended it to include a superimposed axial loading. Little attempt has been made to compare the predictions of the simulations with experimental results, although Van Arsdale *et al.* (1980) observe a qualitative agreement.

## 7.2 The solution of boundary value problems

Hart's equations have been utilized in both infinitesimal and finite strain boundary value problems for viscoplasticity.

**7.2.1 Infinitesimal strain problems.** The use of Hart's equations in boundary value problems where rigid body motions can be assumed negligible has been overviewed by Mukherjee (1982). The approach adopted is one devised for three dimensional isotropic bodies subjected to specified time-varying loads and temperature distributions. It formulates the problem in terms of real time rates and thereby defines an inhomogeneous linear boundary value problem for the stress or displacement-rates. This linear boundary value problem is solved to find the rates of the variables of interest throughout the body at any time, and then these rates are integrated forward in time to obtain their time histories.

The method outlined is not restricted to use with Hart's analysis but may be used with any model of inelastic deformation in which the constitutive relations have the mathematical structure given by equations 7.27 and 7.28.

**7.2.1.1 Formulation of the problem :** The governing differential equations of the problem, in terms of rates are

(a) kinematic

$$\dot{\varepsilon}_{ij}^{(t)} = \dot{\varepsilon}_{ij}^{(e)} + \dot{\varepsilon}_{ij}^{(n)} + \dot{\varepsilon}_{ij}^{(T)} = \frac{1}{2} (\dot{u}_{i,j} + \dot{u}_{j,i}) \quad (7.23)$$

or equivalently the compatibility equation

$$\nabla \times \dot{\varepsilon}^{(t)} \times \nabla = \dot{\varepsilon}_{ij,kl}^{(t)} + \dot{\varepsilon}_{kl,ij}^{(t)} - \dot{\varepsilon}_{ik,jl}^{(t)} - \dot{\varepsilon}_{jl,ik}^{(t)} = 0 \quad (7.24)$$

(b) equilibrium

$$\nabla \cdot \dot{\sigma} + \dot{F} = \dot{\sigma}_{ij,j} + \dot{F}_i = 0 \quad (7.25)$$

(c) constitutive

$$\dot{\varepsilon}_{ij}^{(e)} = \frac{1}{2G} \left( \dot{\sigma}_{ij} - \frac{\nu_p}{1+\nu_p} \dot{\sigma}_{kk} \delta_{ij} \right) \quad (7.26)$$

$$\dot{\varepsilon}_{ij}^{(n)} = f_{ij}(\sigma_{ij}, q_k, T) \quad (7.27)$$

$$\dot{q}_k = g_{ij}(\sigma_{ij}, q_k, T) \quad (7.28)$$

$$\dot{\varepsilon}_{ij}^{(T)} = \Theta \dot{T} \delta_{ij} \quad (7.29)$$

where the subscript comma notation represents a partial derivative with respect to the coordinates  $x_i$ ,  $\dot{\varepsilon}_{ij}^{(T)}$  is the thermal strain,  $u_i$  the displacement vector,  $F_i$  the body force vector per unit volume and  $\Theta$  the coefficient of linear thermal expansion. In general the mechanical state

variables  $q_k$  are tensor quantities (*i.e.* they should be represented as  $q_{ij}^{(k)}$ ), but since in Hart's equations they are scalars the notation is here simplified. As observed previously (§ 7.1.1 ; 7.1.4) the constitutive equations 7.27 and 7.28 depend on the particular version of Hart's model that is employed, although only those for the original model (figure 7.1b) have ever been used.

Equations 7.23 – 7.29 may be combined to define a boundary value problem in either stress-rates or displacement-rates. The stress-rate formulation uses equations 7.23, 7.26 and 7.29 to rewrite the compatibility condition (equation 7.24) as

$$\nabla \times \left[ \frac{1}{2G} \left( \dot{\sigma} - \frac{\nu_p}{1+\nu_p} \dot{\sigma} \cdot I \right) \right] \times \nabla = - \nabla \times \dot{\epsilon}_{ij}^{(n)} \times \nabla - \nabla \times [\Theta \dot{T} I] \times \nabla \quad (7.30)$$

The traction boundary condition is

$$\dot{\sigma}_{ij} n_j = \dot{\tau}_i \quad (7.31)$$

where  $n_i$  is the unit normal vector to the surface  $S$  of the body and  $\dot{\tau}_i$  is the surface traction vector which is prescribed on  $S$ . Equation 7.30 is linear in stress-rates. Furthermore the inhomogeneous term on the right-hand side is known at any time provided the stresses, state variables, temperature and body forces are known at that time.

The displacement-rate formulation uses equations 7.23, 7.26 and 7.29 to rewrite the equilibrium equation (equation 7.25) as

$$\dot{u}_{i,jj} + \frac{1}{1-2\nu_p} \dot{u}_{k,ki} = - \frac{\dot{F}_i}{G} + 2\dot{\epsilon}_{ij,j}^{(n)} + \frac{2(1+\nu_p)}{1-2\nu_p} (\Theta \dot{T})_{,i} \quad (7.32)$$

The boundary conditions involve stresses

$$\begin{aligned} \dot{\tau}_i \text{ on } S &= \dot{\sigma}_{ij} n_j \\ &= G \left[ (\dot{u}_{i,j} + \dot{u}_{j,i}) n_j + \frac{2\nu_p}{1-2\nu_p} \dot{u}_{j,j} n_i - 2 \left( \dot{\epsilon}_{ij,j}^{(n)} n_j + \frac{1+\nu_p}{1-2\nu_p} \Theta \dot{T} n_i \right) \right] \end{aligned} \quad (7.33)$$

and/or displacements

$$\dot{u}_i = \dot{\Delta}_i \text{ on } S \quad (7.34)$$

where  $\dot{\Delta}_i$  is the prescribed displacement vector on the surface of the body. Equations 7.32 and 7.33 are linear in displacement-rates and the inhomogeneous terms are determinable at any time if the stresses, state variables, temperature and body forces are known at that time.

**7.2.1.2 Solution strategy :** The solution strategy (figure 7.4) is similar in general features to that described for the simulations of deformation experiments (§ 7.1.2).

The initial inelastic strain is taken to be zero and the initial distribution of the internal state variables throughout the body  $q_k^{(0)}(x_i)$  is prescribed. The total initial strain then has only elastic and thermal components and so can be determined from the thermoelastic problem with identical material and geometry *i.e.*

$$\begin{aligned} \sigma_{ij}(x_i, 0) &\equiv \sigma_{ij}^{(0)}(x_i) ; \quad \epsilon_{ij}^{(t)}(x_i, 0) \equiv \epsilon_{ij}^{(0)}(x_i) = \epsilon_{ij}^{(e)}(x_i, 0) + \epsilon_{ij}^{(T)}(x_i, 0) \\ \epsilon_{ij}^{(n)}(x_i, 0) &= 0 ; \quad q_k(x_i, 0) = q_k^{(0)}(x_i) \end{aligned} \quad (7.35)$$

where  $\sigma_{ij}^{(0)}$  and  $\epsilon_{ij}^{(0)}$  correspond to the thermoelastic solution. Thus for example, in the stress-rate formulation  $\sigma_{ij}^{(0)}$  and  $\epsilon_{ij}^{(0)}$  are obtained by solving the problem

$$\epsilon^{(0)} = \frac{1}{2G} \left( \sigma^{(0)} - \frac{\nu_p}{1+\nu_p} \sigma^{(0)} \cdot I \right) + \Theta T^{(0)} I$$

$$\nabla \times \left[ \frac{1}{2G} \left( \sigma^{(0)} - \frac{\nu_p}{1+\nu_p} \sigma^{(0)} \cdot I \right) \right] \times \nabla + \nabla \times [\Theta T^{(0)} I] \times \nabla = 0 \quad (7.36)$$

$$\nabla \cdot \sigma^{(0)} = -F^{(0)} ; \quad \sigma^{(0)} \cdot n = \tau^{(0)}$$

where equations 7.36 are tensor relations and  $T^{(0)}$ ,  $F^{(0)}$  and  $\tau^{(0)}$  are the temperature, body force and traction distributions at  $t = 0$ .

Having obtained the initial stresses from the thermoelastic problem, and given  $q_k^{(0)}(x_i)$ , the next step is to determine the value of the inhomogeneous term in equation 7.30 or 7.32 at  $t = 0$ , so that either of these equations may be solved for the stress / displacement-rate at that time. Of the factors in the inhomogeneous term,  $T$  and  $F_i$  are assumed to be independently determinable for all times by prescription. If the temperature is not constant, then provided thermal steady state conditions hold and assuming there is no thermomechanical coupling,  $T(x_i, t)$  is the solution to the heat conduction equation subject to time varying thermal boundary conditions on the surface  $S$ . The remaining factor in the inhomogeneous term is  $\epsilon_{ij}^{(n)}(x_i, 0)$ . This is determined with the constitutive relations (equations 7.27 and 7.28), using the known values of  $\sigma_{ij}$  and  $q_k$  and utilizing the fact that the initial inelastic strains are taken to be zero (cf. § 7.1.2.2).

The next step is to determine the rates of the displacements, stresses and total / elastic strains. In the stress-rate formulation the stress-rate at  $t = 0$  is determined by solving equations 7.30 and 7.25 subject to the boundary condition 7.31. The elastic strain-rate is then given by Hooke's law (equation 7.26) and the total strain-rate from the first half of equation 7.23. In the

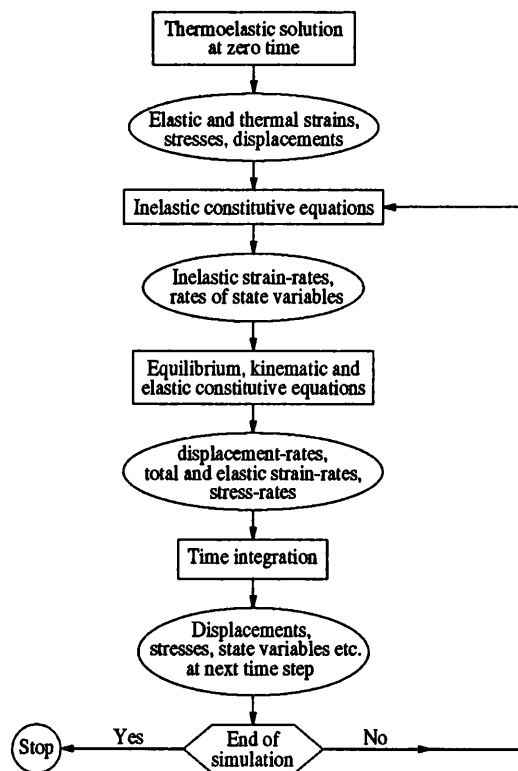


FIG. 7.4. Flow diagram illustrating the solution strategy for boundary value problems in infinitesimal strain (modified after Mukherjee, 1982).

displacement-rate formulation the displacement-rate at  $t = 0$  is determined by solving equation 7.32 subject to the boundary condition 7.33 or 7.34. The total strain-rate is given by the second equality of equation 7.23 and the elastic strain-rate from the first equality of that equation (*i.e.*  $\dot{\epsilon}_{ij}^{(e)} = \dot{\epsilon}_{ij}^{(t)} - \dot{\epsilon}_{ij}^{(n)}$ ). Finally the stress-rate is obtained from the inverted form of Hooke's law.

Time integration to determine the new inelastic strains, stresses, internal state variables proceeds as described previously (§ 7.1.2.3). The viscoplastic limit approximation is equation 7.22 with the deformation-rates changed to the appropriate strain-rates

$$\dot{\alpha} = \frac{s_{ij}^{(a)} \dot{\epsilon}_{ij}^{(n)} / \sigma_a}{1 + (\sigma^* \Gamma / \mathcal{M})} \quad (7.37)$$

while the inelastic strain-rate used in Banthia and Mukherjee's error bound on the time-step size (equation 7.14) is the maximum inelastic strain-rate in the body at the integration time. Since the integrated variables in these problems are functions of space as well as time, the error vector (equation 7.16) is obtained by discretizing each dependent variable at a finite number of space points so that the only difference from the uniaxial deformation case is that a much larger system of equations (equation 7.15) is defined.

Once the new values of inelastic strain, stress and internal state variables are obtained, the constitutive relations (equations 7.27 and 7.28) are used to determine the new rates of inelastic strain and internal state variables and so on as described above, until the final desired time.

**7.2.1.3 Results of problems modelled in this way :** The modelling of multiaxial problems is complicated by the boundary value problem posed by equations 7.25, 7.30 and 7.31 (or equations 7.32 – 7.34), the solution of which is required to find the stress (or displacement) rates at any time. Closed form solutions for this problem are only possible for simple geometries and loading conditions. Published solutions which have been tested with Hart's equations include a thick-walled spherical shell under internal and external pressure, a close-ended thick-walled cylinder under internal and external pressure with an axial force and torque, and a thin circular disc rotating at constant angular velocity (Kumar and Mukherjee, 1976 ; 1977a,b,c). In all these solutions the pressures, forces and temperature distributions were assumed invariant with time. Subsequently the solutions for the spherical shell and the cylinder were generalized to include time-varying (but thermally steady) temperature distributions and a prescribed internal radial displacement (Mukherjee *et al.*, 1978 ; Mukherjee and Harkness, 1979 ; Wire *et al.*, 1981). The problem of the bending of a beam symmetric about the plane of bending under a time-varying moment has been solved by Chang *et al.* (1979). Some of these solutions have been obtained both by a direct combination of the governing differential equations and by the boundary integral method.

Problems involving more complex geometries require use of either finite element or boundary element techniques to solve for the stress / displacement rates at each time increment (and possibly also for the solution of the initial thermoelastic problem). Such techniques have been successfully applied to model the creep of arbitrarily shaped planar bodies (*i.e.* under plane stress and plane strain conditions) under arbitrary loading histories (Mukherjee and Kumar, 1978 ; Morjaria and Mukherjee, 1980a ; Morjaria *et al.*, 1980), the inelastic bending of arbitrarily shaped thin plates with clamped or simply supported edges (Morjaria and Mukherjee, 1980b), the inelastic torsion of prismatic shafts of arbitrary cross section (Mukherjee and

Morjaria, 1981), and the inelastic deformation of a thick-walled cylinder under unsteady temperature conditions (Morjaria and Mukherjee, 1981). Many of these problems have been solved using both finite elements and boundary elements, and for special cases (where possible) these solutions have been compared with the results generated by direct numerical integration. The comparisons with the direct integrations indicate that both finite element and boundary element methods yield accurate results but that the latter are computationally much more efficient (Morjaria *et al.*, 1980 ; Mukherjee, 1982).

The engineering application of the solutions to these problems has as yet been limited. Wire *et al.* (1981) used the solution to the problem of a closed-ended thick-walled cylinder under time-varying temperatures and internal pressures, to simulate the response of the Type 316 stainless steel fuel element cladding tubes used in nuclear reactors, to the extreme mechanical loads and thermal environments they experience during normal service conditions. For the simulations the constitutive relations listed in figure 7.1b were used, together with equation 4.57 for the  $\Gamma$  function and an empirical description of the curves shown on figure 6.20b for the  $\mathfrak{R}$  function. The material parameters were empirically adjusted to account for grain boundary sliding and any thermally induced changes not accommodated in  $\mathfrak{R}$ . The solutions were presented as curves of outside circumferential strain versus : temperature during heating at constant internal pressure and temperature-rate, internal pressure at constant temperature, and time at constant temperature and internal pressure. The results for the first two of these simulations are compared with those directly obtained in experiment in figure 7.5a,b, and it can be seen that the agreement is remarkable given the complexity of the thermal / deformation history.

**7.2.2 Finite strain problems.** The use of Hart's equations in large strain boundary value problems has been overviewed by Mukherjee and Chandra (1984). The approach adopted is one devised for three dimensional isotropic bodies subjected to specified time-varying loads at uniform and constant temperature.

**7.2.2.1 Some definitions :** Referring to the same set of spatially fixed orthogonal cartesian coordinates, the position of a material point in a reference configuration of a three dimensional body is specified by coordinates  $X_i$ , and in the current configuration by coordinates  $x_i$ . The displacement vector  $u_i$  is given by the difference between the two (equation 5.30), and the velocity of the material point is denoted by  $v_i$ .

Of the two conventional measures of strain used in finite strain theory (*i.e.* the Almansi and the Green strains, *e.g.* Fung, 1965, pp. 434f), the Green strain defined as

$$E_{ij} = \frac{1}{2} \left( \frac{\partial u_i}{\partial X_j} + \frac{\partial u_j}{\partial X_i} + \frac{\partial u_k}{\partial X_i} \frac{\partial u_k}{\partial X_j} \right) \quad (7.38)$$

is the one most suited to the following analysis, because in the Lagrangian formulation of the finite strain problem employed, its material derivative equals the deformation-rate, *i.e.*

$$\dot{E}_{ij} = d_{ij} \quad (7.39)$$

(Mukherjee and Chandra, 1984).

The usual distinctions between the Cauchy, Lagrange and Kirchhoff stress tensors are observed (*e.g.* Fung, 1965, pp. 436f). The Cauchy (or Eulerian) stress tensor refers the stress to the instantaneous (current) area of the surface element on which the force vector acts and is the

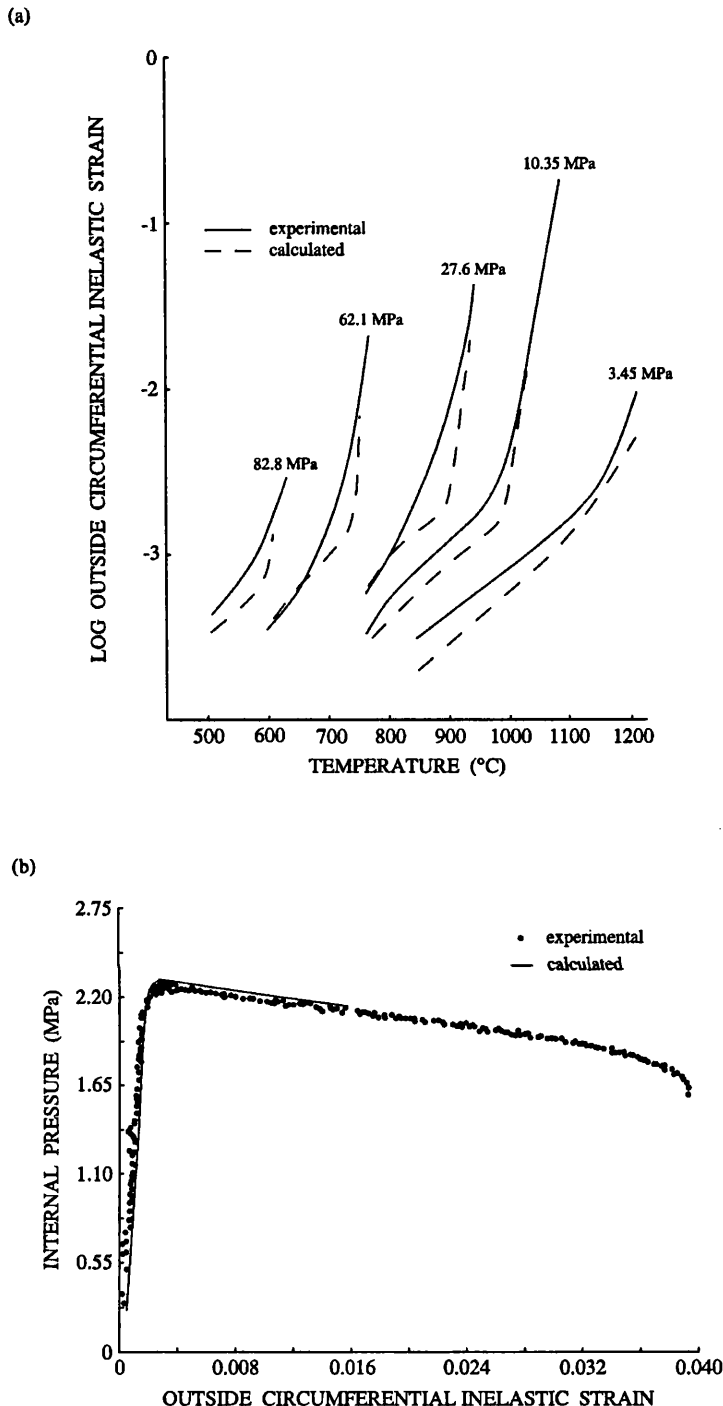


FIG. 7.5. Comparison of measured and simulated behaviour of thin-walled Type 316 stainless steel tubes. (a) Outside circumferential strain as a function of temperature at various constant internal pressures (indicated) and constant temperature-rate. (b) Outside circumferential strain as a function of internal pressure at constant temperature. Simulations were conducted with the multiaxial infinitesimal strain equations for Hart's original model (redrawn after Wire *et al.*, 1981).

stress that has been utilized throughout the preceding discussion. The Lagrangian and Kirchhoff stress tensors (also known respectively, as the first and second Piola-Kirchhoff stress tensors) refer the stress to the initial area of the surface element (as for example, engineering stress

does). The Lagrangian stress resolves the force vector in its current orientation on the initial area, whereas the Kirchhoff stress, before resolving the force vector on the initial area, applies the same transformation to it as experienced by the surface element during the deformation. Thus

$$\begin{aligned} n_j \sigma_{ji} dS &= dT_i \\ n_j^{(0)} \sigma_{ji}^{(L)} dS^{(0)} &= dT_i = dT_i^{(L)} \\ n_j^{(0)} \sigma_{ji}^{(K)} dS^{(0)} &= (\partial X_i / \partial x_j) dT_j = dT_i^{(K)} \end{aligned} \quad (7.40)$$

where  $\sigma_{ij}$ ,  $\sigma_{ij}^{(L)}$  and  $\sigma_{ij}^{(K)}$  are the Cauchy, Lagrange and Kirchhoff stress tensors respectively,  $T_i$  is an applied force vector in its current orientation,  $T_i^{(L)}$  and  $T_i^{(K)}$  the force vector as referred back to the initial (reference) configuration of the element in the Lagrange and Kirchhoff schemes respectively, and the superscripted 0 refers to the initial (reference) configuration of the element. In general, the Lagrange stress tensor is not symmetric but the Kirchhoff stress tensor is. Consequently, although the Lagrange stress leads to a relatively simple stress equilibrium equation, the Kirchhoff stress is more convenient to use in stress / strain relations where the strain tensor is always symmetric. The relationship between the two is therefore significant, and is given by

$$\dot{\sigma}_{ij}^{(K)} = \dot{\sigma}_{ij}^{(L)} + (\sigma_{ik} d_{jk}^{(t)} + \sigma_{kj} d_{ik}^{(t)}) - \sigma_{ik} v_{j,k} \quad (7.41)$$

where the superscripted circle refers to a Jaumann derivative and the square to a material derivative (Hill, 1959). Furthermore, for nearly incompressible deformation

$$\dot{\sigma}_{ij}^{(K)} \approx \dot{\sigma}_{ij} \quad (7.42)$$

(Yamada and Hirakawa, 1978).

**7.2.2.2 Governing equations :** For the solution of finite strain problems using Hart's equations, the configuration of the body at time  $t$  is used as the reference configuration for the time step  $t$  to  $t + \Delta t$ . In this so-called 'updated Lagrangian formulation', the governing equations of the problem in terms of rates are

(a) kinematic

$$d_{ij}^{(t)} = d_{ij}^{(e)} + d_{ij}^{(n)} = \frac{1}{2} (v_{i,j} + v_{j,i}) \quad (7.43)$$

(b) equilibrium

$$\dot{\sigma}_{ij,j}^{(L)} + \rho^{(0)} \dot{F}_i^{(0)} = 0 \quad (7.44)$$

(c) constitutive

$$d_{ij}^{(e)} = \frac{1}{2G} \left( \dot{\sigma}_{ij} - \frac{\nu_p}{1+\nu_p} \dot{\sigma}_{kk} \delta_{ij} \right) \quad (7.45)$$

$$d_{ij}^{(n)} = f_{ij}(\sigma_{ij}, q_k, T) \quad (7.46)$$

$$q_k = g_{ij}(\sigma_{ij}, q_k, T) \quad (7.47)$$

where  $\rho^{(0)}$  and  $F_i^{(0)}$  are respectively, the mass density and body force (per unit mass) in the reference configuration, and where the subscript comma notation in equation 7.43 is the partial derivative with respect to the coordinates  $x_i$  (cf. equation 5.32), while in equation 7.44 it is the partial derivative with respect to the coordinates  $X_i$ . The elastic constitutive relation (equation 7.45) assumes that the material is hypoelastic *i.e.* that the components of the (coordinate frame invariant) stress-rate are homogeneous linear functions of the components of the deformation-rate (Fung, 1965, pp. 444f).

**7.2.2.3 Finite element formulation :** The finite element formulation of the problem is described

in detail by Chandra and Mukherjee (1984a). The governing equations 7.43 - 7.47 are combined using the principle of virtual work

$$\int_{B^{(0)}} [\overset{\circ}{\sigma}_{ij}^{(L)} \delta(v_{j,i})] dV^{(0)} - \int_{\partial B^{(0)}} \overset{\circ}{\tau}_j^{(L)} \delta v_j dS^{(0)} - \int_{B^{(0)}} \rho^{(0)} \overset{\circ}{F}_j^{(0)} \delta v_j dV^{(0)} = 0 \quad (7.48)$$

where  $\overset{\circ}{\tau}_j^{(L)} = \overset{\circ}{\sigma}_{ij}^{(L)} n_j^{(0)}$  is the traction-rate,  $B^{(0)}$  is the domain of the body,  $\partial B^{(0)}$  is that part of the boundary of the body on which the tractions are prescribed, and  $\delta v_j$  is the virtual velocity field. Again the superscripted 0 refers to the reference configuration of the body. Substituting  $\overset{\circ}{\sigma}_{ij}^{(K)}$  for  $\overset{\circ}{\sigma}_{ij}^{(L)}$  using equation 7.41 and using the second equality in equation 7.43, equation 7.48 becomes

$$\begin{aligned} \int_{B^{(0)}} [\overset{\circ}{\sigma}_{ij}^{(K)} \delta(d_{ij}^{(t)}) - \frac{1}{2} \sigma_{ij} \delta(2 d_{ik}^{(t)} d_{kj}^{(t)} - v_{k,i} v_{k,j})] dV^{(0)} \\ - \int_{\partial B^{(0)}} \overset{\circ}{\tau}_j^{(L)} \delta v_j dS^{(0)} - \int_{B^{(0)}} \rho^{(0)} \overset{\circ}{F}_j^{(0)} \delta v_j dV^{(0)} = 0 \end{aligned} \quad (7.49)$$

Now rearranging equation 7.45 and writing it in matrix form

$$\{\overset{\circ}{\sigma}\} = [C]\{d^{(e)}\} = [C](\{d^{(t)}\} - [C]\{d^{(n)}\}) \quad (7.50)$$

where the first equality of equation 7.43 has also been used. A discretized form of equation 7.49 may be obtained in the usual manner by choosing shape functions for the velocity field

$$v = [N]\{v\} \quad (7.51)$$

where  $v$  on the left hand side of the equation is understood in vector form,  $[N]$  is the shape function matrix and  $\{v\}$  are the nodal velocities. From equations 7.43 and 7.51

$$\{d^{(t)}\} = [B]\{v\} \quad (7.52)$$

Using equations 7.42 and 7.50 - 7.52 in equation 7.49 yields in matrix form

$$([K_S] + [K_G] + [K_C])\{v\} = \{P^{(n)}\} + \{P^{(B)}\} \quad (7.53)$$

where to simplify the discussion the prescribed body forces  $F_i^{(0)}$  have been set to zero. The stiffness matrix  $[K_S]$  and the inelastic load vector  $\{P^{(n)}\}$  derive from the first integral of equation 7.49. The second stiffness matrix  $[K_G]$  arises from the second term in equation 7.49 and reflects the inclusion of rotation effects in equation 7.41. The load correction matrix  $[K_C]$  and the load vector  $\{P^{(B)}\}$  derive respectively, from the velocity dependent and the velocity independent terms arising from the surface integral. These two groups of terms arise because the surface integral includes the traction-rate  $\overset{\circ}{\tau}_j^{(L)}$  which is associated with the initial geometry in the virtual work equation (equation 7.48), but which in general involves a deforming surface and rotating normal. Hence by using the spin tensor (equation 5.33) in equation 7.41 then it is observed that

$$\overset{\circ}{\tau}_j^{(L)} = \overset{\circ}{\sigma}_{ij}^{(L)} n_i^{(0)} = \overset{\circ}{\sigma}_{ji}^{(K)} n_i - \sigma_{jk} d_{ki}^{(t)} n_i + \Omega_{jk} \sigma_{ki} n_i \quad (7.54)$$

The solution strategy for the finite element problem is illustrated in figure 7.6. First the elastic problem (without  $[K_G]$  and  $[K_C]$ ) is solved at zero time to obtain the initial stresses, strains and displacements. The inelastic deformation-rate  $d_{ij}^{(n)}$  at zero time is obtained from the constitutive relations 7.46 and 7.47, and  $\{P^{(n)}\}$  is computed from  $d_{ij}^{(n)}$ . The matrices  $[K_G]$  and  $[K_C]$  are evaluated from the initial stresses  $\sigma_{ij}$ . Equation 7.53 is solved for the nodal velocities  $\{v\}$  and the velocity gradients are obtained at zero time. These velocity gradients are used with the definition of the deformation-rate tensor (equation 5.32) and equations 7.43 and 7.45 to

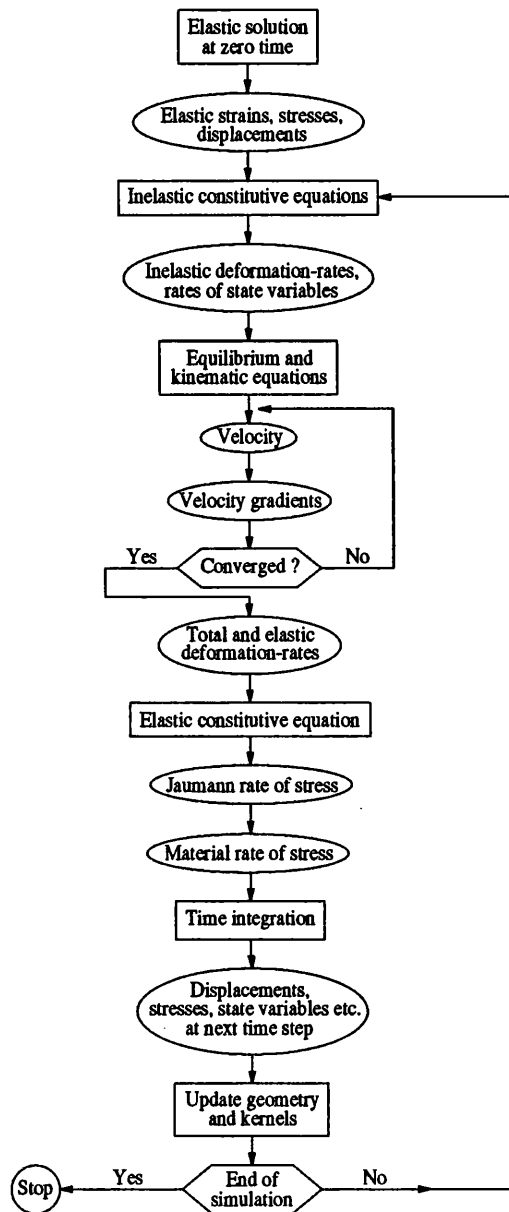


FIG. 7.6. Flow diagram illustrating the solution strategy for boundary value problems in finite strain. The strategy is given for the boundary element formulation but the finite element strategy differs only in not containing the convergence loop (modified after Mukherjee and Chandra, 1984).

determine the initial value of  $\dot{\sigma}_{ij}$ , and from this and the definitions of the spin-rate tensor and the Jaumann and material derivatives (equations 5.33, 5.35 and 5.37),  $\dot{\sigma}_{ij}$  is obtained. Time integration is carried out using the material derivatives so that the integrated values can be obtained in a spatially fixed coordinate frame as a function of  $x_i$  and time. The integration algorithm is as described for the infinitesimal strain problems. After each increment the geometry and matrix  $[K_G]$  are updated and the new inelastic deformation-rates are calculated, *et cetera*.

**7.2.2.4 Boundary element formulation :** The boundary element formulation of the problem is

described in detail by Chandra and Mukherjee (1984b). The governing equations 7.43 - 7.47 are combined using a form of Betti's reciprocal theorem

$$\int_{B^{(0)}} \overset{\circ}{\sigma}_{ij}^{(K)} \varepsilon_{ij}^{(R)} dV^{(0)} = \int_{B^{(0)}} \sigma_{ij}^{(R)} \overset{\circ}{E}_{ij}^{(e)} dV^{(0)} \quad (7.55)$$

where  $\sigma_{ij}^{(R)}$  and  $\varepsilon_{ij}^{(R)}$  are reference stress and strain fields respectively, in an elastic body with the same elastic constants which is undergoing small strain. The equality indicated in equation 7.55 may be seen by observing that in the small strain approximation,  $\sigma_{ij}^{(R)}$  and  $\varepsilon_{ij}^{(R)}$  are related according to equation 7.26, while  $\overset{\circ}{\sigma}_{ij}^{(K)}$  and  $\overset{\circ}{E}_{ij}^{(e)}$  are related by equation 7.45 (using equation 7.39).

Now using equation 7.26 for the relationship between  $\sigma_{ij}^{(R)}$  and  $\varepsilon_{ij}^{(R)}$ , equation 7.23 to replace  $\varepsilon_{ij}^{(R)}$  by  $u_i^{(R)}$ , the equilibrium equation (equation 7.44), and Kelvin's solution for a point force in an infinite three-dimensional elastic body undergoing infinitesimal deformation, then equation 7.55 may be rewritten

$$\begin{aligned} v_j(p) = & \int_{\partial B^{(0)}} [U_{ij}(p, Q) \overset{\circ}{\tau}_i^{(L)}(Q) - T_{ij}(p, Q) v_i(Q)] dS_Q^{(0)} \\ & + \int_{B^{(0)}} \rho^{(0)} \overset{\circ}{F}_i^{(0)}(q) U_{ij}(p, q) dV_q^{(0)} + \int_{B^{(0)}} 2G U_{ij,k}(p, q) d_{ik}^{(n)}(q) dV_q^{(0)} \\ & + \int_{B^{(0)}} U_{ij,m}(p, q) G_{mkl}^*(q) v_{k,l}(q) dV_q^{(0)} \end{aligned} \quad (7.56)$$

where once more  $\overset{\circ}{\tau}_j^{(L)} = \overset{\circ}{\sigma}_{ij}^{(L)} n_j^{(0)}$  is the traction-rate,  $B^{(0)}$  is the domain of the body,  $\partial B^{(0)}$  is that part of the boundary of the body on which the tractions are prescribed,  $U_{ij}$  and  $T_{ij}$  are the two point kernels for the displacements and tractions respectively in Kelvin's solution, and  $p$  and  $q$  are source and field points respectively (lower-case denoting points inside  $B^{(0)}$  and upper-case points on the boundary  $\partial B^{(0)}$ ). The subscript comma notation denotes differentiation at field point  $q$ , and  $G_{mkl}^*$  arises from writing equation 7.41 as

$$\overset{\circ}{\sigma}_{ij}^{(K)} = \overset{\circ}{\sigma}_{ji}^{(L)} + G_{jikl}^* v_{k,l} \quad (7.57)$$

A boundary integral equation for the boundary displacement-rates may be obtained from equation 7.56 by taking the limit as  $p \rightarrow P$ . The velocity gradients may be obtained by differentiating equation 7.56 at  $p$ . Discretization of the three expressions (*i.e.* for velocity, velocity gradients and boundary displacement-rates) yields in each case, a system of equations of the form

$$[A]\{v\} + [B]\{\overset{\circ}{\tau}^{(L)}\} = \{b\} \quad (7.58)$$

where  $[A]$  and  $[B]$  contain integrals of the kernels and the shape functions, and the vector  $\{b\}$  contains the various quantities from the three domain integrals. As in the finite element problem the components  $\overset{\circ}{\tau}_j^{(L)}$  obtained in the local coordinate frame from equation 7.54 must be transformed into the spatially fixed frame before being used in these discretized equations.

The solution strategy (figure 7.6) is similar to that employed in the finite element problem. First the velocity gradient version of equation 7.58 is solved with the inelastic deformation-rates set to zero and the prescribed initial displacements and tractions used instead of velocities and traction-rates. This yields the initial displacement gradients from which the strains (wholly elastic), stresses and rotations are obtained. The constitutive relations 7.46 and 7.47 are solved

to determine the initial inelastic deformation-rates and the material rates of the state variables. The initial boundary velocities are obtained iteratively using the equations for the boundary displacement-rates and the velocity gradients, with the first guesses for the boundary velocity gradients being obtained from a boundary stress-rate algorithm and with the first guesses for the velocity gradients within the body being zero. Once the boundary velocities are obtained, the velocities and velocity gradients within the body can be calculated, and armed with these the solution proceeds exactly as for the finite element problem *i.e.*  $\dot{\sigma}_{ij}$  and from this  $\dot{\sigma}_{ij}$  are obtained, and time integration is carried out using the material derivatives.

**7.2.2.5 Results of problems modelled in this way :** Only problems in either plane strain or plane stress have so far been considered using the full set of Hart's equations. The deformation of planar bodies (with and without traction-free cutouts) which are fixed at one end while being pulled at constant displacement-rate at the other, has been simulated by Chandra and Mukherjee (1984b). In each case the finite element and boundary element formulations yielded similar results but with the finite element solution requiring almost twice the computer time. Although quantitative comparisons were not made, it was observed that the simulation results showed qualitative agreement with the published results of deformation experiments conducted on bodies with the same geometry. The same authors have also used the finite element formulation to simulate the plane strain extrusion of an aluminium billet through a doubly curving die (Chandra and Mukherjee, 1984a). Again no quantitative comparisons with real material behaviour were made, but the potential of the analysis for metal-forming type problems, and in particular for the calculation of residual stresses in the workpiece, was confirmed.

Eggert and Dawson (1987) used finite elements and a simplified version of Hart's model (the anelastic element was omitted), to simulate the axisymmetric deformation of Type 304 stainless steel tapered rods during upset welding. They observed that with little extra cost in computer time, Hart's model compared rather more favourably with real experimental results than did equivalent simulations using a hyperbolic sine (steady-state) flow law (*cf.* equation 1.3).

### 7.3 Limitations of the modelling scheme

The time integration of Hart's inelastic constitutive equations presents the most significant limitation on the numerical modelling scheme outlined above. As observed previously (§ 7.1.2.3), this is a problem inherent in any time-dependent model of inelastic deformation because the constitutive equations must inevitably be a strongly increasing function of stress. Consequently, despite automatic time-step-size control, the numerical modelling of high strain-rate problems (*e.g.* short duration impact of bodies) where the time-steps must be especially small, remains computationally formidable.

In view of this problem it is important that the description of inelastic deformation used is simply applied and requires the storage of as few variables as possible during the calculation. The multiaxial constitutive equations involve the variables  $s_{ij}$ ,  $s_{ij}^{(a)}$ ,  $s_{ij}^{(f)}$ ,  $\sigma$ ,  $\sigma_a$ ,  $\sigma_f$ ,  $\varepsilon_{ij}^{(n)}$ ,  $a_{ij}$ ,  $\alpha_{ij}$ ,  $\varepsilon^{(n)}$ ,  $\dot{a}$ ,  $\alpha$ ,  $\sigma^*$ ,  $T$  and  $t$ . In the three dimensional case this involves forty-five scalar components and hence a considerable memory storage size in finite element applications. However, as observed by Bammann and Krieg (1987), most of the variables appear only as a convenience in

explaining the physical motivation for the deformation model and may be eliminated by appropriate mathematical manipulations (§ A1.5). When this is done the equations of, for example figure 7.1b (together with the elastic constitutive equation), reduce to

$$\dot{s}_{ij} = 2G(\dot{\varepsilon}_{ij}^{(t)} - \dot{\varepsilon}_{ij}^{(n)}) \quad (7.59)$$

$$\dot{\varepsilon}_{ij}^{(n)} = (3/2) \dot{\alpha}^*(\sigma^*, T) \left( \frac{\sigma - \sigma_a}{G} \right)^{M(T)} \frac{s_{ij}}{\sigma} \quad (7.60)$$

$$\dot{\sigma}_a = \mathcal{M} \left[ \dot{\alpha}^*(\sigma^*, T) \left( \frac{\sigma - \sigma_a}{G} \right)^{M(T)} - \left( \ln \frac{\sigma^*}{\sigma_a} \right)^{-1/\lambda} \left( \frac{\sigma^*}{G} \right)^m f_0 \exp \left( \frac{-H}{RT} \right) \right] \quad (7.61)$$

$$\frac{d \ln \sigma^*}{dt} = \left\{ \left[ \left( \ln \frac{\sigma^*}{\sigma_a} \right)^{-1/\lambda} \left( \frac{\sigma^*}{G} \right)^m f_0 \exp \left( \frac{-H}{RT} \right) \right] \Gamma(\sigma^*, \sigma_a) \right\} - \mathfrak{R}(\sigma^*, T) \quad (7.62)$$

$$\sigma = (1.5 s_{ij} \dot{s}_{ij})^{1/2} \quad (7.63)$$

These equations involve only  $s_{ij}$ ,  $\sigma_a$ ,  $\dot{\varepsilon}_{ij}^{(t)}$ ,  $\sigma^*$ ,  $T$  and  $t$  ( $\dot{\varepsilon}_{ij}^{(n)}$  is eliminated by substituting equation 7.60 into 7.59), and the number of scalar components is therefore reduced to sixteen. In some applications this number may be reduced even further. For example, the displacement-rate formulation of the infinitesimal strain problem requires only  $\dot{\varepsilon}_{ij}^{(t)}$ ,  $T$  and  $t$ , *i.e.* just eight memory storage locations are needed. This makes Hart's description of inelastic deformation very attractive in terms of storage requirements in comparison with other state variable type models.

The time integration problems of inelastic state variable models require the numerical modeller to balance the improved description of material behaviour that they afford, against the computational efficiency of classical yield surface plasticity models. Considerable attention has been given to the effect of the material parameters in the constitutive equations on the predicted material response. However, as observed by Bammann and Krieg (1987), a greater appreciation of their effect on the finite element solution (which is likely to be highly problem specific) would perhaps be of greater importance from the modelling perspective.

## **PART II**

### **THE EXPERIMENTAL INVESTIGATION**

## 8 AN OUTLINE OF THE EXPERIMENTAL PROGRAMME

The mechanical data used to illustrate the preceding account comes from a sufficiently wide range of materials to suggest that Hart's state variable description of inelastic deformation can be applied to geological materials as well. However, this data was obtained from experiments conducted at room pressure, whereas in the temperature range over which Hart's model in its original form applies (*i.e.*  $T < 0.45 T_m$ ), most geological materials require the presence of substantial confining pressures to suppress cataclasis at experimentally accessible strain-rates. Although confining pressure is not expected to affect the applicability of Hart's deformation model (throughout the preceding discussion inelastic deformation has been approximated as pressure insensitive), it does pose severe technical limitations on the quality of the mechanical data that can be obtained from the requisite experiments. Consequently, the possibility remains, that Hart's description can account for the inelastic behaviour of geological materials, but that the material parameters in it cannot be evaluated with sufficient accuracy for the approach to be of interest. The major objective of the experimental programme was to investigate this possibility by determining the full set of material parameters in Hart's original model (figure 5.3) for Carrara marble in compression at a confining pressure of 200 MPa and  $T < 0.45 T_m$ .

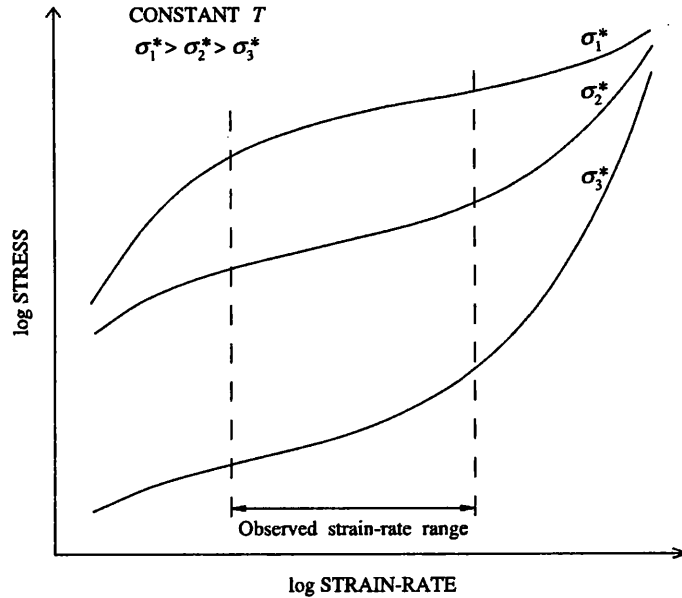
The significance of Hart's deformation model for characterizing the properties of geological materials is also highly dependent on the potential for applying them at  $T > 0.45 T_m$ . This reflects not only the fact that geologically significant inelastic deformation occurs at these temperatures, but also the fact that many important minerals are simply too strong to deform non-catastically in the laboratory at lower temperatures. Hence a second objective of the experimental programme was to investigate the form of a suitable recovery function  $\mathfrak{R}(\sigma^*, T)$  at these elevated temperatures, again using Carrara marble.

The first part of this account of the experimental programme is an outline of the experimental methodology / data gathering procedures (§ 8), and a detailed description / evaluation of the factors which limit the quality of the obtained data (§ 9). The results of the attempt to evaluate the material parameters in the three elements of Hart's original model and in the mechanical state evolution equation are described in § 10, § 11, § 12 and § 13 respectively, while the results of the investigation of the high temperature behaviour are given in § 14. Finally the potential of Hart's approach for geological materials is evaluated and compared with the more widely used steady-state flow laws (§ 15).

### 8.1 The experimental task

To determine the material parameters in Hart's equations of state, the simplest procedure is to choose experimental conditions for which each element of the analogue model (figure 5.3) is in turn, deformation rate controlling. This requires that separate experiments be performed :

- (a) at temperatures less than  $0.45 T_m$  and stresses below the macroplastic yield stress to characterize the anelastic element,
- (b) at temperatures less than  $0.3 T_m$  to characterize the friction element and,



(b)

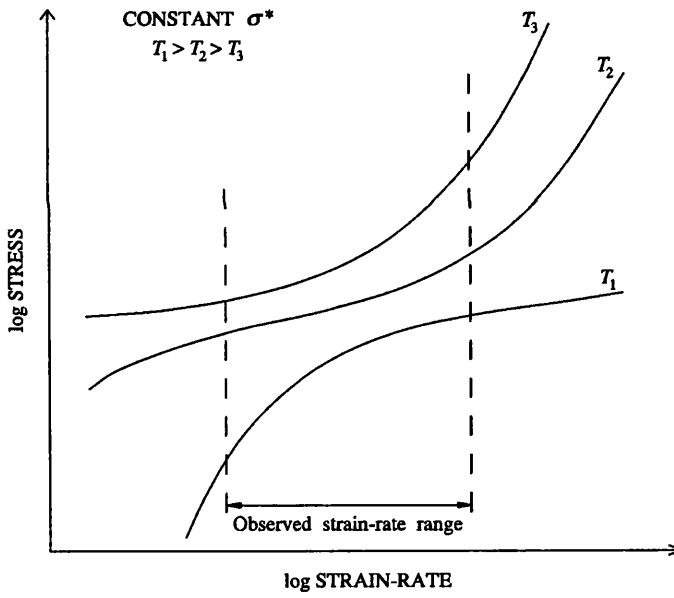


FIG. 8.1. The  $\log \sigma / \log \dot{\varepsilon}^{(n)}$  behaviour predicted by Hart's original deformation model showing the effects of (a) changing mechanical state and (b) changing temperature. Decreasing  $\sigma^*$  and  $T$  leads to the friction element controlling the deformation within the experimentally accessible strain-rate range, and hence allows the material parameters in that element to be determined. Conversely, increasing  $\sigma^*$  and  $T$  allows the parameters in the plastic element to be evaluated (redrawn after Lerner *et al.*, 1979).

(c) at temperatures between 0.3 and 0.45  $T_m$  to characterize the plastic element.

The optimum procedure (in terms of time) is to conduct variants of the isothermal constant displacement-rate test to determine the function  $\sigma(a; \sigma^*; T)$  for the anelastic element, and to conduct isothermal load relaxation tests after loading to stresses greater than the macroplastic

yield stress to determine the functions  $\sigma^*(\sigma, \dot{\epsilon}^{(n)}; T)$  for the friction and plastic elements. The maximum temperature of  $0.3 T_m$  for investigating the friction element, may to some extent be increased by increasing the loading strain-rate (figure 8.1). The stress dip and the creep recovery tests may also be used to determine respectively, the functions  $\sigma^*(\sigma, \dot{\epsilon}^{(n)}; T)$  and  $\sigma(a; \sigma^*; T)$ , but only at a considerable expense in time.

Provided the equations of state have been previously determined, the results of isothermal constant displacement-rate tests at temperatures less than  $0.45 T_m$  may be converted into the function  $\sigma^*(\alpha, \sigma, \dot{\epsilon}^{(n)}; T)$  and used to determine the material parameters in the mechanical state evolution equation. Again provided the equations of state are known, interrupted constant displacement-rate tests where the deformation is at  $T < 0.45 T_m$ , and uninterrupted constant displacement-rate tests at higher temperatures, provide all the mechanical data required to investigate the recovery function  $\mathcal{R}(\sigma^*, T)$ .

The potential utility of Hart's description for geological materials is therefore determined by the quality of the data that can be obtained from constant displacement-rate and load relaxation / stress dip / creep recovery tests under the confining pressures of interest.

## 8.2 The deformation apparatus employed

All the experiments reported here were conducted on two fluid confining medium apparatus, subsequently referred to as HEARD1 and as NIMONIC2. The technical specifications of both apparatus have been outlined elsewhere (see below), and so the present discussion is restricted to those aspects of the design which influence the quality of the mechanical data obtained.

**8.2.1 Basic design.** Both deformation apparatus are similar in basic design. In each the specimen is deformed within a vertically mounted, externally heated, cylindrical pressure vessel. Differential loads are applied to the specimen by a screw which is connected to the loading piston via a non-rotating thrust bearing, and which is driven by a motor through gears of a ratio that can be varied over five orders of magnitude. A computerized data logging system allows the millivolt output of the temperature, confining pressure, pore fluid pressure (though not present in these tests), crosshead displacement and axial load measuring devices to be recorded throughout the experiment. The fastest logging rate for a complete set of readings is approximately once every seven seconds (limited primarily by the settling time required for the digital multimeter as it is switched through the five channels), with a faster rate of once every 0.7 seconds if only one of the readings is required.

The two apparatus differ primarily in the material used for the pressure vessel and hence in the confining medium which can be employed. Consequently, they are used to access different temperature ranges.

**8.2.2 HEARD1.** HEARD1 has a steel (Jessop-Saville H 50 pressure die-casting steel) pressure vessel and uses silicone oil as its confining medium (figure 8.2). This apparatus was built initially to a design by H. C. Heard in 1968, but prior to this experimental programme it was completely (apart from the loading train) re-manufactured. Apart from some minor dimensional modifications introduced during the reconstruction, the use of silicone oil rather than water as the confining medium (to enhance the life of the pressure vessel), and the replacement of chart

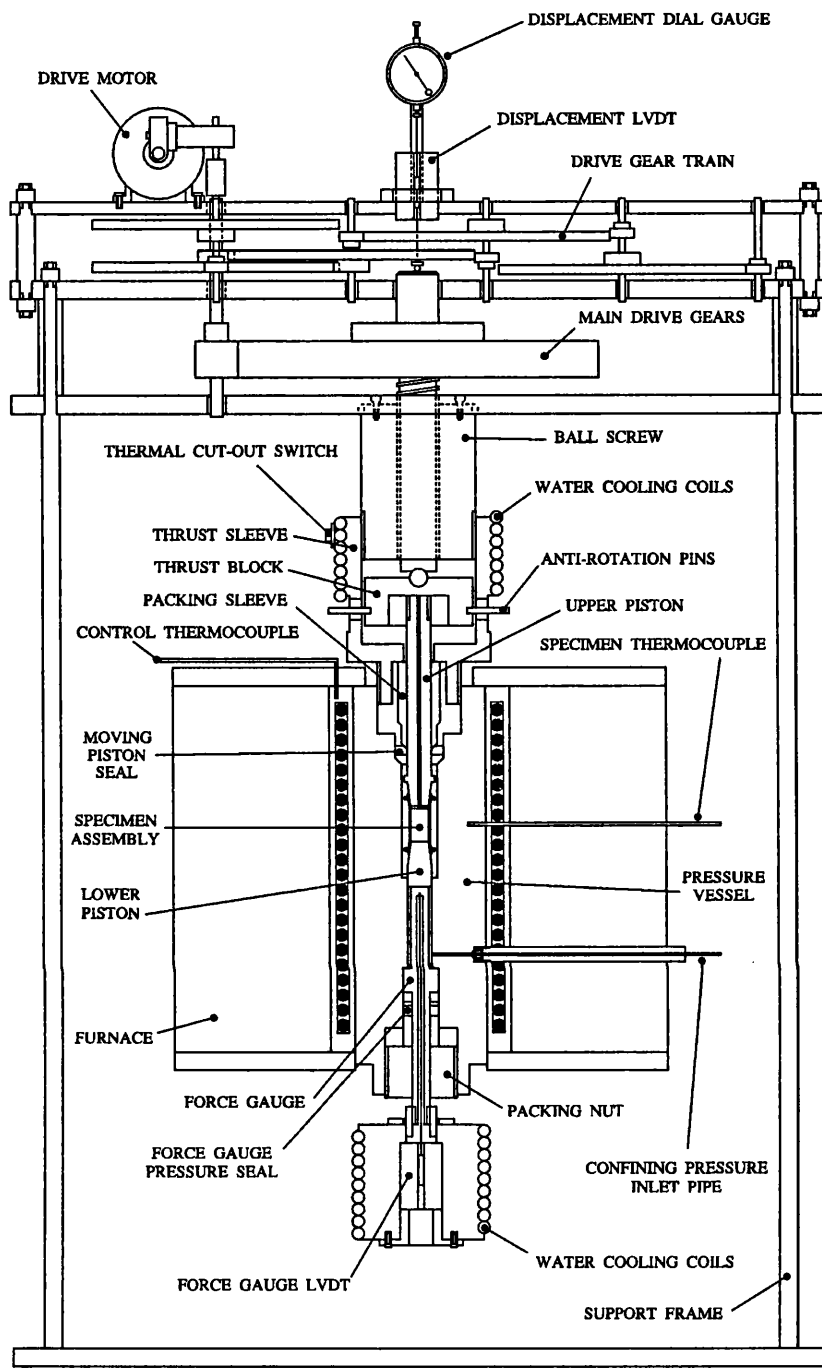


FIG. 8.2. The HEARD1 deformation apparatus (redrawn with modifications after Rutter, 1970).

recorders by the computerized logging system, the apparatus is as described in detail by Rutter (1970 ; 1972).

The confining pressure sealing arrangement may be understood with reference to figure 8.2. The details of the lower pressure seal (which is against the force gauge) are of no consequence to the present discussion. The upper seal is effected by a tool steel ring which, during assembly of the test, is forced by a packing sleeve to deform elastically outwards against the inner surface of the pressure vessel, and inwards against the top piston. During the test the

upper piston is pushed through the seal once sufficient load has been applied to overcome the large frictional forces. The confining pressure is measured by a DC - LVDT transducer operated by the displacement of the bourdon tube inside a bourdon tube pressure gauge located in the pressure line. The pressure vessel is rated to allow confining pressures of upto 400 MPa, although the maximum pressure that can be maintained for long periods is about 250 MPa.

Temperature is supplied by two furnace halves which fit closely around the outer diameter of the pressure vessel. The furnace power supply is controlled by a variable transformer, while the furnace temperature is regulated by a platinum resistance, thermometer actuated, temperature controller which interrupts the power supply according to the output from a control thermocouple placed in a low thermal capacity part of the furnace element. The specimen temperature is measured by a chromel-alumel thermocouple which is placed in a one-eighth inch (3.175 mm) diameter hole drilled in the wall of the pressure vessel opposite the specimen position. The output obtained is given with respect to a temperature regulated (nominally 30°C) reference thermocouple. Water cooling coils positioned at the top and bottom of the axial column maintain a constant thermal gradient along the pressure vessel. The maximum operating temperature of the apparatus is limited by the polymerization of the confining medium, which becomes significant at temperatures greater than about 420°C.

Crosshead displacement is measured by a DC - LVDT transducer. The body of the transducer is clamped to the apparatus frame, and the movable core rests via a steel ball, on top of the screw which drives the loading piston. The upper part of the core is connected, via a brass rod, to a 0.001 inch (0.0254 mm) divided dial gauge which spring loads the LVDT core.

The axial load acting on the specimen is measured by the elastic distortion of a hollow, tool steel column (the force gauge, figure 8.6), which lies directly under the lower piston and experiences the same load as the specimen. An unstressed rod connects the top of this column with the core of a DC - LVDT transducer, the body of which is housed within a water cooled block which is in turn rigidly attached to the other end of the column. In response to the axial deformation of the column, this rod moves through the transducer and produces an output which can be calibrated against the differential load applied. No correction for seal friction is required because the actively deforming length of the force gauge lies entirely between the upper and lower pressure seals.

The pressure, displacement and force transducers are all served with the same regulated 24 volt power supply.

**8.2.3 NIMONIC2.** NIMONIC2 has a Nimonic 105 alloy pressure vessel and uses de-ionized water as its confining medium (figure 8.3). This apparatus was designed and built within the laboratory by R. F. Holloway and E. H. Rutter and carries the additional difference from HEARD1 in that the load is applied from the bottom of the axial column, not the top, an innovation which shortens the turnaround time between tests considerably. It has been operated successfully since 1984 and has been described in detail by Walker (1991).

As with HEARD1 the lower confining pressure seal, which is here the moving piston seal, lies below the active part of the force gauge and has no direct influence on the quality of data obtained from the apparatus. The upper seal arrangement is contained within a stainless steel unit (the top sealing block) which is held in place by eight high tensile bolts which pass through

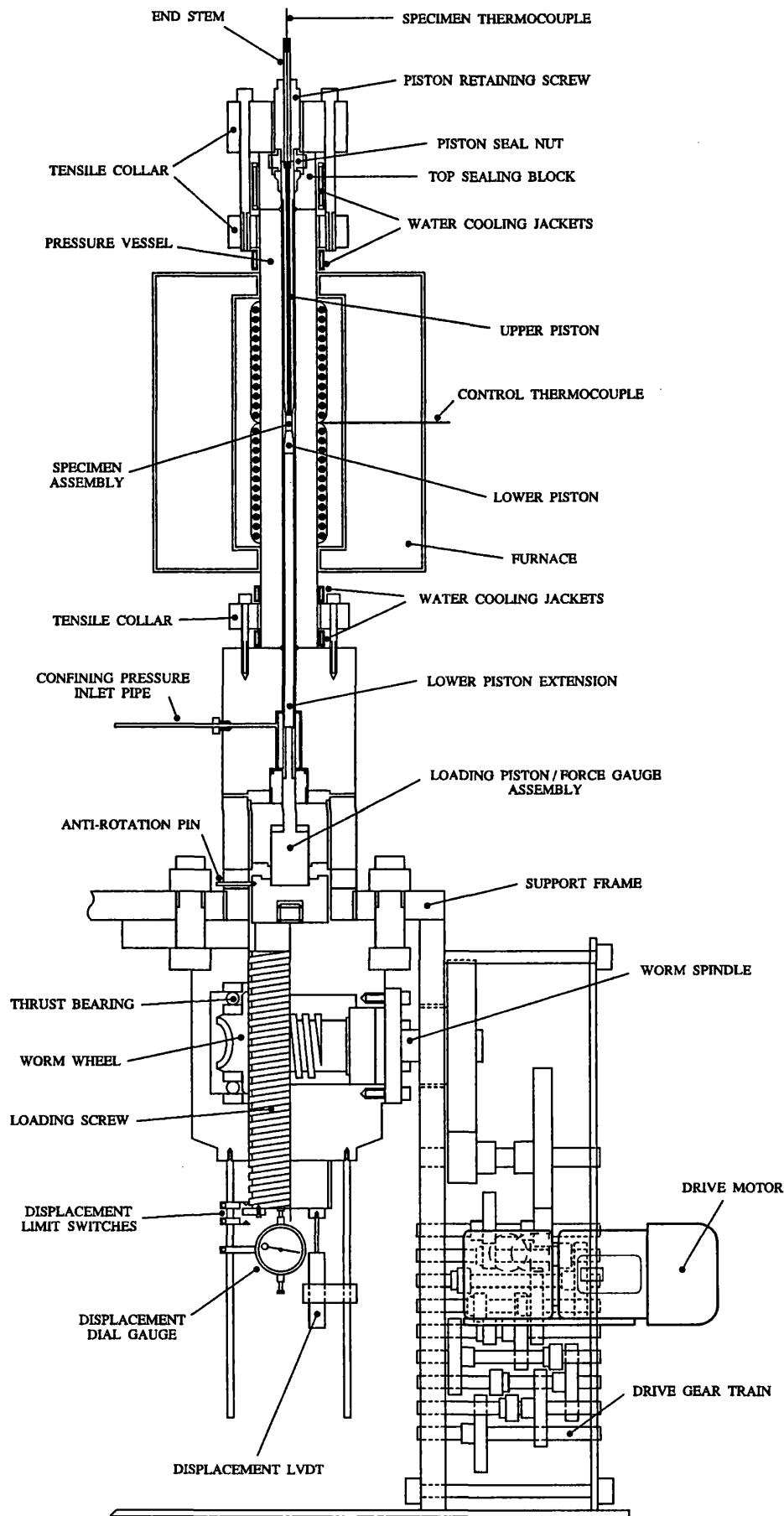


FIG. 8.3. The NIMONIC2 deformation apparatus (redrawn with modifications after Walker, 1991).

a thick collar above the unit, into another collar around the top of the pressure cylinder below it (figure 8.4). The seal is effected by an O-ring which is squeezed by a gland nut between the upper piston and the inner surface of the steel unit. The piston is held in place by a retaining screw, while the seal between the steel unit and the top of the pressure cylinder is effected by a stainless steel delta ring placed at the contact between the two faces, and deformed elastically against the walls of its seat by the force exerted from the eight bolts. The confining pressure is measured both by a pressure transducer and by a bourdon tube gauge, which are connected separately in the pressure line. The pressure vessel is rated to allow confining pressures of upto 300 MPa, but the maximum pressure that can be maintained for long periods is about 180 MPa.

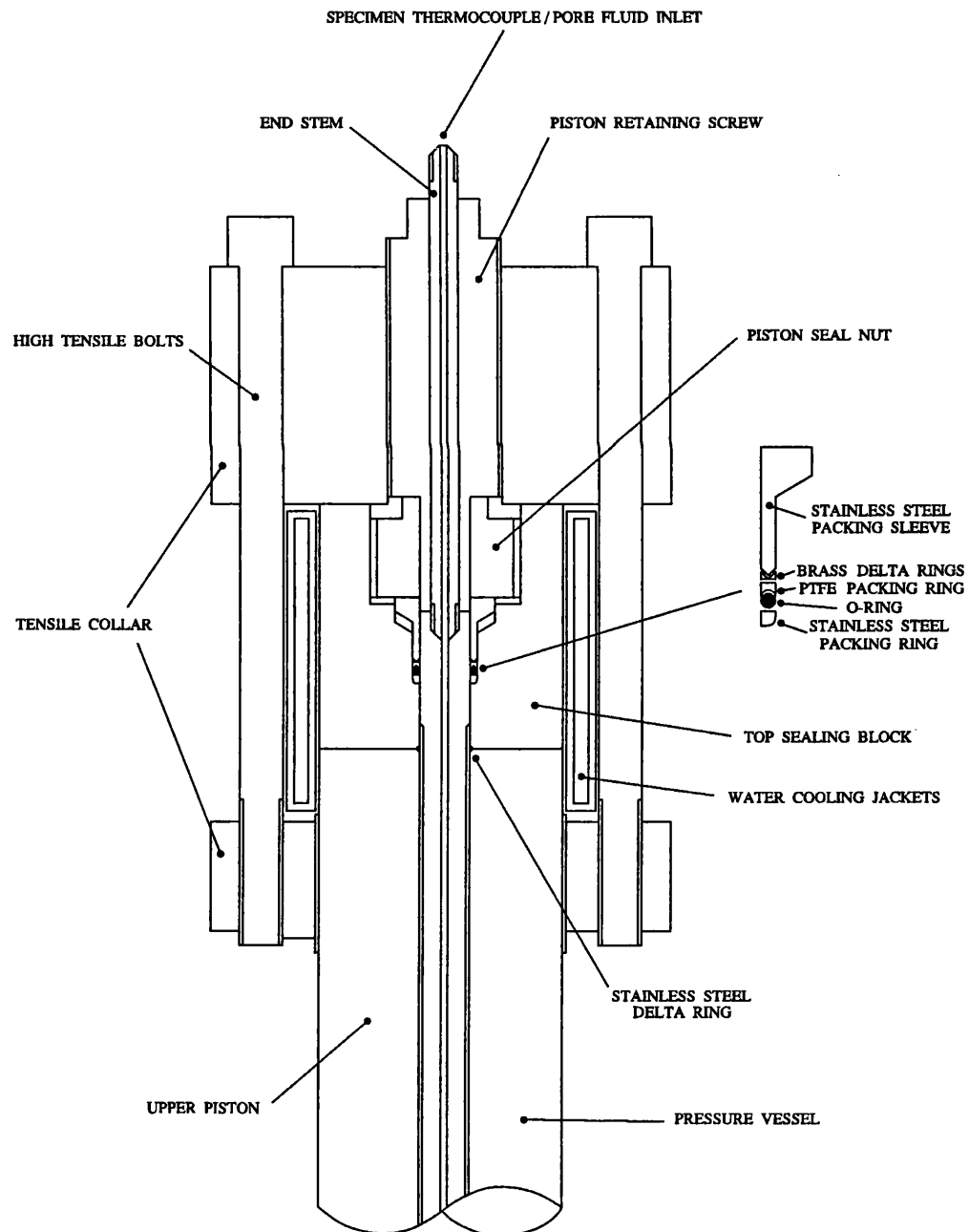


FIG. 8.4. The upper closure assembly of NIMONIC2 (redrawn with modifications after Walker, 1991).

The temperature is supplied in the same way as for HEARD1, except that the furnace temperature is regulated with a combined thyristor and silicon diode power rectifier, operating in fast cycle mode and controlled by a thermocouple located against the outside of the pressure vessel opposite the specimen position. The temperature is measured using a chromel-alumel thermocouple inserted through the pore fluid inlet in the upper piston such that its tip lies a few millimetres from the top of the specimen. Again the temperature is given with respect to a temperature regulated (at 30°C) reference thermocouple, and water cooling coils at either end of the axial column serve to maintain a constant thermal gradient along the axis of the pressure

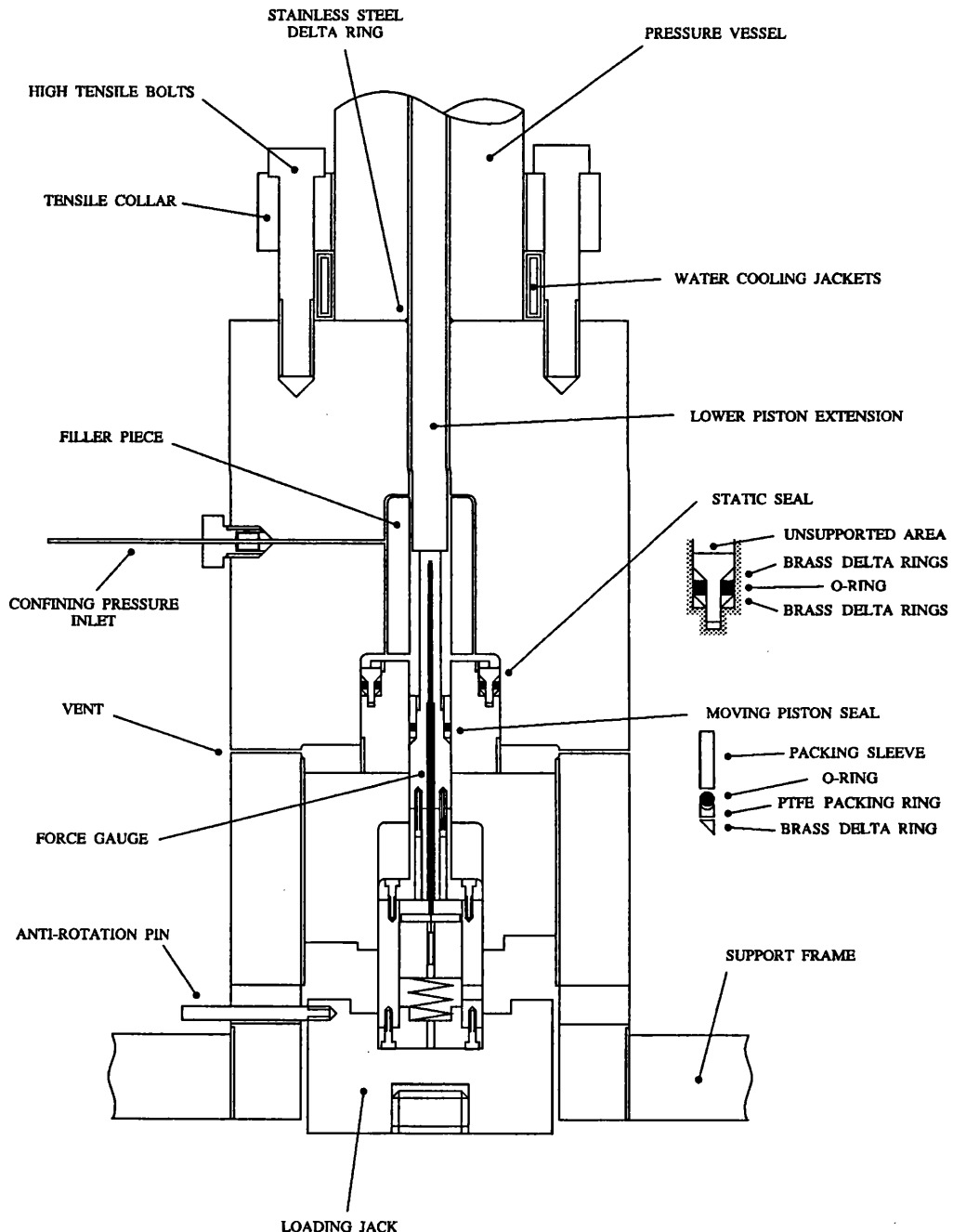


FIG. 8.5. The lower closure assembly of NIMONIC2 (redrawn with modifications after Walker, 1991).

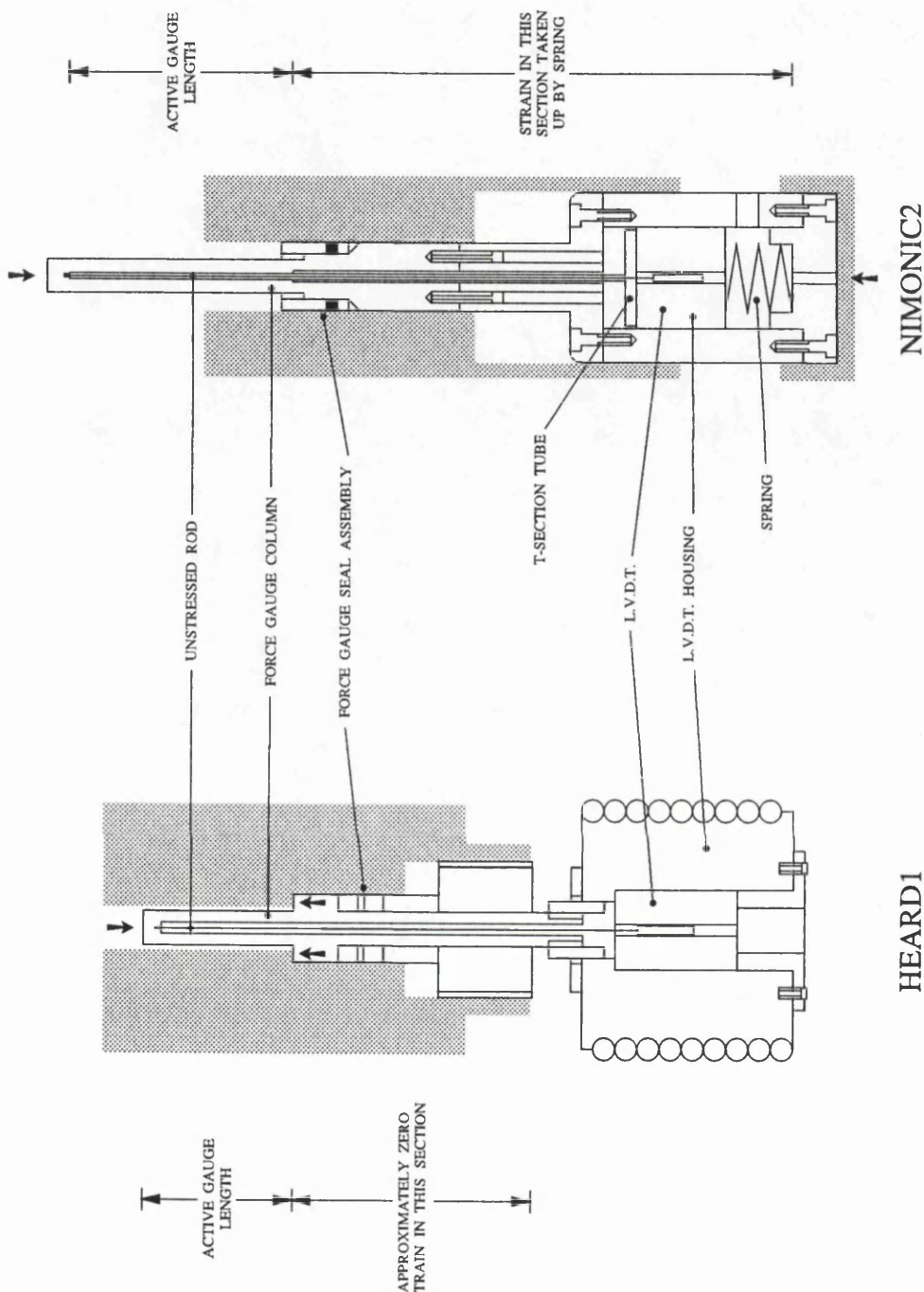


FIG. 8.6. Comparison of the force gauge assemblies of the HEARD1 and NIMONIC2 deformation apparatuses.

vessel. The maximum working temperature is controlled by the strength characteristics of the Nimonic 105 alloy used for the pressure vessel. At 300 MPa confining pressure the maximum operating temperature is approximately 700°C. Temperatures of upto 800°C can be accessed if the confining pressure is decreased, but no such tests were conducted in this study.

Crosshead displacement is measured by a DC - LVDT transducer. The body of the transducer is clamped to the apparatus frame and the movable core is fixed to the bottom of the screw which drives the loading piston. A 0.0001 inch (0.00254 mm) dial gauge separately attached to the rig also measures the displacement of the bottom of the loading screw.

The axial load acting on the specimen is measured, like HEARD1, by the elastic distortion of a hollow, tool steel column as indicated by the displacement of an unstressed rod connecting to the top of the column to the core of a DC - LVDT transducer (figure 8.6). However, on NIMONIC2 the force gauge is located inside the loading piston (figure 8.5). The transducer body is forced firmly by a steel spring against the base of a T-section tube, which in turn is pushed against a shoulder situated midway up the interior of the force gauge column above the level of the moving piston pressure seal. During loading any elastic distortion of the piston below the top of the T-section tube is accommodated by the spring, and the displacement measured by the transducer is due entirely to the shortening of the column between the top of the T-section tube and the top of the unstressed rod. Hence as for HEARD1, the actively deforming length of the force gauge lies entirely between the pressure seals and no correction for seal friction is required.

The pressure, displacement and force transducers are served from two (between them) 12 volt stabilized power supplies.

### 8.3 Experimental procedures

All the experiments conducted in this study were either load relaxations or variants of the constant displacement-rate test. All were conducted in compression at constant temperature (during the deformation phase) and constant confining pressure, and in each case the stress field applied to the specimen was of uniaxial symmetry. HEARD1 was used to determine the material parameters in Hart's original model, while NIMONIC2 was used to investigate the static recovery function.

**8.3.1 The starting material.** Carrara marble is a white marble, quarried for monumental purposes at Carrara in the Northern Apennines of Italy. It was used in the seminal triaxial rock deformation studies of von Kármán (1911, or see Jaeger and Cook, 1979, pp. 152 / Kirby and McCormick, 1984, pp. 155) and von Böker (1915, or see Kirby and McCormick, 1984, pp. 255). More recently, it has been used in several experimental deformation studies of calcitic aggregates to characterize their brittle behaviour (Cooper, 1977 ; Atkinson, 1979, 1984 ; also see Atkinson and Meredith, 1987), their semi-brittle behaviour (Edmond and Paterson, 1972 ; Fredrich *et al.*, 1989 ; Fischer and Paterson, 1989), to determine steady-state flow laws in the intracrystalline slip and grain boundary sliding deformation regimes (Rutter, 1972 ; 1974 ; Schmid *et al.*, 1980), and to observe the development of deformation textures by intracrystalline slip under both coaxial and non-coaxially applied differential loads (Rutter and Rusbridge, 1977 ; Owens and Rutter, 1978 ; Casey *et al.*, 1978 ; Spiers, 1981 ; Laurent *et al.*,

1981 ; Schmid *et al.*, 1987 ; Rowe and Rutter, 1990).

**8.3.1.1 Characterization :** Carrara marble forms part of Alpi Apuane metamorphic complex which is exposed as a large ( $300 \text{ km}^2$ ) tectonic window through an unmetamorphosed cover sequence. It is derived from Lower Liassic massive limestones which were compressively deformed and metamorphosed at mid-crustal levels during the Eocene, which were then extended during the Miocene, and which were finally brought rapidly to the surface during the isostatic uplift and denudation that followed the extensional event (Carmignani and Kligfield, 1990). Despite a large number of thermobarometric and dating studies on the metamorphic complex, details of the precise form of the  $pTt$  curve remain unclear from the information published in the English language literature. The compressional deformation is dated on stratigraphic grounds and by K-Ar and  $^{40}\text{Ar}/^{39}\text{Ar}$  studies to 27 Ma (Kligfield *et al.*, 1986). Post-kinematic chloritoid and kyanite porphyroblasts are used to suggest that the metamorphic peak occurred shortly after the deformation. Petrogenetic grid considerations and calcite-dolomite geothermometry suggest that the peak metamorphic conditions were approximately 400 MPa and 500°C with a small decrease in temperature from the west to the east of the complex (Di Pisa *et al.*, 1985). Cooling to below 300°C following the metamorphic peak must have been very rapid in order to avoid the complete resetting of the argon systems in the metamorphic phengites and the magnesium in the Mg-calcites. Syn-kinematic phengites have been used to date (by  $^{40}\text{Ar}/^{39}\text{Ar}$  methods) the onset of the extension to 12 Ma, while the dates of post-kinematic phengites and various stratigraphic arguments suggest that the deformation was completed by 8 Ma (Kligfield *et al.*, 1986). The syn-kinematic mineral assemblages (chlorite plus coexisting muscovite and phengite) have been used to infer that the extensional deformation occurred at about 300 MPa and 300°C. The timing of the subsequent rapid uplift to the surface is constrained by apatite fission track data (reported in Carmignani and Kligfield, 1990).

Despite this complex tectonothermal history, and despite the observation that breccia units stratigraphically above, below and within the marble formation record large strains (Kligfield *et al.*, 1981), in thin section the rock appears as a granoblastic calcite polycrystal with few deformation features (figure 8.7). The grain-size is uniform with a mean linear intercept of  $147 \pm 9 \mu\text{m}$  (where the error is at the 95% confidence level from eight counts – with an average of 141 grains sampled per count – made from non-overlapping areas using a circular intercept counting net, Abrams, 1971). The grain boundaries are well defined although not straight, suggesting that they have been at least partially mobile at some time. Most grains show an undulose extinction, and many contain a few, mostly thin, straight-sided deformation twins. However, there is no significant shape fabric, and by optical inspection there is little evidence for any crystallographic preferred orientation.

Dark grey inclusion trails, arranged on approximately parallel planes, form a prominent feature of the hand specimen. In thin section these are seen to be composed of widely disseminated but very fine-grained opaques. Where they are particularly concentrated the calcite grain-size may be greatly reduced (to as little as  $20 - 30 \mu\text{m}$ , figure 8.7), but this is only rarely the case and in general the inclusions appear to have no influence on the texture of the marble. In occasional thin sections isolated euhedral crystals of quartz and albite may be found.

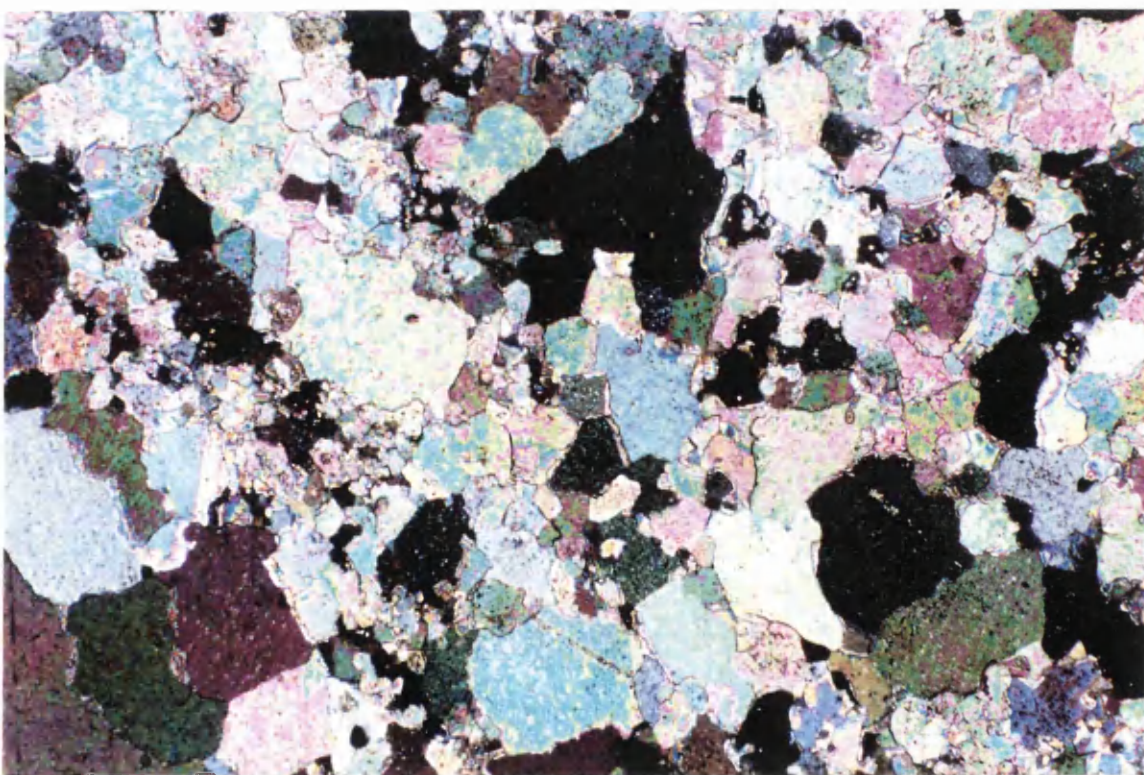


FIG. 8.7. Photomicrographs of the Carrara marble starting material used in the experiments. (top) The typical microstructure. The base of this photomicrograph is 3125  $\mu\text{m}$ . (bottom) An area of the microstructure in which there is a particularly high concentration of finely dispersed opaques and in which correspondingly, the calcite grain-size is much reduced. The base of this photomicrograph is 1250  $\mu\text{m}$ .

These are similar in size to the calcite. The calcite is extremely pure with respect to solute impurities. An ICP analysis of material from the block used for the experiments reported here, yielded the following results

Sr = 97 ppm	Mn = 27 ppm	Ce ≈ 7 ppm	Y ≈ 1.3 ppm
Mg = 2250 ppm	Be < 0.2 ppm	Zn ≈ 1.5 ppm	Ti ≈ 24 ppm
Fe = 12 ppm	Cr = 27 ppm	V < 0.8 ppm	P ≈ 6 ppm
Cu < 1 ppm	Zr < 27 ppm	K = 4 ppm	

(where the potassium result was determined by AAS).

For the purposes of this study therefore, Carrara marble is an approximately isotropic, pure calcite polycrystal which is in an almost completely undeformed state. The implication is that the block of marble used for this work came from a part of the Apuane complex which was locally only mildly affected by the extensional deformation, and that the texture is the product of a recrystallization process involving significant grain boundary migration after the completion of the Eocene compressional event.

**8.3.1.2 Specimen preparation procedures :** All specimens used in this study were right circular cylinders cored in an arbitrary but constant direction from the same block of marble. Two different core diameters were employed ; 0.25 inch (6.35 mm) for the static recovery tests and 0.375 inch (9.525 mm) for all the others. The cores were allowed to oven-dry at 105°C until required for use. Final preparation procedures included cutting the cores to length (a length / diameter aspect ratio of about 2.35 was employed for the recovery tests ; 2.60 for the others), squaring the ends to better than 0.001 inch (0.0254 mm), washing the resulting specimens in alcohol and returning them to the oven for a few minutes.

All specimens were deformed in a thin-walled (0.01 inch, 0.254 mm) commercial purity copper jacket, which served to isolate the specimen from the confining medium (the assembly arrangement is illustrated in figure 9.9a). The jackets were annealed immediately prior to test assembly by heating rapidly to red heat in a butane flame. They were then quenched in cold tap water, soaked for a few seconds in nitric acid to remove the copper oxide formed during the heating, washed in tap water and in alcohol, and were finally placed in the oven for a few minutes to dry.

**8.3.2 The deformation experiments.** The deformation conditions and types of test that can be employed to evaluate the material parameters in Hart's model, are dictated by the need to access its various elements under circumstances where deformation processes not accommodated by the description have a negligible influence on the mechanical behaviour. For Carrara marble this requires that the effects of cataclasis and mechanical twinning be avoided. The strategy adopted was to attempt to negate the former by the choice of deformation environment and the latter, as far as possible, by the choice of the type of test.

**8.3.2.1 The choice of deformation conditions :** At strain-rates of  $10^{-5} \text{ s}^{-1}$  at room temperature, cataclasis is significant (*i.e.* for the purposes of this discussion, the interconnected porosity increases above 0.01) at all confining pressures under 300 MPa (Fredrich *et al.*, 1989), while at the same strain-rate and at effective pressures below 150 MPa it remains significant upto temperatures of 400°C (Fischer and Paterson, 1989). These pressures are near to the maximum long term confining pressures that can be maintained by the two apparatus, and so if cataclasis

is to be avoided it is necessary that the confining pressures and temperatures be as high as possible while the maximum strain-rates investigated be as low as possible. Set against this are the observations made during the course of the experimental programme, that static recovery becomes important at temperatures above 400°C, and that the transition between deformation rate controlled by the friction element and that controlled by the plastic element, occurs at approximately 240°C. Furthermore decreasing the strain-rates during the loading prior to load relaxation, decreases the strain-rate range over which the relaxation data is gathered, while also increasing the time required to complete the experiments.

Given these constraints the confining pressures chosen for the experiments were 200 MPa for the HEARD1 tests and 170 MPa for the NIMONIC2 tests, each of which is close to the maximum long term working pressure for the respective apparatus. The minimum temperature investigated was 120°C, which permits a 120°C temperature range for the investigation of the parameters of the friction element. The maximum strain-rate employed was  $6 \times 10^{-4} \text{ s}^{-1}$  where the results suggest that the influence of cataclasis is just detectable (§ 13.2).

*8.3.2.2 The choice of the type of test :* Mechanical twinning is an important deformation process in Carrara marble throughout the range of conditions that can be accessed by the deformation apparatus. However, it is a process which is critically dependent on the magnitude of the applied differential stress and so can, in principle, be avoided by employing tests in which the mechanical data of interest is collected at stresses below the maximum the specimen has previously experienced.

In all the types of test which have been used previously to determine the material parameters in the friction and plastic elements (*i.e.* the load relaxation, stress dip and creep recovery tests), the data is collected at lower stresses than experienced by the specimen at the end of pre-straining, and so mechanical twinning is not a problem. The parameters in those elements were evaluated in this study by interrupting a constant displacement-rate test several times to conduct load relaxations. At elevated confining pressure the load relaxation test is simpler to conduct, and the required data is more quickly obtained and easier to interpret, than for stress dip and creep recovery tests. In addition, this method of generating a several relaxations from one sample at different strains (*i.e.* mechanical states), removes the effect of specimen variability from results produced at otherwise identical conditions, and permits the absence of any deformation independent changes in mechanical state during the test to be verified (through comparison of the reload stress / strain curves with the stress / strain curve generated from a test without relaxations). Eight different temperatures were investigated at 40°C intervals in the range 120 to 400°C. At each temperature about twelve load relaxations were conducted at approximately 0.015 strain intervals in the range 0.01 to 0.20 logarithmic strain. The average duration of each relaxation was two days, although those at low temperature and low strain were frequently of only one day, while those at high temperature and high strains were of upto ten days. In this way relaxation data was obtained routinely from the loading strain-rate to strain-rates of  $10^{-9} \text{ s}^{-1}$ . For the tests conducted at 120 and 160°C the loading displacement-rate was 0.8 mm / min corresponding to a strain-rate of approximately  $6 \times 10^{-4} \text{ s}^{-1}$ , while for the remaining temperatures the displacement-rate was 0.333 mm / min corresponding to a strain-rate of  $2 \times 10^{-4} \text{ s}^{-1}$  (where the strain-rates are those at a strain of 0.1).

The parameters in the anelastic element were determined from constant displacement-rate tests (at  $0.0333 \text{ mm/min}$  i.e.  $2 \times 10^{-5} \text{ s}^{-1}$ ) as interrupted for complete unloading and reloading at several different strains in the range 0 to 0.3. The required parameters were evaluated from the reload curves and hence were determined at stresses lower than previously experienced by the specimen. Experiments were conducted at 200 and 399°C while a further experiment at 318°C was repeatedly loaded and unloaded at a strain of 0.10 and displacement-rates of 0.333, 0.0333 and 0.00333 mm/min to verify the strain-rate independence of the parameters.

The evaluation of the parameters in the mechanical state evolution equation must involve tests in which mechanical twinning is significant, because any method of changing the magnitude of  $\sigma^*$  inevitably also involves twinning. Hence the only way to prevent a deformation history dependence in the evaluations of the material parameters, is to identify and remove the effect of twinning from the acquired mechanical data (cf. § 9.4.2). In this study the required parameters were determined from constant displacement-rate tests conducted without interruption at the same eight temperatures as the relaxations, and at six different displacement rates corresponding to the strain-rate range  $6 \times 10^{-4}$  to  $6 \times 10^{-7} \text{ s}^{-1}$ . In addition, three suites of relaxation curves were generated at 310°C after pre-straining at displacement-rates corresponding to strain-rates of  $6 \times 10^{-5}$ ,  $2 \times 10^{-5}$  and  $6 \times 10^{-6} \text{ s}^{-1}$ .

The static recovery behaviour was investigated by means of constant displacement-rate tests corresponding to a strain-rate of  $3 \times 10^{-4} \text{ s}^{-1}$ , which were conducted at 420°C (for the choice of temperature see § 9.2.2). After deforming the specimen to a pre-determined strain, the load was removed from the sample and the temperature rapidly raised to a desired value. The specimen was left to anneal for a given period, and was then re-deformed under the initial deformation conditions to allow a comparison between the initial and reload stress / strain curves. Annealing was conducted at 500, 550, 600, 650 and 700°C, all after a pre-strain of 0.17, and at 600°C after pre-strains of 0.08, 0.17 and 0.2725. At each annealing condition about six annealing periods were investigated, equally spaced in log time between 3 hours and 40 days.

#### 8.4 Data reduction

For a deformation experiment in which the applied loads have uniaxial symmetry and the confining pressure and temperature remain constant, the task of the data reduction exercise is to determine at any instant the seven variables

$$\sigma, \varepsilon^{(t)}, \varepsilon^{(e)}, \varepsilon^{(n)}, \dot{\varepsilon}^{(t)}, \dot{\varepsilon}^{(e)}, \dot{\varepsilon}^{(n)}$$

where  $\sigma$  is the differential stress acting on the specimen normal to the deformation axis, and the strain and strain-rate terms are axial. The supplied data is a time record of the differential load  $\mathcal{P}$  acting on the specimen and the displacement  $\mathcal{X}$  of the apparatus crosshead. The initial specimen dimensions are given as a length  $L_0$  and a cross sectional area  $A_0$  (respectively, parallel with and normal to the deformation axis).

Defining  $\mathcal{A}$  and  $\mathcal{L}$  as the cross sectional area and length of the specimen at any instant, and  $L$  as the specimen "elastic length" (i.e. the initial length less the component of inelastic deformation) at that instant, then

$$\sigma = \mathcal{P}/\mathcal{A} \quad (8.1)$$

$$\varepsilon^{(t)} = \ln(\mathcal{L}/L_0) \quad (8.2)$$

The deformation of the specimen at any instant during the experiment is given by

$$\mathcal{X} = \Delta \mathcal{L} + \Delta L_{app} \quad (8.11a)$$

$$= \Delta L_e + \Delta L_p + \Delta L_{app} \quad (8.11b)$$

which may be solved for  $\mathcal{L}$  and  $L$  using equations 8.8 – 8.10 if any two of  $\Delta L_{app}$ ,  $\Delta L_e$  and  $\Delta L_p$  can be determined.  $\dot{\mathcal{L}}$  and  $\dot{L}$  are given by the time derivatives of  $\mathcal{L}$  and  $L$ . To complete the reduction problem, some function relating  $\sigma$  and  $\mathcal{L}$  must be specified so that  $\sigma$  can be found.

**8.4.1.1 The additional relations :** In the subsequent derivations constant volume deformation is assumed so that

$$\sigma = A_0 L_0 / \mathcal{L} \quad (8.12)$$

$\Delta L_{app}$  is given by calibrations of the apparatus stiffness  $\mathcal{S}$

$$\Delta L_{app} = \mathcal{P} / \mathcal{S} \quad (8.13)$$

$\Delta L_e$  is specified by the Young's modulus  $E$  of the specimen

$$\sigma = E \Delta L_e / L \quad (8.14)$$

where the elastic length of the specimen has been used. Substituting equations 8.1 and 8.12 into equation 8.14 yields

$$\Delta L_e = \mathcal{P} \mathcal{L} L / A_0 L_0 E \quad (8.15)$$

**8.4.1.2 The complete solution :** Substituting equation 8.13 into 8.11a, and rewriting for  $\Delta \mathcal{L}$  using equation 8.9

$$\mathcal{L} = L_0 - \mathcal{X} + (\mathcal{P} / \mathcal{S}) \quad (8.16)$$

Substituting equations 8.13 and 8.15 into equation 8.11b, rewriting for  $\Delta L_p$  with equation 8.10 and simplifying with equation 8.16

$$L = \mathcal{L} + (\mathcal{P} \mathcal{L} L / A_0 L_0 E) \quad (8.17)$$

which solving for  $L$  yields

$$L = \mathcal{L} / [1 - (\mathcal{P} \mathcal{L} / A_0 L_0 E)] \quad (8.18)$$

Differentiating equations 8.16 and 8.18 with respect to time

$$\dot{\mathcal{L}} = -\dot{\mathcal{X}} + (\dot{\mathcal{P}} / \mathcal{S}) \quad (8.19)$$

and

$$\dot{L} = [\dot{\mathcal{L}} + (\dot{\mathcal{P}} \mathcal{L}^2 / A_0 L_0 E)] / (\mathcal{L} / L)^2 \quad (8.20)$$

(appendix § A2.1.3) where  $\dot{\mathcal{P}}$  may be found by differentiating the observed load record with respect to time.

**8.4.2 The data reduction procedures employed.** The data reduction equations derived above were applied as they stand, to the data recorded during the deformation experiments. No correction was applied to the differential load data to account for that part of the load supported by the copper jacket (cf. § 9.3).

The initial specimen dimensions were determined using a 0.001 inch (0.0254 mm) divided micrometer. The length was specified as the mean of two measurements, while the cross sectional area was determined from the mean of six diameter measurements using the equation for the area of a circle. No correction was applied to account for the compression of the sample under confining pressure or for the thermal expansion of the sample during heating to the test conditions.

Data processing for each test was conducted in three stages, with the output of each being stored as a data file. First, representative sets of data (where each set comprises the millivolt

output of the five recorded channels plus the time at which the set was logged) were selected visually from the complete data record. Typically about fifty sets were chosen for a constant displacement-rate test with the greatest concentration in the first 0.01 increment of strain, while for a relaxation test about one hundred were selected (the exact number varying with the amount of relaxation) with the density of data reflecting the relaxation-rate.

The second processing stage involved the conversion of the selected millivolt data into SI units using the apparatus calibration information.

The final step was to apply the data reduction formulae derived above. For the constant displacement-rate tests equations 8.12, 8.16 and 8.18 were applied to find  $\sigma$ ,  $\varepsilon^{(t)}$  and  $\varepsilon^{(n)}$  (the Young's modulus used is discussed in § 10.1.1).  $\dot{\varepsilon}^{(t)}$  was determined for the  $i$ th data set from

$$\dot{\varepsilon}^{(t)} = [(\mathcal{L}_i - \mathcal{L}_{i-1}) / \mathcal{L}_{i-1}] / [t_i - t_{i-1}] \quad (8.21)$$

where  $t$  is the time of the data set. Equations 8.19 and 8.20 were not used because of the effort required to determine  $\dot{\mathcal{P}}$ . For the load relaxation tests, the full set of equations 8.12, 8.16 and 8.18 – 8.20 were used to determine  $\sigma$ ,  $\varepsilon^{(t)}$ ,  $\varepsilon^{(n)}$ ,  $\dot{\varepsilon}^{(t)}$  and  $\dot{\varepsilon}^{(n)}$ .  $\dot{\mathcal{P}}$  was determined by fitting a least squares polynomial of requisite order (usually fourth, fifth or sixth) to  $\mathcal{P}$  plotted as a function of  $\ln t$

$$\mathcal{P} = \sum_{i=0}^{n_p} a_i (\ln t)^i \quad (8.22)$$

so that on differentiating

$$\dot{\mathcal{P}} = \sum_{i=1}^{n_p} i a_i (\ln t)^{i-1} / t \quad (8.23)$$

where  $a_i$  are the polynomial coefficients and  $n_p$  is the order of the polynomial. Considerable effort was expended to ensure that the slope of the polynomial provided a true reflection of the data (figure 8.9). It was usually the case that this was only a problem at each end of the data range, and if necessary the data was fitted in two, or occasionally three, segments. Given the polynomial fit, the time for each data set was then used with equations 8.22 and 8.23 to determine  $\mathcal{P}$  and  $\dot{\mathcal{P}}$ , for insertion into the reduction equations.

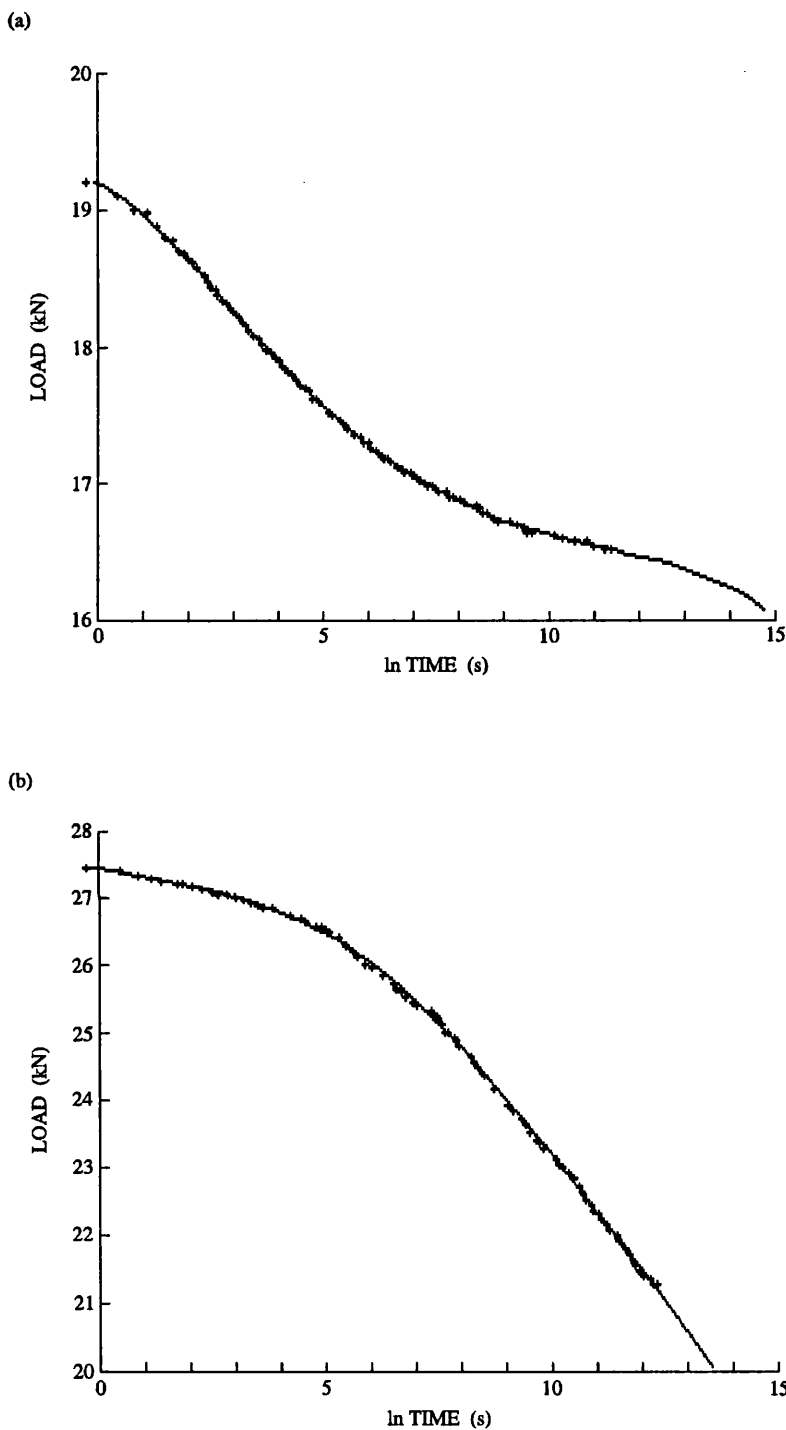


FIG. 8.9. Typical load / time data produced during the load relaxation experiments, together with the polynomial fits to the data. (a) Relaxation B produced at 121°C and yielding a concave upward relaxation curve (*cf.* figure 11.1). (b) Relaxation K produced at 360°C and yielding a concave downward relaxation curve (*cf.* figure 12.1).

## 9 AN EVALUATION OF THE FACTORS LIMITING DATA QUALITY

Two types of problem serve to undermine the quality of the data obtained from the experimental programme. Firstly there are the technical problems associated with the need to maintain confining pressure whilst keeping the confining medium out of the specimen. These have the following consequences :

- (a) they require that the deformation variables be determined remotely during the test and hence introduce calibration errors ;
- (b) they restrict the ability to change the deformation environment instantaneously and hence undermine the quality of the data obtained from the load relaxation and recovery experiments where it is necessary to change the crosshead displacement-rate and the temperature respectively, as quickly as possible, and ;
- (c) they introduce errors into the determination of the differential load experienced by the specimen because of the presence of a jacket around the specimen which supports some of the load.

All these problems are unavoidable, although their significance may be reduced by appropriate design or procedural improvements.

The second type of problems are associated with approximations made about the specimen deformation behaviour which become important, not during data collection, but during the data interpretation stage. These approximations are of two kinds :

- (a) those concerning material behaviour *i.e.* that cataclasis, mechanical twinning and impurities have an identifiable and separable effect on the data, and ;
- (b) those made for the convenience of data reduction and parameter fitting *i.e.* that the deformation is homogeneous, that any variability in confining pressure, temperature and strain-rate between tests under nominally the same condition with respect to those variables is insignificant, and that only one element of Hart's model is controlling the deformation under given conditions.

These problems are, in principle, avoidable, but if the approximations can be made, they simplify the data analysis considerably.

### 9.1 Calibration and data measurement errors

Extensive calibrations (each of six weeks duration) of both deformation apparatus were conducted prior to the experimental programme, and a further two shorter (four weeks) calibrations were conducted on NIMONIC2 following maintenance operations on the force gauge.

**9.1.1 HEARD1.** The calibration of HEARD1 was conducted in August / September 1988, following the reconstruction of the apparatus.

**9.1.1.1 Confining pressure :** The output of the pressure LVDT was calibrated against the apparatus bourdon tube pressure gauge at intervals of 1500 psi (10 MPa) in the range 0 to 60000 psi (0 - 414 MPa). The dependence was approximately linear but a least squares cubic polynomial was fitted giving a root mean square error of 137 psi (0.9 MPa). Most of this error

reflects friction acting on the transducer core.

**9.1.1.2 Temperature :** The calibration data for the specimen thermocouple was provided by the manufacturer at 5°C intervals in the range 0 to 1100°C. The data in the range 0 to 500°C was linearly regressed, presenting a root mean square error of 1.2°C. This error is smaller than that of the manufacturer's data which is quoted at  $\pm 3^\circ\text{C}$  for temperatures below 400°C.

The thermal profile along the specimen axis was investigated using a 0.25 inch (6.35 mm) diameter, 0.5318 inch (13.51 mm) long serpentinite specimen with a hole drilled through its axis. Steel spacers placed under the lower piston located the base of the serpentinite at a level corresponding to the middle of a specimen in the usual assembly. A thermocouple was inserted through the pore fluid inlet in the upper piston to the bottom of the specimen, and then at 10000 psi (69 MPa) confining pressure and at 91, 209, 304 and 397°C (as given by the normal specimen thermocouple), the thermocouple was withdrawn and the temperature difference between it and the specimen thermocouple noted at 1 or 2 mm intervals. The results suggested that at all temperatures, the temperature given by specimen thermocouple is approximately that which the base of a specimen in the normal assembly would experience, while the top of a specimen in the normal assembly would be upto 5°C cooler (the difference increasing to this figure as the test temperature is increased to 400°C). However, given the greater size of the specimen in the normal assembly (effectively replacing the spacers) and hence a corresponding decrease in axial thermal conduction, this thermal gradient must be an overestimate. Even in the worst case *i.e.* tests conducted at 400°C, the thermal gradient along the specimen axis is therefore less than the error in temperature measurement.

**9.1.1.3 Differential load :** The displacement of the unstressed rod used to measure the differential load, is affected by temperature and confining pressure, both because the stiffness of the force gauge column is affected by those variables, and because both variables add a component of force gauge deformation which is independent of the applied differential load.

The calibration of the force gauge at zero differential load (the FGZ calibration) was conducted by determining the output of the force transducer at 2500 psi (17 MPa) increments during depressurization in the range 5000 to 40000 psi (34 - 276 MPa), at each of five temperatures, room, 89, 208, 305 and 398°C. At each temperature the pressure dependence was described by a least squares fitted cubic polynomial. The temperature dependence was accommodated by fitting each of the cubic coefficients as a function of temperature in two linear segments. In this way the FGZ could be calculated at any temperature and pressure with a root mean square error of about 0.02 mV, where all readings are determined to the nearest 0.01 mV, in the range 0 to 20 mV.

The force gauge stiffness was determined using a previously calibrated load cell placed in the position of the thrust block (figure 8.2). The load cell was calibrated against a 10 tonf (99640 kN) proving ring placed in series in a hydraulic press and loaded / unloaded full range three times. Data collected at 0.5 tonf (4982 N) increments, was subsequently linearly regressed producing a fit with a root mean square error of 0.03 tonf (300 N). The force gauge stiffness was then determined at six equally spaced confining pressures in the range 10000 to 50000 psi (69 - 345 MPa) at room temperature, by loading from 0 to 2.5 tonf (0 - 24910 N). At each pressure at least five loadings were conducted, and for each loading the output of the force

transducer and the load cell was continuously recorded on an *x*-*y* chart recorder. Best linear fits were applied visually to the traces and the resulting stiffnesses linearly regressed as a function of pressure. The force gauge stiffness decreased with increasing confining pressure ; the root mean square error of the fit is 0.005 tonf / mV (50 N / mV) which is approximately 1.5% of the force gauge stiffness back extrapolated to room pressure. The force gauge stiffness was not calibrated directly as a function of temperature because the load cell could not be heated. Instead the observed FGZ dependence on temperature was used with the thermal linear expansion coefficient of tool steel, the active length of the force gauge (*i.e.* that part which deforms under differential load, figure 8.6) and the displacement calibration of the force LVDT, to calculate an effective temperature of the force gauge (*i.e.* that required to produce the same thermal expansion of the force gauge if there were no thermal profile along it) as a function of specimen temperature. This was then used with the Young's modulus of tool steel and its dependence on temperature, to correct the force gauge stiffness for temperature.

Given these calibrations the differential load is determined at any instant in an experiment by (a) noting the 'initial' force gauge (FGZ), temperature and pressure outputs immediately before load is applied to the specimen, (b) calculating the 'current' FGZ by using the 'current' temperature and pressure and applying a correction using the 'initial' temperature, pressure and FGZ readings and the FGZ calibration, (c) subtracting the 'current' FGZ from the force gauge output and, (d) by applying the force gauge stiffness as calculated from the 'current' temperature and pressure to the remainder. The effect of the errors in the force gauge calibration are illustrated in figure 9.1 using the stress / strain curve for a Carrara marble specimen of typical dimensions (for HEARD1) deformed at 279°C and  $2.5 \times 10^{-4} \text{ s}^{-1}$ .

The primary source of error in the FGZ calibration is the presence of friction acting on the transducer core. This is manifest in a small (0.01 mV) hysteresis in the forward and reverse sense movement values of the FGZ (*i.e.* the FGZ calibrated during pressurization rather than during depressurization) which affects the magnitude of the FGZ but not the slope of the pressure dependence. In principle such friction could mean that the specimen starts loading before the force gauge registers it, thereby leading to an observed differential load which is smaller than real. However, this effect is barely detectable even for an error on the FGZ value five times that of the calibration error (figure 9.1a).

The errors on the force gauge stiffness are more significant. The calibration procedure, comparing as it does the load experienced by the load cell on one side of the moving piston pressure seal with that experienced by the force gauge on the other, carries the implicit assumption that the frictional forces acting on the moving piston remain constant during loading. If they increase the calibrated stiffness will be an overestimate ; if they decrease the stiffness will be underestimated. The fact that when the upper pressure seal is over-tightened the upper piston progresses by stick-slip events at high temperatures, indicates that the frictional forces change in a complex manner during loading (Jaeger and Cook, 1979, pp. 63-65), as might be expected given that different parts of the piston come into contact with the sealing rings. The observed decrease in force gauge stiffness with increasing confining pressure runs counter to the increase in the Young's modulus of tool steel with that variable, and is at least an order of magnitude too big to be explained by changes in the dimensions of gauge as

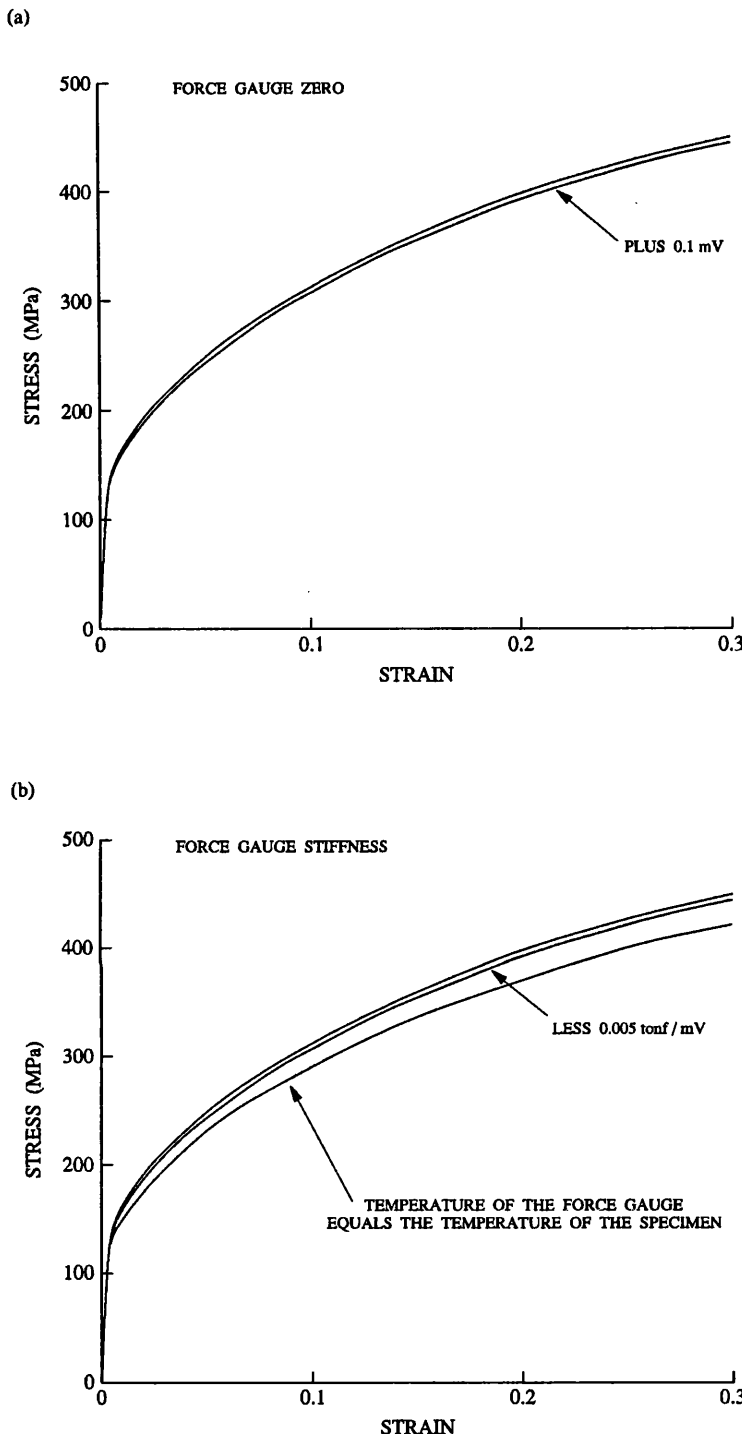


FIG. 9.1 The effect of the HEARD1 force gauge calibration errors on a Carrara marble stress / strain curve generated at 279°C and  $2.5 \times 10^{-4} \text{ s}^{-1}$ .

determined from the compressibility data of tool steel. This therefore suggests that as confining pressure is increased, the frictional forces tend in the direction of decreasing as loading progresses, thereby implying that the force gauge stiffness tends towards an underestimate with increasing confining pressure. It provides no indication of whether this corrects an already overestimated stiffness or worsens an already underestimated one.

The error of 0.005 tonf/mV in the calibration runs produces only a small error in the

differential load calculations (figure 9.1b). Of more importance are the temperature corrections to the force gauge stiffness. The calculations of the effective temperature of the force gauge derive from measurements of the differential expansion of the force gauge column and the unstressed rod, and hence must be an underestimate. At 400°C the effective temperature is 84°C, which expresses a thermal gradient from about 400°C at the top of the gauge to 20°C in the water cooled block, and this is an underestimate of perhaps about one half. The effect of treating the effective temperature as equal to the specimen temperature is to lower a differential stress of 400 MPa by about 30 MPa (figure 9.1b), and hence it may be expected that the indeterminacy of the force gauge stiffness temperature correction alone leads to an overestimate of the differential stress of upto 15 MPa.

The reloading constant displacement-rate experiments used for the evaluation of the parameters in the anelastic element provide some constraint on the force gauge stiffness problem, because provided the assumptions that cataclasis and mechanical twinning are negligible during reloading are valid, the slope of the elastic portion of the reloading stress / strain curves should be given by the Young's modulus of calcite. In fact it is observed that the slope almost always underestimates Young's modulus (table 10.1), suggesting that the force gauge stiffness is underestimated. The implication is that at all temperatures the differential loads are underestimated, but that with increasing temperature this error is reduced because of the underestimated temperature correction.

*9.1.1.4 Specimen displacement* : From equation 8.16 it is apparent that to determine the deformation of a specimen it is necessary to know the crosshead displacement and the component of apparatus deformation.

The crosshead displacement was calculated during the tests by multiplying the crosshead displacement-rate (always zero or constant in these experiments) by the duration of loading. The crosshead displacement-rate was calibrated by dividing the displacement achieved in several hours at low gear ratio (as given by the displacement dial gauge), by the time elapsed. The error is about  $\pm 2.5\%$ .

The output of the displacement LVDT was also calibrated against the displacement dial gauge reading for use in the calibration of apparatus deformation. This output was recorded at 0.0015 inch (0.04 mm) intervals over a range of 0.4 inch (10.16 mm), and the data linearly regressed to provide a fit with root mean square error of 0.0001 inch (0.00254 mm).

The component of apparatus deformation is given by the stiffness of the axial column which varies as a function of temperature and pressure. The apparatus stiffness was determined by sealing the two pistons together with a shortened copper jacket. An x-y chart recorder was used to continuously record the output of the displacement and force transducers during loading from 0 to 2.5 tonf (0 - 24910 N) at 10000, 20000, 30000, and 40000 psi (69, 138, 207, 276 MPa) confining pressure at each of room, 100, 237 and 377°C. At each temperature / pressure condition at least three loadings were conducted. A best linear fit was determined visually for each loading trace and the results converted into apparatus stiffness using the force gauge stiffness and displacement transducer calibrations. At each temperature the pressure dependency of the apparatus stiffness was linearly regressed, and the temperature dependency was accommodated by fitting the two regression coefficients as a function of temperature. In

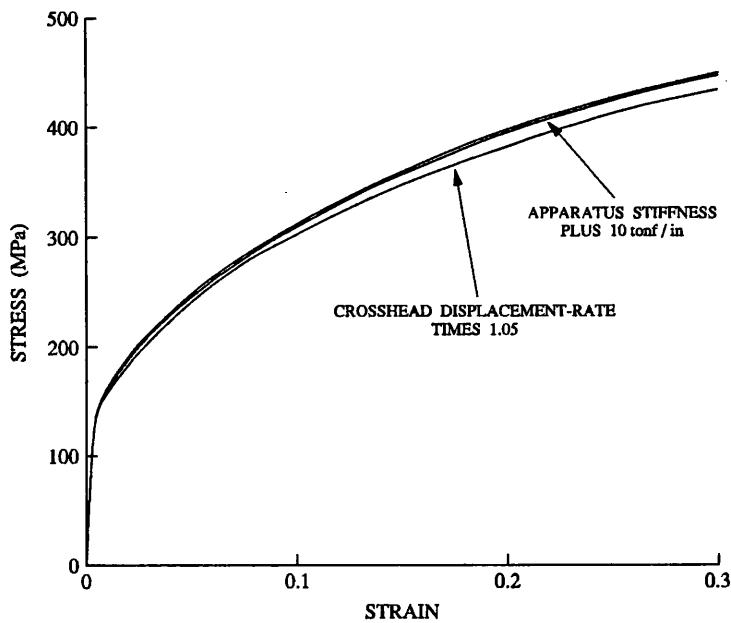


FIG. 9.2. The effect of the HEARD1 apparatus stiffness and crosshead displacement-rate calibration errors on a Carrara marble stress / strain curve generated at 279°C and  $2.5 \times 10^{-4} \text{ s}^{-1}$ .

this way the apparatus stiffness could be determined at any temperature and pressure to within 3 tonf / in ( $1.18 \times 10^6 \text{ N/m}$ ), which is about 2% of the back extrapolated room temperature and pressure value.

In figure 9.2 it may be seen that the error in the determination of apparatus stiffness has negligible effect on the experimental stress / strain curves, but that the error on the displacement-rate becomes significant at strains of greater than 0.1. At strains of 0.2 the error in the specimen strain due to the uncertainty in the displacement-rate is 0.015. The magnitude of the apparent differential stress error this uncertainty produces is determined by its effect on the cross sectional area calculation (equation 8.12) which is small, and by the slope of the stress / strain curve.

**9.1.2 NIMONIC2.** The following discussion refers to the most recent calibration (June 1991), although the procedures and errors in the two previous calibrations were similar.

**9.1.2.1 Confining pressure :** The output of the pressure transducer was calibrated against the apparatus bourdon tube pressure gauge at intervals of 500 psi (3.5 MPa) in the range 0 to 40000 psi (0 - 276 MPa). The data was linearly regressed giving a root mean square error of 125 psi (0.9 MPa).

**9.1.2.2 Temperature :** The calibration data for the specimen thermocouple, provided by the manufacturer at 5°C intervals in the range 0 to 1100°C, was fit by least squares to a cubic polynomial. The root mean square error is 0.8°C which is smaller than the error in the calibration data, quoted at  $\pm 3^\circ\text{C}$  for temperatures below 400°C and  $\pm 0.75\%$  at higher temperatures.

The thermal profile along the specimen axis was determined by R. Maddocks in January 1984 and was not repeated. He followed the same procedure as described for HEARD1 (except

that it was the specimen thermocouple that was retracted), using a 0.25 inch (6.35 mm) diameter, 0.5700 inch (14.48 mm) long specimen (which is of similar dimensions to the specimens used in this study). Thermal profiles were determined at 10000 psi (69 MPa) confining pressure at 338, 461, 592 and 735°C. At each temperature the hottest point was at the base of the specimen with the difference in temperature between the top and bottom of the specimen increasing from 1 to 5°C as the temperature was increased. This difference is smaller than the error in the thermocouple calibration data.

**9.1.2.3 Differential load :** The NIMONIC2 force gauge is affected by temperature and confining pressure in the same manner as that of HEARD1, and consequently again FGZ and force gauge stiffness calibrations are required.

The FGZ calibration was conducted by determining the output of the force transducer at 500 psi (3.5 MPa) increments during two pressurization / depressurizations in the range 5000 to 40000 psi (34 - 276 MPa), at each of eight temperatures equally spaced in the range room to 700°C. At each temperature the pressure dependence was linearly regressed and the temperature dependence accommodated by fitting the two regression coefficients as a function of temperature. In this way the FGZ could be calculated at any temperature and pressure with a root mean square error of about 0.035 mV, where all readings are determined to the nearest 0.01 mV, in the range -1 to 6 mV. This error reflects primarily the hysteresis between the pressurization and depressurization data, which nevertheless have an indistinguishable pressure dependence.

The force gauge stiffness was determined using the arrangement shown in figure 9.3 which, by locating the reference load cell in a cool position, allows the temperature as well as the pressure dependence of the force gauge stiffness to be determined directly. The load cell employed for the HEARD1 calibrations was used, but after recalibration in the range 0 to 7 tonf (0 - 69748 N) against an externally calibrated (according to National Physics Laboratory standards) Instron loading device. The root mean square error of the linear fit to the load / mV data remains 0.03 tonf (300 N). The force gauge stiffness was determined at six equally spaced confining pressures in the range 5000 to 30000 psi (34 - 207 MPa) at each of eight temperatures equally spaced in the range room to 700°C. At each pressure / temperature condition two or three loadings from 0 to 3 tonf (0 - 29892 N) were conducted and the load cell and force gauge outputs continuously recorded on a *y-t* chart recorder. Best linear fits were applied visually to the traces and these were converted into stiffnesses. The stiffnesses were then multiply regressed on temperature and pressure, treating the data from temperatures below 350°C separately from that above. The root mean square error of the fits is approximately 0.0015 tonf / mV (15 N/mV) which is 0.8% of the calculated stiffness at room temperature and pressure.

The differential load during an experiment is determined with these calibrations in the same way as for HEARD1. The effect of the errors in the force gauge calibration are illustrated in figure 9.4 using the stress / strain curve for a Carrara marble specimen of typical dimensions (for NIMONIC2) deformed at 417°C and  $3.4 \times 10^{-4} \text{ s}^{-1}$ .

As for HEARD1 the error in the FGZ calibration has a negligible effect on the calculated stress / strain curves (figure 9.4a). However, it is frequently observed that after large movements of the loading piston especially when accompanied by large temperature changes

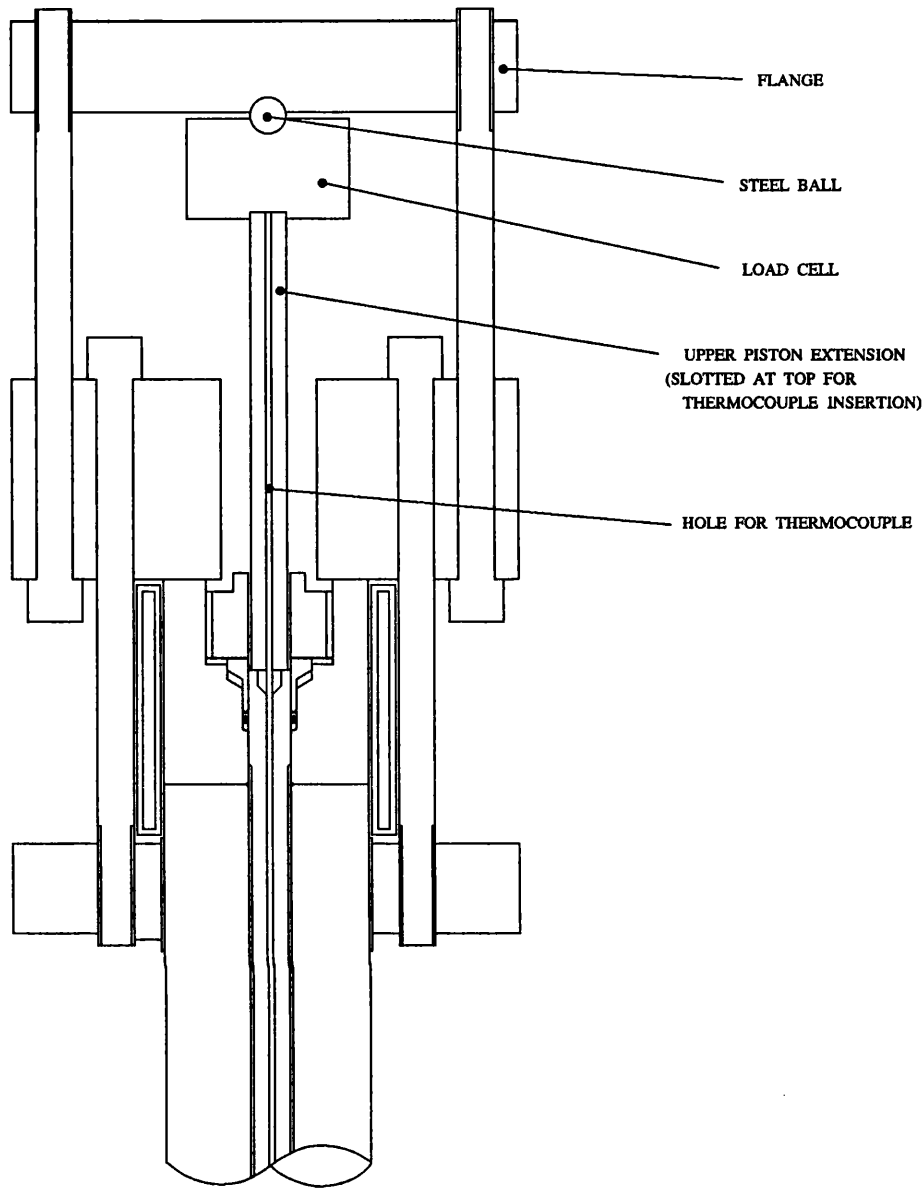


FIG. 9.3. The NIMONIC2 upper closure assembly used for the calibration of the force gauge stiffness (cf. figure 8.4).

(i.e. between experiments), there are differences of upto 0.5 mV in the value of the FGZ under the same pressure / temperature conditions (this effect was circumvented in the calibrations by not moving the piston until all the FGZ calibrations had been completed). 0.6 mV represents a transducer core displacement of just 0.00012 inch (3.05  $\mu$ m) which may be the result of oxide particles opening a gap between the transducer body and the T-section tube or, more probably, at the top of the T-section tube where it is pressed against the interior of the force gauge column. If so, and if during loading the gap is closed (a change of  $\pm 0.3$  mV in the force gauge output would not be noticed in the initial stages of loading), the effect would be an error in the initial FGZ which at 0.6 mV corresponds to about 20 MPa differential stress for the NIMONIC2 experiments in this study. A reproducibility error of this magnitude is observed

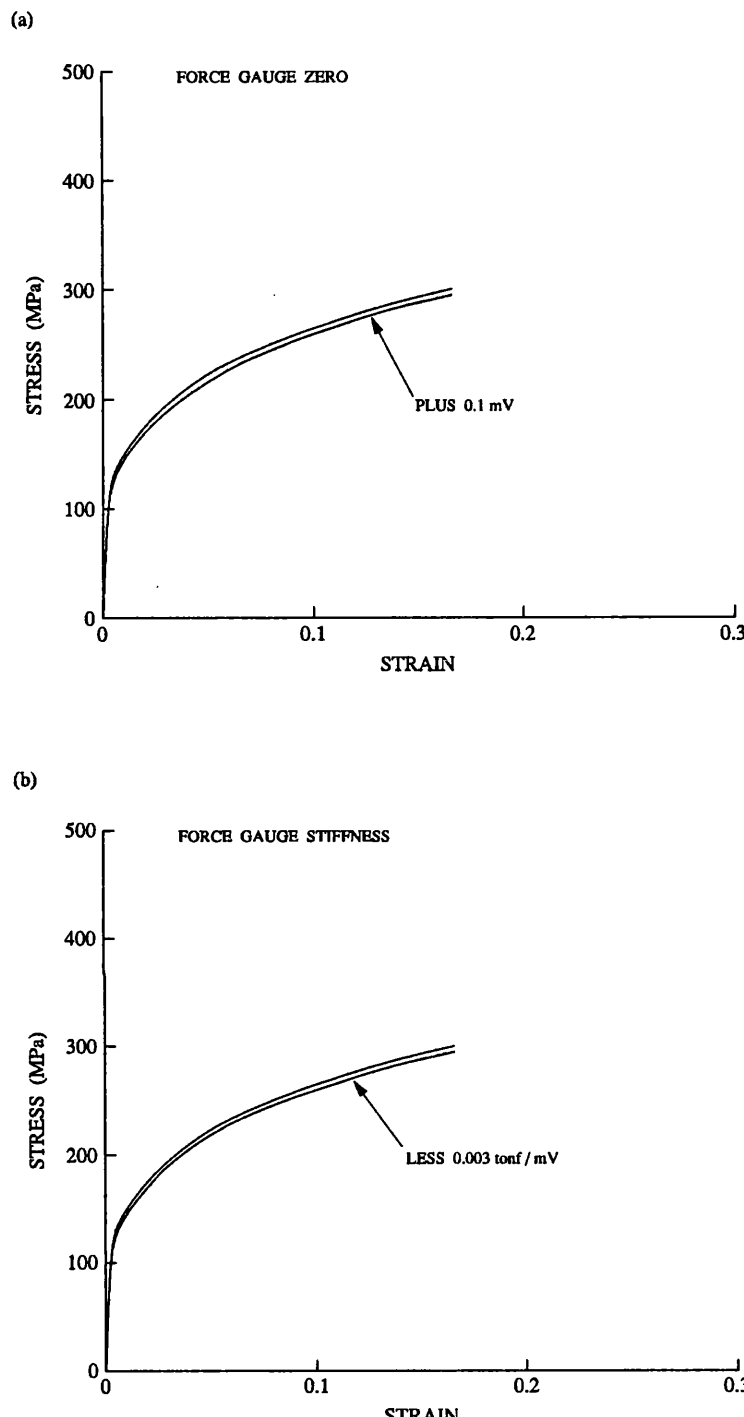


FIG. 9.4. The effect of the NIMONIC2 force gauge calibration errors on a Carrara marble stress / strain curve generated at 417°C and  $3.4 \times 10^{-4} \text{ s}^{-1}$ .

(figure 9.6).

The error in the force gauge stiffness calibration has a negligible effect on the observed stress / strain curves (figure 9.4b). However, as for HEARD1 the calibration procedure carries the implicit assumption that during loading the rate of change of differential load experienced by the load cell is the same as that experienced by the force gauge *i.e.* in this case that the frictional forces acting between the O-ring and the upper piston remain constant during loading.

The lower frictional forces and smaller (only elastic) displacement through the seal, suggests that this assumption is less significant for NIMONIC2, but again the magnitude of the problem is difficult to evaluate precisely.

**9.1.2.4 Specimen displacement :** The output of displacement LVDT and the displacement dial gauge reading were recorded at 0.01 inch (0.254 mm) intervals over a range of 0.5 inch (12.7 mm), and the data linearly regressed to provide a displacement transducer calibration with root mean square error of 0.002 inch (0.05 mm).

The apparatus stiffness was determined with a tungsten carbide dummy in place of the specimen at six equally spaced confining pressures in the range 5000 to 30000 psi (34 - 207 MPa) at each of eight temperatures equally spaced in the range room to 700°C. At each pressure / temperature condition two or three loadings from 0 to 3 tonf (0 - 29892 N) were conducted and the displacement LVDT and force gauge outputs continuously recorded on a y-t chart recorder. Best linear fits were applied visually to the traces and these were converted into stiffnesses using the displacement transducer and force gauge stiffness calibrations after subtracting the elastic deformation of the tungsten carbide dummy. The stiffnesses were then multiply regressed on  $T^2$ ,  $T$  and  $p$ , where  $T$  is the temperature and  $p$  the confining pressure. The root mean square error of the fits is approximately 0.6 tonf / in ( $2.35 \times 10^5$  N / m) which is 0.8% of the calculated stiffness at room temperature and pressure.

The crosshead displacement-rate was determined as the average of the displacement-rates calculated, from the time elapsed and the amount of displacement achieved, in each loading used for the apparatus stiffness calibration. The error is about  $\pm 2.5\%$ .

The error in the determination of apparatus stiffness has negligible effect on the experimental stress / strain curves while the error on the displacement-rate, being the same magnitude as that of HEARD1, has the same effect on the stress / strain curves (figure 9.5).

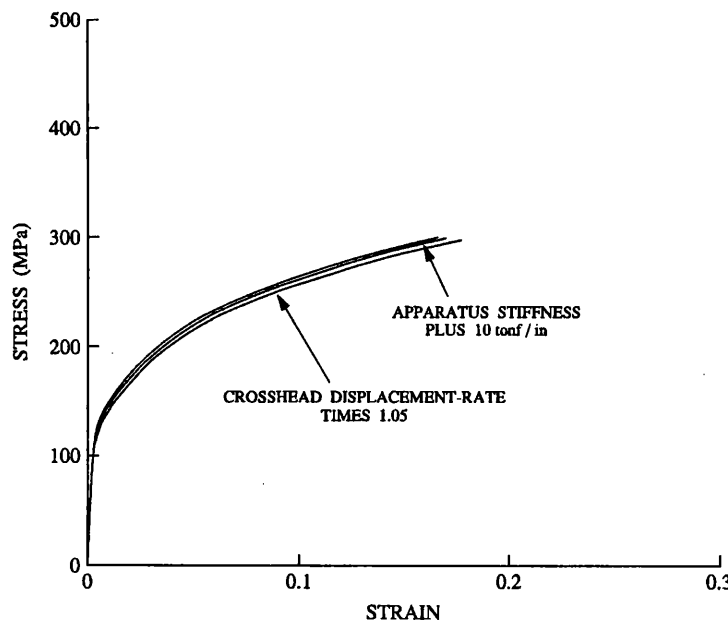


FIG. 9.5. The effect of the NIMONIC2 apparatus stiffness and crosshead displacement-rate calibration errors on a Carrara marble stress / strain curve generated at 417°C and  $3.4 \times 10^{-4} \text{ s}^{-1}$ .

**9.1.3 Summary of the data measurement problems.** The data measurement problems described above have various degrees of significance for the determination of the deformation variables.

**9.1.3.1 Confining pressure :** On both apparatus the error on the confining pressure measurement is less than  $\pm 1$  MPa.

**9.1.3.2 Temperature :** For temperatures below  $400^{\circ}\text{C}$  the error on the temperature measurement is  $\pm 3^{\circ}\text{C}$ , while at higher temperatures it rises to about  $\pm 5^{\circ}\text{C}$  at  $700^{\circ}\text{C}$ . These errors reflect the small thermal profile that exists along the specimen axis and errors in the thermocouple calibration data.

**9.1.3.3 Strain :** For both apparatus, the error in the specimen strain increases from 0 to  $\pm 0.01$  at a strain of 0.3 due primarily to the uncertainty in the crosshead displacement-rate. This is reflected in an error of  $\pm 2.5\%$  on the strain-rates as calculated from equation 8.21 at a strain of 0.1.

**9.1.3.4 Differential stress :** On HEARD1 the differential stress is underestimated by an amount which decreases with increasing temperature. This is due to the uncertainty in the force gauge stiffness calibration and although it is difficult to evaluate, it is considered to be of the order of 10 - 20 MPa. On NIMONIC2 the unpredictable variability of the FGZ produces an error of upto  $\pm 10$  MPa on the differential stress determined in different tests. The error on the NIMONIC2 force gauge stiffness calibration is believed to be small.

In principle, a comparison of the stress / strain curves generated under identical conditions on HEARD1 and NIMONIC2 offers some constraint on the differential load calibration problems because the seal friction effects are very different for each apparatus. In figure 9.6, a

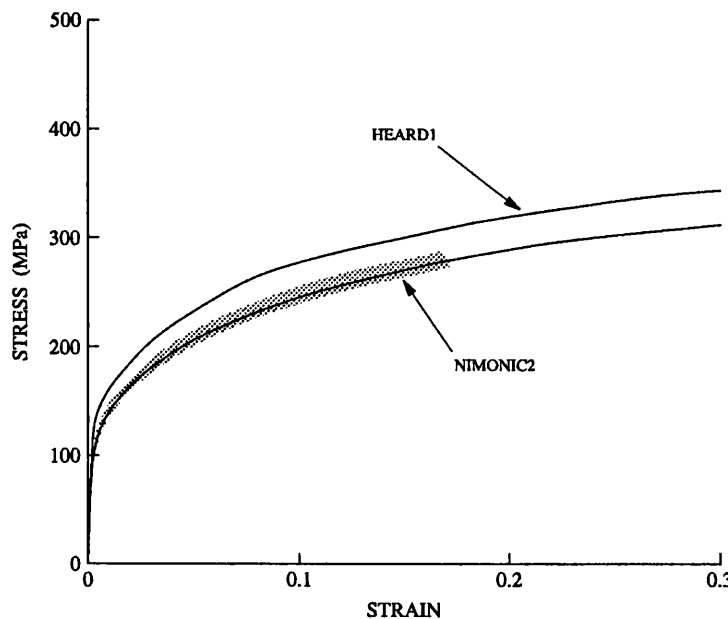


FIG. 9.6. Comparison of the stress / strain curves of two Carrara marble specimens deformed under nominally the same conditions, one in HEARD1 and the other in NIMONIC2. Both curves are corrected for the load supported by the copper jacket. The shaded area indicates the reproducibility band of the NIMONIC2 experiments that were conducted to a total strain of 0.17.

curve generated at  $2.6 \times 10^{-4} \text{ s}^{-1}$ , 418°C and 206 MPa on HEARD1 is compared with a NIMONIC2 curve produced at  $3.4 \times 10^{-4} \text{ s}^{-1}$ , 417°C and 174 MPa (and lying near the middle of the  $\pm 10$  MPa range produced by the FGZ variability). The curves have been corrected for the differential load supported by the copper jacket, which is easily done for a constant displacement-rate test (§ 9.3.2.2) and which is necessary in this instance because of the different specimen diameters (and hence different cross section areal fraction of copper). Beyond a strain of 0.01 the NIMONIC2 curve is about 25 MPa weaker, a difference which if the statements made above concerning the force gauge stiffness calibrations are accurate, must be in reality even larger. The differences in the strain-rates and confining pressures are too small to account for this discrepancy, and hence the source of the problem is not understood. However, it is observed that under the smaller loads experienced by the NIMONIC2 specimen (the specimen is smaller), 25 MPa corresponds to a force gauge transducer core displacement of the order of only 3.5  $\mu\text{m}$ , and hence may simply reflect a force gauge design limitation.

## 9.2 Problems caused by instantaneous changes in the deformation variables

The apparatus design poses significant limitations on the ability to change the deformation variables instantaneously during a test. For the experiments undertaken here, this affects on HEARD1, the load relaxation test where it is necessary to change instantly the displacement-rate to zero, and on NIMONIC2, the interrupted constant displacement-rate tests where the temperature must be changed as quickly as possible.

**9.2.1 The load relaxation test.** To commence a load relaxation test after a period of loading, the motor driving the crosshead is stopped. However, the inertia of the loading train is such that the loading piston continues to move (for upto two seconds at the highest displacement-rates) until overcome by the frictional forces in the moving piston seal. This has two consequences for the quality of data obtained from the relaxation. First, it makes it difficult to define the start of the relaxation. However, this problem becomes insignificant after a few seconds because the interesting features of a relaxation occur over a logarithmic timescale.

The second consequence derives from the load differential which, by the manner in which the piston comes to rest, is inevitably set up between either side of the moving piston seal. If sufficiently large this load differential is re-equilibrated during the relaxation, thereby reloading the specimen and introducing anelastic effects into relaxation curves which, in this experimental programme, are used to determine purely plastic properties.

The task of correcting relaxation curves for anelastic effects introduced by load re-equilibration is sufficiently formidable for it to have been decided to abandon any experiment in which it was detected. The problem posed by such load changes then reduces to one of detection. Load re-equilibration may occur either by a stick-slip event which instantaneously reloads the specimen or by a gradual 'creep-through', both recognizable on the load / time curve by small rises in load during the relaxation (figure 9.7). Detection difficulties arise when 'creep-through' type re-equilibration is too slow relative to the rate of relaxation for the total load to rise. To circumvent this detection problem as far as possible, the first relaxation of a suite was always conducted at low strain (0.015) and for a long time (several days). In such circumstances the rate of relaxation rapidly becomes very small. A further check is afforded by

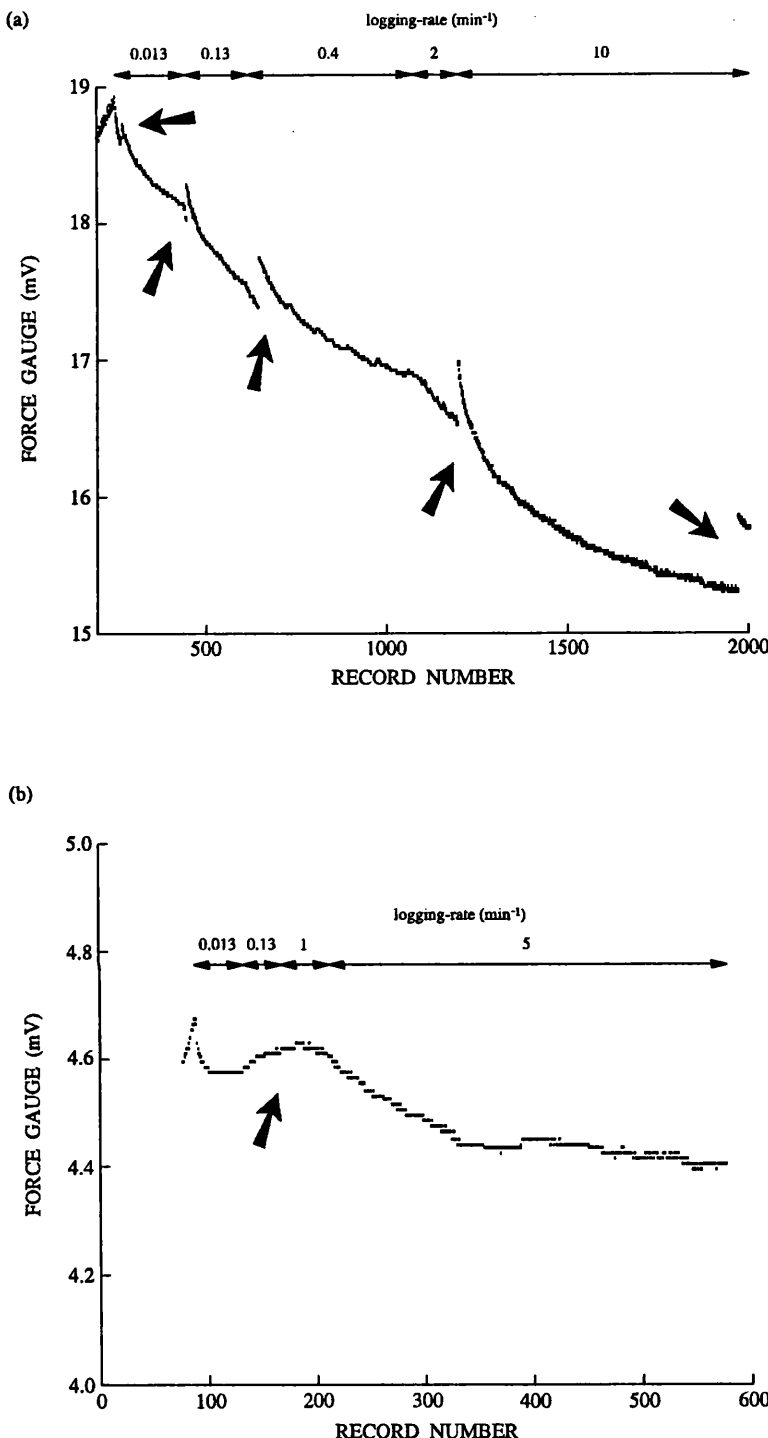


FIG. 9.7. The effect on the load / time data of a re-equilibration of the load differential set up on either side of the HEARD1 moving piston seal prior to / at the onset of a load relaxation test. (a) Stick-slip type behaviour. (b) 'Creep-through' type behaviour.

the fact that 'creep-through' if present should vary with temperature and between tests (since the occurrence of load re-equilibration reflects factors influencing seal friction *i.e.* it varies with temperature, with the condition of the sealing rings and with the tightness of the seal), and consequently will affect the ability to describe the relaxation curves generated at different temperatures and on different samples as members of a single family. Hence if such a family is

found then it can be inferred that 'creep-through' was negligible (although the failure to find such a family does not mean necessarily that 'creep-through' occurred). All the relaxations conducted in this programme were closely inspected for indications of 'creep-through' and if it was suspected then the relaxations from that specimen were discarded.

**9.2.2 The interrupted constant displacement-rate tests.** The use of interrupted constant displacement-rate tests to determine the change in mechanical state during a given anneal period, provides data which must be treated (in the first instance at least) as if the heating / cooling periods at either end of the anneal are instantaneous (*i.e.* as if no recovery occurred during them). However, the use of an externally heated pressure vessel of large thermal mass constrains the rate of temperature change that can be applied. The presence of a finite heating / cooling time requires an arbitrary definition of the start and end of the anneal period and therefore introduces an error into the measured duration of annealing. Moreover, it restricts the minimum anneal period that can be investigated. The presence of a large thermal mass also means that there is inevitably a temperature overshoot during heating if the temperature is increased rapidly.

To minimize these problems, the cold-working in the experiments reported here was conducted at a temperature which was as high as possible without the deformation being influenced by the recovery processes under investigation. Figure 9.8 shows a typical thermal history of a specimen from the end of initial loading to the start of reloading. Heating / cooling times were upto 40 minutes (depending on the anneal temperature) with a further 30 minutes required for complete thermal equilibrium. Temperature overshoots of about 15°C during heating were usual. The anneal period was defined from the moment the anneal temperature was attained (before equilibrium) until the moment cooling was initiated. For all tests longer than 3 hours the error in anneal duration is negligible given that the interesting changes are

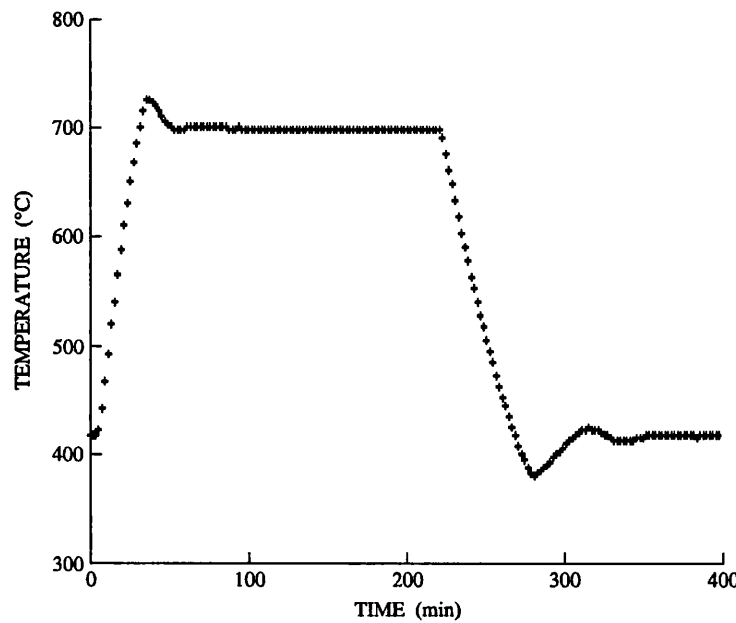


FIG. 9.8. The typical thermal history of a specimen during the anneal period of an interrupted constant displacement-rate test conducted on NIMONIC2.

measured over a logarithmic timescale. The shortest duration anneal investigated given the aforementioned difficulties was 3 hours. This minimum period poses a highly significant constraint for it accounts for the first four of the seven orders of magnitude of anneal time investigated.

Although the heating / cooling rates in the recovery experiments were constrained by the design of the apparatus, the large thermal expansion anisotropy of calcite also constrains the rate of temperature change that can be applied. At the fastest cooling rates in this study (7°C/min) this is just sufficient to cause a minor amount of mechanical twinning, and hence if twinning influences the mechanical state of the calcite, then still faster temperature change rates would have introduced errors into the calculations of the change of  $\sigma^*$  with anneal duration.

### 9.3 Problems caused by the copper jacket

The data reduction procedures employed in the experimental programme (§ 8.4) make no correction for that part of the total differential load supported by the specimen jacket, and therefore overestimate the differential load experienced by the specimen. No attempt was made to accommodate this error because although the jacket correction for a constant displacement-rate test is simple to determine and apply, this is not the case for a load relaxation test.

**9.3.1 Formulation of the problem.** The jacket sealing arrangement employed in these experiments is shown in figure 9.9a. To apply a jacket correction it is necessary to replace the single branch analogue model of the deformation of the specimen assembly (figure 8.8), with the two branch model of figure 9.9b. The identity of the elements of this analogue remains the same as before, but one branch represents the elastic / inelastic deformation of the specimen while the other represents the elastic / inelastic deformation of the jacket.

Using the same definitions as previously but with the subscripts *spec* and *jack* to refer to the specimen and jacket elements respectively, and observing that the axial shortening of the jacket equals that of the specimen, then in response to the displacement of the crosshead there is a total shortening of the assembly given by

$$\begin{aligned}\Delta\mathcal{L} &= (\Delta\mathcal{L})_{spec} \\ &= (\Delta L_e)_{spec} + (\Delta L_p)_{spec}\end{aligned}\quad (9.1a)$$

$$\begin{aligned}&= (\Delta\mathcal{L})_{jack} \\ &= (\Delta L_e)_{jack} + (\Delta L_p)_{jack}\end{aligned}\quad (9.1b)$$

so that

$$\begin{aligned}\mathcal{L} &= L_0 - (\Delta\mathcal{L})_{spec} \\ &= L_0 - (\Delta L_e)_{spec} - (\Delta L_p)_{spec}\end{aligned}\quad (9.2a)$$

$$\begin{aligned}&= L_0 - (\Delta\mathcal{L})_{jack} \\ &= L_0 - (\Delta L_e)_{jack} - (\Delta L_p)_{jack}\end{aligned}\quad (9.2b)$$

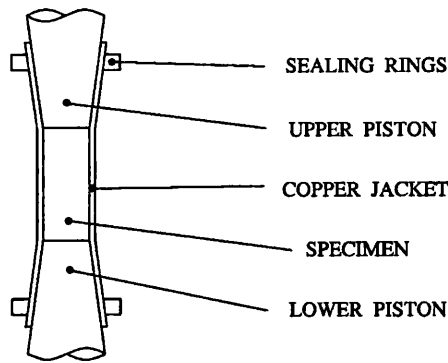
and also

$$\begin{aligned}(L)_{spec} &= L_0 - (\Delta L_p)_{spec} \\ &= \mathcal{L} + (\Delta L_e)_{spec}\end{aligned}\quad (9.3a)$$

$$\begin{aligned}(L)_{jack} &= L_0 - (\Delta L_p)_{jack} \\ &= \mathcal{L} + (\Delta L_e)_{jack}\end{aligned}\quad (9.3b)$$

In response to a total differential load  $\mathcal{P}$  the deformation of the specimen assembly is specified

(a)



(b)

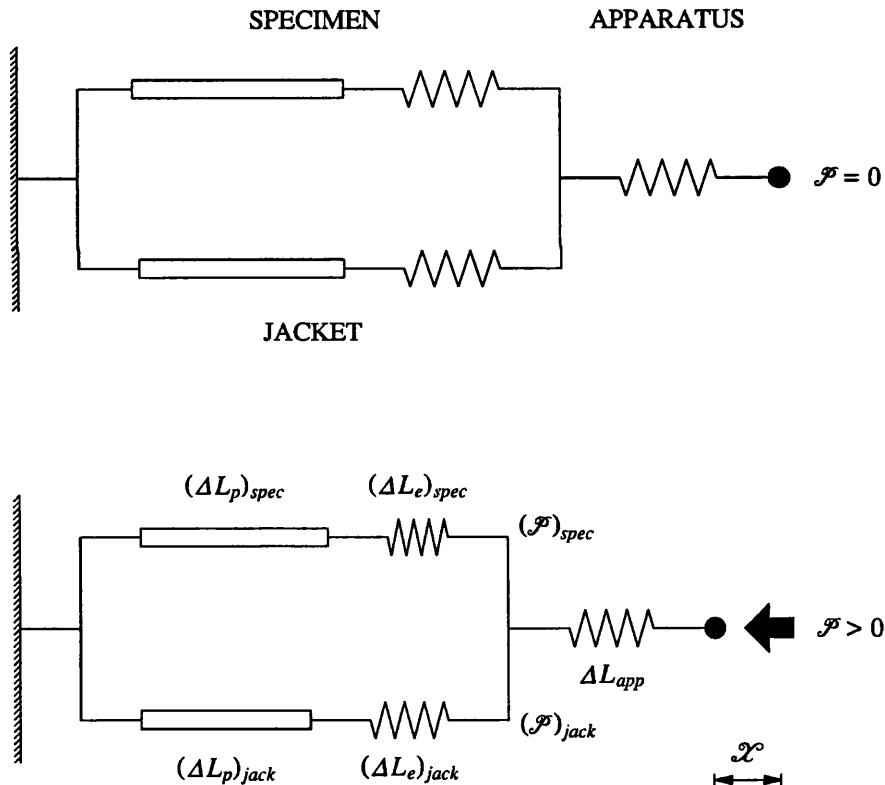


FIG. 9.9. Correcting for the load supported by the copper jacket. (a) The specimen assembly in both the HEARD1 and NIMONIC2 experiments. (b) An analogue model representing the deformation of the apparatus axial column during a deformation experiment and which distinguishes the differential load supported by the jacket from that supported by the specimen (cf. figure 8.8).

by the four equations

$$\mathcal{P} = (\mathcal{P})_{spec} + (\mathcal{P})_{jack} \quad (9.4a)$$

$$\mathcal{X} = \Delta \mathcal{L} + \Delta L_{app} \quad (9.4b)$$

$$= (\Delta L_e)_{spec} + (\Delta L_p)_{spec} + \Delta L_{app} \quad (9.4c)$$

$$= (\Delta L_e)_{jack} + (\Delta L_p)_{jack} + \Delta L_{app} \quad (9.4d)$$

which may be solved completely from equations 9.1 - 9.3 if any four of  $(\Delta L_e)_{spec}$ ,  $(\Delta L_p)_{spec}$ ,  $(\Delta L_e)_{jack}$ ,  $(\Delta L_p)_{jack}$  and  $\Delta L_{app}$  are determinable. In practice,  $\Delta L_{app}$  is given from the apparatus stiffness calibration by equation 8.13, and  $(\Delta L_e)_{spec}$  and  $(\Delta L_e)_{jack}$  are given by

$$(\Delta L_e)_{spec} = (\mathcal{P})_{spec} \mathcal{L} (L)_{spec} / (A_0)_{spec} L_0 (E)_{spec} \quad (9.5a)$$

$$(\Delta L_e)_{jack} = (\mathcal{P})_{jack} \mathcal{L} (L)_{jack} / (A_0)_{jack} L_0 (E)_{jack} \quad (9.5b)$$

(cf. equation 8.15). Using equations 8.13 and 9.5, then equations 9.4 become (cf. equation 8.18)

$$\mathcal{P} = (\mathcal{P})_{spec} + (\mathcal{P})_{jack} \quad (9.6a)$$

$$(L)_{spec} = \mathcal{L} / \{ 1 - [(\mathcal{P})_{spec} \mathcal{L} / (A_0)_{spec} L_0 (E)_{spec}] \} \quad (9.6b)$$

$$(L)_{jack} = \mathcal{L} / \{ 1 - [(\mathcal{P})_{jack} \mathcal{L} / (A_0)_{jack} L_0 (E)_{jack}] \} \quad (9.6c)$$

which contains the four unknowns  $(\mathcal{P})_{spec}$ ,  $(\mathcal{P})_{jack}$ ,  $(L)_{spec}$ ,  $(L)_{jack}$ . Hence the jacket correction problem reduces to one of determining  $(L)_{jack}$  or  $(\mathcal{P})_{jack}$  during the experiment.

**9.3.2 Special case solutions.** Two special cases exist where the jacket correction is readily determinable.

**9.3.2.1 Purely elastic deformation :** For purely elastic deformation

$$(\Delta L_p)_{spec} = (\Delta L_p)_{jack} = 0 \quad (9.7)$$

so that from equations 9.2

$$(L)_{spec} = (L)_{jack} = \mathcal{L} \quad (9.8)$$

Using this result to equate equations 9.6b and 9.6c, substituting 9.6a and rearranging, then

$$(\mathcal{P})_{spec} = \mathcal{P} / \{ 1 + [(A_0)_{jack} (E)_{jack}] / [(A_0)_{spec} (E)_{spec}] \} \quad (9.9)$$

which is the result given by Murrell and Chakravarty (1973).

**9.3.2.2 Constant displacement-rate test :** During a constant displacement-rate test the jacket and specimen deform independently (although at the same rate). By replacing the specimen with a dummy made of the jacket material, the data reduction equations derived in § 8.4 may be used to determine the stress supported by the jacket as a function of strain at the temperatures, confining pressures and strain-rates of interest. Then in a normal test the stress supported by the jacket can be determined at any instant from the jacket strain (as given from equation 9.4b), and this in turn can be converted into  $(\mathcal{P})_{jack}$  by using the constant volume deformation assumption. Data reduction can then proceed as outlined in § 8.4 but with  $(\mathcal{P})_{spec}$  (determined from equation 9.6a) in place of  $\mathcal{P}$ .

**9.3.3 The errors arising from neglecting a jacket correction.** The possibility of making an empirical correction for the load supported by the jacket in a constant displacement-rate test derives from the fact that the jacket and specimen deform independently. However, during a load relaxation test this is not the case because although once more the total length of each (i.e.  $\mathcal{L}$ ) remains equal, in this instance that length is controlled by the relaxation behaviour of whichever of the two supports the greater load (this determines the apparatus deformation) and not by external bounds on the deformation (i.e. the position of the crosshead). Given this constraint the deformation of jacket and specimen proceeds as illustrated in the analogue model

of the deformation system (figure 9.9b) where it may be seen that although the total length of each branch is the same, the partitioning of the deformation between the elastic and inelastic elements within each branch can change. In such circumstances, and for all subsequent reloads (the reload jacket stress / strain curve cannot be expected to retrace the uninterrupted one), the jacket correction can only be determined if a deformation history independent set of constitutive equations for the inelastic deformation of the jacket material is known. These can then be integrated using the boundary condition  $\mathcal{L}$  (supplied by equation 9.4b) and the elastic behaviour of the jacket (equation 9.5b) to determine  $(\mathcal{P})_{jack}$  at any instant. In this study this requires that the whole experimental programme be first conducted on commercial purity copper dummies.

**9.3.3.1 The deformation behaviour of commercial purity copper :** A substantial number of experiments (23 constant displacement-rate tests and approximately 200 load relaxations ranging in duration from a few minutes to several days) were conducted at the beginning of the experimental programme to characterize the deformation behaviour of commercial purity copper. Dummies of the same dimensions as the HEARD1 specimens (§ 8.3.1.2) were manufactured from commercial purity copper rod obtained from three different sources (referred to as IMPERIAL1, IMPERIAL2 and MANCHESTER1). The same preparation procedure as used for the jackets was followed, and the deformation experiments were conducted on HEARD1 under the same conditions as those for the Carrara marble experiments on that apparatus.

Figures 9.10a and 9.10b show some of the stress / strain curves produced at 200 MPa confining pressure and at the same displacement-rate but various temperatures, and at the same temperature but various displacement-rates, respectively. The solid curves on each figure were generated by IMPERIAL2 dummies and are reproducible to within  $\pm 5$  MPa on repeat runs. The dashed curves were produced by the MANCHESTER1 dummies and are consistently about 15 MPa (*i.e.* approximately 10%) weaker under identical conditions than those of IMPERIAL2. This difference is interpreted to be due to the different impurity content of copper from the different sources but this has not been confirmed.

The reloading stress / strain curves generated after load relaxation experiments indicate that in the IMPERIAL2 dummies the mechanical state of the copper is influenced by recovery during relaxation at all temperatures greater than about 320°C. At lower temperatures the relaxation curves are either poorly reproducible or are difficult to fit to the Hart's model. This may reflect the influence of the impurities on the relaxation behaviour but was not systematically investigated. At 310°C and a strain-rate of  $10^{-5} \text{ s}^{-1}$ , some of the MANCHESTER1 dummies have oscillating stress / strain curves. This is diagnostic of dynamic recrystallization and indicates that in these dummies recovery of the mechanical state begins at lower temperatures than in those from the IMPERIAL2 source.

**9.3.3.2 Assessment of the copper jacket effect :** The aim of determining a set of deformation history dependent equations for commercial purity copper was abandoned when the variability of mechanical properties with the source of the copper dummies was discovered, and when it became apparent that a full recovery function for temperatures greater than about 300°C would have to be determined.

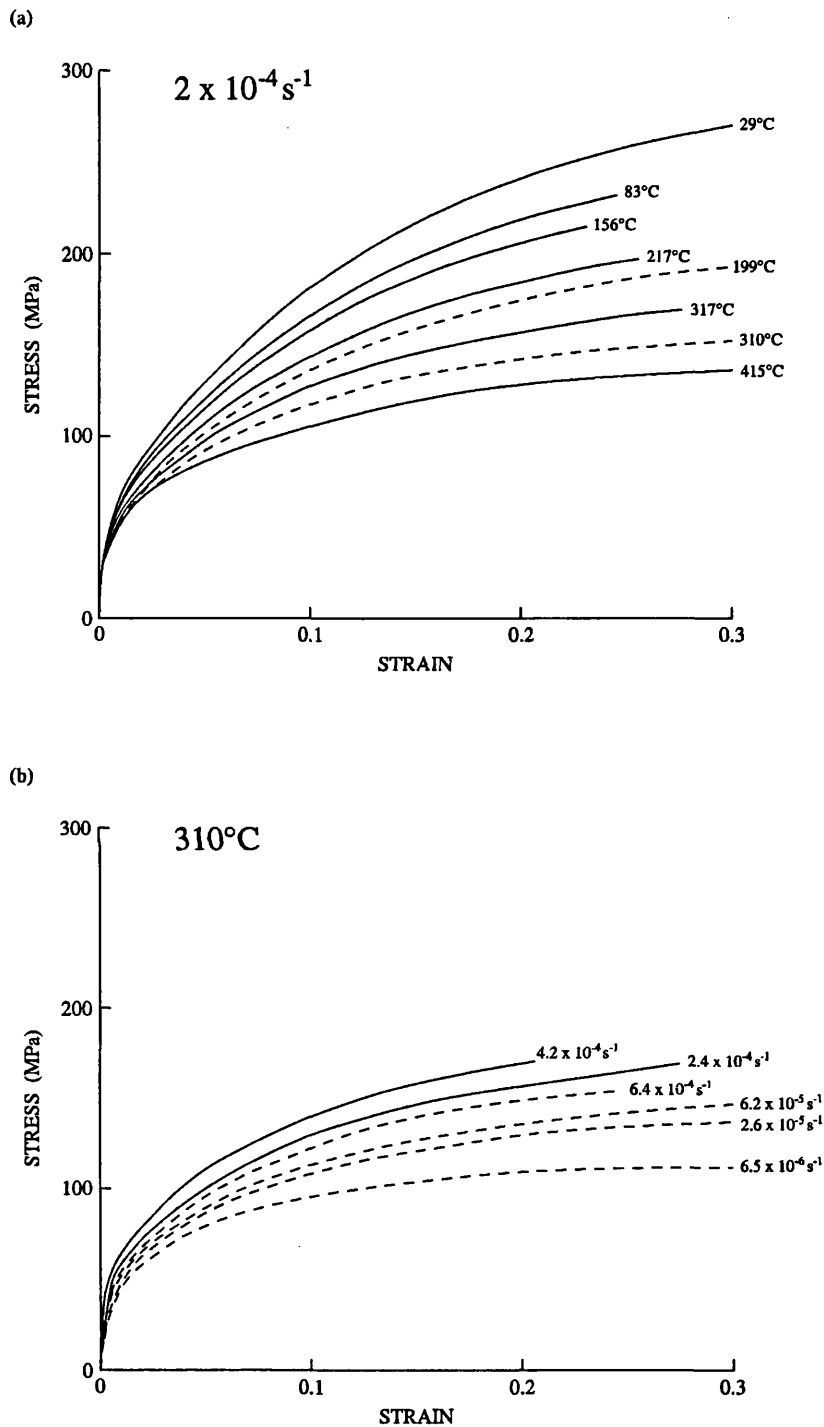
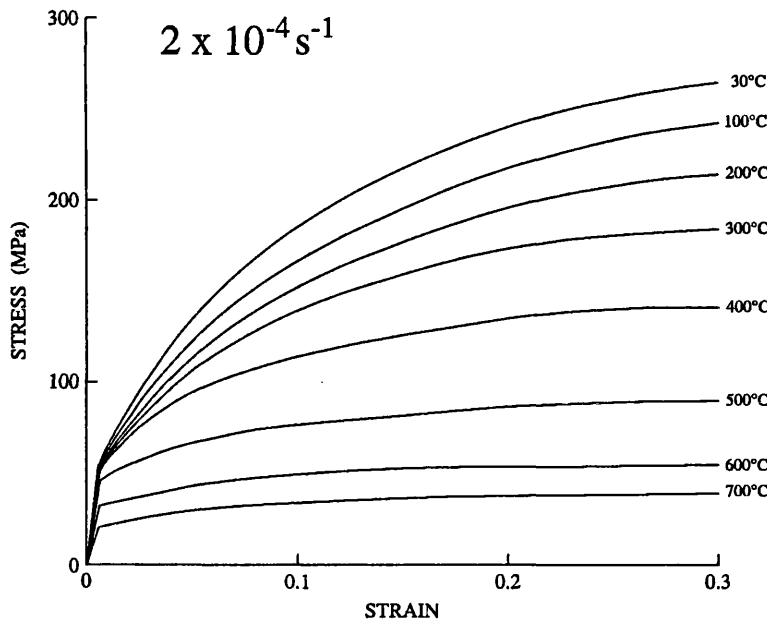


FIG. 9.10. Stress / strain curves generated from constant displacement-rate tests conducted at 200 MPa confining pressure on commercial purity copper. (a) Tests at the same strain-rate but various temperatures. (b) Tests at the same temperature but various strain-rates. The solid curves were generated from the IMPERIAL2 copper rod ; the dashed curves from the MANCHESTER1 rod.



#### Elastic deformation

$$\sigma = 129800 \{1 - [3 \times 10^{-4}(T - 15)]\} \epsilon^{(t)}$$

else

$$\sigma = A_1 + A_2(\epsilon^{(t)}) + A_3(\epsilon^{(t)})^2 + A_4(\epsilon^{(t)})^3 + A_5(\epsilon^{(t)})^4 + A_6(\epsilon^{(t)})^5$$

where at  $T < 450^\circ\text{C}$

$$\begin{aligned} A_1 &= 39.28959271 + (3.443423349 \times 10^{-2} T) - (1.962290763 \times 10^{-4} T^2) + (3.37448856 \times 10^{-7} T^3) \\ A_2 &= 2793.882471 - (7.162773073 T) + (2.127590118 \times 10^{-2} T^2) - (2.706149075 \times 10^{-5} T^3) \\ A_3 &= -18162.94807 + (24.80883337 T) + (3.022451074 \times 10^{-2} T^2) - (1.831462956 \times 10^{-4} T^3) \\ A_4 &= 77934.08551 + (29.82777344 T) - (1.113252883 T^2) + (2.677767568 \times 10^{-3} T^3) \\ A_5 &= -185231.1141 - (243.3340883 T) + (4.001695313 T^2) - (9.117138557 \times 10^{-3} T^3) \\ A_6 &= 177964.6477 + (266.0696135 T) - (4.307180142 T^2) + (9.962335836 \times 10^{-3} T^3) \end{aligned}$$

and at  $T > 450^\circ\text{C}$

$$\begin{aligned} A_1 &= -115.8386299 + (1.05263833 T) - (2.086639432 \times 10^{-3} T^2) + (1.225451325 \times 10^{-6} T^3) \\ A_2 &= 459.9577153 + (12.64131453 T) - (3.832193036 \times 10^{-2} T^2) + (2.846288227 \times 10^{-5} T^3) \\ A_3 &= 60885.45432 - (463.6351646 T) + (0.9673320211 T^2) - (6.190932299 \times 10^{-4} T^3) \\ A_4 &= -495905.2483 + (3360.5932 T) - (6.707451139 T^2) + (4.193048608 \times 10^{-3} T^3) \\ A_5 &= 1424254.574 - (9328.29781 T) + (18.3279034 T^2) - (1.134604515 \times 10^{-2} T^3) \\ A_6 &= -1395729.067 + (8992.187824 T) - (17.50635764 T^2) + (1.076597566 \times 10^{-2} T^3) \end{aligned}$$

FIG. 9.11. The fitted stress / strain curves for the IMPERIAL2 commercial purity copper rod at 200 MPa confining pressure and  $2 \times 10^{-4} \text{ s}^{-1}$  strain-rate. The curves for  $T < 450^\circ\text{C}$  were obtained on HEARD1 and those for  $T > 450^\circ\text{C}$  (not required in this study) were obtained by A. N. Walker on NIMONIC2. All stresses are in MPa ; all temperatures in  $^\circ\text{C}$ .

To evaluate the effect of neglecting the jacket correction each of the IMPERIAL2 stress / strain curves in figure 9.10a was fitted to a fifth order least squares polynomial and the six polynomial coefficients were each described as a function of temperature by cubic polynomial fits. The resulting calculated stress / strain curves (figure 9.11) agree within 5 MPa to the experimental ones. Using this calibration it is found that the jacket supports about 4% of the total differential load in the HEARD1 specimens and 7% in the NIMONIC2 specimens (figure 9.12a). This corresponds to about 15 and 20 MPa respectively, in the stress / strain curves generated at 420°C. The same Carrara marble stress / strain curve as employed to indicate the errors caused by the apparatus measuring devices in figures 9.1 and 9.2, is shown with and without the jacket correction in figure 9.12b. This specimen was deformed at 279°C, at which temperature the neglect of the load supported by the jacket leads to an overestimate of about 20 MPa in the differential stress.

The real load relaxation curve of a Carrara marble specimen is bracketed by the curve produced under the assumption that the load on the jacket is zero throughout the relaxation (*i.e.* as assumed in the results reported here) and that produced assuming that the load remains the same as that supported at the start of the relaxation. Figure 9.13a shows these 'brackets' for two Carrara marble relaxations of opposite concavity. The real curve must migrate from the high strain-rate end of the lower bracket towards the upper bracket as strain-rate decreases, and hence the real marble relaxation curves exhibit less concavity than those reported here. The load supported by the jacket remains an approximately constant fraction of the total load at strains greater than 0.01 (figure 9.12a) indicating that the separation of the bracketing curves is similar for all the relaxations conducted. However, the rate of migration away from the lower bracket may be expected to change with factors influencing the copper relaxation-rate. Hence the overestimate of the concavity of the real relaxation curve increases with pre-strain and temperature. The worst case situation arises if the copper recrystallizes during the relaxation (figure 9.13b), but this is a potential problem only in the highest temperature relaxations conducted in this study. All these factors, if significant, will be reflected in the quality of the fit of the relaxation data to a single family of curves.

#### 9.4 Assumptions about material behaviour

In fitting Hart's equations it is assumed that the results from different specimens, deformed under different conditions, are directly comparable. For the Carrara marble experiments this entails the assumptions that the effects of cataclasis, mechanical twinning and impurities in the starting material can be avoided, or at least identified and separated from the observed mechanical behaviour.

**9.4.1 Cataclasis.** The primary problem posed by cataclasis is that by accommodating a strain, it complicates the determination of  $\Gamma = d \ln \sigma^* / d\alpha$ . Given the choice of deformation conditions employed in this study, cataclasis if present will affect only those tests conducted at the highest strain-rates and lowest temperatures (§ 8.3.2.1). The influence of any cataclasis on the shape of the stress / strain curve is therefore easily identified by plotting the stress supported at given strain as a function strain-rate and temperature respectively to determine if the high strain-rate / low temperature data exhibits an anomalous (in comparison with the rest of the data)

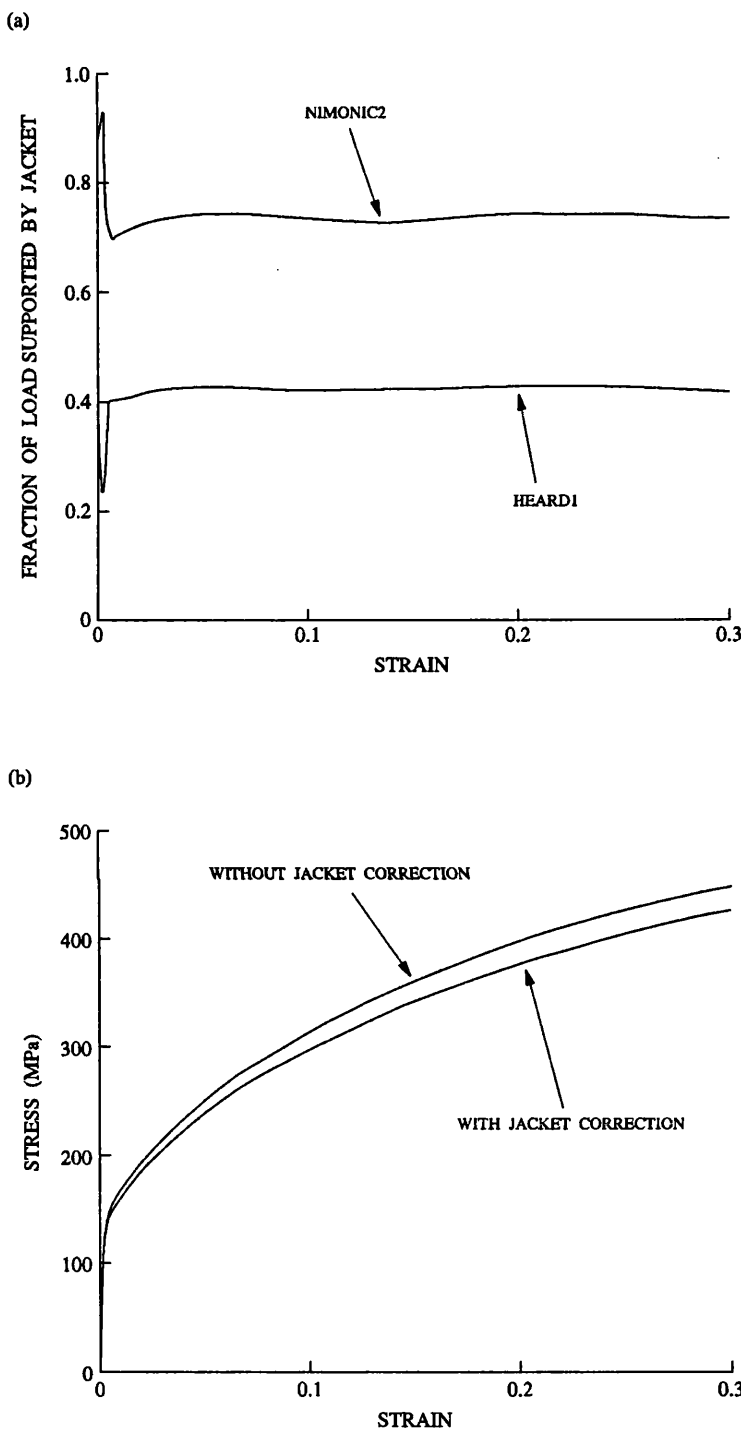
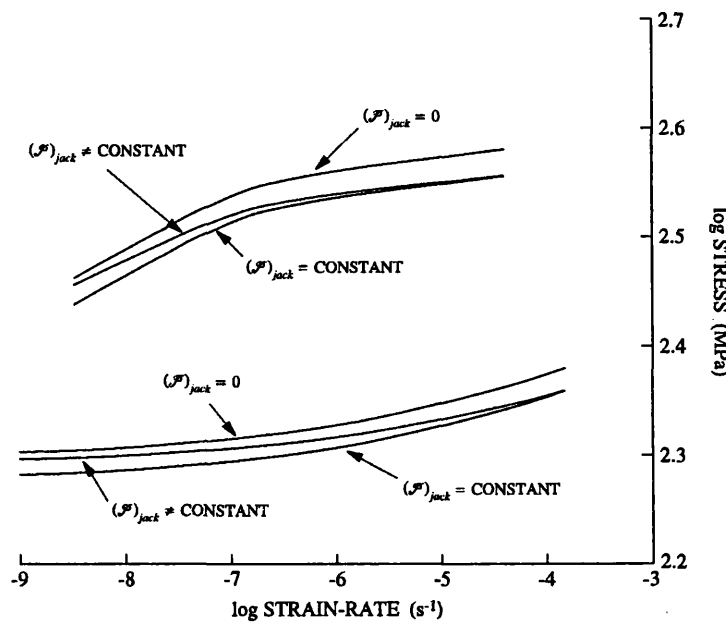


FIG. 9.12. The effect of neglecting the copper jacket correction in constant displacement-rate experiments. (a) The fraction of the total differential load which is supported by the jacket during constant displacement-rate tests conducted at 418°C on specimens of 0.25 inch (6.35 mm, NIMONIC2) and 0.375 inch (9.525 mm, HEARD1) diameter. (b) The effect of neglecting the copper jacket correction on a Carrara marble stress / strain curve generated on HEARD1 at 279°C and  $2.5 \times 10^{-4} \text{ s}^{-1}$ .

(a)



(b)

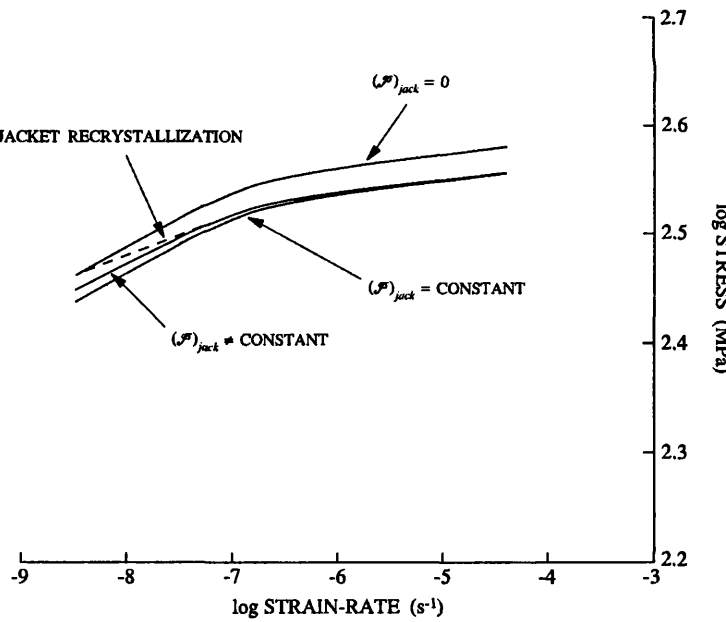


FIG. 9.13. The effect of neglecting the copper jacket correction on the shape of load relaxation curves.  $(\mathcal{P})_{jacket} = 0$  represents the curve without a jacket correction (as in this study);  $(\mathcal{P})_{jacket} = \text{constant}$  represents the curve where the load on the jacket is assumed to remain the same as at the start of the relaxation;  $(\mathcal{P})_{jacket} \neq 0$  represents the true relaxation curve. (a) The effect on relaxation curves of opposite concavity (relaxation A at 121°C in figure 11.1, and the highest strain relaxation at 320°C in figure 12.1). The  $(\mathcal{P})_{jacket} \neq 0$  curves are schematic. (b) The complicating influence of rapid recovery / recrystallization in the jacket material (again schematically drawn).

dependence on those variables.

Since the mechanical data used to evaluate the parameters in the three elements of Hart's model is obtained at stresses below those experienced previously by the specimen, it is inferred that any cataclasis effects on the evaluations of those parameters should be negligible. For the friction and plastic elements, the quality of the fit of all the relaxation curves obtained at different temperatures (and hence presumably under different amounts of cataclasis) to a one parameter family serves as a test of this assumption. The presence of cataclasis in the reloads used to determine the parameters of the anelastic element, is in principle (excepting the effects of all other errors), indicated by a deviation of the initial part of the stress / strain curve from that predicted by the Young's modulus.

**9.4.2 Mechanical twinning.** The primary problem presented by mechanical twinning is, like cataclasis, posed for the determination of  $\Gamma$ . In the range of conditions investigated it is a deformation process which is inevitably involved in any experiment which increases the magnitude of  $\sigma^*$ , and so unlike cataclasis it cannot be sidestepped. The effects of twinning on the determination of  $\Gamma$  are potentially twofold. Firstly, twinning accommodates a strain which must be subtracted from the stress / strain curves before  $\Gamma$  is evaluated. In principle, this strain may be calculated from a function relating volume fraction twinning and differential stress. Secondly, by presenting obstacles to dislocation motion, twin boundaries may exert an influence on the work hardening behaviour similar to that of grain boundaries (§ 6.3.3). Since the spacing of twin boundaries is large (tens of microns or more), it is anticipated that this effect is small, but again in principle, this can be tested by varying the deformation history (specifically the stress history and hence the twin density) used to attain given values of  $\sigma^*$ . No attempt to correct for the effects of twinning has been made in this study. Consequently, the mechanical state evolution equation presented may be deformation history dependent.

The influence of mechanical twinning on the evaluation of the material parameters in the three elements of Hart's model is believed to be negligible, again because the mechanical data was obtained at stresses lower than those previously experienced by the specimen. As for cataclasis, this assumption is tested by the quality of the fit of all the relaxation curves, obtained after straining to different stresses (and hence different twin density), to a one parameter family (friction and plastic elements), and by comparison of the slope of the initial portion of the reloading stress / strain curves with that predicted by Young's modulus (anelastic element).

The effects of mechanical twinning may be of significance for the static recovery function because twin boundaries are potential nucleation sites for recrystallization. Hence when recovery is accommodated by recrystallization, the recovery-rate may be a function of twin density. Microstructural examination of the annealed textures is required to evaluate the importance of this effect.

**9.4.3 The effect of impurities.** Any effect that the solute and second phase impurities in Carrara marble have on the deformation behaviour, can be recognized and accommodated as described in § 6.3.1 and § 6.3.2. If these effects are present but are not recognized, then they will be reflected in an anomalous variation of the material parameters with the deformation variables and, for the second phase impurities (given their non-uniform distribution), in a poor reproducibility of the results obtained from different specimens.

## 9.5 Assumptions made for the convenience of the data processing

A number of assumptions have been made to simplify both the data reduction and the fitting of the material parameters.

**9.5.1 Assumptions used in the data reduction.** Implicit in the use of equation 8.12 is that as deformation proceeds, the specimen remains a perfectly parallel-sided cylinder of constant volume, and that the differential load is applied over the entire cross sectional area. These assumptions are approximations because as deformation proceeds the pistons do not increase in cross sectional area at the same rate as the specimen. The lateral constraint then posed at the ends of the specimen by the jacket, leads to a cone-shaped region of low strain immediately adjacent to each piston, with a geometrically forced zone of high shear strain separating it from a zone of more uniformly distributed strain in the centre of the specimen (figure 9.14a). The result is that for specimens with an initial length / diameter ratio greater than 2.5 (*i.e.* of HEARD1 dimensions) only the central portion of the specimen remains parallel-sided, while for lower initial aspect ratios (*i.e.* of NIMONIC2 dimensions), there is a tendency for the specimen to barrel (figure 9.14b). For specimens with an aspect ratio of about 2.5, the deviation in shape is small relative to the total cross sectional area, being visually noticeable only at strains greater than about 0.25. Hence the error arising in the calculated differential stresses must be small.

A further deviation from a perfectly cylindrical shape arises when the axis of deformation does not exactly coincide with the axis of the specimen. In such circumstances the specimen tends to develop a 'kidney' shape (figure 9.14b). Again the deviations in shape are small but if significant, they will be reflected in the reproducibility of the stress / strain curves.

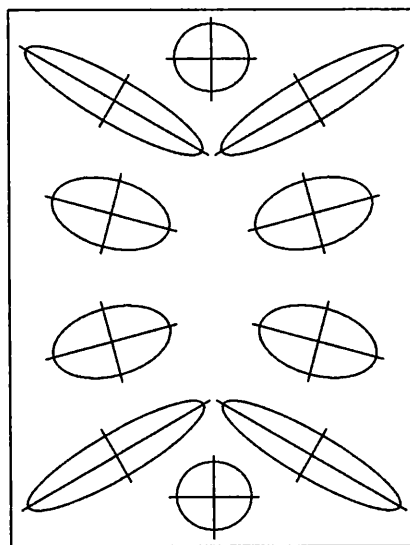
**9.5.2 Assumptions used for parameter fitting.** In determining the material parameters in Hart's equations the deformation is treated as if it is homogenous *i.e.* as if local variations in the deformation variables within the specimen have a negligible influence on the analysis. Given the strain heterogeneities arising within a specimen because of the end constraints (§ 9.5.1, figure 9.14), this is clearly an approximation, but no attempt has been made to evaluate its significance (through for example, comparison with the results of tension tests).

It is assumed that any variations of confining pressure throughout the experimental programme have no effect on the fitted equations. This primarily involves the assumption, used to determine the evolution of  $\sigma^*$  in the recovery tests, that the difference in confining pressure between the HEARD1 and NIMONIC2 experiments (about 30 MPa) and between experiments conducted on the same apparatus (upto 10 MPa), has a negligible influence on the mechanical behaviour. However, also included is the assumption that any gradual pressure leaks during a given test are insignificant. In a six week experiment in which a suite of relaxations was obtained, these latter leaks were upto 20 MPa.

Similarly it is assumed that any temperature fluctuations during a test (always less than  $\pm 1.5^\circ\text{C}$  and usually less than  $\pm 1^\circ\text{C}$ ) have negligible significance.

An important approximation for the evaluation of the  $\sigma^*$  evolution equation is that the constant displacement-rate tests can be treated as constant plastic strain-rate tests. For the specimen dimensions used here the plastic strain-rate increases linearly with strain by about 150% between strains of 0.01 and 0.30. This is small compared with the strain-rate range

(a)



STRAIN DISTRIBUTION IN A SPECIMEN

(b)

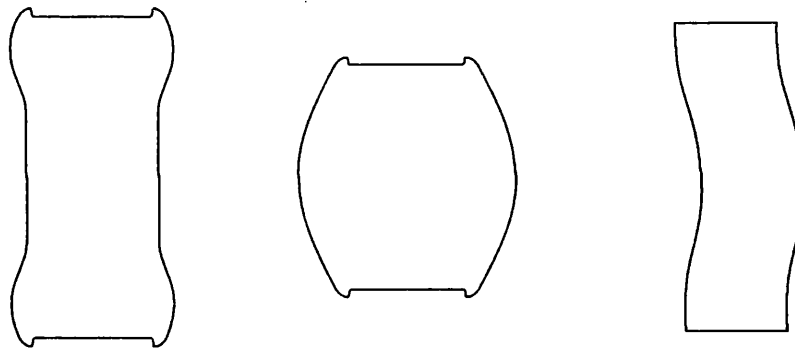
INITIAL ASPECT RATIO  
GREATER THAN 2.5INITIAL ASPECT RATIO  
LESS THAN 2.5LOADING NOT PRECISELY  
AXIAL

FIG. 9.14. Inhomogeneous deformation in the tests. (a) The strain distribution within a specimen deformed in compression and (b) the consequences of that heterogeneous strain distribution on the external morphology of the deformed specimens.

investigated but is sufficiently large to allow at strains greater than 0.01, the further simplifying approximation  $\varepsilon^{(n)} = \varepsilon^{(t)}$ . The errors that result are negligible because the  $\sigma^*$  evolution equation is not very strain-rate sensitive at the deformation conditions investigated (§ 13.2).

A final assumption employed in fitting the material parameters is that at each temperature investigated, in the strain-rate range of interest, only one element of Hart's analogue model (figure 5.3) is deformation rate controlling. This assumption has been widely used for fitting Hart's equations in the materials' science literature, although non-linear data correlation procedures which do not require it have been formulated (appendix A3.2).

## 9.6 Summary

The most significant factors limiting the quality of the data obtained in this experimental programme concern the determination of the differential stress acting on the specimen. For the HEARD1 experiments it is considered that the stress / strain curves are approximately accurate, with the underestimate in differential load due to inaccuracies in the force gauge stiffness calibration being cancelled by the neglect of a copper jacket correction. The neglect of the jacket correction however, leads to an overestimate of the concavity of the the load relaxation curves. For the NIMONIC2 experiments there is an uncertainty of  $\pm 10$  MPa due to the variability of the FGZ, while the neglect of the jacket correction means that the differential stresses are overestimated by an additional 20 MPa. There remains however, a discrepancy of unknown origin between the stresses given by the two apparatus.

Of the other problems, the most significant is the influence of mechanical twinning on the data utilized from constant displacement-rate tests. Although this can in principle, be accommodated, no attempt to do so has been made here. All other problems are either negligible or can be identified and accounted for when significant.

## 10 EQUATION OF STATE I. THE ANELASTIC ELEMENT

The anelastic element in Hart's original model is described by (equation 5.9)

$$\sigma_a = \mathcal{M}a \quad (10.1)$$

where the anelastic modulus  $\mathcal{M}$  is an unspecified function of mechanical state and temperature (§ 6.2.1). In this study  $\mathcal{M}$  was evaluated using the constant displacement-rate test, but in other investigations it has also been determined from the results of stress dip tests (§ 5.1.3.3).

### 10.1 Fitting the anelastic modulus

In a deformation experiment at stresses between the elastic and anelastic limits, the total strain is given by (equation 2.1)

$$\epsilon^{(t)} = \epsilon^{(e)} + a \quad (10.2)$$

Differentiating equation 10.2 with respect to the applied stress and using equation 5.7

$$\frac{d\epsilon^{(t)}}{d\sigma} = \frac{d\epsilon^{(e)}}{d\sigma} + \frac{da}{d\sigma} = \frac{d\epsilon^{(e)}}{d\sigma} + \frac{da}{d\sigma_a + d\sigma_f} \quad (10.3)$$

Also between the elastic and anelastic limits

$$\dot{\epsilon}^{(n)} = \dot{a} = \dot{\sigma}/\mathcal{M} \quad (10.4)$$

Hence if in the test it can be shown that  $\dot{\sigma}$  is constant, then it follows that  $\dot{\epsilon}^{(n)}$  and therefore (equation 5.12)  $\sigma_f$  are also constant. Equation 10.3 then becomes, with equation 10.1

$$\frac{d\epsilon^{(t)}}{d\sigma} = (1/E) + (1/\mathcal{M}) \quad (10.5)$$

where  $E$  is the Young's modulus of the specimen.

Over a small strain interval in a constant displacement-rate test  $\dot{\sigma}$  is approximately constant if the stress / total strain curve in that interval is linear. Hence it follows that if the stress / total strain curve between the elastic and anelastic limits in a constant displacement-rate test is linear, then its slope is described by equation 10.5, and given  $E$ ,  $\mathcal{M}$  may be determined.

**10.1.1 The Young's modulus of calcite.** The Young's modulus of calcite used in this study was calculated from the bulk and rigidity moduli given by Sumino and Anderson (1984) as Voight-Reuss-Hill averages of the calcite elastic constants (original data of Dandekar, 1968a,b ; Dandekar and Ruoff, 1968) :

$$\begin{aligned} K_0 &= 7.612 \times 10^{10} \text{ Pa} & ; & G_0 = 3.174 \times 10^{10} \text{ Pa} \\ K_0 &= 7.468 \times 10^{10} \text{ Pa} & ; & G_0 = 3.181 \times 10^{10} \text{ Pa} \\ (dK/dp)_T &= 5.38 \\ (dK/dT)_p &= -2.85 \times 10^7 \text{ Pa/}^\circ\text{C} \\ (dG/dp)_T &= -1.50 \\ (dG/dT)_p &= -9.70 \times 10^6 \text{ Pa/}^\circ\text{C} \end{aligned}$$

where  $K$  is the bulk modulus and  $G$  the rigidity modulus and the subscript 0 indicates the room temperature / pressure value (for which there are two estimates for each modulus). The Young's modulus is given by

$$E = 9KG/(3K+G) \quad (10.6)$$

(e.g. Fung, 1965, pp. 130). The temperature dependency of  $E$  was determined by calculating  $K$  and  $G$  (using their temperature dependencies) and hence  $E$  (using equation 10.6) at ten equally

spaced intervals in the range 0 to 1000°C (room pressure) and then linearly regressing the results. This was repeated for each  $K_0$ ,  $G_0$  pair and the fractional change in  $E$  with temperature (the slope divided by  $E$  at 20°C) for each fit was averaged. The pressure dependency was determined in the same way in the range 0 to 500 MPa (room temperature). Hence

$$E = 8.358 \times 10^{10} \{1 - [3.334 \times 10^{-11} p] - [3.151 \times 10^{-4} (T - 293)]\} \quad (10.7)$$

where  $E$  and  $p$  are in pascals and  $T$  is in kelvin, and where the error on the estimate of  $E$  produced by the linear fits is far smaller than that introduced by the different values of  $K_0$  and  $G_0$ .

**10.1.2 Determining the elastic and anelastic limits.** In order to determine the slope of the stress / total strain curve between the elastic and anelastic limits it is necessary that those limits be clearly defined. Provided there is a sufficient difference in the magnitudes of  $E$  and  $\mathcal{M}$ , the elastic limit is easily determined. The anelastic limit may, in principle, be located precisely by plotting  $\dot{\epsilon}^{(n)}$  against  $\sigma$ , since below the anelastic limit  $d\dot{\epsilon}^{(n)}/d\sigma = 0$  (*i.e.* the slope of the stress / strain curve is constant), while above it  $d\dot{\epsilon}^{(n)}/d\sigma$  increases (*i.e.* the slope of the stress / strain curve decreases).

The inability to determine the elastic and anelastic limits in the reloading curves in the load relaxation experiments and in the unloading curves from these anelasticity experiments prevents those curves from being utilized to yield additional values of  $\mathcal{M}$ . In the former case, reloading generally begins at stresses close to or above the elastic limit, while in the latter case seal friction problems complicate the form of the stress / strain curve in the anelastic region (*i.e.* in the latter stages of unloading, figure 6.2a).

## 10.2 Results

The composite stress / strain curves generated in multiple loading / unloading tests at 200 and 399°C are shown in figure 10.1. In each case except for the highest strain reload at 399°C, the reloading curve rejoins that obtained in an uninterrupted constant displacement-rate test. Hence it is inferred that apart from the one exception in which some recovery apparently took place,  $\sigma^*$  remained constant during each unloading.

Apart from the first two reloads at 399°C where the anelastic region covered too small a stress range, the initial part of all of the reload stress / strain curves can be described unambiguously by two linear segments (figure 10.2a), corresponding to the elastic and anelastic regions respectively (*cf.* figure 6.2b). Where both linear regions can be discerned, the  $\dot{\epsilon}^{(n)}$  against  $\sigma$  plots show that  $d\dot{\epsilon}^{(n)}/d\sigma = 0$  below the anelastic limit (thereby validating the use of equation 10.5), and that  $d\dot{\epsilon}^{(n)}/d\sigma$  increases sharply beyond the limit (figure 10.2b).

**10.2.1 Parameter evaluation.** The full results of the fitting procedure to determine  $\mathcal{M}$  are presented in table 10.1 in the following form :

- (i) the strain is the total inelastic pre-strain experienced prior to reloading as calculated from the differential stress supported at the end of the previous loading period using the stress / total strain curve generated under identical conditions without unload / reload interruptions ;
- (ii) the strain-rate is the total strain-rate corresponding to a strain of 0.10 during an uninterrupted test conducted at the same displacement-rate on a specimen of the same dimensions ;

- (iii) the differential stress is that supported at the end of the previous loading ;
- (iv) the value of the mechanical state is that calculated from the appropriate equation of state (§ 11.2.4 and § 12.2.4) using the total strain-rate (and the approximation  $\dot{\epsilon}^{(n)} = \dot{\epsilon}^{(t)}$ , § 9.5.2), and the final stress achieved in the previous loading (*cf.* § 13.1.1). For the final reload at 399°C the reload macroplastic yield stress was used, which is equivalent to assuming that none of the observed static recovery occurred during the reloading phase ;
- (v)  $E_{obs}$  is the slope of the observed stress / strain curve in the elastic region as defined by a visual fit made with the aid of a rule ;
- (vi)  $E$  is the Young's modulus calculated from equation 10.7 ;
- (vii)  $\mathcal{M}_{obs}$  is given by equation 10.5 using  $E$  (not  $E_{obs}$ ) and the slope of the observed stress / strain curve in the anelastic region (defined as for  $E_{obs}$  by a visual fit made with the aid of a rule) ;
- (viii)  $\mathcal{M}$  is the final value used for the anelastic modulus as given by

$$\mathcal{M} = \tan [ (\tan^{-1} E) - (\tan^{-1} E_{obs}) + (\tan^{-1} \mathcal{M}_{obs}) ] \quad (10.8)$$

*i.e.* it is the value given by rotating the observed stress / strain curve about (0,0) so that  $E_{obs}$  becomes coincident with  $E$ .

**10.2.2 The observed values of the anelastic modulus.** The values of  $\mathcal{M}$  given in table 10.1 yield an  $\mathcal{M}/E$  ratio of approximately 2.5 which is similar to that observed for pure aluminium (Alexopoulos *et al.*, 1981). They are plotted as a function of mechanical state and temperature on figure 10.3 where it may be seen that  $\mathcal{M}$  decreases with both  $\sigma^*$  and  $T$ . Repeated reloads at the same mechanical state and strain-rate, and at the same mechanical state but different strain-rates, show that  $\mathcal{M}$  is both reproducible at given  $\sigma^*$  and is strain-rate independent.

The decrease of  $\mathcal{M}$  with  $\sigma^*$  is linear and independent of  $T$ , and so the values of  $\mathcal{M}$  at 200 and 399°C together with the arithmetic mean of the values of  $\mathcal{M}$  at 318°C, were multiply regressed on the equation

$$\mathcal{M} = A + B\sigma^* + CT \quad (10.9)$$

where  $A$ ,  $B$  and  $C$  are the regression coefficients. The resulting regression equation (shown on figure 10.3) is

$$\mathcal{M} = 5.304 \times 10^{11} - 704.3 \sigma^* - 1.940 \times 10^8 T \quad (10.10)$$

where the stress dimensions are pascals,  $T$  is in kelvin, and the root mean square error is 5166 MPa.

**10.2.3 Uncertainties in the values of the anelastic modulus.** Although the results presented on figure 10.3 show that  $\mathcal{M}$  varies systematically with mechanical state and temperature, and that it is reproducible and independent of strain-rate, the slope of the stress / strain curve between the elastic and anelastic limits is not very sensitive to  $\mathcal{M}$  given the range of values found in these experiments (figure 10.4), and consequently any uncertainties in  $\mathcal{M}$  are of considerable significance.

Accurate knowledge of the specimen dimensions at the start of each reload is important for the calculations of both differential stress and strain during reloading. Two sources of error arise in the calculations of these dimensions. Firstly, although strictly they are given by the initial dimensions less the prior plastic strain, in the data reduction procedures employed here they were given as the initial dimensions less the inelastic strain *i.e.* a small error is introduced by the

incorrect subtraction of the anelastic deformation. Secondly, the method of calculating the specimen pre-strain from the stress / strain curves of uninterrupted tests, assumes that the stress / strain curves from the interrupted tests reproduce them perfectly at the end of the reloading. This strategy was preferred over the alternative of summing the strains in the previous loadings because it does not allow the errors arising from the inaccurate location of the initiation of loading in each reload (due to moving seal friction effects) to accumulate. Measurements of the final lengths of the specimens made after disassembly of the experiments correspond to within a strain of 0.004 with those calculated for the end of the final loading, and hence the errors on  $\mathcal{M}$  due to inaccurate knowledge of the specimen dimensions must be small.

A further source of error is that introduced by the visual fitting. The accuracy of these fits is increased as the 'length' of the fitted curve (*i.e.* the difference between the elastic and anelastic limits) is increased for this serves to define the anelastic limit more clearly. This is important because, although plots of  $\dot{\varepsilon}^{(n)}$  against  $\sigma$  show that  $\dot{\varepsilon}^{(n)}$  rises sharply from a constant level at the anelastic limit (figure 10.2b), the onset of this increase is not defined sufficiently precisely to aid the fitting. The error introduced by the fitting is most significant at low  $\sigma^*$  where  $\mathcal{M}$  is largest (and deviations in the fitted slope have their biggest influence on  $\mathcal{M}$ , figure 10.4) and the difference between the elastic and anelastic limits smallest. By doing repeat fits the error on  $\mathcal{M}$  was found to be less than  $\pm 5000$  MPa, and was generally much smaller.

By far the largest potential source of error lies in the procedure of correcting  $\mathcal{M}_{obs}$  to  $\mathcal{M}$  using equation 10.8. The use of equation 10.8 is an attempt to remove errors introduced by any factor which affects the data quality in these experiments (§ 9). The most significant of these errors (given the small strain interval and rapidly rising stress) arise from the uncertainty on the force gauge stiffness (§ 9.1.1.3) and from any permanent strain occurring at stresses below the anelastic limit (*e.g.* by cataclasis / mechanical twinning, § 9.4, or by 'early' yielding of the more highly stressed grains of the polycrystal). The magnitude of neither of these errors is precisely determinable, although it was found for the reloading curves that the difference between  $E_{obs}$  and  $E$  was approximately half (in terms of angle) that for the initial loading curves, suggesting that the procedure of using reloads to estimate  $\mathcal{M}$  in order to avoid the effect of permanent strains at low stresses was at least partially successful. The use of equation 10.8 assumes that all the deviation of  $E_{obs}$  from  $E$  results from these errors and, as suggested by the fact that the stress / strain curves are linear in the elastic and anelastic regions, that the net magnitude of the errors remains linearly dependent on stress upto the anelastic limit.

**10.2.4 Final statement of the equation of state.** The constitutive equation for the anelastic element is given by

$$\sigma_a = \mathcal{M}a$$

where

$$\mathcal{M} = 5.304 \times 10^{11} - 704.3 \sigma^* - 1.940 \times 10^8 T$$

and SI units have been employed.

### 10.3 Discussion

The behaviour of the anelastic element is as envisaged by Hart's original model. As required, the value of  $\mathcal{M}$  at given  $\sigma^*$  and  $T$  is strain-rate and deformation history independent

(§ 5.1.1.1, § 5.1.3.3). Furthermore, as anticipated from the continuum dislocation theory analysis of Hart's model where  $\mathcal{M}$  is shown to be given by

$$\mathcal{M} = G / (\pi l^2 \mathcal{N}^0) \quad (10.11)$$

in which  $l$  is the half distance between the long range barriers to dislocation motion and  $\mathcal{N}^0$  is the slip-zone density, it is also a function of  $\sigma^*$  and  $T$  (§ 6.2.1). The decrease  $\mathcal{M}$  with  $\sigma^*$  implies a corresponding increase in  $(l^2 \mathcal{N}^0)$ . Similarly, since the decrease in  $\mathcal{M}$  with  $T$  is an order of magnitude greater than that of  $G$ ,  $(l^2 \mathcal{N}^0)$  must also increase with temperature. It is unlikely that  $l$  increases in either instance, and so it is inferred that the decrease in  $\mathcal{M}$  with temperature and mechanical state reflects primarily the increased activation of slip-zones.

Although the results described here fit the anticipated behaviour of the anelastic element, they are strongly dependent on the validity of using equation 10.8 to determine  $\mathcal{M}$  from  $\mathcal{M}_{obs}$ . Since there is no independent justification of this procedure the results should be treated with caution. It is for this reason that a more extensive investigation of the variation of  $\mathcal{M}$  with  $\sigma^*$  and  $T$  was not attempted, and it is a problem which must be addressed before any attempt is made to apply the refined Hart model (figure 6.3).

Table 10.1. The data used to fit the anelastic element.

$\epsilon^{(n)}$	$\epsilon^{(t)} (s^{-1})$	$\sigma$ (MPa)	$\sigma^*$ (MPa)	$E_{obs}$ (MPa)	$E$ (MPa)	$\mathcal{M}_{obs}$ (MPa)	$\mathcal{M}$ (MPa)
<i>T = 200°C</i>							
0.0164	$2 \times 10^{-5}$	193	183	58635	78254	131988	303012
0.0467	$2 \times 10^{-5}$	255	241	62636	78254	148086	280382
0.0867	$2 \times 10^{-5}$	312	294	62636	78254	131988	227798
0.1297	$2 \times 10^{-5}$	360	338	56637	78249	101290	200173
0.1636	$2 \times 10^{-5}$	392	368	64892	78246	123797	183559
0.2087	$2 \times 10^{-5}$	429	402	58448	78243	91438	151336
<i>T = 318°C</i>							
0.0978	$2 \times 10^{-5}$	303	313	64509	75141	130301	182452
0.0978	$2 \times 10^{-5}$	303	313	72507	75139	159703	173057
0.0978	$2 \times 10^{-5}$	303	313	73374	75139	194035	206884
0.0994	$2 \times 10^{-6}$	305	321	70941	75139	168762	194622
0.1044	$2 \times 10^{-4}$	309	315	73777	75139	193894	203589
<i>T = 399°C</i>							
0.0791	$2 \times 10^{-5}$	275	294	67328	73019	155568	189738
0.1257	$2 \times 10^{-5}$	302	328	72815	73017	172797	173926
0.1606	$2 \times 10^{-5}$	316	345	74695	73017	168875	160534
0.2013	$2 \times 10^{-5}$	327	360	67754	73014	123398	142028

The variations in the values of  $E$  at nominally the same conditions are due to small changes in the confining pressure. The fitted data was taken to ten significant figures.

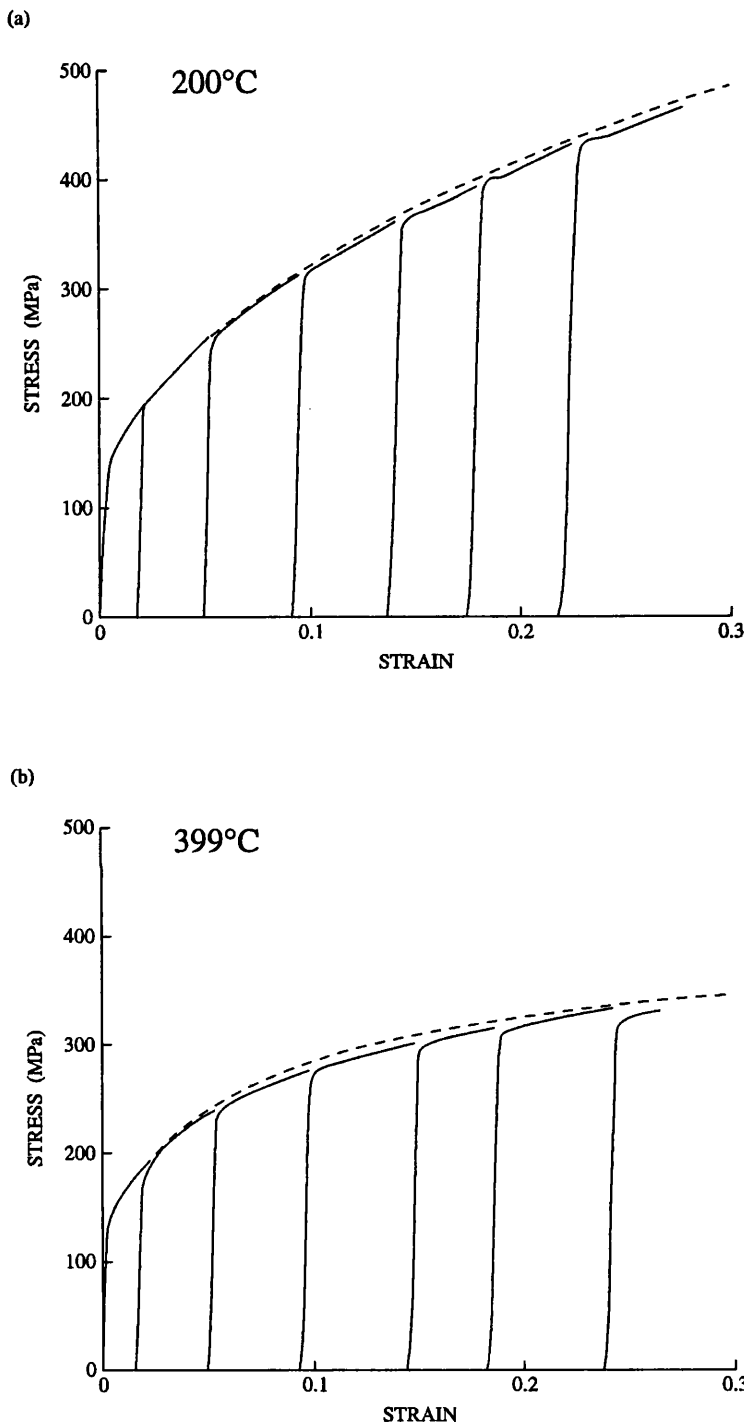


FIG. 10.1. The composite stress / strain curves generated in multiple loading / unloading constant displacement-rate experiments at a strain-rate of  $2 \times 10^{-5} \text{ s}^{-1}$  and at (a) 200°C and (b) 399°C. The dashed stress / strain curves are from uninterrupted constant displacement-rate experiments conducted on different specimens at the same conditions.

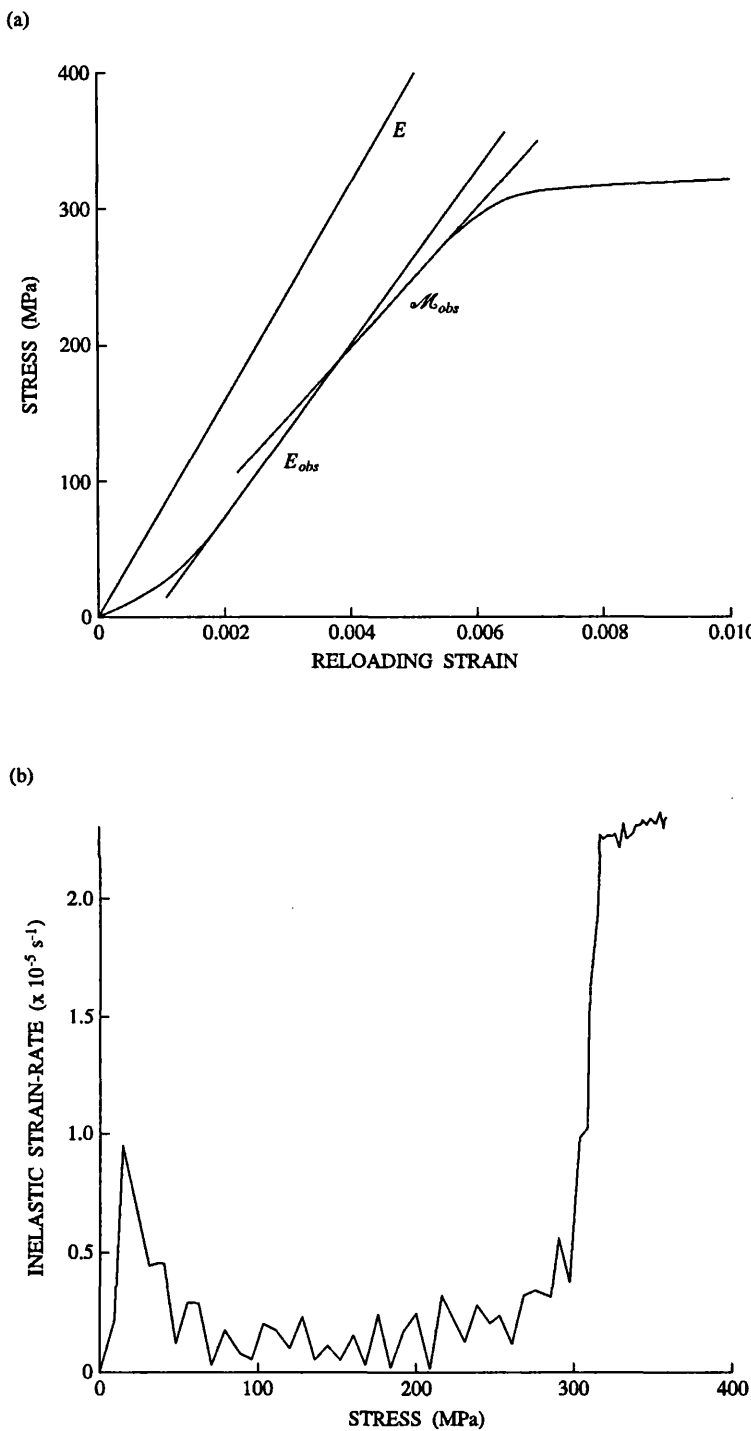


FIG. 10.2. The fourth loading (third reloading) conducted at 200°C. (a) The stress / strain curve showing the excellent definition of the elastic and anelastic regions. (b) The corresponding inelastic strain-rate / stress curve. The ragged form of the strain-rate / stress curve reflects the use of equation 8.21 (cast in terms of the 'elastic length') to determine the inelastic strain-rate rather than a smoothed load / time function.

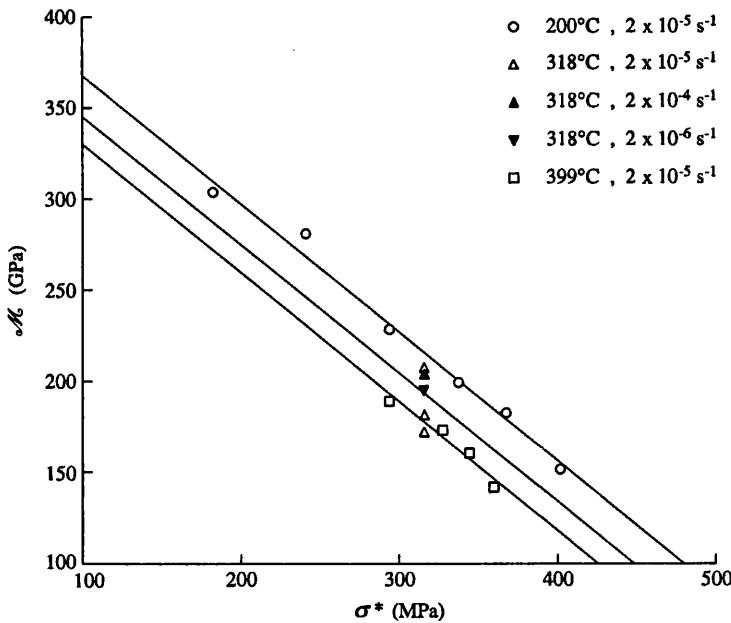


FIG. 10.3. The variation of the anelastic modulus with mechanical state together with the fitted curves expressing this variation (equation 10.10).

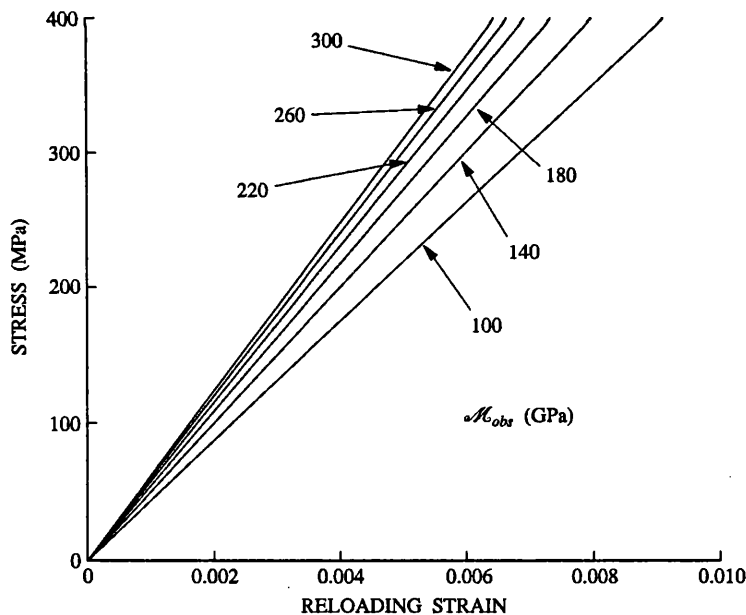


FIG. 10.4. The slope of the stress / strain curves in the anelastic region for various values of the anelastic modulus as determined from equation 10.5 using a Young's modulus of 78285 MPa (200°C and 200 MPa confining pressure). For large  $\mathcal{M}$  the slope of the curves is not very sensitive to the magnitude of  $\mathcal{M}$  and hence there are potentially large errors in its evaluation.

## 11 EQUATION OF STATE II. THE FRICTION ELEMENT

The friction element in Hart's original model is described by (equation 5.12)

$$\dot{\epsilon}^{(n)} = \dot{\alpha}^* (\sigma_f / G)^M \quad (11.1)$$

where in pure polycrystalline materials

$$\dot{\alpha}^* = \dot{\alpha}^* [(\sigma^* / G)^B \exp(C/T)] \quad (11.2)$$

$$M = M(1/T) \quad (11.3)$$

in which  $B$  and  $C$  are material constants (§ 6.2.2). In this study values for  $\dot{\alpha}^*$  and  $M$  were obtained from the load relaxation test, but in other investigations they have also been determined from the results of stress dip tests (§ 5.1.3.3).

### 11.1 Fitting the parameters

The following procedure for determining  $\dot{\alpha}^*$  and  $M$  from load relaxation curves depends upon the assumption that both remain constant during any given relaxation, and that each relaxation is isothermal and truly at constant  $\sigma^*$ .

**11.1.1 Determining  $M$ .** From equation 5.7 and the approximation  $\sigma_a = \sigma^*$  (§ 5.1.3.2), then equation 11.1 becomes

$$\dot{\epsilon}^{(n)} = \dot{\alpha}^* [(\sigma - \sigma^*) / G]^M \quad (11.4)$$

which may be rewritten as

$$\sigma = \sigma^* + \sigma \nu M \quad (11.5)$$

where  $\nu = d \log \sigma / d \log \dot{\epsilon}^{(n)}$  (§ A3.1.1). Hence, when plotted as  $\sigma$  against  $\sigma \nu$ , relaxation data should be linear with slope  $M$  and intercept  $\sigma^*$ . This method of obtaining  $M$  is to be preferred over the use of the reciprocal of the scaling slope (widely employed in the literature) which ignores the expected dependence of  $\dot{\alpha}^*$  on  $\sigma^*$  (§ 6.2.2.1).

### 11.1.2 Determining $\dot{\alpha}^*$ . Rearranging equation 11.4

$$\sigma = \sigma^* + [G / \dot{\alpha}^{*(1/M)}] [\dot{\epsilon}^{(n)}]^{(1/M)} \quad (11.6)$$

The relaxation data should therefore be linear, with slope  $[G / \dot{\alpha}^{*(1/M)}]$  and intercept  $\sigma^*$ , when plotted as  $\sigma$  against  $[\dot{\epsilon}^{(n)}]^{(1/M)}$ . Hence, with the value of  $M$  given by equation 11.5, and using

$$G = 3.1775 \times 10^{10} - 1.5p - 9.7 \times 10^6 (T - 293) \quad (11.7)$$

(§ 10.1.1, where the arithmetic mean of the two values of  $G_0$  is used),  $\dot{\alpha}^*$  may be calculated.

### 11.2 Results

The stress / strain curves generated in the multiple load relaxation experiments at 120, 160, 200 and 240°C, together with the corresponding relaxation curves, are shown in figure 11.1. The stress / strain curves show reloading peaks which become less pronounced with increasing stress and decreasing temperature. These peaks are, however, transient features, and within a reload strain of 0.01 the stress / strain curves rejoin those obtained from uninterrupted experiments, with the implication that the cause of the peaks does not also cause a change in  $\sigma^*$  during the relaxation.

The relaxation curves show a decreasing degree of upward concavity as temperature increases, and by 240°C they contain an inflexion point such that they become concave

downward at low strain-rates. The concave upward portions of all curves generated at given temperature may be superposed onto one master relaxation curve by a rigid body translation in fixed direction, but the shape of the master curve and the translation direction changes with temperature (figure 11.2).

**11.2.1 Parameter evaluation.** The full results of the fitting procedure as applied to the relaxation curves shown in figure 11.1 are given in table 11.1. The stresses and strains in the table are those at the start of each relaxation as given by the data reduction procedure (§ 8.4). The values of  $\dot{a}^*$ ,  $M$  and  $\sigma^*$  for each relaxation curve were determined in the following way :

- (i) the  $\log \sigma / \log \dot{\epsilon}^{(n)}$  data were fitted to a cubic polynomial ;
- (ii) using the experimentally observed strain-rates to calculate  $\sigma$  from the cubic polynomial and  $\nu$  from the derivative of that equation, the data was replotted as  $\sigma$  against  $\sigma\nu$  and linearly regressed to determine  $M$  ( $M_{obs}$  in table 11.1) ;
- (iii) the mean value of  $M_{obs}$  at each temperature was determined and these were then linearly regressed in accordance with equation 11.3, on the equation

$$MT = A + BT \quad (11.8)$$

where  $A$  and  $B$  are the regression coefficients ;

- (iv) using the values of  $M$  given by equation 11.8 and the relaxation temperature, the experimentally observed stress / strain-rate relaxation data were replotted as  $\sigma$  against  $[\dot{\epsilon}^{(n)}]^{(1/M)}$ , and linearly regressed to determine  $\dot{a}^*$  ( $\dot{a}_{obs}^*$  in table 11.1) and  $\sigma^*$  ;
- (v) the values of  $\dot{a}_{obs}^*$  and  $\sigma^*$  determined in (iv) were multiply regressed in accordance with equation 11.2, on the equation

$$\ln \dot{a}^* = A + B \ln (\sigma^* / G) + (C / T) \quad (11.9)$$

where  $A$ ,  $B$  and  $C$  are again regression coefficients.

**11.2.2 The observed values of the material parameters.** The values of  $M$  cover almost the entire range of values recorded for other materials. They are plotted according to equation 11.8 on figure 11.3a. The regression equation is

$$MT = 8489 - 13.61T \quad (11.10)$$

where  $T$  is in kelvin and the root mean square error on  $MT$  is 62.71 K.

The observed values of  $\dot{a}^*$  are plotted according to equation 11.9 on figure 11.3b. The regression equation is

$$\ln \dot{a}^* = -99.19 - 5.369 \ln (\sigma^* / G) + (45280 / T) \quad (11.11)$$

where the stress dimensions are pascals, the rate dimensions are per second and temperature is in kelvin. The root mean square error on  $\ln \dot{a}^*$  is 0.7799 which corresponds to a root mean square error on the  $\log \dot{\epsilon}^{(n)}$  location of the relaxation curves of 0.3387. Comparison with other materials is difficult because of the extreme dependence of  $\dot{a}^*$  on the value of  $M$ , but the observed values of  $[G / \dot{a}^{*(1/M)}]$  are of the same order of magnitude.

**11.2.3 Uncertainties in the values of the material parameters.** Figure 11.4a-c shows example plots from the three relaxation data curve fitting exercises – parts (i), (ii) and (iv) of the parameter fitting procedure. The root mean square errors on the  $\log \sigma / \log \dot{\epsilon}^{(n)}$  fits at all temperatures are about 1 MPa, whereas on the other two fits they are generally substantially less than 0.5 MPa.

The errors on the fits suggest that the value of  $M$ , which controls the shape of the fitted

relaxation curve, and that of  $\dot{\alpha}^*$ , which controls its strain-rate location, are well constrained for each relaxation. However, there is a broadly defined increase in  $M$  with  $\sigma^*$  at all temperatures (cf.  $M_{obs}$ , table 11.1) which was ignored in fitting equation 11.10 on the assumption that it was within error (and in particular within the error on  $\nu$  arising through neglect of the upper jacket correction, § 9.3.3.2). In fact the shape of the fitted relaxation curves is not very sensitive to the choice  $M$  within the observed range of values (figure 11.5a), and consequently by appropriate changes in  $\dot{\alpha}^*$ , a wide range of  $M$  values can be made to fit the data. This is emphasized in figure 11.5b, where using  $M = 10$  for all the relaxation data plotted in figure 11.4 irrespective of the observed  $M$  value (which for these curves lies between 2.9 and 5.5), apparently has no significant effect on the linearity of the  $\sigma$  versus  $[\dot{\varepsilon}^{(n)}]^{(1/M)}$  curves. The consequences for the values of  $\dot{\alpha}^*$  are enormous – the  $\dot{\alpha}^*$  obtained from the  $M = 10$  fits are fifteen orders of magnitude larger than the corresponding ones in table 11.1. Under these circumstances, the fitting procedure used to determine the values of  $M$  and  $\dot{\alpha}^*$  is clearly of great importance and presents a highly significant constraint on their interpretation.

**11.2.4 Final statement of the equation of state.** The constitutive equation for the friction element is given by

$$\dot{\varepsilon}^{(n)} = \dot{\alpha}^* (\sigma_f / G)^M$$

where

$$\dot{\alpha}^* = 8.322 \times 10^{-44} (\sigma^* / G)^{-5.369} \exp(376500 / RT)$$

$$G = 3.1775 \times 10^{10} - 1.5p - 9.7 \times 10^6 (T - 293)$$

$$M = -13.61 + (8489 / T)$$

and SI units have been employed. The fits to the relaxation data using this equation (in the form equation 11.4) and the values of  $\sigma^*$  in table 11.1, are shown on figure 11.1. With the exception of the highest stress relaxations at 120°C, the fits describe the relaxations within the regression error on  $\dot{\alpha}^*$ .

### 11.3 Discussion

In principle, the linear scaling behaviour of the relaxation curves suggests that the friction element behaves as envisaged for Hart's original model. As anticipated, the scaling slope is given by

$$\mu = (M + \partial \log \dot{\alpha}^* / \partial \log \sigma^*)^{-1} \quad (11.12)$$

(equation 4.46) with the implications that  $\dot{\alpha}^*$  and  $M$  are constant during each relaxation, that  $M$  is not a function of  $\sigma^*$ , and that there is a power law relationship between  $\dot{\alpha}^*$  and  $\sigma^*$  (§ 4.1.2.2). However,  $MT$  is not constant as expected (§ 6.2.2.2), and the rate parameter  $\dot{\alpha}^*$  decreases with increasing temperature. Moreover,  $\dot{\alpha}^*$  decreases with increasing  $\sigma^*$ , leading to the unlikely conclusion that the mobile dislocation density decreases with increasing strain (§ 6.2.2.1).

The exceptionally small slope of the relaxation curves at low strain-rates (particularly at low  $\sigma^*$  and at relatively high  $T$ ) and the existence of the reloading peaks, suggest that the observed mechanical behaviour may be influenced by impurities (cf. § 6.3.1.2, § 6.3.2.2). Of the impurities in the Carrara marble only the Mg solutes and the finely dispersed opaque inclusions are present in sufficient amounts to be of potential significance (§ 8.3.1.1). Since no correlation between the mechanical properties and the amount of inclusions in the starting

specimen was observed in this experimental programme, it is inferred that any impurity effect must be due to the Mg solutes. The systematic variation of the size of the reloading peaks with temperature and strain is consistent with this inference. At given temperature the size of the peaks is expected to be largest at low strains before the impurities have been incorporated into the immobile dislocation network, and after the longest duration relaxations reflecting the increased amount of solute segregation during the relaxation. The former is evident from figure 11.1 ; the latter is confirmed by the observation that the reloading peaks in the 200°C unloading / reloading tests used to characterize the anelastic element, are very small (figure 10.1a). With increasing temperature the size of the reloading peaks is expected to rise to a maximum and then to decrease in correspondence with the magnitude of the solute-dislocation interactions and with changes in the solute mobility. Again the results are in accord with this expectation ; the peaks increase to their maximum size at 240°C (figure 11.1) and then diminish to non-existence at 320°C (figure 12.1).

The limited experimental data available suggests that solute impurities affect  $M$  but not  $\alpha^*$  (§ 6.3.1.4). The implication is that ongoing solute segregation during relaxation causes a corresponding decrease in  $M$  which is not sufficient to affect significantly the linearity of the  $\sigma$  versus  $[\varepsilon^{(n)}]^{(1/M)}$  curves, and which does not sufficiently depend on the pre-strain or the relaxation duration to prevent scaling. However, this decrease in  $M$  is sufficient to affect the evaluation of  $\alpha^*$  and hence the apparent dependence of  $\alpha^*$  on  $\sigma^*$ . It may be that the Mg solute concentration is simply too small to produce the expected breakdown in scaling behaviour at given temperature, and hence the solute effect is made apparent only through its temperature dependence.

In view of these comments it is apparent that while the inelastic deformation of Carrara marble at 200 MPa confining pressure and low homologous temperatures can be described by the constitutive relation for the friction element, the material parameters evaluated in this study are probably strongly influenced by the effect of Mg solute impurities. Hence prior to a full parameterization for solute impurity effects, it seems inevitable that the equation of state presented here will not be applicable to other calcitic aggregates of different impurity composition.

Table 11.1. The data used to fit the friction element.

$T$ (°C)	$\dot{\varepsilon}^{(n)}$	$\sigma$ (MPa)	$\sigma^*$ (MPa)	$M_{obs}$	$\dot{\alpha}_{obs}^*$ (s <sup>-1</sup> )
$\dot{\varepsilon}^{(n)} = 6 \times 10^{-4}$ s <sup>-1</sup>					
A	121	0.020	240	189	5.907
B	121	0.032	272	219	6.144
C	120	0.043	299	241	6.348
D	120	0.055	323	259	8.788
E	120	0.068	342	279	6.736
F	121	0.081	364	300	7.591
G	121	0.095	383	315	8.335
H	121	0.112	404	333	9.268
I	121	0.133	426	354	8.531
J	121	0.161	454	373	10.04
K	121	0.195	485	396	19.54 †
L	120	0.239	524	422	10.56
Mean $M_{obs} = 8.02$					
$\dot{\varepsilon}^{(n)} = 6 \times 10^{-4}$ s <sup>-1</sup>					
A	162	0.020	222	193	6.683
B	161	0.031	251	219	4.474
C	161	0.042	276	242	5.050
D	161	0.054	298	262	6.054
E	161	0.068	320	282	6.226
F	161	0.079	340	299	6.931
G	161	0.091	357	313	6.572
H	161	0.109	378	335	7.711
I	161	0.128	398	352	6.137
J	161	0.147	415	369	5.920
K	161	0.167	433	384	6.879
Mean $M_{obs} = 6.06$					
$\dot{\varepsilon}^{(n)} = 2 \times 10^{-4}$ s <sup>-1</sup>					
A	200	0.012	182	167	3.877
B	200	0.020	205	190	3.990
C	200	0.028	227	211	3.274
D	200	0.036	247	228	3.129
E	200	0.046	264	243	3.263
F	200	0.055	280	259	3.502
G	200	0.065	296	273	3.456
H	200	0.076	312	287	3.680
I	200	0.089	329	303	3.607
J	200	0.101	345	316	4.166
K	200	0.114	359	328	4.347
L	200	0.131	378	347	4.652
M	200	0.144	393	361	5.464
N	200	0.161	406	372	5.779
O	200	0.179	424	389	5.123
Mean $M_{obs} = 4.09$					
$\dot{\varepsilon}^{(n)} = 2 \times 10^{-4}$ s <sup>-1</sup>					
216	0.025	223	204	3.004	1.398 x 10 <sup>8</sup>
216	0.037	247	228	2.745	1.834 x 10 <sup>8</sup>
216	0.050	273	246	3.034	1.162 x 10 <sup>8</sup>
217	0.066	297	272	3.809	3.842 x 10 <sup>7</sup>
217	0.088	324	296	4.162	1.708 x 10 <sup>7</sup>
215	0.112	349	317	5.097	1.880 x 10 <sup>7</sup>
Mean $M_{obs} = 3.82$					
$\dot{\varepsilon}^{(n)} = 2 \times 10^{-4}$ s <sup>-1</sup>					
B	238	0.020	178	191	3.773
C	240	0.028	222	214	2.541
D	241	0.036	241	231	1.803
E	241	0.044	258	247	2.803
F	241	0.053	273	262	3.175
G	241	0.064	288	276	2.888
H	241	0.082	311	297	2.146
I	241	0.102	335	319	2.700
J	241	0.125	360	343	2.918
K	241	0.149	384	364	3.470
L	241	0.176	407	385	4.069
Mean $M_{obs} = 2.94$					

† data which was not used in the fits. The fitted data was taken to ten significant figures.

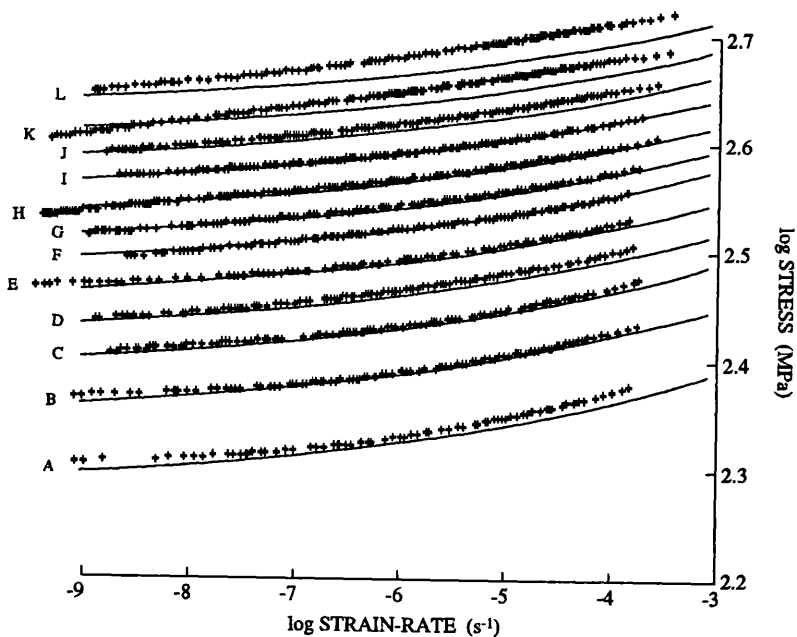
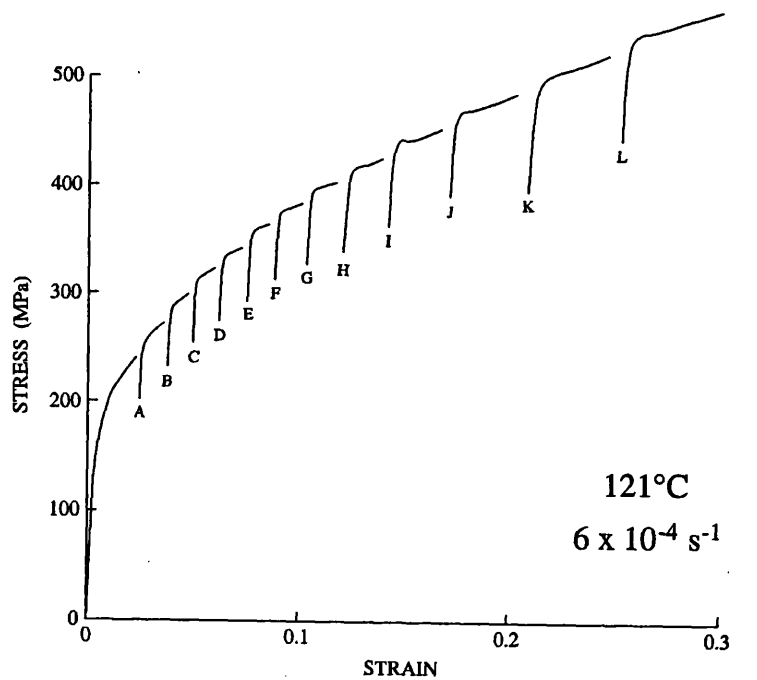


FIG. 11.1. The stress / strain and corresponding load relaxation curves from the multiple relaxation experiment conducted at  $121^{\circ}\text{C}$ . The solid relaxation curves are the fits to the data using the final equation of state (§ 11.2.4) and the values of  $\sigma^*$  in table 11.1. A  $\log \dot{\epsilon}^{(n)}$  shift of -0.03 has been applied to all the fitted curves.

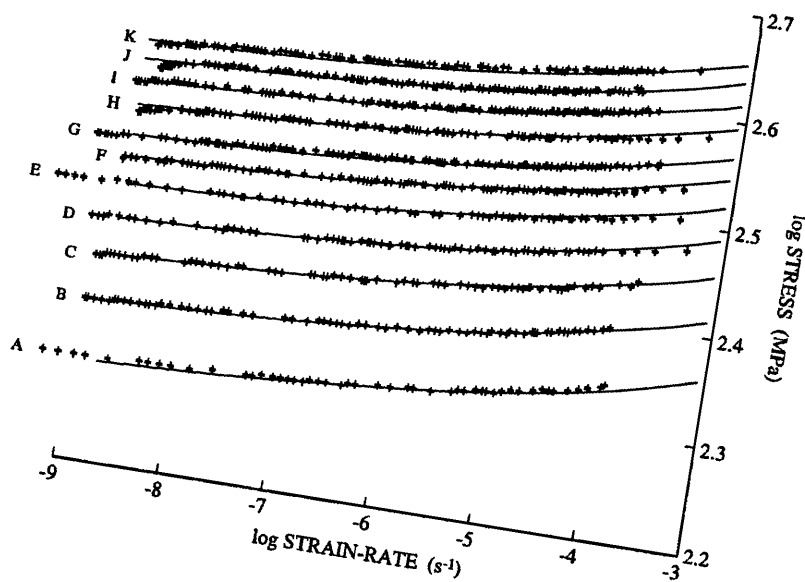
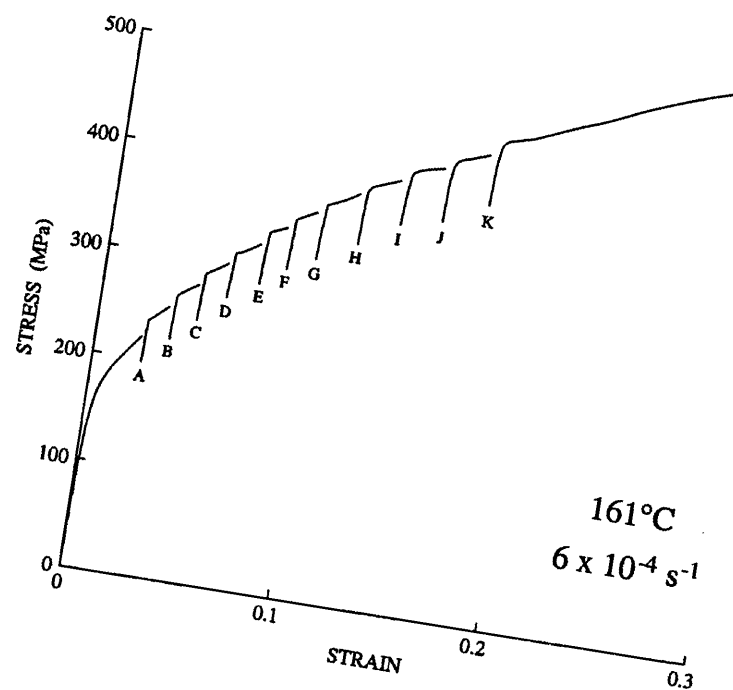


FIG. 11.1 contd. The results of the multiple relaxation experiment conducted at 161°C. The fitted relaxation curves have been given a  $\log \dot{\epsilon}^{(n)}$  shift of +0.28.

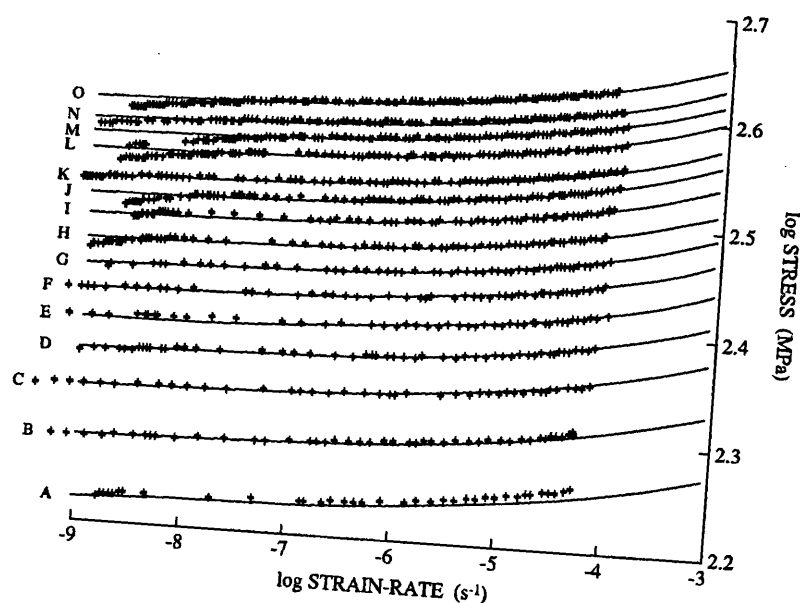
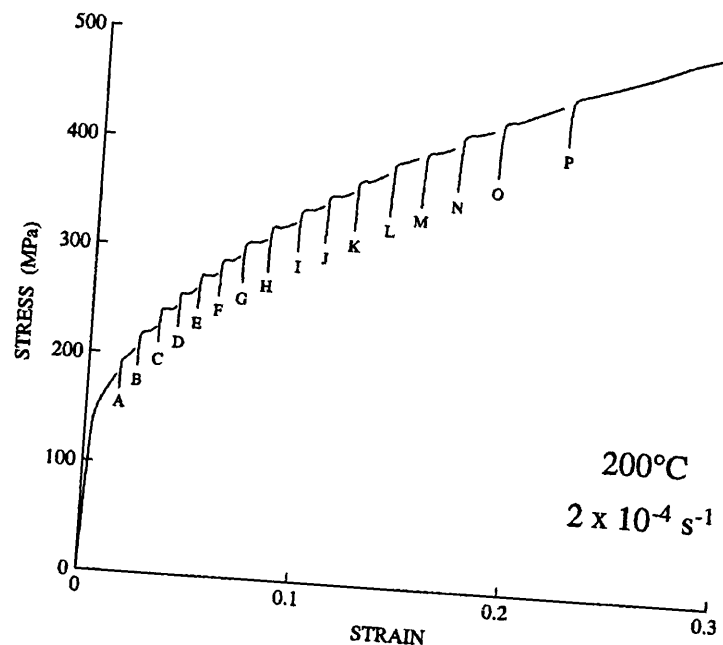


FIG. 11.1 contd. The results of the multiple relaxation experiment conducted at 200°C. No  $\log \dot{\epsilon}^{(n)}$  shift has been applied to the fitted relaxation curves.

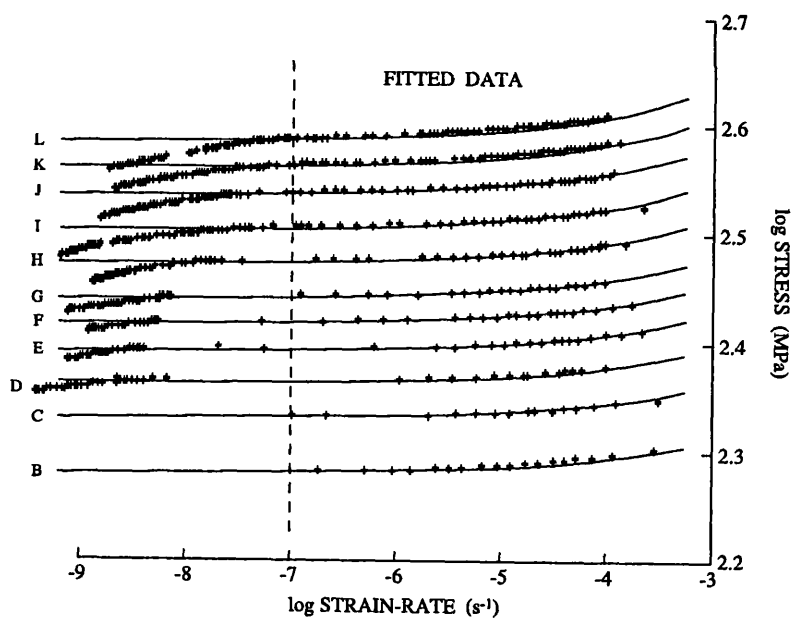
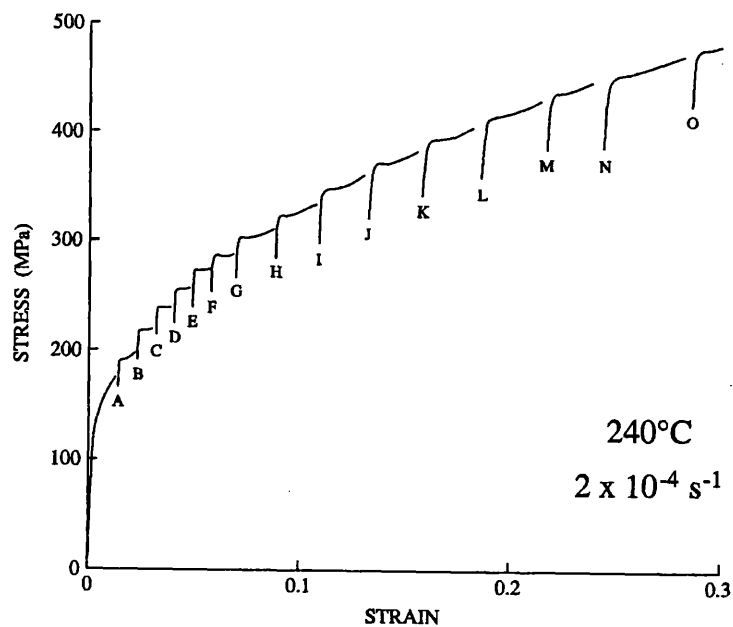


FIG. 11.1 contd. The results of the multiple relaxation experiment conducted at  $240^{\circ}\text{C}$ . The fitted relaxation curves have been given a  $\log \dot{\epsilon}^{(n)}$  shift of -0.21.

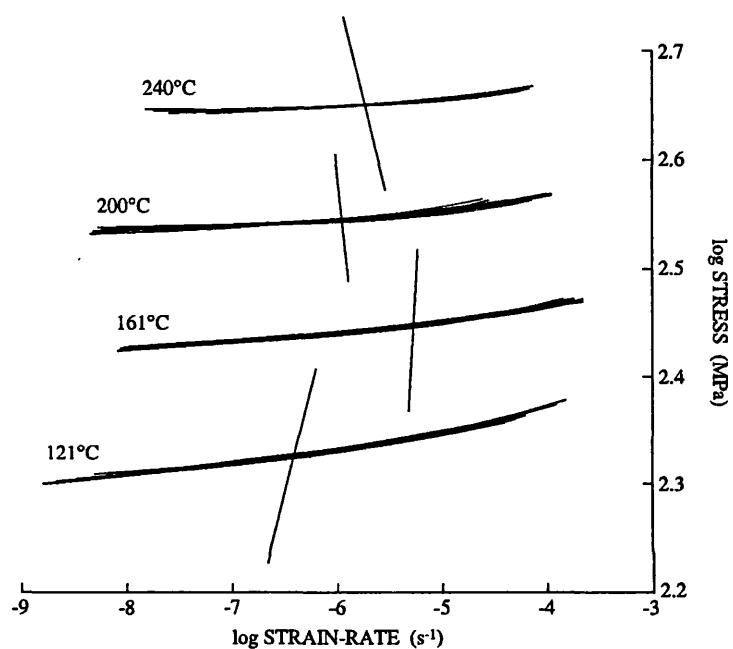


FIG. 11.2. The master  $\sigma^*$  curves for each temperature as generated by translating the experimental data within the fitted range of strain-rates (generally  $\log \dot{\varepsilon}^{(n)} > -8$ ) in the indicated directions (given by equation 11.12). Each of the master curves has a different value of  $\sigma^*$ .

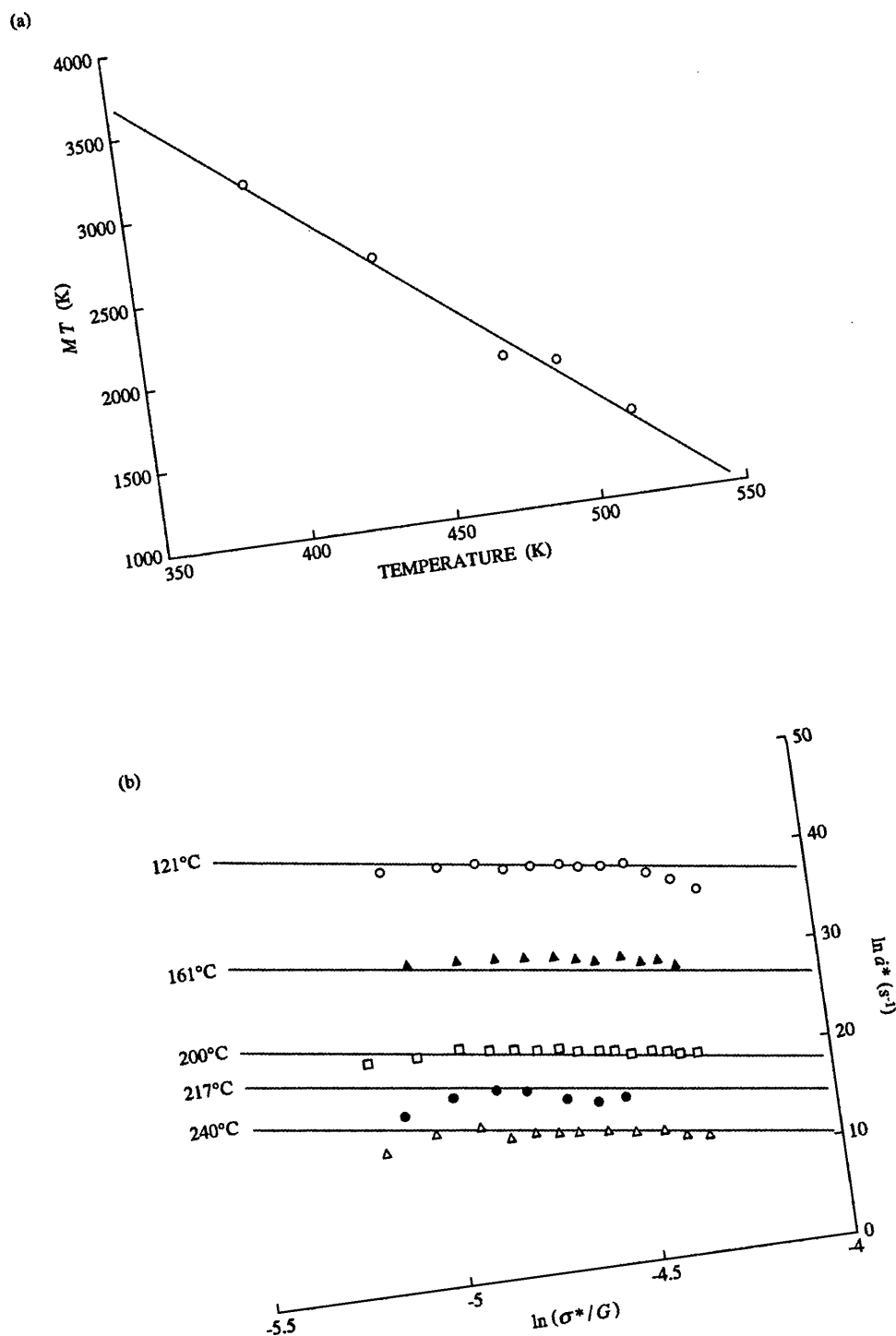
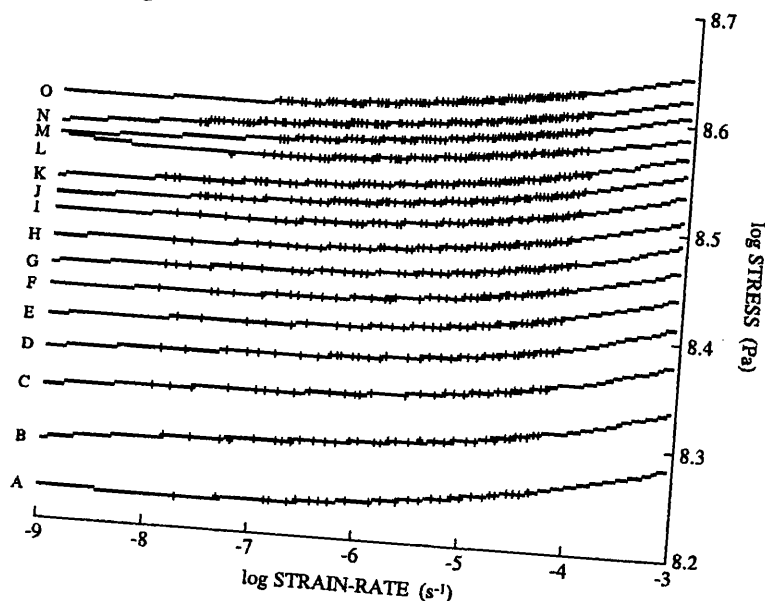


FIG. 11.3 The variation of material parameters of the friction element. (a) The variation of  $MT$  with  $T$  and the fit expressing that variation (equation 11.10). (b) The variation of  $\dot{\alpha}^*$  with  $\sigma^*$  and  $T$  and the fits expressing that variation (equation 11.11).

(a)

200°C



(b)

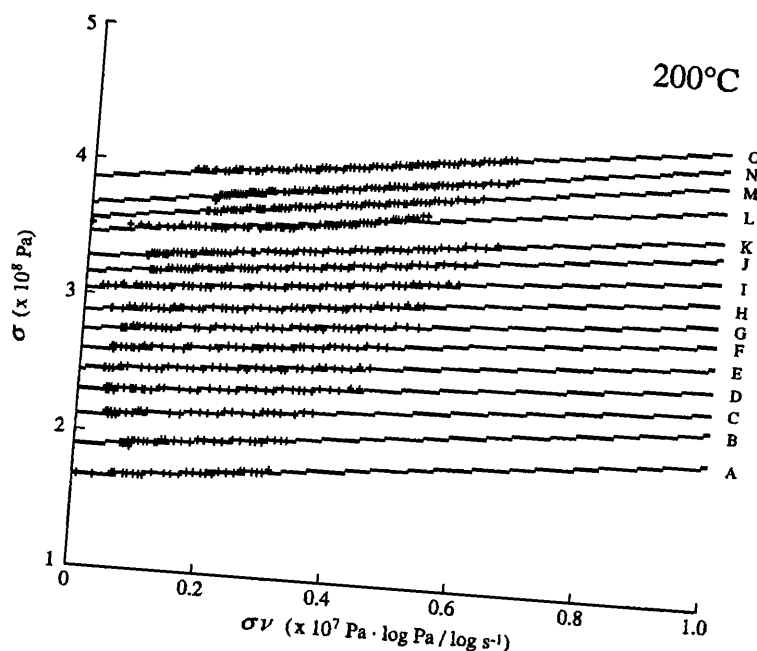


FIG. 11.4. Typical plots from the three relaxation data fitting exercises. (a) Polynomial fits to the  $\log \sigma / \log \dot{\epsilon}^{(n)}$  data. (b) Linear fits to the relaxation data cast as  $\sigma$  vs.  $\sigma\nu$ .

(c)

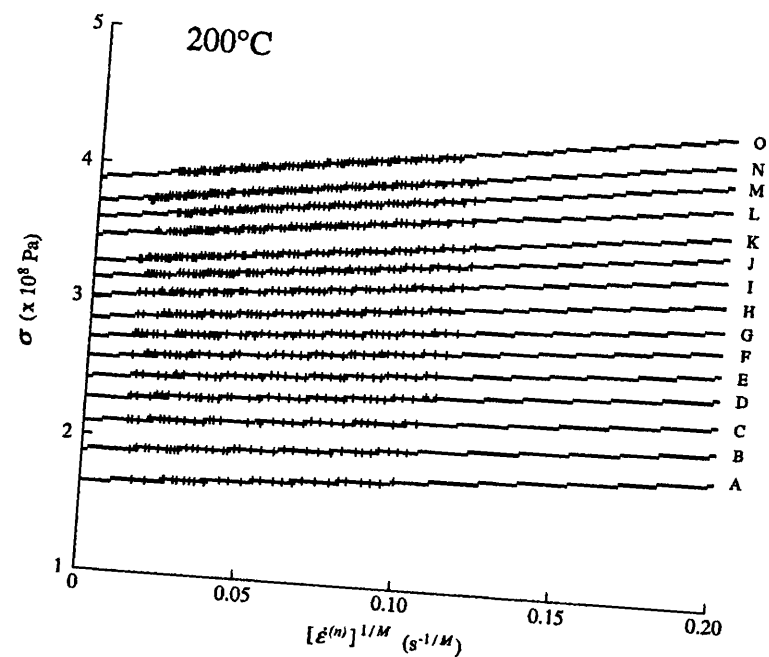


FIG. 11.4 contd. (c) Linear fits to the relaxation data cast as  $\sigma$  vs.  $[\dot{\epsilon}^{(n)}]^{1/M}$ .

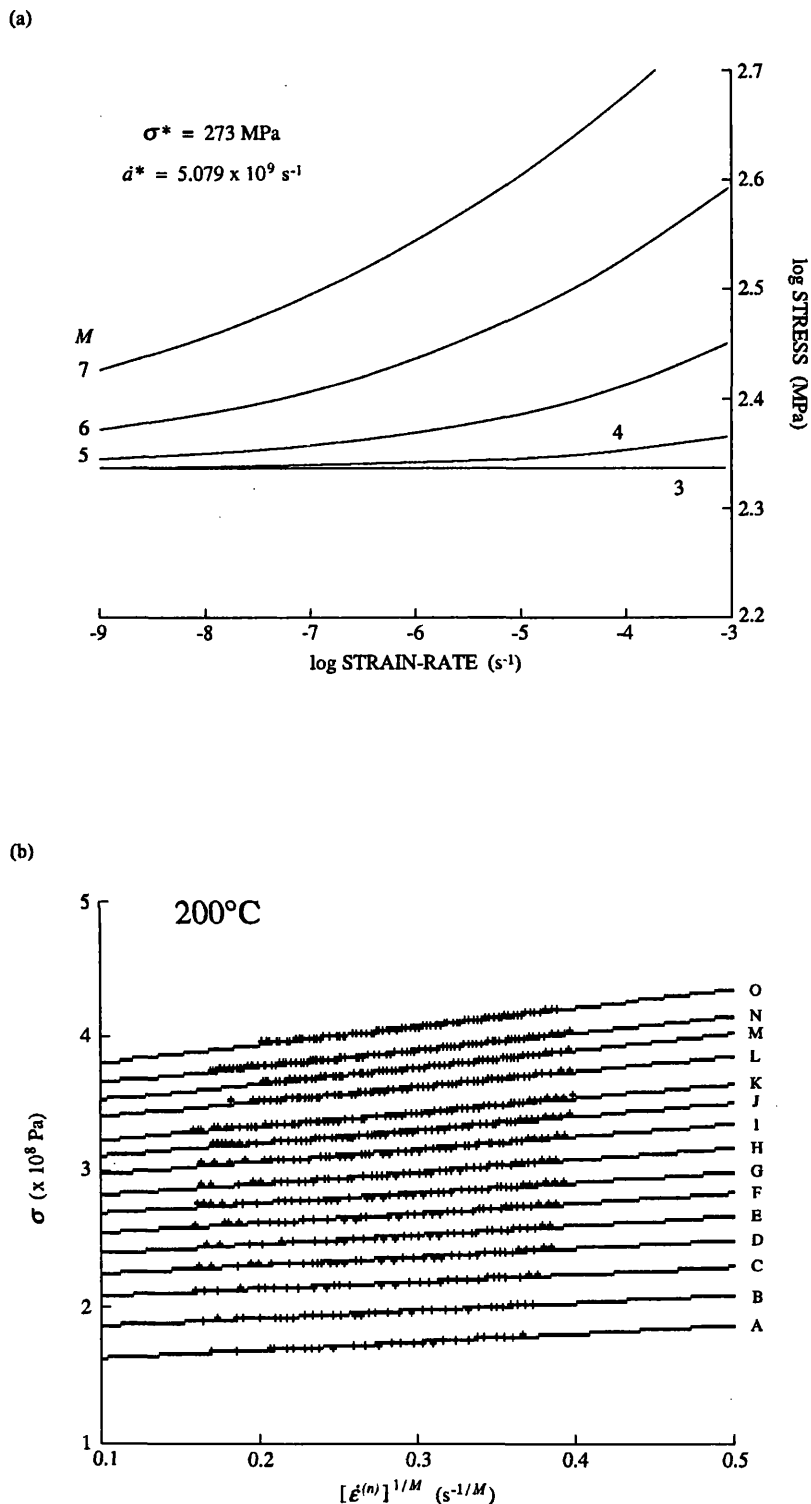


FIG. 11.5. The effect of the parameter fitting errors. (a) The effect of  $M$  on the shape of the relaxation curves at constant  $\dot{\epsilon}^*$  and  $\sigma^*$  (the values of relaxation G at 200°C). (b) Linear fits to the relaxation data cast as  $\sigma$  vs.  $[\dot{\epsilon}^{(n)}]^{1/M}$  using  $M = 10$ , and showing that the linearity of this data is not very sensitive to the magnitude of  $M$  (cf. figure 11.4c where the same data is described with  $M = 4.34$ ).

## 12 EQUATION OF STATE III. THE PLASTIC ELEMENT

The plastic element in Hart's original model is described by (equations 5.10 and 5.11)

$$\ln(\sigma^*/\sigma_a) = (\dot{\varepsilon}^*/\dot{\alpha})^\lambda \quad (12.1)$$

where

$$\dot{\varepsilon}^* = (\sigma^*/G)^m f_0 \exp(-H/RT) \quad (12.2)$$

in which the material parameters  $\lambda$ ,  $m$ ,  $f_0$  and  $H$  are all independent of temperature and mechanical state. In this study values for these parameters were obtained from the load relaxation test, but in other investigations they have also been determined from the results of stress dip tests (cf. § 6.1.3.4 ; Korhonen *et al.*, 1985a). Both types of test provide the same mechanical information and consequently the method of fitting the parameters is the same in each case.

### 12.1 Fitting the parameters

The following procedure for determining the requisite material parameters from relaxation curves depends upon the assumption that they all remain constant during any given relaxation, and that each relaxation is isothermal and truly at constant  $\sigma^*$ .

**12.1.1 Determining  $\lambda$ .** Making the approximation  $\dot{\alpha} = \dot{\varepsilon}^{(n)}$  (§ 5.1.3.2), then equation 12.1 can be rearranged to show that the slope of a constant mechanical state relaxation curve is given by

$$\nu = d\log \sigma / d\log \dot{\varepsilon}^{(n)} = \lambda (\dot{\varepsilon}^* / \dot{\varepsilon}^{(n)})^\lambda \quad (12.3)$$

(§ A3.1.2). Substituting this result back into equation 12.1 and rearranging, then with  $\sigma = \sigma_a$  (§ 5.1.3.2)

$$\ln \sigma = \ln \sigma^* - (\nu / \lambda) \quad (12.4)$$

Hence relaxation data should be linear, with slope  $(-1/\lambda)$  and intercept  $\ln \sigma^*$ , when plotted as  $\ln \sigma$  against  $\nu$ .

**12.1.2 Determining  $\sigma^*$  and  $\dot{\varepsilon}^*$ .** Rearranging equation 12.1 and using  $\dot{\alpha} = \dot{\varepsilon}^{(n)}$  and  $\sigma = \sigma_a$ ,

$$\ln \sigma = \ln \sigma^* - (\dot{\varepsilon}^*)^\lambda (1/\dot{\varepsilon}^{(n)})^\lambda \quad (12.5)$$

The relaxation data should therefore be linear, with slope  $-(\dot{\varepsilon}^*)^\lambda$  and intercept  $\ln \sigma^*$ , when plotted as  $\ln \sigma$  against  $(1/\dot{\varepsilon}^{(n)})^\lambda$ . Hence, with the value of  $\lambda$  given by equation 12.4,  $\sigma^*$  and  $\dot{\varepsilon}^*$  may be found.

**12.1.3 Determining  $m, f_0$  and  $H$ .** Rewriting equation 12.2 as

$$\ln \dot{\varepsilon}^* = m \ln(\sigma^*/G) + \ln f_0 - (H/RT) \quad (12.6)$$

then with the values of  $\sigma^*$  and  $\dot{\varepsilon}^*$  given by equation 12.5 for all the relaxations of interest, and with

$$G = 3.1775 \times 10^{10} - 1.5p - 9.7 \times 10^6(T - 293) \quad (12.7)$$

(§ 10.1.1, where the arithmetic mean of the two values of  $G_0$  is used), then  $m, f_0$  and  $H$  may be found by conducting a multiple linear regression of  $\ln \dot{\varepsilon}^*$  on  $\ln(\sigma^*/G)$  and  $(1/T)$ . For a suite of relaxations generated at constant temperature,  $m$  is also the reciprocal of the scaling slope (§ 4.1.2.1).

## 12.2 Results

The stress / strain curves generated in the multiple load relaxation experiments at 240, 280, 310, 320, 360 and 400°C, together with their corresponding relaxation curves, are shown in figure 12.1. The reloading peaks present in the corresponding stress / strain curves at lower temperatures (figure 11.1) disappear at temperatures above 280°C, and the reloading curves simply rejoin the uninterrupted stress / strain curve, albeit with a transient which occupies an increasing strain as the total strain and temperature is increased. Hence, it is inferred that there were no changes in  $\sigma^*$  during any relaxation (with the possible exception of the two highest strain relaxations J and K at 400°C), and that the size of the reloading transients reflects only increased weak barrier recovery as temperature and  $\sigma^*$  are increased (§ 6.1.4).

The relaxation curves show an increasing degree of downward concavity as temperature is increased, but no change in concavity with the loading strain-rate. At each temperature all the curves may be superposed onto one master relaxation curve by a rigid body translation in a fixed direction, and this direction is independent of temperature (figure 12.2).

**12.2.1 Parameter evaluation.** The full results of the fitting procedure as applied to the relaxation curves shown in figure 12.1 are given in table 12.1. The stresses and strains in the table are those at the start of each relaxation as given by the data reduction procedure (§ 8.4). The values of the material parameters were determined in the following way :

- (i) the  $\log \sigma / \log \dot{\varepsilon}^{(n)}$  data were fitted to a cubic polynomial ;
- (ii) using the experimentally observed strain-rates to calculate  $\sigma$  from the cubic polynomial and  $\nu$  from the derivative of that equation, the data was replotted as  $\ln \sigma$  against  $\nu$  and linearly regressed to determine  $\lambda$  ( $\lambda_{obs}$  in table 12.1) ;
- (iii) the  $\lambda_{obs}$  from every utilized relaxation were sorted into size classes 0.05 wide and a value between the mode and the arithmetic mean was adopted as  $\lambda$  ;
- (iv) using the value of  $\lambda$  obtained from (iii), the experimental stress / strain-rate relaxation data was replotted as  $\ln \sigma$  against  $(1/\dot{\varepsilon}^{(n)})^\lambda$ , and linearly regressed to determine  $\sigma^*$  and  $\dot{\varepsilon}^*$  ;
- (v) the values of  $\sigma^*$  and  $\dot{\varepsilon}^*$  given by (iv) for every utilized relaxation, were multiply regressed on the equation

$$\ln \dot{\varepsilon}^* = A + B \ln (\sigma^* / G) + (C/T) \quad (12.8)$$

and  $f_0$ ,  $m$  and  $H$  determined from the regression coefficients  $A$ ,  $B$  and  $C$  respectively. As a comparison, a value of  $m$  ( $m_{obs}$  in table 12.1) was also determined for each suite of relaxations by linearly regressing the values of  $\sigma^*$  and  $\dot{\varepsilon}^*$  given by (iv) on

$$\ln \dot{\varepsilon}^* = A + B \ln \sigma^* \quad (12.9)$$

where  $m_{obs}$  is the regression coefficient  $B$ .

**12.2.2 The observed values of the material parameters.** The frequency diagram of  $\lambda_{obs}$  values is shown in figure 12.3a. The adopted value of  $\lambda$  was

$$\lambda = 0.2 \quad (12.10)$$

which compares with a mean  $\lambda_{obs}$  of 0.25 and a root mean square error about that mean of 0.13. This value of  $\lambda$  is close to the average of that obtained from other materials.

The observed values of  $\dot{\varepsilon}^*$  are plotted according to equation 12.8 on figure 12.3b. The regression equation is

$$\ln \dot{\varepsilon}^* = 46.91 + 9.170 \ln (\sigma^* / G) - (19880/T) \quad (12.11)$$

where the stress dimensions are pascals, the rate dimensions are per second and temperature is in kelvin. The root mean square error on  $\ln \dot{\varepsilon}^*$  is 0.5736 which corresponds to a root mean square error on the  $\log \dot{\varepsilon}^{(n)}$  location of the relaxation curves of 0.2491. Hence

$$f_0 = 2.367 \times 10^{20} \text{ s}^{-1} ; m = 9.170 ; H = 165.3 \text{ kJ mol}^{-1} \quad (12.12)$$

The mean  $m_{obs}$  is 9.05 with a root mean square error of 1.03. This value of  $m$  lies within the range observed for other materials.

**12.2.3 Uncertainties in the values for the material parameters.** Figure 12.4a-c shows example plots from the three relaxation data curve fitting exercises – parts (i), (ii) and (iv) of the parameter fitting procedure. The root mean square errors on the  $\log \sigma / \log \dot{\varepsilon}^{(n)}$  fits at all temperatures are generally less than 0.5 MPa ; for the  $\ln \sigma / \nu$  fits at temperatures less than 350°C they are generally less than 0.75 MPa, but at higher temperatures they increase to more than 5 MPa as the  $\ln \sigma / \nu$  curves become markedly non-linear (figure 12.5a) ; while for the  $\ln \sigma / (1/\dot{\varepsilon}^{(n)})^\lambda$  fits they are generally less than 1 MPa.

The most significant uncertainty in the values of the material parameters concerns that of  $\lambda$ .  $\lambda$  controls the shape of the fitted relaxation curves such that increasing  $\lambda$  increases the concavity of the relaxation curves, although this effect is only noticeable (within the range of  $\lambda$  values observed in these experiments) near their point of maximum curvature (figure 12.5b). This latter observation is significant because the relaxation curves at the lower temperatures all lie to the high strain-rate side of the point of maximum curvature of the master relaxation curve, whereas those at 360 and 400°C contain this point of maximum curvature near the middle of their accessed strain-rate range. Hence it may be expected that the most reliable estimates of  $\lambda$  are those obtained at 360 and 400°C. Unfortunately it is at  $T > 350^\circ\text{C}$  that the actual fitting errors are largest, for it is at these temperatures that the  $\ln \sigma / \nu$  fits used to evaluate  $\lambda$  are least linear.

The departure of the  $\ln \sigma / \nu$  curves from linearity implies, in principle, that one or more of the material parameters change during relaxation. This would invalidate the use of these plots to determine  $\lambda$ . However,  $\nu$  is extremely sensitive to factors influencing the apparent load / time data and in particular to the neglect of the copper jacket correction. Since the observed departure from linearity is such that it indicates that the observed  $\log \sigma / \log \dot{\varepsilon}^{(n)}$  relaxation curves are too linear at low strain-rates, it is assumed that the non-linearity is an artifact of the neglect of the copper jacket correction under circumstances where rapid recovery / recrystallization is ongoing in the jacket material (§ 9.3.3.2).

Given these observations, it seems unwarranted to assert that  $\lambda$  is dependent on any of the deformation variables.  $\lambda_{obs}$  shows no significant variation with  $\sigma^*$  or with the strain-rate during pre-straining, and the apparent decrease of  $\lambda_{obs}$  with temperature for  $T < 320^\circ\text{C}$  (figure 12.5c) is interpreted to reflect the lack of sensitivity of these relatively flat relaxation curves to the value of  $\lambda$ . The adoption of a value of  $\lambda$  which is less than the mean  $\lambda_{obs}$ , accords with the higher temperature values of  $\lambda_{obs}$ , while also reflecting the observation that overestimates of  $\lambda$  produce a much larger departure from linearity on  $\ln \sigma / (1/\dot{\varepsilon}^{(n)})^\lambda$  plots than underestimates of the same magnitude. Indeed attempts to fit the relaxation data to  $\lambda > 0.2$  were inadequate at 360 and 400°C and so it is anticipated that the adopted value of  $\lambda = 0.2$  is an overestimate rather than an underestimate.

Inspection of figure 12.3b shows that the error on the  $\varepsilon^*$  fits reflects primarily the 360°C results which behave more as if they were generated at 350°C, and the 320°C results which behave as if they were generated at 330°C. The slope of the curves (*i.e.*  $m$ ) is well defined, as is their temperature location (*i.e.*  $H$ ) when considered over the full temperature range. This is confirmed by the excellent fit of all the relaxations to a single temperature-parameterized, master  $\sigma^*$  curve (figure 12.2b). In consequence, excepting the uncertainty introduced into the magnitude of  $\varepsilon^*$  by the uncertainty on  $\lambda$ , it is considered that the errors on  $m$ ,  $f_0$  and  $H$  are small.

**12.2.4 Final statement of the equation of state.** The constitutive equation for the plastic element is given by

$$\ln(\sigma^*/\sigma_a) = (\varepsilon^*/\dot{\alpha})^\lambda$$

where

$$\lambda = 0.2$$

$$\varepsilon^* = (\sigma^*/G)^m f_0 \exp(-H/RT)$$

$$m = 9.170 ; f_0 = 2.367 \times 10^{20} \text{ s}^{-1} ; H = 165.3 \text{ kJ mol}^{-1}$$

$$G = 3.1775 \times 10^{10} - 1.5p - 9.7 \times 10^6(T - 293)$$

and SI units have been employed unless specified. The fits of the relaxation data using this equation and the values of  $\sigma^*$  in table 12.1, are shown in figure 12.1. The fits describe the relaxations within the multiple regression error on  $\varepsilon^*$ .

### 12.3 Discussion

The behaviour of the plastic element is as envisaged by the original Hart model. All of the material parameters are apparently independent of the deformation variables and all are of a comparable magnitude to those found for other materials. The greatest uncertainty concerns the magnitude of  $\lambda$  but the value obtained is nevertheless close to the average found for other materials, which is significant given that it is often assumed that the value of  $\lambda$  is material independent.

It appears therefore that of the three elements in Hart's original model, the fitted equations for the plastic element are the most reliable. However, given effect of Mg solute impurities on the parameters of the friction element, the potential influence of those impurities on the parameters of the plastic element cannot be precluded. An assessment of this possibility and hence of the general applicability of the evaluated equations to other calcitic aggregates, is rendered difficult by the lack of a micromechanical interpretation for equations 12.1 and 12.2.

Table 12.1. The data used to fit the plastic element.

$T$ (°C)	$\dot{\epsilon}^{(n)}$	$\sigma$ (MPa)	$\sigma^*$ (MPa)	$\lambda_{obs}$	$\dot{\epsilon}_{obs}^* (s^{-1})$
$\dot{\epsilon}^{(n)} = 2 \times 10^{-4} s^{-1}$					
D	241	0.036	241	0.436	$5.182 \times 10^{-16}$
E	241	0.044	258	0.816	$1.251 \times 10^{-16}$
F	241	0.053	273	0.733	$5.872 \times 10^{-17}$
G	241	0.064	288	0.539	$4.323 \times 10^{-16}$
H	241	0.082	311	0.553	$5.863 \times 10^{-15}$
I	241	0.102	335	0.374	$5.116 \times 10^{-15}$
J	241	0.125	360	0.420	$9.079 \times 10^{-15}$
K	241	0.149	384	0.352	$1.299 \times 10^{-14}$
L	241	0.176	407	0.326	$4.598 \times 10^{-14}$
$m_{obs} = 11.27$					
$\dot{\epsilon}^{(n)} = 2 \times 10^{-4} s^{-1}$					
F	281	0.083	311	0.405	$4.149 \times 10^{-14}$
G	281	0.110	341	0.409	$1.050 \times 10^{-13}$
H	281	0.133	361	0.293	$2.331 \times 10^{-13}$
I	282	0.154	375	0.337	$3.366 \times 10^{-13}$
J	281	0.171	387	0.348	$6.162 \times 10^{-13}$
K	281	0.189	401	0.266	$5.146 \times 10^{-13}$
L	281	0.209	412	0.277	$7.153 \times 10^{-13}$
M	281	0.231	424	0.250	$7.252 \times 10^{-13}$
N	281	0.254	438	0.259	$1.033 \times 10^{-12}$
$m_{obs} = 9.03$					
$\dot{\epsilon}^{(n)} = 2 \times 10^{-4} s^{-1}$					
B	320	0.024	206	0.393	$2.672 \times 10^{-14}$
C	320	0.036	231	0.282	$4.811 \times 10^{-14}$
D	321	0.046	247	0.253	$1.651 \times 10^{-13}$
E	322	0.062	270	0.169	$3.684 \times 10^{-13}$
F	324	0.085	297	0.206	$1.449 \times 10^{-12}$
G	324	0.109	319	0.255	$1.768 \times 10^{-12}$
H	324	0.140	346	0.249	$4.664 \times 10^{-12}$
I	322	0.174	375	0.215	$1.186 \times 10^{-11}$
	319	0.178	381	0.236	$8.200 \times 10^{-12}$
$m_{obs} = 9.62$					
$\dot{\epsilon}^{(n)} = 2 \times 10^{-4} s^{-1}$					
A	362	0.014	182	0.153	$3.967 \times 10^{-14}$
B	362	0.024	209	0.117	$1.195 \times 10^{-13}$
C	362	0.034	228	0.397	$3.969 \times 10^{-13}$
D	363	0.043	249	0.150	$4.609 \times 10^{-13}$
E	362	0.053	265	0.150	$1.133 \times 10^{-12}$
F	363	0.062	276	0.149	$1.354 \times 10^{-12}$
G	362	0.075	289	0.136	$2.183 \times 10^{-12}$
H	362	0.091	301	0.179	$5.204 \times 10^{-12}$
I	362	0.109	307	0.120	$3.682 \times 10^{-12}$
J	362	0.129	323	0.132	$7.291 \times 10^{-12}$
K	362	0.159	346	0.130	$1.347 \times 10^{-11}$
L	364	0.207	379	0.132	$4.728 \times 10^{-11}$
$m_{obs} = 8.95$					
$\dot{\epsilon}^{(n)} = 2 \times 10^{-4} s^{-1}$					
A	400	0.008	171	0.118	$3.131 \times 10^{-13}$
B	399	0.015	193	0.162	$1.815 \times 10^{-12}$
C	400	0.025	210	0.111	$1.215 \times 10^{-12}$
D	402	0.035	231	0.167	$4.330 \times 10^{-12}$
E	402	0.046	247	0.151	$7.730 \times 10^{-12}$
F	402	0.060	259	0.117	$9.109 \times 10^{-12}$
G	402	0.075	272	0.131	$2.012 \times 10^{-11}$
H	401	0.103	299	0.157	$4.708 \times 10^{-11}$
I	401	0.144	326	0.161	$1.120 \times 10^{-10}$
$m_{obs} = 8.73$					
$\dot{\epsilon}^{(n)} = 6 \times 10^{-5} s^{-1}$					
B	313	0.033	230	0.317	$7.743 \times 10^{-14}$
C	313	0.047	255	0.242	$1.736 \times 10^{-13}$
D	314	0.061	275	0.245	$2.687 \times 10^{-13}$
E	314	0.077	293	0.217	$5.053 \times 10^{-13}$
F	314	0.092	309	0.218	$1.028 \times 10^{-12}$
G	313	0.105	318	0.238	$9.934 \times 10^{-13}$
H	313	0.120	332	0.222	$1.554 \times 10^{-12}$
I	314	0.140	348	0.147	$2.539 \times 10^{-12}$

	$T$ (°C)	$\varepsilon^{(n)}$	$\sigma$ (MPa)	$\sigma^*$ (MPa)	$\lambda_{obs}$	$\varepsilon_{obs}^* (s^{-1})$
J	313	0.163	362	378	0.175	$4.385 \times 10^{-12}$
K	314	0.187	374	389	0.159	$4.400 \times 10^{-12}$
				$m_{obs} = 8.48$		
$\varepsilon^{(n)} = 2 \times 10^{-5} s^{-1}$						
C	311	0.042	247	254	0.332	$8.805 \times 10^{-14}$
D	311	0.056	268	278	0.357	$2.665 \times 10^{-13}$
E	311	0.070	287	297	0.244	$4.694 \times 10^{-13}$
F	310	0.086	305	317	0.232	$9.080 \times 10^{-13}$
G	311	0.100	316	326	0.223	$6.403 \times 10^{-13}$
H	310	0.117	332	347	0.181	$1.689 \times 10^{-12}$
I	313	0.142	350	366	0.151	$2.547 \times 10^{-12}$
J	313	0.178	375	394	0.176	$5.362 \times 10^{-12}$
				$m_{obs} = 8.93$		
$\varepsilon^{(n)} = 6 \times 10^{-6} s^{-1}$						
B	314	0.020	203	212	0.335	$3.373 \times 10^{-14}$
C	314	0.031	226	236	0.170	$5.882 \times 10^{-14}$
D	314	0.041	245	258	0.279	$1.455 \times 10^{-13}$
E	313	0.053	263	275	0.160	$2.300 \times 10^{-13}$
F	314	0.070	282	295	0.111	$2.517 \times 10^{-13}$
G	313	0.087	299	313	0.075	$3.880 \times 10^{-13}$
H	314	0.102	313	332	0.165	$1.029 \times 10^{-12}$
I	314	0.120	326	345	0.164	$1.196 \times 10^{-12}$
J	313	0.136	336	357	0.163	$1.606 \times 10^{-12}$
K	314	0.156	348	369	0.133	$1.750 \times 10^{-12}$
				$m_{obs} = 7.41$		

The fitted data was taken to ten significant figures.

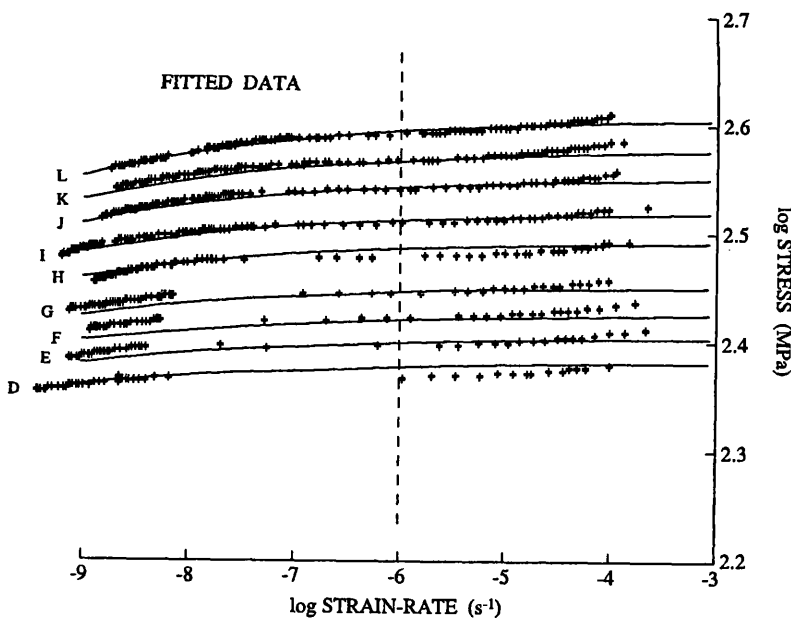
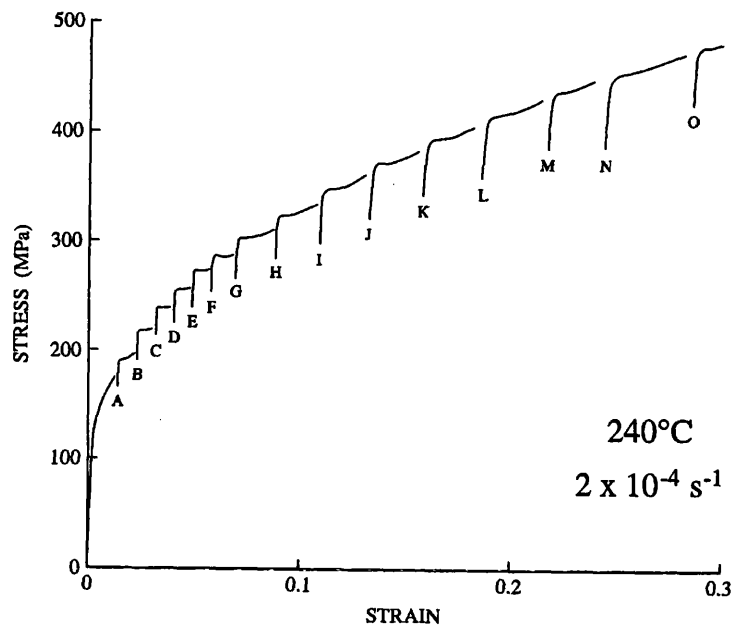


FIG. 12.1. The stress / strain and corresponding load relaxation curves from the multiple relaxation experiment at 240°C. The solid relaxation curves are the fits using the final equation of state (§ 12.2.4) and the values of  $\sigma^*$  in table 12.1. No  $\log \dot{\varepsilon}^{(n)}$  shift has been applied to the fitted curves.

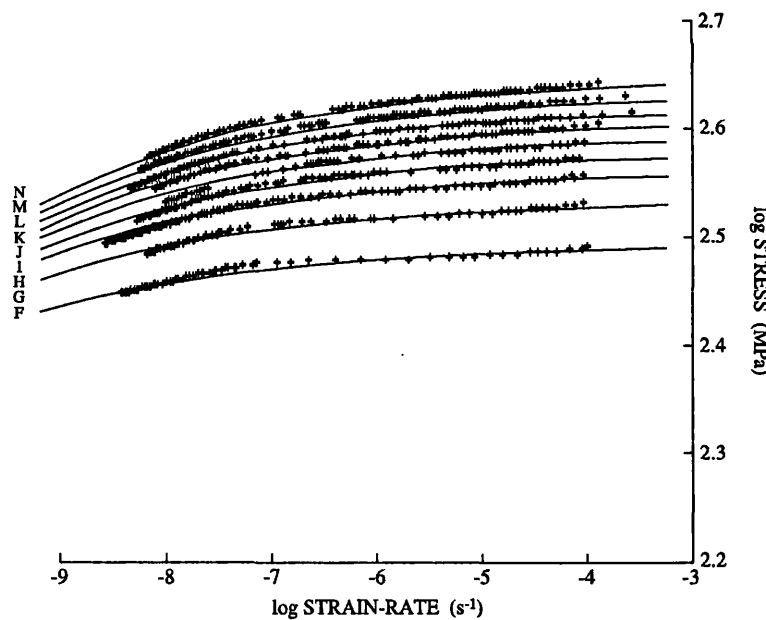
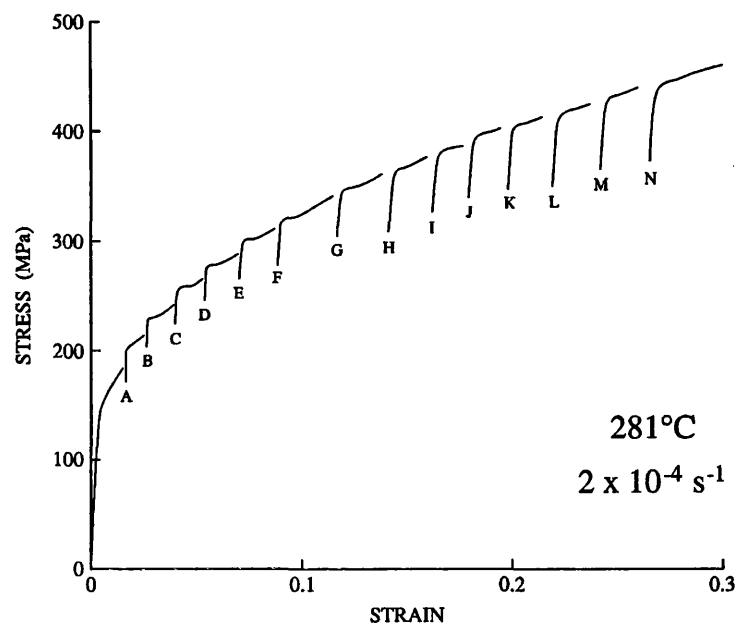


FIG. 12.1 contd. The results of the multiple relaxation experiment at 281°C. The fitted relaxation curves have been given a  $\log \dot{\epsilon}^{(n)}$  shift of -0.18.

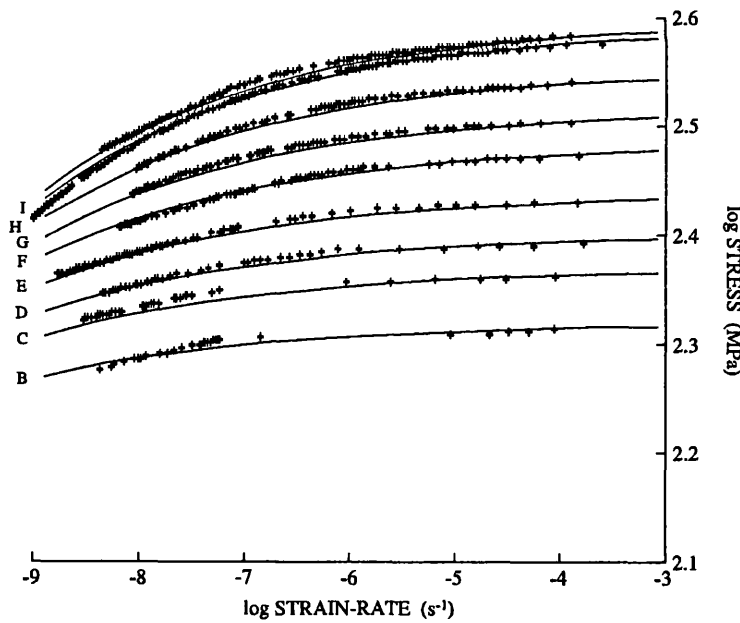
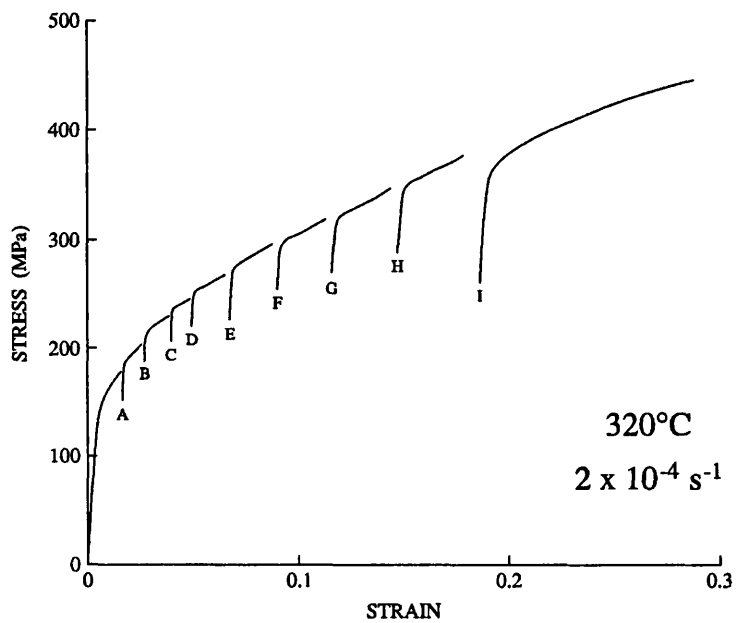


FIG. 12.1 contd. The results of the multiple relaxation experiment at 320°C. The highest strain relaxation was generated from a different specimen at the same conditions. The fitted relaxation curves have been given a  $\log \dot{\epsilon}^{(n)}$  shift of +0.12.

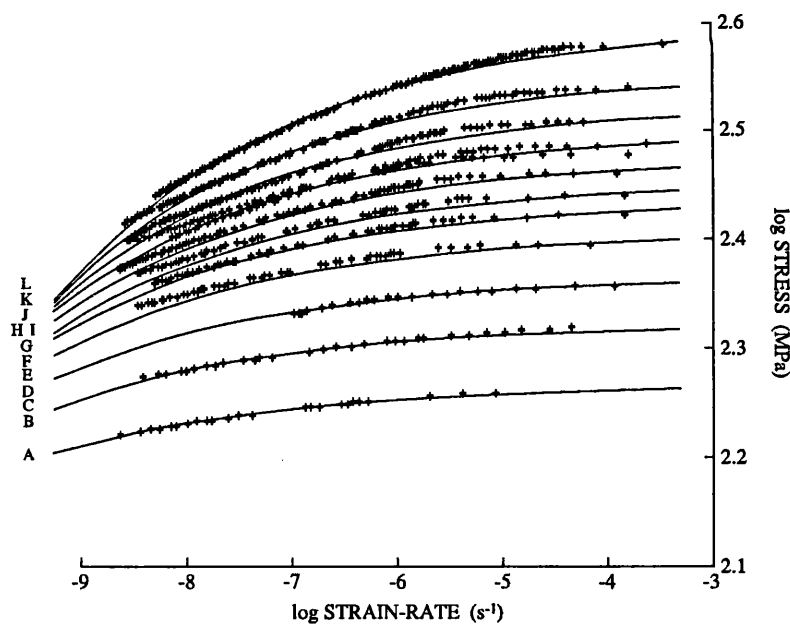
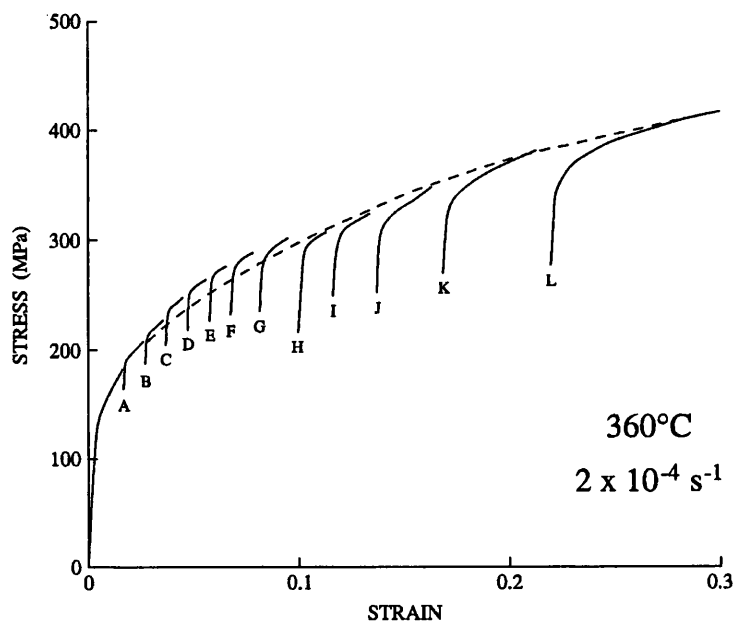


FIG. 12.1 contd. The results of the multiple relaxation experiment at 360°C. The dashed stress / strain curve was generated from a different specimen in an uninterrupted constant displacement-rate test at the same conditions. The fitted relaxation curves have been given a  $\log \dot{\epsilon}^{(n)}$  shift of -0.26.

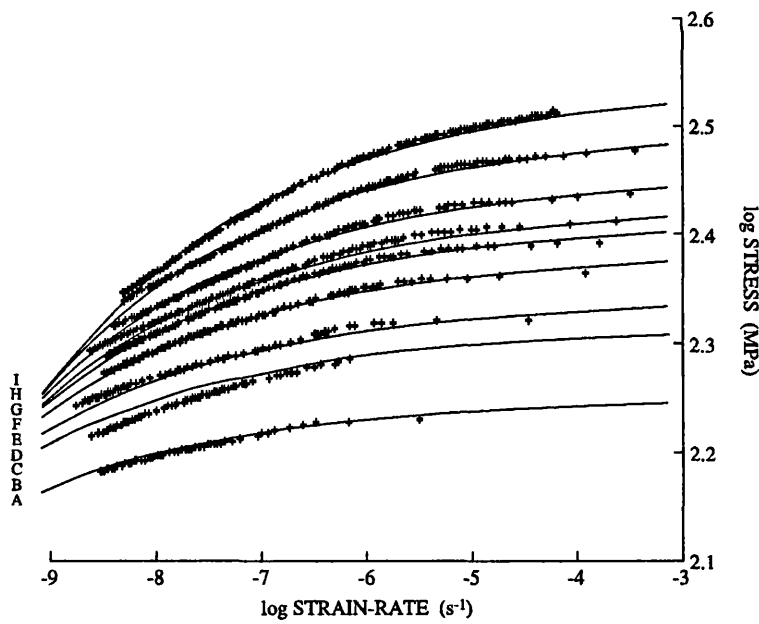
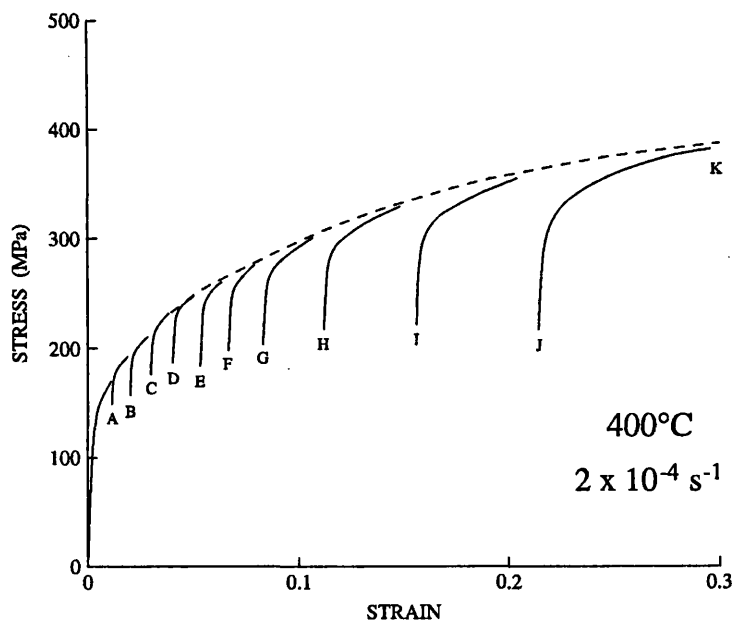


FIG. 12.1 contd. The results of the multiple relaxation experiment at 400°C. The dashed stress / strain curve was generated from a different specimen in an uninterrupted constant displacement-rate test at the same conditions. The fitted relaxation curves have been given a  $\log \dot{\varepsilon}^{(n)}$  shift of -0.09.

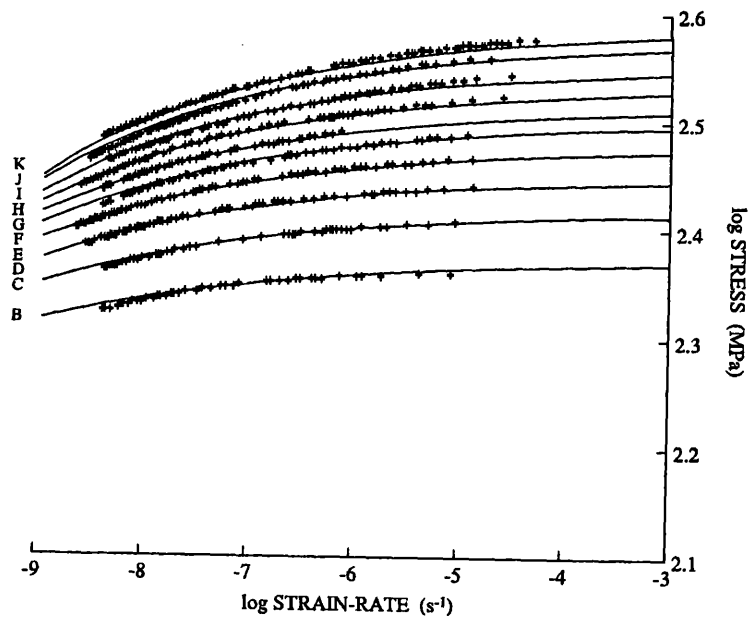
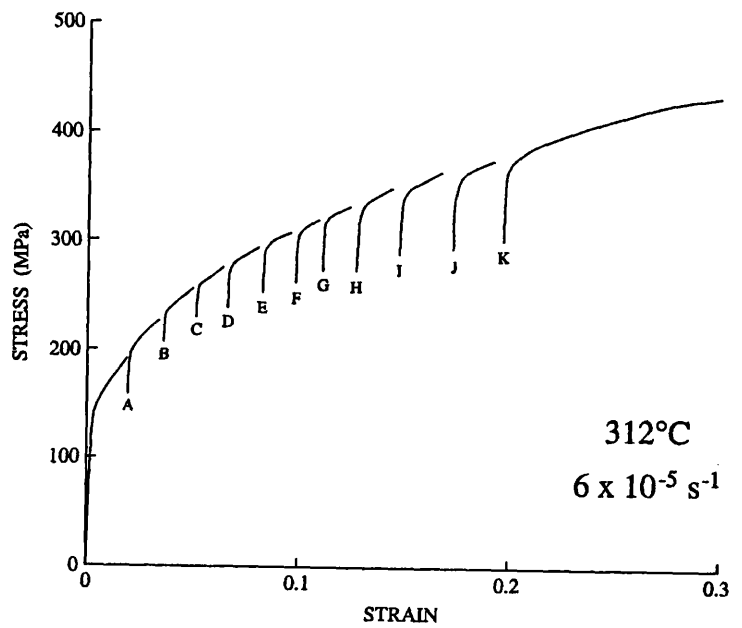


FIG. 12.1 contd. The results of the multiple relaxation experiment at 312°C and  $6 \times 10^{-5} \text{ s}^{-1}$  loading strain-rate. The fitted relaxation curves have been given a  $\log \varepsilon^{(n)}$  shift of +0.04.

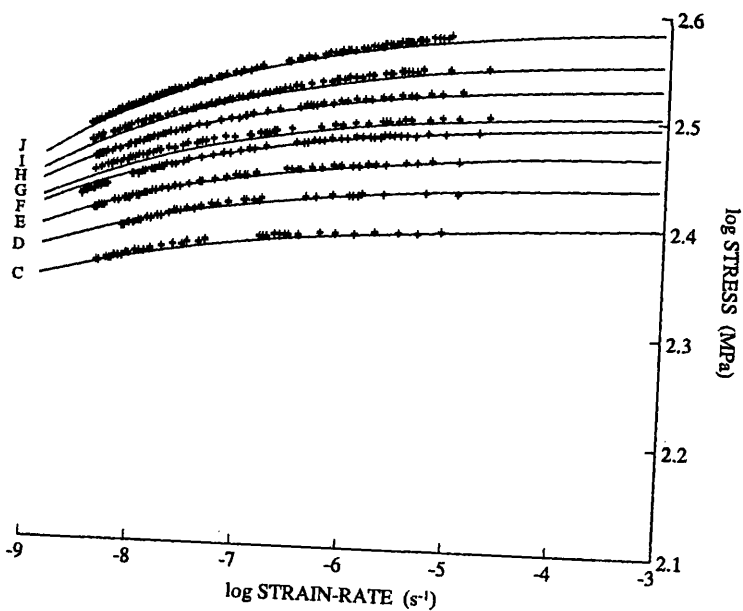
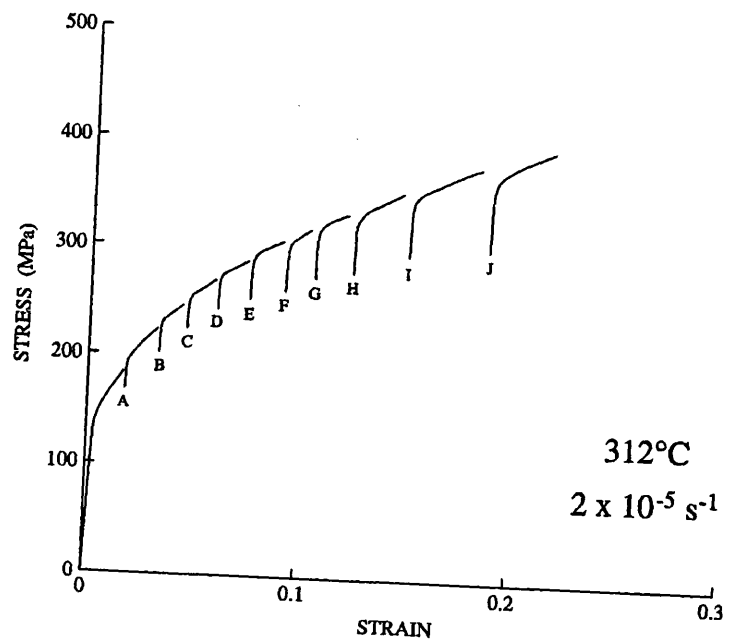


FIG. 12.1 contd. The results of the multiple relaxation experiment at 312°C and  $2 \times 10^{-5} \text{ s}^{-1}$  loading strain-rate. The fitted relaxation curves have been given a  $\log \dot{\epsilon}^{(n)}$  shift of +0.11.

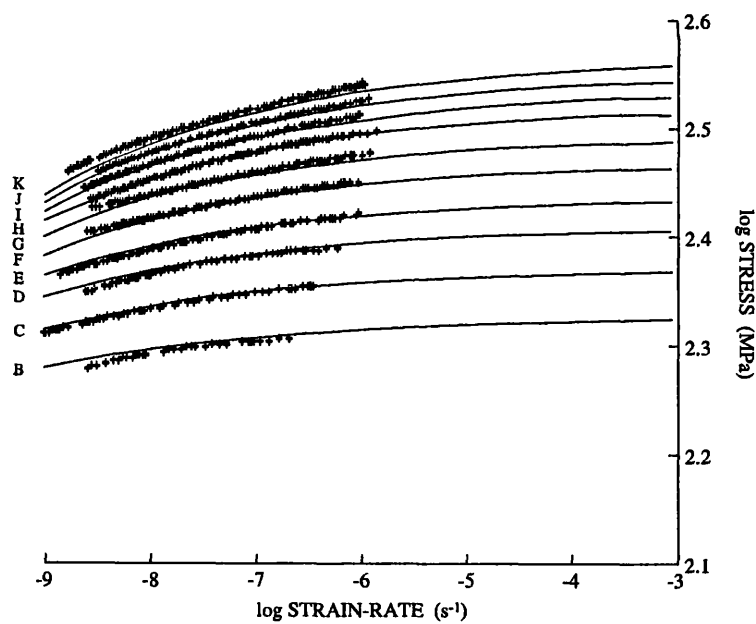
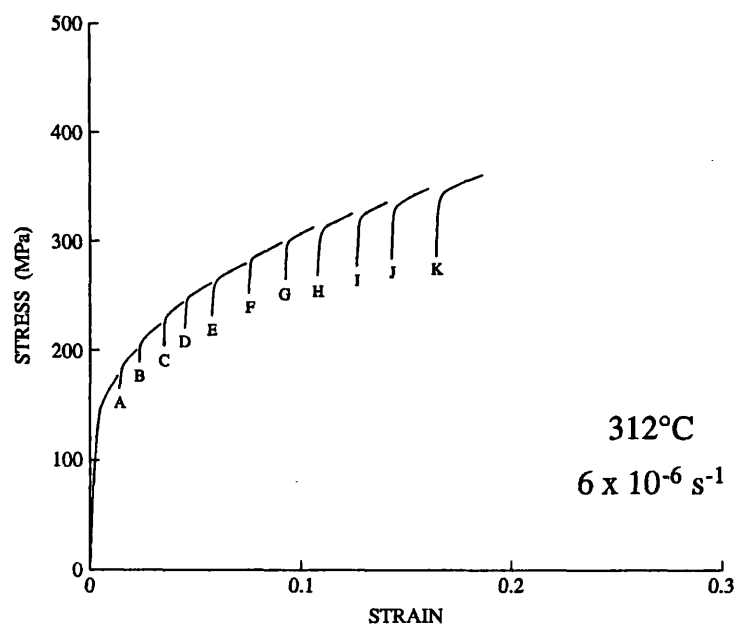
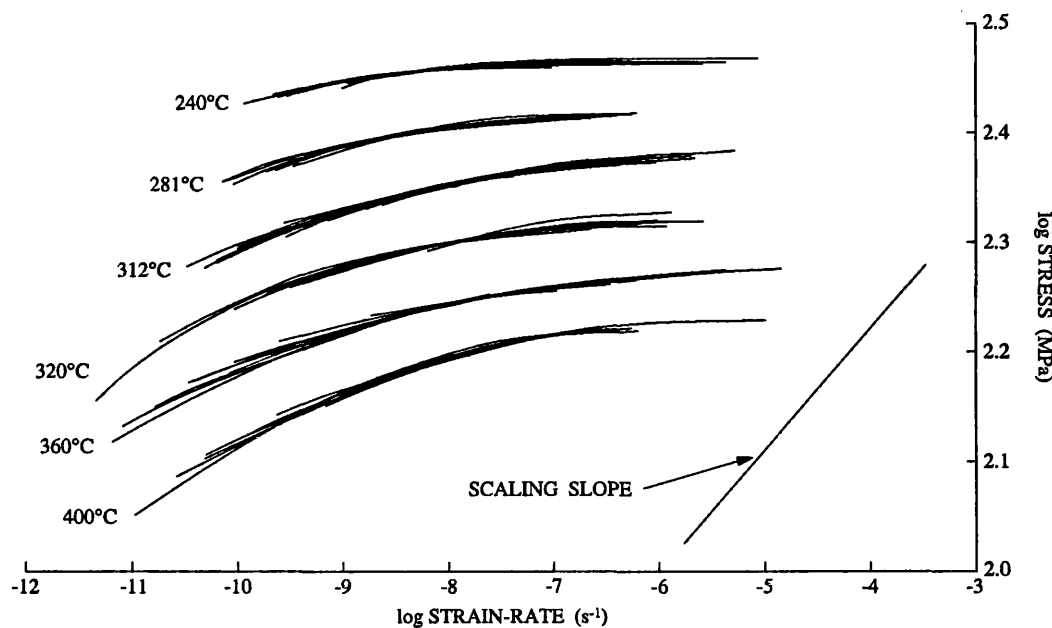


FIG. 12.1 contd. The results of the multiple relaxation experiment at 312°C and  $6 \times 10^{-6} \text{ s}^{-1}$  loading strain-rate. No  $\log \dot{\epsilon}^{(n)}$  shift has been applied to the fitted relaxation curves.

(a)



(b)

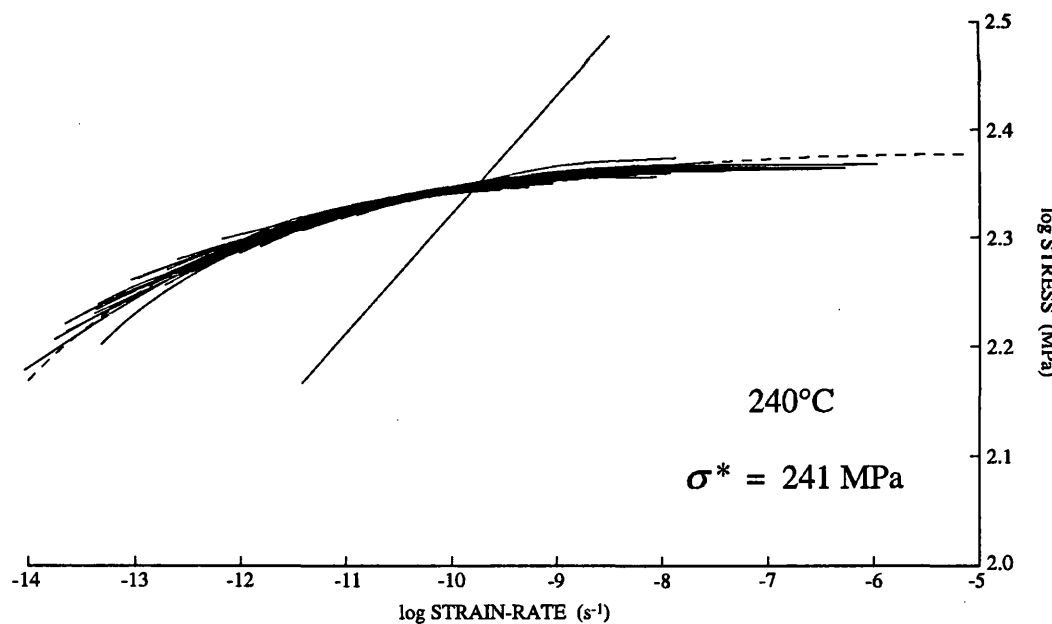


FIG. 12.2. The high homologous temperature master  $\sigma^*$  curves. (a) The master curves for each temperature generated by translating the experimental data within the fitted range of strain-rates (generally  $\log \dot{\epsilon}^{(n)} < -5$ ) in the indicated direction (given by  $1/m$ ). Each of the master curves has a different value of  $\sigma^*$ . The curves from different temperatures do not superpose along the scaling direction because the strain-rates are not temperature parameterized. (b) Composite master curve generated by correcting all (76) of the fitted relaxations to a common temperature and  $\sigma^*$  using the final equation of state, § 12.2.4. The dashed curve is the  $\sigma^*$  curve for this  $\sigma^*$  and temperature, also as given by the final equation of state.

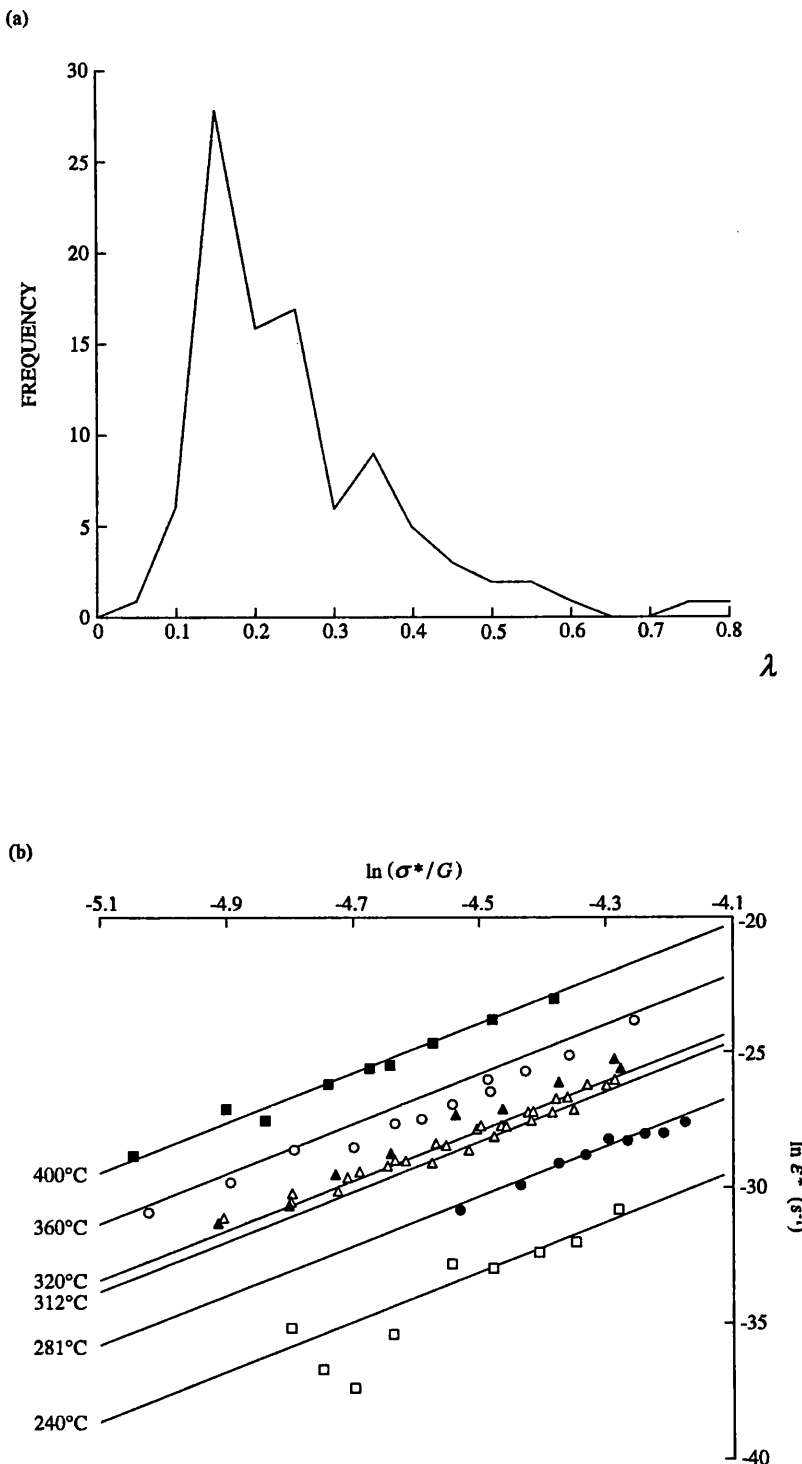


FIG. 12.3. The variation of the material parameters in the plastic element. (a) A frequency plot of the values of  $\lambda_{obs}$ . (b) The variation of  $\dot{\epsilon}^*$  with  $\sigma^*$  and  $T$  and the fits expressing this variation (equation 12.11). The slope of these curves is the reciprocal of the scaling slope shown in figure 12.2.

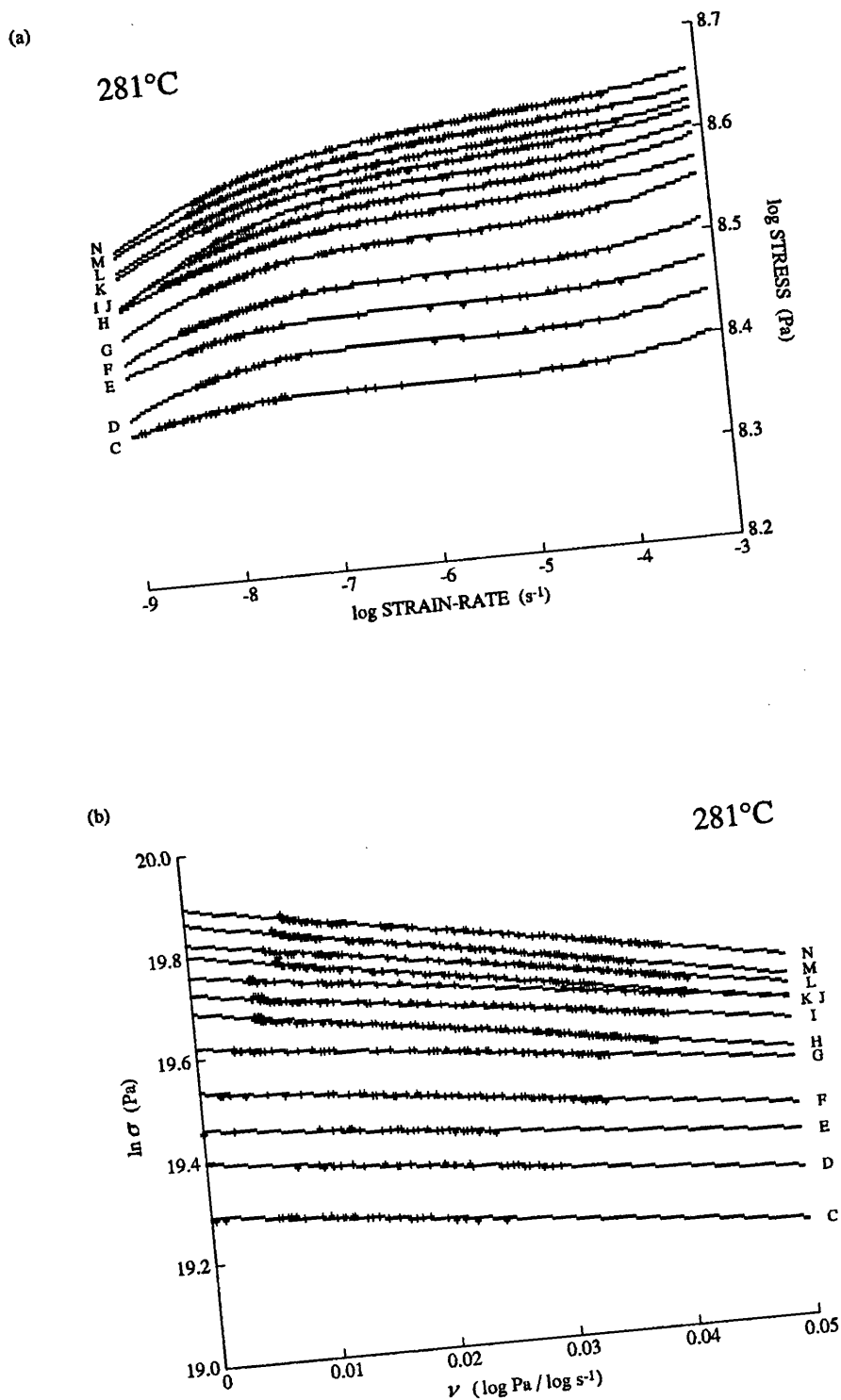


FIG. 12.4. Typical plots from the three relaxation data curve fitting exercises. (a) Polynomial fits to the  $\log \sigma / \log \dot{\varepsilon}^{(n)}$  data. (b) Linear fits to the relaxation data cast as  $\ln \sigma$  vs.  $\nu$ .

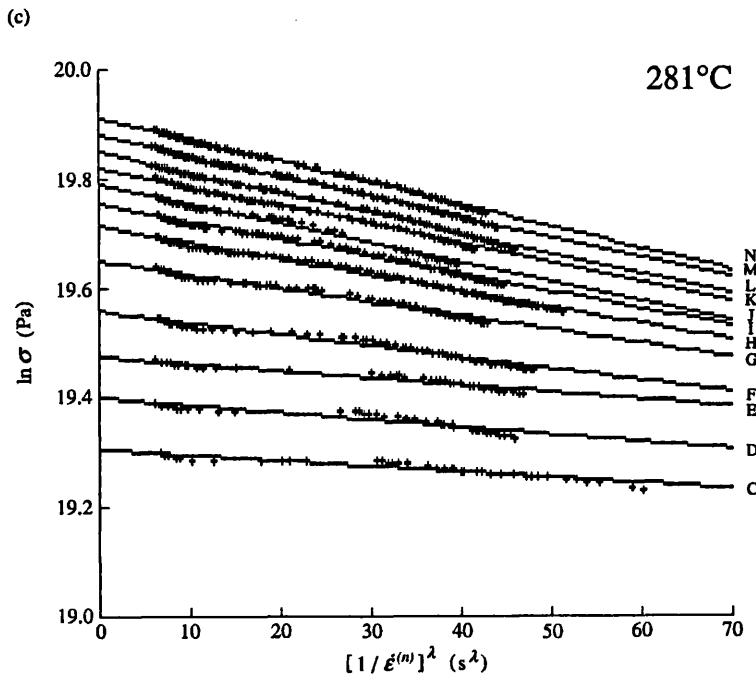


FIG. 12.4 contd. (c) Linear fits to the relaxation data cast as  $\ln \sigma$  vs.  $[1/\dot{\varepsilon}^{(n)}]^\lambda$ .

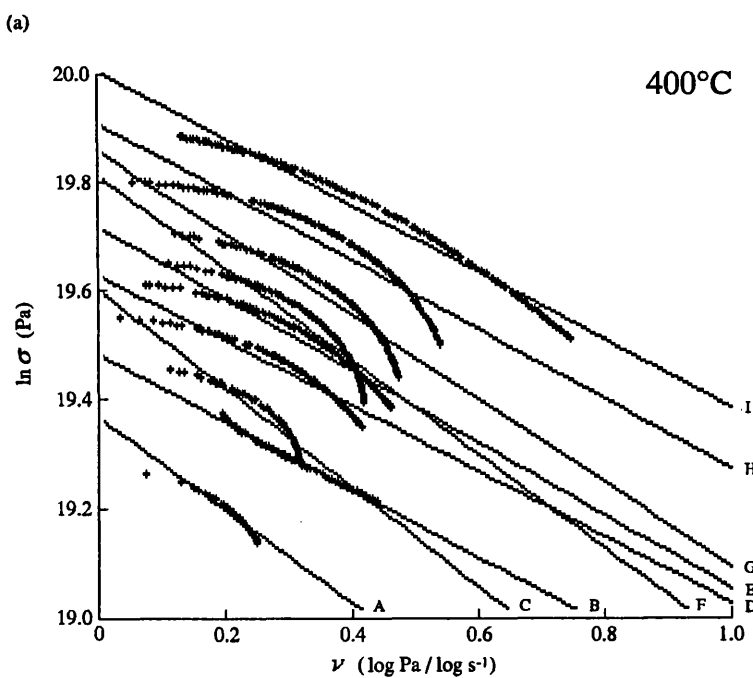


FIG. 12.5. The effect of the parameter fitting errors. (a) The  $\ln \sigma$  vs.  $\nu$  plots of the relaxation data obtained at 400°C showing its markedly non-linear nature.

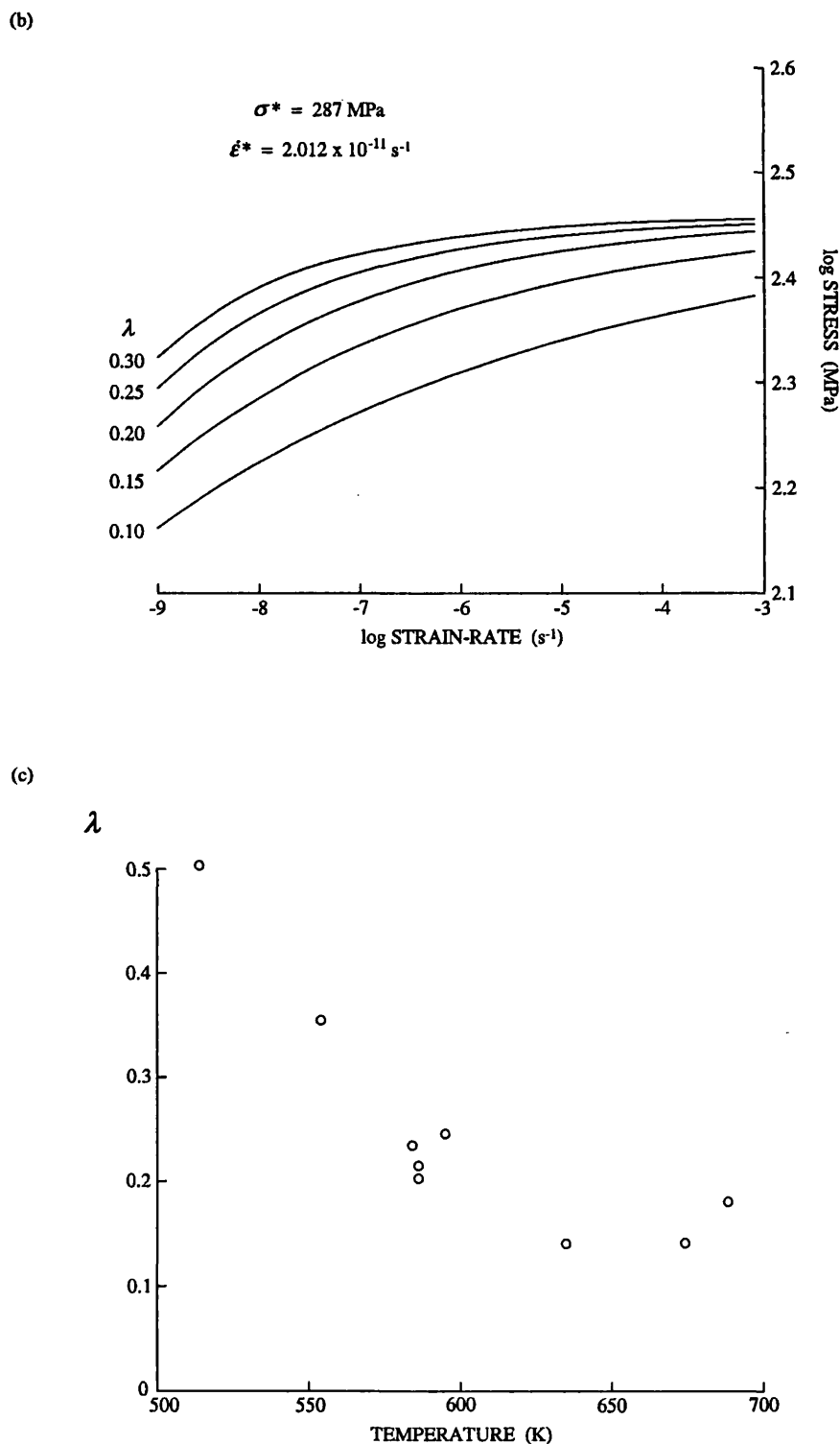


FIG. 12.5 contd. (b) The effect of  $\lambda$  on the shape of the relaxation curves at constant  $\sigma^*$  and  $\dot{\epsilon}^*$  (the values for relaxation G at 400°C). (c) The variation of the mean values of  $\lambda$  obtained at each temperature as a function of temperature.

### 13 EVOLUTION EQUATION I. $T < 0.45 T_m$

The mechanical state evolution equation at  $T < 0.45 T_m$  is described by (equations 5.13 - 5.16)

$$\Gamma = d \ln \sigma^* / d \alpha = \Gamma^* \exp [-(\dot{\alpha}^* / \dot{\alpha})^\Lambda] \quad (13.1)$$

where

$$\Gamma^* = [\zeta / (\sigma^* - \sigma_0^*)]^\eta \quad (13.2)$$

$$\dot{\alpha}^* = (\Gamma^*)^{m^*} f_0^* \exp (-H^*/RT) \quad (13.3)$$

in which the material parameters  $\Lambda$ ,  $\zeta$ ,  $\eta$ ,  $\sigma_0^*$ ,  $m^*$ ,  $f_0^*$  and  $H^*$  are all independent of temperature and mechanical state. In this study values for these parameters were obtained from constant displacement-rate tests conducted at several different displacement-rates and temperatures. This follows the experimental strategy employed in the only other investigation of these parameters (Korhonen *et al.*, 1985b), although the temperature dependence of equations 13.1 - 13.3 has never before been experimentally determined.

#### 13.1 Fitting the parameters

In order to evaluate the parameters in equations 13.1 - 13.3 it is first necessary to determine curves of  $\ln \sigma^*$  against  $\alpha$ . The slope of these curves is  $\Gamma$ , and hence the dependence of  $\Gamma$  on the variables  $\sigma^*$ ,  $\dot{\alpha}$  and  $T$  may be found from the dependence of that slope on these variables.

The following procedure for determining the requisite material parameters from constant displacement-rate stress / strain curves, makes the approximations that the anelastic component of the inelastic strain is negligible so that  $\alpha = \varepsilon^{(n)}$  and  $\dot{\alpha} = \dot{\varepsilon}^{(n)}$  (§ 5.1.3.2), and that the deformation is at constant strain-rate where also  $\varepsilon^{(n)} \approx \dot{\varepsilon}^{(t)}$  (§ 9.5.2).

**13.1.1 Determining  $\sigma^*$ .** The magnitude of  $\sigma^*$  at any time in an isothermal constant inelastic strain-rate test may be determined from the appropriate equations of state using the inelastic strain-rate, temperature and differential stress supported at that time. At  $T < 0.3 T_m$  the appropriate equation of state is the constitutive relation for the friction element, while at  $T > 0.3 T_m$  it is the constitutive relation for the plastic element. These equations may be solved for  $\sigma^*$  using the Newton-Raphson method (§ A3.1.3), by respectively writing them (to avoid mathematical stiffness problems, § 7.1.2.3) as

$$0 = [A \exp(C/T)] [\sigma^*/G]^B [(\sigma - \sigma^*)/G]^M - \dot{\varepsilon}^{(n)} \quad (13.4)$$

(equations 11.4 and 11.9) and

$$0 = \ln \sigma^* - \ln \sigma - \left[ \frac{f_0 \exp(-H/RT)}{\dot{\varepsilon}^{(n)}} \right]^\lambda [G]^{-\lambda m} [\sigma^*]^{\lambda m} \quad (13.5)$$

(equations 12.1 and 12.2).

**13.1.2 Determining  $\Lambda$ .** Equation 13.1 has the same form as equation 12.1 and hence  $\Lambda$  may be determined in the same way as  $\lambda$  (§ 12.1.1). First  $\Gamma$  is determined as a function of  $\sigma^*$  and  $\dot{\varepsilon}^{(n)}$  from the isothermal, constant inelastic strain-rate stress / strain data plotted as curves of  $\ln \sigma^*$  against  $\dot{\varepsilon}^{(n)}$ . The  $\Gamma$  data is then plotted as constant  $\sigma^*$  curves of  $\log \Gamma$  against  $\log \dot{\varepsilon}^{(n)}$ . The slope of these curves is given by

$$(d \log \Gamma / d \log \dot{\varepsilon}^{(n)})_{\sigma^*} = \Lambda (\dot{\alpha}^* / \dot{\varepsilon}^{(n)})^\Lambda \quad (13.6)$$

(§ A3.1.4) which on substituting back into equation 13.1 yields

$$\ln \Gamma = \ln \Gamma^* - [(d \log \Gamma / d \log \dot{\varepsilon}^{(n)})_{\sigma^*} / \Lambda] \quad (13.7)$$

Hence the isothermal  $\Gamma$  data should be linear with slope  $(-1/\Lambda)$  and intercept  $\ln \Gamma^*$ , when plotted as constant  $\sigma^*$  curves of  $\ln \Gamma$  against  $(d \log \Gamma / d \log \dot{\varepsilon}^{(n)})$ .

**13.1.3 Determining  $\Gamma^*$  and  $\dot{\alpha}^*$ .** Equation 13.1 may be written as

$$\ln \Gamma = \ln \Gamma^* - (\dot{\alpha}^*)^A (1/\dot{\varepsilon}^{(n)})^A \quad (13.8)$$

Hence the isothermal  $\Gamma$  data should be linear with slope  $-(\dot{\alpha}^*)^A$  and intercept  $\ln \Gamma^*$ , when plotted as constant  $\sigma^*$  curves of  $\ln \Gamma$  against  $(1/\dot{\varepsilon}^{(n)})^A$ . Therefore with the value of  $\Lambda$  given by equation 13.7,  $\Gamma^*$  and  $\dot{\alpha}^*$  may be found.

**13.1.4 Determining  $\zeta$ ,  $\eta$  and  $\sigma_0^*$ .** If  $\sigma_0^* = 0$ , then equation 13.2 may be written as

$$\ln \Gamma^* = \eta \ln \zeta - \eta \ln \sigma^* \quad (13.9)$$

Hence the values of  $\Gamma^*$  given by equation 13.8, when plotted as  $\ln \Gamma^*$  against  $\ln \sigma^*$ , should be linear with slope  $-\eta$  and intercept  $\eta \ln \zeta$ . If  $\sigma_0^* \neq 0$ , then equation 13.2 may be written as

$$\sigma^* = \sigma_0^* + \zeta \Gamma^{*(-1/\eta)} \quad (13.10)$$

$\zeta$ ,  $\eta$  and  $\sigma_0^*$  may then be found from a non-linear least squares fitting routine. Alternatively, with the correct value of  $\eta$  the values of  $\Gamma^*$  given by equation 13.8, when plotted as  $\sigma^*$  against  $\Gamma^{*(-1/\eta)}$ , should be linear with slope  $\zeta$  and intercept  $\sigma_0^*$ . The value of  $\eta$  can then be chosen as the one which provides the best linear description of the data.

**13.1.5 Determining  $m^*$ ,  $f_0^*$  and  $H^*$ .** Rewriting equation 13.3 as

$$\ln \dot{\alpha}^* = m^* \ln \Gamma^* + \ln f_0^* - (H^*/RT) \quad (13.11)$$

then with the values of  $\Gamma^*$  and  $\dot{\alpha}^*$  given by equation 13.8,  $m^*$ ,  $f_0^*$  and  $H^*$  may be found by conducting a multiple linear regression of  $\ln \dot{\alpha}^*$  on  $\ln \Gamma^*$  and  $(1/T)$ . For a suite of isothermal constant  $\sigma^*$  curves of  $\log \Gamma$  against  $\log \dot{\varepsilon}^{(n)}$ ,  $m^*$  is also the reciprocal of the scaling slope (§ 4.2.2.3).

## 13.2 Results

The stress / strain curves generated in the constant displacement-rate experiments are presented as curves at the same strain-rate but various temperatures in figure 13.1, and as curves at the same temperature but various strain-rates in figure 13.2. To avoid the errors that arise from the indeterminacy of the precise time at which loading begins, the stress / strain curves have been stress and/or strain shifted so that they all have a common stress at a strain of about 0.01. In practice this shifting was necessary for only a few of the curves (all at the highest strain-rates), and the shifts applied were always less than a stress of 5 MPa and a strain of 0.005. All the curves demonstrate an excellently systematic decrease in the stress supported at given strain as temperature is increased and, with the exception of the curves generated at the highest strain-rate ( $6 \times 10^{-4} \text{ s}^{-1}$ ), in the stress supported at given strain as strain-rate is decreased. The difference in the behaviour of the  $6 \times 10^{-4} \text{ s}^{-1}$  curves may reflect the effects of cataclasis (§ 9.4.1), but is sufficiently small to be ignored.

The stresses supported at  $\dot{\varepsilon}^{(t)} = 0.10$  together with the values of  $\sigma^*$  at this strain are given in table 13.1.

**13.2.1 Parameter evaluation.** The values of the material parameters in equations 13.1 - 13.3 were determined in the following way.

(i) The stress / total strain curves were digitized using approximately fifty points per curve in the strain interval 0.01 to 0.32, and were then fitted to a fourth order least squares polynomial as curves of  $\varepsilon^{(t)}$  against  $\sigma$ .

(ii) Each stress / strain curve was converted to a curve of  $\ln \sigma^*$  against  $\varepsilon^{(n)}$ . First the Newton-Raphson method was used to solve the  $\varepsilon^{(t)} / \sigma$  polynomial of the curve for the stress at fifty equally spaced (in strain) points in the strain interval 0.015 to 0.30. Then using these stresses, the inelastic strain was calculated at each point by subtracting the the elastic strain  $\varepsilon^{(e)}$  from  $\varepsilon^{(t)}$ , where

$$\varepsilon^{(e)} = \ln \{1/[1 - (\sigma/E)]\} \quad (13.12)$$

(§ A3.1.5) in which  $E$  is the calcite Young's modulus (equation 10.7). The stresses were also used with the temperature and strain-rate of the test, to calculate  $\sigma^*$  at each point from either equation 13.4 or 13.5. Equation 13.4 was used for the curves generated at  $T < 250^\circ\text{C}$ , and equation 13.5 for the curves generated at higher temperatures. Finally the  $\ln \sigma^* / \varepsilon^{(n)}$  points for each curve were fitted to a sixth order least squares polynomial.

The final  $\ln \sigma^* / \varepsilon^{(n)}$  curves for each temperature are shown in figure 13.3. At temperatures below  $200^\circ\text{C}$  these curves are strain-rate independent *i.e.*  $\Gamma$  (the slope of the curves) is strain-rate independent. At higher temperatures a strain-rate dependence to  $\Gamma$  becomes apparent at the smallest strain-rate.

(iii)  $\Gamma$  ( $= d \ln \sigma^* / d \varepsilon^{(n)}$ ) was determined from each isothermal constant inelastic strain-rate  $\ln \sigma^* / \varepsilon^{(n)}$  curve at 20 MPa intervals of  $\sigma^*$  in the range 200 to 440 MPa (or the maximum  $\sigma^*$  value of the curve). This was done by using the Newton-Raphson method to solve the  $\ln \sigma^* / \varepsilon^{(n)}$  polynomial for  $\varepsilon^{(n)}$  at each required  $\sigma^*$  value, and then by using the  $\varepsilon^{(n)}$  to evaluate the derivative of that polynomial at that  $\sigma^*$ .

The results of this exercise are plotted in figure 13.4 as constant  $\sigma^*$  curves of  $\log \Gamma$  against  $\log \varepsilon^{(n)}$  for all the temperatures investigated. These plots confirm that only at temperatures above  $300^\circ\text{C}$  is  $\Gamma$  appreciably strain-rate dependent, and then only at the highest values of  $\sigma^*$ .

(iv) The constant  $\sigma^*$ ,  $\log \Gamma / \log \varepsilon^{(n)}$  data is not sufficiently smooth to permit a reliable estimate of  $\Lambda$  by the method described above (§ 13.1.2). Hence it was assumed that  $\Lambda = \lambda$  as seems to be warranted from experiments on other materials (§ 4.2.2.3).

(v) Using the value of  $\Lambda$  given by (iv), the data presented on figure 13.4 (determined in iii) was replotted as  $\ln \Gamma$  against  $(1/\varepsilon^{(n)})^\Lambda$ . The data belonging to each value of  $\sigma^*$  and  $T$  was then linearly regressed to determine  $\Gamma^*$  and  $\alpha^*$  at those values of  $\sigma^*$  and  $T$ .

(vi) The values of  $\Gamma^*$  determined from (v) were plotted as  $\ln \Gamma^*$  against  $\ln \sigma^*$  and were linearly regressed on the equation

$$\ln \Gamma^* = A + B \ln \sigma^* \quad (13.13)$$

and  $\zeta$  and  $\eta$  determined from the regression coefficients  $A$  and  $B$ . For the final fits only the data from  $T < 250^\circ\text{C}$  was used. The data from higher temperatures had the same slope (*i.e.* the same value of  $B$ ) but at given  $\Gamma^*$  were shifted to a value of  $\sigma^*$  which was 15 MPa larger than that observed at lower temperatures. Since this is about the same difference in  $\sigma^*$  as arises from fitting the equations for the friction and plastic elements to the same mixed concavity relaxation curves at  $240^\circ\text{C}$  (*cf.* tables 11.1 and 12.1), it was interpreted as reflecting the errors arising from the use of two different equations of state (equations 13.4 and 13.5) to evaluate  $\sigma^*$  rather than

any real change in  $A$ .

The  $\ln \Gamma^* / \ln \sigma^*$  plot is shown in figure 13.5a and is compared with the  $\sigma^* / \Gamma^{*(1/\eta)}$  plot generated using the determined value of  $\eta$  (figure 13.5b).

(vii) the values  $\dot{\alpha}^*$  given by (v) were multiply regressed on the equation

$$\ln \dot{\alpha}^* = A + B \ln \Gamma^* + (C/T) \quad (13.14)$$

and  $f_0^*$ ,  $m^*$  and  $H^*$  determined from the regression coefficients  $A$ ,  $B$  and  $C$  respectively. For each value of  $\dot{\alpha}^*$  the value of  $\Gamma^*$  was determined from equation 13.13 using the appropriate  $\sigma^*$  ( $\sigma^* - 15$  MPa for all  $T > 250^\circ\text{C}$ ) value. Since many of the  $\ln \Gamma / (1/\dot{\varepsilon}^{(n)})^\Lambda$  curves of (v) yielded  $\dot{\alpha}^* = 0$  within the fitting error, only those  $(\dot{\alpha}^*, \Gamma^*, T)$  data sets in which  $\dot{\alpha}^*$  was significantly greater than zero were used. The remaining data is shown in figure 13.6.

### 13.2.2 The observed values of the material parameters. From (iv)

$$\Lambda = 0.2 \quad (13.15)$$

The regression equation 13.13 is

$$\ln \Gamma^* = 50.52 - 2.522 \ln \sigma^* \quad (13.16)$$

where the stress dimensions are pascals and the root mean square error on  $\ln \Gamma^*$  is 0.0509.

Hence

$$\zeta = 499.4 \text{ MPa} ; \eta = 2.522 ; \sigma_0^* = 0 \quad (13.17)$$

The values of  $\zeta$  and  $\eta$  are of similar magnitude to those obtained in other materials, while the value of  $\sigma_0^*$  is consistent with the large grain-size of Carrara marble (§ 4.2.2.3).

The regression equation 13.14 is

$$\ln \dot{\alpha}^* = 45.32 - 11.42 \ln \Gamma^* - (29880/T) \quad (13.18)$$

where the stress dimensions are pascals, the rate dimensions are per second, temperature is in kelvin, and where the root mean square error on  $\ln \dot{\alpha}^*$  is 1.302. Hence

$$f_0^* = 4.787 \times 10^{19} \text{ s}^{-1} ; m^* = -11.42 ; H^* = 248.4 \text{ kJ mol}^{-1} \quad (13.19)$$

The value of  $m^*$  is similar to that of OFHC copper, the only other material for which it has been determined. The value of  $H^*$  is the same (within error) as reported previously for the apparent activation enthalpy of exponential law creep (equation 1.1) in Carrara marble (Rutter, 1974).

**13.2.3 Uncertainties in the values of the material parameters.** Figure 13.7a shows an example of the  $\dot{\varepsilon}^{(t)} / \sigma$  fits from which it is apparent that the fitted polynomials provide an excellent description of the experimental stress / strain curves. The same is true of the  $\ln \sigma^* / \dot{\varepsilon}^{(n)}$  fits (figure 13.3), and hence it follows that these two polynomial fitting exercises do not introduce any significant error into the determinations of  $\Gamma(\sigma^*, \dot{\varepsilon}^{(n)})$ . However, the value of  $\Gamma$  is extremely sensitive to the slope of the experimental stress / strain curves. Hence even very small non-systematic variations in this slope as a function of temperature and strain-rates (*i.e.* departures of the stress / strain curves from perfect reproducibility) lead to a scatter when the data from different experiments is combined to plot a constant  $\sigma^*$  curve of  $\log \Gamma$  against  $\log \dot{\varepsilon}^{(n)}$  (figure 13.4). This scatter presents a highly significant constraint on the parameter fitting exercise because it prevents  $\Lambda$  from being reliably determined, and because it causes a scatter on the  $\ln \Gamma / (1/\dot{\varepsilon}^{(n)})^\Lambda$  plots (figure 13.7b) which are used to determine  $\Gamma^*$  and  $\dot{\alpha}^*$  and hence all the other parameters.

The assumption that  $\Lambda = \lambda$  seems justified on the grounds that it makes explicit the correspondence between flow and work hardening behaviour as a function of strain-rate and

temperature (cf. equations 12.1 and 13.1), *i.e.* a transition in flow behaviour results in a transition of work hardening behaviour and *vice versa* (Korhonen *et al.*, 1985b). Hence since the uncertainty on  $\lambda$  is believed to be small (§ 12.3), then that should also be true of  $\Lambda$ .

The scatter of the  $\Gamma$  data is approximately the same for each constant  $\sigma^*$  curve, and consequently it has much less significance on the value of  $\eta$  than on  $\zeta$  when the magnitudes of both are determined from the values of  $\Gamma^*$  given by the intercepts of the  $\ln \Gamma / (1/\dot{\varepsilon}^{(n)})^\Lambda$  linear fits. The uncertainty of  $\eta$  seems to be small given the quality of the linear fit to the  $\ln \Gamma^* / \ln \sigma^*$  data (figure 13.5a). Moreover, given the quality of the linear fit there is no justification for fitting  $\sigma_0^* \neq 0$  even though the  $\sigma^* / \Gamma^{*(1/\eta)}$  plot using  $\eta = 2.522$  (figure 13.5b) is linear and yields  $\sigma_0^* = 63.56$  MPa (and  $\zeta = 445.7$  MPa).

The scatter of the  $\Gamma$  data on the  $\ln \Gamma / (1/\dot{\varepsilon}^{(n)})^\Lambda$  fits influences significantly the slope of those fits and hence the value of  $\alpha^*$ . This problem is compounded by the fact that within the temperature and strain-rate range investigated the variation in  $\alpha^*$  is small. The uncertainty on  $\alpha^*$  is reflected in the non-linearity observed between  $\ln \alpha^*$  and  $\ln \Gamma^*$  (figure 13.6). However, excepting this non-linearity, the slope of the  $\ln \alpha^* / \ln \Gamma^*$  relationship (*i.e.*  $m^*$ ) and the temperature dependence of  $\ln \alpha^*$  (*i.e.*  $H^*$ ), both appear to be well constrained.

**13.2.4 Final statement of the evolution equation.** The  $\sigma^*$  evolution equation at  $T < 0.45 T_m$  is

$$\Gamma = d \ln \sigma^* / d \alpha = \Gamma^* \exp [-(\alpha^*/\alpha)^\Lambda]$$

where

$$\begin{aligned} \Lambda &= 0.2 \\ \Gamma^* &= [\zeta / (\sigma^* - \sigma_0^*)]^\eta \\ \zeta &= 499.4 \text{ MPa} \quad ; \quad \eta = 2.522 \quad ; \quad \sigma_0^* = 0 \\ \alpha^* &= (\Gamma^*)^{m^*} f_0^* \exp (-H^*/RT) \\ f_0^* &= 4.787 \times 10^{19} \text{ s}^{-1} \quad ; \quad m^* = -11.42 \quad ; \quad H^* = 248.4 \text{ kJ mol}^{-1} \end{aligned}$$

and SI units have been employed unless specified. The fits to the  $\log \Gamma / \log \dot{\varepsilon}^{(n)}$  data using this equation are shown in figure 13.4. For all  $T > 250^\circ\text{C}$  the fitted curves correspond to a value of  $\sigma^*$  which is 15 MPa less than that of the plotted  $\Gamma$  data (cf. § 13.2.1).

### 13.3 Discussion

Within the parameter fitting constraints posed by the difficulty of precisely reproducing the values of  $\Gamma$  in different tests, the behaviour of the  $\sigma^*$  evolution equation is as envisaged by Korhonen *et al.* (1985b) and adopted here for use in Hart's original model. All of the material parameters are apparently independent of the deformation variables and all are of a magnitude which corresponds with that expected. However, despite this, the general applicability of the values obtained for the material parameters remains unclear. This reflects partly the uncertainty on the parameters due to the fitting errors, and partly the unknown influence of mechanical twinning on the results.

To reduce the uncertainty on the parameters due to the fitting errors it is necessary either to reduce the scatter in  $\Gamma$  values primarily responsible for those errors, or to reduce the influence of that scatter on the parameter fitting procedures. Since the reproducibility of the stress / strain curves generated in this study is excellent given the technical limitations imposed by conducting experiments at elevated confining pressure, it seems unlikely that the scatter in  $\Gamma$

values can ever be significantly reduced. To reduce the influence of the scatter in  $\Gamma$  on the fitting procedures, it is necessary to obtain more data under conditions in which  $\Gamma$  is strain-rate sensitive. However, even at the highest permissible temperatures (400°C) this would require experiments conducted at a strain-rate of at least an order of magnitude slower than the slowest employed here, while at lower temperatures strain-rates substantially smaller than this would be necessary. Such tests would be of a prohibitively long duration.

If the observation that  $\sigma_0^* = 0$  is accurate then it suggests that as expected the overall deformation behaviour is not significantly influenced by any interactions between the dislocations and the twin boundaries (§ 9.4.2). However, twinning must be responsible for some of the strain experienced by the aggregate and hence it will affect the apparent value of  $\Gamma$ . Without knowing the magnitude of this strain as a function of the applied stress, it is difficult to ascertain precisely how significant this effect is.

If significant, these uncertainties pose considerable problems not only for the application of the equations to other deformation histories / calcitic aggregates, but also for the extrapolation of the equations (and hence Hart's model, § 6.4.3.3) to  $T > 0.45 T_m$ . In the absence of theoretical constraints, some insight into the significance of the problems may be gained by using the equations to simulate deformation tests and by then comparing the results with actual experimental data (*cf.* § 7.1). Although this is a simple task, it has yet to be attempted.

Table 13.1. The stresses supported at a total strain of 0.10 in the constant displacement-rate experiments.

$T$ (°C)	$\dot{\epsilon}^{(i)}$ ( $s^{-1}$ )	$\sigma$ (MPa)	$\sigma^*$ (MPa)
121	$6 \times 10^{-4}$	383	309
121	$2 \times 10^{-4}$	365	302
121	$6 \times 10^{-5}$	352	298
121	$2 \times 10^{-5}$	347	299
121	$6 \times 10^{-6}$	344	302
121	$6 \times 10^{-7}$	335	300
161	$6 \times 10^{-4}$	360	302
163	$2 \times 10^{-4}$	351	303
160	$6 \times 10^{-5}$	339	300
159	$2 \times 10^{-5}$	334	301
161	$6 \times 10^{-6}$	325	298
161	$6 \times 10^{-7}$	324	303
200	$6 \times 10^{-4}$	333	293
200	$2 \times 10^{-4}$	338	306
199	$6 \times 10^{-5}$	327	302
200	$2 \times 10^{-5}$	323	304
199	$6 \times 10^{-6}$	321	306
199	$6 \times 10^{-7}$	318	308
217	$2 \times 10^{-4}$	332	307
240	$6 \times 10^{-4}$	320	297
239	$2 \times 10^{-4}$	325	308
241	$6 \times 10^{-5}$	318	307
241	$2 \times 10^{-5}$	315	308
240	$6 \times 10^{-6}$	317	312
240	$6 \times 10^{-7}$	311	308
281	$6 \times 10^{-4}$	314	317
279	$2 \times 10^{-4}$	317	321
280	$6 \times 10^{-5}$	310	315
279	$2 \times 10^{-5}$	310	316
281	$6 \times 10^{-6}$	309	317
277	$6 \times 10^{-7}$	303	314
311	$6 \times 10^{-4}$	307	312
312	$6 \times 10^{-5}$	308	315
314	$2 \times 10^{-5}$	306	316
313	$6 \times 10^{-6}$	307	319
320	$6 \times 10^{-4}$	302	307
321	$2 \times 10^{-4}$	310	317
321	$6 \times 10^{-5}$	302	310
319	$2 \times 10^{-5}$	302	311
319	$6 \times 10^{-6}$	306	319
320	$6 \times 10^{-7}$	289	308
360	$6 \times 10^{-4}$	298	305
362	$2 \times 10^{-4}$	303	313
359	$6 \times 10^{-5}$	297	309
361	$2 \times 10^{-5}$	297	313
359	$6 \times 10^{-6}$	296	316
358	$6 \times 10^{-7}$	277	305
400	$6 \times 10^{-4}$	291	301
401	$2 \times 10^{-4}$	299	313
400	$6 \times 10^{-5}$	285	302
401	$2 \times 10^{-5}$	287	309
400	$6 \times 10^{-6}$	287	317
397	$6 \times 10^{-7}$	256	291
418	$2 \times 10^{-4}$	289	305

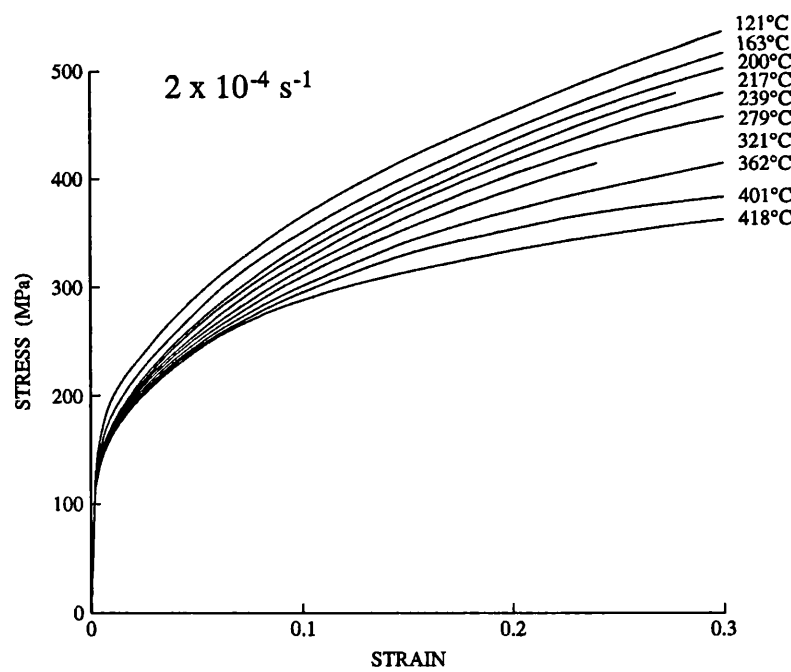
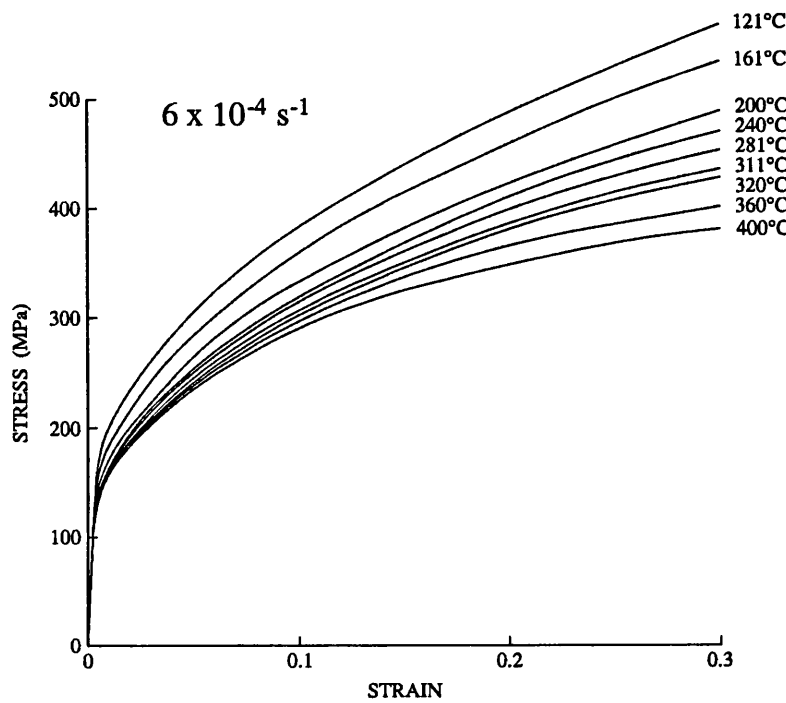


FIG. 13.1 The stress / strain curves generated in the uninterrupted constant displacement-rate experiments plotted as a function of temperature at constant 'strain-rate'.

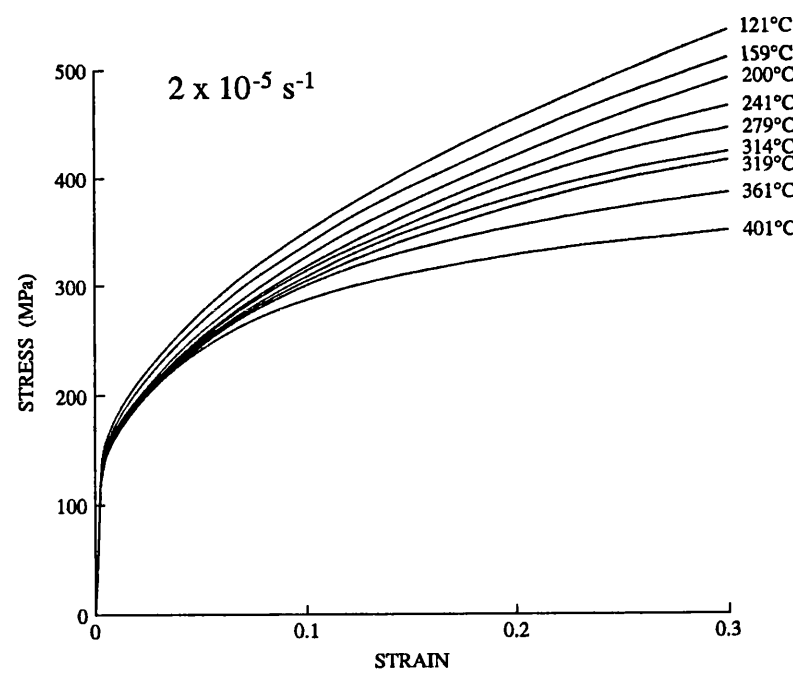
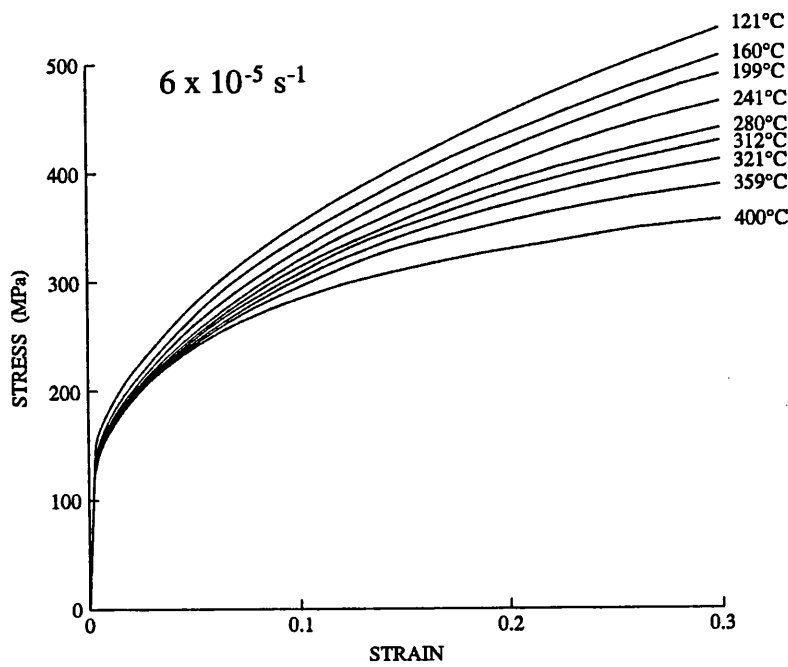


FIG. 13.1 contd.

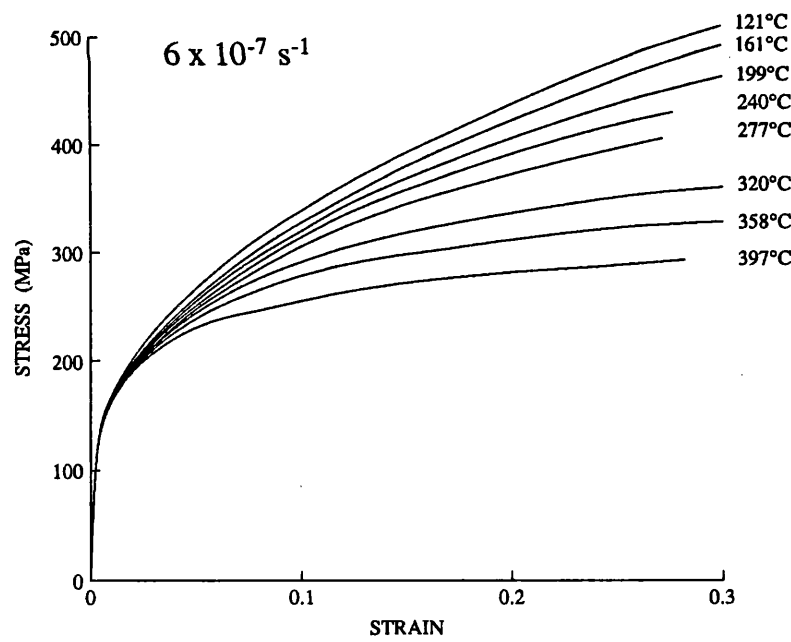
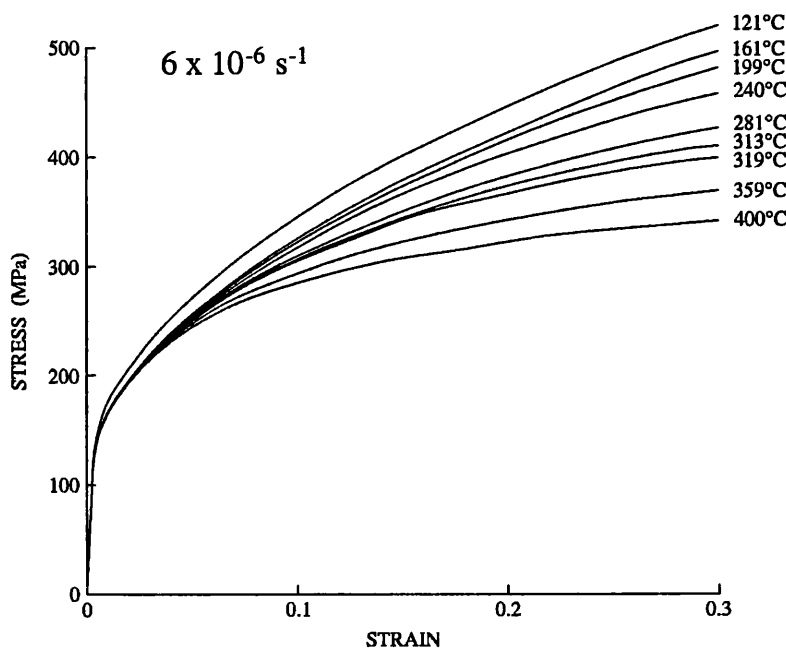


FIG. 13.1 contd.

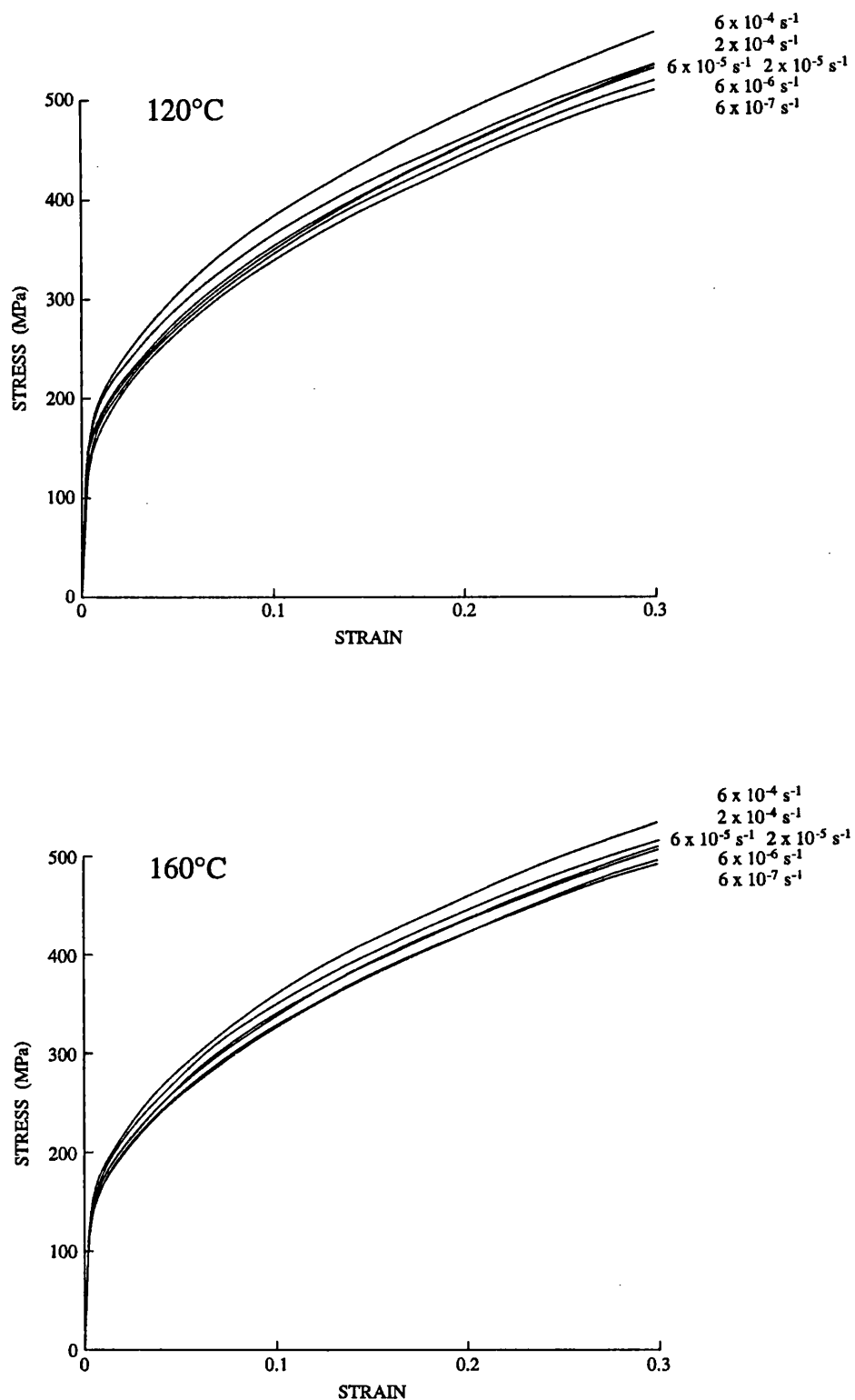


FIG. 13.2. The stress / strain curves of figure 13.1 replotted as a function of strain-rate at constant temperature.

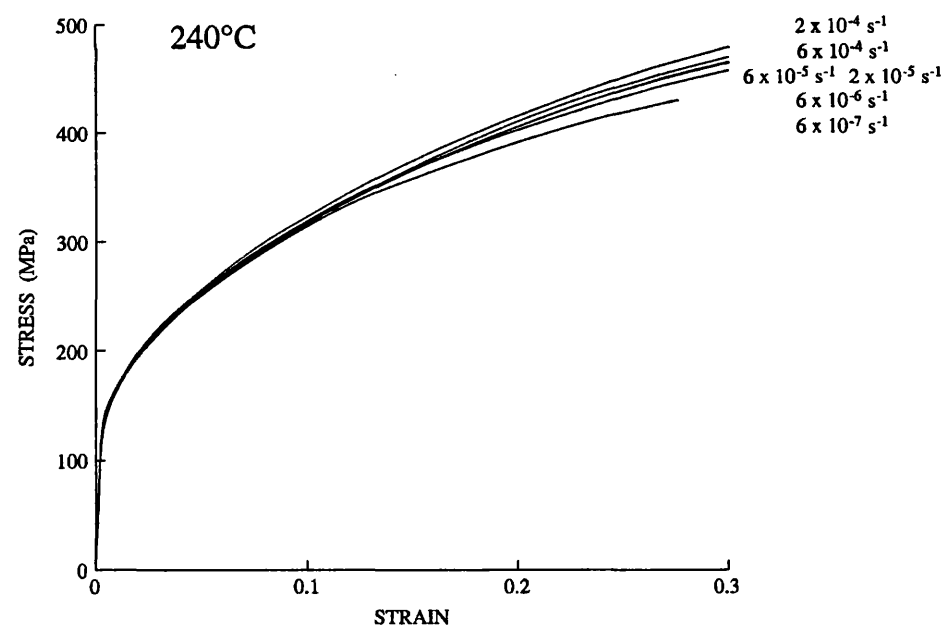
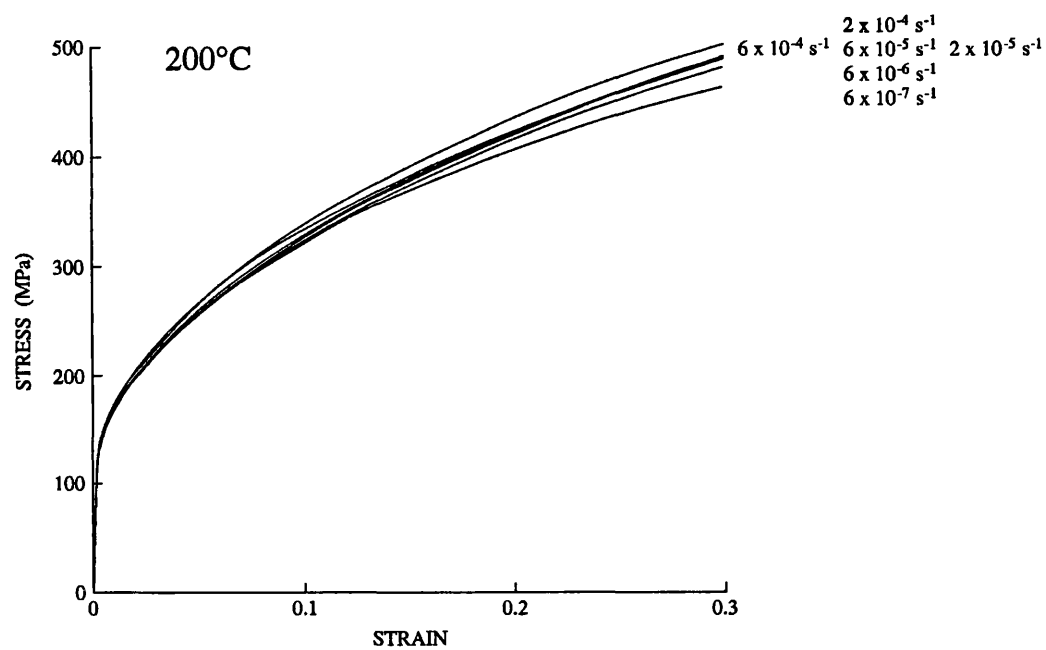


FIG. 13.2 contd.

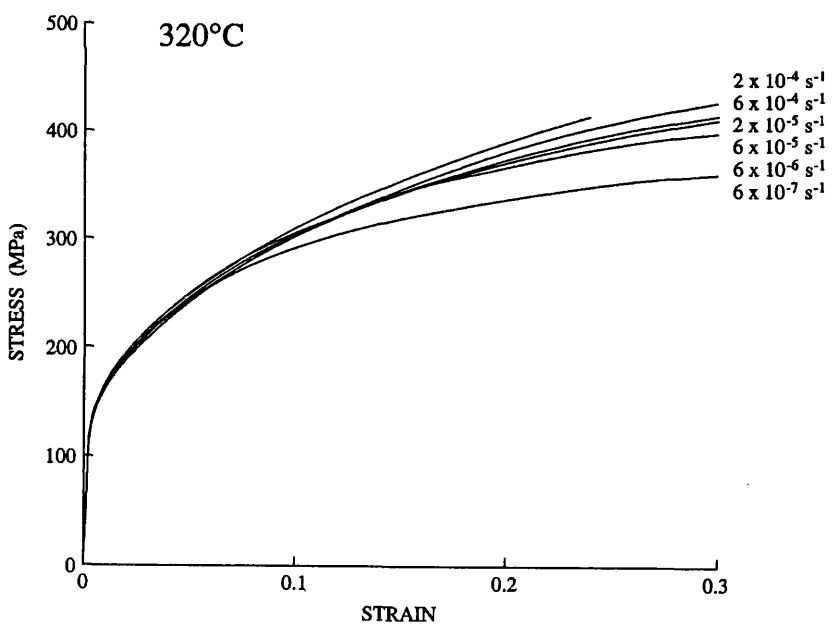
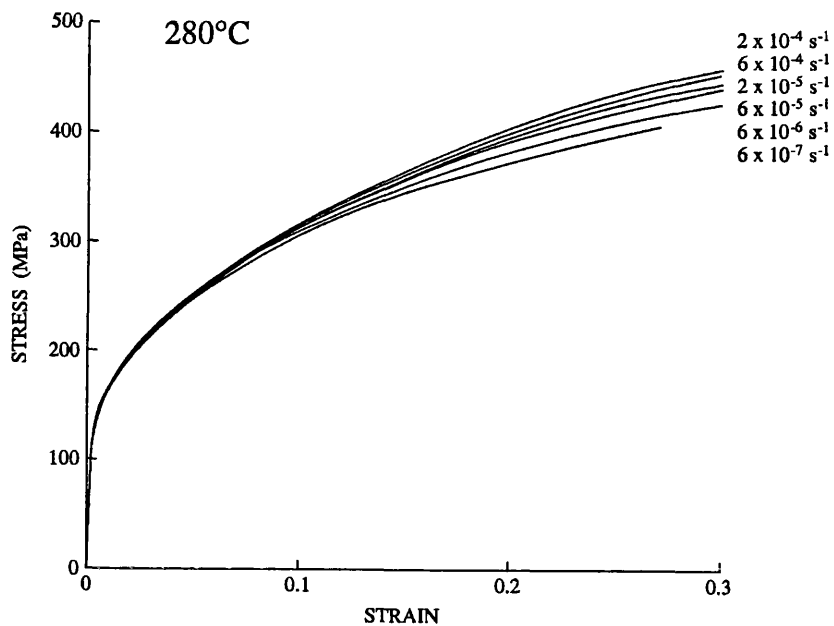


FIG. 13.2 contd.

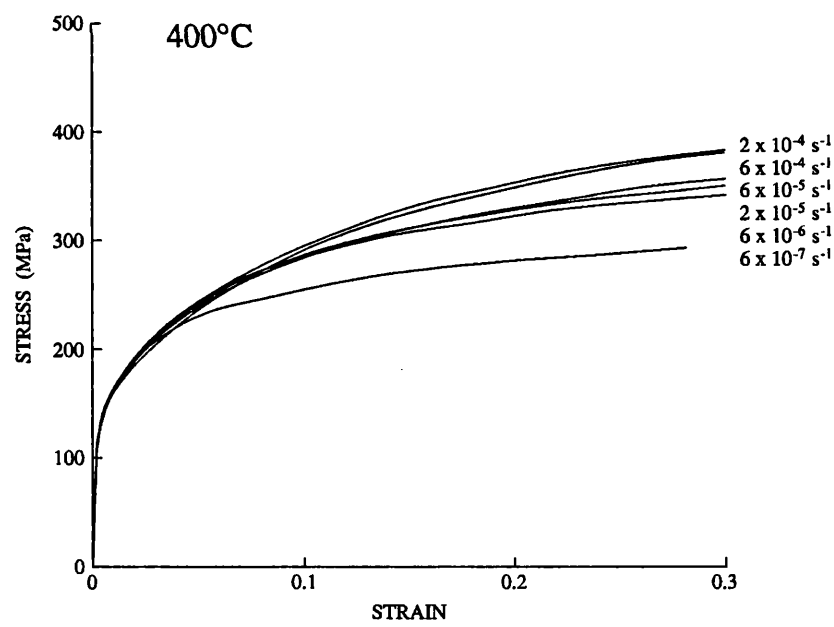
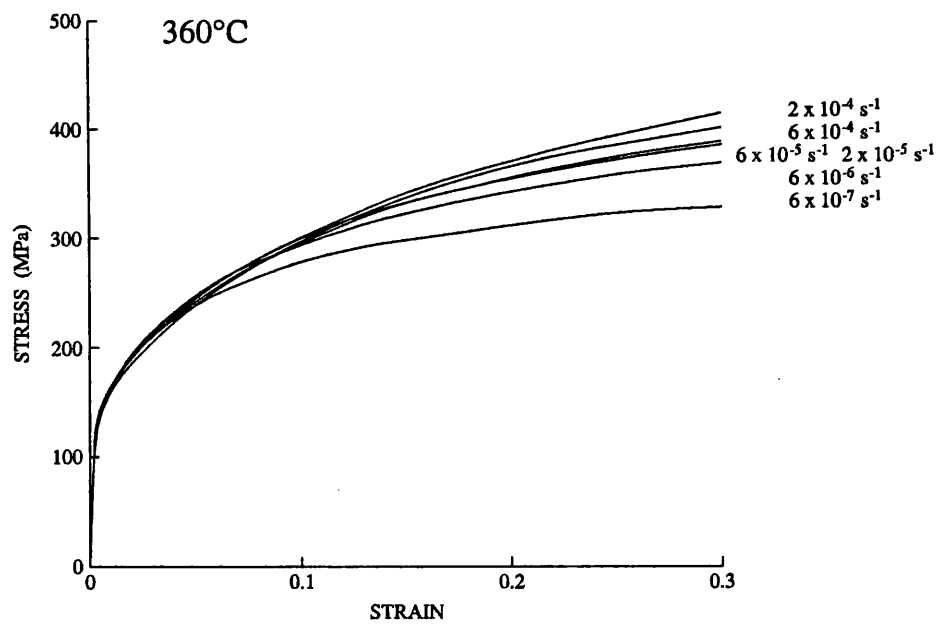


FIG. 13.2 contd.

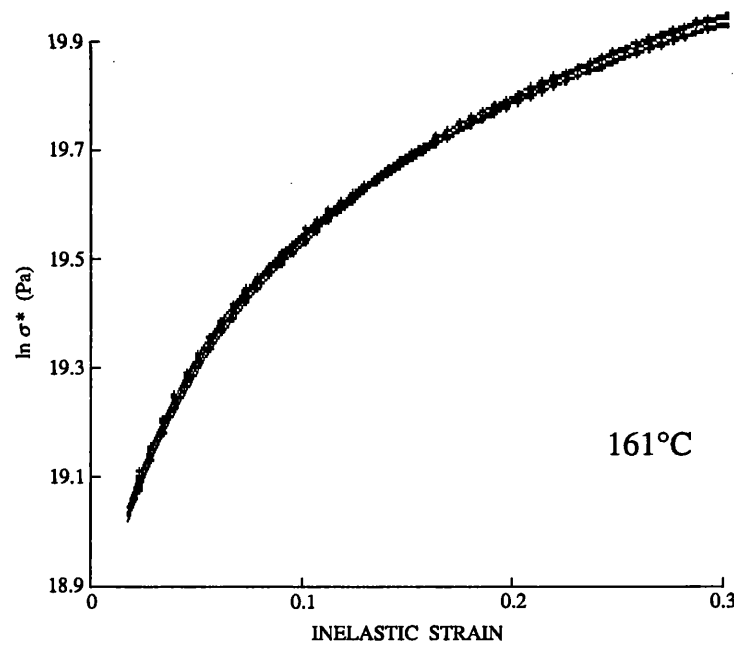
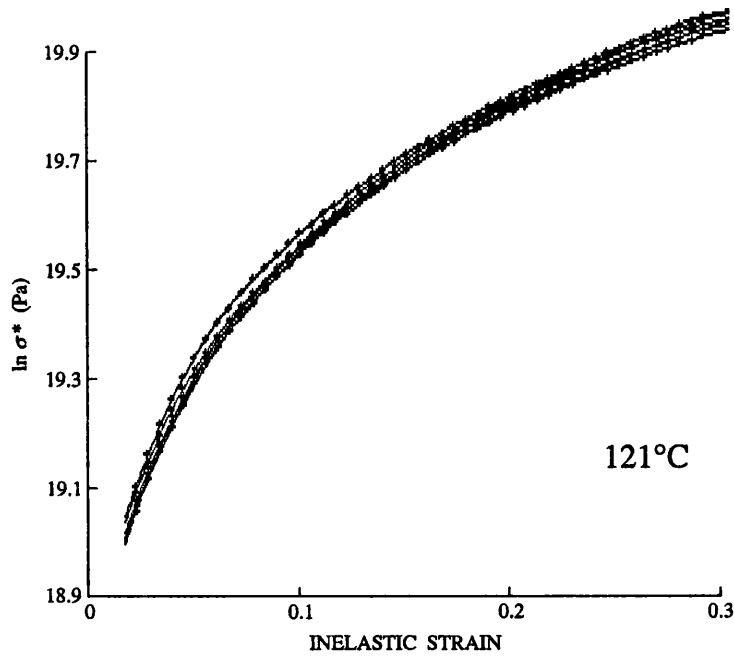


FIG. 13.3. The stress / strain curves of figure 13.2 replotted as curves of  $\ln \sigma^*$  vs.  $\varepsilon^{(n)}$ . The slope of these curves is  $\Gamma$ .

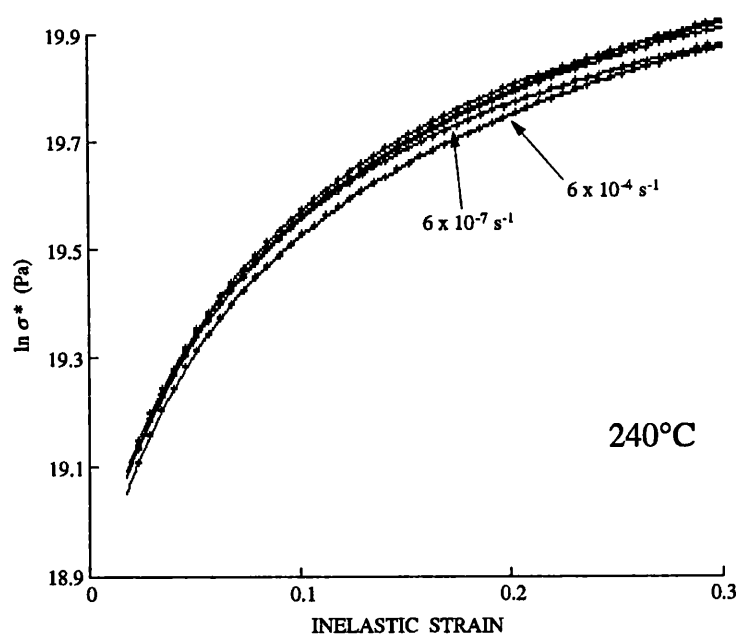
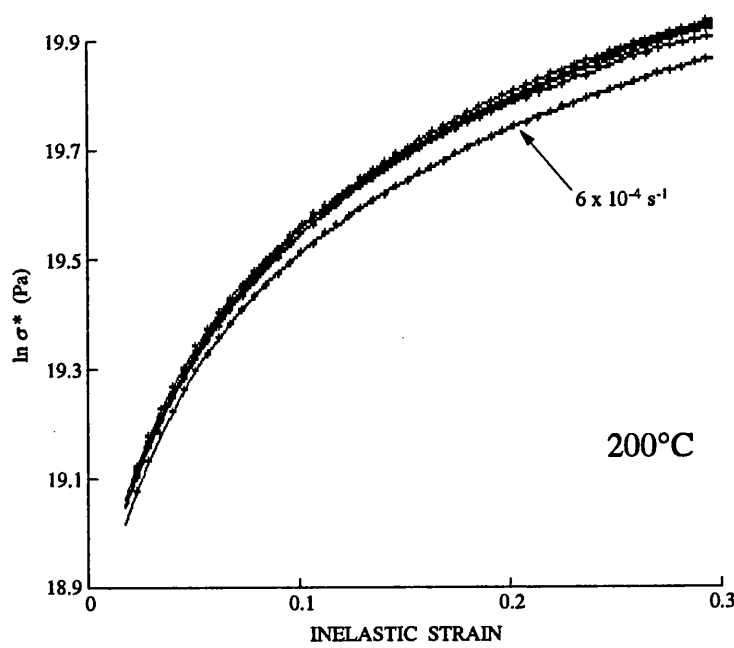


FIG. 13.3 contd.

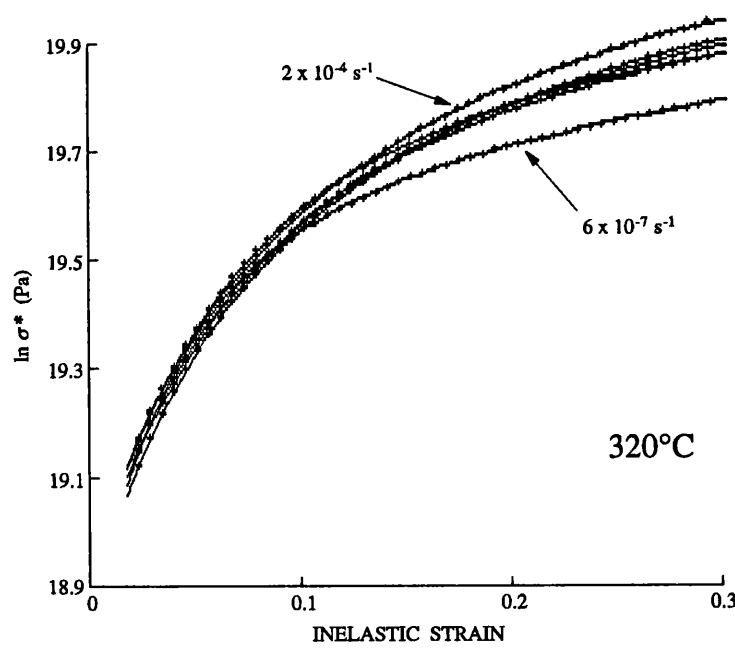
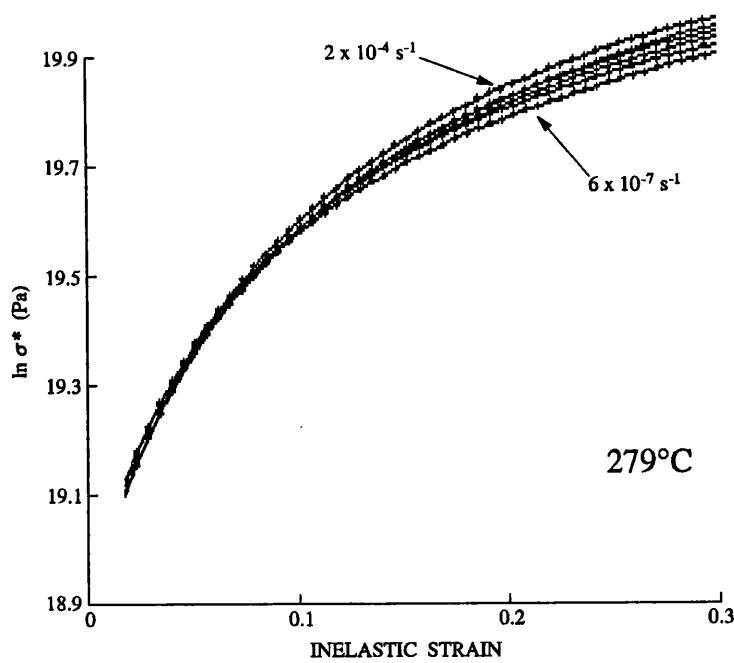


FIG. 13.3 contd.

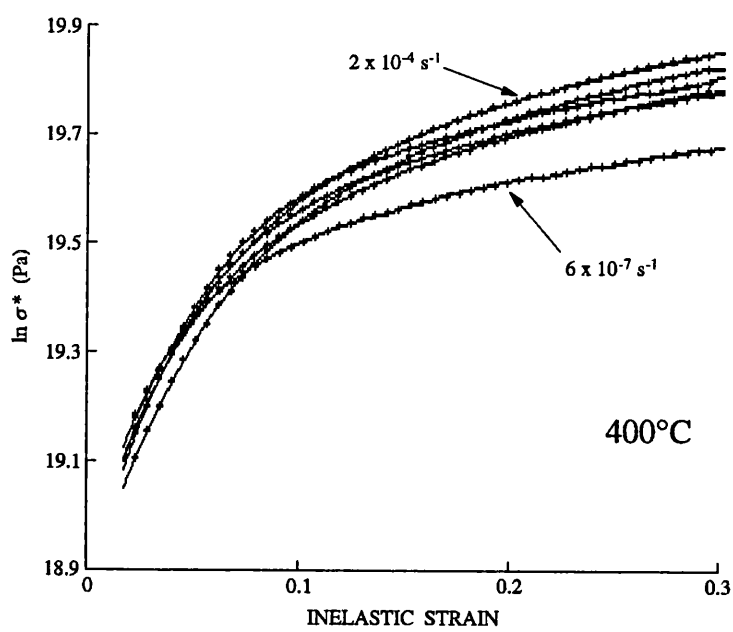
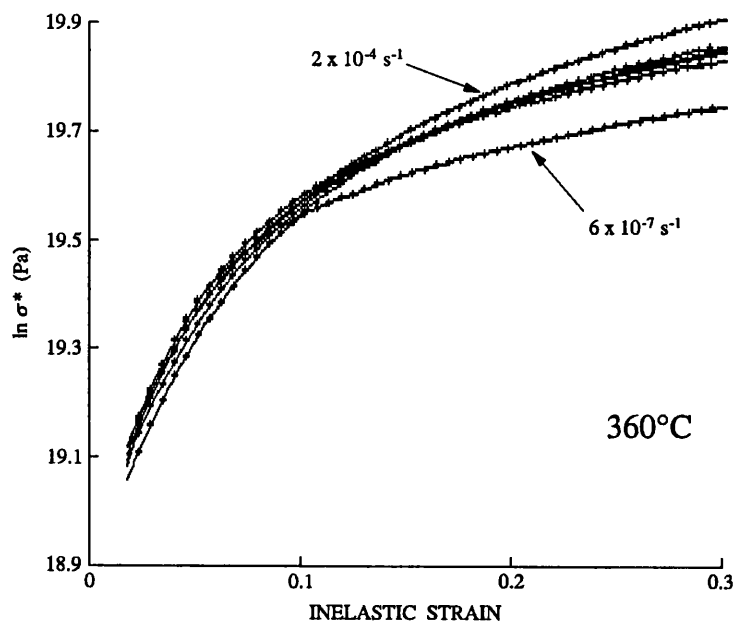


FIG. 13.3 contd.

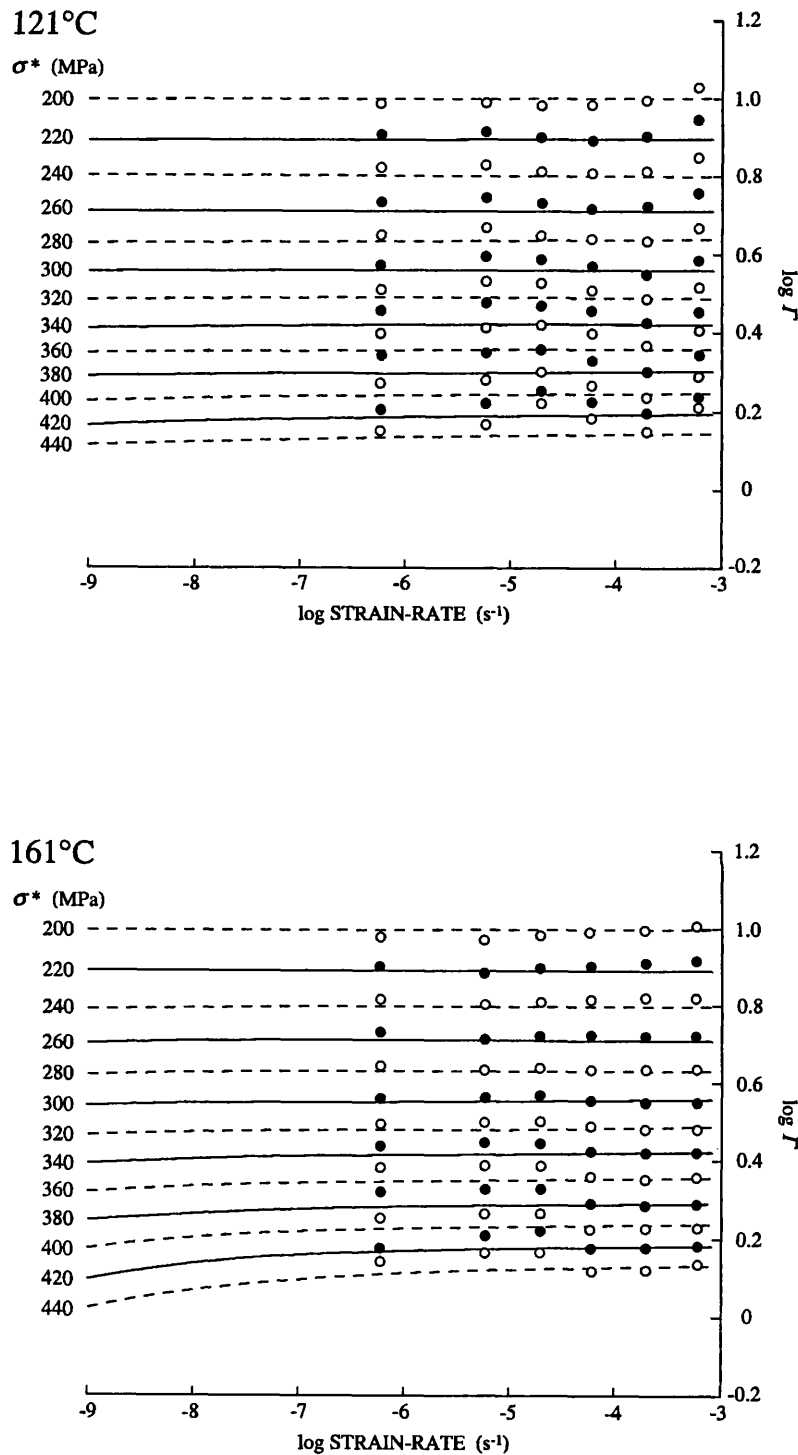


FIG. 13.4. The values of  $\Gamma$  determined from the data presented in figure 13.3 plotted as a function of  $\log \dot{\varepsilon}^{(n)}$  at the indicated  $\sigma^*$ . The curves are the fits to the data as given by the final evolution equation (§ 13.2.4). The alternating dash / solid curves and open / filled symbols are merely for presentation purposes.

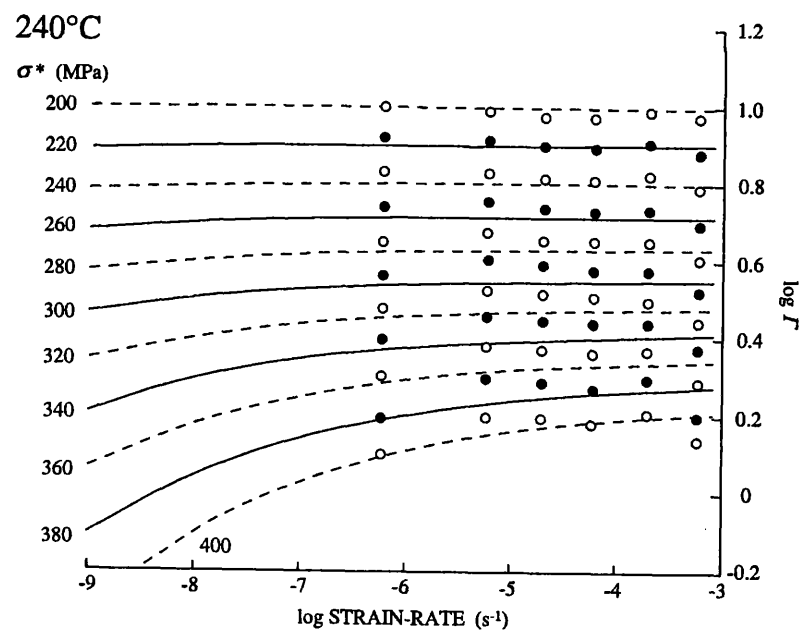
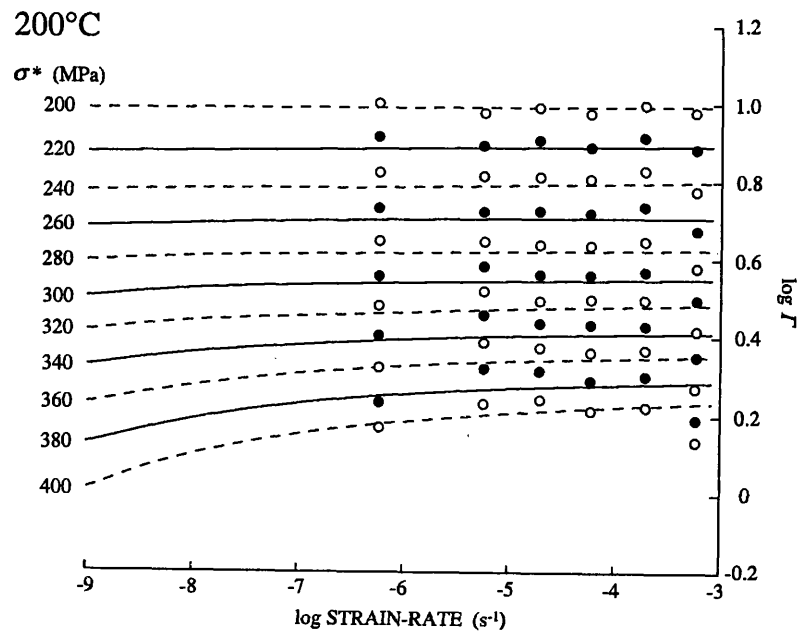


FIG. 13.4 contd.

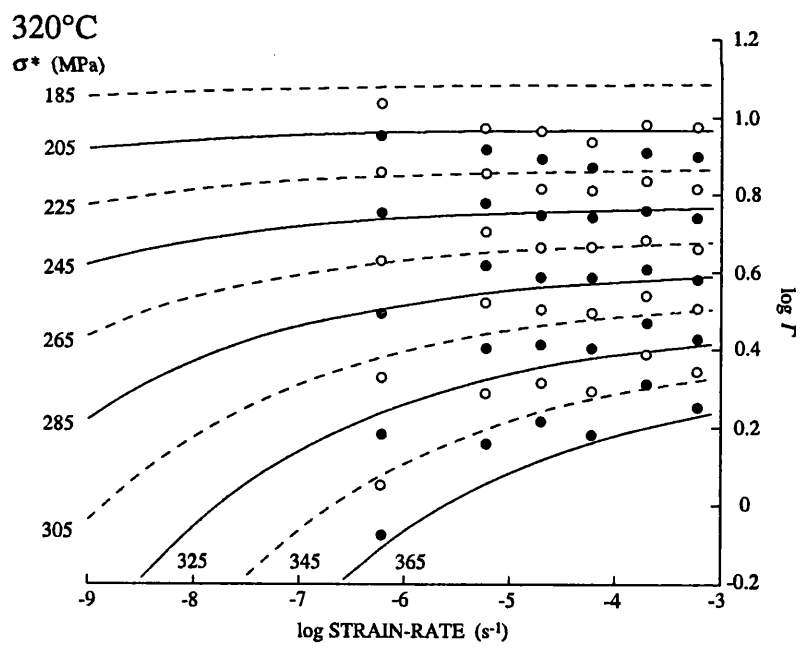
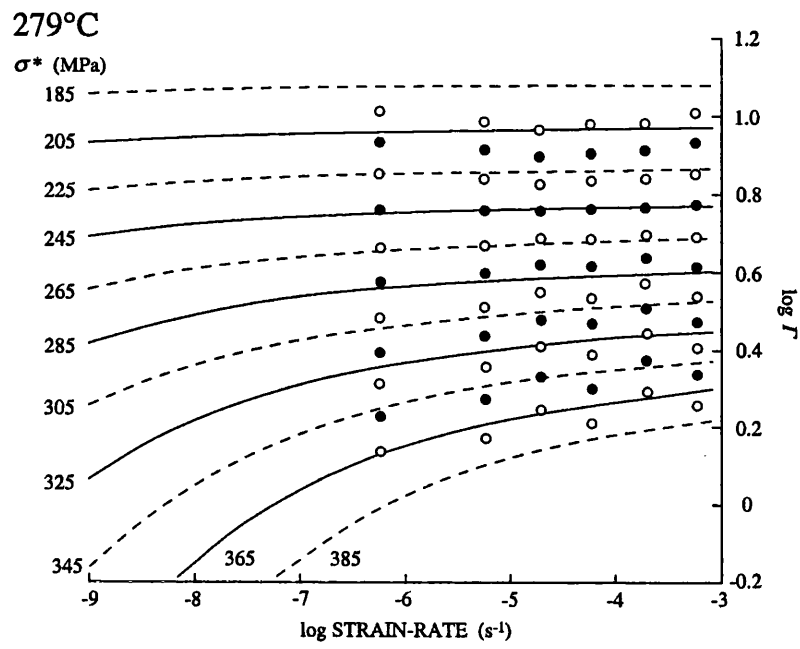


FIG. 13.4 contd.

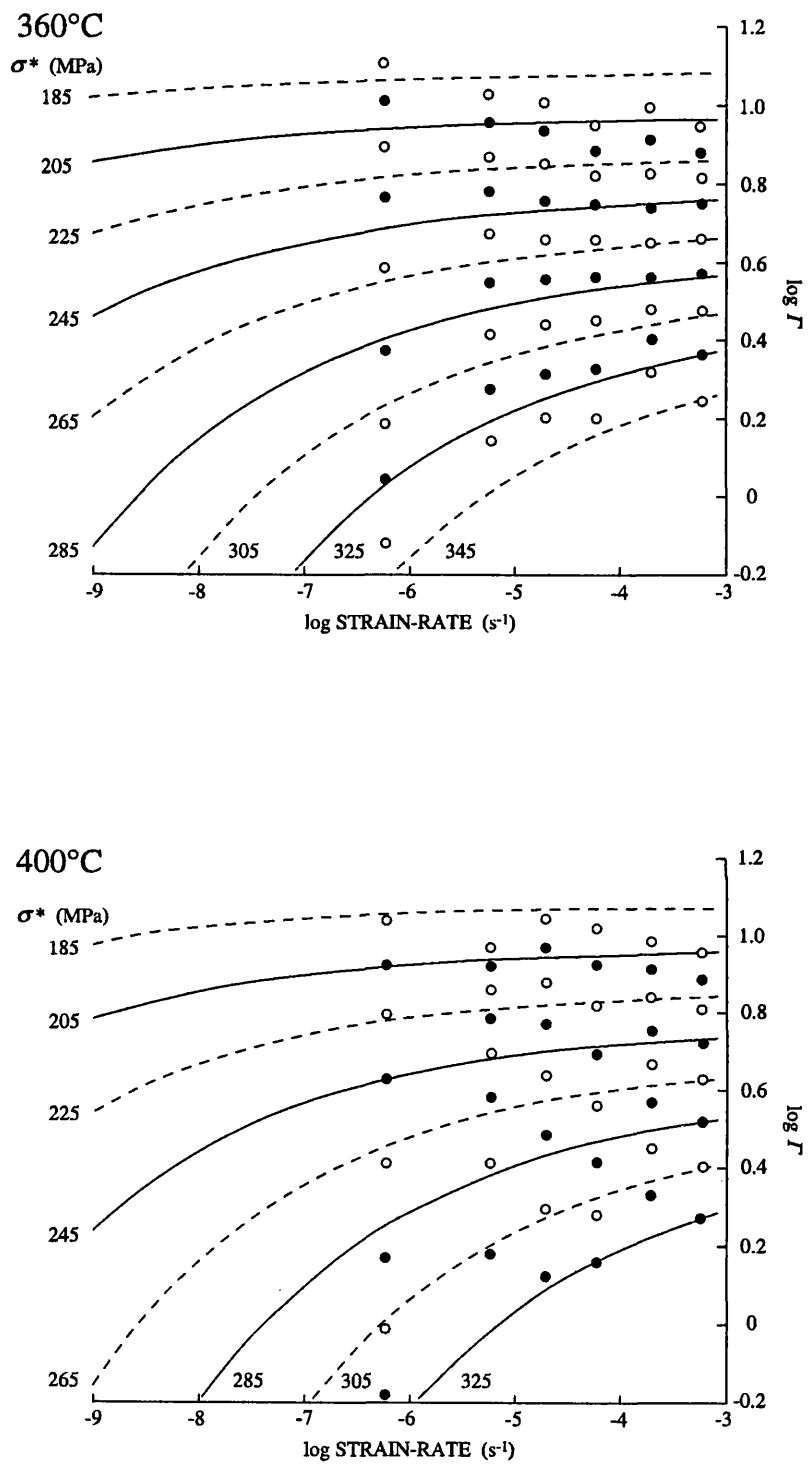


FIG. 13.4 contd.

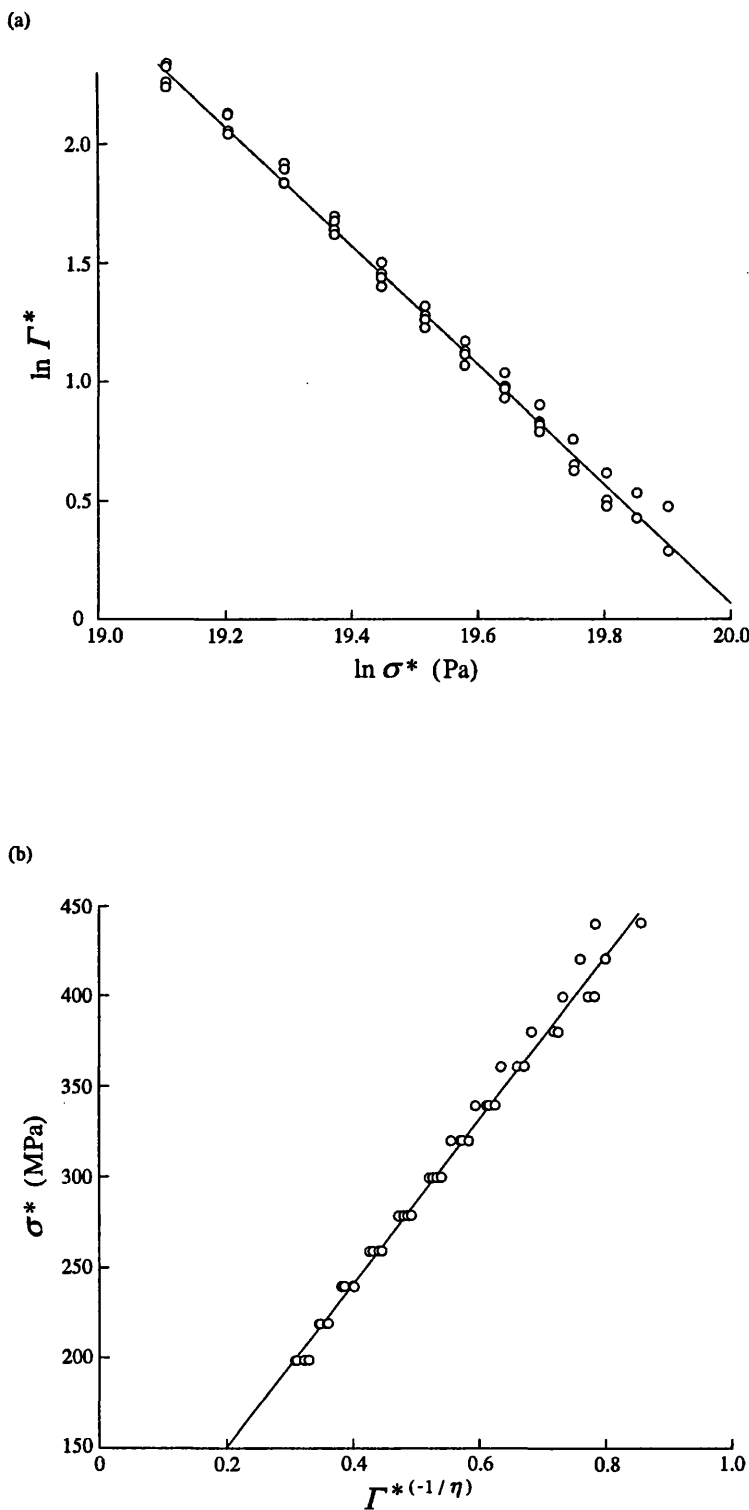


FIG. 13.5. The  $I^*$  values for  $T < 250^\circ\text{C}$  plotted according to (a) equation 13.9 and (b) equation 13.10. The linearity of plot (a) implies that  $\sigma_0^* = 0$  although plot (b) yields a small value of 64 MPa for this parameter.

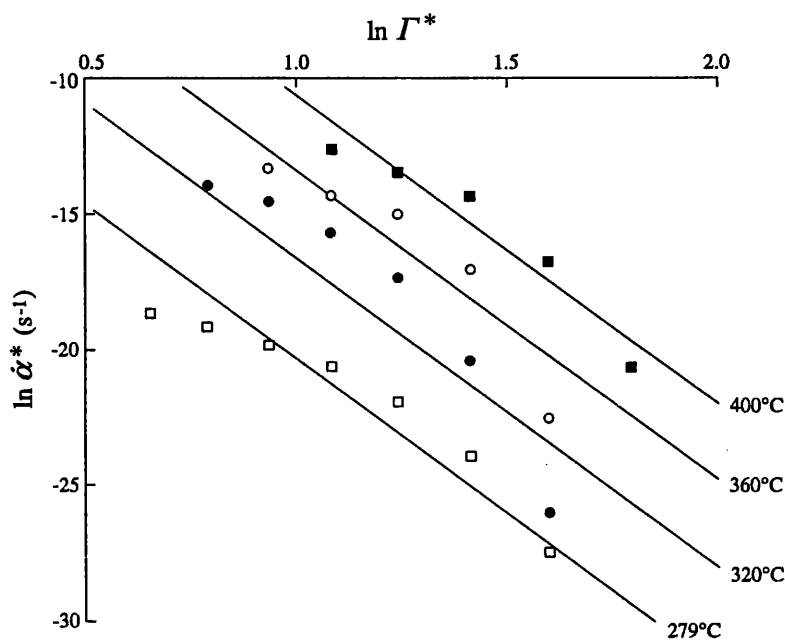


FIG. 13.6. The variation of  $\dot{\alpha}^*$  with  $\Gamma^*$  and  $T$  together with the fits expressing this variation (equation 13.18). The slope of these curves is the reciprocal of the scaling slope for the  $\log \Gamma^* / \log \dot{\varepsilon}^{(n)}$  curves shown in figure 13.4.

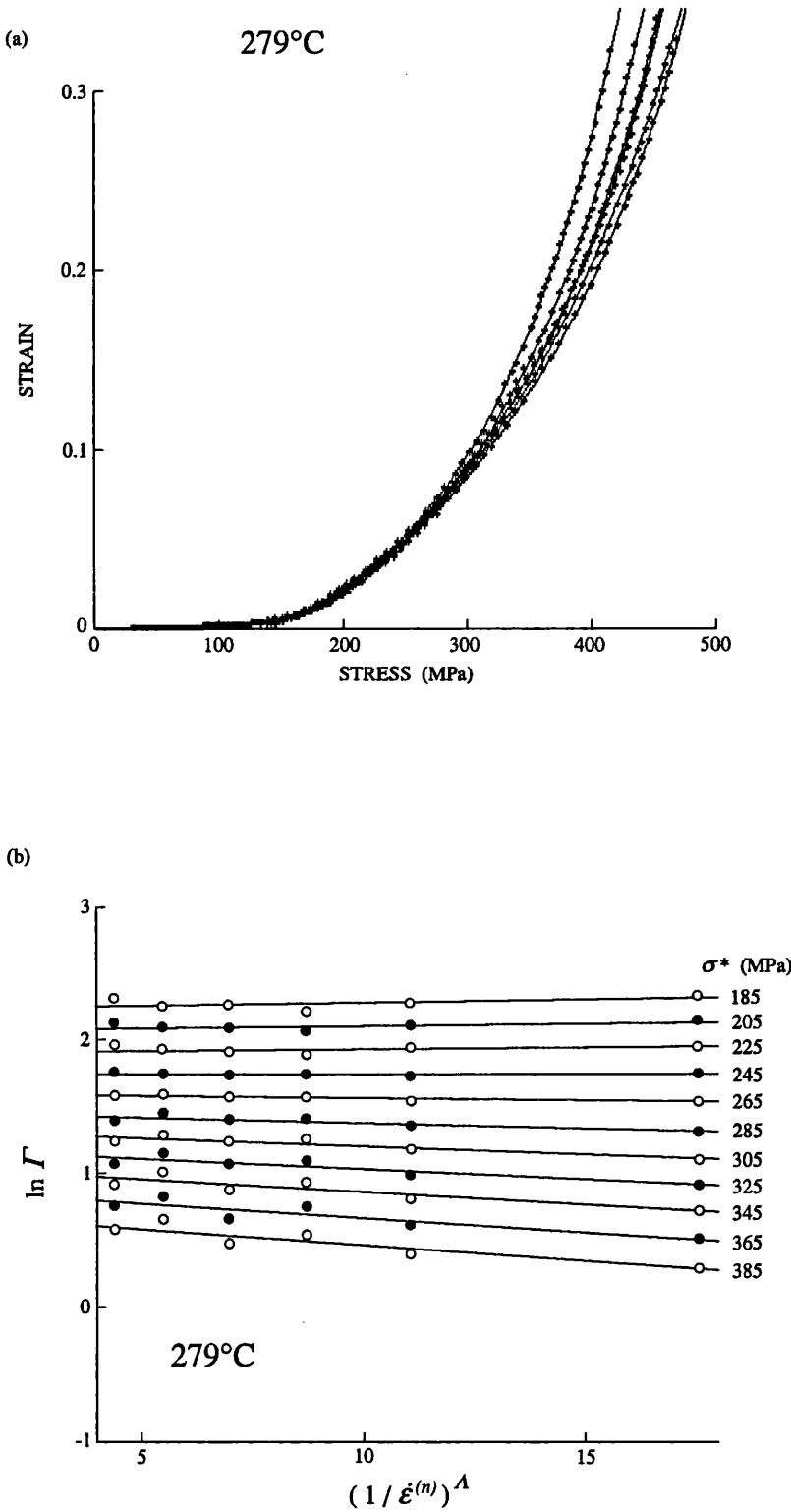


FIG. 13.7. Errors in the evaluation of the evolution equation. (a) A typical example of the strain / stress polynomial fits of the data presented in figure 13.2. (b) Typical fits to the  $\Gamma$  data plotted as  $\ln \Gamma$  vs.  $[1/\dot{\epsilon}^{(n)}]^A$  in order to determine  $\dot{\alpha}^*$ . The  $\Gamma$  data corresponds to that determined for the appropriate strain-rate at the indicated  $\sigma^* + 15$  MPa (i.e. the strategy employed for all  $T > 250^\circ\text{C}$ , § 13.2.1).

## 14 EVOLUTION EQUATION II. STATIC RECOVERY

Nominally deformation independent changes in mechanical state at  $T > 0.45 T_m$  (*i.e.* static recovery, § 6.4.1) are accommodated within Hart's original model as the term

$$d\ln \sigma^*/dt = -\mathfrak{R}(\sigma^*, T) \quad (14.1)$$

in the mechanical state evolution equation (equation 5.13). The functional form of  $\mathfrak{R}(\sigma^*, T)$  was not stipulated by Hart, and there have been few attempts to determine it by experiment (*cf.* § 6.4.3).

In principle provided the appropriate recovery absent equation of state is known, the functional form of  $\mathfrak{R}(\sigma^*, T)$  may be investigated by interrupting any deformation test (conducted under conditions where that equation applies) for a period of isostatic annealing at elevated temperature, and then on completion of the anneal, by continuing the test at the initial deformation conditions. The equation of state can then be used to calculate  $\sigma^*$  both before and after annealing from the corresponding deformation behaviour. By repeating the experiment for different anneal durations, a curve of  $\sigma^*$  as a function of anneal time may be generated and hence  $d\ln \sigma^*/dt$  can be evaluated. The functional dependence of  $d\ln \sigma^*/dt$  on  $\sigma^*$  and  $T$  may then be ascertained by generating several such curves at different anneal temperatures and after different pre-strains (the latter permitting access to a wider range of  $\sigma^*$ ).

This strategy contains the separate problems of (a) evaluating  $d\ln \sigma^*/dt$  from a given experiment, and of (b) finding an appropriate function to describe the observed dependence of  $d\ln \sigma^*/dt$  on  $\sigma^*$  and  $T$ . In this study only the first of these problems is addressed, although the second is given some consideration in the discussion of the results (§ 14.4). The changes in  $\sigma^*$  during annealing are determined from stress / strain curves generated by constant displacement-rate tests conducted at 420°C and  $3 \times 10^{-4} \text{ s}^{-1}$ .

### 14.1 Evaluating the recovery function

The ideal behaviour required for evaluating  $d\ln \sigma^*/dt$  from the results of an interrupted constant displacement-rate test is illustrated in figure 14.1a. The specimen is first loaded to stress  $\sigma_3$ , offloaded and then annealed for given period. On reload the specimen yields at stress  $\sigma_2$ , where if static recovery has taken place  $\sigma_2 < \sigma_3$ , and thereafter retraces the initial stress / strain curve, although along a path displaced from it by  $\Delta\varepsilon$ . In such circumstances, the magnitude of  $\sigma^*$  both before and after annealing, can be calculated from the appropriate (for the deformation conditions) equation of state using  $\sigma_3$  and  $\sigma_2$  respectively.

Real behaviour however, is complicated by reloading transients. At low homologous temperatures these may be due to factors such as solute impurities (§ 6.3.1.2), but at  $T > 0.35 T_m$  of greater significance are the reloading transients attributable within the framework of the refined Hart model (§ 6.1) to weak barrier recovery. Weak barrier recovery does not affect the propensity for the reloading curve to rejoin the stress / strain curve generated in an uninterrupted test (*i.e.* it does not affect  $\sigma^*$ ), but it modifies the shape (decreases the observed stresses at given strains) of the initial part of that curve. Such transients may persist over reload strains of several percent and hence lead to an underestimate of the post-annealing value of  $\sigma^*$ .

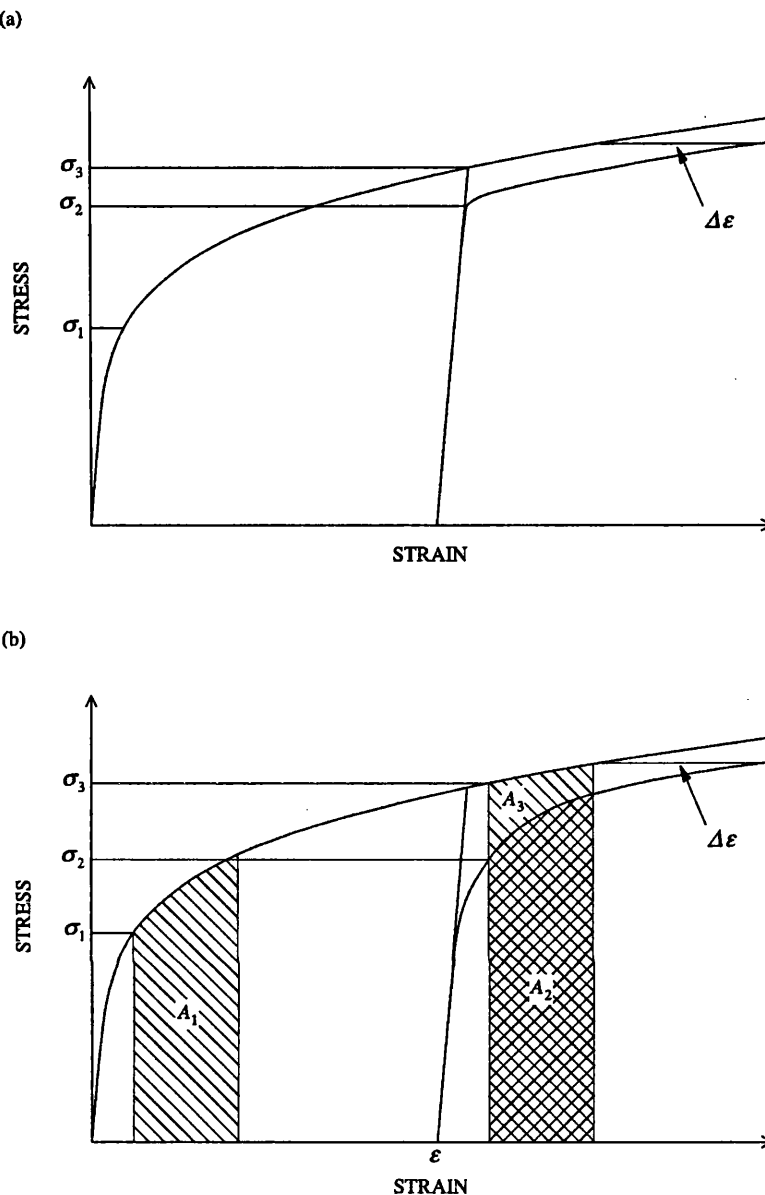


FIG. 14.1. Methods of estimating recovery from a comparison of the stress / strain curves generated by constant displacement-rate deformation before and after a period of annealing. (a) Ideal reloading behaviour permitting recovery to be unambiguously estimated by using the indicated stresses in equation 14.3. (b) Definition of the various terms (in equations 14.2 to 14.3) used to estimate recovery when there is a reloading transient.

if the latter is calculated using  $\sigma_2$ .

The influence of weak barrier recovery turns the evaluation of  $d\ln \sigma^*/dt$  into a two part problem. First it is necessary to determine a method for making the comparison of the initial and reload curves *i.e.* to determine a recovery estimate, and then secondly, it is necessary to translate that estimate into a change in  $\sigma^*$ .

**14.1.1 Obtaining an estimate of recovery.** In principle, the most suitable (for evaluating  $d\ln \sigma^*/dt$ ) comparison of initial and reload stress / strain curves is to determine  $\Delta\epsilon$  (*i.e.* the translation parallel to the strain axis required to superpose the reload curve onto the initial

curve), since this requires the use of the transient-free portion of the reload curve and is therefore unaffected by weak barrier recovery. Normalizing with respect to the final strain attained in the first loading  $\varepsilon$ , the fractional recovery is

$$\varepsilon_{rec} = \Delta\varepsilon/\varepsilon \quad (14.2)$$

However, if the slope of the stress / strain curve is small in the strain range of interest, the estimate of  $\Delta\varepsilon$  is highly sensitive to the determined differential stresses and even small errors in these (reflecting for example, the accuracy of differential load determination) cause large errors in  $\varepsilon_{rec}$ .

Two other methods of comparing initial and reload stress / strain curves have been widely used in static recovery investigations (figure 14.1b). The first is a stress based estimate in which the fractional recovery is defined as

$$\sigma_{rec} = (\sigma_3 - \sigma_2)/(\sigma_3 - \sigma_1) \quad (14.3)$$

where  $\sigma_1$  is the yield stress in the initial loading,  $\sigma_2$  the yield stress in reloading and  $\sigma_3$  the flow stress that would have pertained at the total strain at which the yielding occurred in the reload, had the test not been interrupted for annealing. The second is an area based estimate in which the fractional recovery is defined as

$$A_{rec} = (A_3 - A_2)/(A_3 - A_1) \quad (14.4)$$

where  $A_1$  is the area under the initial loading curve in a given strain interval,  $A_2$  is the area under the reload curve in the same strain interval, and  $A_3$  is the area under the initial loading curve that would have pertained in the same interval of total strain as used for  $A_2$  if the test had not been interrupted. Both the stress and area based estimates ignore transient effects and therefore include a component of weak barrier recovery. Since the effect of weak barrier recovery on the shape of the reloading curves decreases with increasing reloading strain, each may be expected to be sensitive to the choice of the strains used for defining the yield stresses and the bounds of the areas respectively, and the area based estimate should be less affected by weak barrier recovery than the stress based one.

The stress and area based estimates are much more easily determined and subject to far smaller measurement errors, than the strain based estimate. However, by ignoring transient effects, they transfer the difficulties posed by weak barrier recovery onto the problem of converting the recovery estimate into changes in  $\sigma^*$ .

**14.1.2 Correlating the recovery estimate with changes of  $\sigma^*$ .** The value of  $\sigma^*$  after annealing may be readily calculated by finding the stress on the initial loading curve which corresponds to the strain  $(\varepsilon - \Delta\varepsilon)$ , and then by using it in the appropriate equation of state. This presents no problem for the strain based recovery estimate, but for the other two recovery estimates it becomes necessary to find the functions  $\Delta\varepsilon(\sigma_{rec})$  and  $\Delta\varepsilon(A_{rec})$  respectively. In principle, this requires a precise knowledge of the effect of weak barrier recovery on the shape of the stress / strain curves *i.e.* a weak barrier recovery function is needed. However, in practice, by determining all three recovery estimates it may be possible to find some empirical expression for these functions.

## 14.2 Results I. The recovery estimates

The observation of substantial reloading transients in the multiple relaxation experiments

conducted at  $T > 300^\circ\text{C}$  (figure 12.1) suggests that weak barrier recovery must have a significant effect on the reloading behaviour observed in the recovery tests conducted here. Consequently, all three recovery estimates (equations 14.2 - 14.4) were evaluated for each experiment.

**14.2.1 Procedures employed.** The most significant problem in determining the recovery estimates is that posed by the  $\pm 10 \text{ MPa}$  error in differential stress due to the NIMONIC2 FGZ variability (§ 9.1.2.3). The potential errors introduced by this variability are very large, and consequently the recovery analysis procedures employed here were chosen to minimize their effect.

**14.2.1.1 Characterizing the loading curves :** The initial loading behaviour was characterized by selecting a reference stress / total strain curve from the highest density part of the 20 MPa range of initial loading curves actually produced from experiments (figure 9.6). The reference curve was then fitted by a fourth order polynomial (root mean square error of 1.75 MPa) to allow the stress corresponding to any given strain, and the area under the curve between any two strains, to be readily determined.

The initial specimen dimensions for use in the data reduction procedure for the reloading were the elastic length at the end of the first loading (as given by equation 8.18) and the corresponding cross sectional area (assuming constant volume deformation). Otherwise the observed stress / strain curve given by the data reduction procedure was used for the reloading behaviour, with that part of it between reloading strains of approximately 0.008 and 0.100 fitted by a fourth order polynomial to allow  $\sigma_2$  and  $A_2$  to be determined.

**14.2.1.2 Evaluating equations 14.2 - 14.4 :**  $\Delta\varepsilon$  for use in equation 14.2 was determined by finding the translation distance (by visual inspection) required to superpose the observed reloading curve onto the reference initial loading curve.

The stresses for use in equation 14.3 were those corresponding to the following strains

$$\sigma_1 ; \text{ total strain} = 0.01$$

$$\sigma_2 ; \text{ reload strain} = 0.01$$

$$\sigma_3 ; \text{ total strain} = \varepsilon - \varepsilon^{(e)} + 0.01$$

where the stresses  $\sigma_1$  and  $\sigma_3$  were calculated from the reference initial loading curve polynomial and  $\sigma_2$  from the observed reloading curve polynomial, and where  $\varepsilon$  is the total strain at the end of the initial loading and  $\varepsilon^{(e)}$  is the corresponding elastic component of that strain as given by

$$\varepsilon^{(e)} = \ln \{1/[1 - (\sigma/E)]\} \quad (14.5)$$

where  $E$  is the calcite Young's modulus (equation 10.7) and  $\sigma$  is the stress corresponding to  $\varepsilon$  on the reference curve (§ A3.1.5).

The areas for use in equation 14.4 were calculated from the areas under the stress / strain curves between the following strains

$$A_1 ; \text{ total strain} = 0.01 \text{ and total strain} = 0.06$$

$$A_2 ; \text{ reload strain} = 0.01 \text{ and reload strain} = 0.06$$

$$A_3 ; \text{ total strain} = \varepsilon - \varepsilon^{(e)} + 0.01 \text{ and total strain} = \varepsilon - \varepsilon^{(e)} + 0.06$$

using for  $A_1$  and  $A_3$  the reference initial loading curve polynomial and for  $A_2$  the observed reloading curve polynomial, and where  $\varepsilon$  and  $\varepsilon^{(e)}$  are as defined for the stresses.

**14.2.2 The observed values of the recovery estimates.** The values of  $\sigma_{rec}$ ,  $A_{rec}$  and  $\varepsilon_{rec}$

obtained in this investigation are given in table 14.1 and are plotted as a function of time in figure 14.2 for the two cases constant anneal temperature / various pre-strains, and constant pre-strain / various anneal temperatures.

**14.2.2.1 A qualitative description of the results :** The fractional recovery / log time curves constructed for each recovery estimate are sigmoidal *i.e.* the slopes of the curves vary from shallow to steep to shallow as time increases. The curves at anneal temperatures of less than 600°C show only the top part of this sigmoid, those at temperatures greater than 600°C only the bottom part, while those at 600°C show the full curve. The effect of increasing the pre-strain while keeping the anneal temperature constant is to displace the steep portion of the curves to shorter anneal times. These results are similar to those observed for other materials (§ 6.4.2.2).

**14.2.2.2 A comparison of the recovery estimates :** As expected given the predicted influence of weak barrier recovery on each of the recovery estimates,  $\sigma_{rec} > A_{rec} > \varepsilon_{rec}$ . When plotted against each other (figure 14.3), it is apparent that the relationship between the estimates is non-linear, although the non-linearity is only strongly developed at small recoveries, and then primarily in the relationship between the stress based estimate and the other two.

**14.2.3 Errors in the estimates.** The most significant errors in the recovery estimates arise from the reloading part of the experiments. These include the errors resulting from the assumption of homogeneous deformation, and in particular from the assumption that the specimen remains a perfect right circular cylinder during deformation (§ 9.5.1), and those resulting from the  $\pm 10$  MPa uncertainty in the differential stress due to the FGZ variability (§ 9.1.2.3). The former are unimportant compared with the latter, but are expected to be more significant for the high pre-strain experiments where reloading data upto a total strain of 0.45 were used. The error due to the FGZ variability is expected, given the slope of the stress / strain curve, to be more significant for the estimate of  $\varepsilon_{rec}$  than for the other two estimates, and to be more important at low pre-strains when the denominator terms in equations 14.2 - 14.4 are small. These expectations are confirmed by the observed scatter in the data presented in figures 14.2 and 14.3.

All other errors, such as those arising in the calculation of the initial specimen dimensions for the reloads, and those arising from the polynomial fitting to the reference and reload curves, are negligible.

### 14.3 Results II. Changes in mechanical state

All three recovery estimates were utilized to determine the change in  $\sigma^*$  during a given annealing period.

**14.3.1 Procedures employed.** To determine the post-annealing value of  $\sigma^*$  it is necessary to select a value for  $\Delta\varepsilon$ . The values used to determine  $\varepsilon_{rec}$  may be employed or alternatively, by fitting some function  $\varepsilon_{rec}(\sigma_{rec})$  or  $\varepsilon_{rec}(A_{rec})$  to the results presented on figure 14.3,  $\Delta\varepsilon$  may be determined using the estimates of  $\sigma_{rec}$  or  $A_{rec}$  and equation 14.2. A variant of the second procedure was employed here. First the three recovery estimates from all the experiments were least squares regressed on the equation

$$\varepsilon_{rec} = A(\sigma_{rec})^2 + B\sigma_{rec} + CA_{rec} + D \quad (14.6)$$

where  $A$ ,  $B$ ,  $C$  and  $D$  are the regression coefficients, and the  $(\sigma_{rec})^2$  term is included to

accommodate the observed non-linear relationship between the recovery estimates. Equation 14.6 was then used with equation 14.2 to calculate  $\Delta\varepsilon$  for each experiment from the values of  $\sigma_{rec}$  and  $A_{rec}$  for that experiment.

The stresses used to solve the equation of state for the value of  $\sigma^*$  before and after annealing, were respectively those given by the strains  $\varepsilon$  and  $(\varepsilon - \Delta\varepsilon)$ , as applied to a polynomial fit of a  $\varepsilon^{(t)}/\sigma$  curve generated on HEARD1 under the same deformation conditions used for the recovery experiments. In this way the apparatus dependent differences between the HEARD1 and NIMONIC2 experiments (§ 9.1.3.4) were eliminated from the analysis. The equation of state for the plastic element (§ 12.2.4) in the form given by equation 13.5 was used, with  $\sigma^*$  being determined using a Newton-Raphson procedure (cf. § A3.1.3).

**14.3.2 The observed changes in mechanical state.** The regression equation for the corrected  $\varepsilon_{rec}$  (equation 14.6) is

$$\varepsilon_{rec} = 0.2306(\sigma_{rec})^2 - 0.6086\sigma_{rec} + 1.231A_{rec} + 0.0587 \quad (14.7)$$

with a root mean square error on  $\varepsilon_{rec}$  of 0.0804. The values given by equation 14.7 are presented in table 14.1, are shown with respect to the uncorrected  $\varepsilon_{rec}$  in figure 14.3, and are plotted as a function of log time in figure 14.4. The features of the fractional recovery / log time plots are qualitatively the same as described for the three types of recovery estimate.

The corresponding post-annealing values of  $\sigma^*$  are also given in table 14.1, and are shown as a function of time in figures 14.5 and 14.6. Plotted as a function of  $t$ , it is apparent that the recovery of  $\sigma^*$  is initially very rapid. Plotted as a function of  $\log t$ , the change in  $\sigma^*$  with time displays the same sigmoidal form as the fractional recovery curves.

**14.3.3 Errors in the post-annealing values of  $\sigma^*$ .** The use of equation 14.7 only provides a consistent relationship between the three recovery estimates determined for each test (primarily to give a more confident value for  $\varepsilon_{rec}$ ) ; it does not remove the errors inherent in those estimates, and consequently they remain in the values of  $\sigma^*$ . From figure 14.5 it is apparent that these errors are of most significance (for  $d\ln\sigma^*/dt$ ) at long anneal times, when the recovery rates become very small.

The errors in the equation of state for the plastic element (§ 12.2.3) are present in all the determined values of  $\sigma^*$ . In using the same equation of state to determine the pre- and post-annealing values of  $\sigma^*$ , it is assumed that any changes that occur during annealing do not also change the values of the material parameters in that equation. The observation that it is possible to translate the reloading curves onto the initial loading curves indicates that this assumption is valid.

#### 14.4 Discussion

Qualitatively, the static recovery behaviour of Carrara marble observed in this study is as expected. The sigmoidal form of the fractional recovery curves matches that observed in other materials, suggesting that as for those materials the initial shallow portion of the curves corresponds to recovery by dislocation annihilation and subgrain formation, the steep portion marks the onset and progression of migration recrystallization, and the final shallow portion of the curves corresponds to the further reorganization of those dislocations remaining after complete recrystallization.

Preliminary microstructural analyses of specimens which were annealed but not reloaded, confirm this interpretation of the results. At 700°C rapid grain boundary migration begins within minutes of the anneal temperature being attained, and within an hour the whole aggregate is recrystallized. The grain boundaries in the resulting microstructure are highly sinuous with the grain-size being approximately the same as in the starting material. Subsequently over a period of a few days, a second wave of recrystallization begins in which the recrystallization nuclei are formed by subgrain mechanisms (§ 6.4.1.2). This process continues upwards of fifty days and leads to a marked reduction in grain-size and the development of excellent foam textures. Microstructures generated at lower anneal temperatures verify that the start of the steep portion of the recovery curves corresponds approximately to the onset of the migration recrystallization, and that prior to this point recovery is primarily by dislocation rearrangement.

In the strategy outlined previously for the incorporation of recovery into Hart's analysis (§ 6.4.3), it was suggested that two recovery functions may be required, one describing recovery by dislocation motion, and the other describing recovery by boundary migration. It was observed that recovery by dislocation motion might be described by (equation 6.45)

$$\sigma^* = A - B(\ln t - H_r/RT) \quad (14.8)$$

where  $A$  and  $B$  are constants and  $H_r$  is some activation enthalpy, while recovery by boundary migration might be described via an Avrami type equation (equation 6.46)

$$X_f = 1 - \exp(-At^B) \quad (14.9)$$

where  $A$  and  $B$  are again constants and  $X_f$  is the volume fraction of recrystallized material. The results described here are compatible with these suggestions. The data corresponding to recovery by dislocation motion show a linear dependence of  $\sigma^*$  on  $\log t$  (figure 14.6), with  $d\sigma^*/d\log t$  being temperature sensitive, both as predicted by equation 14.8. Recovery apparently continues at a rate which is independent of the magnitude of  $\sigma^*$  until the requisite incubation time for migration recrystallization is attained. Once migration recrystallization begins  $d\sigma^*/d\log t$  becomes much larger, as expected from equation 14.9 (cf. figure 6.21c). The results from 600°C suggest that the incubation time may be uniquely specified by  $\sigma^*$  (*i.e.* the three  $\sigma^*/\log t$  curves merge) as might be expected, but its extreme temperature sensitivity (*i.e.* it is very short at  $T > 600^\circ\text{C}$  and very long at  $T < 600^\circ\text{C}$ ) renders confirmation of this at other temperatures difficult.

Further constraints on the recovery function(s) must remain speculative until the mechanical data presented here is supported with quantitative microstructural information. In particular information concerning the progress of recrystallization with annealing time is required in order to test the application of the Avrami equation.

Table 14.1. The data used to fit the plastic element.

$t$ (s)	$\sigma_{rec}$	$A_{rec}$	$\varepsilon_{rec}$	$\varepsilon_{smooth}$	$\sigma_{end}^*$ (MPa)
$T_{anneal} = 600^\circ\text{C}$	$\varepsilon^{(t)} = 0.08$	$\sigma_{start}^* = 287 \text{ MPa}$			
11520	0.63	0.46	0.06 †	0.33	256
61854	0.75	0.51	0.06 †	0.36	252
229120	0.76	0.59	0.25	0.46	240
231567	0.75	0.59	0.25	0.46	240
503548	0.78	0.60	0.37	0.46	240
925400	0.80	0.61	0.25	0.47	239
1017144	0.85	0.72	0.66	0.59	220
2222487	0.93	0.75	0.62	0.62	217
$T_{anneal} = 600^\circ\text{C}$	$\varepsilon^{(t)} = 0.17$	$\sigma_{start}^* = 349 \text{ MPa}$			
11423	0.72	0.50	0.29	0.36	314
15388	0.78	0.52	0.26	0.36	313
61548	0.76	0.54	0.40	0.39	309
235963	0.87	0.68	0.46	0.54	287
495420	0.96	0.76	0.63	0.62	272
1109465	1.03	0.86	0.71	0.74	245
2795938	1.02	0.89	0.81	0.77	234
$T_{anneal} = 600^\circ\text{C}$	$\varepsilon^{(t)} = 0.27$	$\sigma_{start}^* = 385 \text{ MPa}$			
11040	0.70	0.49	0.50	0.35	350
65918	0.85	0.65	0.62	0.51	328
239956	1.06	0.84	0.71	0.71	287
936747	1.04	0.93	0.88	0.82	249
2987020	1.08	0.95	0.91	0.84	241
$T_{anneal} = 500^\circ\text{C}$	$\varepsilon^{(t)} = 0.17$	$\sigma_{start}^* = 349 \text{ MPa}$			
13346	0.34	0.21	0.14	0.14	337
60223	0.49	0.31	0.26	0.20	331
63372	0.56	0.35	0.34	0.22	329
244726	0.45	0.30	0.26	0.20	331
946538	0.61	0.40	0.26	0.27	324
952624	0.62	0.37	0.23	0.23	328
2060936	0.58	0.42	0.37	0.30	320
$T_{anneal} = 550^\circ\text{C}$	$\varepsilon^{(t)} = 0.17$	$\sigma_{start}^* = 349 \text{ MPa}$			
10690	0.48	0.28	0.15	0.16	330
60464	0.57	0.38	0.33	0.25	321
218780	0.59	0.42	0.36	0.30	316
928266	0.62	0.43	0.33	0.30	316
1447126	0.67	0.46	0.27	0.32	313
3273781	0.92	0.75	0.76	0.62	268
$T_{anneal} = 650^\circ\text{C}$	$\varepsilon^{(t)} = 0.17$	$\sigma_{start}^* = 349 \text{ MPa}$			
11675	1.05	0.81	0.71	0.67	257
44680	1.09	0.90	0.82	0.78	229
233853	1.08	0.93	0.83	0.82	216
400411	1.03	0.87	0.73	0.75	237
925695	1.19	0.98	0.85	0.87	198
$T_{anneal} = 700^\circ\text{C}$	$\varepsilon^{(t)} = 0.17$	$\sigma_{start}^* = 349 \text{ MPa}$			
11316	1.07	0.91	0.76	0.79	228
80703	1.10	0.95	0.83	0.84	212
316983	1.15	1.04	0.94	0.94	165
433517	1.06	0.94	0.83	0.83	215
1050307	1.15	1.02	0.89	0.92	178
2065827	1.16	1.01	0.90	0.91	184
2413634	1.12	1.01	0.91	0.91	183

† values not used for fitting equation 14.6

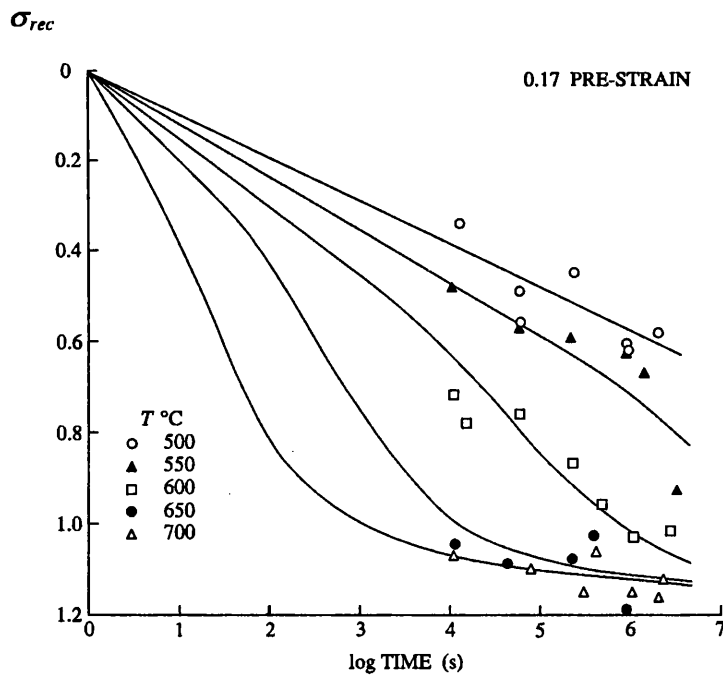
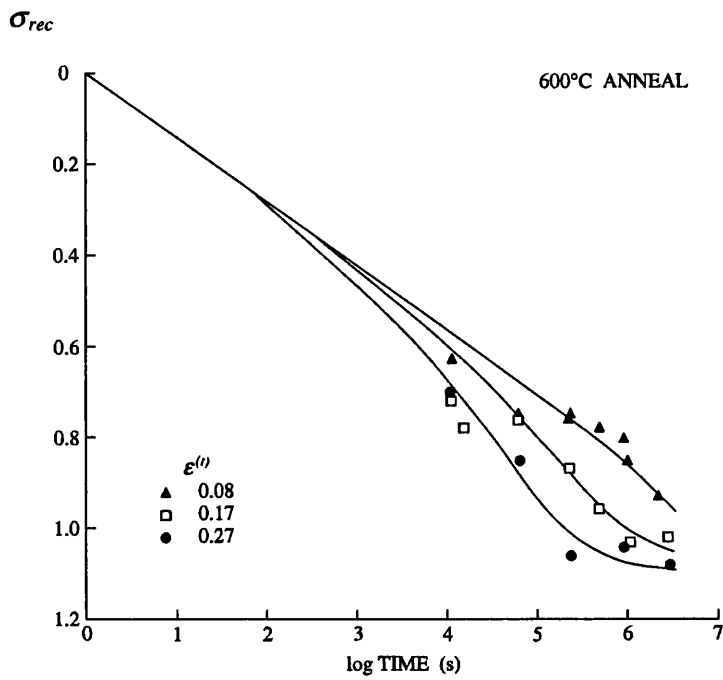


FIG. 14.2. Stress based fractional recovery (equation 14.3) curves for Carrara marble after annealing at constant temperature but various pre-strains (top) and at constant pre-strain but various temperatures (bottom). The curves show trends in the data only and are not fits.

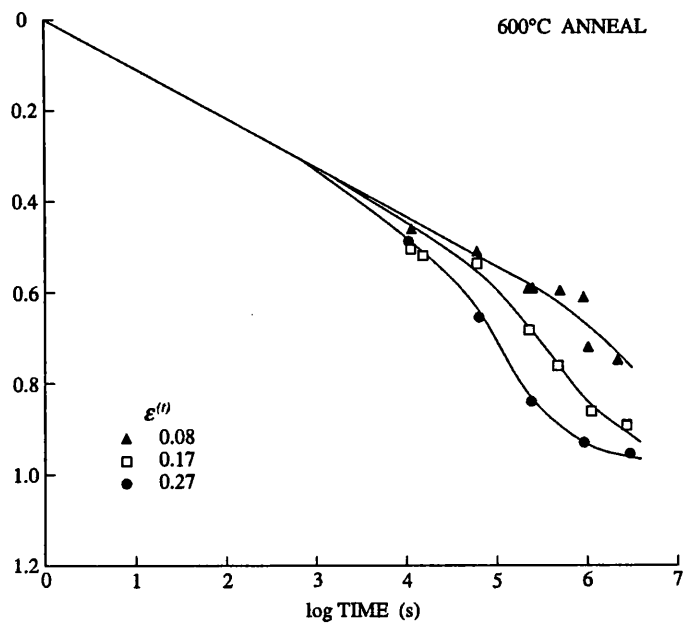
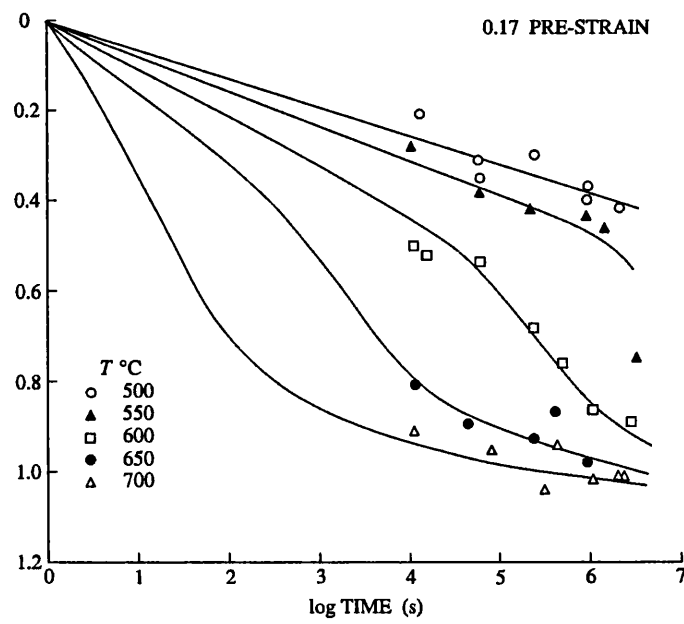
$A_{rec}$  $A_{rec}$ 

FIG. 14.2 contd. Area based fractional recovery (equation 14.4) curves for Carrara marble.

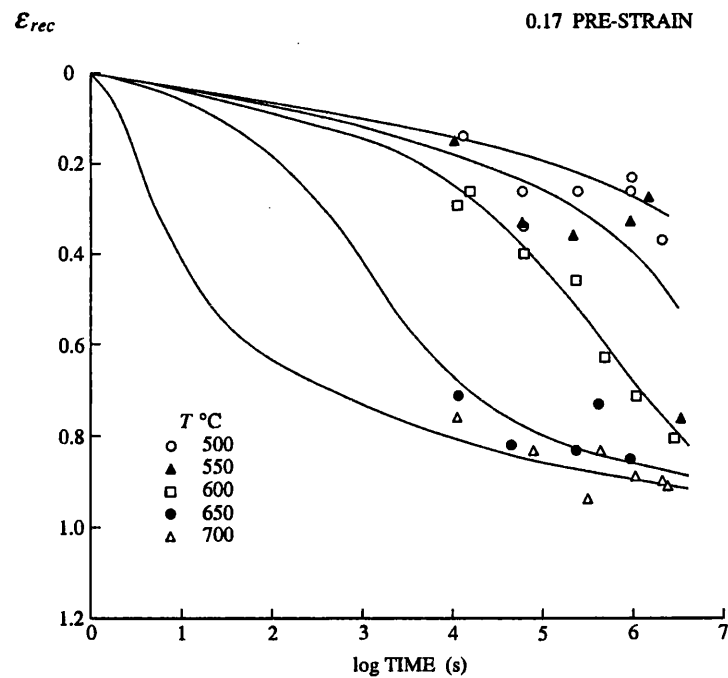
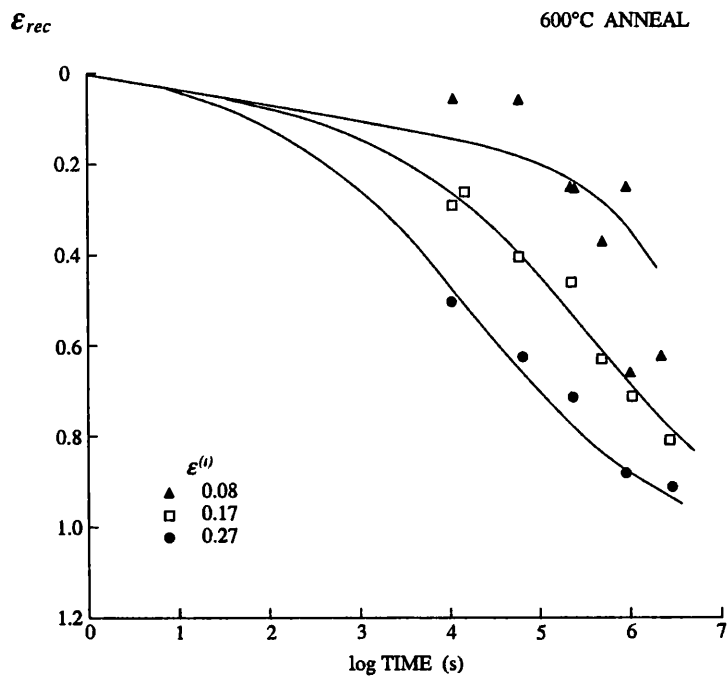


FIG. 14.2 contd. Strain based fractional recovery (equation 14.2) curves for Carrara marble.

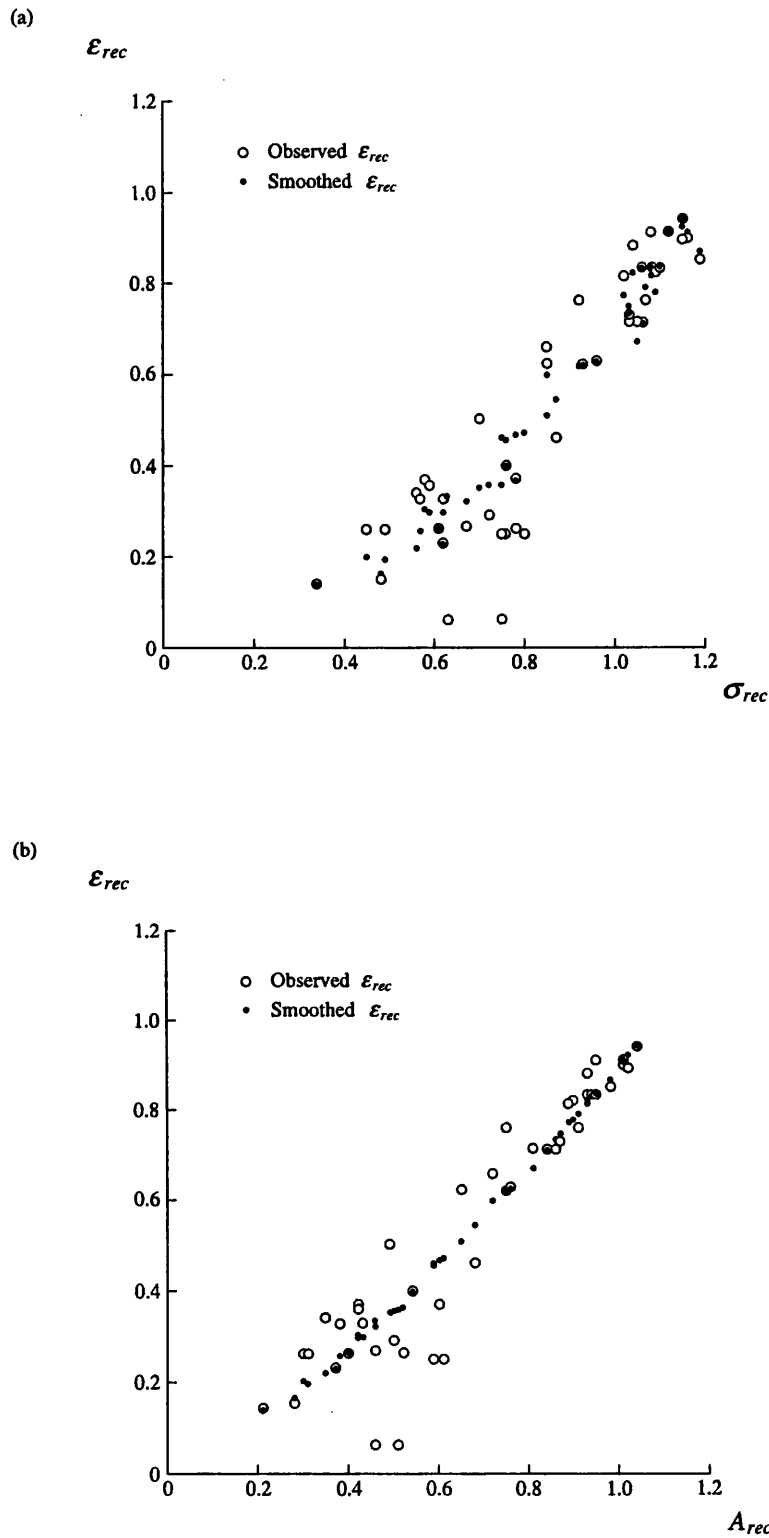


FIG. 14.3. Comparison of (a) the strain and stress based and (b) the strain and area based fractional recovery estimates. The smoothed strain based values are those given by equation 14.7 using the observed stress and area based values.

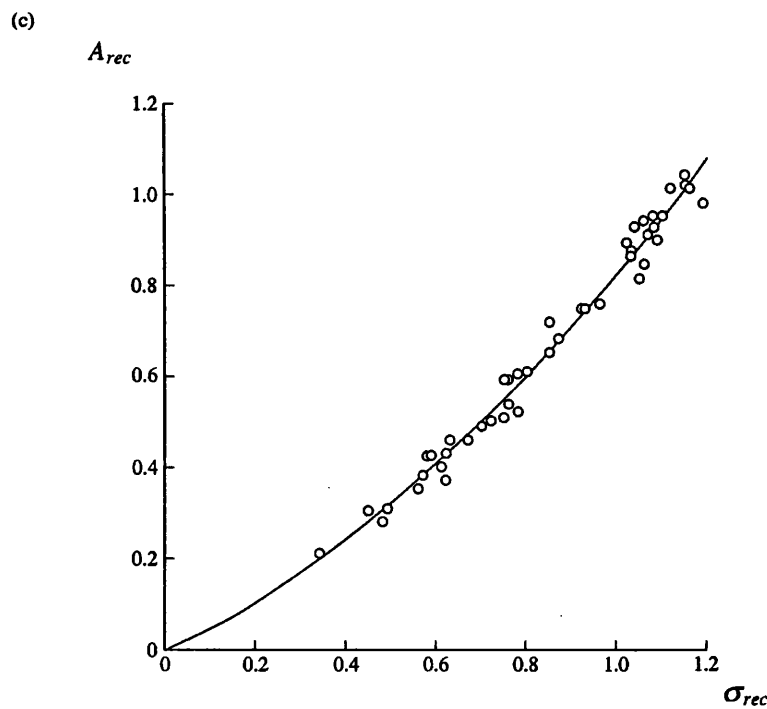


FIG. 14.3 contd. (c) Comparison of the area and stress based fractional recovery estimates with the best least squares fitted quadratic polynomial to the data.

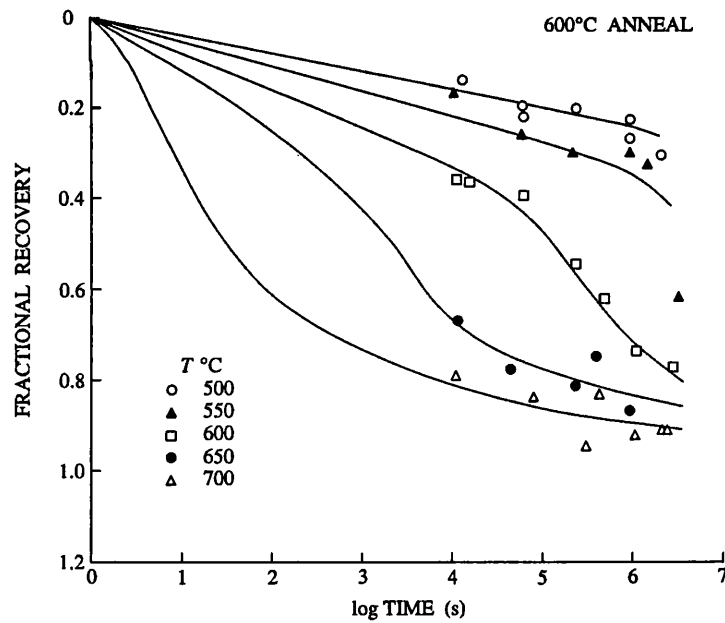
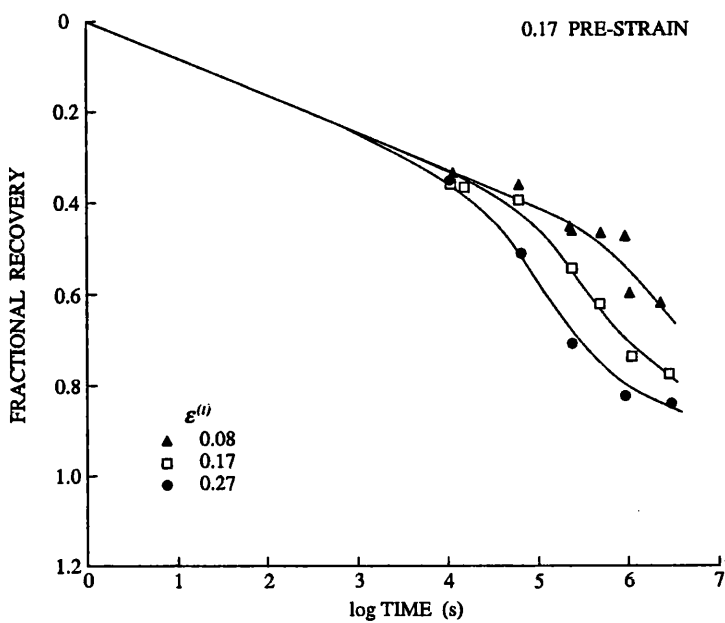


FIG. 14.4. The smoothed fractional recovery (equation 14.7) curves for Carrara marble after annealing at constant temperature but various pre-strains (top) and at constant pre-strain but various temperatures (bottom). The curves show trends in the data only and are not fits.

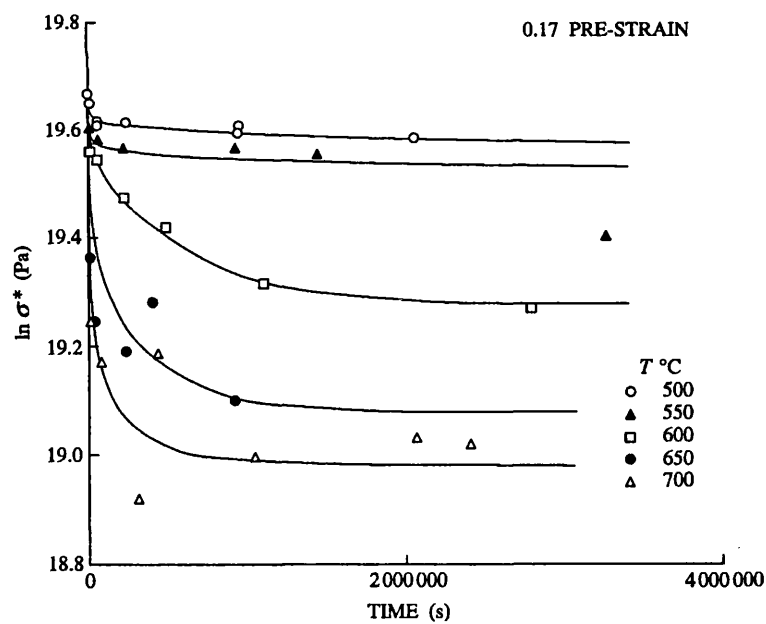
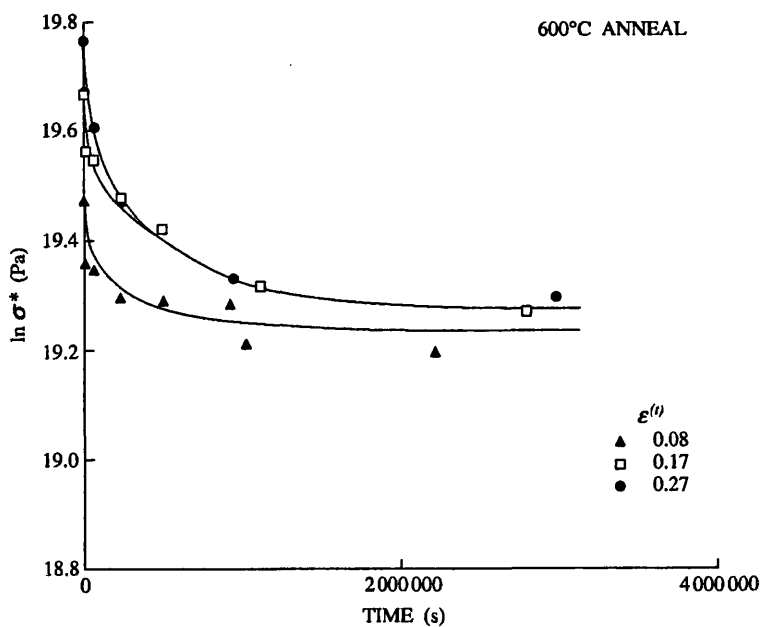


FIG. 14.5. The change in mechanical state as a function of anneal duration for Carrara marble after annealing at constant temperature but various pre-strains (top) and at constant pre-strain but various temperatures (bottom). The curves show trends in the data only and are not fits.  $\mathfrak{R}$  is the slope of these curves.

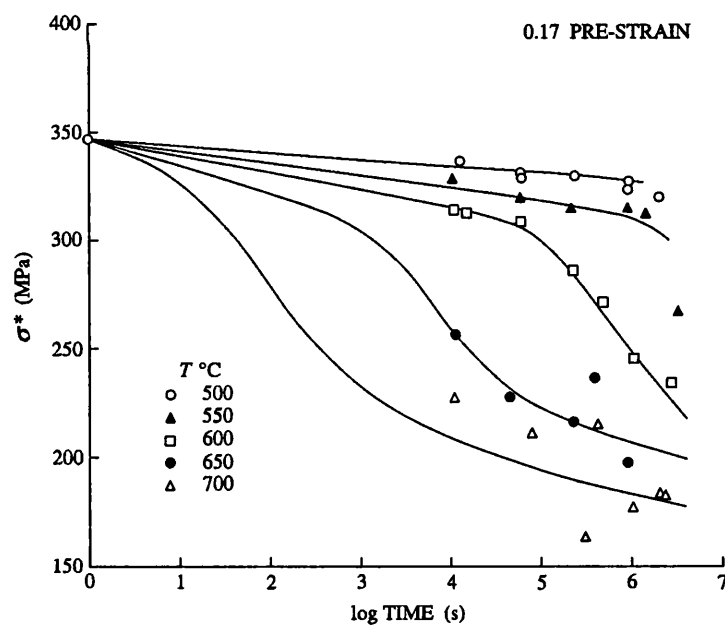
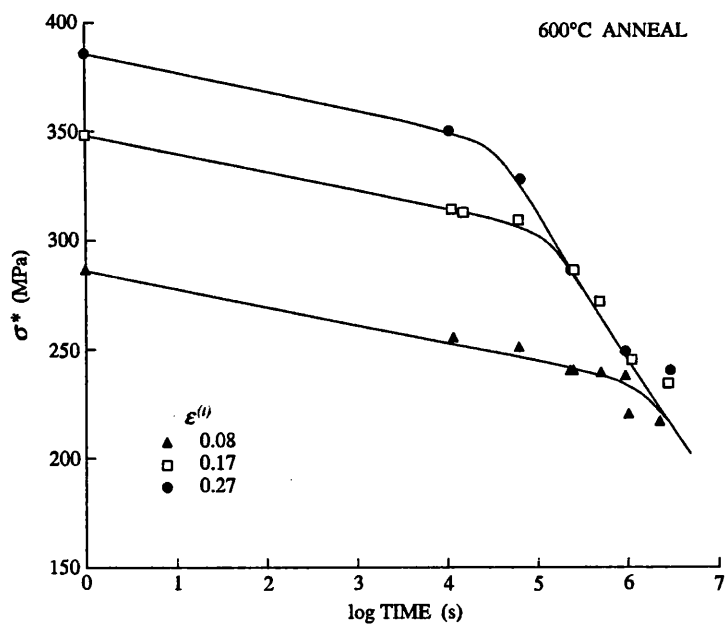


FIG. 14.6. The change in mechanical state as a function of log anneal duration for Carrara marble after annealing at constant temperature but various pre-strains (top) and at constant pre-strain but various temperatures (bottom). The curves show trends in the data only and are not fits.

## 15 SUMMARY AND COMPARISON WITH STEADY-STATE FLOW LAWS

The research presented in this thesis is an exploration of the possibility of applying a fully deformation history independent set of constitutive equations to characterize the inelastic deformation properties of geological materials at elevated confining pressure. For this task the inelastic constitutive equations proposed by Hart (1976) were chosen, because they have been successfully applied to a wide range of materials at room pressure, because they contain material parameters which are relatively easy to evaluate and which are relatively few in number, and because they have been shown to be particularly efficient in numerical modelling applications. Carrara marble was chosen as the material for investigation because it is one of the few geologically significant materials which can be deformed experimentally at low temperatures and confining pressures without cataclasis. Hence the choice of both the constitutive equations and the material present a best case test of the problem.

### 15.1 Summary of the work

There work presented here had two specific aims

- (a) to determine if the material parameters in Hart's equations could be evaluated with sufficient accuracy at elevated confining pressures for the equations to be of use in the geophysical modelling of geological deformation processes and,
- (b) to determine the feasibility of extending Hart's equations to accommodate factors not initially considered in the initial model (*e.g.* the role of impurities, deformation at  $T > 0.45 T_m$ ) but which are nevertheless of great importance in the characterization of geological materials.

Hart's inelastic deformation model was outlined in detail in § 2 - 5, and the attempts to evaluate the material parameters in it for Carrara marble at 200 MPa confining pressure and  $T < 0.45 T_m$  described in § 10 - 13. The experimental results demonstrate unequivocally that the requisite material parameters can be evaluated with sufficient accuracy. However, some of the parameters appear to be influenced by Mg solute impurities in the marble (§ 11), and hence there may be problems in applying the evaluated equations to other calcitic aggregates of different impurity composition. Since the marble is extremely pure (there is only 0.2 wt% Mg), and since such a concentration of impurities is commonplace in all geological starting materials (including synthetic aggregates), the importance of extending Hart's equations to accommodate solute impurity effects is emphasized.

The extension of Hart's model to accommodate factors of geological importance was considered in § 6. Of particular significance is the ability to accommodate compositional, microstructural (grain-size) and environmental (*e.g.* the presence of  $H_2O$ ) variables. However, by far the most significant problem is the extension of the model to  $T > 0.45 T_m$  because all the most important geological materials (*i.e.* quartz, feldspar, olivine and pyroxene) require such temperatures if they are to be deformed without cataclasis at experimentally accessible (on fluid and gas medium apparatus) confining pressures. To augment the semi-theoretical discussion of how such an extension may be achieved (§ 6.4), the deformation independent change of mechanical state which occurs during annealing at elevated temperatures was investigated

(§ 14). Qualitatively, the experimental results support the proposed method of extending Hart's model to higher temperatures.

Numerical simulation of performable deformation experiments is required before the quality of the experimental results can be fully assessed. This has yet to be attempted, although in principle, it is not a difficult task (§ 7.1).

## 15.2 Comparison with steady-state flow laws

As a description of material behaviour, a fully deformation history independent characterization of the inelastic properties of geological materials is clearly superior to that provided by the steady-state flow laws usually chosen for this purpose. However, given that such descriptions are more difficult and time consuming to evaluate, it is important to establish that they make a significant difference to the results of geophysical models of geological deformation processes. This can now be done by using the results presented above and the procedures outlined in § 7.

Modelling of geological deformation processes using Hart's equations has yet to be attempted. However, the case for preferring those equations over steady-state flow laws is given substantial support from a consideration of the problems posed for the latter, by the requirement that experimental results be interpreted in terms of the steady-state approximation. In the following discussion the relationship of the steady-state approximation to Hart's analysis is described, and the problems of applying it to experimental data are outlined. From this perspective the results of previous experimental investigations of the steady-state inelastic deformation properties of Carrara marble are considered, and these are then compared with those presented here.

**15.2.1 The steady-state approximation.** The steady-state approximation is widely applied in two senses. In terms of Hart's analysis, steady-state deformation occurs when

$$d(\ln \sigma^*)/dt = \dot{\alpha}(\Gamma^* - R^*) - \mathfrak{R} = 0 \quad (15.1)$$

(cf. equation 6.43) *i.e.* deformation is described as steady-state when it occurs at constant  $\sigma^*$ . In this sense the steady-state flow law is a constant  $\sigma^*$  curve which describes the relationship between stress and strain-rate at the steady-state value of  $\sigma^*$ .

More frequently, isothermal, plastic deformation is described as steady-state when

$$\gamma = (\partial \ln \sigma / \partial \alpha)_{\dot{\alpha}} = 0 \quad \text{and} \quad (\partial \ln \dot{\alpha} / \partial \alpha)_{\sigma} = 0 \quad (15.2)$$

The steady-state flow law then describes the relationship between the stresses and strain-rates required to satisfy these conditions *i.e.* it describes a  $\gamma = 0$  curve. This description is well suited to the widely employed steady-state creep equations (equations 1.1 - 1.3), which are usually evaluated from constant strain-rate or constant stress experiments conducted at various strain-rates and stresses respectively.

The two descriptions are not the same. The former requires the deformation to be at constant material structure. However, the latter does not because although it specifies that a material deform at constant mechanical state in a constant strain-rate or constant stress test, it does not require the value of the mechanical state in one steady state condition (*i.e.* at one strain-rate or stress) to be the same as that in all others. Hence in a test in which the stress and strain-rate vary, then provided the steady-state conditions (equation 15.2) hold at every instant,

the deformation may still be described as steady-state even when the material structure ( $\sigma^*$ ) is evolving. This difference between the two steady-state descriptions is manifested in the frequent observation (e.g. Hart, 1970 ; Poirier, 1985, pp. 31-33) that the slope of constant  $\sigma^*$  curves is less than the slope of the  $\gamma = 0$  curve when both are plotted in  $\log \sigma / \log \dot{\varepsilon}^{(n)}$  space (i.e. generally  $\nu < 1/n$ , where  $n$  and  $\nu$  are defined in equations 1.1 - 1.3 and equation 2.3 respectively).

**15.2.1.1 Problems of evaluating  $\gamma = 0$  steady-state flow laws :** In the geological literature inelastic constitutive equations are almost always of the  $\gamma = 0$  steady-state type. For these to be successful as steady-state flow laws, it is critical that the deformation is stable when the stress / strain-rate points used to build up the  $\gamma = 0$  curve are determined. Generally the requisite stress / strain-rate points are taken as the stress in a constant strain-rate test when the stress / strain curve becomes flat-topped, or as the strain-rate in a constant stress test when the strain / time curve becomes linear. However, in all tests conducted to a sufficiently large strain (where the deformation is by grain matrix processes), the former is found to be a stress maximum and the latter a strain-rate minimum. It then becomes necessary to determine if this reflects the interruption of steady-state deformation by an instability induced by the geometric constraints acting on the specimen (e.g. § 9.5.1), or whether it is a fundamental consequence of the deformation mechanism(s) operating and therefore indicates that there is no steady-state regime. This is not a simple problem.

The starting point of Hart's analysis is the description of the isothermal, grain matrix, plastic deformation occurring in some increment of time by (equation 2.2)

$$d \ln \sigma = \gamma d\alpha + \nu d \ln \dot{\alpha} \quad (15.3)$$

where  $\gamma$  and  $\nu$  are (equation 2.3)

$$\gamma = (\partial \ln \sigma / \partial \alpha)_\alpha : \nu = (\partial \ln \sigma / \partial \ln \dot{\alpha})_\alpha \quad (15.4)$$

By definition, unstable deformation occurs when the load bearing capacity of an element of a deforming specimen decreases with increasing strain. Combining equation 15.3, the assumption of constant volume deformation and the definitions of stress, strain and strain-rate (cast in terms of cross-sectional areas), it can then be shown that deformation is unstable in tension if

$$\gamma + \nu < 1 \quad (15.5)$$

(Hart, 1967 ; Lin *et al.*, 1981). Since generally  $\nu < 1$ , then when  $\gamma = 0$  the deformation must be unstable. In fact as observed by Hart (1981), generally  $\nu \ll 1$  (cf. figure 12.4b for the values of  $\nu$  for Carrara marble at 281°C), and hence the deformation is unstable for a considerable range of values of  $\gamma$  greater than zero. The implication is that steady-state deformation can never be attained in circumstances where the deformation is fully described by equation 15.3, which for Hart's analysis is at all  $T < 0.45 T_m$ . It therefore follows that  $\gamma = 0$  type steady-state flow laws cannot be applied to describe inelastic properties at these temperatures.

At higher temperatures, the possibility of stable deformation is permitted by the operation of nominally deformation independent recovery processes. However, deformation stability may be difficult to verify as such. When constant  $\sigma^*$  curves are very closely spaced substantial strains may be required to produce an observable change in strain-rate (constant stress test) or stress (constant strain-rate test). For Carrara marble at 400°C the  $\sigma^*$  curves are indeed extremely closely spaced at low strain-rates (figure 15.1a). At higher temperatures this region

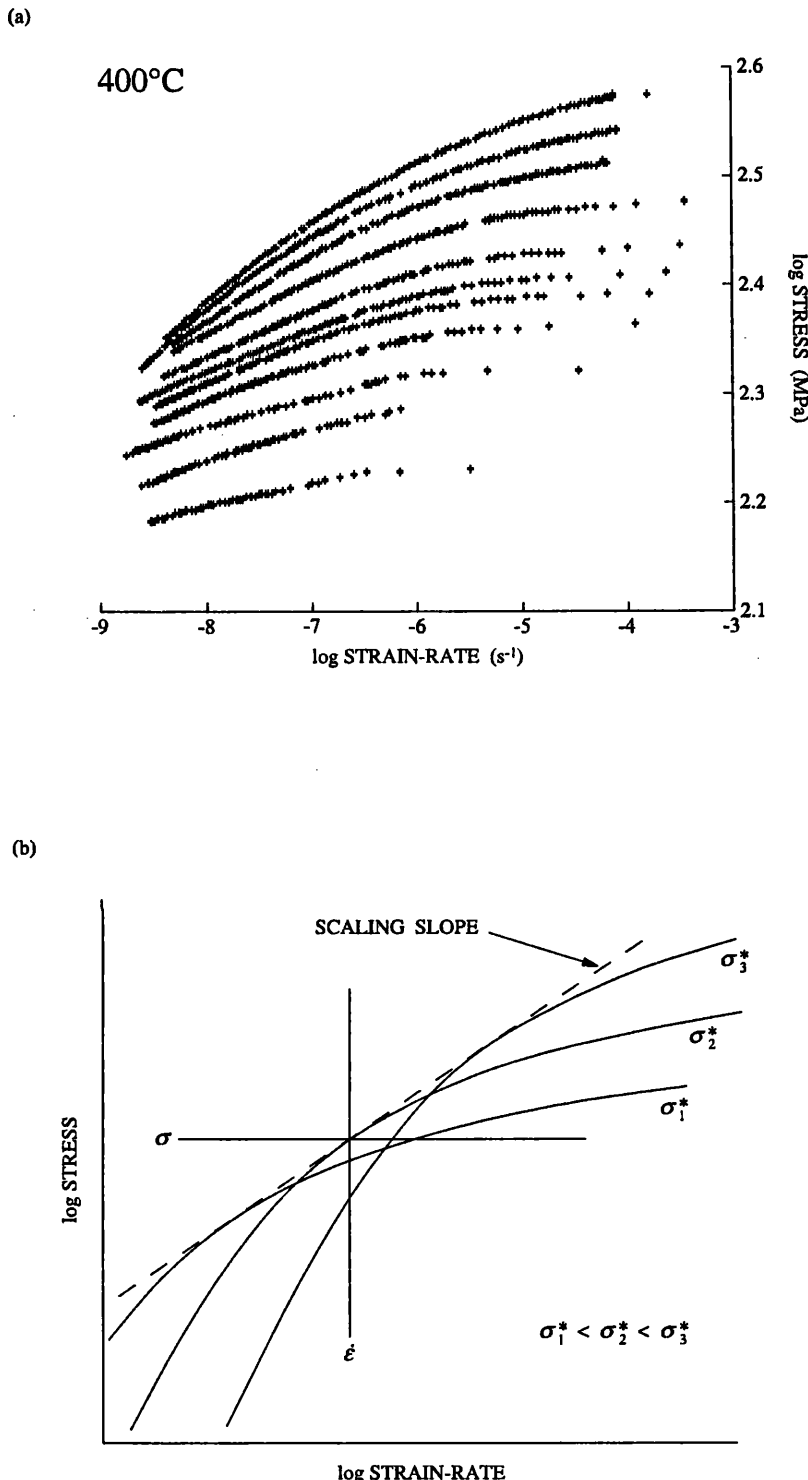


FIG. 15.1. The question of steady-state deformation. (a) The results of the multiple relaxation experiment on Carrara marble at 400°C (cf. figure 12.1) showing also the two highest strain relaxations (J and K) in which there was a small amount of recovery. At low strain-rates the curves become sufficiently close together to indicate that large changes in mechanical state are required to change the flow stress significantly. (b) Crossing constant mechanical state curves leading to a strain-rate minimum in a constant stress creep test and a stress maximum in a constant strain-rate test (redrawn with modifications after Hart *et al.*, 1975).

of closely spaced curves occurs at strain-rates which are accessible in constant strain-rate and constant stress experiments. Close spacing of the  $\sigma^*$  curves is controlled by the values of the material parameters  $\lambda$  and  $m$  in the equation of state for the plastic element. Since the values of these parameters for Carrara marble are similar to those observed in a wide range of other materials, this may be expected to be a common phenomenon.

The errors that arise from treating inherently unstable deformation as stable are illustrated in figure 15.1b. When deformation is unstable, curves of constant  $\sigma^*$  cross. Referring to figure 15.1b, then as the deformation proceeds in a constant stress creep test, the specimen moves from the curves  $\sigma_1^*$  to  $\sigma_2^*$  to  $\sigma_3^*$  with a corresponding decrease and then increase in strain-rate. Similarly, in a constant strain-rate test the path from  $\sigma_1^*$  to  $\sigma_2^*$  to  $\sigma_3^*$  leads to an increase and then decrease in stress (*i.e.* there is work softening even though  $\sigma^*$  is increasing). The creep-rate minimum (or stress maximum) occurs at  $\sigma_2^*$ , but at other stresses (strain-rates) occurs at other  $\sigma^*$  such that the locus of strain-rate minima (stress maxima) as a function of stress (strain-rate) is parallel to the scaling direction of the  $\sigma^*$  curves. This locus clearly does not provide a steady-state flow law, although in  $\log \sigma / \log \dot{\alpha}$  space it is linear and may therefore be confused with the behaviour expected of power law creep (equation 1.2).

Steady-state flow laws of the  $\gamma = 0$  type therefore carry significant problems of evaluation. It appears that they cannot be applied to deformation occurring at  $T < 0.45 T_m$ . At higher temperatures it is essential to achieve large strains without geometric constraint problems, in order to verify that the deformation is truly stable. The observation that the curves of constant  $\sigma^*$  for many materials are closely spaced at elevated temperature in the experimentally accessible strain-rate range, suggests that verification of deformation stability may require strains too great to be achievable in compression testing, and hence emphasizes the importance of tension testing in the determination of steady-state flow laws of this type.

**15.2.1.2 Problems for evaluating constant  $\sigma^*$  steady-state flow laws :** There have been few attempts to determine constant structure steady-state flow laws in the geological literature.

At  $T < 0.45 T_m$  deformation at constant  $\sigma^*$  requires that the athermal work hardening rate equal the dynamic recovery (*sensu stricto*, § 6.4.1.1) rate

$$d(\ln \sigma^*)/d\alpha = \Gamma = \Gamma^* - R^* = 0 \quad (15.6)$$

In such circumstances the steady-state  $\sigma^*$  curve overlies the  $\Gamma = 0$  curve in  $\log \sigma / \log \dot{\alpha}$  space (figure 4.3b). This has never been observed, and as argued above, it is expected from deformation stability considerations, that it never will be.

At  $T > 0.45 T_m$  deformation at constant  $\sigma^*$  occurs when the rate of increase of  $\sigma^*$  due to the deformation equals the rate of decrease of  $\sigma^*$  due to nominally deformation independent processes

$$d(\ln \sigma^*)/dt = \dot{\alpha}\Gamma - \mathfrak{R} = 0 \quad (15.7)$$

Such circumstances are entirely feasible from the perspective of Hart's analysis. However, at these temperatures the operation of deformation independent recovery processes complicates the task of determining mechanical properties at constant  $\sigma^*$ . Load relaxation curves are not in general curves of constant  $\sigma^*$ , because during relaxation  $\sigma^*$  is not dynamically maintained, and so  $\sigma^*$  must change when  $\mathfrak{R}$  is non-zero. In practice this problem may not be as significant as it appears. If the constant  $\sigma^*$  curves are very closely spaced in the accessible strain-rate range,

then changes in  $\sigma^*$  during relaxation have little effect on the  $\log \sigma / \log \alpha$  location of the relaxation curve. As observed above, this may be true for many materials. In the case that the rates of recovery are critically dependent on  $\sigma^*$ , then there is a maximum  $\sigma^*$  curve above which recovery to that maximum  $\sigma^*$  is effectively instantaneous, and below which rates of recovery are negligibly small. The maximum  $\sigma^*$  curve then provides steady-state properties. Such a case was postulated by Hart (1981), but the recovery results presented here (cf. figure 14.5) indicate that the  $\sigma^*$  dependence of the rate of recovery is not sufficiently critical for this to be true of Carrara marble.

Isostructural properties may be determined from strain-rate or stress change experiments, but the interpretation of these tests is complicated by the transient period after each change (cf. figure 6.7a), and by the possibility of recovery induced changes in  $\sigma^*$  during those transients.

Steady-state flow laws of the constant  $\sigma^*$  type therefore may also be difficult to evaluate. At  $T < 0.45 T_m$  deformation is not expected ever to be at steady-state, while at higher temperatures nominally deformation independent recovery processes complicate the evaluation of the steady-state  $\sigma^*$  curve. The significance of the latter problem depends on the spacing of the constant  $\sigma^*$  curves in the strain-rate range of interest. In practice it may be necessary to confirm that the experimentally determined steady-state  $\sigma^*$  curve conforms to that expected from the evaluations of the  $\Gamma$  and  $\mathfrak{R}$  functions in equation 15.7.

**15.2.2 Previously published flow laws for Carrara marble.** Given the previous observations, it is anticipated that it is impractical to fit any steady-state flow law to describe the inelastic deformation of Carrara marble at  $T < 0.45 T_m$  (*i.e.* at  $T < 450^\circ\text{C}$ ). At higher temperatures steady-state flow laws of either type may be determined, but the results must be interpreted with caution with respect to the stability of the deformation ( $\gamma = 0$  type) and with respect to the complicating influence of recovery processes (constant  $\sigma^*$  type).

**15.2.2.1 Outline of the previous data :** Steady-state flow laws of  $\gamma = 0$  type for Carrara marble have been published by Rutter (1974) and by Schmid *et al.* (1980). The experiments of Rutter were conducted on an apparatus of the same design as HEARD1, in the temperature range 20 to  $500^\circ\text{C}$  and at a confining pressure of 150 MPa. The effect of a pore fluid was also investigated but was shown to be negligible at constant effective confining pressure. The experiments of Schmid *et al.* were conducted on a gas medium apparatus, in the temperature range 600 to  $1050^\circ\text{C}$  and at a confining pressure of 300 MPa. In both experimental programmes the material parameters in the steady-state flow laws were evaluated from the stresses supported at a total strain of 0.10 in constant displacement-rate tests conducted at various displacement-rates. At their highest temperatures, Schmid *et al.* also utilize the  $\gamma = 0$  (not isostructural) flow stresses obtained from strain-rate change tests.

In all the experiments conducted at  $T < 400^\circ\text{C}$ , the rate of work hardening was sufficiently large at 0.10 strain to prevent any attempt to fit a steady-state flow law. At higher temperatures it was considered to be sufficiently small to allow the stress / strain curve to be approximated as flat-topped. At these higher temperatures, three regimes of deformation behaviour were recognized ;

(a) at stresses above 100 MPa the mechanical data is described by an exponential flow law (equation 1.1)

$$\dot{\varepsilon}^{(n)} = A \exp(B\sigma) \exp(-H_s/RT) \quad (15.8)$$

where

$$\log A = 5.77 \text{ (s}^{-1}) \quad : \quad B = 0.088 \text{ MPa}^{-1} \quad : \quad H_s = 260 \text{ kJmol}^{-1}$$

(Rutter, 1974, but note his typographic error in the value of  $B$ );

(b) at stresses between 20 and 100 MPa the data is described by a power law creep equation (equation 1.2)

$$\dot{\varepsilon}^{(n)} = A \sigma^n \exp(-H_s/RT) \quad (15.9)$$

where

$$\log A = 3.10 \text{ (MPa}^{-n} \text{s}^{-1}) \quad : \quad n = 7.6 \quad : \quad H_s = 419 \text{ kJmol}^{-1}$$

(Schmid *et al.*, 1980);

(c) at stresses below 20 MPa a power law creep equation also describes the data but with

$$\log A \approx 8.10 \text{ (MPa}^{-n} \text{s}^{-1}) \quad : \quad n \approx 4.2 \quad : \quad H_s \approx 427 \text{ kJmol}^{-1}$$

(Schmid *et al.*, 1980).

At constant temperature the data presented in  $\log \sigma / \log \dot{\varepsilon}^{(n)}$  space therefore defines a broad, downwardly concave curve which is fitted in three segments.

Schmid *et al.* also present some load relaxation curves generated at the end of several of their constant displacement-rate tests. These show qualitatively the same features as the  $\gamma = 0$  data in  $\log \sigma / \log \dot{\varepsilon}^{(n)}$  space but no attempt was made to fit a constant  $\sigma^*$  type flow law to them.

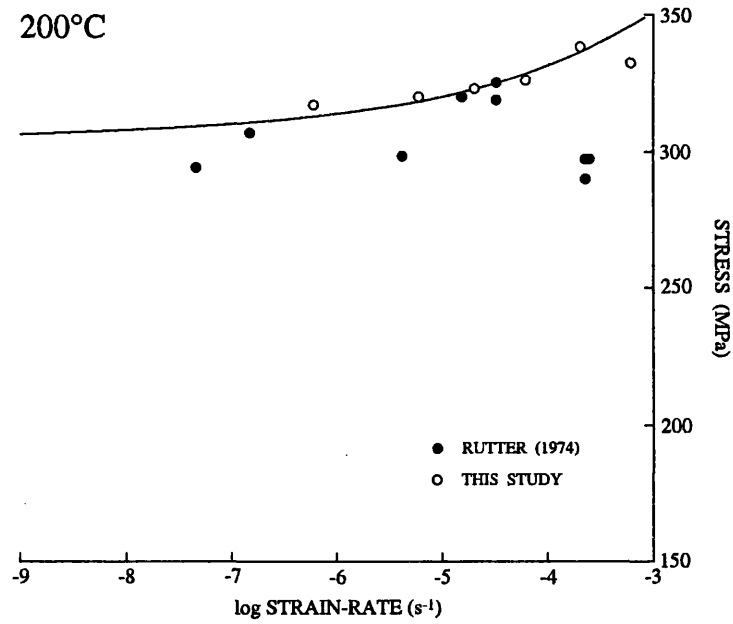
**15.2.2.2 Comparisons with the data presented here :** Only Rutter's results generated at 200 and 400°C may be directly compared with the results of this study. His data includes a correction for the load supported by the copper jacket in the experiment, and a temperature correction to the force gauge stiffness which assumes that the force gauge is at the same temperature as the specimen. Hence to be directly comparable with the data of this study, 20 to 30 MPa must be added to his stresses at 200°C and 30 to 40 MPa at 400°C (§ 9.1.1.3, § 9.3.3.2). After this correction the data correspond well (figure 15.2).

At both temperatures, the change in  $\sigma^*$  with strain is approximately strain-rate independent in the range of strain-rates employed in these studies (*cf.* figure 13.4). Consequently, the data from 0.10 strain are at approximately constant  $\sigma^*$  ( $\approx 305$  MPa, table 13.1) and should be described by a constant  $\sigma^*$  curve. This is indeed the case (figure 15.2). At 400°C the constant  $\sigma^*$  curve may be compared with the fitted exponential creep equation (equation 15.8). Both describe the data within the error on the data (figure 15.2b). However, it should be recalled that the constant  $\sigma^*$  curve describes the relaxation data for this  $\sigma^*$  very closely (relaxation H at 400°C, figure 12.1), *i.e.* the exponential creep equation is a poor description of that data.

**15.2.2.3 Steady-state deformation in Carrara marble :** Clearly the steady-state approximation cannot be applied to the experimental results generated on Carrara marble at  $T < 400^\circ\text{C}$ . Deformation history independent flow laws are therefore the only appropriate characterization of its inelastic properties at these temperatures, and the results presented in this study are the first attempt to do this.

The capacity of the fitted exponential steady-state flow law (equation 15.8) to describe the high stress behaviour at  $T > 400^\circ\text{C}$  is questionable. With the exception of Rutter's lowest strain-rate (less than  $1 \times 10^{-5} \text{ s}^{-1}$ ) data at 500°C, none of the stress / strain curves from this regime are

(a)



(b)

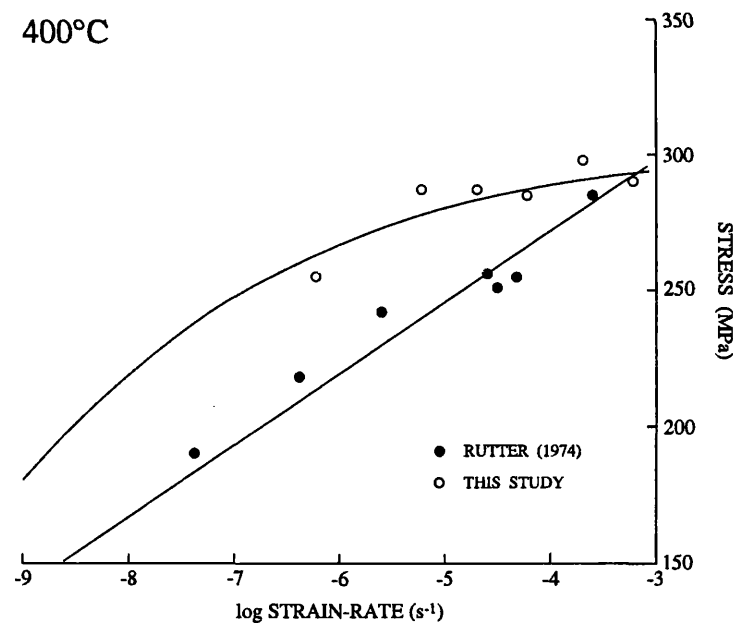


FIG. 15.2. Comparison of the stresses supported at  $\dot{\varepsilon}^{(t)} = 0.10$  in constant displacement-rate experiments conducted by Rutter (1974) and in this study. For consistent calibration procedures 20-30 MPa must be added to Rutter's stresses at 200°C, and 30-40 MPa to those stresses at 400°C.  $\sigma^* = 305$  MPa curves are shown in both figures, while the linear fit at 400°C is Rutter's exponential law creep fit (equation 15.8) to his 400 and 500°C data.

flat-topped, even when plotted over a small strain range (0 to 0.12). The implication is that the deformation was not at steady-state in these experiments, and this is most certainly true of the 400°C results obtained in this study.

The power law fits (equation 15.9) applicable at lower differential stresses may have greater validity, particularly at the higher temperatures. However, all the data was obtained at rather small strains and so the stability of the deformation remains open to question.

The full significance of these conclusions is difficult to ascertain in advance of the results of numerical modelling using the various equations.

### 15.3 The scope for further work

Although the experimental results presented in this study indicate that Hart's description of inelastic deformation can be applied successfully to mechanical data obtained at elevated confining pressures, several problems are remain to be addressed if the approach is to have general application for geological materials. The most significant of these include ;

- (a) a parameterization of the equations for the effects of solute impurities, finely dispersed second phase inclusions and grain-size,
- (b) a modification of the equations to accommodate other deformation variables, and in particular pressure and the presence of fluids,
- (c) a closer consideration of the  $\sigma^*$  evolution equation, particularly with respect to the complicating influence that mechanical twinning has on the evaluation of the material parameters in that equation, and with respect to the mechanical significance of a developing crystallographic preferred orientation / shape fabric as the deformation is taken to large strains,
- (d) a full determination of the recovery function with an accompanying quantitative evaluation of the ability to extend Hart's analysis to  $T > 0.45 T_m$ , and
- (e) an evaluation the material parameters in the grain boundary sliding extension of the deformation model.

Problems (b), (c) and (d) may be addressed by further experiments on Carrara marble. Problems (a) and (e) will inevitably require experiments on synthetic aggregates because of the need to control carefully the variables under consideration. Experiments conducted in tension will be necessary for the large strain problems (c and e). Large strain tension experiments will also provide a more systematic evaluation of the steady-state approximation and hence of the case for employing non-steady-state inelastic constitutive relations.

Numerical modelling with the equations, both of deformation experiments and of geological deformation processes, is essential in order to test the evaluated material parameters and to determine the difference (particularly with respect to steady-state flow laws) the equations make on the results of such modelling.

Of outstanding geological significance would be the identification of  $\sigma^*$  with some observable feature of the deformation microstructure. In principle, it would then be possible to determine the mechanical state of a material (and hence its deformation properties) merely by inspection. This in turn would allow a much closer integration of field based metamorphic  $pTt$  type studies with geophysical deformation models.

## REFERENCES

ABRAMS, H. (1971) Grain-size measurement by the intercept method. *Metallogr.* **4**, 425-441.

ALDEN, T. H. (1967) The origin of superplasticity in Sn - 5% Bi alloy. *Acta Metall.* **15**, 469-480.

ALEXOPOULOS, P. S., CHO, C. W., HU, C. P. and LI, C.-Y. (1981) Determination of the anelastic modulus for several metals. *Acta Metall.* **29**, 569-577.

ALEXOPOULOS, P. S., KEUSSEYAN, R. L., WIRE, G. L. and LI, C.-Y. (1982) Experimental investigation of nonelastic deformation emphasizing transient phenomena by using a state variable approach. In *Mechanical Testing for Deformation Model Development* (eds. R. W. ROHDE and J. C. SWEARENGEN), pp. 148-184. ASTM STP 765.

ASHBY, M. F. (1971) The deformation of plastically non-homogeneous alloys. In *Strengthening Methods in Crystals* (eds. A. KELLY and R. B. NICHOLSON), pp. 137-192. Applied Science Publishers.

ATKINSON, B. K. (1979) Fracture toughness of Tennessee sandstone and Carrara marble using the double torsion testing method. *Int. J. Rock Mech. Min. Sci. Geomech. Abstr.* **16**, 49-53.

ATKINSON, B. K. (1984) Subcritical crack growth in geological materials. *J. Geophys. Res.* **89**, 4077-4114.

ATKINSON, B. K. and MEREDITH, P. G. (1987) Experimental fracture mechanics data for rocks and minerals. In *Fracture Mechanics of Rock* (ed. B. K. ATKINSON), pp. 477-525. Academic Press.

BAMMANN, D. and KRIEG, R. D. (1987) Summary and Critique. In *Unified Constitutive Equations for Creep and Plasticity* (ed. A. K. MILLER), pp. 303-336. Elsevier Applied Science.

BANTHIA, V. and MUKHERJEE, S. (1985) On an improved time integration scheme for stiff constitutive models of inelastic deformation. *J. Engng. Mater. Technol.* **107**, 282-285.

BARRETT, C. R. and NIX, W. D. (1965) A model for steady state creep based on the motion of jogged screw dislocations. *Acta Metall.* **13**, 1247-1258.

BIROCHEAU, J. and OYTANA, C. (1983) Experimental analysis of the relationship between dip test techniques and the plastic equation of state. In *Strength of Metals and Alloys*, Proc. 6th Int. Conf. on the Strength of Metals and Alloys, 1982, Melbourne (ed. R. C. GIFFINS), pp. 569-574. Pergamon Press.

BLOOMFIELD, J. P. and COVEY-CRUMP, S. J. (1992) Correlating mechanical data with microstructural observations in deformation experiments on synthetic two-phase aggregates. *J. Struct. Geol.* (in press).

BÖKER, R. VON (1915) Die mechanik der bleibenden formänderung in kristallinisch aufgebauten körpern. *Ver. Deut. Ing. Mitt. Forsch.* **175**, 1-51.

BORN, M. (1949) *Natural Philosophy of Cause and Chance*. Oxford University Press.

BOYCE, W. E. and DI PRIMA, R. C. (1986) *Elementary Differential Equations and Boundary Value Problems*, 4th edn., 654 pp. John Wiley & Sons.

BUCHDAHL, H. A. (1949) On the theorem of Carathéodory. *Am. J. Phys.* **17**, 44-46.

BUCHDAHL, H. A. (1955) Simplification of a proof of Carathéodory's theorem. *Am. J. Phys.* **23**, 65-66.

CARATHÉODORY, C. (1909) Untersuchungen über die grundlagen der thermodynamik. *Math. Ann.* **67**, 355-386.

CARMIGNANI, L. and KLIGFIELD, R. (1990) Crustal extension in the Northern Apennines : the transition from compression to extension in the Alpi Apuane core complex. *Tectonics* **9**, 1275-1303.

CASEY, M., RUTTER, E. H., SCHMID, S. M., SIDDANS, A. W. B. and WHALLEY, J. S. (1978) Texture development in experimentally deformed calcite rocks. In *Textures of Materials*, Proc. 5th Int. Conf. on Textures of Materials, 1978, Aachen (eds. G. GOTTSSTEIN and K. LÜCKE), 2, 231-240. Springer-Verlag.

CHANDRA, A. and MUKHERJEE, S. (1984a) A finite element analysis of metal-forming problems with an elastic-viscoplastic material model. *Int. J. Num. Meth. Engng.* **20**, 1613-1628.

CHANDRA, A. and MUKHERJEE, S. (1984b) Boundary element formulations for large strain-large deformation problems of viscoplasticity. *Int. J. Solids Struct.* **20**, 41-53.

CHANG, K. J., LANCE, R. and MUKHERJEE, S. (1979) Inelastic bending of beams under time-varying moments – a state variable approach. *J. Press. Vessel Technol.* **101**, 305-310.

CHEN, I. W. and ARGON, A. S. (1979) Steady state power law creep in heterogeneous alloys with coarse microstructures. *Acta Metall.* **27**, 785-791.

COOPER, G. A. (1977) Optimization of the three-point bend test for fracture energy measurement. *J. Mater. Sci.* **12**, 277-289.

CORDTS, D. and KOLLMANN, F. G. (1986) An implicit time integration scheme for inelastic constitutive equations with internal state variables. *Int. J. Num. Meth. Engng.* **23**, 533-554.

DANDEKAR, D. P. (1968a) Variation of the elastic constants of calcite with temperature. *J. Appl. Phys.* **39**, 3694-3699.

DANDEKAR, D. P. (1968b) Pressure dependence of the elastic constants of calcite. *Phys. Rev.* **172**, 873-877.

DANDEKAR, D. P. and RUOFF, A. L. (1968) Temperature dependence of the elastic constants of calcite between 160° and 300°K. *J. Appl. Phys.* **39**, 6004-6009.

DI PISA, A., FRANCESCHELLI, M., LEONI, L. and MECCHERI, M. (1985) Regional variation of the metamorphic temperatures across the Tuscanid I Unit and its implications on the alpine metamorphism (Apuan Alps, N. Tuscany). *N. Jb. Miner. Abh.* **151**, 197-211.

DOTSENKO, V. I. (1979) Stress relaxation in crystals. *Phys. Stat. Sol. (b)* **93**, 11-43.

EDMOND, J. M. and PATERSON, M. S. (1972) Volume changes during the deformation of rocks at high pressures. *Int. J. Rock Mech. Min. Sci.* **9**, 161-182.

EGGERT, G. M. and DAWSON, P. R. (1987) On the use of internal variable constitutive equations in transient forming processes. *Int. J. Mech. Sci.* **29**, 95-113.

ELLIS, F. V., WIRE, G. L. and LI, C.-Y. (1975) Effects of cold work and mechanical equation of state in 1100 aluminium alloy. *J. Engng. Mater. Technol.* **97**, 338-342.

FERRON, G. and MLIHA-TOUATI, M. (1982) Plastic instability and the mechanical equation of state in simple tension. *Scripta Metall.* **16**, 911-916.

FISCHER, G. J. and PATERSON, M. S. (1989) Dilatancy during rock deformation at high temperatures and pressures. *J. Geophys. Res.* **94**, 17607-17617.

FISCHMEISTER, H. and KARLSSON, B. (1977) Plasticity of two-phase materials with coarse microstructure (in German). *Z. Metallk.* **68**, 311-327.

FORTES, M. A. and EMILIA ROSA, M. (1984) The form of a constitutive equation of plastic deformation compatible with stress relaxation data. *Acta Metall.* **32**, 663-670.

FREDRICH, J. T., EVANS, B. and WONG, T.-F. (1989) Micromechanics of the brittle to plastic transition in Carrara marble. *J. Geophys. Res.* **94**, 4129-4145.

FUNG, Y. C. (1965) *Foundations of Solid Mechanics*, 525 pp. Prentice-Hall Inc.

GOLOMB, M. and SHANKS, M. (1950) *Elements of Ordinary Differential Equations*, 356 pp. McGraw-Hill.

GREENBERG, M. D. (1978) *Foundations of Applied Mathematics*, 638 pp. Prentice-Hall Inc.

GUPTA, I. and LI, J. C. M. (1970) Stress relaxation, internal stress and work hardening in some bcc metals and alloys. *Metall. Trans.* **1**, 2323-2330.

GURLAND, J. (1979) A structural approach to the yield strength of two-phase alloys with coarse microstructures. *Mater. Sci. Engng.* **40**, 59-71.

GYPEN, L. A. and DERUYTTERE, A. (1982) Thermally activated deformation in tantalum base solid solutions. *J. Less Comm. Met.* **86**, 219-240.

HARRIS, J. (1977) *Rheology and non-Newtonian Flow*, 338 pp. Longman Group Ltd.

HART, E. W. (1967) Theory of the tensile test. *Acta Metall.* **15**, 351-355.

HART, E. W. (1970) A phenomenological theory for plastic deformation of polycrystalline metals. *Acta Metall.* **18**, 599-610.

HART, E. W. (1975) The plastic equation of state at high and low temperatures. In *Rate Processes in Plastic Deformation*, Proc. of J. E. Dorn Memorial Symposium, Oct. 1972, Cleveland, Ohio (eds. J. C. M. LI and A. K. MUKHERJEE), pp. 284-297. ASM.

HART, E. W. (1976) Constitutive equations for the nonelastic deformation of metals. *J. Engng. Mater. Technol.* **98**, 193-202.

HART, E. W. (1978) Constitutive equations for nonelastic deformation. *Nucl. Engng. Design* **46**, 179-185.

HART, E. W. (1979) Load relaxation testing and material constitutive relations. In *Stress Relaxation Testing* (ed. A. FOX), pp. 5-20. ASTM STP 676.

HART, E. W. (1981) A critical examination of steady state creep. In *Creep in Structures* (eds. A. R. S. PONTER and D. R. HAYHURST), pp. 90-102. Springer.

HART, E. W. (1982) The effects of material rotations in tension-torsion testing. *Int. J. Solids Struct.* **18**, 1031-1042.

HART, E. W. (1984) A micromechanical basis for constitutive equations with internal state variables. *J. Engng. Mater. Technol.* **106**, 322-325.

HART, E. W. and LI, C.-Y. (1977) The use of state variables in the description of irradiation creep and deformation of metals. In *Zirconium in the Nuclear Industry* (eds. A. L. LOWE JR. and G. W. PARRY), pp. 315-325. ASTM STP 633.

HART, E. W. and SOLOMON, H. D. (1973) Load relaxation studies of polycrystalline high purity aluminium. *Acta Metall.* **21**, 295-307.

HART, E. W., LI, C.-Y., YAMADA, H. and WIRE, G. L. (1975) Phenomenological theory : a guide to constitutive relations and fundamental deformation properties. In *Constitutive Equations in Plasticity* (ed. A. S. ARGON), pp. 149-197. MIT Press.

HAUSER, F. E. (1966) Techniques for measuring stress / strain relations at high strain-rates. *Exp. Mech.* **6**, 395-402.

HENDERSON, D. W., KUO, R. C. and LI, C.-Y. (1984) The applicability of Hart's state variable model to large strain-rate ranges. *Scripta Metall.* **18**, 1021-1023.

HILDEBRAND, F. B. (1976) *Advanced Calculus for Applications*, 2nd edn., 733 pp. Prentice-Hall.

HILL, R. (1959) Some basic principles in the mechanics of solids without a natural time. *J. Mech. Phys. Solids* **7**, 209-225.

HIRTH, J. P. and LOTHE, J. (1982) *Theory of Dislocations*, 2nd edn., 857 pp. John Wiley & Sons.

HONEYCOMBE, R. W. K. (1968) *The Plastic Deformation of Metals*, 477pp. Edward Arnold (Publishers) Ltd.

HUANG, F. H., ELLIS, F. V. and LI, C.-Y. (1977) Comparison of load relaxation data of Type 316 stainless steel with Hart's deformation model. *Metall. Trans. A* **8A**, 699-704.

HUANG, F. H., SABOL, G. P., McDONALD, S. G. and LI, C.-Y. (1979) Load relaxation studies of zircaloy-4. *J. Nucl. Mater.* **79**, 214-226.

HUI, C.-Y. (1985) A uniformly valid asymptotic solution of Hart's equations for constant, nonelastic, extensional strain rate. *Int. J. Sol. Struct.* **21**, 411-421.

JACKSON, M. S., CHO, C. W., ALEXOPOULOS, P. and LI, C.-Y. (1981) A phenomenological model for transient deformation based on state variables. *J. Engng. Mater. Technol.* **103**, 314-325.

JAEGER, J. C. and COOK, N. G. W. (1979) *Fundamentals of Rock Mechanics*, 3rd edn., 593 pp. Chapman and Hall.

JOHNSON, G. D., STRAALSUND, J. L. and WIRE, G. L. (1977) A new approach to stress to rupture data correlation. *Mater. Sci. Engng.* **28**, 69-75.

JOHNSTON, W. G. and GILMAN, J. J. (1959) Dislocation velocities, dislocation densities and plastic flow in lithium fluoride crystals. *J. Appl. Phys.* **30**, 129-144.

KÁRMÁN, T. VON (1911) Festigkeitsversuche unter allseitigem druck. *Z. Ver. Deut. Ingr.* **55**, 1749-1757.

KEUSSEYAN, R. L., WANAGEL, J., OCKEN, H., ROBERTS, J. T. A. and LI, C.-Y. (1981) The effect of fabrication variables on the load relaxation behaviour of unirradiated zircaloy sheet. *J. Nucl. Mater.* **98**, 86-97.

KIRBY, S. H. and MCCORMICK, J. W. (1984) Inelastic properties of rocks and minerals. In *Handbook of Physical Properties of Rocks* (ed. R. S. CARMICHAEL), 3, 139-280. CRC Press.

KLIGFIELD, R., CARMIGNANI, L. and OWENS, W. H. (1981) Strain analysis of a Northern Apennine shear zone using deformed marble breccias. *J. Struct. Geol.* **3**, 421-436.

KLIGFIELD, R., HUNZIKER, J., DALLMEYER, R. D. and SCHAMEL, S. (1986) Dating of deformation phases using K-Ar and  $^{40}\text{Ar}/^{39}\text{Ar}$  techniques : results from the Northern Apennines. *J. Struct. Geol.* **8**, 781-798.

KOCKS, U. F., ARGON, A. S. and ASHBY, M. F. (1975) Thermodynamics and kinetics of slip. *Prog. Mater. Sci.* **19**.

KORHONEN, M. A. and LI, C.-Y. (1982) Deformation modelling of aluminium during repeated stress relaxation runs. *Scripta Metall.* **16**, 951-955.

KORHONEN, M. A., LI, C.-Y. and GIBELING, J. C. (1985a) A state variable approach to transient creep deformation in stress reduction experiments. *Mater. Sci. Engng.* **74**, 179-188.

KORHONEN, M. A., HANNULA, S.-P. and LI, C.-Y. (1985b) Work hardening correlations based on state variables in some fcc metals in monotonic loading. *Metall. Trans. A* **16A**, 411-420.

KORHONEN, M. A., HANNULA, S.-P. and LI, C.-Y. (1987) State variable theories based on Hart's formulation. In *Unified Constitutive Equations for Creep and Plasticity* (ed. A. K. MILLER), pp. 89-137. Elsevier Applied Science.

KUMAR, V. and MUKHERJEE, S. (1976) Creep analysis of structures using a new equation of state type constitutive relation. *Comp. Struct.* **6**, 429-437.

KUMAR, V. and MUKHERJEE, S. (1977a) Time-dependent inelastic analysis of metallic media using constitutive relations with state variables. *Nucl. Engng. Design* **41**, 27-43.

KUMAR, V. and MUKHERJEE, S. (1977b) Creep analysis of metallic structures in the presence of thermal gradients using newer constitutive relations. *J. Press. Vessel Technol.* **99**, 272-280.

KUMAR, V. and MUKHERJEE, S. (1977c) A boundary integral equation formulation for time-dependent inelastic deformation in metals. *Int. J. Mech. Sci.* **19**, 713-724.

KUMAR, V., MORJARIA, M. and MUKHERJEE, S. (1980) Numerical integration of some stiff constitutive models of inelastic deformation. *J. Engng. Mater. Technol.* **102**, 92-96.

KWON, O. and DEARDO, A. J. (1990) On the recovery and recrystallization which attend static softening in hot-deformed copper and aluminium. *Acta Metall.* **38**, 41-54.

LAASRAOUI, A. and JONAS, J. J. (1991) Recrystallization of austenite after deformation at high temperatures and strain-rates – analysis and modelling. *Metall. Trans. A* **22A**, 151-160.

LAURENT, P., BERNARD, P., VASSEUR, G. and ETCHECOPAR, A. (1981) Stress tensor determination from the study of  $e$  twins in calcite : a linear programming method. *Tectonophys.* **78**, 651-660.

LERNER, I. and KOHLSTEDT, D. L. (1981) Effect of radiation on plastic flow of NaCl. *J. Am. Ceram. Soc.* **64**, 105-108.

LERNER, I. and KOHLSTEDT, D. L. (1982) Load relaxation studies of AgCl. *Acta Metall.* **30**, 225-233.

LERNER, I., CHIANG, S.-W. and KOHLSTEDT, D. L. (1979) Load relaxation studies of four alkali halides. *Acta Metall.* **27**, 1187-1196.

LI, C.-Y. (1981) State variable theories for nonelastic deformation. In *Metallurgical Treatises* (eds. J. K. TIEN and G. F. ELLIOTT), pp. 469-485. TMS-AIME.

LI, C.-Y., ELLIS, F. V. and HUANG, F. H. (1976) Mechanical equations of state. In *Alloy and Microstructural Design* (eds. J. K. TIEN and G. S. ANSELL), pp. 403-424. Academic Press.

LIN, I.-H., HIRTH, J. P. and HART, E. W. (1981) Plastic instability in uniaxial tension tests. *Acta Metall.* **29**, 819-827.

LUTON, M. J. and SELLARS, C. M. (1969) Dynamic recrystallization in nickel and nickel-iron alloys during high temperature deformation. *Acta Metall.* **17**, 1033-1043.

MACEWEN, S. R. (1982) The mechanical equation of state and strengthening mechanisms for the deformation of crystal-bar zirconium. *Acta Metall.* **30**, 1431-1442.

MILLER, A. K., ed. (1987) *Unified Constitutive Equations for Creep and Plasticity*, 342 pp. Elsevier Applied Science.

MORJARIA, M. and MUKHERJEE, S. (1980a) Improved boundary-integral equation method for time-dependent inelastic deformation in metals. *Int. J. Num. Meth. Engng.* **15**, 97-111.

MORJARIA, M. and MUKHERJEE, S. (1980b) Inelastic analysis of transverse deflection of plates by the boundary element method. *J. Appl. Mech.* **47**, 291-296.

MORJARIA, M. and MUKHERJEE, S. (1981) Finite element analysis of time-dependent inelastic deformation in the presence of transient thermal stresses. *Int. J. Num. Meth. Engng.* **17**, 909-921.

MORJARIA, M., SARIHAN, V. and MUKHERJEE, S. (1980) Comparison of boundary element and finite element methods in two-dimensional inelastic analysis. *Res Mech.* **1**, 3-20.

MUKHERJEE, S. (1982) Time-dependent inelastic deformation of metals by boundary element methods. In *Developments in Boundary Element Methods – 2* (eds. P. K. BANERJEE and R. P. SHAW), pp. 111-142. Applied Science Publishers.

MUKHERJEE, S. and CHANDRA, A. (1984) Boundary element formulations for large strain – large deformation problems of plasticity and viscoplasticity. In *Developments in Boundary Element Methods – 3* (eds. P. K. BANERJEE and S. MUKHERJEE), pp. 27-58. Elsevier Applied Science.

MUKHERJEE, S. and HARKNESS, S. D. (1979) Mechanical analysis of a first wall model by using a state variable approach. *J. Nucl. Mater.* **85 & 86**, 183-187.

MUKHERJEE, S. and KUMAR, V. (1978) Numerical analysis of time-dependent inelastic deformation in metallic media using the boundary integral equation method. *J. Appl. Mech.* **45**, 785-790.

MUKHERJEE, S. and MORJARIA, M. (1981) Comparison of boundary element and finite element methods in the inelastic torsion of prismatic shafts. *Int. J. Num. Meth. Engng.* **17**, 1576-1588.

MUKHERJEE, S., KUMAR, V. and CHANG, K. J. (1978) Elevated temperature inelastic analysis of metallic media under time varying loads using state variable theories. *Int. J. Solids Struct.*

14, 663-679.

MÜLLER, D. and HARTMANN, G. (1989) Identification of materials parameters for inelastic constitutive models using principles of biologic evolution. *J. Engng. Mater. Technol.* **111**, 299-305.

MURRELL, S. A. F. and CHAKRAVARTY, S. (1973) Some new rheological experiments on igneous rocks at temperatures upto 1120°C. *Geophys. J. R. Astron. Soc.* **34**, 211-250.

NABARRO, F. R. N. (1989) Work hardening and dynamical recovery of fcc metals in multiple glide. *Acta Metall.* **37**, 1521-1546.

NIR, N., HART, E. W. and LI, C.-Y. (1976) Anelastic deformation of high purity aluminium at room temperature. *Scripta Metall.* **10**, 189-194.

NIR, N., HUANG, F. H., HART, E. W. and LI, C.-Y. (1977) Relationship between anelastic and nonlinear viscoplastic behaviour of 316 stainless steel at low homologous temperature. *Metall. Trans. A* **8A**, 583-588.

OLDROYD, J. G. (1950) On the formulation of rheological equations of state. *Proc. R. Soc. (London) A* **200**, 523-541.

OLDROYD, J. G. (1958) Non-Newtonian effects in steady motion of some idealized elastico-viscous liquids. *Proc. R. Soc. (London) A* **245**, 278-297.

OROWAN, E. (1940) Problems of plastic gliding. *Proc. Phys. Soc. (London)* **52**, 8-22.

OWENS, W. H. and RUTTER, E. H. (1978) The development of magnetic susceptibility anisotropy through crystallographic preferred orientation in a calcite rock. *Phys. Earth Planet. Int.* **16**, 215-222.

PATERSON, M. S. (1973) Nonhydrostatic thermodynamics and its geological applications. *Rev. Geophys. Space Phys.* **11**, 355-389.

PAXTON, M. M. (1974) *Hanford Engineering Development Laboratory Report* HEDL-TME-74-41.

POIRIER, J.-P. (1985) *Creep of Crystals*, 260 pp. Cambridge University Press.

POVOLO, F. (1981) On the analysis of stress relaxation data. *J. Nucl. Mat.* **96**, 178-186.

POVOLO, F. (1985) Scaling relationships in a constitutive equation with one structure variable. *J. Mater. Sci. Lett.* **4**, 619-623.

POVOLO, F. and CAPITANI, J. C. (1984) Influence of temperature and stress-relieving treatment on the stress relaxation in bending of zircaloy-4 near 673K. *J. Mater. Sci.* **19**, 2969-2979.

POVOLO, F. and FONTELOS, N. (1987a) Procedure to determine if a set of experimental curves are really related by scaling. *Res Mech.* **22**, 185-198.

POVOLO, F. and FONTELOS, N. (1987b) Time-temperature superposition principle and scaling behaviour. *J. Mater. Sci.* **22**, 1530-1534.

POVOLO, F. and HIGA, M. (1980) Stress relaxation in bending, at 673K, of stress-relieved and cold-worked zircaloy-4. *J. Nucl. Mater.* **91**, 189-199.

POVOLO, F. and MARZOCCA, A. J. (1981) Representation of creep and stress relaxation data either in terms of Hart's phenomenological theory or a hyperbolic sine function. *J. Nucl. Mater.* **99**, 317-319.

POVOLO, F. and MARZOCCA, A. J. (1983a) On the scaling behaviour in a  $\log \sigma - \log \dot{\epsilon}$  diagram. *J. Mater. Sci.* **18**, 1426-1432.

POVOLO, F. and MARZOCCA, A. J. (1983b) On the description of stress relaxation behaviour by a stress-partitioned power law. *Trans. Jpn. Inst. Met.* **24**, 111-114.

POVOLO, F. and PESZKIN, P. N. (1983) Stress relaxation in bending of zircaloy-4 as a function of cold work. *Res Mech.* **6**, 233-253.

POVOLO, F. and REGGIARDO, J. F. (1988) Stress relaxation in bending of Inconel 718, at 773

and 823K. *J. Mater. Sci.* **23**, 241-247.

POVOLO, F. and RUBILO, G. H. (1983a) Scaling relationship in the  $\log \sigma - \log \dot{\epsilon}$  creep and stress-relaxation curves and the plastic equation of state. *J. Mater. Sci.* **18**, 821-826.

POVOLO, F. and RUBILO, G. H. (1983b) The interpretation of the scaling relationship shown by the  $\log \sigma - \log \dot{\epsilon}$  creep and stress-relaxation curves. In *Strength of Metals and Alloys*, Proc. 6th Int. Conf. on the Strength of Metals and Alloys, 1982, Melbourne (ed. R. C. GIFFINS), pp. 589-594. Pergamon Press.

POVOLO, F. and TINIVELLA, R. (1984a) Stress relaxation in bending of Type AISI 304 and A-286 steels at 773K. *J. Mater. Sci.* **19**, 1851-1862.

POVOLO, F. and TINIVELLA, R. (1984b) Load relaxation of stainless steel Type AISI 304 near 563K. *J. Mater. Sci.* **19**, 2373-2377.

POVOLO, F., MARZOCCA, A. J. and RUBILO, G.H. (1984) Connection between the plastic equation of state and scaling behaviour. *Res Mech.* **12**, 27-40.

ROBERTS, J. T. A. (1974) Mechanical equation of state and high temperature deformation ( $> 0.5 T_m$ ) of uranium dioxide. *Acta Metall.* **22**, 873-878.

ROHDE, R. W., JONES, W. B. and HICKS, D. L. (1981) Deformation modelling of aluminium : stress relaxation, transient behaviour and search for microstructural correlations. *Acta Metall.* **29**, 41-52.

ROWE, K. J. and RUTTER, E. H. (1990) Palaeostress estimation using calcite twinning : experimental calibration and application to nature. *J. Struct. Geol.* **12**, 1-17.

RUTTER, E. H. (1970) *An Experimental Study of the Factors Affecting the Rheological Properties of Rocks in Simulated Geological Environments*. Unpubl. Ph.D. Thesis, University of London.

RUTTER, E. H. (1972) The influence of interstitial water on the rheological behaviour of calcite rocks. *Tectonophys.* **14**, 13-33.

RUTTER, E. H. (1974) The influence of temperature, strain-rate and interstitial water in the experimental deformation of calcite rocks. *Tectonophys.* **22**, 311-334.

RUTTER, E. H. and RUSBRIDGE, M. (1977) The effect of non-coaxial strain paths on crystallographic preferred orientation development in the experimental deformation of a marble. *Tectonophys.* **39**, 73-86.

SCHMID, S. M., PATERSON, M. S. and BOLAND, J. N. (1980) High temperature flow and dynamic recrystallization in Carrara marble. *Tectonophys.* **65**, 245-280.

SCHMID, S. M., PANZZO, R. and BAUER, S. (1987) Simple shear experiments on calcite rocks : rheology and microfabric. *J. Struct. Geol.* **9**, 747-778.

SELLARS, C. M. (1978) Recrystallization of metals during hot deformation. *Phil. Trans. R. Soc. (London) A* **288**, 147-158.

SNEDDON, I. N. (1957) *Elements of Partial Differential Equations*, 327 pp. McGraw-Hill.

SPIERS, C. J. (1981) *The Development of Deformation Textures in Calcite Rocks*. Unpubl. Ph.D. Thesis, University of London.

STONE, D. S. (1991) Scaling laws in dislocation creep. *Acta Metall.* **39**, 599-608.

SUMINO, Y. and ANDERSON, O. L. (1984) Elastic constants of minerals. In *Handbook of Physical Properties of Rocks* (ed. R. S. CARMICHAEL), 3, 39-138. CRC Press.

SUZUKI, H., OKUBO, T. and ISHIZAKA, H. (1982) Nonelastic behaviour of zircaloy fuel cladding tubes at 473K. *J. Nucl. Sci. Technol.* **19**, 133-144.

SUZUKI, H. and OKUBO, T. (1984) A study on the nonelastic behaviour of zircaloy fuel cladding. In *Zirconium in the Nuclear Industry : Sixth International Symposium* (eds. D. G. FRANKLIN and R. B. ADAMSON), pp. 157-175. ASTM STP 824.

SWEARENGEN, J. C., ROHDE, R. W. and HICKS, D. L. (1976) Mechanical state relations for inelastic deformation of iron : the choice of variables. *Acta Metall.* **24**, 969-975.

TANOUE, K. (1991) Cottrell-Stokes Law and scaling loci of stress relaxation curves in copper single crystals. *Scripta Metall.* **25**, 565-569.

TANOUE, K. and MATSUDA, H. (1982) Mechanical equation of state in molybdenum. *Trans. Jpn. Inst. Met.* **23**, 234-242.

TANOUE, K. and MATSUDA, H. (1984) The characteristics of stress relaxation curves and thermally activated deformation in molybdenum. *Trans. Jpn. Inst. Met.* **25**, 89-95.

TANOUE, K., NAKANO, O. and MATSUDA, H. (1983) The shape of stress relaxation curves and the mechanical equation of state in molybdenum. *Trans. Jpn. Inst. Met.* **24**, 205-215.

TANOUE, K., YAMASHITA, K., NISHIMURA, T. and MATSUDA, H. (1988) Mechanical equation of state in metallic single crystals. *Scripta Metall.* **22**, 379-384.

THOMAS, JR., J. F. and YAGEE, F. L. (1975) Stress relaxation in solution-annealed and 20 pct cold-worked Type 316 stainless steel. *Metall. Trans. A* **6A**, 1835-1837.

TILLER, W. A. (1991) *The Science of Crystallization : Microscopic Interfacial Phenomena*, 391 pp. Cambridge University Press.

TONEJC, A. and POIRIER, J.-P. (1975) Mechanical equation of state and superplastic materials. *Scripta Metall.* **9**, 555-558.

UNDERWOOD, E. E. (1970) *Quantitative Stereology*, 274 pp. Addison-Wesley.

VAN ARSDALE, W. E., HART, E. W. and JENKINS, J. T. (1980) Elongation upon torsion in a theory for the inelastic behaviour of metals. *J. Appl. Phys.* **51**, 953-958.

WALKER, A. N. (1991) *An Experimental Study of Grain-Size Sensitive Flow of Hot-Pressed Synthetic Rocks*. Unpubl. Ph.D. Thesis, University of London.

WIRE, G. L., YAMADA, H. and LI, C.-Y. (1974) Mechanical equation of state and grain boundary sliding in lead in monotonic loading. *Acta Metall.* **22**, 505-512.

WIRE, G. L., ELLIS, F. V. and LI, C.-Y. (1976) Work hardening and mechanical equation of state in some metals in monotonic loading. *Acta Metall.* **24**, 677-685.

WIRE, G. L., CANNON, N. S. and JOHNSON, G. D. (1979) Prediction of transient mechanical response of Type 316 stainless steel cladding using an equation of state approach. *J. Nucl. Mater.* **82**, 317-328.

WIRE, G. L., DUNCAN, D. R., CANNON, N. S., JOHNSON, G. D., ALEXOPOULOS, P. S., MUKHERJEE, S. and LI, C.-Y. (1981) A state variable analysis of inelastic deformation of thin walled tubes. *J. Engng. Mater. Technol.* **103**, 305-313.

WOODFORD, D. A. (1975) Measurement of the mechanical state of a low alloy steel at elevated temperature. *Metall. Trans. A* **6A**, 1693-1697.

WOODFORD, D. A. (1976) Load relaxation testing of a superplastic superalloy. *Metall. Trans. A* **7A**, 1244-1246.

YAMADA, H. (1977) Effect of heat treatment on the mechanical state of 20% cold worked Type 316 austenitic stainless steel. *Scripta Metall.* **11**, 321-325.

YAMADA, H. and LI, C.-Y. (1973) Stress relaxation and mechanical equation of state in austenitic stainless steels. *Metall. Trans. A* **4A**, 2133-2136.

YAMADA, Y. and HIRAKAWA, H. (1978) Large deformation and instability analysis in metal forming process. In *Numerical Modelling of Manufacturing Processes* (eds. H. ARMEN and R. F. JONES), pp. 27-38. ASME AMD-28.

ZENER, C. and HOLLOWAY, J. H. (1944) Plastic flow and rupture of metals. *Trans. Am. Soc. Met.* **33**, 163-215.

## **APPENDICES**

## A1 DERIVATIONS ASSOCIATED WITH THE CONSTITUTIVE EQUATIONS

### A1.1 Theory of Pfaffian forms

The expression

$$\sum_{i=1}^N F_i(x_1, x_2, \dots, x_N) dx_i \quad (A1.1)$$

in which the  $F_i$  are functions of some or all of the  $N$  independent variables  $x_1, x_2, \dots, x_N$  is called a Pfaffian differential form in  $N$  variables. The relation

$$\sum_{i=1}^N F_i dx_i = 0 \quad (A1.2)$$

is called a Pfaffian differential equation.

Aspects of the theory of Pfaffian forms / equations are described in all introductory texts concerned with first order, non-linear ordinary differential equations, although the name *Pfaffian* is not always applied. The most systematic account, given the requirements of Hart's analysis, may be found in Sneddon (1957, pp. 18-42).

**A1.1.1 Pfaffian forms in two variables.** In the case of two variables, equation A1.2 may be written

$$P(x,y)dx + Q(x,y)dy = 0 \quad (A1.3)$$

or equivalently, as

$$dy/dx = f(x,y) = -P/Q \quad (A1.4)$$

**A1.1.1.1 Existence and uniqueness of a solution to equation A1.3 :** The existence of a unique solution  $y(x)$  to the initial value problem

$$dy/dx = f(x,y) ; \quad y(x_0) = y_0 \quad (A1.5)$$

in the rectangle  $A_1 < x < A_2$ ,  $B_1 < y < B_2$ , is guaranteed by the *Existence and Uniqueness Theorem*, provided the functions  $f$  and  $\partial f / \partial y$  are continuous in that rectangle. The proof of this theorem was first given by Picard in 1890 and is described in many advanced calculus texts (e.g. Golomb and Shanks, 1950, pp. 315-319 ; Greenberg, 1978, pp. 400-403 ; or see the simpler discussion of Boyce and DiPrima, 1986, pp. 95-103).

**A1.1.1.2 The solution of equation A1.3 :** For Pfaffian forms of two variables there always exists a function  $f(x,y)$  and a function  $\Upsilon(x,y)$  such that

$$df(x,y) = \Upsilon(x,y)[P(x,y)dx + Q(x,y)dy] \quad (A1.6)$$

and hence that the equation

$$Pdx + Qdy = 0 \quad (A1.7)$$

must possess an integral solution of the form

$$f(x,y) = C \quad (A1.8)$$

where  $C$  is an arbitrary constant. This may be seen as follows. Writing equation A1.8 in differential form

$$df = \frac{\partial f}{\partial x} dx + \frac{\partial f}{\partial y} dy = 0 \quad (A1.9)$$

and substituting equation A1.4, it follows that there always exists a function  $\Upsilon(x,y)$  such that

$$\frac{1}{P} \frac{\partial f}{\partial x} = \frac{1}{Q} \frac{\partial f}{\partial y} = \Upsilon \quad (\text{A1.10})$$

On multiplying equation A1.3 by  $\Upsilon$

$$\Upsilon(Pdx + Qdy) = 0 \quad (\text{A1.11})$$

and the result is exact, *i.e.*

$$\frac{\partial(\Upsilon P)}{\partial y} = \frac{\partial(\Upsilon Q)}{\partial x} \quad (\text{A1.12})$$

Hence there must exist a function  $f(x, y)$  such that

$$df = \Upsilon(Pdx + Qdy) \quad (\text{A1.13})$$

(*e.g.* Hildebrand, 1976, pp. 32-33).

The function  $\Upsilon$  which makes the Pfaffian equation exact, is termed the integrating factor. It is easy to show (Sneddon, 1957, pp. 23-24) that if one integrating factor of a Pfaffian equation (of any number of variables) exists, then so do an infinity of others.

The general solution to any Pfaffian equation in two variables (*i.e.* equation A1.8) defines a one-parameter family of curves in the  $xy$  plane. These are isoclines to the direction field given by equation A1.4 (*cf.* Boyce and DiPrima, 1986, pp. 34-35). The uniqueness of the solution ensures that at constant  $C$  there passes through every point of the  $xy$  plane, one and only one curve of the one-parameter system.

**A1.1.2 Pfaffian forms in more than two variables.** A Pfaffian form in more than two variables does not necessarily possess an integrating factor which makes the corresponding Pfaffian equation exact. This may be illustrated with respect to a Pfaffian equation in three variables

$$P(x, y, z)dx + Q(x, y, z)dy + R(x, y, z)dz = 0 \quad (\text{A1.14})$$

If an integrating factor exists, equation A1.14 has the solution

$$f(x, y, z) = C \quad (\text{A1.15})$$

In differential form this yields

$$\frac{\partial f}{\partial x}dx + \frac{\partial f}{\partial y}dy + \frac{\partial f}{\partial z}dz = 0 \quad (\text{A1.16})$$

and so on comparison of equations A1.14 and A1.16, it must be that

$$\frac{1}{P} \frac{\partial f}{\partial x} = \frac{1}{Q} \frac{\partial f}{\partial y} = \frac{1}{R} \frac{\partial f}{\partial z} = \Upsilon \quad (\text{A1.17})$$

which is true only if (Sneddon, 1957, pp. 21-23)

$$X \cdot \text{curl } X = 0 \quad (\text{A1.18})$$

where  $X$  is the vector  $(P, Q, R)$ . Since this is not necessarily true, an integrating factor does not necessarily exist.

Pfaffian forms for which an integrating factor exists are said to be integrable, although this does not imply that non-integrable Pfaffian forms do not have solutions (Sneddon, 1957, pp. 25-26). There is no reason why  $N$  arbitrarily prescribed functions  $F_i$  (equation A1.1) should in every case be derivable by differentiation from a single function (*cf.* equation A1.16)).

**A1.1.3 Carathéodory's theorem.** The observation for Pfaffian forms of two variables that at constant  $C$  there passes through every point of the  $xy$  plane one and only one curve of the one-parameter system of solutions, implies that from any given point in the  $xy$  plane there are neighbouring points which cannot be reached along curves which satisfy the differential

equation, *i.e.* there are points which are not accessible from the given point. This conclusion may be generalized to state that if a Pfaffian equation of any number of variables is integrable, then in the neighbourhood of any given point there exist points which are inaccessible along curves which satisfy the equation. The important contribution of Carathéodory was to prove the converse *i.e.* that if in the neighbourhood of a given point there are points which are inaccessible along curves which are solutions to the Pfaffian equation, then that equation must be integrable.

Several versions of the proof of Carathéodory's theorem exist. Sneddon (1957, pp. 35-38) describes two ; that due to Buchdahl (1949, for a simplification and generalization of this proof see Buchdahl, 1955 and the references cited therein), and that due to Born (1949).

## A1.2 Derivations of the constitutive equations

The following derivations are associated with the equations of § 4.

### A1.2.1 Constraints on the constitutive relations.

#### A1.2.1.1 Derivation of equation 4.4 : From equation 4.3

$$F = g(u) - B_i x_i \quad ; \quad u = A_i x_i \quad (A1.19)$$

Hence

$$\frac{\partial F}{\partial x_i} = \frac{dg}{du} \frac{du}{dx_i} - B_i \quad (A1.20)$$

multiplying by  $\Delta x_i$  and using the notation employed in equation 4.4

$$F_i \Delta x_i = g'(u)(A_i \Delta x_i) - B_i \Delta x_i \quad (A1.21)$$

#### A1.2.1.2 Derivation of equation 4.7 : From equation 4.5 and 4.6 respectively

$$A_i \Delta x_i + A_j \Delta x_j + A_k \Delta x_k = 0 \quad (A1.22)$$

$$B_i \Delta x_i + B_j \Delta x_j + B_k \Delta x_k = 0 \quad (A1.23)$$

Rearranging both equation A1.22 and A1.23 for  $\Delta x_j$  and equating the two equations, then equation 4.7 follows from the result by algebraic manipulation.

#### A1.2.1.3 Derivation of equations 4.15 and 4.16 : When

$$F = F(x, y, z) \quad \text{but} \quad z = \psi(x, y) \quad (A1.24)$$

then

$$\left( \frac{\partial F}{\partial x} \right)_y = \frac{\partial F}{\partial x} \frac{\partial x}{\partial x} + \frac{\partial F}{\partial y} \frac{\partial y}{\partial x} + \frac{\partial F}{\partial z} \frac{\partial z}{\partial x} \quad (A1.25)$$

Since  $y$  is independent of  $x$ ,  $\partial y / \partial x = 0$  and equation A1.25 becomes

$$\left( \frac{\partial F}{\partial x} \right)_y = \frac{\partial F}{\partial x} + \frac{\partial F}{\partial z} \frac{\partial z}{\partial x} \quad (A1.26)$$

Rearranging

$$\psi_x = \frac{\partial z}{\partial x} = - \frac{\partial F / \partial x}{\partial F / \partial z} \quad (A1.27a)$$

Similarly

$$\psi_y = \frac{\partial z}{\partial y} = - \frac{\partial F / \partial y}{\partial F / \partial z} \quad (A1.27b)$$

Also

$$\frac{\partial^2 F}{\partial y \partial x} = \left( \frac{\partial}{\partial y} + \frac{\partial z}{\partial y} \frac{\partial}{\partial z} \right) \left( \frac{\partial F}{\partial x} + \frac{\partial z}{\partial x} \frac{\partial F}{\partial z} \right) \quad (A1.28)$$

Expanding and rearranging

$$\frac{\partial^2 z}{\partial y \partial x} = - \left( \frac{\partial^2 F}{\partial y \partial x} + \frac{\partial z}{\partial x} \frac{\partial^2 F}{\partial y \partial z} + \frac{\partial z}{\partial y} \frac{\partial^2 F}{\partial z \partial x} + \frac{\partial z}{\partial y} \frac{\partial z}{\partial x} \frac{\partial^2 F}{\partial z^2} \right) + \left( \frac{\partial F}{\partial z} \right) \quad (A1.29a)$$

which is  $\psi_{xy}$ , and similarly

$$\frac{\partial^2 z}{\partial x \partial y} = - \left( \frac{\partial^2 F}{\partial x \partial y} + \frac{\partial z}{\partial y} \frac{\partial^2 F}{\partial x \partial z} + \frac{\partial z}{\partial x} \frac{\partial^2 F}{\partial z \partial y} + \frac{\partial z}{\partial x} \frac{\partial z}{\partial y} \frac{\partial^2 F}{\partial z^2} \right) + \left( \frac{\partial F}{\partial z} \right) \quad (A1.29b)$$

which is  $\psi_{yx}$ .

From equation 4.12

$$F(x, y, z) = g(A_1 x + A_2 y + A_3 z) - B_1 x - B_2 y - B_3 z - B_4 \quad (A1.30)$$

Using equation A1.20 with  $x, y, z$  in place of the 1, 2, 3 nomenclature

$$\begin{aligned} \frac{\partial F}{\partial x} &= g'(u)A_1 - B_1 & \frac{\partial F}{\partial y} &= g'(u)A_2 - B_2 \\ \frac{\partial F}{\partial z} &= g'(u)A_3 - B_3 \\ \frac{\partial^2 F}{\partial x^2} &= g''(u)A_1^2 & \frac{\partial^2 F}{\partial y^2} &= g''(u)A_2^2 \\ \frac{\partial^2 F}{\partial z^2} &= g''(u)A_3^2 \\ \frac{\partial^2 F}{\partial x \partial y} &= g''(u)A_1 A_2 & \frac{\partial^2 F}{\partial y \partial x} &= g''(u)A_1 A_2 \\ \frac{\partial^2 F}{\partial x \partial z} &= g''(u)A_1 A_3 & \frac{\partial^2 F}{\partial z \partial x} &= g''(u)A_1 A_3 \\ \frac{\partial^2 F}{\partial y \partial z} &= g''(u)A_2 A_3 & \frac{\partial^2 F}{\partial z \partial y} &= g''(u)A_2 A_3 \end{aligned} \quad (A1.31)$$

Equations 4.15 and 4.16 then follow by substituting the relevant equations A1.31 into equations A1.27 and A1.29 respectively.

**A1.2.2 The equation of state for the plastic element.** The equation of state for the plastic element is

$$\ln(\sigma^*/\sigma) = (\dot{\epsilon}^*/\dot{\alpha})^\lambda \quad (A1.32)$$

**A1.2.2.1 Derivation of equations 4.26a, b** : Rearranging equation A1.32 and making the change in variables  $\sigma_0 = \sigma^*$  and  $\beta = \lambda$

$$\sigma/\sigma_0 = \exp[-(\dot{\alpha}/\dot{\epsilon}^*)^{-\beta}] \quad (A1.33)$$

Making the change in variables  $x = \log(\sigma/\sigma_0)$ ,  $y = \log(\dot{\alpha}/\dot{\epsilon}^*)$  and  $z = \log \beta$  equation A1.33 becomes

$$f(x, y, z) = \exp[-(10^y)^{-10^z}] - 10^x = 0 \quad (A1.34)$$

Recalling that  $z$  is an implicit function of  $x$  and  $y$ , the following derivatives are found

$$\frac{\partial f}{\partial x} = -(10^x \ln 10) \quad (A1.35)$$

$$\begin{aligned} \frac{\partial f}{\partial y} &= \left\{ \exp[-(10^{-y} 10^z)] \right\} \left\{ \frac{\partial}{\partial y} [-(10^{-y} 10^z)] \right\} \\ &= \left\{ \exp[-(10^{-y} 10^z)] \right\} \{10^{z-y} 10^z \ln 10\} \end{aligned} \quad (A1.36)$$

$$\begin{aligned} \frac{\partial f}{\partial z} &= \left\{ \exp[-(10^{-y} 10^z)] \right\} \left\{ \frac{\partial}{\partial z} [-(10^{-y} 10^z)] \right\} \\ &= - \left\{ \exp[-(10^{-y} 10^z)] \right\} \{10^{-y} 10^z \ln 10\} \left\{ \frac{\partial}{\partial z} (-y 10^z) \right\} \\ &= \left\{ \exp[-(10^{-y} 10^z)] \right\} \{y 10^{z-y} 10^z \ln 10 \ln 10\} \end{aligned} \quad (A1.37)$$

Applying equation A1.27a

$$\begin{aligned}
 h &= \frac{\partial z}{\partial x} = -\frac{\partial f/\partial x}{\partial f/\partial z} \\
 &= \frac{-[-(10^x \ln 10)]}{\{\exp[-(10^{-y} 10^z)]\} \{y 10^{z-y} 10^z \ln 10 \ln 10\}} \\
 &= \frac{10^x}{10^x y 10^{z-y} 10^z \ln 10} = \frac{1}{\beta(\dot{\alpha}/\dot{\varepsilon}^*)^{-\beta} \ln(\dot{\alpha}/\dot{\varepsilon}^*)}
 \end{aligned} \tag{A1.38}$$

Similarly, applying equation A1.27b

$$\begin{aligned}
 g &= \frac{\partial z}{\partial y} = -\frac{\partial f/\partial y}{\partial f/\partial z} \\
 &= \frac{-\{\exp[-(10^{-y} 10^z)]\} \{10^{z-y} 10^z \ln 10\}}{\{\exp[-(10^{-y} 10^z)]\} \{y 10^{z-y} 10^z \ln 10 \ln 10\}} \\
 &= \frac{-1}{y \ln 10} = \frac{-1}{\ln(\dot{\alpha}/\dot{\varepsilon}^*)}
 \end{aligned} \tag{A1.39}$$

A1.2.2.2 *Derivation of equation 4.31* : Rearranging equation A1.32

$$\ln \sigma = \ln \sigma^* - \{\exp[\lambda(\ln \dot{\varepsilon}^* - \ln \dot{\alpha})]\} \tag{A1.40}$$

Dividing through by  $\ln 10$  and using

$$\log \dot{\varepsilon}^* = \log C + m \log \sigma^* \tag{A1.41}$$

(equation 4.30 with  $m = 1/\mu$ ), then equation A1.40 becomes

$$\log \sigma = \log \sigma^* - \{[1/(\ln 10)] \exp[\lambda(\ln 10)(\log C + m \sigma^* - \log \dot{\alpha})]\} \tag{A1.42}$$

Making the change in variables  $x = \log \sigma$ ,  $y = \log \dot{\alpha}$  and  $z = \log \sigma^*$  then

$$z - y - [1/(\ln 10)] \{\exp[\lambda(\ln 10)(\log C + mz - x)]\} = 0 \tag{A1.43}$$

A1.2.2.3 *Derivation of equation 4.33* : If

$$g(A_1x + A_2y + A_3z) - B_1x - B_2y - B_3z - B_4 = 0 \tag{A1.44}$$

(equation 4.12) then equation A1.43 yields (with  $u = A_1x + A_2y + A_3z$ )

$$\begin{aligned}
 g(u) &= -[1/(\ln 10)] \{\exp[\lambda(\ln 10)(\log C + mz - x)]\} \\
 u &= -x + mz
 \end{aligned} \tag{A1.45}$$

Hence

$$\begin{aligned}
 g'(u) &= \frac{dg}{du} = \frac{d\{-[1/(\ln 10)] \exp[\lambda(\ln 10)(\log C + mz - x)]\}}{d(mz - x)} \\
 &= \lambda \exp[\lambda(\ln 10)(\log C + mz - x)] \\
 &= -\lambda(\dot{\varepsilon}^*/\dot{\alpha})^\lambda
 \end{aligned} \tag{A1.46}$$

Using equation A1.46 in equation 4.17

$$\lambda(\dot{\varepsilon}^*/\dot{\alpha})^\lambda \neq 1/m \tag{A1.47}$$

and hence from equation A1.32

$$\ln(\sigma^*/\sigma) \neq 1/\lambda m \tag{A1.48}$$

A1.2.3 **The equation of state for the friction element.** Making the approximation  $\dot{\alpha} = \dot{\varepsilon}^{(n)}$ , the equation of state for the friction element is

$$\dot{\alpha} = \dot{\alpha}^*[(\sigma - \sigma^*)/G]^M \tag{A1.49}$$

A1.2.3.1 *Equivalence of equations 4.35 and 4.37* : Substituting equations 4.36 and 4.38 into

equation 4.35 and rearranging yields

$$\dot{\alpha} = \dot{\varepsilon}^* \{ \ln [1 + (\sigma_f/\sigma^*)] \}^{1/\lambda} \quad (\text{A1.50})$$

Taking a Taylor series expansion of equation A1.50 using only the first term, *i.e.*

$$\begin{aligned} f(x) &= f(A) + f'(A)(x-A) + \dots \\ f(x) &= f(\sigma_f/\sigma^*) = \ln [1 + (\sigma_f/\sigma^*)] \\ f'(x) &= f'(\sigma_f/\sigma^*) = [1 + (\sigma_f/\sigma^*)]^{-1} \end{aligned} \quad (\text{A1.51})$$

then about  $A = 0$

$$\ln [1 + (\sigma_f/\sigma^*)] = (\sigma_f/\sigma^*) \quad (\text{A1.52})$$

Hence

$$\dot{\varepsilon}^* \{ \ln [1 + (\sigma_f/\sigma^*)] \}^{1/\lambda} = \dot{\varepsilon}^* (\sigma_f/\sigma^*)^{1/\lambda} \quad (\text{A1.53})$$

On using equation A1.50 this becomes

$$\dot{\alpha} = \dot{\varepsilon}^* (\sigma_f/\sigma^*)^{1/\lambda} \quad (\text{A1.54})$$

which is the same as equation 4.37 with

$$1/\lambda = M ; \dot{\varepsilon}^* = \dot{\alpha}^* (\sigma^*/G)^M \quad (\text{A1.55})$$

*A1.2.3.2 Derivation of equations 4.43a,b* : Rearranging equation A1.49 and making the change in variables  $\sigma_0 = \sigma^*$ ,  $\dot{\varepsilon}^* = \dot{\alpha}^* (\sigma^*/G)^M$  and  $\beta = 1/M$

$$\sigma/\sigma_0 = 1 + (\dot{\alpha}/\dot{\varepsilon}^*)^\beta \quad (\text{A1.56})$$

Making the change in variables  $x = \log(\sigma/\sigma_0)$ ,  $y = \log(\dot{\alpha}/\dot{\varepsilon}^*)$  and  $z = \log \beta$  equation A1.56 becomes

$$f(x, y, z) = 1 + (10^y)^{10^z} - 10^x = 0 \quad (\text{A1.57})$$

Recalling that  $z$  is an implicit function of  $x$  and  $y$ , the following derivatives are found

$$\frac{\partial f}{\partial x} = -(10^x \ln 10) \quad (\text{A1.58})$$

$$\frac{\partial f}{\partial y} = 10^{z+y} 10^z \ln 10 \quad (\text{A1.59})$$

$$\begin{aligned} \frac{\partial f}{\partial z} &= \{ 10^{-y} 10^z \ln 10 \} \left\{ \frac{\partial}{\partial z} (y 10^z) \right\} \\ &= y 10^{z+y} 10^z \ln 10 \ln 10 \end{aligned} \quad (\text{A1.60})$$

Applying equation A1.27a

$$\begin{aligned} h &= \frac{\partial z}{\partial x} = -\frac{\frac{\partial f}{\partial x}}{\frac{\partial f}{\partial z}} \\ &= \frac{-[-(10^x \ln 10)]}{y 10^{z+y} 10^z \ln 10 \ln 10} = \frac{\sigma/\sigma_0}{\beta (\dot{\alpha}/\dot{\varepsilon}^*)^\beta \ln (\dot{\alpha}/\dot{\varepsilon}^*)} \end{aligned} \quad (\text{A1.61})$$

Similarly, applying equation A1.27b

$$\begin{aligned} g &= \frac{\partial z}{\partial y} = -\frac{\frac{\partial f}{\partial y}}{\frac{\partial f}{\partial z}} \\ &= \frac{-10^{z+y} 10^z \ln 10}{y 10^{z+y} 10^z \ln 10 \ln 10} = \frac{-1}{y \ln 10} = \frac{-1}{\ln (\dot{\alpha}/\dot{\varepsilon}^*)} \end{aligned} \quad (\text{A1.62})$$

*A1.2.3.3 Derivation of equation 4.47* : Rearranging equation A1.49

$$\ln \dot{\alpha} = \ln \dot{\alpha}^* - M \ln G + M \ln \sigma^* + M \ln \{ [\exp(\ln \sigma - \ln \sigma^*)] - 1 \} \quad (\text{A1.63})$$

Dividing through by  $\ln 10$  and making the change in variables  $x = \log \sigma$ ,  $y = \log \dot{\alpha}$  and  $z = \log \sigma^*$  then

$$(\log \dot{\alpha}^* - M \log G) + Mz - x + M \log \{ \exp[\ln 10(y - z)] - 1 \} = 0 \quad (\text{A1.64})$$

which is equation 4.47. Using

$$\log \dot{\alpha}^* = A + B \log \sigma^* \quad (\text{A1.65})$$

(equation 4.48), then equation A1.64 becomes

$$(A - M \log G) + (B + M)z - x + M \log \{ \exp[\ln 10(y - z)] - 1 \} = 0 \quad (\text{A1.66})$$

A1.2.3.4 *Derivation of equation 4.50* : If

$$g(A_1x + A_2y + A_3z) - B_1x - B_2y - B_3z - B_4 = 0 \quad (\text{A1.67})$$

(equation 4.12) then equation A1.66 yields (with  $u = A_1x + A_2y + A_3z$ )

$$\begin{aligned} g(u) &= M \log \{ \exp[\ln 10(y - z)] - 1 \} \\ u &= y - z \end{aligned} \quad (\text{A1.68})$$

Hence

$$\begin{aligned} g'(u) &= \frac{dg}{du} = \frac{d \{ M \log \{ \exp[\ln 10(y - z)] - 1 \} \}}{d(y - z)} \\ &= \left\{ \frac{M}{\ln 10 \{ \exp[\ln 10(y - z)] - 1 \}} \right\} \left\{ \frac{\partial \{ \exp[\ln 10(y - z)] - 1 \}}{\partial(y - z)} \right\} \\ &= \frac{M \exp[\ln 10(y - z)]}{\exp[\ln 10(y - z)] - 1} = \frac{M}{1 - \{ \exp[\ln 10(z - y)] \}} \\ &= M/[1 - (\sigma^*/\sigma)] \end{aligned} \quad (\text{A1.69})$$

Using equation A1.69 in equation 4.17

$$M/[1 - (\sigma^*/\sigma)] \neq B + M \quad (\text{A1.70})$$

which on rearranging yields

$$(\sigma^*/\sigma) \neq B/(B + M) \quad (\text{A1.71})$$

A1.2.4 *Derivation of equation 4.54*. The change in mechanical state during deformation is given by

$$d \ln \sigma^* = (\Gamma/\gamma) (d \ln \sigma - \nu d \ln \dot{\alpha}) \quad (\text{A1.72})$$

(equation 4.52). Along the scaling path for constant  $\sigma^*$  curves  $d \ln \sigma^* = d \ln \sigma$ , and so

$$d \ln \sigma [1 - (\Gamma/\gamma)] = -(\nu \Gamma/\gamma) d \ln \dot{\alpha} \quad (\text{A1.73})$$

Also on the scaling path  $(d \ln \sigma / d \ln \dot{\alpha}) = \mu$  and therefore

$$\mu [1 - (\Gamma/\gamma)] = -\nu \Gamma/\gamma \quad (\text{A1.74})$$

which on rearranging yields

$$\Gamma = \gamma \mu / (\mu - \nu) \quad (\text{A1.75})$$

### A1.3 Derivation of the form of anelastic load relaxation curves

During completely anelastic deformation, Hart's original inelastic model (figure 5.3) predicts that

$$\sigma = G(\dot{\varepsilon}^{(n)}/\dot{\alpha}^*)^{1/M} + \mathcal{M}a \quad (\text{A1.76})$$

(equations 5.7, 5.9 and 5.12). Rearranging

$$(\sigma - \mathcal{M}a)/G = (\dot{\varepsilon}^{(n)}/\dot{\alpha}^*)^{1/M} \quad (\text{A1.77})$$

The integrated form of the stress relaxation equation (equation 5.17) when the deformation is entirely anelastic is

$$(\sigma - \sigma_0) = \kappa(a - a_0) \quad (\text{A1.78})$$

where  $\kappa$  is an effective modulus for the specimen and load train, and the subscript 0 refers to the

start of the relaxation.

Rearranging equation A1.78 for  $a$  and substituting the result into the left-hand side of equation A1.77

$$\begin{aligned}
 \frac{\sigma - \mathcal{M}a}{G} &= \frac{\sigma}{G} - \frac{\mathcal{M}}{G} \left[ \frac{(\sigma - \sigma_0)}{\kappa} + a_0 \right] \\
 &= \left( \frac{1}{G} - \frac{\mathcal{M}}{G\kappa} \right) \sigma + \frac{\mathcal{M}}{G\kappa} \left( \frac{\kappa - \mathcal{M}}{\kappa - \mathcal{M}} \right) (\sigma_0 - \kappa a_0) \\
 &= \left( \frac{1}{G} - \frac{\mathcal{M}}{G\kappa} \right) \sigma + \frac{\mathcal{M}}{G} \left( \frac{1}{\kappa - \mathcal{M}} - \frac{\mathcal{M}}{\kappa(\kappa - \mathcal{M})} \right) (\sigma_0 - \kappa a_0) \\
 &= \left( \frac{1}{G} - \frac{\mathcal{M}}{G\kappa} \right) \sigma + \frac{\mathcal{M}}{G[(\kappa/\mathcal{M}) - 1]} \left( \frac{1}{\mathcal{M}} - \frac{1}{\kappa} \right) (\sigma_0 - \kappa a_0) \\
 &= \left( \frac{1}{G} - \frac{\mathcal{M}}{G\kappa} \right) \left( \sigma + \frac{(\sigma_0 - \kappa a_0)}{[(\kappa/\mathcal{M}) - 1]} \right)
 \end{aligned} \tag{A1.79}$$

Defining

$$\frac{1}{\mathcal{M}^{(a)}} \equiv \left( \frac{1}{G} - \frac{\mathcal{M}}{G\kappa} \right) ; \quad \sigma_a^{(a)} \equiv \frac{-(\sigma_0 - \kappa a_0)}{[(\kappa/\mathcal{M}) - 1]} \tag{A1.80}$$

then equation A1.79 becomes in equation A1.77

$$[\sigma - \sigma_a^{(a)}]/\mathcal{M}^{(a)} = (\dot{\varepsilon}^{(n)}/\dot{a}^*)^{1/M} \tag{A1.81}$$

#### A1.4 Derivation of the viscoplastic limit equations

The following derivations apply for Hart's original inelastic deformation model (figure 5.3).

##### A1.4.1 The uniaxial case. Substituting equation 5.9 into equation 5.8

$$\dot{\varepsilon}^{(n)} = (\dot{\sigma}_a/\mathcal{M}) + \dot{\alpha} \tag{A1.82}$$

Making the approximation  $\dot{\sigma}_a = \dot{\sigma}^*$

$$\dot{\varepsilon}^{(n)} = (\dot{\sigma}^*/\mathcal{M}) + \dot{\alpha} \tag{A1.83}$$

which on substituting equation 5.13 (assuming  $\mathfrak{R} = 0$ ) becomes

$$\dot{\varepsilon}^{(n)} = (\dot{\alpha}\sigma^*\Gamma/\mathcal{M}) + \dot{\alpha} \tag{A1.84}$$

Rearranging equation A1.84

$$\dot{\alpha} = \dot{\varepsilon}^{(n)}/[1 + (\sigma^*\Gamma/\mathcal{M})] \tag{A1.85}$$

##### A1.4.2 The multiaxial case. Substituting equation 5.28 into equation 5.26

$$\dot{\varepsilon}_{ij}^{(n)} = (3/2)(\dot{a}/\sigma_a) s_{ij}^{(a)} + (3/2)(\dot{\alpha}/\sigma_a) s_{ij}^{(a)} \tag{A1.86}$$

Substituting equation 5.9

$$\dot{\varepsilon}_{ij}^{(n)} = (3/2)[\dot{\sigma}_a/(\mathcal{M}\sigma_a)] s_{ij}^{(a)} + (3/2)(\dot{\alpha}/\sigma_a) s_{ij}^{(a)} \tag{A1.87}$$

Again using  $\dot{\sigma}_a = \dot{\sigma}^*$  and substituting equation 5.13 (assuming  $\mathfrak{R} = 0$ )

$$\dot{\varepsilon}_{ij}^{(n)} = (3/2)[(\dot{\alpha}\sigma^*\Gamma)/(\mathcal{M}\sigma_a)] s_{ij}^{(a)} + (3/2)(\dot{\alpha}/\sigma_a) s_{ij}^{(a)} \tag{A1.88}$$

which on rearranging becomes

$$\dot{\alpha} = [(2/3)(\sigma_a \dot{\varepsilon}_{ij}^{(n)}/s_{ij}^{(a)})]/[1 + (\sigma^*\Gamma/\mathcal{M})] \tag{A1.89}$$

Observing also that

$$\sigma_a = [(3/2)s_{ij}^{(a)} s_{ij}^{(a)}]^{1/2} \tag{A1.90}$$

(equation 5.29) which on rearranging becomes

$$(2/3)(\sigma_a/s_{ij}^{(a)}) = s_{ij}^{(a)}/\sigma_a \tag{A1.91}$$

Substituting equation A1.91 into A1.89 yields

$$\dot{\alpha} = \frac{s_{ij}^{(a)} \dot{\epsilon}_{ij}^{(n)} / \sigma_a}{1 + (\sigma^* \Gamma / \mathcal{M})} \quad (\text{A1.92})$$

For finite strain applications the derivation proceeds in the same manner but with the substitution of the appropriate rate variables.

### A1.5 Reduction of the number of variables in Hart's equations

Bammann and Krieg (1987) observe that many of the variables that appear in Hart's constitutive equations do so only as a convenience in explaining the physical motivation behind the deformation model, and that consequently with the appropriate mathematical manipulations, several may be eliminated. Their method of doing this is outlined here for the multiaxial infinitesimal strain case.

#### A1.5.1 Reducing the number of stress and strain-rate variables.

From equations 5.28b,c

$$\dot{\alpha}_{ij} / \dot{\alpha} = \dot{a}_{ij} / \dot{a} = (3/2)(s_{ij}^{(a)} / \sigma_a) \quad (\text{A1.93})$$

Substituting equation A1.93 into equation 5.26

$$\dot{\epsilon}_{ij}^{(n)} = (3/2)(s_{ij}^{(a)} / \sigma_a) \dot{\alpha} + (3/2)(s_{ij}^{(a)} / \sigma_a) \dot{a} \quad (\text{A1.94})$$

Substituting equation 5.8 into equation A1.94

$$\dot{\epsilon}_{ij}^{(n)} / \dot{\epsilon}^{(n)} = (3/2)(s_{ij}^{(a)} / \sigma_a) \quad (\text{A1.95})$$

Substituting equation 5.28a into equation A1.95

$$s_{ij}^{(f)} / \sigma_f = s_{ij}^{(a)} / \sigma_a \quad (\text{A1.96})$$

Rearranging equation A1.96 for  $s_{ij}^{(f)}$ , substituting the result into equation 5.27 and dividing through by  $\sigma$

$$s_{ij} / \sigma = [s_{ij}^{(a)} + (\sigma_f s_{ij}^{(a)} / \sigma_a)] / \sigma \quad (\text{A1.97})$$

Substituting equation 5.7 into the right-hand side of equation A1.97

$$s_{ij} / \sigma_f = s_{ij}^{(a)} / \sigma_a \quad (\text{A1.98})$$

Hence from equations A1.93, A1.95, A1.96 and A1.98 it follows that

$$\begin{aligned} \dot{\alpha}_{ij} / \dot{\alpha} &= \dot{a}_{ij} / \dot{a} = \dot{\epsilon}_{ij}^{(n)} / \dot{\epsilon}^{(n)} \\ &= (3/2)(s_{ij}^{(a)} / \sigma_a) = (3/2)(s_{ij}^{(f)} / \sigma_f) = (3/2)(s_{ij} / \sigma) \end{aligned} \quad (\text{A1.99})$$

This collinearity allows  $\dot{\alpha}_{ij}$ ,  $\dot{a}_{ij}$ ,  $\dot{\epsilon}_{ij}^{(n)}$ ,  $s_{ij}^{(a)}$  and  $s_{ij}^{(f)}$  to be eliminated by stating them in terms of  $\dot{\alpha}$ ,  $\dot{a}$ ,  $\dot{\epsilon}^{(n)}$ ,  $\sigma_a$  and  $\sigma_f$  respectively, along with the directionality of  $s_{ij}$ .

**A1.5.2 Reducing the number of equations.** Defining the elastic strain-rate as  $\dot{s}_{ij} / 2G$  (but cf. equation 7.26) the kinematic equation (which stipulates that the total strain-rate is the sum of the elastic and inelastic parts) becomes

$$\dot{s}_{ij} = 2G(\dot{\epsilon}_{ij}^{(t)} - \dot{\epsilon}_{ij}^{(n)}) \quad (\text{A1.100})$$

Substituting equation 5.7 into 5.12 to remove  $\sigma_f$ , the result into equation 5.28a to make equation 5.12 multiaxial, and using equation A1.99 to remove  $s_{ij}^{(f)} / \sigma_f$ , then

$$\dot{\epsilon}_{ij}^{(n)} = (3/2) \dot{a}^*(\sigma^*, T) \left( \frac{\sigma - \sigma_a}{G} \right)^{M(T)} \frac{s_{ij}}{\sigma} \quad (\text{A1.101})$$

Differentiating equation 5.9 with respect to time and substituting the result into equation 5.8

$$\dot{\sigma}_a = \mathcal{M}(\dot{\epsilon}^{(n)} - \dot{\alpha}) \quad (\text{A1.102})$$

Substituting equation 5.7 into 5.12 to remove  $\sigma_f$  and the result into equation A1.102 to remove

$\dot{\varepsilon}^{(n)}$ , and substituting equation 5.11 into 5.10 to remove  $\varepsilon^*$  and the result into equation A1.102 to remove  $\alpha$  then

$$\dot{\sigma}_a = \mathcal{M} \left[ \dot{\alpha}^*(\sigma^*, T) \left( \frac{\sigma - \sigma_a}{G} \right)^{M(T)} - \left( \ln \frac{\sigma^*}{\sigma_a} \right)^{-1/\lambda} \left( \frac{\sigma^*}{G} \right)^m f_0 \exp \left( \frac{-H}{RT} \right) \right] \quad (\text{A1.103})$$

Substituting equation 5.11 into 5.10 to remove  $\varepsilon^*$  and the result into equation 5.13 to remove  $\alpha$  then

$$\frac{d \ln \sigma^*}{dt} = \left\{ \left[ \left( \ln \frac{\sigma^*}{\sigma_a} \right)^{-1/\lambda} \left( \frac{\sigma^*}{G} \right)^m f_0 \exp \left( \frac{-H}{RT} \right) \right] \Gamma(\sigma^*, \sigma_a) \right\} - \mathcal{R}(\sigma^*, T) \quad (\text{A1.104})$$

Finally from equation 5.29

$$\sigma = [(3/2) s_{ij} s_{ij}]^{1/2} \quad (\text{A1.105})$$

Hart's equations are therefore reduced to equations A1.100, A1.101, A1.103, A1.104 and A1.105 in which the independent variables are  $\dot{\varepsilon}^{(t)}$ ,  $s_{ij}$ ,  $\sigma_a$ ,  $\sigma^*$ ,  $T$  and time.

## A2 DERIVATIONS ASSOCIATED WITH THE DATA REDUCTION EQUATIONS

### A2.1 Derivation of the data reduction equations

In the following derivations use is made of the familiar product and quotient rules, respectively

$$\frac{d}{dx}(uv) = u\frac{dv}{dx} + v\frac{du}{dx} ; \quad \frac{d}{dx}\left(\frac{u}{v}\right) = \frac{v(du/dx) - u(dv/dx)}{v^2} \quad (\text{A2.1})$$

in which  $u$  and  $v$  are functions of  $x$ .

#### A2.1.1 Derivation of equations 8.5 and 8.7. From equation 8.2

$$\dot{\varepsilon}^{(t)} = d[\ln(\mathcal{L}/L_0)]/dt \quad (\text{A2.2})$$

where  $\mathcal{L}$  is a function of  $t$ . Therefore

$$\dot{\varepsilon}^{(t)} = (L_0/\mathcal{L})[d(\mathcal{L}/L_0)/dt] \quad (\text{A2.3})$$

and hence

$$\dot{\varepsilon}^{(t)} = \dot{\mathcal{L}}/\mathcal{L} \quad (\text{A2.4})$$

Similarly

$$\dot{\varepsilon}^{(n)} = \dot{L}/L \quad (\text{A2.5})$$

#### A2.1.2 Derivation of equation 8.6. From equation 8.3

$$\dot{\varepsilon}^{(e)} = d[\ln(\mathcal{L}/L)]/dt \quad (\text{A2.6})$$

where both  $\mathcal{L}$  and  $L$  are a function of  $t$ . Therefore

$$\dot{\varepsilon}^{(e)} = (L/\mathcal{L})[d(\mathcal{L}/L)/dt] \quad (\text{A2.7})$$

which from the quotient rule yields

$$\dot{\varepsilon}^{(e)} = (L/\mathcal{L})[(L\dot{\mathcal{L}} - \dot{L}\mathcal{L})/L^2] \quad (\text{A2.8})$$

and hence

$$\dot{\varepsilon}^{(e)} = (L\dot{\mathcal{L}} - \dot{L}\mathcal{L})/L\mathcal{L} \quad (\text{A2.9})$$

#### A2.1.3 Derivation of equation 8.20. From equation 8.18

$$\dot{L} = d\{\mathcal{L}/[1 - (\mathcal{P}\mathcal{L}/A_0 L_0 E)]\}/dt \quad (\text{A2.10})$$

where both  $\mathcal{L}$  and  $\mathcal{P}$  are a function of  $t$ . Making the substitutions

$$u = \mathcal{L} ; \quad v = [1 - (\mathcal{P}\mathcal{L}/A_0 L_0 E)]$$

and applying the quotient rule

$$\dot{L} = \frac{\dot{\mathcal{L}}[1 - (\mathcal{P}\mathcal{L}/A_0 L_0 E)] - \mathcal{L}d[1 - (\mathcal{P}\mathcal{L}/A_0 L_0 E)]/dt}{[1 - (\mathcal{P}\mathcal{L}/A_0 L_0 E)]^2} \quad (\text{A2.11})$$

Making the substitutions

$$u = \mathcal{P} ; \quad v = -\mathcal{L}/A_0 L_0 E$$

and applying the product rule

$$\dot{L} = \frac{\dot{\mathcal{L}}[1 - (\mathcal{P}\mathcal{L}/A_0 L_0 E)] - \mathcal{L}[-(\mathcal{P}\dot{\mathcal{L}}/A_0 L_0 E) - (\dot{\mathcal{P}}\mathcal{L}/A_0 L_0 E)]}{[1 - (\mathcal{P}\mathcal{L}/A_0 L_0 E)]^2} \quad (\text{A2.12})$$

which on clearing terms becomes

$$\dot{L} = [\dot{\mathcal{L}} + (\mathcal{P}\mathcal{L}^2/A_0 L_0 E)]/[1 - (\mathcal{P}\mathcal{L}/A_0 L_0 E)]^2 \quad (\text{A2.13})$$

Observing from equation 8.18 that

$$(\mathcal{L}/L) = [1 - (\mathcal{P}\mathcal{L}/A_0 L_0 E)] \quad (\text{A2.14})$$

then

$$\dot{L} = [\dot{\mathcal{L}} + (\mathcal{P}\mathcal{L}^2/A_0L_0E)]/(\mathcal{L}/L)^2 \quad (\text{A2.15})$$

## A2.2 Experimental loading histories cast as stress-rates

In the following derivations use is again made of the product and quotient rules (equation A2.1).

### A2.2.1 Constant load creep test.

During any deformation test from equation 8.1

$$\dot{\sigma} = d(\mathcal{P}/\mathcal{A})/dt \quad (\text{A2.16})$$

where  $\mathcal{P}$  and  $\mathcal{A}$  are a function of  $t$ . Applying the quotient rule

$$\dot{\sigma} = (\mathcal{A}\dot{\mathcal{P}} - \mathcal{P}\dot{\mathcal{A}})/\mathcal{A}^2 \quad (\text{A2.17})$$

In a constant load creep test  $\dot{\mathcal{P}} = 0$  and so

$$\dot{\sigma} = (-\mathcal{P}\dot{\mathcal{A}}/\mathcal{A}^2) = -\sigma(\dot{\mathcal{A}}/\mathcal{A}) \quad (\text{A2.18})$$

Also during any deformation test the rate of change of volume is given by

$$\dot{\mathcal{V}} = d(\mathcal{A}\mathcal{L})/dt = \mathcal{A}\dot{\mathcal{L}} + \mathcal{L}\dot{\mathcal{A}} \quad (\text{A2.19})$$

(using the product rule). Assuming constant volume deformation, equation A2.19 becomes

$$\dot{\mathcal{L}}/\mathcal{L} = -\dot{\mathcal{A}}/\mathcal{A} \quad (\text{A2.20})$$

which on substituting into equation A2.18 and using equation 8.5 (equation A2.4) yields

$$\dot{\sigma} = \sigma\dot{\epsilon}^{(t)} \quad (\text{A2.21})$$

### A2.2.2 Constant displacement-rate test.

During any deformation test the apparatus crosshead displacement  $\mathcal{X}$  is given by (cf. figure 8.6 and equation 8.11b)

$$\dot{\mathcal{X}} = (\mathcal{P}/\mathcal{S}_{\text{eff}}) + \Delta L_p \quad (\text{A2.22})$$

where  $\Delta L_p$  is the inelastic shortening of the specimen and  $(\mathcal{P}/\mathcal{S}_{\text{eff}})$  is the combined elastic shortening of the apparatus and specimen. The combined apparatus and specimen stiffness  $\mathcal{S}_{\text{eff}}$  is used to define an effective Young's modulus  $\kappa$  for the combined apparatus and specimen such that

$$\mathcal{S}_{\text{eff}} = \mathcal{A}\kappa/L \quad (\text{A2.23})$$

In passing it is observed that since

$$(\mathcal{P}/\mathcal{S}_{\text{eff}}) = \Delta L_{\text{app}} + \Delta L_e = (\mathcal{P}/\mathcal{S}) + \mathcal{P}L/\mathcal{A}E \quad (\text{A2.24})$$

(equations 8.12, 8.13 and 8.15), then (using equation A2.23 in A2.24)

$$(1/\kappa) = (\mathcal{A}/L\mathcal{S}) + (1/E) \quad (\text{A2.25})$$

which is the usual definition of  $\kappa$  employed in the literature (e.g. Dotsenko, 1979, eqn. 6).

Differentiating equation A2.22 with respect to time

$$\dot{\mathcal{X}} = d(\mathcal{P}/\mathcal{S}_{\text{eff}})/dt + d(\Delta L_p)/dt \quad (\text{A2.26})$$

From the quotient rule

$$d(\mathcal{P}/\mathcal{S}_{\text{eff}})/dt = (\mathcal{S}_{\text{eff}}\dot{\mathcal{P}} - \mathcal{P}\dot{\mathcal{S}}_{\text{eff}})/\mathcal{S}_{\text{eff}}^2 \quad (\text{A2.27})$$

Again applying the quotient rule to equation A2.23 then

$$\dot{\mathcal{S}}_{\text{eff}} = \kappa[(L\dot{\mathcal{A}} - \mathcal{A}\dot{L})/L^2] \quad (\text{A2.28})$$

Substituting equations A2.23 and A2.28 into A2.27 and rearranging

$$\frac{d}{dt}\left(\frac{\mathcal{P}}{\mathcal{S}_{\text{eff}}}\right) = \left(\frac{\mathcal{A}\dot{\mathcal{P}} - \mathcal{P}\dot{\mathcal{A}}}{\mathcal{A}^2}\right)\left(\frac{L}{\kappa}\right) + \left(\frac{\mathcal{P}}{\mathcal{A}}\right)\left(\frac{\dot{L}}{\kappa}\right) \quad (\text{A2.29})$$

Substituting equations 8.1 and A2.17 this becomes

$$d(\mathcal{P}/\mathcal{S}_{\text{eff}})/dt = \dot{\sigma}L/\kappa + \sigma\dot{L}/\kappa \quad (\text{A2.30})$$

Also from equation 8.10

$$d(\Delta L_p)/dt = d(L_0 - L)/dt = -\dot{L} \quad (\text{A2.31})$$

Substituting equations A2.30 and A2.31 into A2.26 and dividing through by  $L$  then with equation 8.7 (equation A2.5)

$$\dot{\mathcal{X}}/L = \dot{\sigma}/\kappa + \dot{\varepsilon}^{(n)}[(\sigma/\kappa) - 1] \quad (\text{A2.32})$$

Since for most deformation apparatus  $\sigma \ll \kappa$  then

$$\dot{\mathcal{X}}/L \approx \dot{\sigma}/\kappa - \dot{\varepsilon}^{(n)} \quad (\text{A2.33})$$

**A2.2.3 Load relaxation test.** During a load relaxation test  $\dot{\mathcal{X}} = 0$  and so equation A2.33 becomes

$$\dot{\sigma} = \kappa \dot{\varepsilon}^{(n)} \quad (\text{A2.34})$$

In the usually quoted expression for the stress-rate during a load relaxation, the left-hand side of equation A2.34 is negative. This results from a different sign convention for the change in length of a specimen during deformation *i.e.* from prescribing

$$L = L_0 + \Delta L_p \quad (\text{A2.35a})$$

(reflecting application to tests conducted in tension) rather than (equation 8.10)

$$L = L_0 - \Delta L_p \quad (\text{A2.35b})$$

(reflecting here application to tests conducted in compression). If equation A2.35a is used in equation A2.31, then the usual expression results.

### A3 DERIVATIONS ASSOCIATED WITH MATERIAL PARAMETER FITTING

#### A3.1 The fitting procedures employed in this study

The following derivations support the material parameter fitting procedures outlined in § 11 to § 13. Use is made of the differentiation formulae

$$\frac{d}{dx} (\log_A u) = \frac{1}{u \ln A} \frac{du}{dx} \quad (A3.1)$$

$$\frac{d}{dx} (CA^u) = CA^u \ln A \frac{du}{dx} \quad (A3.2)$$

where  $u$  is a function of  $x$  and  $A$  and  $C$  are constants.

**A3.1.1 Derivation of equation 11.5.** The equation of state for the friction element may be written (equation 11.4)

$$\dot{\varepsilon}^{(n)} = \dot{\alpha}^* [(\sigma - \sigma^*)/G]^M \quad (A3.3)$$

Rearranging

$$\sigma = \sigma^* + G(\dot{\varepsilon}^{(n)}/\dot{\alpha}^*)^{1/M} \quad (A3.4)$$

Making the substitutions  $x = \log \dot{\varepsilon}^{(n)}$  and  $y = \log \sigma$

$$y = \log [\sigma^* + G(10^x/\dot{\alpha}^*)^{1/M}] \quad (A3.5)$$

At constant  $\sigma^*$  using equation A3.1

$$\frac{dy}{dx} = \frac{1}{\ln 10 [\sigma^* + G(10^x/\dot{\alpha}^*)^{1/M}]} \frac{d}{dx} [\sigma^* + G(10^x/\dot{\alpha}^*)^{1/M}] \quad (A3.6)$$

Using equation A3.2 with

$$A = 10 \quad ; \quad C = G(\dot{\alpha}^*)^{1/M} \quad ; \quad u = x/M$$

this becomes

$$\frac{dy}{dx} = \frac{G(10^x/\dot{\alpha}^*)^{1/M}}{M [\sigma^* + G(10^x/\dot{\alpha}^*)^{1/M}]} \quad (A3.7)$$

and so

$$\nu = \frac{d \log \sigma}{d \log \dot{\varepsilon}^{(n)}} = \frac{G(\dot{\varepsilon}^{(n)}/\dot{\alpha}^*)^{1/M}}{M [\sigma^* + G(\dot{\varepsilon}^{(n)}/\dot{\alpha}^*)^{1/M}]} \quad (A3.8)$$

Rearranging

$$G(\dot{\varepsilon}^{(n)}/\dot{\alpha}^*)^{1/M} = \nu M [\sigma^* + G(\dot{\varepsilon}^{(n)}/\dot{\alpha}^*)^{1/M}] \quad (A3.9)$$

Substituting equation A3.9 into A3.4

$$\sigma = \sigma^* + \nu M [\sigma^* + G(\dot{\varepsilon}^{(n)}/\dot{\alpha}^*)^{1/M}] \quad (A3.10)$$

and substituting equation A3.4 into A3.10

$$\sigma = \sigma^* + \sigma \nu M \quad (A3.11)$$

**A3.1.2 Derivation of equation 12.3.** Rearranging the equation of state for the plastic element (equation 12.1)

$$\ln \sigma = \ln \sigma^* - [(\dot{\varepsilon}^*/\dot{\alpha})^\lambda] \quad (A3.12)$$

Making the substitutions  $x = \log \dot{\alpha}$  and  $y = \log \sigma$

$$y = \log \sigma^* - [(\dot{\varepsilon}^*/10^x)^\lambda / \ln 10] \quad (A3.13)$$

At constant  $\sigma^*$  using equation A3.2 with

$$A = 10 \quad ; \quad C = -(\dot{\varepsilon}^*)^\lambda / \ln 10 \quad ; \quad u = -\lambda x$$

then

$$\frac{dy}{dx} = \lambda(\dot{\varepsilon}^*/10^x)^\lambda \quad (\text{A3.14})$$

and so

$$\nu \equiv d\log \sigma / d\log \dot{\alpha} = \lambda(\dot{\varepsilon}^*/\dot{\alpha})^\lambda \quad (\text{A3.15})$$

**A3.1.3 Determining  $\sigma^*$  from the equations of state.** The magnitude of  $\sigma^*$  at known  $\sigma$  and  $\dot{\varepsilon}^{(n)}$  was determined by using the Newton-Raphson method (e.g. Hildebrand, 1976, pp. 367-370) to solve the appropriate equation of state i.e.  $\sigma^*$  was determined iteratively by writing the appropriate equation of state as  $f(\sigma^*) = 0$  and employing the formula

$$\sigma_{k+1}^* = \sigma_k^* - \frac{f(\sigma_k^*)}{f'(\sigma_k^*)} \quad (\text{A3.16})$$

where  $\sigma_k^*$  is the value of  $\sigma^*$  after the  $k$ th iteration step.

**A3.1.3.1 The equation of state for the friction element :** The equation of state for the friction element may be written as

$$\dot{\varepsilon}^{(n)} = [A \exp(C/T)] [\sigma^*/G]^B [(\sigma - \sigma^*)/G]^M \quad (\text{A3.17})$$

(equation 11.4 with equation 11.2 to account for the  $\sigma^*$  and  $T$  dependence of  $\dot{\alpha}^*$ ). Hence at constant temperature

$$f(\sigma^*) = 0 = A_1 [\sigma^*/G]^B [(\sigma - \sigma^*)/G]^M - \dot{\varepsilon}^{(n)} \quad (\text{A3.18})$$

where

$$A_1 = A \exp(C/T) \quad (\text{A3.19})$$

Employing the product rule (equation A2.1)

$$\begin{aligned} f'(\sigma^*) &= \frac{BA_1}{G^B} (\sigma^*)^{B-1} [(\sigma - \sigma^*)/G]^M - \frac{MA_1(\sigma^*/G)^B}{G^M} (\sigma - \sigma^*)^{M-1} \\ &= \frac{BA_1}{\sigma^*} (\sigma^*/G)^B [(\sigma - \sigma^*)/G]^M - \frac{MA_1(\sigma^*/G)^B}{(\sigma - \sigma^*)} \left[ \frac{(\sigma - \sigma^*)}{G} \right]^M \\ &= \left[ \frac{B}{\sigma^*} - \frac{M}{(\sigma - \sigma^*)} \right] [f(\sigma^*) + \dot{\varepsilon}^{(n)}] \end{aligned} \quad (\text{A3.20})$$

**A3.1.3.2 The equation of state for the plastic element :** The equation of state for the plastic element may be written

$$\ln \sigma = \ln \sigma^* - \left[ \frac{f_0 \exp(-H/RT)}{\dot{\varepsilon}^{(n)}} \right]^\lambda [G]^{-\lambda m} [\sigma^*]^{\lambda m} \quad (\text{A3.21})$$

(equation 12.1 with equation 12.2). Hence at constant temperature

$$f(\sigma^*) = 0 = \ln \sigma^* - A_1 (\sigma^*)^{\lambda m} - \ln \sigma \quad (\text{A3.22})$$

where

$$A_1 = [f_0 \exp(-H/RT)/\dot{\varepsilon}^{(n)}]^\lambda [G^{-\lambda m}] \quad (\text{A3.23})$$

and

$$f'(\sigma^*) = [1/\sigma^*] - [A_1 \lambda m (\sigma^*)^{\lambda m-1}] \quad (\text{A3.24})$$

**A3.1.4 Derivation of equation 13.6.** Rearranging the mechanical state evolution equation (equation 13.1)

$$\ln \Gamma = \ln \Gamma^* - [(\dot{\alpha}^*/\dot{\alpha})^A] \quad (\text{A3.25})$$

Making the substitutions  $x = \log \dot{\alpha}$  and  $y = \log \Gamma$

$$y = \log \Gamma^* - [(\dot{\alpha}^*/10^x)^A / \ln 10] \quad (\text{A3.26})$$

At constant  $\Gamma^*$  (i.e. at constant  $\sigma^*$ , equation 13.2) using equation A3.2 with

$$A = 10 \quad ; \quad C = -(\dot{\alpha}^*)^A / \ln 10 \quad ; \quad u = -\lambda x$$

then

$$[\frac{d\log \sigma}{d\log \dot{\alpha}}]_{\sigma^*} = A(\dot{\alpha}^*/\dot{\alpha})^A \quad (\text{A3.27})$$

an A3.1.5 Derivation of equation 13.12. The elastic strain is given by

$$\varepsilon^{(e)} = \ln(\mathcal{L}/L) \quad (\text{A3.28})$$

A (equation 8.3). Substituting equation 8.18 for  $L$

$$\varepsilon^{(e)} = \ln \{ 1 / [1 - (\mathcal{P}\mathcal{L}/A_0 L_0 E)] \} \quad (\text{A3.29})$$

(e) Recalling that

$$\sigma = \mathcal{P}/\mathcal{A} = \mathcal{P}\mathcal{L}/A_0 L_0 \quad (\text{A3.30})$$

R (equations 8.1 and 8.12) then equation A3.30 becomes

$$\varepsilon^{(e)} = \ln \{ 1 / [1 - (\sigma/E)] \} \quad (\text{A3.31})$$

(equations 8.1 and 8.12) then equation A3.30 becomes

$$\varepsilon^{(e)} = \ln \{ 1 / [1 - (\sigma/E)] \} \quad (\text{A3.32})$$

### A3.2 Alternative fitting procedures

The fitting procedures employed to evaluate the material parameters of the friction and plastic elements in this study, require the approximation for any given relaxation curve that only one of these elements is deformation rate controlling in the fitted strain-rate range (§ 9.5.2). This approximation may be avoided by using non-linear fitting routines to fit the full equation for plastic deformation

$$\sigma = G(\dot{\alpha}/\dot{\alpha}^*)^{1/M} + \sigma^* \exp[-(\dot{\varepsilon}^*/\dot{\alpha})^M] \quad (\text{A3.33})$$

(equation 5.21) to each relaxation curve. Two attempts to do this have been described in the literature.

Huang *et al.* (1977, also see Huang *et al.*, 1979, for a minor modification of this procedure) use an iterative process to fit a series of constant  $\sigma^*$  curves all generated at approximately the same value of  $\sigma^*$  but at different temperatures. Values of  $\sigma^*$  and  $\dot{\varepsilon}^*$  were obtained from the highest temperature curve (which is dominated by the plastic element) using  $\lambda = 0.15$ . Using this value of  $\sigma^*$ ,  $M$  was determined from the lowest temperature curve (which is dominated by the friction element). With the values of  $\lambda$ ,  $\sigma^*$  and  $M$ , equation A3.33 was then fitted to the highest temperature data using a non-linear least squares method to determine  $G(\dot{\alpha}/\dot{\alpha}^*)^{1/M}$  and a better estimate of  $\dot{\varepsilon}^*$ . Using a pre-determined activation enthalpy, the value of  $\dot{\varepsilon}^*$  at the second highest temperature was then calculated. With this value and the previous values of  $\lambda$  and  $M$ , the non-linear least squares method was used to fit equation A3.33 to determine  $G(\dot{\alpha}/\dot{\alpha}^*)^{1/M}$  and an estimate of  $\sigma^*$  for that temperature. This process was then repeated for all the temperatures. If the final fits were not satisfactory or the values of  $\sigma^*$  for each curve were not sufficiently close together, the whole procedure was repeated using new values of  $\sigma^*$  and  $\dot{\varepsilon}^*$  for the highest temperature curve.

Müller and Hartmann (1989) describe a stochastic optimization method for finding Hart's material parameters. In this procedure guesses of the values of each material parameter are repeatedly modified until a good description of the mechanical data is obtained. The

optimization is multidimensional *i.e.* it is carried out over all the material parameters simultaneously. The modification scheme is designed to simulate biological evolution. Random 'mutations' (within prescribed limits) are applied to the parameter vector (*i.e.* the vector which has the material parameters as components). If the resulting (daughter) vector describes the data better, the previous (parent) vector is released and daughter is used as the parent for the next mutation. This procedure (the asexual heredity stage) is continued until the population of 'released' vectors reaches a prescribed size (for Müller and Hartmann this is 10). Subsequently, each daughter vector is generated by randomly selecting her components from the vectors in the population (the sexual heredity stage). Random mutations are also carried out on the daughter. Whenever a daughter provides a superior description of the mechanical data than the worst member of the population, she is retained in the population and the worst member is discarded. In this way the population size is held constant. This process is continued until some prescribed quality limit is attained, until the difference between the best and worst members of the population falls below some prescribed limit, or until the number of generations exceeds some prescribed limit.

Both the method of Huang *et al.* (1977) and that of Müller and Hartmann (1989) require optimizing. As described the method of Huang *et al.* ignores the expected dependence of  $M$  on  $T$ , and therefore although the description of the relaxation curves is very good (figure 3.2e), the physical interpretation of the evaluated parameters is complicated (§ 11.2.3). Müller and Hartmann applied their method to some experimental data for 25CrMo4-steel and found it to be efficient. However, the quality of their fits is rather poorer than that achieved by the more usual methods, although again this may reflect the fact that they ignored the dependence of  $M$  on  $T$  and of  $\dot{\alpha}^*$  on  $\sigma^*$ .